Connecting core-collapse supernova remnants and their central neutron stars

An X-ray study using Chandra and SRG/eROSITA

Martin Georg Friedrich Mayer

SIGILL. UNIVERSITAT. LUDOVIC. MAXIM.

München 2023

Connecting core-collapse supernova remnants and their central neutron stars

An X-ray study using Chandra and SRG/eROSITA

Martin Georg Friedrich Mayer

Dissertation
der Fakultät für Physik
der Ludwig-Maximilians-Universität
München

vorgelegt von
Martin Georg Friedrich Mayer
aus Burghausen

München, den 27.02.2023

Erstgutachter: Prof. Dr. Werner Becker
Zweitgutachter: Prof. Dr. Bruno Leibundgut
Tag der mündlichen Prüfung: 04.04.2023

Contents

List of Figures

List of Tables

Glossary: acronyms and recurring terms

2TNT double-thermal, single-nonthermal spectral model used for modelling the Vela SNR (`TBabs*(vapec+vapec+powerlaw)`). 154, 157, 159, 161, 167, 179

ACIS Advanced CCD Imaging Spectrometer on board the *Chandra* telescope. 63

apec astrophysical plasma emision code, widely used model for thermal X-ray emission of collisionally ionized gas (Smith et al. 2001). 117, 154

ARF ancillary response file, encoding the energy-dependent effective area of the instrument. 107, 116

CCO central compact object. 4, 20, 37, 59, 105

CIAO *Chandra* interactive analysis of observations, general tool for data reduction and analysis. 39, 64

CIE collisional ionization equlibrium. 26, 120, 122, 154, 227

eRASS eROSITA All-Sky Survey; eRASS:n indicates the nth cumulative survey. 35, 147, 153, 172

eSASS eROSITA science analysis software. 107, 147

GTI good time interval, during which the telescope was detecting photons nominally. 107, 148

HRC High-Resolution Camera on board the *Chandra* telescope. 39, 63

ISM interstellar medium. 1, 12, 140, 173

LSR local standard of rest, the expected motion of an object co-rotating with the Galaxy at the given position. 68

MCMC Markov chain Monte Carlo, a class of methods allowing to sample from a probability distribution using random numbers. 156, 183, 222

NEI non-equilibrium ionization. 26, 116, 154, 169

NS neutron star. 3, 37, 59, 137

ObsID observation ID. 39, 107, 204

PSF point spread function. 40, 66

PWN pulsar wind nebula. 4, 23, 145, 178, 221

RMF redistribution matrix file, mapping incident photon energy to detected signal, encoding the spectral resolution. 116

Sherpa `CIAO` package for spatial and spectral modelling and fitting. 43, 66

SN supernova. 1, 7, 9

SNR supernova remnant. 1, 59, 105, 145

TBabs Tübingen-Boulder X-ray absorption model (Wilms et al. 2000). 31, 116, 126, 154

TM eROSITA telescope module. 33, 106, 148

TNT single-thermal, single-nonthermal spectral model used for modelling the Vela SNR (`TBabs*(vpshock+powerlaw)`). 154, 159, 161, 166, 227

vpshock model for a plane-parallel shocked plasma with variable abundances, and a uniform distribution of ionization timescales (Borkowski et al. 2001). 116, 126, 154

WCS world coordinate system, in which absolute positions can be described. 40

Xspec X-ray spectral fitting package (Arnaud 1996). 116, 153

Zusammenfassung

Als Kernkollaps-Supernovae (SNe) bezeichnet man die Explosionen massereicher Sterne oberhalb von 8 $M_\odot$. Sie gehören zu den energiereichsten durch Beobachtungen zugänglichen Phänomenen im Universum. Die Wechselwirkung der während der Explosion freigesetzten Ejecta mit dem umgebenden interstellaren Medium (ISM) führt zur Entstehung eines Supernovaüberrests (SNR), in dem Schockwellen sowohl die Ejecta als auch das umgebende ISM auf Temperaturen der Größenordnung 10^7 K erhitzen. Plasmen dieser Temperatur strahlen den Großteil ihrer Energie im Röntgenband ab, weshalb sich dieses ideal für die Charakterisierung von SNRs eignet. Die Röntgenemission kann verwendet werden, um die Temperatur und den Ionisationszustand des heißen Plasmas in einem SNR räumlich aufgelöst zu bestimmen, sowie um die Zusammensetzung der durch die SN freigesetzten Ejecta festzustellen. Damit können Röntgenbeobachtungen von SNRs wertvolle Hinweise auf die Explosionsenergie, die Masse des Vorgängersterns, oder die nukleosynthetischen Produkte der SN liefern.

Man erwartet, dass der Großteil aller Kernkollaps-SNe während der Explosion einen Neutronenstern (NS) produziert. Ein NS ist der von der Explosion zurückgelassene Überrest des kompakten stellaren Kerns, welcher aufgrund supranuklearer Dichten eine neutronenreiche Zusammensetzung aufweist. NSe zeigen für Beobachter eine vielfältige Phänomenologie: Viele NSe werden als rotationsgetriebene Pulsare beobachtet, pulsierende, primär nichtthermische Quellen, die von Radio- bis zu Röntgen- und Gamma-Energien detektierbar sind. Ihre Emission wird durch die Rotation des enormen Magnetfelds des Pulsars um dessen Achse verursacht, was zur Beschleunigung relativistischer geladener Teilchen in dessen Magnetosphäre führt. Diese energetischen, vom Pulsar emittierten Teilchen manifestieren sich oft ebenfalls in diffusen, nichtthermischen Pulsarwind-Nebeln (PWN). Im Gegensatz dazu zeichnen sich die als zentrale kompakte Objekte (CCOs) bezeichneten NSe durch ihre rein thermische Emission und vermeintlich schwachen Magnetfelder aus, sowie durch ihre Assoziation mit jungen SNRs. Gegenwärtig ist nicht sicher, welcher Prozess zu dieser phänomenologischen Separation führt, aber die Akkretion zurückfallenden Materials kurz nach der Explosion wurde als Ursache vorgeschlagen.

Gegenstand der vorliegenden Arbeit ist die Untersuchung der Physik von Kernkollaps-SNRs und ihrer zentralen Neutronensterne, durch die beobachtende Analyse ihrer Röntgenemission, mit Schwerpunkt auf deren physikalische Wechselwirkung und zusammenhängende Entwicklung. Im Einzelnen untersuche ich die Kinematik von SNRs in Relation zu ihren zentralen Neutronensternen durch die astrometrische Analyse von abbildenden *Chandra*-Daten. Ferner wende ich spektrale und bildgebende Techniken auf eROSITA-Daten der SNRs Puppis A und Vela an, um das schockerhitzte ISM und die Ejecta zu charakterisieren, und um die mit dem Vela-Pulsar

assoziierte relativistische Teilchenpopulation aufzudecken.

Eine grundlegende untersuchte Frage ist die der Geschwindigkeitsverteilung von Neutronensternen, insbesondere die von CCOs. Es gilt als sicher, dass NSe hohe Geschwindigkeiten von mehreren $100\,\mathrm{km\,s^{-1}}$ aufweisen, da sie während der Explosion durch den sogenannten “Kick”, den Rückstoß durch einen asymmetrischen Massenauswurf, einen signifikanten Impuls erhalten (Wongwathanarat et al. 2013). Um dieses fast ausschließlich auf Radio-Daten von Pulsaren basierende Bild zu vervollständigen, stelle ich eine Stichprobe aus sieben CCOs zusammen, deren Bewegung mit existierenden Daten messbar ist, um deren Geschwindigkeit in der Himmelsebene zu bestimmen. Dies wird erreicht durch die Analyse mehrerer abbildender Röntgendatensätze des *Chandra*-Teleskops, welche Gesamtzeiträume von 8 bis 19 Jahren umfassen. Um systematische Fehler in der Analyse zu minimieren, werden die einzelnen Beobachtungen sorgfältig mithilfe von *Gaia*-Kalibrationsquellen angeglichen. Ebenfalls wird die komplexe Punktbildfunktion des Teleskops abseits der optischen Achse modelliert. Dies ermöglicht, die Eigenbewegung der untersuchten Objekte mit typischen Messfehlern der Größenordnung $\sim 10\,\mathrm{mas\,yr^{-1}}$ zu bestimmen, was an der Grenze des im Röntgenband erreichbaren Auflösungsvermögens liegt.

Die untersuchten CCOs zeigen keine Hinweise auf eine Kick-Geschwindigkeit größer als der theoretisch erwartete Grenzwert $\sim 1000\,\mathrm{km\,s^{-1}}$. Ebenfalls ist die Bandbreite der beobachteten Geschwindigkeiten ähnlich der von Radio-Pulsaren, für die es eine viel größere Stichprobe gibt. Im Detail finde ich eine projizierte Geschwindigkeit von $(760 \pm 70)\,\mathrm{km\,s^{-1}}$ (einen Abstand von 2 kpc annehmend) für das CCO RX J0822−4300 im SNR Puppis A, wobei dessen Bewegung in Richtung Südwesten mit großer Genauigkeit eingeschränkt wird. Der Umstand, dass der NS im Expansionszentrum des SNRs entstanden sein muss, erlaubt, das Alter von Puppis A zu (4600 ± 700) Jahren abzuschätzen. Dies wird erreicht durch die Kombination von dessen Trajektorie mit optischen Expansionsmessungen des SNRs, was als unabhängige Verifikation des Expansionsalters von (3700 ± 300) Jahren dient (Winkler et al. 1988). Auf ähnliche Weise, nämlich durch Verwendung externer Expansionsmessungen und der ermittelten Obergrenze auf die Bewegung des CCOs, schränke ich das Alter des SNRs RX J1713.7−3946 auf < 1700 Jahre ein. Dies stellt die bislang strikteste Obergrenze auf dessen Alter dar.

Für drei untersuchte SNRs erlauben die Röntgendaten zusätzlich die direkte Messung von deren Expansion. Zwei Objekte (G15.9+0.2 und Kes 79) zeigen marginal signifikante Hinweise auf einheitliche Expansion (2.5σ bzw. 2σ), die in der Zukunft dazu dienen könnte, deren Alter präzise zu messen. Demgegenüber zeichnet sich das dritte Objekt, der SNR G350.1−0.3, durch rasante Expansion mit bis zu $6000\,\mathrm{km\,s^{-1}}$ aus, wie ich mithilfe meiner eigenen Methoden unabhängig von kürzlich veröffentlichten Ergebnissen belege (Borkowski et al. 2020). Das macht dieses Objekt zum drittjüngsten bekannten Kernkollaps-SNR unserer Galaxie, mit einem Alter von höchstens 700 Jahren. Außerdem verstärkt der Umstand, dass das CCO sich relativ langsam bewegt, die extreme intrinsische Asymmetrie dieses außergewöhnlichen SNRs, die wahrscheinlich durch dessen Expansion in ein inhomogenes ISM verursacht wird.

Der zweite wesentliche Abschnitt dieser Arbeit beschreibt die detaillierte bildgebende Spektroskopie der SNRs Puppis A und Vela mithilfe von Röntgendaten des kürzlich gestarteten Teleskops *SRG*/eROSITA (Predehl et al. 2021). Die hohe Effizienz von eROSITA in der Durchmusterung großer Gebiete, sowie dessen verbesserte Spektralauflösung verglichen mit anderen Röntgenobservatorien, machen das Instrument ideal zur Durchführung von Untersuchungen dieser beiden ausgedehnten Objekte. Dank dieser Eigenschaften offenbart meine Bildgebung eine bemerkenswerte Energieabhängigkeit der Morphologie der zwei SNRs, wobei in Puppis A Klumpen reich an Ejecta durch deren Linienemission hervortreten, während in Vela weiche, schalenartige von harter, plerionischer Emission getrennt wird. Um die beiden SNRs quantitativ zu charakterisieren, ist mein wesentliches Analysewerkzeug die ortsaufgelöste Spektroskopie mehrerer Hundert unabhängiger Regionen. Dies erlaubt die Messung der räumlichen Verteilung des heißen Plasmas über die SNRs, sowie die Quantifikation von dessen Temperatur, Ionisationszustand, und Zusammensetzung. Ebenfalls kann eine mögliche nichtthermische Komponente der Emission isoliert werden.

Mithilfe der Ergebnisse dieser Modellierung wird zum ersten Mal die Fortbewegung des Schocks durch den SNR Puppis A rekonstruiert, durch die Bestimmung eines charakteristischen "Schock-Alters" für jedes Spektrum. Dank dieser neuartigen Methode lassen sich Regionen identifizieren, die kürzlich von einer Schockwelle erhitzt wurden, inklusive einiger kompakter Klumpen und Filamente und des "hellen östlichen Knotens", wo die Schockwelle eine dichte molekulare Wolke komprimiert. Ferner erlaubt die Analyse, die Gesamtmenge des geschockten interstellaren Mediums in Puppis A zu bestimmen. Dadurch lässt sich die Explosionsenergie der SN einschränken. Dies zeigt, dass die häufig angenommene Distanz zu Puppis A von 2 kpc recht unwahrscheinlich ist, da sie eine relativ hohe Explosionsenergie von 10^{52} erg implizieren würde.

Schließlich erfasst unsere Beobachtung zum ersten Mal die Verteilung schwerer Elemente über den gesamten SNR, mit dem Ergebnis, dass der Großteil röntgenheller Ejecta sich in einem ausgedehnten Klumpen in dessen Nordosten befindet, was aus zwei Gründen außergewöhnlich erscheint: Erstens ist dieser Ejecta-Klumpen unerwartet reich an Silizium, was in scheinbarem Widerspruch dazu steht, dass Kernkollaps-SNe bevorzugt leichtere Metalle produzieren sollten. Zweitens weicht die Position des Klumpens signifikant ($\sim 60^\circ$) von der theoretischen Erwartung ab, nach der während der Explosion synthetisierte Ejecta in der entgegensetzten Richtung zur Bewegung des Neutronensterns konzentriert sein sollten (Katsuda et al. 2018). Diese Befunde könnten sich eignen, um numerische Modelle von Kernkollaps-SNRs zu überprüfen, sowohl den kinematischen als auch den nukleosynthetischen Aspekt betreffend.

Der Vela SNR ist wesentlich älter als Puppis A mit $\sim 30\,000$ Jahren, und ist einer der ausgedehntesten SNRs am Himmel, mit einem Durchmesser von 8°. Außerdem enthält er kein assoziiertes CCO, sondern den energetischen Vela-Pulsar, welcher sich durch einen hellen PWN (Vela X) manifestiert. Angesichts seiner enormen Größe stellen die eROSITA-Daten von Vela dessen erste vollständige Röntgenabbildung seit der *ROSAT*-Ära dar, wobei sie eine wesentlich höhere Spektralauflösung bieten. Meine Analyse zeigt, dass Röntgenstrahlen von Vela generell recht wenig vom Vordergrund absorbiert werden ($N_{\mathrm{H}} < 10^{21}\,\mathrm{cm}^{-2}$), mit einem deutlichen Nord-Süd-Gradienten. Dieser Gradient scheint antikorreliert mit der räumlichen Verteilung der optischen Extinktion in Richtung Vela, was entweder auf die Zerstörung von Staub innerhalb der SNR-Schale, oder auf eine starke Klumpung des röntgenhellen Materials im Süden hindeuten könnte.

Die thermische Emission lässt sich insgesamt gut durch ein Plasma mit vergleichsweise niedriger Temperatur ($kT \sim 0.19\,\mathrm{keV}$) beschreiben, wobei sich über den SNR verteilt heiße Klumpen finden, die reich an leichten Ejecta-Elementen sind. Interessanterweise sind die relativen Konzentrationen von Neon und Magnesium verglichen mit Sauerstoff überall signifikant höher als erwartet, mit etwa dem Doppelten des solaren Verhältnisses, was im Konflikt mit Nukleosynthese-Modellen zu stehen scheint (Sukhbold et al. 2016). Mögliche Erklärungen hierfür sind entweder physikalische Prozesse, die in den eindimensionalen theoretischen Modellen nicht berücksichtigt werden, oder die unvollständige Detektion der Ejecta im Röntgenband. In diesem Kontext untersucht meine Arbeit ein dem SNR eigenes, "Schrapnell D" genanntes, Merkmal, ein dichter Ejecta-Klumpen, welcher der SNR-Schale voraus ins ISM geschleudert wurde. Unsere Beobachtung trennt deutlich den breiten Bugschock, hinter dem erhitztes ISM weiche Röntgenstrahlung emittiert, vom heißen und extrem Neon- und Magnesium-reichen Material an der Spitze des Schrapnells. Die vergleichsweise hohe Temperatur des dichten Ejecta-Klumpens könnte auf dessen zusätzliche Erhitzung während Bewegung nach außen hindeuten, da rein hydrodynamische Simulationen eine im Vergleich zur Umgebung niedrigere Temperatur vorhersagen.

Zuletzt wird in den eROSITA-Daten zum ersten Mal das volle Ausmaß der mit dem PWN assoziierten, nichtthermischen Synchrotronkomponente deutlich. Es zeigt sich ein weit ausgedehntes, radial abfallendes Helligkeitsprofil, das bis zu 3° vom Pulsar detektierbar ist, und eine integrierte Leuchtkraft von 1.5×10^{-3} des momentanen Rotationsenergieverlusts des Pulsars aufweist. Die Größe des Röntgen-PWN entspricht einem physikalischen Radius von 14 pc, was die detektierte Struktur wesentlich größer als seine Radio- und Gamma-Gegenstücke macht. Das Profil der in meinen Spektralmodellen gemessenen Photon-Indizes zeigt einen radialen Anstieg, in Übereinstimmung mit der erwarteten Versteilerung des Spektrums durch Energieverluste an Synchrotron-Emission und inverse Compton-Streuung. Diese ausgedehnte Struktur wird als die Signatur hochenergetischer Elektronen interpretiert, die aus dem Kern des PWN entwichen sind, und deren Transport durch relativ langsame Diffusion reguliert wird, ähnlich wie bei einigen Pulsar-Halos beobachtet (Abeysekara et al. 2017). Dies zeigt, dass Vela X, trotz seines vergleichsweise jungen Alters, möglicherweise verwandt mit der Klasse der TeV-Gammastrahlen-Halos ist, die kürzlich um einige ältere Pulsare, wie Geminga, detektiert wurden. Allerdings ist ein fehlendes "Puzzleteil" in diesem Szenario die Existenz eines Gamma-Gegenstücks zur ausgedehnten Röntgen-Struktur, welches durch inverse Compton-Streuung der energetischen Elektronenpopulation sichtbar werden sollte, aber bisher nicht in TeV-Beobachtungen gefunden wurde.

Diese Arbeit schließt mit einer Diskussion der grundlegenden Herausforderungen und Probleme, mit denen die Analysen konfrontiert sind, und zeigt auf, wie diese in der Zukunft behoben werden könnten. Zum Beispiel ließen sich die Unsicherheiten vieler präsentierter Geschwindigkeitsmessungen innerhalb dieses Jahrzehnts mit mäßig aufwändigen *Chandra*-Beobachtungen mehr als halbieren, alternativ dazu mit einer potentiellen Nachfolgemission. Ebenfalls könnte die Spektroskopie linienreicher thermischer Plasmen in naher Zukunft revolutioniert werden, da die Verwendung von Mikrokalorimeter-Detektoren in der Röntgenastronomie die verfügbare spektrale Auflösung im Vergleich zu CCD-Detektoren stark verbessern wird. Um hingegen die Parameter der hier entdeckten Synchrotronemission des Vela PWN genauer zu bestimmen, wären Instrumente mit besserer Empfindlichkeit für harte Röntgenstrahlen, oder mit Sensitivität auf dessen Polarisation, entscheidend. Zusätzlich könnten zukünftige Beobachtungen der assoziierten Gammastrahlung mit höherer Sensitivität für ausgedehnte Emission entscheidend dazu beitragen, einen der größten jemals detektierten Röntgen-PWN genauer zu charakterisieren.

Abstract

Core-collapse supernovae (SNe) are the violent explosions of massive stars above 8 $M_\odot$, which are among the most energetic observationally accessible phenomena in the universe. The interaction of the expanding ejecta released during the explosion and the surrounding interstellar medium (ISM) leads to the formation of a supernova remnant (SNR), in which shock waves heat both the ejecta and the surrounding ISM to temperatures on the order of 10^7 K. Plasmas of this temperature radiate most of their energy in the X-ray band, which makes X-rays ideally suited for the characterization of SNRs. The X-ray emission can be used to measure the quantity, temperature, and ionization state of the hot plasma in an SNR in a spatially resolved manner, as well as to characterize the composition of the ejecta produced during the SN. Thus, X-ray observations of SNRs may provide valuable constraints on explosion energy, progenitor mass or nucleosynthetic products of the SN.

The majority of core-collapse SNe is thought to produce a neutron star (NS) during the explosion. A NS is the remnant of the compact stellar core left behind by the explosion, in which supranuclear densities induce a neutron-rich composition. Observationally, NSs exhibit a diverse phenomenology: many are visible as rotation-powered pulsars, pulsating, primarily nonthermal sources detectable from radio up to X-ray and gamma-ray energies. Their emission is caused by the misaligned rotation of the pulsar's strong magnetic field around the spin axis, which leads to the acceleration of relativistic charged particles in its magnetosphere. These energetic particles emitted by the pulsar often manifest themselves in diffuse, nonthermally radiating pulsar wind nebulae (PWNe). In contrast, NSs known as central compact objects (CCOs) are observed as purely thermal emitters with weak magnetic fields, which intriguingly are found to be associated to particularly young SNRs. It is unclear which process drives this separation in the observed phenomenology, but the accretion of fallback material shortly after the explosion has been suggested to play a role.

This thesis investigates the physics of core-collapse SNRs and their central NSs from an observational point of view using their X-ray emission, with special emphasis on the physical interaction and evolutionary connection between the two. In particular, I investigate the kinematics of SNRs in relation to their central NSs through astrometric analysis of *Chandra* imaging data. Furthermore, I apply spectro-imaging techniques to eROSITA data of the SNRs Puppis A and Vela to characterize the shock-heated ISM and ejecta, as well as to reveal the relativistic particle population associated to the Vela pulsar.

A fundamental question I tackle is that of the velocity distribution of NSs, in particular that of CCOs. It is well known that NSs are high-velocity objects, at speeds of several 100 km s^{-1},

as they receive a significant amount of momentum during the "kick", that is, the recoil induced by the anisotropic ejection of mass during the explosion (Wongwathanarat et al. 2013). In order to complement the observational picture, which is almost entirely based on radio observations of pulsars, a sample of seven CCOs whose proper motions are directly measurable with available X-ray data is compiled, to constrain their projected velocities in the celestial plane. These measurements are performed via the analysis of multiple X-ray imaging data sets from the *Chandra* X-ray Observatory, spanning baselines between 8 and 19 years. In order to avoid systematic biases in this analysis, special care is taken in the astrometric alignment of the individual observations using *Gaia* calibrator sources, and in modelling the telescope's complex point spread function off the optical axis. This allows extracting proper motion constraints with typical uncertainties on the order of $\sim 10\,\mathrm{mas\,yr^{-1}}$, which is close to the limit of achievable resolution in the X-ray band.

No evidence is found in any of the investigated CCOs for a kick velocity beyond the theoretically expected limit $\sim 1000\,\mathrm{km\,s^{-1}}$. Further, the spread in observed velocities is similar to that seen for radio pulsars, for which a much larger sample size is available. Specifically, a projected velocity of $(760 \pm 70)\,\mathrm{km\,s^{-1}}$ (assuming a distance of 2 kpc) is measured for the CCO RX J0822−4300 in the SNR Puppis A, with tight constraints on its direction of motion toward the southwest. The fact that the NS must have been born at the SNR's center of expansion allows estimating an age of (4600 ± 700) yr for Puppis A, via the combination of the NS's trajectory with optical expansion measurements. This serves as an independent verification of the expansion age of (3700 ± 300) yr (Winkler et al. 1988). In a similar manner, I use external X-ray expansion measurements of the nonthermal SNR RX J1713.7−3946 and the measured upper limit on its CCO's proper motion, to derive the most constraining upper limit on its age thus far, at < 1700 yr.

For three of the host SNRs, the available X-ray data sets allow searching for direct signatures of expansion. Two objects (G15.9+0.2 and Kes 79) show marginal evidence for uniform expansion (2.5σ and 2σ), which, if confirmed, may help accurately constrain their ages in the future. In contrast, the third object, SNR G350.1−0.3, exhibits rapid and highly significant expansion at up to $6000\,\mathrm{km\,s^{-1}}$, which confirms recently published results (Borkowski et al. 2020), using an independent methodology. This makes the object the third youngest known core-collapse SNR in the Milky Way, with an age of at most 700 yr. Further, the fact that its CCO is moving relatively slowly reinforces this peculiar SNR's extreme intrinsic asymmetry observed at multiple wavelengths, which is likely caused by its expansion into an ISM density gradient.

The second major effort presented in this thesis consists in detailed imaging spectroscopy of the Puppis A and Vela SNRs, using X-ray data from the recently launched *SRG*/eROSITA telescope (Predehl et al. 2021). The enormous survey efficiency of eROSITA, and improved spectral resolution compared to other X-ray observatories, make the instrument ideally suited for performing sensitive X-ray studies of these two extended objects. Thanks to these capabilities, a remarkable energy dependence in their morphologies is found through narrowband imaging alone, which reveals ejecta-rich clumps in Puppis A through their line emission, and separates soft shell-like and hard plerionic contributions to the emission of Vela. In order to characterize the two SNRs more quantitatively, I perform spatially resolved spectroscopy of several hundred independent regions, using physically motivated models for the instrumental and astrophysical backgrounds, collisionally ionized shocked plasma and/or synchrotron emission of relativistic electrons. This allows measuring the spatial distribution of thermally emitting plasma across the SNRs, quantifying its temperature, ionization state, and composition, as well as isolating the contribution from nonthermal emission in the Vela SNR.

In Puppis A, the models are used to reconstruct for the first time the history of shock propagation through the SNR, by estimating a characteristic "shock age" in each region. This newly derived method identifies regions which have interacted with the forward or reverse shock recently, including several ejecta-rich clumps and filaments, and the "bright eastern knot", where the blast wave is crushing a dense clump in a molecular cloud. Furthermore, my analysis allows weighing the total amount of shocked ISM in Puppis A, and thereby estimating the explosion energy of its SN. This indicates that the commonly assumed distance of 2 kpc to Puppis A is in fact rather unlikely, as it would imply a quite large explosion energy above 10^{52} erg.

Finally, a census of elemental abundances throughout the entire SNR reveals that the majority of X-ray-bright ejecta appears to be concentrated in a single extended clump in the northeast, which seems peculiar for two reasons: first, this ejecta clump appears unexpectedly rich in silicon, in apparent contradiction to the expectation for core-collapse SNe to produce mostly lighter metals. Second, the location of this clump with respect to the SNR center deviates quite significantly ($\sim 60^\circ$) from the expectation that explosively synthesized ejecta should be concentrated in the direction opposite the NS recoil (Katsuda et al. 2018). These findings, if not caused by observational biases, may prove useful for testing numerical models of core-collapse SNe, concerning both the kinematic and nucleosynthetic aspect.

The Vela SNR is several times older than Puppis A, at $\sim$ 30 kyr, and is one of the most extended SNRs on the sky, at a diameter of 8°. Further, it does not contain an associated CCO, but the energetic rotation-powered Vela pulsar, which powers a bright PWN (Vela X). In view of its large size, our eROSITA data set of Vela constitutes the first complete X-ray view of the entire SNR since the *ROSAT* era, while providing a much higher spectral resolving power than the latter. My work shows that X-rays from Vela generally experience little foreground absorption ($N_\mathrm{H} < 10^{21}\,\mathrm{cm}^{-2}$), with a clearly visible north-south gradient. This gradient appears anticorrelated with the spatial distribution of optical extinction toward Vela, which may be a signature of either dust destruction in the SNR shell, or a strong clumping of the X-ray emitting material in the south.

The thermal emission of Vela is overall well describable by a plasma with a comparatively low temperature ($kT \sim 0.19$ keV), but several clumps of hotter material rich in light-element ejecta are revealed throughout the SNR. Intriguingly, the relative concentrations of neon and magnesium with respect to oxygen are quite uniform throughout the SNR, and significantly higher than expected, at around twice the solar ratio. This is in apparent conflict with predictions from nucleosynthetic models (Sukhbold et al. 2016), and may be explained either by physical processes not considered in the one-dimensional theoretical models, or by biases in the observational detection of ejecta in the X-ray band. In this context, one particular feature is investigated, the so-called "shrapnel D", a dense ejecta clump which has been catapulted past the main SNR shell into the ISM. Our data set clearly separates the hot, extremely ejecta-rich material at the apex of the feature, from the wide bow-shock associated to cooler, shocked ISM. The comparatively high temperature of the dense ejecta clump may point toward additional heating experienced during its outward propagation, since purely hydrodynamical simulations predict it to remain colder than its surroundings.

Finally, the eROSITA data set for the first time reveals the full size of the nonthermal X-ray synchrotron component associated to Vela X. It exhibits an extremely extended, smoothly declining radial brightness profile, detectable up to 3° from the pulsar, with an integrated luminosity corresponding to 1.5×10^{-3} of the pulsar's current rotational energy loss. The size of this X-ray PWN corresponds to a characteristic physical radius of 14 pc, making the detected structure significantly larger than its radio and gamma-ray counterparts. The measured nonthermal photon indices in my spectral models exhibit an increase out to larger radii, consistent with the expectation for spectral steepening caused by electron energy losses to synchrotron and inverse Compton emission. The extended structure is interpreted as the signature of high-energy electrons that have escaped from the inner part of the PWN, and whose transport is regulated by relatively slow diffusion, at a similar rate as seen for several pulsar halos (Abeysekara et al. 2017). This shows that Vela X, despite its rather low age, may be related to the class of TeV gamma-ray halos which have recently been detected around much older pulsars, such as Geminga. However, a missing "puzzle piece" in this scenario is the existence of a gamma-ray counterpart to the extended X-ray structure, which should be visible through inverse Compton emission of the energetic electron population, but has so far eluded detection at TeV energies.

This thesis concludes by describing fundamental challenges and issues faced by the presented work, and laying out how these may be resolved in the future. For instance, I show that the statistical and systematic uncertainties of many proper motion measurements carried out here could be reduced by a factor > 2 within this decade, through reasonably expensive observations with *Chandra* or a potential successor mission. Concerning the spectroscopy of thermal plasma, the limitations in the analysis of line-rich X-ray spectra of diffuse sources may be overcome through the usage of microcalorimeter detectors in X-ray astronomy, which will greatly improve the available spectral resolution, compared to CCD detectors. Finally, present-day or future X-ray instrumentation with better response to hard X-rays than eROSITA, or with sensitivity to X-ray polarization, would be crucial for improving the constraints on the synchrotron emission of the Vela PWN. Additionally, gamma-ray observations with higher sensitivity to degree-scale emission than currently available would be essential for confirming and further characterizing the structure of Vela X, one of the largest X-ray PWNe ever detected.

Chapter 1

Introduction

1.1 Context

Few events in the cosmos are as spectacular, for the public interest and astronomers alike, as stellar explosions, commonly referred to as supernovae (SNe). SNe occur either due to the core-collapse of massive stars ($> 8\,M_\odot$), or due to thermonuclear runaway burning of a white dwarf in a binary system. Due to the extreme amounts of energy released during these cataclysmic events ($\sim 10^{51}$ erg), they can briefly outshine entire galaxies, making them visible with telescopes billions of light years away.

Thanks to their enormous brightness, historically, SNe were observed as "guest stars" long before the invention of telescopes (e.g., Green & Stephenson 2003; Stephenson & Green 2009). The most prominent historical SNe, such as the ones studied by Tycho Brahe (SN 1572) and Johannes Kepler (SN 1604), were often bright enough to be seen during the day, even though their origin was not understood yet. It was not until 1931, that the term "supernova" was coined by Walter Baade and Fritz Zwicky (1934a; 1934b), in order to distinguish the phenomenon from normal "novae", which obtained their Latin name due to their appearance as "new stars". Unfortunately, in the last 400 years, no Galactic SN has been directly observed, so that our direct observations of the phenomenon are entirely based on extragalactic SNe. However, in the year 1987, a stellar explosion (SN1987A) occurred in the Large Magellanic Cloud, a Milky Way satellite. Thanks to its relative proximity, this SN has been observable in great detail for the last 35 years (e.g. McCray & Fransson 2016). This continued observational effort has shown its spectacular temporal evolution, as SN1987A gradually started to interact with its environment, revealing a complicated circumstellar morphology with multiple rings of dense material.

As the example of SN1987A shows, SNe do not cease to impact their surroundings after the optical light from the explosion fades. Instead, the expansion into the interstellar medium (ISM) of ejecta released during the explosion leads to the emergence of supersonic shock waves, whose interaction with the ISM produces a supernova remnant (SNR). The expanding SNR enriches and heats up the ISM to millions of degrees, and accelerates particles to relativistic energies at the shock front. The complex morphologies of SNRs are observable for around one hundred thousand years, especially through thermal X-ray emission from shock-heated gas, and synchrotron

Figure 1.1: Examples of the diverse SNR morphologies visible through X-ray eyes with the *Chandra* telescope. The *left* panel shows the shell-type SNR Cas A, with different colors (red, yellow, green, purple) reflecting different ejecta elements (Si, S, Ca, Fe), and the blue band tracing synchrotron emission behind fast shocks. The SNR's quiescent central compact object can be seen as a "white" point source close to the geometric SNR center. The *right* panel shows the pulsar wind nebula of the extremely energetic Crab pulsar. Red and blue colors indicate soft and hard X-ray emission, respectively. The pulsar itself is seen as a point-like source, surrounded by a complicated morphology of tori and jets. Image credit: NASA/CXC/SAO

emission of accelerated electrons in the radio band (Frail et al. 1994). Hence, not only do SNRs tend to produce beautiful images in X-rays, optical, or radio (see Fig. 1.1), but they are also fascinating from an astrophysical point of view, as a plethora of physical processes contributes to their formation, evolution, and emitted radiation. Thus, despite the scarcity of nearby SNe, their explosion mechanism and environmental impact can be studied indirectly through the observation of Galactic SNRs.

For instance, taking advantage of their characteristic thermal line emission in the X-ray regime, typical ejecta elements in SNRs can be identified, located, and quantified. The ejecta composition may allow for inferring the SN type and mass of the progenitor star, and constraining the nucleosynthetic processes during the explosion (e.g., Hwang & Laming 2012). The location of heavy-element ejecta or shocked X-ray emitting gas may also serve as an indicator of asymmetries, whether they are intrinsic to the explosion (e.g., Katsuda et al. 2018), or extrinsic (i.e., caused by ISM inhomogeneities). Further, in the case of exploding massive stars, the shock wave is expected to sweep up a significant amount of material released by the progenitor during its final years, such that its pre-SN evolution can be reconstructed from the density and composition of shocked circumstellar material in young SNRs (e.g., Lundqvist & Fransson 1996). Similarly, a more evolved SNR will have swept up a large amount of ISM, so that the

X-ray emitting material can be used to trace the typical ISM density and composition at its location. Finally, much of the microphysics of the collisionless shocks typical for SNRs is still quite uncertain. For instance, it is unclear to what degree individual particle species are thermally equilibrated immediately behind the shock, which may be investigated via high-resolution X-ray observations of thermally emitting SNR blast waves (e.g., Rakowski et al. 2003). In contrast, it is quite certain that the shocks of SNRs are excellent particle accelerators (see Cas A in Fig. 1.1), provided the shock velocity is high enough (Reynolds 2008), and likely contribute a significant fraction of the local cosmic ray budget. It is nonetheless uncertain whether SNRs are PeVatrons, meaning whether they are capable of accelerating particles to the highest energies observed for Galactic cosmic rays (Vink 2022). This question may be investigated via the nonthermal X-rays and gamma-rays emitted by their shock fronts, to infer the maximum energies of the particle population (e.g., Tsuji et al. 2021; Ahnen et al. 2017).

These themes are not only relevant for the investigation of SNe or SNRs individually, but tie in with the topic of galaxy evolution as a whole. On one hand, SNe are one of the main sources of metals in the ISM, in particular from oxygen to the iron group (Iwamoto et al. 1999; Woosley & Weaver 1995), and thereby impact their host galaxy's metallicity evolution and hence the formation and evolution of future generations of stars. On the other hand, ISM heating and cosmic ray injection by SNRs are relevant for the total galactic energy budget. For instance, SNR shock waves are suspected to be capable of triggering cloud collapse to form new stars (Herbst & Assousa 1977), whereas, at the same time, they likely contribute to the quenching of star formation by removing cold gas from low-mass galaxies (supernova feedback, Hopkins et al. 2012). Furthermore, SNe have a complex impact on the galactic dust budget, as they are thought to both produce dust in their ejecta (e.g., Rho et al. 2009), and destroy ISM dust particles in their shock waves (e.g., Arendt et al. 2010). In addition to the uncertainties in the individual processes described above, a final relevant question for galaxy evolution is that of the global SN rate of a galaxy. Counting the number of known Milky Way SNRs, one arrives at around 300 objects (Green 2019; Ferrand & Safi-Harb 2012), whereas a Galactic SN rate of three per century (Li et al. 2011b,a) and a radio-observable SNR lifetime of > 60 kyr (Frail et al. 1994) would predict almost 2000 Galactic SNRs. This discrepancy is likely caused by the selection effects against small or faint SNRs in past radio surveys (see Becker et al. 2021), implying that Galactic SNR searches in sensitive radio, X-ray or optical observations harbor a large discovery potential.

It is well known that the death of a massive star in a core-collapse SN often leaves behind a neutron star (NS), which is the compact neutron-rich remnant of the stellar core, characterized by extreme densities, temperatures, and magnetic fields. The idea of a NS being formed in a stellar explosion can once again be traced back to Baade and Zwicky (1934c), whereas the first investigations of their possible structure were conducted by Oppenheimer & Volkoff (1939). The observational discovery of the first isolated NS did not occur until 30 years later, when Jocelyn Bell-Burnell and Anthony Hewish (1968) observed a regularly pulsating Galactic radio source. It was soon suggested (e.g., Pacini 1967; Gold 1968) that the origin of this pulsed radio emission could be a rapidly rotating magnetized NS, which we nowadays refer to as a (rotation-powered) pulsar.

Pulsars are still by far the most commonly detected type of NS, with around 3000 objects currently known (Manchester et al. 2005). They are characterized by nonthermal radiation visible in the radio, and often X-ray and gamma-ray bands, and are detectable for millions to billions of years. Their high-energy particle wind frequently powers surrounding diffuse emission, visible as bow shocks or pulsar wind nebulae (PWNe), such as the Crab nebula shown in Fig. 1.1. However, the "neutron star zoo" (Harding 2013) exhibits several further exotic species, including magnetars, the most strongly magnetized NSs at up to 10^{15} G, or central compact objects (CCOs, De Luca 2017), purely thermal X-ray emitters within young SNRs, which appear to be weakly magnetized (visible in Cas A in Fig. 1.1).

NSs are of interest for astrophysicists and fundamental physicists alike: firstly, PWNe are excellent accelerators of leptonic cosmic rays (Gaensler & Slane 2006), and may be the dominant local source thereof (Vink 2022). The maximum energy of accelerated particles and the efficiency of particle transport in PWNe can be characterized through observations in the X-ray or gamma-ray bands (e.g., H. E. S. S. Collaboration et al. 2019; Abeysekara et al. 2017). Furthermore, the interior composition of NSs probes a regime of the nuclear force which is inaccessible in terrestrial laboratories, resulting in their equation of state, which relates pressure and density, being unknown. This equation of state can be probed by measuring NS masses and radii, for instance in binary systems (Abbott et al. 2017; Kramer et al. 2021; Clark et al. 2023b), through spectral modelling (Doroshenko et al. 2022), or by constraining their cooling mechanisms through their surface X-ray radiation (Page 2009). Finally, it is currently not understood why NSs appear in so many different observational flavors, showing thermally or nonthermally dominated emission, which may be pulsed, bursting, or even quiescent. The characterization of large samples of the different NS types may thus contribute to finding a "unified theory" of NSs (Enoto et al. 2019).

1.2 Questions addressed in this thesis

In practice, oftentimes, NSs and SNRs are studied separately, as pulsars usually outlive their SNRs, not all SNRs contain a NS, and the two objects are traditionally detected via different channels (timing and imaging). However, much synergy lies in the joint investigation of core-collapse SNRs and their central NSs, as they are inherently connected in their formation and evolution for $\sim 10^5$ yr. With this cumulative dissertation, I aim to provide new insights into the physics of core-collapse SNRs and their central NSs based on the detailed analysis of X-ray observations of individual systems, exploiting in particular the connection between the two at different stages. Chapter 2 gives an overview of the physics and phenomenology of SNe, SNRs, and NSs, with an emphasis on their X-ray emission and its detection. I then present the results of four research projects[1], in which several X-ray observations of SNRs and their central NSs by the *Chandra* and *SRG*/eROSITA telescopes were analyzed. Broadly speaking, Chapters 3 and 4 investigate the kinematics of NSs and SNRs via astrometric analysis in the imaging domain, whereas Chapters 5 and 6 characterize the X-ray emission of SNRs through methods of imaging

---

[1] Three of these projects have been published under my first-authorship in refereed journals, with the final first-author paper foreseen for submission in the near future. In Appendix A, papers which I have co-authored are listed, highlighting my respective contributions. As these publications have originated from substantial collaborative effort, I frequently use the pronoun "we" to describe the work carried out in the following chapters.

spectroscopy. Finally, Chapter 7 summarizes and connects the results presented, emphasizing the remaining challenges in the analysis and discussing how these may be resolved in the future. In the following, I give an overview of the main scientific questions which motivate the individual research projects presented in Chapters 3 to 6.

1.2.1 Kinematics of CCOs and core-collapse SNRs

It is well known that the asymmetric ejection of material during a core-collapse SN explosion leads to a substantial transfer of momentum onto the compact object, most likely via gravitational interaction (Wongwathanarat et al. 2013; Janka 2017b). The strength of the resulting "kick" velocities of NSs is relatively well constrained for radio pulsars, with mean physical velocities $\sim 400\,\mathrm{km\,s^{-1}}$ observed for large samples (Hobbs et al. 2005; Verbunt et al. 2017), but little is known for other NS types, including CCOs. The phenomenology of CCOs, which are observed as purely thermal X-rays emitters with weak magnetic fields, is believed to be related to the enhanced accretion of fallback material after the explosion (e.g., Ho 2011). Hence, it is imaginable that the interaction with slow ejecta could be stronger for CCOs than for other NS types. To test whether this might cause a modified kick velocity distribution in CCOs, we investigate the kinematics of a total of seven CCOs, via the measurement of their proper motions, in Chapters 3 and 4.

However, the meaningfulness of such proper motion measurements is not limited to estimating NS velocities. They may also serve as valuable constraints on time and location of the parent SN, since its explosion site must necessarily intersect with the past trajectory of the NS. In combination with a second constraint on the explosion site, for instance from the SNR's expansion, the NS trajectory can thus be used to estimate the absolute age of an SNR in a relatively model-independent manner. This is applied in Chapters 3 and 4, where we combine our measured NS trajectories with (external as well as newly performed) measurements of the expansion of the parent SNRs, yielding competitive age estimates for several objects.

Finally, we can investigate the connection between the intrinsic asymmetry traced by the NS kick and the expansion of its host SNR. On one hand, this is done by comparing our constraints on SNR explosion sites with their present-day X-ray emission, to reveal strong intrinsic asymmetries in their morphology (Chapter 4). On the other hand, we perform a direct comparison between the NS kick direction and the location of heavy-element ejecta in the SNR Puppis A, revealed via spatially resolved spectroscopy (Chapter 5). Thereby, we can test the theoretical expectation that explosively synthesized ejecta, like silicon and iron, should be preferentially expelled in the direction opposite the kick (Wongwathanarat et al. 2013; Katsuda et al. 2018).

1.2.2 Interaction of ejecta, shocks, and ISM

One fundamental advantage of X-ray observations of SNRs is that the thermal emission from hot shocked ISM and ejecta is directly observable, which allows us to perform a census of ejecta clumps in reasonably extended SNRs. Here, such an analysis is performed for the X-ray-bright Puppis A and Vela SNRs in Chapters 5 and 6. In the absence of strong contamination by ISM, we can use spectroscopically measured elemental abundances to infer the approximate composition of the ejecta produced in the explosion. This can then be compared to theoretical predictions from models of core-collapse SN nucleosynthesis (Woosley & Weaver 1995; Rauscher et al. 2002; Sukhbold et al. 2016), both as a test for their reliability, and in order to constrain the type of the progenitor star.

Furthermore, taking advantage of the good statistics and spatial resolution offered by our data set of Puppis A, compact regions which have recently interacted with a shock wave can be isolated via searching for signatures of non-equilibrium ionization (NEI) in spectral modelling (Chapter 5). In this way, the forward shock's propagation history into the ISM can be traced, and signatures of the reverse shock reheating ejecta can be identified in this medium-age SNR. In addition, by carrying out a complete census of the X-ray emitting shocked gas, we are able to weigh the amount of material swept up by the blast wave, and, via comparison with simple evolutionary models, infer the approximate explosion energy of the SN that formed Puppis A. A unique characteristic of the comparatively older Vela SNR is the visibility of prominent "shrapnels" (Aschenbach et al. 1995). These features are visible through X-ray-bright bow shocks, and are thought to be caused by dense ejecta clumps which have propagated past the main shell, and are now protruding into the unperturbed ISM. The data presented in Chapter 6 allow for resolving the energy-dependent morphology of the brightest such shrapnel. This provides an opportunity to investigate the resulting temperature distribution of in an isolated clump supersonically penetrating the ISM, in comparison with theoretical predictions for the shrapnels (Miceli et al. 2013).

Finally, owing to the large sizes of the two SNRs studied in Chapters 5 and 6, the spatial variation in foreground X-ray absorption on degree-scales is probed by our data. This allows us to study the properties of the absorbing material, via comparison with multiwavelength data tracing the emission of dust in the mid-infrared (Arendt et al. 2010) and the dust-induced optical extinction (Anders et al. 2022; Lallement et al. 2019). In particular, we explore the possibilities that a significant amount of X-ray absorption occurs within the SNR itself, and that the interaction of the expanding SNR blast wave with intervening material may lead to an observable effect of dust destruction.

1.2.3 Evolution of PWNe

It is clear that the observational characteristics of PWNe change over their lifetime, as they co-evolve with their host SNRs. Giacinti et al. (2020) presented an evolutionary picture in which a young compact PWN evolves through a stage of interaction with the SNR's reverse shock, which compresses the expanding PWN, and may induce asymmetries in its observed morphology. Eventually, the pulsar is thought to leave the shell of its parent SNR and form a degree-scale gamma-ray halo of energetic electrons diffusing through the ISM, as observed for instance for the middle-aged pulsar Geminga (Abeysekara et al. 2017). The PWN of the Vela pulsar is currently in the intermediate stage, in which strong interaction with the reverse shock has significantly modified its morphology, leading to the appearance of an X-ray "cocoon" (Blondin et al. 2001; Slane et al. 2018). Our X-ray observation of the Vela SNR (Chapter 6) for the first time allows for isolating the nonthermal synchrotron emission associated to the PWN from the SNR's ambient thermal emission on large angular scales. This provides the currently most sensitive view of the distribution of high-energy electrons escaped from the PWN core, with which we can study their diffusion and radiative energy loss.

Chapter 2

Scientific background

In this chapter, I outline the theoretical and observational background behind this thesis, including a brief description of the different supernova types and an overview of the characteristics of their compact and extended remnants. Finally, the main processes giving rise to the X-ray emission of these objects are discussed, along with the instruments used in this thesis for their detection and characterization.

2.1 Supernovae and their classification

Traditionally, SNe are classified observationally based on their optical spectra, with the major division being between type I and type II SNe without and with hydrogen lines, respectively. This classification does however not reflect the physical reality of SN explosion mechanisms which separates between thermonuclear and core-collapse explosions, which I briefly characterize here.

2.1.1 Thermonuclear supernovae

Thermonuclear SNe (or type Ia SNe, according to their spectroscopic classification) are the explosions of white dwarfs via the runaway nuclear burning of their degenerate material. It is generally accepted that the progenitors of thermonuclear explosions are binary systems containing a (carbon-oxygen) white dwarf. The nature of the white dwarf's companion star and of the trigger of the thermonuclear explosion are however heavily debated (see Hoeflich 2017; Maguire 2017).

In the classical "single-degenerate" scenario (illustrated in the left panel of Fig. 2.1), the white dwarf continually accretes matter from a nondegenerate companion star via Roche-lobe overflow, until it has reached a critical mass limit, the Chandrasekhar mass $M_{\mathrm{Ch}} \sim 1.4\,M_{\odot}$. At this point, carbon burning sets in, producing a deflagration flame propagating subsonically through the white dwarf, leading to a rise in temperature. As the pressure in the white dwarf is mainly provided by the Fermi pressure of degenerate electrons, this increase in temperature does not lead to an expansion, but does enhance the reaction rate, ultimately causing a thermonuclear runaway. During this runaway, according to the so-called delayed detonation model (Khokhlov

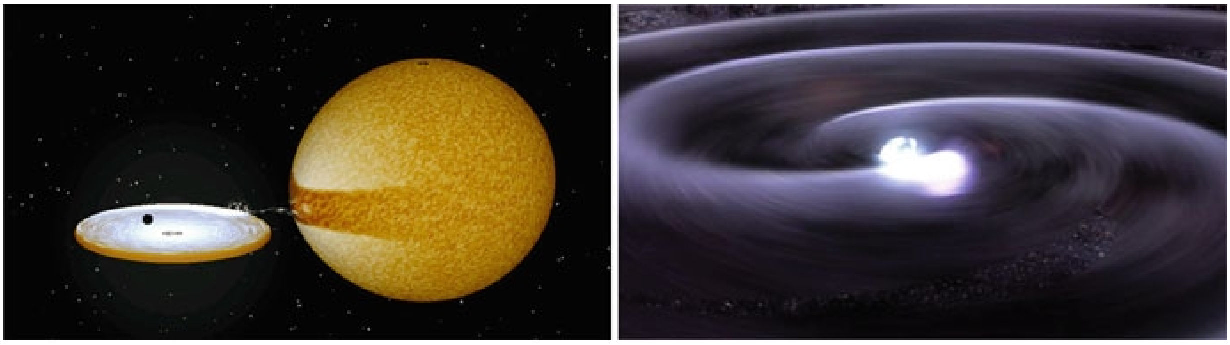

Figure 2.1: Artistic sketches of the single-degenerate (*left*) and double-degenerate (*right*) scenarios of thermonuclear SNe. Image credit: Hoeflich (2017), R. Hines & NASA/GSFC, T. Stromayer

1991), the subsonic deflagration flame is expected to trigger a supersonic detonation, burning a large fraction of the available fuel into iron and nickel, but also producing a considerable amount of intermediate-mass elements (Iwamoto et al. 1999). In contrast, in the "double-degenerate" scenario (right panel in Fig. 2.1), the primary white dwarf merges with a secondary white dwarf, either violently or over timescales of up to $\sim 10^5$ yr (Maguire 2017). This places the white dwarf above the Chandrasekhar limit, triggering the subsequent explosion. Type Ia explosions are expected to unbind the explosively burning matter completely, leaving no compact remnant, and releasing a large amount of ejecta rich in iron-group elements into the ISM (Iwamoto et al. 1999).

The fact that, in many models, all type Ia supernovae are expected to originate from a progenitor of similar mass makes them a popular choice for a cosmological "standard candle", as the peak absolute brightness of different events should be approximately standardizable. Hence, type Ia supernovae have been – and are still being – used to derive fundamental cosmological insights, such as the discovery of the acceleration of the universe's expansion (Riess et al. 1998; Perlmutter et al. 1999).

2.1.2 Core-collapse supernovae

In contrast to lighter stellar objects, massive stars with initial masses $\gtrsim 8\,M_\odot$ are believed to end their lives in core-collapse explosions (spectroscopic types Ib, Ic, II). The routes of differently massive stars through the central density-temperature plane to their death are indicated in Fig. 2.2: during their evolution over millions of years, massive stars pass through several nuclear burning stages, each at a hotter temperature and shorter duration than the previous one. More massive stars are capable of reaching higher core temperatures, and thereby later burning stages.

While stars of initial masses below $8\,M_\odot$ are eventually stabilized by the degeneracy pressure of electrons and end up as white dwarfs, heavier stars are expected to obtain a gravitationally unstable core, characterized by an adiabatic index $\gamma < 4/3$, leading to its subsequent collapse. Stars in the narrow initial mass range $8\,M_\odot \lesssim M_* \lesssim 9\,M_\odot$, develop cores rich in oxygen, neon, and magnesium, but are unable to reach the next burning stages. Eventually, the degenerate electrons in the core reach sufficiently high Fermi energies to be captured on neon and magnesium atoms.

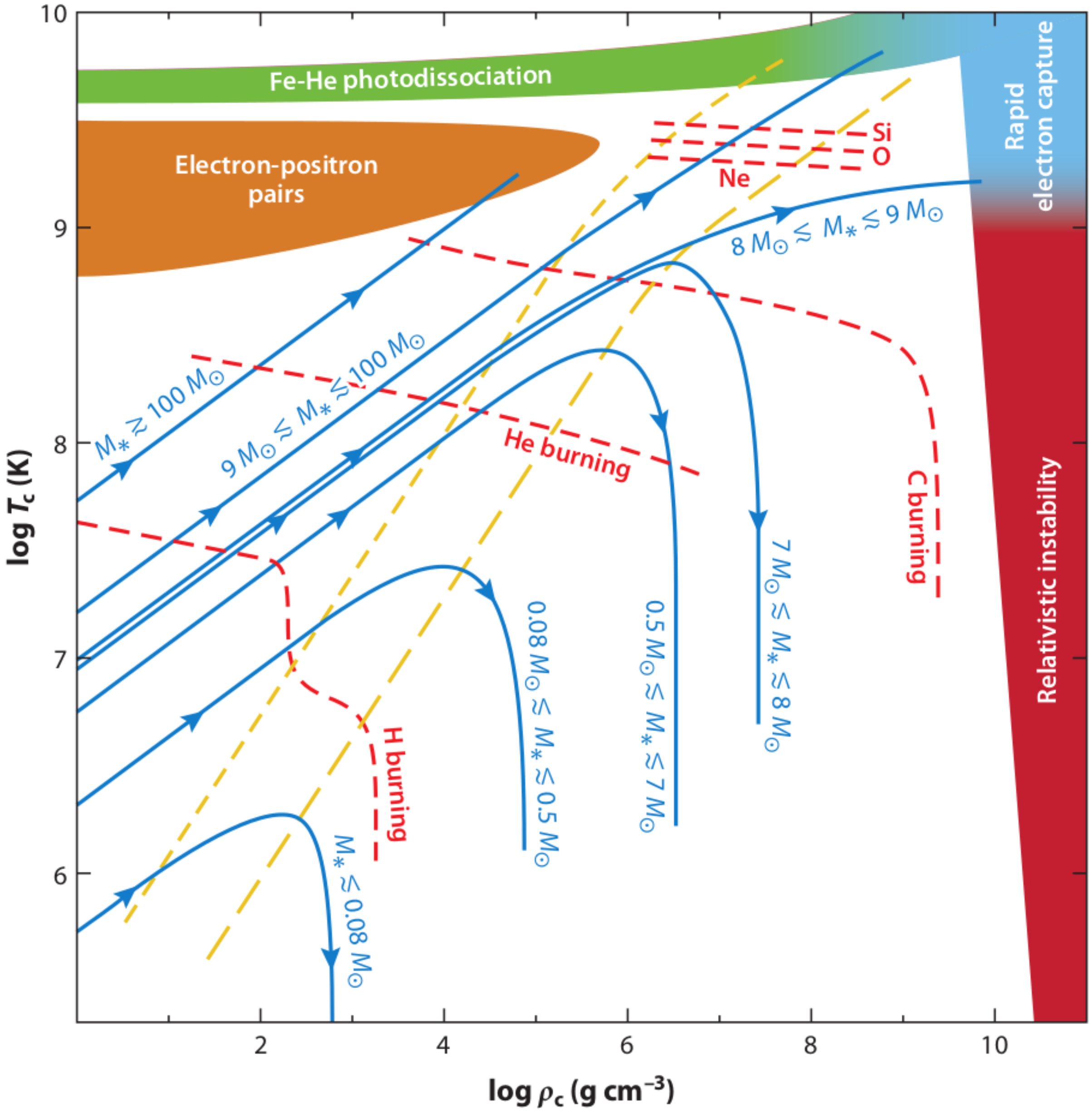

Figure 2.2: Stellar death regions and stellar evolutionary tracks in the plane of central density ρ_c and central temperature T_c for different initial masses M_*. The various nuclear burning stages are indicated in red, and the yellow lines mark the transition of the electron plasma in the core into different regimes of degeneracy. Figure courtesy to Janka (2012).

This process causes the collapse of the core and the star's subsequent explosion in an electron-capture supernova. While the estimated mass range for electron-capture SNe is narrow, the steep nature of the stellar initial mass function implies that a significant fraction of exploding massive stars produce electron-capture SNe, especially in low-metallicity environments (up to

30%, Wanajo et al. 2009; Janka 2012). In contrast to this process, more massive stars reach the hydrostatic neon, oxygen, and silicon burning stages, ultimately forming an iron core. This core eventually becomes so hot and dense that a nuclear statistical equilibrium is established, which allows for the photodissociation of nuclei into α particles. This, in combination with electron capture on free protons and nuclei, reduces the effective adiabatic index, and allows for the core's rapid collapse (Janka 2017a).

The core collapse is halted and reversed once nuclear densities are reached, and the repulsive component of the nuclear force becomes felt, which produces an outward-propagating shock wave. This shock wave is however stalled due to energy losses to the photodissociation of infalling matter. At this point, different mechanisms have been proposed to power the subsequent revival of the shock wave and explosion of the star (see Janka 2012), but the delayed neutrino heating-mechanism seems particularly promising. In this scenario, the enormous density of the infalling matter leads to the trapping of neutrinos radiated from the proto-neutron star, which are produced via electron capture reactions under enormous pressure and density, leaving behind homogeneous neutron-rich nuclear-density matter. On time scales of several 100 ms, the energy deposition by neutrinos becomes large enough to revive the shock wave and cause its outward motion against the infalling matter. Modern simulations of this process show that three-dimensional effects, such as convective flows or standing accretion shock instabilities (see Janka 2017a, and references therein), lead to large-scale nonradial motions of the material at this stage, and amplify the efficiency of neutrino heating. The shock wave propagates outward through the progenitor star on time scales of hours, causing the explosive nucleosynthesis of radioactive elements and ultimately gravitationally unbinding the star.

At its center, the core-collapse explosion leaves behind a compact remnant, in most cases a hot neutron star, which is expected to spin rapidly (periods at most on the order of 0.1 s) due to the nonradial hydrodynamical flows during the explosion (Janka 2012). In addition, anisotropic gravitational forces exerted on the NS by slow ejecta lead to it receiving a strong "kick" in the seconds after the shock revival, via the gravitational "tug-boat" mechanism (Wongwathanarat et al. 2013). This kick manifests itself in large neutron star space velocities of several 100 km s^{-1}, which are measurable as such for millions of years (Hobbs et al. 2005).

There are further, albeit more exotic, SN types originating from massive stars. These include hypernovae, in which the rapid rotation of the stellar core produces collimated ultrarelativistic jets, manifesting themselves in gamma-ray bursts (Janka 2012). These explosions may be linked to the formation of black holes at the center of the collapsing star (MacFadyen & Woosley 1999). Furthermore, in extremely massive stars ($> 100\,M_\odot$), pair instability sets in after carbon burning, meaning that temperature and pressure allow for the formation of electron-positron pairs from thermal photons, decreasing the effective adiabatic index, and leading to stellar implosion. Depending on the progenitor mass, this collapse may either directly form a black hole, or lead to an ignition of the available fuel, and an explosion in a pair-instability SN (Heger et al. 2003).

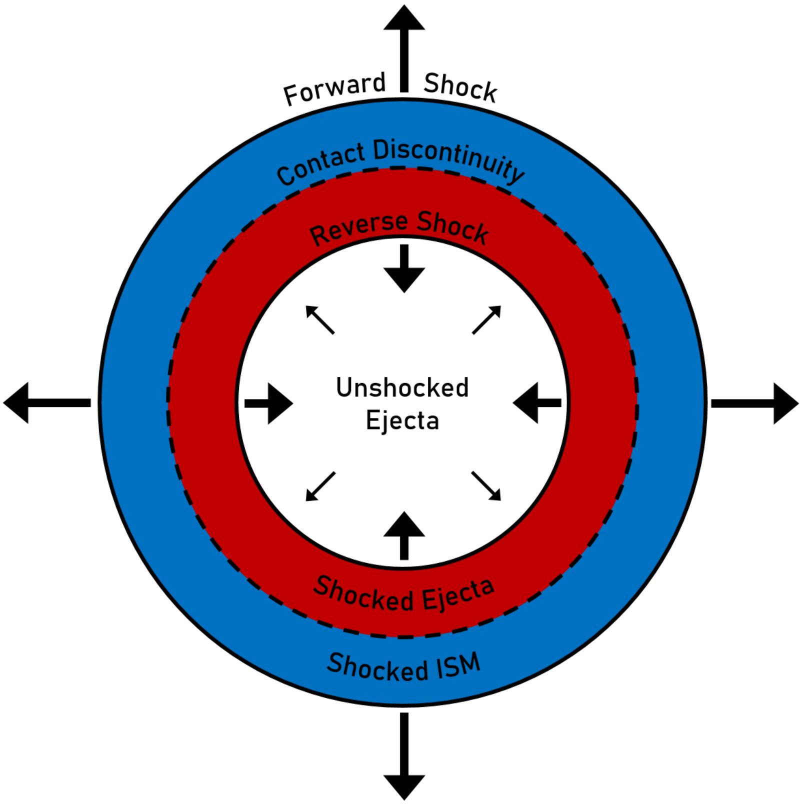

Figure 2.3: Schematic of the shock structure in an idealized SNR (without compact object), inspired by Reynolds (2017).

2.2 Physics of supernova remnants

Although it is difficult to quantify the exact moment at which an SN transforms into a supernova remnant (SNR), a defining property of an SNR is that the observable emission is powered by the interaction between its blast wave and the surrounding medium, rather than the radioactive decay of elements or the heat released during the explosion. Here, I give a compact overview of the evolution, morphological characteristics, and astrophysical impact of SNRs.

2.2.1 Evolutionary stages

In order to broadly characterize the evolution of an SNR, one usually assumes a spherically symmetric model (sketched in Fig. 2.3), in which the explosion releases an amount of kinetic energy on the order of $E \sim 10^{51}$ erg, in the form of rapidly expanding ejecta. The time-dependent SNR size is characterized by the radius of its forward shock R_{FS}, which expands over time into an ISM of density ρ, which is often assumed to be uniform but may also be radially decreasing. The forward shock is usually assumed to be in the non-relativistic strong-shock regime, implying a compression of the shocked material by a factor of 4. The ejecta of total mass M_{ej} are assumed to be expanding behind the forward shock and are often characterized by a steeply decreasing radial density profile. The deceleration of the freely expanding ejecta leads to the formation of a reverse shock with radius $R_{\rm RS}$, moving backward in the frame of the ejecta. Shocked ISM and reverse-shocked ejecta are separated by a contact discontinuity in this idealized case.

One can broadly divide the idealized evolution of an SNR into four qualitatively distinct regimes:

- **Ejecta-dominated stage:** As long as the swept-up ISM mass is much smaller than the ejecta mass, $4\pi/3\,\rho R_{\rm FS}^3 \ll M_{\rm ej}$, the ejecta expand relatively freely, at velocities on the order of $5000\,{\rm km\,s^{-1}}$ and $10000\,{\rm km\,s^{-1}}$, for core-collapse and type Ia SNRs, respectively (Reynolds 2017). During this initial free expansion, the ejecta cool adiabatically, only to be reheated once they are struck by the reverse shock. At this stage, the forward shock expansion behavior depends on the density structure of both the ejecta and surrounding ISM, and usually follows a self-similar behavior of type $R_{\rm FS} \propto t^m$, dependent on the expansion parameter m. Observational constraints on the value of m during this initial stage imply values of $m \sim 0.8$ in SN 1993J (Marcaide et al. 2009), several thousand days after its explosion, and $m \sim 0.65$ in the 350-year-old SNR Cas A (Patnaude & Fesen 2009).

- **Sedov-Taylor stage:** Once the swept-up ISM mass becomes dominant over the available ejecta mass, $4\pi/3\,\rho R_{\rm FS}^3 \gg M_{\rm ej}$, the majority of the explosion energy is no longer contained in the unshocked ejecta, but in the kinetic energy of the adiabatically expanding shell (Vink 2020). Both density and pressure inside the SNR show a sharp outward rise and are maximal at the location of the forward shock (Cox & Anderson 1982). In the idealized case of a point explosion in a uniform medium, the evolution of the forward shock radius with time t can be described exactly using the self-similar Sedov-Taylor solution (Sedov 1959; Truelove & McKee 1999):

  $$R_{\rm FS} = 1.15\left(\frac{Et^2}{\rho}\right)^{1/5}. \tag{2.1}$$

  While highly idealized, the fact that this phase lasts for many thousand years makes the Sedov-Taylor formula approximately applicable and highly useful for many moderately evolved SNRs, as it allows for crude estimates of their ages, ISM densities, or explosion energies. In practice, the transition between the first two evolutionary phases is of course not abrupt but smooth, and the shock radii can be described by the generalized (but not self-similar) solutions developed by Truelove & McKee (1999), which depend on the density profile of both ejecta and ISM.

- **Radiative stage:** After tens of thousands of years, once the forward shock has decelerated to a speed on the order of $\dot{R}_{\rm FS} \sim 200\,{\rm km\,s^{-1}}$ (Reynolds 2017), energy losses from radiative cooling become relevant to the total energy budget. This cooling occurs mostly via line emission from metals around optical wavelengths, and is expected to lead to the formation of a cool and dense SNR shell. The Conservation of momentum of the blast wave implies an expansion with $R_{\rm FS} \propto t^{1/4}$. At this point, the assumption of a spherically symmetric structure is most likely quite unrealistic, as a realistic SNR would probably exhibit a strongly fragmented structure at this point (see SNR Simeis 147 in Drew et al. 2005, for an example), even when expanding into a roughly uniform medium. In the radiative phase, SNRs are expected to be visible at optical and radio wavelengths mostly, since low temperatures and shock velocities imply weak X-ray emission.

- **Merging stage:** Once the shock wave velocity becomes comparable to the local ISM sound speed, the shock fronts will dissipate, as the swept-up material mixes subsonically with the local ISM. At this point, while a bubble of heated material may be left behind, the SNR will no longer be recognizable as such.

2.2.2 Morphological properties

Ideally, the classification of SNRs by their progenitor type would be desirable. However, in the absence of an associated compact object or other clues on the explosion type (e.g., Galactic location or light-echo spectra), performing this distinction in practice often requires detailed knowledge of the X-ray spectrum. The spectrum may reveal signatures of elements typical for type Ia or core-collapse SNe (Hughes et al. 1995), or the characteristic location of the centroid of iron K-shell line emission (Yamaguchi et al. 2014). Since X-ray images, let alone spectra, are not always available in practice, SNRs have traditionally been classified based on their imaging morphology. This scheme divides SNRs into the following types (see also Vink 2020), illustrated with prototypical examples in Fig. 2.4:

- **Shell-type SNRs** may well be described as the "traditional" class of SNRs, characterized by an edge-brightened ring-like morphology. If an SNR appears shell-like in X-rays, meaning its emission is concentrated on the region behind the forward shock, an association with the Sedov-Taylor or radiative evolutionary stages appears likely.

- **Plerionic SNRs:** Frequently termed "center-filled" SNRs, plerions do not correspond to SNRs in the traditional sense. Instead, the centrally bright morphological structure usually corresponds to synchrotron emission from a pulsar wind nebula produced by a core-collapse SN (see Sect. 2.3.2).

- **Composite SNRs** can be described as a combination of the above two types, with signatures of shell-type diffuse emission and a central plerion visible at the same wavelength.

- **Mixed-morphology SNRs** show signatures of a synchrotron-dominated shell in the radio band, but exhibit a filled center in X-rays. In contrast to the composite type, the nature of the center-filled X-ray emission is thermal (Rho & Petre 1998) and frequently appears to originate from ejecta material. This justifies grouping mixed-morphology objects into a separate class of SNRs, which are typically relatively old (see Chapter 10 in Vink 2020, for a recent overview).

Naturally, SNRs are not always clearly classifiable into a single one of these categories, or may show features which do not fit into any of these simple pictures. For instance, the mature Vela SNR exhibits several interesting morphological features dubbed "shrapnels", which were

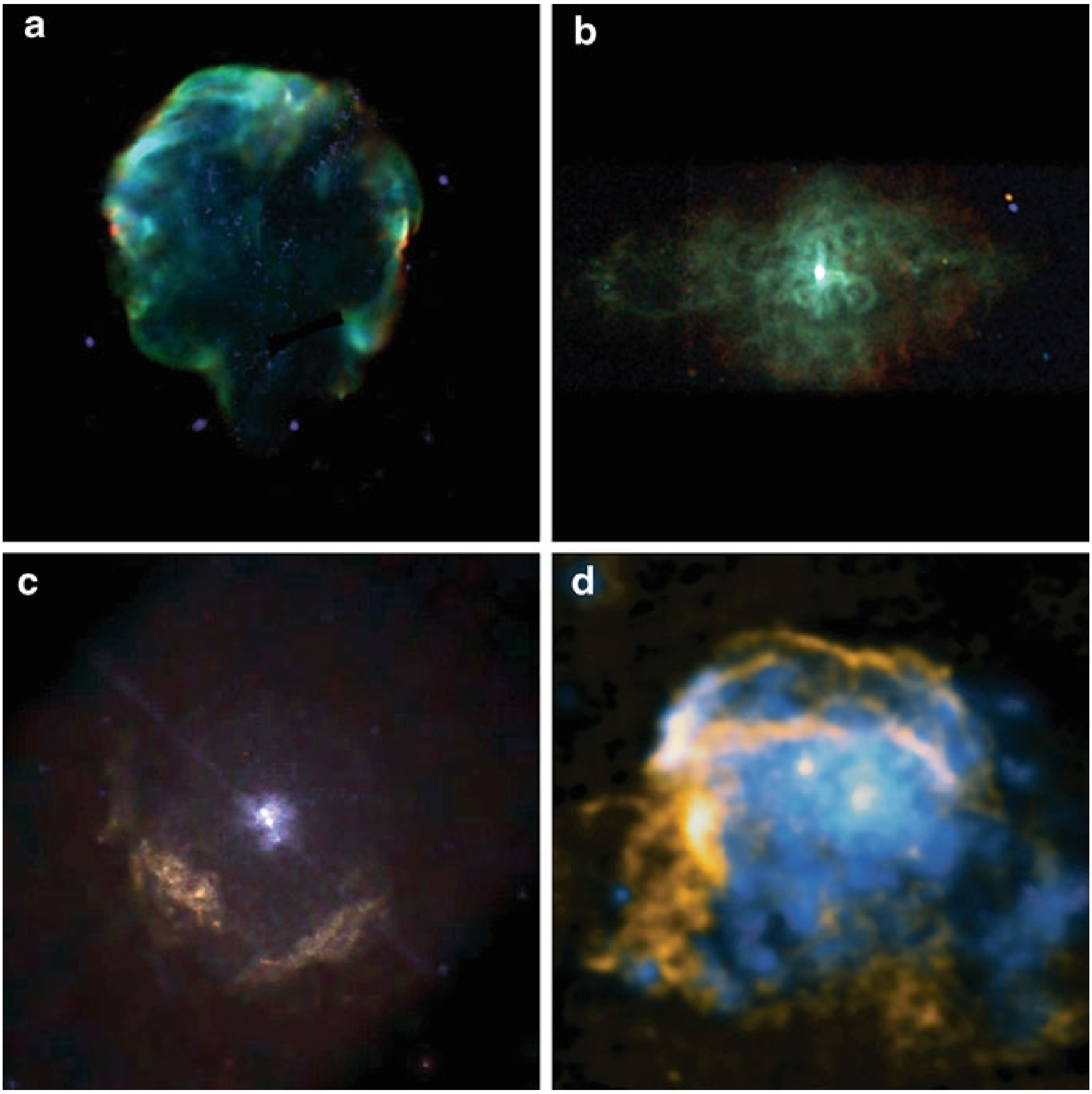

Figure 2.4: Examples of SNR morphologies, mainly displayed using X-ray imaging. (a) The Cygnus loop, an old shell-type SNR (Levenson et al. 1998); (b) 3C58, a plerionic SNR (Slane et al. 2004); (c) The composite SNR Kes 75 (Helfand et al. 2003); (d) W28, a mixed-morphology SNR, with X-rays shown in blue, and radio data (Dubner et al. 2000) in orange (credit: *Chandra* press office[1]); This figure was reproduced from Vink (2020).

discovered in X-rays with *ROSAT* (Aschenbach et al. 1995). These features are located outside the main SNR shell, and exhibit bow shocks of varying opening angles. They are believed to contain dense ejecta clumps which have overtaken the forward shock, and are now penetrating into the ambient medium, which is supported by elemental abundance measurements via X-ray spectroscopy (Katsuda & Tsunemi 2005, 2006; Yamaguchi & Katsuda 2009). A further example of extraordinary features in SNRs is the apparent jet-counterjet structure visible in the young core-collapse SNR Cas A. The X-ray emitting material in these jets is known to contain a large amount of silicon (Hwang et al. 2004), and to expand away from the center at a much higher velocity than other ejecta (Fesen et al. 2006). This may indicate an anisotropic explosion with a preferred axis similar to the jet direction. Finally, in practice, strong asymmetries in SNR shells may also be caused by extrinsic effects, such as the expansion into an inhomogeneous ISM, which may give rise to lobes or "ears" in the observed morphology of the SNR (e.g., Chiotellis et al. 2021), or lead to a strongly asymmetric brightness profile.

2.2.3 SNRs in a broader astrophysical context

While the complex morphologies of SNRs and their tendency to produce stunning images may arguably provide sufficient motivation to engage in their study, SNRs are relevant to a broad range of astrophysical fields. A selection of examples of the influence of SNRs on their galactic environment is briefly given in the following.

Particle acceleration

Young shell-type SNRs are well-known sites of cosmic ray acceleration, likely through the diffusive shock acceleration (DSA) mechanism. This is supported by the ubiquitous detection of synchrotron radiation at radio and X-ray wavelengths from SNR shells (e.g., Shklovsky 1968; Koyama et al. 1995), originating from electrons at GeV and TeV energies, respectively. The question whether SNRs could be the dominant source of Galactic cosmic rays at the location of earth, and whether they may be capable of accelerating particles to PeV energies, may be answerable through the observational and theoretical study of the DSA mechanism in SNRs. The basic principle of the DSA mechanism (see Vink 2020) in a collisionless shock is that of particles crossing the shock front multiple times while diffusing through a chaotic magnetic field. On average, each passage is expected to increase the particle's energy by a constant factor dependent on the shock velocity, leading to the exponential growth of the particle energy with the number of crossings. In the idealized case of an infinitely strong shock, the DSA mechanism gives rise to a power-law energy spectrum of the accelerated particles ($\mathrm{d}N/\mathrm{d}E \propto E^{-p}$), with a characteristic index of $p = 2$ (Vink 2020). In practice, in the case of leptons being the dominant emitting species, this will be modified by radiative losses due to synchrotron (and inverse Compton) emission, and by the finite time available for acceleration given by the SNR age, both of which lead to a smooth high-energy cutoff in the spectrum (Reynolds 2008). In the hadronic case, the main energy loss occurs via the collision with ambient material, leading to the production of pions, whose subsequent decay ($\pi^0 \rightarrow \gamma\gamma$) is responsible for the emitted gamma-radiation.

By studying SNRs in the X-ray and radio bands, the energy-dependent spectral index of their nonthermal synchrotron emission can be measured (e.g., Lopez et al. 2015; Tsuji et al. 2021; Sapienza et al. 2022), from which one may learn about the underlying acceleration mechanism,

---

[1] `https://chandra.harvard.edu/photo/2008/w28/more.html`

in particular the importance of radiative losses or nonlinear effects, in which the cosmic ray acceleration modifies the underlying shock structure. Furthermore, polarization measurements of SNRs at radio and, very recently, X-ray energies (Vink et al. 2022), reveal the polarization fraction and angle of synchrotron emission. This can be used to infer physical orientation and degree of uniformity of the magnetic field in the shock front, often revealing turbulent or radially oriented field lines in young SNRs (Anderson et al. 1995). Finally, by using high-resolution imaging to study the width of nonthermal filaments in young X-ray SNR shells, such as Cas A, Kepler, or Tycho (e.g. Vink & Laming 2003; Berezhko et al. 2003; Ballet 2006), the strength of the magnetic field and the efficiency of diffusion can be inferred, as strong magnetic fields (on the order of several $100\,\mu$G) and inefficient diffusion lead to narrow synchrotron filaments (Helder et al. 2012).

Nucleosynthesis

SNe are an important site of nucleosynthesis in the cosmos for many elements between oxygen and the iron group. Initially produced during stellar explosions, the study of SNRs reveals how these metal ejecta interact and mix with the ISM. Furthermore, X-ray emission of ejecta in SNRs reveals their elemental composition, which can be used to infer the nature of the explosion and the type of progenitor star.

In the case of core-collapse SNRs, a large fraction of observable light-element ejecta are produced during hydrostatic burning phases prior to the explosion, so that the observed ejecta composition is a tracer of both the progenitor composition and the explosive nucleosynthesis. Qualitatively, heavier progenitor stars tend to produce a larger fraction of oxygen compared to iron-group elements, whereas the converse is true for lighter progenitors (Woosley & Weaver 1995; Nomoto et al. 2013; Sukhbold et al. 2016). This is because of the more efficient production of α-elements during hydrostatic burning phases of helium and carbon, whose yield roughly scales with the initial progenitor mass. While core-collapse SNe dominate the cosmic budget of light elements like oxygen, neon, and magnesium, type Ia SNe produce a comparable amount of intermediate-mass elements (e.g., silicon) and the majority of heavier elements, including iron and nickel (Iwamoto et al. 1999).

An issue in the quantitative interpretation of nucleosynthetic predictions for arrays of core-collapse SNe of different progenitor masses (e.g. Woosley & Weaver 1995; Sukhbold et al. 2016) is the fact that present-day resources only allow their computation via one-dimensional models. This is due to the large cost of numerically modelling three-dimensional neutrino-driven explosions taking into account all relevant physical processes, including nuclear reactions and neutrino transport, which is mostly feasible for single progenitor masses only (e.g. Wongwathanarat et al. 2017; Bollig et al. 2021). One-dimensional models likely provide realistic predictions for total yields of light elements produced during hydrostatic burning phases, such as oxygen, neon, or magnesium. However, yield predictions of elements heavier than silicon, which are produced during explosive burning phases (Woosley et al. 2002), or even individual isotope ratios, are presently still quite uncertain, since one-dimensional explosion models are unable to take into account nonradial motions and turbulence during the explosion, or the clumping of the produced ejecta.

Dust production and destruction

Supernovae and their remnants are expected to have a significant impact on the dust budget of their host galaxies. In fact, it has been established that a significant amount of dust must be produced in the ejecta of high-redshift core-collapse supernovae, since the amount of dust visible in distant quasar absorption spectra would be difficult to explain otherwise (Dwek et al. 2007). Furthermore, large amounts of heated dust are clearly also present in many Galactic core-collapse SNRs (Ghavamian & Williams 2016; Tappe et al. 2006; Rho et al. 2009). This dust manifests itself in a very high flux in the mid-infrared band, which often even dominates the entire spectral energy distribution and is thus the dominant channel of radiative energy loss in young SNRs (e.g. Dubner et al. 2013). The dust particles in SNRs are thought to be produced early-on after the explosion, during the adiabatic cooling of the expanding ejecta, as soon as their temperatures are low enough to allow for the condensation of refractory elements (Vink 2020). The dust grains are visible in emission due to collisional heating experienced during the interaction with hot ion and electron populations, leading to the emission of thermal continua and emission lines at mid- and far-infrared wavelengths (e.g. De Looze et al. 2017). The dust mass is found to be concentrated in relatively dense ejecta regions, at least in the prototypical case of Cas A (Lagage et al. 1996). Observational estimates for the integrated dust budget produced in individual SNe are dependent on modelling assumptions, but typical values for core-collapse SNRs are in the range $\sim 0.1 - 1\,M_\odot$ (Gomez et al. 2012; De Looze et al. 2017; Arendt et al. 2010).

Despite the well-established production of dust in core-collapse SNRs, it is not clear whether SNe in the local universe have a net positive effect on the galactic dust budget, as there is also considerable evidence for the contrary process, dust destruction, in SNRs. On one hand, this concerns freshly produced dust in the cooled ejecta which may be reheated and destroyed upon its passage through the reverse shock; on the other hand, preexisting dust in the ISM may also be destroyed or affected by sputtering (i.e., grain size reduction) through collision with the forward shock associated to an SNR shell (Vink 2020; Zhu et al. 2019). A beautiful piece of evidence for this process was provided by Arendt et al. (2010), who found a very strong correlation on all spatial scales between mid-infrared and X-ray emission of the medium-age SNR Puppis A. The fact that shock-heated gas and warm dust appear to exist cospatially in narrow filaments, as well as the direct observation of the lack of typical dust molecules in the spectrum of a shocked region, directly trace the ongoing dust destruction through the forward shock of Puppis A.

2.3 Phenomenology of neutron stars

There is ample observational and theoretical evidence that most core-collapse SNe leave behind a compact remnant in the form of a neutron star (NS). With supranuclear densities above $2.8 \times 10^{14}\,\mathrm{g\,cm^{-3}}$ and initial core temperatures of several hundred million Kelvin (Page 2009), NSs are among the densest and hottest objects in the universe. Other extreme physical conditions exhibited by certain types of NSs include rapid rotation at millisecond spin periods, and enormous magnetic fields up to $10^{15}\,\mathrm{G}$. Thus, NSs may be seen as laboratories for investigating the behavior of matter under conditions which are inaccessible on earth.

As implied by their name, NSs are believed to contain a large fraction of free neutrons, but their exact composition and structure is unclear and a subject of intensive research. This is because the composition of matter under the densities inside NSs is sensitive to the nuclear forces at play under such extreme conditions, which are not fully known. It has been suggested that exotic baryonic or mesonic matter, or even free (deconfined) quarks may exist under the enormous pressure and supranuclear densities in the NS core. In practice, this composition gives rise to a certain equation of state (see Weber et al. 2009, for a review), which can be probed via observational constraints on NS cooling and their mass-radius relation.

In this section, I give a brief overview of our physical knowledge of the NS population and its observational phenomenology.

2.3.1 Observational properties

As the majority of NSs are detected as radio pulsars, their primary observables are related to their timing properties, most importantly the spin period P, and its first temporal derivative $\dot{P}$. Commonly, the NS population is organized in a $P-\dot{P}$ diagram, such as the one shown in Fig. 2.5. As can be seen in the diagram, NSs exhibit spin periods spanning four orders of magnitude, ranging between 1.4 ms (Hessels et al. 2006) and around 10 s. The observational range of spin period derivatives extends over more than ten orders of magnitude between around $10^{-10}\,\mathrm{s\,s^{-1}}$ and $10^{-21}\,\mathrm{s\,s^{-1}}$.

The timing properties of NSs can be interpreted physically in the framework of the magnetic dipole braking model (see e.g., Becker 2009): Assuming a “canonical” NS radius and mass of $R = 10\,\mathrm{km}$ and $M = 1.4\,M_\odot$, its approximate moment of inertia (assuming a solid sphere of uniform density) is given by $I \approx 2/5\,MR^2 \approx 1.1 \times 10^{45}\,\mathrm{g\,cm^2}$. Its spin-down power (i.e., the rotational energy loss due to the increase of the spin period) is given by

$$\dot{E} = 4\pi^2 I P^{-3} \dot{P}. \tag{2.2}$$

If one assumes this spin-down to occur due to the energy radiated away by a nonaligned magnetic dipole rotating around the spin axis, one can estimate the necessary magnetic dipole field strength of the NS as (Ostriker & Gunn 1969)

$$B = 3.2 \times 10^{19} \left(\frac{P\dot{P}}{1\,\mathrm{s}}\right)^{1/2}\,\mathrm{G}. \tag{2.3}$$

The spin-down behavior over time can be described by $\dot{P} \propto P^{2-n}$, with the braking index having the value $n = 3$ in the case of braking via magnetic dipole radiation. If one further makes the assumption that the NS was born rotating infinitely fast (or at least much faster than today), one can derive the “characteristic age” of the NS given by

$$\tau = \frac{P}{(n-1)\,\dot{P}} = \frac{P}{2\dot{P}}. \tag{2.4}$$

The input assumptions for the computation of τ are however not unproblematic: first, there is substantial evidence that NSs are not always born with much smaller rotation periods than today,

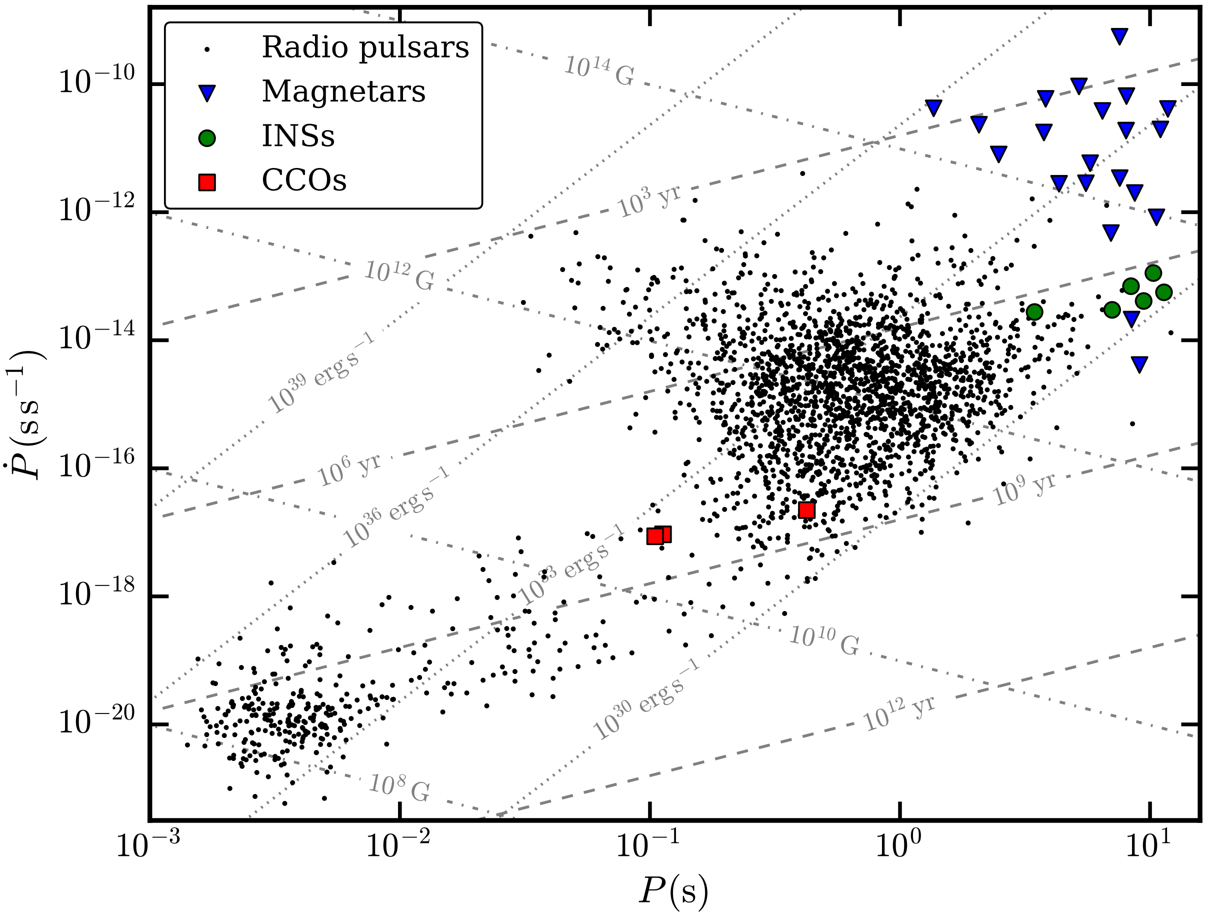

Figure 2.5: Diagram of pulse period P versus its temporal derivative $\dot{P}$ for known NSs. Different classes of NSs are indicated with different symbols, as described in the legend. The superimposed dashed lines mark constant spin-down ages τ, the dotted lines constant spin-down luminosity $\dot{E}$, and the dash-dotted lines constant characteristic magnetic fields B. This figure was created using data from the ATNF Pulsar Catalogue (version 1.69; Manchester et al. 2005).

for instance in the case of the NS hosted by the SNR Puppis A (Gotthelf et al. 2013a). Second, the assumed braking index requires that magnetic dipole radiation indeed be the dominant channel of energy loss, rather than for example energy carried away by a pulsar wind, which would imply $n = 1$ (Pétri 2019). In fact, observations of the timing properties of several objects imply that braking indices $n \sim 2$ may be common among pulsars (Espinoza et al. 2017). Thus, while estimates of the dipole magnetic field B and characteristic age τ of NSs are often useful for their rough characterization, they do not constitute exact measurements of the actual surface magnetic field or NS age.

2.3.2 The neutron star “zoo”

As can be recognized in Fig. 2.5, the observational landscape of non-accreting NSs exhibits considerable diversity in its timing properties alone, and can be divided into various physical subgroups (see Harding 2013; Enoto et al. 2019, for detailed reviews), as we briefly illustrate here.

Magnetars

Magnetars are NSs whose primary energy source is their immense magnetic field (or the decay thereof), rather than their rotation. Magnetars are the class of NSs with the highest magnetic fields, with their timing properties indicating dipole fields in the range $B \sim 10^{14} - 10^{15}\,\mathrm{G}$. Observationally, they appear as bright X-ray emitters with a dominant thermal contribution to their quiescent soft X-ray emission, and luminosities significantly exceeding their spin-down energy loss. In addition, many magnetars exhibit a flat nonthermal emission component visible in the hard X-ray band (e.g., den Hartog et al. 2008), indicating ongoing particle acceleration. Magnetars manifest themselves in two different observational flavors, historically thought to be separate types of objects: soft gamma-ray repeaters undergo episodes of outbursts with typical energy releases of $10^{40} - 10^{41}$ erg, peaking in the soft gamma-ray regime (i.e., around 100 keV, Woods & Thompson 2006). In contrast, anomalous X-ray pulsars are observed as bright, slowly pulsating, thermal X-ray sources with typical blackbody temperatures of $0.5 - 1.0$ keV and luminositites of $10^{35}\,\mathrm{erg\,s^{-1}}$ (Harding 2013).

Isolated neutron stars

Members of the relatively rare class of (X-ray-dim) isolated neutron stars (INSs) are quite similar to magnetars, in the sense that they are observed as thermally emitting X-ray sources, albeit with much smaller luminosities and lower temperatures of at most ~ 0.1 keV. All the “magnificent seven” well-established INSs have been discovered in the *ROSAT* all-sky survey (Haberl 2007), as soft X-ray sources without bright optical counterparts. Similarly to magnetars, INSs are too X-ray bright to be powered by rotational energy loss, and exhibit slow rotation and relatively high magnetic dipole fields in excess of 10^{13} G (Kaplan 2008). It is thus possible that there is an evolutionary connection between these two NS classes (Enoto et al. 2019).

Central compact objects

Central compact objects (CCOs) are a peculiar class of young NSs, observed as bright X-ray sources close to the center of SNRs (De Luca 2017). The around ten known CCOs appear as stable thermal X-ray emitters with typical blackbody temperatures of $0.2 - 0.5$ keV, whose emitting area seems to be consistent with relatively small hotspots on the NS surface. In contrast to all other NS classes, no emission has been detected from CCOs at other wavelengths, thus far. X-ray pulsations in the 100 ms regime have only been detected for the three CCOs in Kes 79, Puppis A, and PKS 1209−51/52 (Gotthelf et al. 2005; Gotthelf & Halpern 2007, 2009), with no pulsations detected for other objects, despite intensive searches (Alford & Halpern 2023). The origin of the pulsed emission has been attributed to the existence of hotspots on the NS surface moving in and out of the visible area. Subsequently, longer X-ray timing campaigns revealed very small period derivatives for all three pulsating CCOs (Gotthelf et al. 2013a; Halpern & Gotthelf 2010a). These imply low magnetic dipole fields on the order of $\lesssim 10^{11}$ G, which has led to the somewhat controversial classification of CCOs as "anti-magnetars". Recently, timing campaigns of the CCO in PKS 1209−51/52 have revealed evidence for glitches, sudden increases in spin frequency, a type of behavior that is usually only expected for NSs with higher magnetic fields (Gotthelf & Halpern 2020).

A fundamental issue with the description of CCOs as a homogeneous class is the lack of X-ray pulsations detected from the majority of CCOs, which makes the existence of pronounced hotspots on the surface of every CCO statistically unlikely. Furthermore, the existence of such localized stable surface hotspots may be difficult to explain if one assumes the low measured magnetic dipole fields (De Luca 2017) to be representative for the global magnetic field strength of the NS. Finally, the lack of older "orphan CCOs" with similar timing properties, but without a host SNR, in the observed NS population is puzzling, as, in principle, CCOs should not move substantially in $P - \dot{P}$ space (Kaspi 2010; Gotthelf et al. 2013b). A solution to these problems has been suggested to lie in the accretion of material falling back on the NS shortly after the SN explosion: a fraction of a solar mass of accreted material may bury the magnetic field beneath the NS surface, leading to a small emergent surface dipole component (Ho 2011). The potentially chaotic or toroidal structure of the hidden magnetic field could explain the existence of surface hotspots through anisotropic heat transport (Shabaltas & Lai 2012). On longer timescales, the internal magnetic field would be expected to resurface via diffusion, and CCOs could turn into "regular" radio pulsars in a different region of $P - \dot{P}$ space (Bogdanov 2014; Luo et al. 2015).

Rotation-powered pulsars

The vast majority of all known NSs are rotation-powered pulsars, with around 3000 such objects listed in the latest iteration of the ATNF Pulsar Catalogue[2] (version 1.69; Manchester et al. 2005). As indicated by the name, their rotational energy loss due to magnetic field braking is thought to be the main powering source of the nonthermal emission of pulsars. Even though emission from pulsars has been detected at virtually every wavelength, the vast majority is detected and investigated in the radio band, via the dedicated search for stable pulsed signals. Nonetheless, recent years have brought the detection of a significant number of radio-quiet rotation-powered pulsars, through the discovery of pulsed emission in the X-ray or gamma-ray bands (e.g., Marelli et al. 2011; Abdo et al. 2013).

The origin of nonthermal radiation from pulsars is not completely understood. While the radio emission most likely originates from a coherent process (e.g., Gil et al. 2004), multiple scenarios exist for the spatial origin of higher-energy magnetospheric radiation from pulsars. One popular class of models suggests an origin of X-ray and gamma-ray photons at the location of open magnetic field lines at the polar caps, right above the NS surface. Alternative scenarios predict their production in the "outer gap", close to the light cylinder, where co-rotation with the

---

[2] `https://www.atnf.csiro.au/research/pulsar/psrcat/`

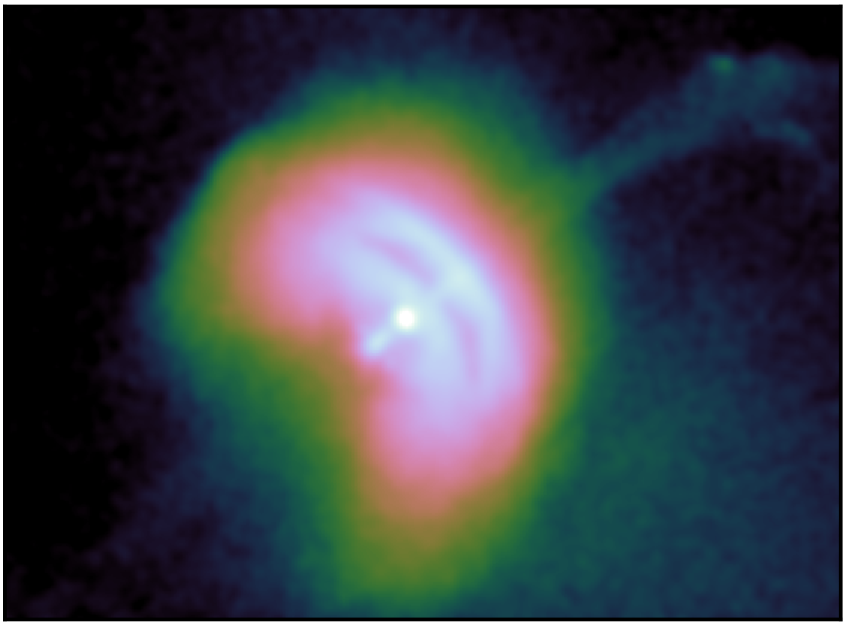

Figure 2.6: X-ray morphology of the inner PWN around the Vela pulsar, as seen by *Chandra*. The bright pulsar, the equatorial toroidal arcs, the inner and outer parts of the jet toward the northwest, and the counterjet toward the southeast are visible. This image shows an area of $3.0' \times 2.2'$, and was created from *Chandra* observations 10135−10139 and 12073−12075, using the `cubehelix` color scheme (Green 2011).

NS implies motion at the speed of light (see Cheng 2009, for a review). The latter acceleration zone exhibits the advantage of allowing easier escape of the photons out of the magnetosphere, as one-photon pair production in the presence of a strong magnetic field is suppressed at larger radii (Cheng et al. 1986). Observationally, the efficiency of conversion of rotational energy to electromagnetic radiation is found to increase toward higher energies, with the highest efficiency observed in the gamma-ray band (Enoto et al. 2019). The conversion efficiency into nonthermal X-ray luminosity L_X exhibits large scatter, but most pulsars seem to lie in the range $L_X/\dot{E} \sim 10^{-5} - 10^{-3}$ (Becker & Trümper 1997; Shibata et al. 2016; Enoto et al. 2019).

Rotation-powered pulsars can be grouped into the following categories based on their age, energetics, and (X-ray) emission behavior (Becker 2009):

- **Crab-like pulsars** are named after one of the most energetic known pulsars, and include young pulsars below $\sim 10^4$ yr. This class of objects usually exhibits bright, hard, and strongly pulsed nonthermal emission in the X-ray band.

- **Vela-like pulsars** exhibit ages in the range $10^4 - 10^5$ yr. They differ from younger pulsars in that they show less strongly pulsed X-ray emission, as well as significant thermal contributions from the NS surface.

- **Cooling NSs** are middle-aged pulsars in the range $10^5 - 10^6$ yr. Popular examples include the nearby pulsars nicknamed the “three musketeers” (Becker & Trümper 1997), all of which exhibit dominant thermal emission in the soft X-ray regime, and nonthermal magnetospheric emission at higher energies. Spectral modelling shows that the thermal emission is likely composed of contributions from the warm entire NS surface and hot polar caps (De Luca et al. 2005).

- **Old nearby pulsars:** The radiation of (non-recycled) pulsars older than the above types is typically dominated by nonthermal magnetospheric emission in the X-ray band (Becker et al. 2004). Somewhat surprisingly, signatures of heated polar caps from particle bombardment (Harding & Muslimov 2002) appear to be scarce.

- **Millisecond pulsars** (or recycled pulsars) are fundamentally different from the other pulsar types discussed here, not only in their small periods $\lesssim 10\,\mathrm{ms}$, and large characteristic ages $\sim 10^9 - 10^{10}\,\mathrm{yr}$, but in the fact that binary evolution plays an important role in their formation. Millisecond pulsars are believed to be the endpoint of low-mass X-ray binary systems, in which the NS accretes material from a lighter companion star. The resulting transfer of angular momentum leads to a spin-up ("recycling") of the pulsar. An especially interesting subtype of this class includes the so-called spider systems, in which the particle wind from the pulsar continually ablates its binary companion star (Roberts 2013).

In contrast to most other types of NSs, pulsars produce a considerable amount of nonthermal diffuse emission in the form of pulsar wind nebulae (PWNe), which are visible mainly at radio, X-ray and gamma-ray energies. PWNe are the manifestation of particles accelerated at the termination shock (Kirk et al. 2009), where the ordered flow of the relativistic "striped" pulsar wind interacts with the ambient medium. The accelerated particles stream outward, emitting synchrotron or inverse Compton radiation over an extended region, and giving rise to complex spatial structures (see Gaensler & Slane 2006; Kargaltsev et al. 2015). In young PWNe, axisymmetric structures are often visible on small scales, consisting of an equatorial torus, and a mildly relativistic jet-counterjet structure along the rotation axis (see the X-ray image of the Vela pulsar in Fig. 2.6). While the toroidal structure is understood to be related to the termination shock, the nature of the jet-like structure is less clear, but may be related to the magnetic collimation of polar outflows from the pulsar (Komissarov & Lyubarsky 2004; Bogovalov et al. 2005).

In contrast, older pulsars supersonically traversing the ISM often show bow-shocks and cometary tails at radio, optical, and X-ray energies, caused by the anisotropic ram pressure due to their high space velocity (Gaensler & Slane 2006). Recently, signatures of large-scale halos on multi-degree scales have been discovered around middle-aged pulsars in the TeV gamma-ray band (e.g., Abeysekara et al. 2017). These bow shocks and TeV halos can be understood as a late stage of the PWN evolution, after it has interacted with the reverse shock and escaped its host SNR, and is now travelling through the unperturbed ISM (see the sketch of different stages in Fig. 2.7, taken from Giacinti et al. (2020)). At this stage, high-energy electrons can escape from confinement in the PWN core, and propagate to large distances via diffusion through the ambient medium, producing diffuse gamma-ray emission via inverse Compton scattering. Thus far, no X-ray emission has been detected from these halos, even though, in principle, energetic electrons should emit detectable synchrotron radiation in the ambient magnetic field (Li et al. 2022).

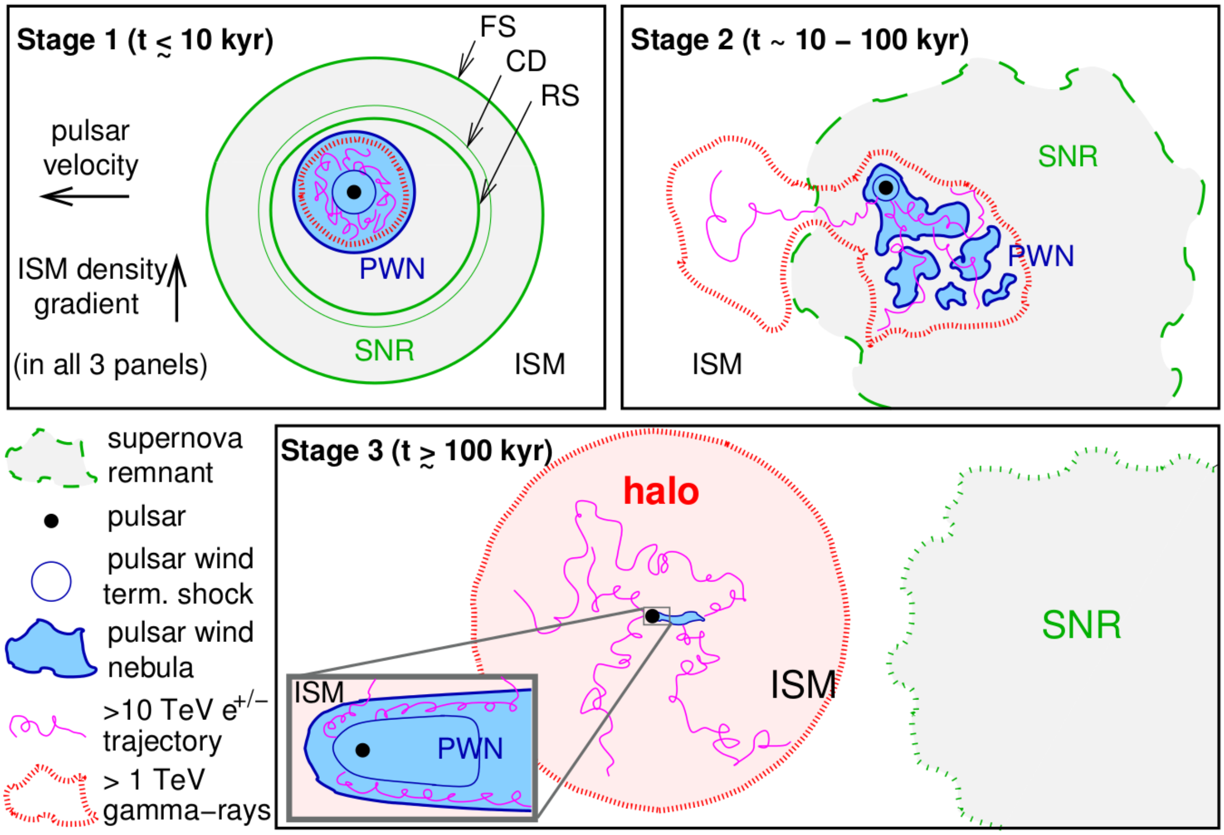

Figure 2.7: Schematic illustration of evolutionary stages of a PWN in its parent SNR. The three stages correspond to a relatively undisturbed expanding PWN in the center of its SNR, a deformed or disrupted relic PWN after the interaction with the reverse shock, and a pulsar which has escaped from its SNR, exhibiting a bow-shock PWN and an extended halo visible at TeV energies. This illustration was adopted from Giacinti et al. (2020).

2.3.3 Physical applications of neutron stars and pulsars

Particle acceleration in PWNe

It appears to be clear that particles are efficiently accelerated in pulsar winds, as many PWNe are detected in emission in X-rays and gamma-rays (Kargaltsev et al. 2015), and even seem to be plausible candidates to explain recently detected emission up to PeV energies (Breuhaus et al. 2022; Cao et al. 2021). PWNe are known to be accelerators of leptonic cosmic rays, electrons and positrons produced via the pair-production mechanism, with an uncertain possible secondary contribution of hadrons (Atoyan & Aharonian 1996; Bednarek & Bartosik 2003). Therefore, it is thought that they cannot be the dominant local cosmic ray source up to the highest energies, as the composition of the most energetic Galactic cosmic rays is known to be primarily hadronic (Antoni et al. 2005; Vink 2022). It seems possible, however, that PWNe are the dominant source of local leptonic cosmic rays. Evidence for this is provided by the detection of electrons escaping into large-scale pulsar halos in the TeV band (Giacinti et al. 2020). However, the fact that their propagation is regulated by relatively slow diffusion (Abeysekara et al. 2017) seems to make it unlikely that PWNe are the reason for the high flux of cosmic ray positrons at earth (Accardo et al. 2014), at least for the case of the Geminga pulsar. Further detections of large-scale diffuse emission around pulsars could be useful to constrain the behavior of escaping electrons and positrons from the pulsar wind.

Tests of fundamental and nuclear physics

Isolated and binary NSs may be used as tools to learn about other branches of physics, including general relativity and nuclear physics at extreme densities. An important system in this context is the famous Hulse-Taylor binary system PSR B1913+16, consisting of a pulsar and a second NS (Hulse & Taylor 1975). The ability to precisely trace the time of arrival of the pulsed radio emission during the orbit of the pulsar around its companion allows for precise tests of the predictions of general relativity. In particular, this system was used to provide the first experimental evidence for gravitational wave emission, based on the detection of the binary orbital shrinkage caused by the energy loss to gravitational radiation (Taylor & Weisberg 1982).

A further unique binary system is the double pulsar PSR J0737−3039A/B (Burgay et al. 2003). The fact that pulsed signals originating from two bodies orbiting each other within little more than two hours can be detected, has allowed for further fundamental tests of strong-field gravity. In particular, seven post-Keplerian parameters, which describe corrections to a Keplerian orbit in the general-relativistic case, as well as several higher-order effects, have been measured for the system (Kramer et al. 2021). Combining the post-Keplerian parameters not only allows for extremely precise measurements of the pulsar masses, but also for several independent tests of general relativity, all of which the theory has passed, thus far (Kramer et al. 2021).

A completely different flavor of physics, namely nuclear physics, can be probed by constraining the nuclear equation of state, relating pressure and density inside the NS. This can be achieved on one hand by comparing observed masses and radii of NSs (e.g., Abbott et al. 2017; Clark et al. 2023b) to their theoretically expected range. On the other hand, the equation of state of extremely dense matter is also encoded in the cooling behavior of NSs (see Page 2009). In practice, this implies the measurement of the surface temperatures of a sample of thermally X-ray emitting isolated NSs with no internal heating source (such as magnetic field decay), and comparing these to their estimated ages. In the absence of internal heating, the cooling of NSs is expected to be regulated by the combination of energy losses due to neutrinos radiated from the interior and thermal electromagnetic radiation at the surface. Thus, measurements of the age dependence of the NS temperature act as an indirect constraint on the neutrino emissivity inside the NS. The latter depends sensitively on several processes, including the formation of neutron Cooper pairs, and the occurrence of the efficient direct URCA process. This process is equivalent to the (inverse) beta decay of a free neutron, without the necessity for a second neutron to conserve momentum (Yakovlev & Pethick 2004). Since these effects depend on the core density and composition, NS cooling is a valuable tracer of the internal structure of NSs, which leads back to the high-density regime of nuclear physics behind the NS equation of state. Currently, there is no unambiguous observational evidence for cooling beyond the “minimal cooling” scenario (Page et al. 2004). In this scenario, the direct URCA process is absent, indicating comparatively

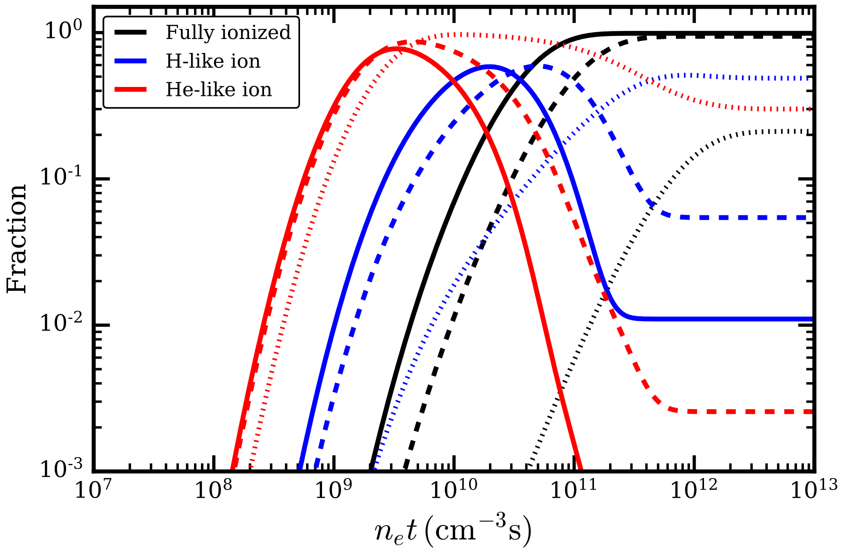

Figure 2.8: Ionization state distribution for underionized oxygen of different temperatures, in dependence on the assumed ionization timescale $n_e t$. The fractions of He-like (O VII), H-like (O VIII), and fully ionized oxygen are indicated in red, blue, and black, respectively. Dotted, dashed, and solid lines indicate electron temperatures of $kT_e = 0.2, 0.5, 1.0\,\mathrm{keV}$, respectively. This figure was created using the AtomDB code (Foster et al. 2012).

low core densities (Lattimer et al. 1991).

2.4 Relevant X-ray emission processes

In this chapter, I give a brief summary of the main physical processes giving rise to, and modifying, the observable X-ray emission from SNRs and their central NSs.

2.4.1 Thermal processes

Non-equilibrium ionization

The thermal X-ray emission associated to SNRs is generally assumed to be caused by hot, collisionally ionized, and optically thin gas, with typical densities $\sim 1\,\mathrm{cm}^{-3}$. This is not fundamentally different from the emission of the hot intra-cluster medium in galaxy clusters or the coronal X-ray emission from stars. Importantly however, the hot plasma in galaxy clusters or stellar coronae is usually in collisional ionization equilibrium (CIE), meaning that the distribution of ionization states of the individual elements is stable over time. In contrast, SNRs frequently exhibit non-equilibrium ionization (NEI), with separate temperatures of electrons and ions. Young SNRs in particular often exhibit underionized plasma, where lower ionization states are preferentially occupied compared to the CIE expectation for a given electron temperature (Borkowski et al. 2001). This underionization is caused by the fact that the shock interaction with the SNR blast wave leads to a very small initial electron-to-ion temperature ratio (approximately $T_e/T_i \sim m_e/m_i$), and insufficient time has passed for equilibration (see Rakowski et al. 2003). In contrast, old SNRs are sometimes found to be overionized (e.g., Yamaguchi et al. 2009), probably due to rapid cooling of the plasma after reaching CIE, for instance caused by its adiabatic expansion.

In practice, the degree of NEI can be very well parametrized by the ionization timescale $n_e t$, the product of post-shock electron density and the time passed since shock heating (see Fig. 2.8). This is because this quantity serves as a proxy for the number of electron-ion collisions that an ion has experienced since crossing the shock. Observationally, timescales $n_e t \gtrsim 10^{12}-10^{13}\,\mathrm{cm}^{-3}\,\mathrm{s}$ tend to produce spectra almost indistinguishable from CIE.

Bremsstrahlung

Bremsstrahlung, or free-free emission, is caused by the acceleration of a free electron by the interaction with the electric field of an ion, usually hydrogen or helium. The luminosity of thermal bremsstrahlung from a given volume is regulated by the so-called emission measure (EM), which depends on the electron and ion densities (n_e and n_i) and ion charges (Z_i) as

$$\mathrm{EM} \propto \int \mathrm{d}V\, n_e \sum_i n_i Z_i^2 \approx 1.7 \int \mathrm{d}V\, n_\mathrm{H}^2, \tag{2.5}$$

where the last equality approximately holds for ionized plasma with cosmic abundances.[3] The scaling with n_H^2 implies that, for inhomogeneous volumes, the intensity of thermal emission is dominated by the densest portions of the volume, making it necessary to estimate volume filling factors in astrophysical applications.

For a thermal distribution of electron velocities (i.e., a Maxwell distribution of temperature T_e), the total bremsstrahlung spectrum S at a radiation frequency ν is proportional to (Vink 2020)

$$S(T_e, \nu) \propto \mathrm{EM}\, g_\mathrm{ff}(T_e, \nu) T_e^{-1/2} \exp\left(-\frac{h\nu}{kT_e}\right), \tag{2.6}$$

where g_ff is the Gaunt factor, a slowly varying function of order unity of the parameters, which takes into account quantum-mechanical corrections to the classical formula. As can be seen by the expression, the resulting intensity spectrum is approximately constant for a given temperature, up to an exponential cutoff at a photon energy of kT_e.

Line emission

Analogously to other fields of astronomy, X-ray line emission is created by transitions between two bound states of different energy levels in the same ion. X-ray emission lines are collisionally ionized "coronal" lines, in the sense that they are formed under high temperatures $\gtrsim 10^6$ K, and originate from highly ionized species, as typical for stellar coronae. In particular, for light

---

[3] Note that, in the spectral fitting program `Xspec` (Arnaud 1996), EM is defined via the product $n_e n_\mathrm{H}$, instead of the sum over all ions, slightly modifying its quantitative interpretation.

elements (starting from carbon), X-ray lines mostly originate from transitions in the atomic K-shell of hydrogen- or helium-like ions, meaning ions with only one or two bound electrons. For heavier elements, most prominently iron, transitions in the L-shell of lower ionization states are also observable in the X-ray band.

The intensity of line emission is naturally a good tracer of absolute and relative metal abundances. In addition, the ratios of different lines from the same element are a powerful tool for inferring its average ionization state, and thereby the temperature and ionization timescale of the plasma. Conveniently, the absolute volume emissivity of X-ray line emission for a given ionization state is proportional to the local density squared, due to collisional ionization being a two-body process. Thus, the emission measure can be used as a global normalization of the composite thermal spectrum, while the relative level of emission lines is regulated by ionization states and elemental abundances.

Radiative recombination continua

Radiative recombination describes the process of a free electron being captured by an ion, leading to the emission of a photon with the combination of the electron's kinetic energy and the ionization energy of the resulting state. This process of free-bound emission leads to the formation of broad radiative recombination continuum contributions of metals to thermal SNR spectra. These continua are relatively faint for underionized plasma in young SNRs and hard to identify with the resolution of present-day instrumentation, but are detectable in old, overionized objects, especially mixed-morphology SNRs (Yamaguchi et al. 2009; Ozawa et al. 2009; Uchida et al. 2012). In addition, they may become crucial in the identification of emission from pure ejecta clumps in young SNRs with future high-resolution instruments (Greco et al. 2020).

Charge-exchange emission

A final increasingly relevant emission process in SNRs is charge-exchange emission, which may contribute significantly whenever tenuous and hot ionized material associated to an SNR shock wave interacts with dense neutral matter, for instance a molecular cloud (Lallement 2004). As the ions strip electrons from the neutral material, it is left heated and ionized, whereas the ions are left in an excited state after recombination. In the X-ray band, the subsequent de-excitation produces a pure emission line spectrum, with the effect of modifying observed line ratios of individual species, compared to the expectation for collisional ionization. The process of charge exchange may justifiably be considered nonthermal, and in practice also occurs in the absence of a thermal distribution of ion velocities, as for instance in the solar wind (Smith et al. 2014). However, its observational signature is very similar to truly thermal spectra of optically thin, collisionally ionized plasma, which is why we include it here.

The effect of charge exchange has been observed in SNRs several times, for instance in a bright knot in the medium-age SNR Puppis A, where Katsuda et al. (2012) found evidence for emission line ratios within helium-like nitrogen, oxygen, and neon, which were inconsistent with simple expectations. In particular, the ratio of the forbidden to the resonance line[4] flux in

---

[4] The resonant line is created by the transition from the singlet state of the excited ion to the ground state

the Heα triplets was found to be abnormally high, and not explicable by other processes, such as recombining plasma. Instead, they showed that charge exchange with a dense cold cloud may lead to an enhancement of the forbidden line emission by the right order of magnitude to reproduce their observation.

Blackbody radiation

Thermal emission from an optically thick emitter, such as a hot NS, will approximately follow the law of blackbody emission derived by Max Planck, where the frequency-dependent intensity per unit area and solid angle of an emitter of temperature T follows

$$S(\nu, T) = \frac{2h\nu^3}{c^2} \frac{1}{\exp(h\nu/kT) - 1}. \tag{2.7}$$

Integrated over all frequencies and solid angles, this yields the total luminosity emitted by the object, following the Stefan-Boltzmann law:

$$L(T) = \sigma T^4 A, \tag{2.8}$$

with A being the surface area, and the Stefan-Boltzmann constant being $\sigma = 5.67 \times 10^{-5}\,\mathrm{erg\,cm^{-2}\,s^{-1}\,K^{-4}}$. In X-ray astronomy, both temperature and photon energy are frequently measured in the same units, such as keV, so it makes sense to define the Wien displacement law, describing the frequency ν_{max} at which the intensity S is maximized, in the following dimensionless form:

$$h\nu_{\mathrm{max}} \approx 2.82\,kT. \tag{2.9}$$

Thus, a blackbody emits its maximum intensity at an energy corresponding to around three times its surface temperature.

In practice, the thermal emission from NS surfaces can be well described by (the sum of) blackbody spectra, but the resulting emitting areas are frequently much smaller than the total NS surface (e.g. Hui & Becker 2006b). This may be alleviated by physical models of NS atmospheres (e.g. Suleimanov et al. 2009), which tend to imply larger emitting areas than ideal blackbodies for the same spectra. However, much of the microphysics of a NS atmosphere necessary for their computation is still uncertain, given the typically encountered extreme magnetic fields.

2.4.2 Nonthermal processes

Synchrotron radiation

Astrophysical synchrotron radiation in PWNe and SNR shells is emitted by relativistic charged particles, usually electrons, due to the acceleration they experience while gyrating around magnetic field lines. As a result, an individual electron will emit a radiation spectrum with peak

---

($1s2p$ to $1s^2$), whereas the forbidden line originates from the triplet state ($1s2s$ to $1s^2$), violating the relevant selection rules regarding electron spin and orbital angular momentum (see Sect. 13.5.4 in Vink 2020).

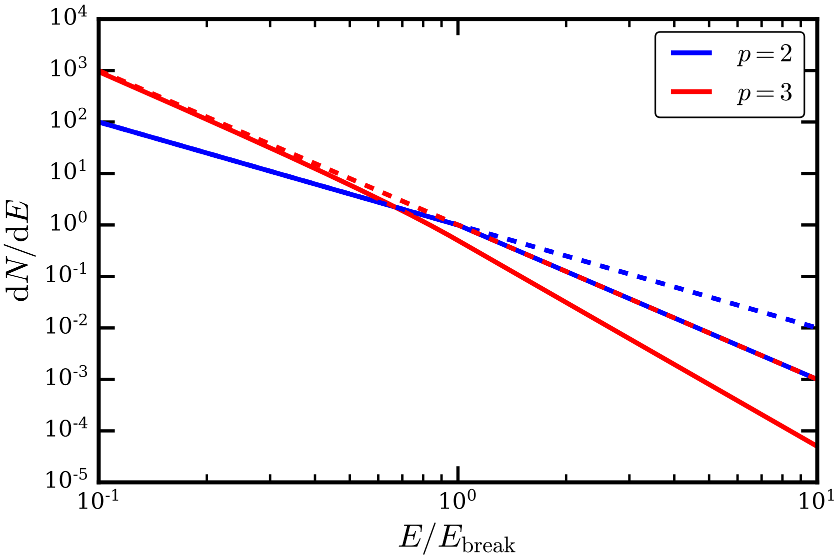

Figure 2.9: Integrated electron spectra of a source continuously injecting particles over time for different spectral indices p (solid lines). The energy loss to synchrotron radiation leads to a cooling break in the spectrum at an age-dependent energy E_{break}, where the electron spectrum steepens by $\Delta p = 1$ (implying a steepening of the synchrotron spectrum by $\Delta\Gamma = 1/2$). The dashed lines show the corresponding uncooled energy distributions to illustrate the location and strength of the cooling break. This figure was inspired by Vink (2020).

intensity at $\nu_{\mathrm{max}} = 0.29\nu_c$, with the critical frequency given by (Vink 2020)

$$\nu_c = \frac{3eB_\perp}{2m_e c}\gamma^2, \tag{2.10}$$

where γ is the Lorentz factor of the relativistic electron, e and m_e are the electron charge and mass, and $B_\perp$ is the perpendicular magnetic field component (with respect to the direction of motion). This implies that the emission of a typical X-ray synchrotron photon at an energy $h\nu \sim 1\,\mathrm{keV}$ in a magnetic field $B_\perp \sim 10\,\mu\mathrm{G}$ requires an electron energy around 70 TeV.

Realistic nonthermal particle energy distributions will frequently follow a power law of type $\mathrm{d}N/\mathrm{d}E \propto E^{-p}$. The combination of the radiation from the individual particles will produce a power-law synchrotron spectrum in which the volume emissivity follows $\epsilon(\nu) \propto \nu^{-\alpha}$, where the spectral index equals

$$\alpha = \Gamma - 1 = \frac{p-1}{2}. \tag{2.11}$$

Here, Γ describes the photon index, quantifying the number of photons emitted per energy bin, as is commonly done in X-ray astronomy.

An electron's emission of synchrotron radiation leads to the loss of kinetic energy proportional to the magnetic field energy density and to the electron energy squared, following (Vink 2020)

$$\frac{\mathrm{d}E}{\mathrm{d}t} = -\frac{4\,ce^4}{9\,(m_e c^2)^4}\,B_\perp^2 E^2. \tag{2.12}$$

An electron will thus lose its energy on a characteristic timescale $\tau = -E/\,(\mathrm{d}E/\mathrm{d}t)$, which in practice is relatively short for X-ray emitting particles. For instance, the example electron from above would have a lifetime of only around 500 yr, giving it relatively little time to move away from its source and stay detectable. This phenomenon known as synchrotron "cooling", meaning the rapid energy loss of the most energetic particles, tends to introduce high-energy cutoffs or cooling breaks in the observed X-ray spectra of PWNe and nonthermal SNR shells (see Fig. 2.9).

Curvature radiation

A mechanism closely related to synchrotron radiation which is likely important for the magnetospheric X-ray (as well as radio and gamma-ray) emission of pulsars is curvature radiation. In contrast to the former process, where high-energy electrons radiate due to their gyration around magnetic field lines, here, the strong curvature of the magnetic field lines itself is the dominant mechanism of deflecting the particles. In analogy to synchrotron radiation, the characteristic energy up to which a relativistic electron emits in the curvature regime is given by (Ochelkov & Usov 1980)

$$\nu_c = \frac{3\gamma^3 c}{2r}, \tag{2.13}$$

where γ is the Lorentz factor of the electron, and r is the radius of curvature of the magnetic field lines, rather than the gyroradius of the electron under a given magnetic field strength (as in the synchrotron case). This implies that for an assumed curvature radius $r \sim 10^8$ cm, emitting nonthermal X-rays with $h\nu \sim 1$ keV requires particle energies around 40 TeV, independently of the exact magnetic field strength.

2.4.3 Photoelectric absorption

Absorption in the X-ray regime occurs primarily via photoionization, affecting the K- and L-shell electrons of abundant metals, although hydrogen and helium do play a minor role at low energies (illustrated in Fig. 2.10). Despite the rather minor importance of hydrogen for X-ray absorption above 0.5 keV, the optical depth to X-ray emission is usually parametrized using the equivalent hydrogen column density N_H, in combination with a model- and frequency-dependent cross-section $\sigma(\nu)$, such as that given by the Tübingen-Boulder model (`TBabs`, Wilms et al. 2000). Thus, the absorbed spectrum $S\,(\nu)$ results from the intrinsic spectrum $S_0(\nu)$ following

$$S\,(\nu) = S_0(\nu)\, \exp\left(-N_\mathrm{H}\sigma(\nu)\right). \tag{2.14}$$

It is well known that the X-ray absorption cross-section scales approximately as $\sigma(\nu) \propto \nu^{-3}$ (see Fig. 2.10), because of the sharp decline of the photoionization cross-section beyond the threshold energy of a transition (Kahn 2005). Therefore, the degree of absorption often varies by orders of magnitude between the soft and hard portions of an X-ray spectrum.

Apart from the atomic physics contributing to the absorption cross-sections of individual processes, the computation of $\sigma(\nu)$ requires the knowledge of the exact composition and ionization state of the intervening ISM toward the source (Wilms et al. 2000). While the limited spectral

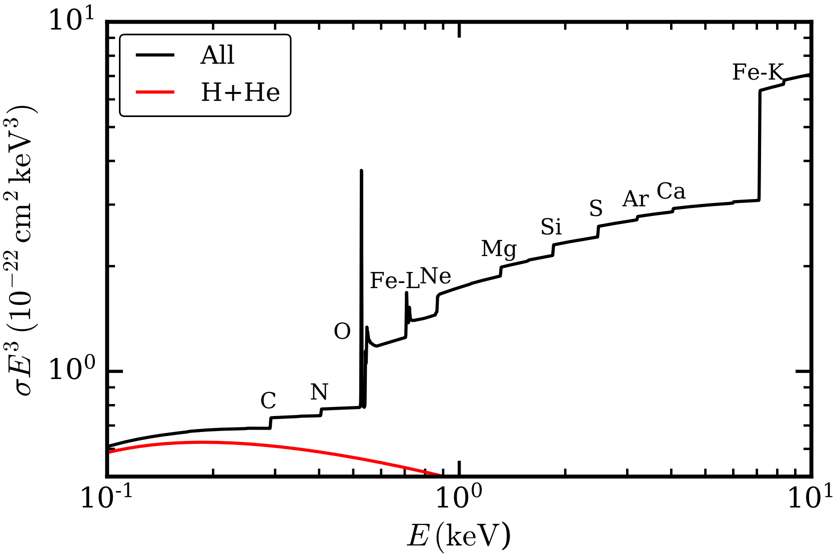

Figure 2.10: Energy-dependent X-ray absorption cross-section of the ISM for a typical composition, following the model of Wilms et al. (2000). The y-axis displays the cross-section σ rescaled with the third power of photon energy E, to emphasize the effect of the absorption edges at the indicated atomic shells. For the oxygen K-shell and iron L-shell, strong substructure is visible in the transition edges, whereas analogous substructure is missing at the edges of other elements. The contribution from hydrogen and helium alone is indicated in red. Figure inspired by Morrison & McCammon (1983).

resolution of present-day CCD detectors does not yet reveal the contributions of individual elements to absorption, future high-resolution spectroscopy may require the modelling of elemental abundances not only in emission but also in absorption (see Gatuzz & Churazov 2018). In contrast to the attenuation of optical light, which occurs mostly on condensed dust grains, X-ray absorption is not strongly dependent on the phase of the absorbing material, so that a comparison of the two energy bands can be useful to infer the ISM dust content (e.g., Predehl & Schmitt 1995; Zhu et al. 2017).

2.5 Involved X-ray instrumentation

The analysis presented in this thesis is largely based on observations in the soft X-ray band from two telescopes, namely *Chandra* and eROSITA. In this section, I will briefly introduce the telescopes and their instruments, discussing their main strengths and characteristics.

2.5.1 *Chandra* X-ray observatory

NASA's *Chandra* X-ray observatory is one of the flagship X-ray missions of the early 21st century, having been launched on July 23, 1999. Thanks to its four extremely smooth nested mirror shells, the primary strength of the telescope is its on-axis angular resolution of 0.5″,[5] which is unparalleled in the X-ray domain. Thus, even though the effective area of its mirror assembly is much smaller than that of its contemporary, *XMM-Newton* (Strüder et al. 2001; Turner et al. 2001), *Chandra* is ideally suited for all tasks requiring high spatial resolution or astrometric accuracy in X-rays. The observatory contains four science instruments, two of which are diffraction grating spectrometers, the Low-Energy and High-Energy Transmission Gratings (Brinkman et al. 2000; Canizares et al. 2005). As they are dedicated to high-resolution X-ray spectroscopy of bright point-like sources, these two instruments are not immediately relevant to the analysis presented in this work.

The Advanced CCD Imaging Spectrometer (ACIS, Garmire et al. 2003) is one of the two imaging detectors aboard *Chandra*. Its two sub-instruments, ACIS-I and ACIS-S, combine a total of ten CCD detector chips, two of which are back-illuminated for an improved soft response, which are sensitive to X-rays in the approximate range $0.5 - 10\,\mathrm{keV}$. Its low intrinsic background level and decent energy resolution, combined with the telescope's high astrometric resolution, make ACIS the ideal instrument for the detection, localization, and rough spectral characterization of many sources in the field of view. It has however been realized that, during the lifetime of *Chandra*, the buildup of contaminant on its optical blocking filter (Marshall et al. 2004) has severely reduced the response of ACIS to X-ray emission below $\sim 2\,\mathrm{keV}$, limiting its usefulness for the analysis of soft sources.

The second imaging instrument, the High-Resolution Camera (HRC, Murray et al. 2000), consists of two sub-detectors, designed for precise imaging (and timing) analysis (HRC-I) and grating spectrometer readout (HRC-S), respectively. The microchannel plate detectors allow for the reconstruction of event positions on a continuous grid, rather than on discretized pixels, leading to a higher on-axis spatial resolution than ACIS, at the expense of spectral resolving power. In practice, the comparatively higher background rate implies that the HRC's imaging capabilities are only superior to those of ACIS for relatively bright sources.

2.5.2 *SRG*/eROSITA

The eROSITA X-ray telescope (extended Roentgen Survey with an Imaging Telescope Array, Predehl et al. 2021) was launched on July 13, 2019, aboard the German-Russian *Spectrum-Roentgen-Gamma* satellite (*SRG*, Sunyaev et al. 2021). The *SRG* mission is located in a halo orbit around the second Lagrange point of the Sun-Earth system (L2), around 1 500 000 km from Earth. The eROSITA telescope is built from seven largely identical telescope modules (TMs), each consisting of 54 nested gold-coated Wolter-I mirror shells, combined with X-ray baffles for the suppression of stray light, and pn-CCD detectors in their focus. The individual mirror modules reach a spatial resolution characterized by a half-energy width around 18″ on the optical axis, and 26″ when averaged over the field of view (Predehl et al. 2021).

The detectors used in each TM are single-chip pn-CCD detectors sensitive in the $0.2 - 10\,\mathrm{keV}$ energy band, similarly to those of EPIC on board *XMM-Newton* (Strüder et al. 2001), with 384 × 384 pixels spread over a field of view of 1.03° diameter. Unlike EPIC-pn, the detec-

---

[5] `https://chandra.harvard.edu/about/specs.html`

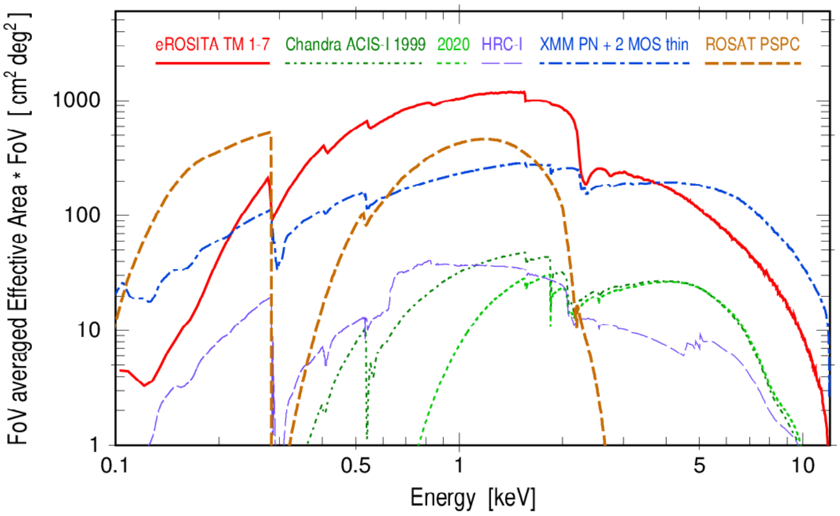

Figure 2.11: Survey efficiency of eROSITA. This figure shows the energy-dependent grasp, the product of field of view and effective area, of eROSITA compared to other X-ray missions. These include the PSPC on board *ROSAT* (Trümper 1982), *XMM-Newton* EPIC (Strüder et al. 2001; Turner et al. 2001), and the HRC and ACIS detectors of *Chandra*. Figure courtesy to Predehl et al. (2021).

tors of eROSITA contain a framestore area, virtually eliminating the existence of "out-of-time" events recorded during the detector readout, which occurs every 50 ms (Meidinger et al. 2020). All but two TMs are equipped with an on-chip optical blocking filter, as TMs 5 and 7 were designed with the goal of improved low-energy spectroscopy. Unfortunately, these two TMs are subject to a temporally variable "light leak" due to solar optical light reaching the detectors. Its complicated spatial distribution and temporal variability presently limits the usefulness of TMs 5 and 7 for X-ray spectroscopy (Predehl et al. 2021).

The combination of the seven TMs yields an on-axis effective area slightly above that of *XMM-Newton* in the soft band, with an average over the field of view of $\sim$ 1200 cm^2 at 1 keV (Predehl et al. 2021). However, the response of eROSITA shows a sharp decrease at an absorption edge associated to the gold M-shell at 2.2 keV, making the instrument significantly less sensitive to hard X-rays. The primary strength of eROSITA is its ability to carry out large-scale surveys efficiently. This is quantified by the so-called grasp, the product of the field of view and the average effective area, whose behavior is illustrated in Fig. 2.11. It can be seen that eROSITA significantly outperforms all other existing or past X-ray missions in the soft X-ray band 0.5 – 2.0 keV. Apart from its large survey efficiency, a key feature of the eROSITA detectors for our analysis is their improved spectral resolution and reduced low-energy redistribution[6], with respect to their predecessor, the EPIC-pn detector of *XMM-Newton*, as illustrated in Fig. 2.12. Specifically, at 1.5 keV, the post-launch full-width half-maximum resolution of EPIC-pn was around 110 eV, whereas eROSITA provides an average resolution of around 80 eV at that energy

---

[6] In this context, low-energy redistribution refers to the detection of individual X-ray photons at significantly underestimated energies, due to incomplete charge generation or collection in the detector. This leads to significant non-Gaussian low-energy tails in detected spectra.

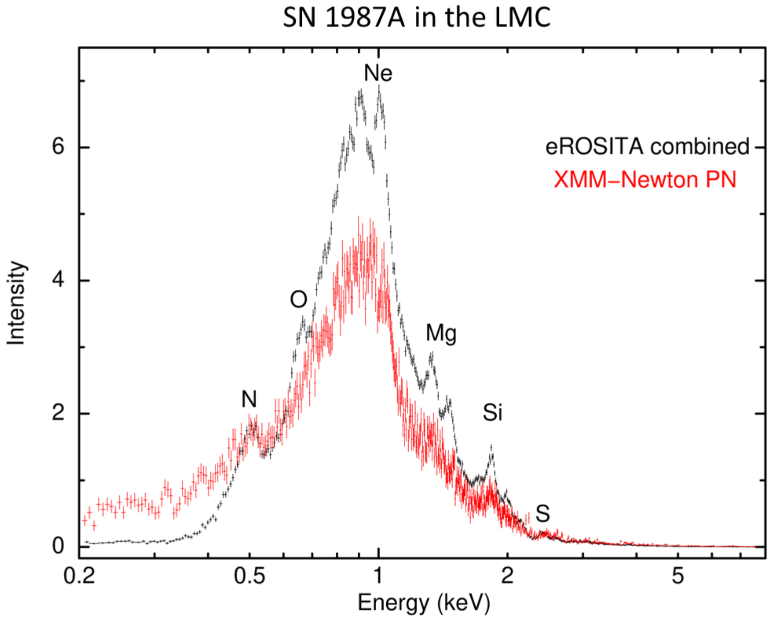

Figure 2.12: Comparison of X-ray spectra of SN 1987A taken by eROSITA and *XMM-Newton* EPIC-pn (Maitra et al. 2022), illustrating the two detectors' different responses. The labels indicate the location of the most important emission lines. Figure credit to C. Maitra and F. Haberl (MPE/IKI)[7].

(Strüder et al. 2001; Meidinger et al. 2020; Predehl et al. 2021). The instrumental background of eROSITA, caused by electronic noise, high-energy particles, and instrumental fluorescence lines, is at a somewhat higher level than predicted before launch. However, owing to the L2 environment of eROSITA, it is quite stable over time and exhibits little flaring, allowing for a reliable quantification of its effect on the observed X-ray emission (Freyberg et al. 2020).

eROSITA's main mission target is the execution of a four-year all-sky X-ray survey in the 0.2 – 10 keV energy band. This observational effort is divided into eight individual all-sky surveys (labeled eRASS1−8), during which the sky is continually scanned along great circles intersecting at the ecliptic poles, with one revolution every four hours. Averaged over the whole sky, the resulting on-source time in the final survey (eRASS:8) is expected to be on the order of 2.5 ks (Predehl et al. 2021). eRASS:8 is expected to be more than 20 times deeper than the previous *ROSAT* all-sky survey in the soft band, while providing the first X-ray imaging survey in the band above 2.4 keV, ever (Merloni et al. 2012). The design-driving science goal of the mission is the detection of 100 000 galaxy clusters across the whole sky, through the emission of hot gas in their intra-cluster medium. This will allow the detailed reconstruction of the growth of large-scale structure across cosmic time, thus constraining cosmological models (Pillepich et al. 2012). Furthermore, unprecedentedly large detected samples of active galactic nuclei and coronally X-ray emitting stars are anticipated (Merloni et al. 2012). Finally, the study of stellar endpoints is expected to benefit strongly from eROSITA's all-sky survey data. A (somewhat biased) list of example science questions includes the search for X-ray detected SNRs in previously inaccessible regions of parameter space, or the characterization of the X-ray properties of large, uniformly selected samples of SNRs or rotation-powered pulsars. Furthermore, the all-sky survey data provides the unique opportunity to study the full size of nearby extended SNRs at unprecedented sensitivity and resolution in X-rays, which would not be feasible with other instruments, due to their limited field of view.

The science exploitation rights of eROSITA survey data are divided equally between the involved consortia based in Germany and Russia, respectively, with the German consortium having access to the "western" Galactic hemisphere ($180° \leq l \leq 360°$). Owing to the German-Russian nature of the mission, on Feb 26, 2022, eROSITA was placed into safe mode in response to the Russian invasion of Ukraine[8], with science operations being halted since then. A future resumption of eROSITA science operations is however possible.

---

[7] https://www.mpe.mpg.de/7360702/presskit-erosita-firstlight

[8] https://www.mpe.mpg.de/7856215/news20220303

Chapter 3

A refined proper motion measurement for the CCO in Puppis A

This chapter is based on a work published as "The proper motion of the central compact object RX J0822−4300 in the supernova remnant Puppis A, revisited" (Mayer et al. 2020) in the Astrophysical Journal, Volume 899, 138.

3.1 Introduction

After their death in violent core-collapse supernovae (i.e. types Ib, Ic, II), massive stars leave behind compact remnants such as black holes or neutron stars. The latter constitute an opportunity to directly observe matter under some of the most extreme conditions in the universe. Over the years, observations have revealed a diverse "zoo" of neutron stars: While most young neutron stars are detected as non-thermal pulsed sources in the radio, optical, X- or gamma-ray regime (for an overview, see e.g. Becker 2009; Harding 2013), members of the class of central compact objects (CCOs) are seen exclusively as isolated hot, steady thermal emitters in X-rays, located at (or near) the center of supernova remnants (SNRs), but without characteristic pulsar wind nebulae. In particular, CCOs have been found associated with relatively young, oxygen-rich Galactic remnants of core-collapse supernovae such as Cas A (Tananbaum 1999; Chakrabarty et al. 2001) and Puppis A (Petre et al. 1996). In total, the sample of Galactic SNRs with confirmed CCOs consists of around 10 objects, including G266.1−1.2, PKS 1209−51/52, G330.2+1.0, G347.3−0.5, G350.1−0.3, Kes 79, G353.6−0.7 and G15.9+0.2 (see De Luca 2017, and references therein)[1].

While X-ray pulsations of CCOs have been detected in a few cases, these can be fully explained by the rotational modulation of thermal emission from hotspots on the neutron star surface (e.g. Gotthelf et al. 2010) and are therefore not comparable to strong pulsations across the electromagnetic spectrum seen from typical young pulsars. The exact reason for the existence of these hotspots is still unclear since heating through accretion or particle bombardment seems unlikely (De Luca 2017). The lack of nonthermal emission from CCOs can likely be attributed

---

[1] See also `http://www.iasf-milano.inaf.it/~deluca/cco/main.htm`

to their comparatively weak magnetic field, which is inferred from small spin-down rates, justifying their designation as "anti-magnetars" (Gotthelf et al. 2013a). An issue with the description of CCOs as a homogeneous class is the paucity of their descendants, since one would expect to find many more "orphaned" compact objects (Halpern & Gotthelf 2010a) without visible SNRs in a similar region of the $P - \dot{P}$ parameter space than are observed in practice (Kaspi 2010).

The dynamical imprint of a violent supernova explosion on its remnant can be studied by observing the kinematics of the ejecta, for instance, fast-moving optical filaments, but also by studying the proper motion of the neutron star itself. Typically, contemporary simulations of core-collapse supernovae predict significant explosion asymmetries, which manifest themselves as bipolar jets, large-scale anisotropies, and/or strong natal kicks to the compact object. These birth kicks can be made plausible simply by conservation of momentum: If a large ejecta mass is expelled at high velocity preferentially in a certain direction, one would naturally expect the compact remnant to experience recoil in the opposite direction.

After it was found from optical observations that ejecta in Puppis A generally expand toward north and east (Winkler & Kirshner 1985; Winkler et al. 1988), it was expected that a possible compact remnant would be moving toward the southwest. Following the discovery of the CCO RX J0822−4300 by Petre et al. (1996), the measurement of its kinematics thus became very interesting, even though it is challenging to achieve sufficient astrometric accuracy for an object that emits exclusively in X-rays. Such a study became possible only after the launch of *Chandra* owing to its unparalleled spatial resolution, once a sufficiently long temporal baseline of 5.3 years (December 1999 - April 2005) between observations had been acquired.

Two studies successfully measured a proper motion toward the southwest, with marginally consistent results for its absolute value: Hui & Becker (2006a) found $\mu_{\mathrm{tot}} = (107 \pm 34)\,\mathrm{mas\,yr^{-1}}$, while Winkler & Petre (2007) measured an even larger value of $\mu_{\mathrm{tot}} = (165 \pm 25)\,\mathrm{mas\,yr^{-1}}$. Combined with an approximate distance to the SNR of 2 kpc, the measurement by Winkler & Petre (2007) implied a very high transverse velocity on the order of $1600\,\mathrm{km\,s^{-1}}$, leading to the designation of RX J0822−4300 as a "cosmic cannonball."[2] While constituting an exciting result on its own, this finding was in conflict not only with observations of pulsar birth velocities being on the order of $\sim 500\,\mathrm{km\,s^{-1}}$ (Caraveo 1993; Frail et al. 1994; Hobbs et al. 2005), but also with theoretical predictions from simulations of supernova explosions. However, Becker et al. (2012) repeated the above study including a new *Chandra* HRC observation taken in August 2010, and found a more conservative value of $\mu_{\mathrm{tot}} = (71 \pm 12)\,\mathrm{mas\,yr^{-1}}$ which corresponds to a velocity of $(672 \pm 115)\,\mathrm{km\,s^{-1}}$, a result in better agreement with theory and the general distribution of measured pulsar proper motion velocities.

In order to finally "pin down" the proper motion of RX J0822−4300 in direction and magnitude, this work incorporates a new *Chandra* observation from early 2019, almost doubling the previously available time baseline. In Section 3.2, we give an overview of the data set we used and the initial data processing. In Section 3.3, we describe the analysis steps we used to obtain the CCO proper motion value from our data. We then discuss the implications on neutron star kick velocity and remnant age in Section 3.4 and summarize our findings in Section 3.5.

---

[2] In the analysis of Becker et al. (2012), it was found that this high velocity was attributable to a subtle bug in the *Chandra* software for fitting and locating the off-axis reference stars. See Section 3.3.1 of this paper.

Table 3.1: *Chandra* observations of RX J0822−4300

Instrument	ObsID	Date	OnTime (s)	Exposure Time (s)
HRC-I	749	1999 Dec 21/22	18014	9860
HRC-I	4612	2005 Apr 25	40165	21317
HRC-I	11819	2010 Aug 10/11	33681	15467
HRC-I	12201	2010 Aug 11	38681	17808
HRC-I	20741	2019 Feb 02	40175	19790

Notes. The 2010 observation was carried out as two consecutive ObsIDs (11819 & 12201), without intervening repointing (Becker et al. 2012). Therefore, we merged the two event files after the reprocessing step using `dmmerge`.

3.2 Observations and data reduction

In total, RX J0822−4300 has been observed five times with *Chandra*'s high resolution camera (HRC). Four of these observations were taken with the HRC-I detector (optimized for imaging), and one with the HRC-S (optimized for spectroscopic readout). In order to reduce the influence of possible small but relevant systematic deviations between the detectors (e.g. due to differences in the degap correction or slight misalignments of the detector axes), we exclude the HRC-S observation from our analysis, leaving four observations spanning 19.18 years. These consist of three archival observations, and a new one carried out on February 2, 2019. A journal of the relevant observation IDs, dates, and durations is given in Table 3.1.

We acquired the archival observations from the *Chandra* Data Archive[3] and reprocessed the data using the standard `CIAO` (*Chandra* Interactive Analysis of Observations, Fruscione et al. 2006) script `chandra_repro` to create new level 2 event files on which we based our analysis. In this and all subsequent steps, we used `CIAO` version 4.9 and CALDB version 4.7.4. We checked the observations for flares by inspecting the light curves of point-source-free regions. For the latest observation (ID 20741), we found a background flare affecting the data during around 8% of the time. Therefore, we excluded the affected time intervals for an effective exposure of 18195 s, yielding a significantly reduced particle background while hardly affecting the number of source counts.

Based on the previous results, we can see that we need to achieve an absolute astrometric accuracy significantly below the arcsecond level in order to obtain sufficient precision on our measurement of the proper motion of the CCO. Therefore, while the absolute positional accuracy of *Chandra* is unparalleled for X-ray telescopes at $\sim 0.8''$[4], we still have to improve on the raw astrometric position by a factor of a few in order to obtain a clean signal for the neutron star motion. Our method closely follows that of Becker et al. (2012), albeit with some changes which we will highlight in the next sections. As in the previous works on this topic, we use three nearby

---

[3] `https://cda.harvard.edu/chaser/mainEntry.do`

[4] `http://cxc.harvard.edu/cal/ASPECT/celmon/`

Table 3.2: IDs, positions and proper motions of the three reference stars.

Designation		Position (Epoch 2015.5)		Proper Motion	
Short	*Gaia* Source ID	R.A. (ICRS) (h:m:s)	Decl. (ICRS) (d:m:s)	μ_α (mas yr^{-1})	μ_δ (mas yr^{-1})
A	5526323497671973632	08:21:46.2788	−43:02:03.590	−11.68 ± 0.03	2.70 ± 0.03
B	5526324631543374464	08:22:24.0044	−42:57:59.261	−0.35 ± 0.03	8.49 ± 0.03
C	5526323527726140416	08:21:48.8067	−43:01:28.211	−51.05 ± 0.04	6.82 ± 0.04

Notes. Data as listed in the *Gaia* DR2 catalog (Gaia Collaboration et al. 2018). The stated 1σ uncertainties of Right Ascension & Declination at the reference epoch are significantly below milliarcsecond-level, and would only become relevant at the sixth & fifth decimal digit, respectively. The proper motion along the Right Ascension & Declination axes are labelled as μ_α & μ_δ, respectively.

optical calibrator stars (designated as A, B, and C) that are detected in X-rays to obtain a precise reference for the world coordinate system (WCS). We take advantage of the *Gaia* DR2 catalog[5] which offers strongly improved precision on the positions and proper motions of our astrometric calibrators (Gaia Collaboration et al. 2016, 2018) compared to the UCAC3 catalog (Zacharias et al. 2010). In Table 3.2, we list the optical properties of the stars, and we indicate their relative location to RX J0822−4300 (designated as NS in the following) in Figure 3.1.

The X-ray image demonstrates the general difficulty of detecting weak point sources on top of diffuse background emission from the SNR. While being very faint in X-rays, source C is located in a region of relatively low diffuse emission and can therefore reliably be detected despite the low associated count rate. Source B, however, is superimposed on bright diffuse emission, which hampers its precise localization. Furthermore, all three calibrator sources are located well off-axis, where the *Chandra* point spread function (PSF) becomes increasingly degraded. Comparing these limitations in the X-ray regime to the exquisite precision of the optical positions of the stars in the *Gaia* catalog, we can infer that the dominant error source will lie in the determination of source positions in X-rays, and not in the input astrometric calibration values.

As a first approximation, we used `CIAO`'s wavelet detection algorithm `wavdetect` to estimate the positions and to verify the detectability of all calibrator sources in each observation. We then extracted sub-images centered on each source for each observation to reduce computation times in the subsequent steps. In order not to significantly oversample the PSF, we used bin sizes of 1 × 1 pixels for the NS, and 2 × 2 pixels for sources A, B, C. Since the calibrator sources are located well off-axis (where the PSF broadens) and have fewer counts compared to the CCO, we did not lose a significant amount of information with the 2 × 2 pixel binning and we suppressed pixel-to-pixel fluctuations for the faint sources.

---

[5] `https://www.cosmos.esa.int/web/gaia/dr2`

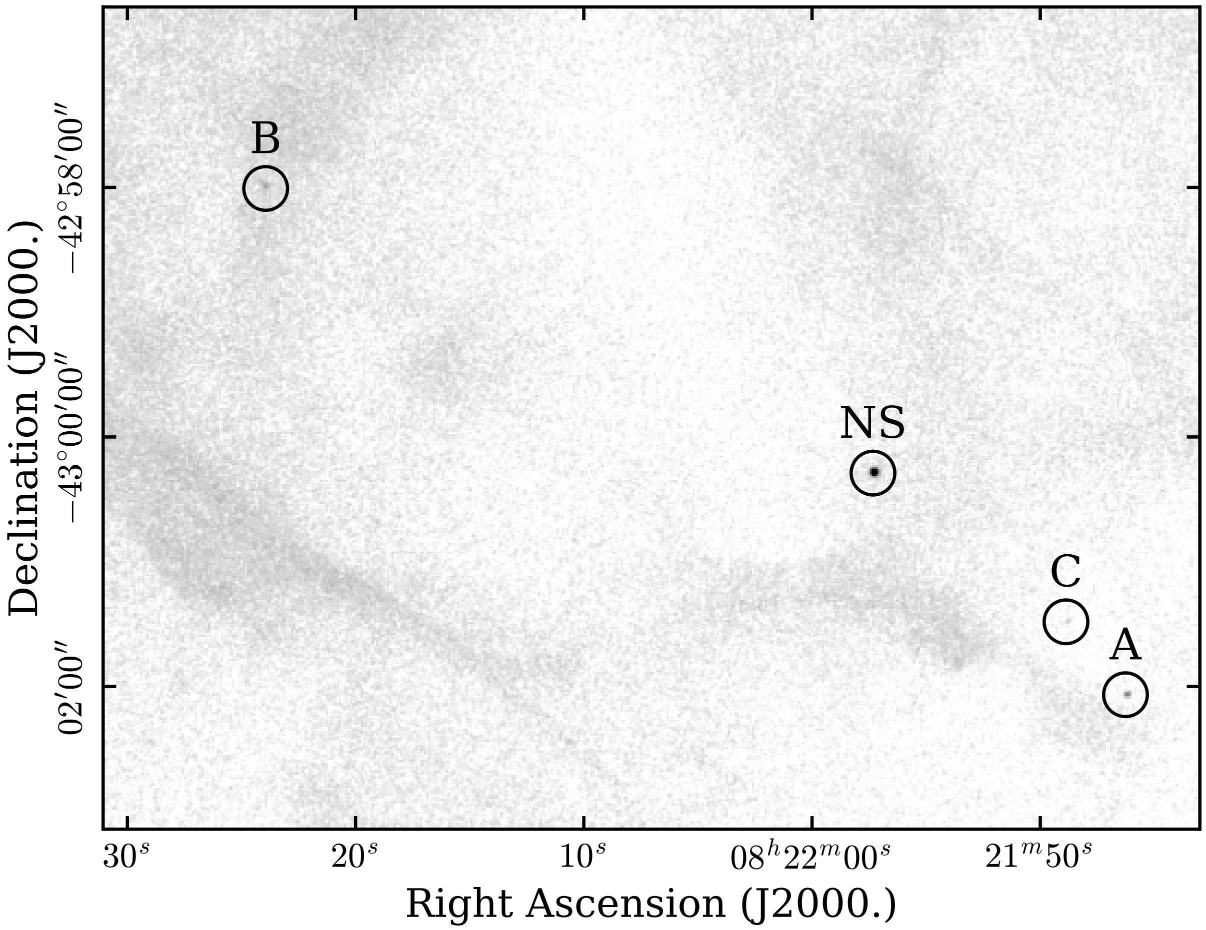

Figure 3.1: Image of the observation from 2010 with the positions of RX J0822−4300 and the astrometric calibrator stars indicated. The scale is logarithmic and the image has been slightly smoothed with a Gaussian of width 0.5″. The field measures around 8.8′ × 6.6′.

3.3 Spatial analysis

In order to measure the proper motion of RX J0822−4300 from our data, we applied a method similar to that described in Becker et al. (2012): We determined the position of all sources (NS, A, B, C) in each data set by modelling and fitting an appropriate PSF to the data (Section 3.3.1). Combining the measured positions of the calibrator stars with their optical positions, we determined an optimal transformation from *Chandra*'s coordinate system to the WCS, which we then applied to the X-ray position of the CCO. In this step, special care was taken in the propagation of uncertainties from each individual fit to the final corrected position of RX J0822−4300, effectively reducing the final size of the error contours (Section 3.3.2). From the absolute positions of the CCO at four epochs, we then straightforwardly determined a new best-fit estimate for its proper motion in two dimensions (Section 3.3.3).

3.3.1 PSF modelling and fitting

In order to get the most reliable estimate for the source positions, we simulated a PSF model for each source in each observation. This is necessary to get results which are unbiased by e.g. the telescope roll angle and pointing, since the off-axis PSF is very broad and, more importantly, distorted. Therefore, the location of peak flux in the PSF does not necessarily correspond to the actual source location. For our simulations, we used the online *Chandra* Ray Tracer tool (`ChaRT`[6]) which incorporates the best available model of the *Chandra* high resolution mirror assembly (HRMA). `ChaRT` uses an input source position in combination with the aspect solution of the observation to trace the photon trajectories from the sky through the HRMA up to the detector plane. Key parameters are the assumed source monochromatic energy, which we set to 1.0 keV (see Becker et al. 2012) and the source photon flux, which we set to the maximal value of $1 \times 10^{-2}\,\mathrm{cm}^{-2}\,\mathrm{s}^{-1}$, in order to minimize the influence of Poisson fluctuations on our PSF model. PSF models with a lower simulated source flux may better resemble the actual images qualitatively, but quantitative fits performed with those yield underestimated positional errors and show larger systematic fluctuations. The `ChaRT` documentation explicitly discourages artificially scaling up source flux to create more rays. However, this warning applies mostly to simulations where one attempts to model nonlinear detection effects like photon pile-up in CCD cameras. The HRC also experiences effects at high rates, such as count rate nonlinearity and deadtime effects, but these do not impact the imaging quality of the source. In total, we created five statistically independent simulations for each source.

The five ray files created by `ChaRT` were then fed simultaneously into `MARX`[7] (Davis et al. 2012, version 5.4.0) which we used to project the rays onto the HRC-I detector and to simulate its response to the photons. We finally obtained PSF model images for each source, with the respective binning matching the data. An impression of the morphology of the PSF models is given in the central panel of Figure 3.2. We found that, in order for the PSF to accurately reflect the observed image, we needed to set the model detector behavior to “non-ideal.” This applies additional blurring (induced by the HRC detector) to the PSF, leading to a closer match between model and data for on-axis sources than would be the case otherwise.

We would like to highlight two more subtle points: First, the PSF image is projected on a grid of sky pixels that exactly matches the pixel grid of the actual observation. Therefore, the “true” source position (i.e. the positional input into `ChaRT`) is not located exactly at the central pixel of the PSF image, but slightly offset from it by a sub-pixel margin. This offset is an effect which we later corrected for by adding its value to the fitted position of the source. Ignore this effect, we found deviations between fits of the same source at different image bin sizes.

Second, when comparing the “true” source position for the PSF of the on-axis (off-axis angle $< 30''$) source with the location of the apparent centroid (or “center of mass”) of the simulated PSF, we found that they do not coincide as perfectly as one would expect. Instead, there is a systematic offset on the order of $0.1''$ which always appears to point in the same direction on the detector even for different simulated roll angles. This behavior is also observed when performing the entire ray-tracing simulation with `MARX` only. The *Chandra* Help Desk confirmed that this

---

[6] `http://cxc.harvard.edu/chart/index.html`

[7] `http://space.mit.edu/CXC/MARX/`

Table 3.3: Optical and "raw" fitted X-ray positions and properties for all sources at all four epochs.

ObsID	Epoch	Source	X-ray R.A. (J2000.) (h:m:s)	X-ray Decl. (J2000.) (d:m:s)	Counts	Optical (*Gaia* DR2) R.A. (J2000.) (h:m:s)	Optical (*Gaia* DR2) Decl. (J2000.) (d:m:s)
749	1999.97	NS	08:21:57.4040(006)	−43:00:16.539(005)	3123		
		A	08:21:46.2906(049)	−43:02:03.308(132)	45	08:21:46.2953(0)	−43:02:03.632(0)
		B	08:22:24.0205(146)	−42:57:59.362(109)	109	08:22:24.0049(0)	−42:57:59.393(0)
		C	08:21:48.8703(103)	−43:01:28.104(180)	13	08:21:48.8790(1)	−43:01:28.316(1)
4612	2005.31	NS	08:21:57.3817(003)	−43:00:17.223(004)	6854		
		A	08:21:46.3002(052)	−43:02:03.919(042)	121	08:21:46.2896(0)	−43:02:03.618(0)
		B	08:22:24.0203(070)	−42:57:59.549(149)	178	08:22:24.0047(0)	−42:57:59.348(0)
		C	08:21:48.8849(130)	−43:01:28.597(178)	9	08:21:48.8542(0)	−43:01:28.280(0)
11819/12201	2010.61	NS	08:21:57.3262(002)	−43:00:17.463(005)	10490		
		A	08:21:46.2617(036)	−43:02:04.089(063)	199	08:21:46.2840(0)	−43:02:03.603(0)
		B	08:22:23.9851(111)	−42:57:59.491(225)	170	08:22:24.0046(0)	−42:57:59.303(0)
		C	08:21:48.8535(135)	−43:01:28.861(123)	19	08:21:48.8295(0)	−43:01:28.244(0)
20741	2019.09	NS	08:21:57.3078(003)	−43:00:17.017(004)	6208		
		A	08:21:46.3035(074)	−43:02:03.284(101)	81	08:21:46.2749(0)	−43:02:03.580(0)
		B	08:22:24.0607(339)	−42:57:58.841(193)	77	08:22:24.0043(0)	−42:57:59.231(0)
		C	08:21:48.8239(145)	−43:01:27.880(211)	18	08:21:48.7900(0)	−43:01:28.186(0)

Notes. The X-ray positions shown here correspond to the best-fit source position in sky coordinates returned by `Sherpa`, uncorrected for any astrometric offsets. The errors on X-ray source positions correspond to the maximum one-sided one-sigma error returned by the `conf` task and are therefore just a crude estimate of the associated uncertainties. The optical positions have been corrected for the proper motions of the respective calibrator stars. For illustrative purposes, we also list rounded "errors" on the last digits of the optical positions, demonstrating that they are of very little importance for the overall uncertainty budget. The column "Counts" lists the amplitude of the Gaussian model which was convolved with the PSF. This therefore corresponds to an estimate for the number of source counts with subtracted background.

behavior is unexpected, and probably indicative of the achievable limit on astrometric precision. The presence of subtle systematic effects at a sub-pixel level therefore must be considered with much care in our analysis.

In the next step, we fitted the PSF models to the individual images of RX J0822−4300 and A, B, C using `Sherpa`[8], a modelling and fitting package developed for *Chandra* (Freeman et al. 2001). We followed the thread "Accounting for PSF Effects in 2D Image Fitting", according to which we convolved the PSF Image (which is normalized to one) with a narrow Gaussian of fixed width, but free to vary in (x, y)-position and amplitude. Additionally, our model incorporated a small, spatially uniform background component across the relevant image area. The convolution with a Gaussian of finite width is necessary to perform meaningful interpolations between pixels so that non-integer position values are possible, and the source position is not "quantized" to the grid of image pixels.

Due to the Poisson nature of the data, we used the fit statistic `cstat`, an implementation of Poisson likelihood that can in principle be used similarly to χ^2 for model comparison, but regardless of the number of counts per pixel.[9] Furthermore, we used the differential evolution algorithm implemented as `moncar` for optimization. After performing the fit, we used the methods `conf` to

---

[8] `http://cxc.harvard.edu/sherpa/`

[9] See `https://cxc.cfa.harvard.edu/sherpa/statistics/`

get a rough estimate of fitting uncertainties, and `reg_proj` to obtain a precise view of the error contours (or equivalently the likelihood profile) in the (x, y)-plane.

During the refinement of the fit parameters, we noticed that the reference point for the convolution does not seem to naturally coincide with what we specify as PSF `center` parameter. This behavior is very similar to the one produced by the `CIAO` software bug reported in Becker et al. (2012) which led to the extreme proper-motion velocity reported by Winkler & Petre (2007) and constitutes a potentially serious problem for the analysis of the fit results, since for off-axis sources, this can result in an offset from the best-fit position by as much as a few pixels. Therefore, in order to actually “fixate” the center of the PSF, we additionally needed to specify the hidden parameter `origin` which makes the convolution process behave as expected. As an example, a complete impression of data and fitted models for a single observation (epoch 2010) is given in Figure 3.2. In Table 3.3, we list all best-fit positions for the individual epochs.

There are several things to note about the fitting process: First, as expected, the fitting of two of the calibrator sources proved to be difficult, due to very high background emission (source B) and the quite limited photon statistics (source C). This made the statistical errors on the astrometric calibration for these sources at least an order of magnitude larger than for the fit of the CCO position on the detector. Second, there are systematic offsets between the best-fit X-ray positions and the known optical positions for the stars. This proves that an astrometric correction is justified and needed in order to obtain the highest possible precision on the final result. Also, we would like to highlight that the uncertainties represented by the fit contours cannot be described well with simple independent Gaussian errors in x and y, since they show significant irregularities and interdependencies.

Finally, we observed small but significant deviations between our best-fit positions and the ones in Becker et al. (2012), most noticeably for the NS. This is probably related to differences between the actual PSF models fitted to the data, since it seems unlikely that the data themselves are altered this drastically by our reprocessing. The differences between the two fits were found to be partly explainable by the deviations between nominal centroid and center of mass of the PSF model, which we indicated earlier. At worst, this corresponds to a systematic error in the NS position of around $0.1''$, which could in principle severely bias our final proper motion estimate. However, any minor coordinate offset that is constant over the detector or scales only linearly with x and y will naturally be compensated by our coordinate transformation in Section 3.3.2, since it would apply to all sources equally.

3.3.2 Transformation to the world coordinate system

In principle, there are many ways imaginable to align the coordinate systems of the individual observations. However, given the small number of calibrators, we attempted only two very common types of transformations to the WCS, similar to those applied in Winkler & Petre (2007):

- **Translation:** For each observation, we determined an optimal transformation with two degrees of freedom, corresponding to a simple coordinate offset $(\Delta x, \Delta y)$ in an arbitrary direction:

$$\begin{pmatrix} x' \\ y' \end{pmatrix} = \begin{pmatrix} x \\ y \end{pmatrix} + \begin{pmatrix} \Delta x \\ \Delta y \end{pmatrix}, \tag{3.1}$$

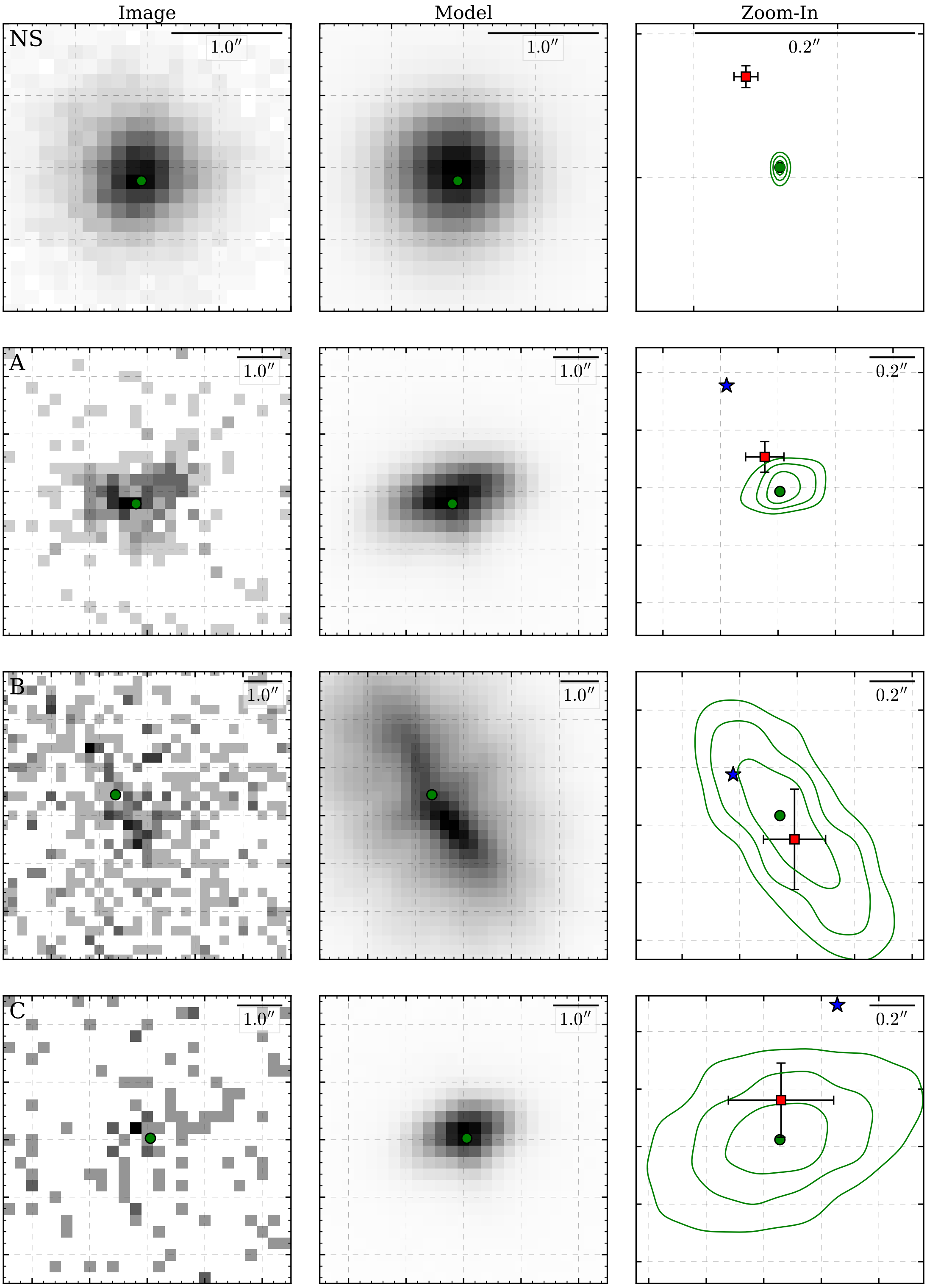

Figure 3.2: Illustration of the PSF fits for the four sources in the 2010 observation (ObsIDs 11819 & 12201). *Left:* Input images; *Center:* Best-fit model, i.e. PSF image convolved with best-fit narrow Gaussian; *Right:* Zoom-in on the source position. We indicate the best-fit (x, y)-position (green circle; as in Table 3.3) with its 1, 2, and 3σ uncertainty contours returned by `reg_proj`; For comparison, we plot the raw best-fit position given in Becker et al. (2012) (red square) and the optical position from *Gaia* projected on our coordinate system (blue star). Data and model images have been binned by a factor of 2 for sources A, B, C and a square-root intensity scale was used to display them.

where x and y correspond to *Chandra* sky coordinates, and x' and y' represent WCS locations projected onto the sky coordinate system.

- **Scaling & Rotation:** In addition to the simple translation, we allowed for a small scale factor of the coordinate system r and a rotation by a small angle θ:

$$\begin{pmatrix} x' \\ y' \end{pmatrix} = \begin{pmatrix} r\cos\theta & -r\sin\theta \\ r\sin\theta & r\cos\theta \end{pmatrix} \begin{pmatrix} x \\ y \end{pmatrix} + \begin{pmatrix} \Delta x \\ \Delta y \end{pmatrix}. \tag{3.2}$$

These two methods are analogous to the available modes of `CIAO`'s standard `wcs_match` script. For the determination of the optimal transformation parameters, we weighted all three calibrators evenly. Thereby, their "center of mass" was relatively close to the actual position of the NS (i.e. the location of the calibrators was not heavily biased toward a certain side of the detector).

Given that a simple Gaussian description of the error is likely an oversimplification, we chose a slightly different approach than Becker et al. (2012) to determine an absolute position of the NS: For each source, we took into account the values of the fit statistic on a finely spaced (x, y)-grid around the best fit, rather than propagating the best-fit and Gaussian uncertainties. The statistic values were extracted using the `Sherpa` task `reg_proj`. For each star i ($i = A, B, C$), the "C statistic" C_i corresponds to the twice the negative logarithm of the Poissonian likelihood $\mathcal{L}_i$. Therefore, we can obtain probability values $P_i(x, y)$ for the position of the star at every point on the grid around the best-fit value by normalizing the total likelihood to one:

$$P_i(x, y) = \frac{\mathcal{L}_i(x, y)}{\sum_{\hat{x},\hat{y}} \mathcal{L}_i(\hat{x}, \hat{y})} = \frac{\exp\left(-\frac{1}{2}\, C_i(x, y)\right)}{\sum_{\hat{x},\hat{y}} \exp\left(-\frac{1}{2}\, C_i(\hat{x}, \hat{y})\right)}, \tag{3.3}$$

where we implicitly assumed a flat prior over our (x, y)-grid, meaning that all viable (and realistic) fit locations are assumed to be within the range of our grid.

From this, we were able to propagate our fit uncertainties without making any strong assumptions on their shape. For the translation method, this is relatively straightforward if we space all our grid points evenly: For each star i, we took the differential between the *Gaia* location at (x', y') and the coordinates of the probability contours at $(x,\ y)$ to obtain a distribution of translation vectors:

$$T_i(\Delta x, \Delta y) \;=\; P_i(x = x' - \Delta x,\ y = y' - \Delta y). \tag{3.4}$$

We then averaged over the three stars by convolving these distributions (corresponding to a summation of the components) and dividing the resulting translation vector by 3. We convolved this average distribution with the distribution of the NS location $P_{\rm NS}(x, y)$ to obtain an estimate of its corrected WCS location.

For the scaling & rotation method, we could not use the same principle since a rotation will automatically "mix" the x and y coordinates, so convolving them on a Cartesian grid is not sensible. Instead, we used the following numerical Monte Carlo technique: For each of the four objects (NS, A, B, C), we sampled $N = 10^6$ points (e.g. $x_{i,1}$, $x_{i,2}$,..., $x_{i,N}$) from their individual probability distributions $P_i(x, y)$. From the samples of A, B, C, we obtained a distribution of the four transformation parameters Δx_n, Δy_n, r_n, and θ_n by fitting them in Equation 3.2. This corresponds to solving the following equation in a standard least-squares manner for each of the N samples.

$$\begin{pmatrix} x_A & -y_A & 1 & 0 \\ y_A & x_A & 0 & 1 \\ x_B & -y_B & 1 & 0 \\ y_B & x_B & 0 & 1 \\ x_C & -y_C & 1 & 0 \\ y_C & x_C & 0 & 1 \end{pmatrix} \begin{pmatrix} r\cos\theta \\ r\sin\theta \\ \Delta x \\ \Delta y \end{pmatrix} \approx \begin{pmatrix} x'_A \\ y'_A \\ x'_B \\ y'_B \\ x'_C \\ y'_C \end{pmatrix}. \tag{3.5}$$

We then applied the individual transformations as in Equation 3.2 to the simulated sample of neutron star locations, to obtain the probability distribution for its absolute location. This method automatically provides us with an estimate for the most likely location of the CCO and detailed uncertainty contours, since it takes into account all likely positions of the individual calibrators. In contrast, we found that standard Gaussian error propagation of only the diagonal elements of the covariance matrix for the transformation parameters leads to an overestimation of the final error on $(x'_{\mathrm{NS}}, y'_{\mathrm{NS}})$, since the transformation parameter values are strongly dependent on each other (i.e. there are large off-diagonal elements in the covariance matrix).

By applying both methods to the PSF fits of each observation, and converting the resulting distributions from sky coordinates to celestial coordinates,[10] we got a clear impression of the motion of the CCO, as can be seen in Figure 3.3. We note that here, as in the following sections, we choose to plot the results from the scaling & rotation method, as it constitutes the more robust coordinate transformation, and its results barely differ from those from the translation method. The corresponding absolute positions, including uncertainties, for both methods are listed in Table 3.4. Here, as everywhere else in this paper, listed uncertainty ranges correspond to the 68 % central interval of the probability distribution of the respective quantity. We note that the relatively large uncertainty on the NS position in 2019 is caused by difficulties in the fitting of the position of source B. In that epoch, it was found to appear significantly fainter than in e.g., the observation from 2005, despite having comparable exposure times.

3.3.3 The proper motion of RX J0822−4300

From the probability distributions for the NS position at four epochs spanning 19.18 years, we were able to determine the most likely value of its proper motion in a relatively straightforward way. We determined the best-fit values μ_α, μ_δ fulfilling the following equation, describing motion at constant speed in two dimensions:

$$\begin{pmatrix} \alpha(t) \\ \delta(t) \end{pmatrix} = \begin{pmatrix} \mu_\alpha \\ \mu_\delta \end{pmatrix} \cdot (t - t_0) + \begin{pmatrix} \alpha_0 \\ \delta_0 \end{pmatrix}, \tag{3.6}$$

where we have introduced the labels α and δ for Right Ascension and Declination, t describes the epoch of the observations in years (with $t_0 = 2019.09$, corresponding to the time of our latest

---

[10] Here, the term “sky coordinates” refers to a tangent-plane system aligned with celestial R.A. and Dec., but measured in pixels (see `https://cxc.cfa.harvard.edu/ciao/ahelp/coords.html`).

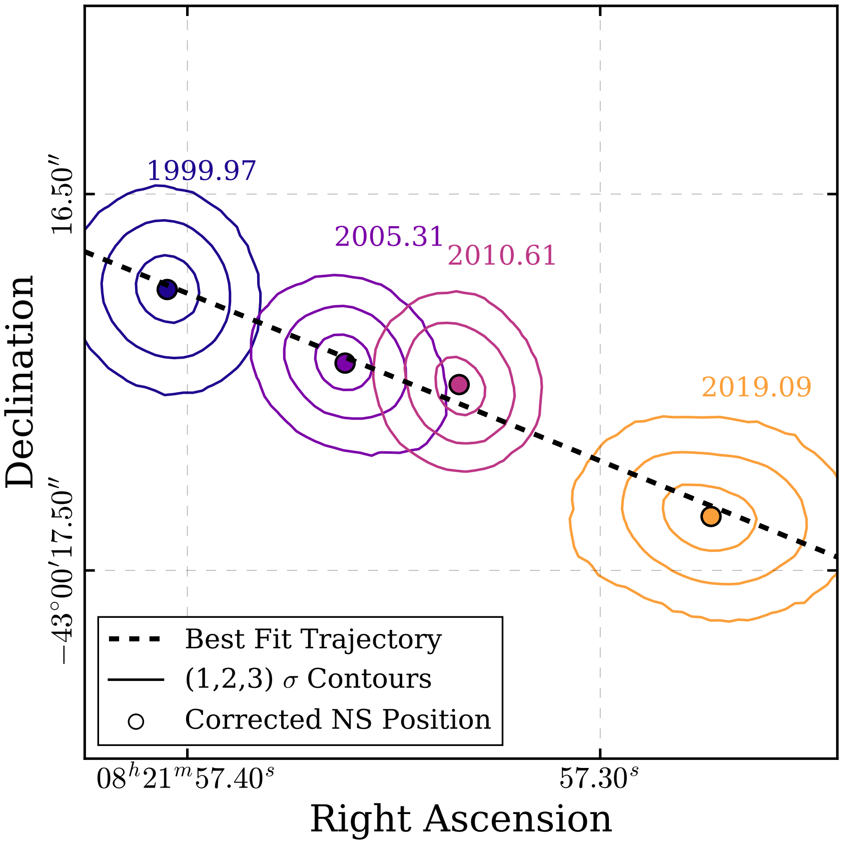

Figure 3.3: Motion of RX J0822−4300. We plot the absolute positions of the NS at the four epochs by indicating the mode and the 1, 2, and 3σ contours (i.e. the smallest regions containing the corresponding fractions of cumulative probability) derived from their distribution. In addition, we indicate the direction of motion (i.e. the best-fit position angle ϕ_0 as determined in Section 3.3.3) with a dashed line. This figure corresponds to an area of $2'' \times 2''$ on the sky.

observation), and α_0, δ_0 correspond to the NS location at t_0. We define μ_α such that a positive value describes an increase in Right Ascension, that is, motion from west to east.

In practice, we performed the fit by again drawing representative samples from the distributions for the individual epochs and then performing a least-squares fit for each sample, leading to a final distribution of proper motion values in (μ_α, μ_δ)-space. With this method, we also obtained an absolute astrometric reference point (α_0, δ_0) for RX J0822−4300, corresponding to its position at the time of our latest observation (epoch 2019.09). By sampling simultaneously in α and δ, we included the effect of any possible interdependence between these parameters, even though the position contours in Figure 3.3 appear to be quite well-behaved. We show representative one-dimensional projections onto the WCS axes of this fit (using the scaling & rotation method) in Figure 3.4 and display the corresponding distribution of proper motion values in Figure 3.5.

The individual corrected positions at the four epochs agree well with the expected linear trajectory. Also, the probability distributions for the source locations and proper motion compo-

Table 3.4: Absolute positions of RX J0822−4300 during four epochs

Epoch	Method	R.A. (J2000.) (h:m:s)	Dec. (J2000.) (d:m:s)
1999.97	Translation	$08{:}21{:}57.402^{+0.008}_{-0.008}$	$-43{:}00{:}16.70^{+0.07}_{-0.10}$
	Scaling & rotation	$08{:}21{:}57.405^{+0.008}_{-0.008}$	$-43{:}00{:}16.75^{+0.09}_{-0.09}$
2005.31	Translation	$08{:}21{:}57.360^{+0.008}_{-0.007}$	$-43{:}00{:}16.93^{+0.08}_{-0.07}$
	Scaling & rotation	$08{:}21{:}57.362^{+0.007}_{-0.007}$	$-43{:}00{:}16.95^{+0.07}_{-0.08}$
2010.61	Translation	$08{:}21{:}57.331^{+0.007}_{-0.008}$	$-43{:}00{:}17.00^{+0.07}_{-0.07}$
	Scaling & rotation	$08{:}21{:}57.334^{+0.007}_{-0.006}$	$-43{:}00{:}17.01^{+0.08}_{-0.08}$
2019.09	Translation	$08{:}21{:}57.271^{+0.014}_{-0.011}$	$-43{:}00{:}17.33^{+0.08}_{-0.09}$
	Scaling & rotation	$08{:}21{:}57.273^{+0.012}_{-0.011}$	$-43{:}00{:}17.36^{+0.09}_{-0.09}$

Notes. We list the median values and 68 % central intervals of the marginalized distributions for Right Ascension & Declination at the given epochs.

nents appear well-behaved and can be described with reasonable accuracy by Gaussian distributions.

In order to exclude large systematic errors in our result due to a possibly biased PSF centroid (see Section 3.3.1), we also tried an alternative approach for the conversion of the fit results to the final proper motion value, by taking the “center of mass” of the PSF image as the precise source location instead of its nominal centroid position. From this analysis, we obtained results that differ by only $\sim 0.5\,\mathrm{mas\,yr^{-1}}$ from the ones shown here. This demonstrates that the effect of such minor potential offsets on the fit output can be balanced by our coordinate transformation method, which inherently compensates for linear distortions of the detector scale.

In order to extract more illustrative quantities from our measurement, we converted the proper motion vector to polar coordinates by defining the total proper motion, μ_{tot}, and the position angle east of north, ϕ_0, as:

$$\mu_{\mathrm{tot}} = \sqrt{\mu_\alpha^2 + \mu_\delta^2} \tag{3.7}$$

$$\tan\phi_0 = \frac{\mu_\alpha}{\mu_\delta}. \tag{3.8}$$

By applying these simple relations to our sample of proper motion vectors, we obtained final probability distributions of the magnitude of the proper motion and of its direction, which we show in Figure 3.6.

We display the resulting astrometric solutions and uncertainties in Table 3.5. The results of the two transformation methods agree very well with each other. Since it constitutes the more robust coordinate transformation, we quote our proper motion from the scaling & rotation method as final: $\mu_{\mathrm{tot}} = 80.4^{+7.7}_{-7.6}\,\mathrm{mas\,yr^{-1}}$ and $\phi_0 = 247.^\circ8^{+4.3}_{-4.4}$.

In general, our values agree within uncertainties with those given in Becker et al. (2012) ($\mu_{\mathrm{tot}} = (71 \pm 12)\,\mathrm{mas\,yr^{-1}}$, $\phi_0 = (244 \pm 11)^\circ$), with our median values corresponding to slightly

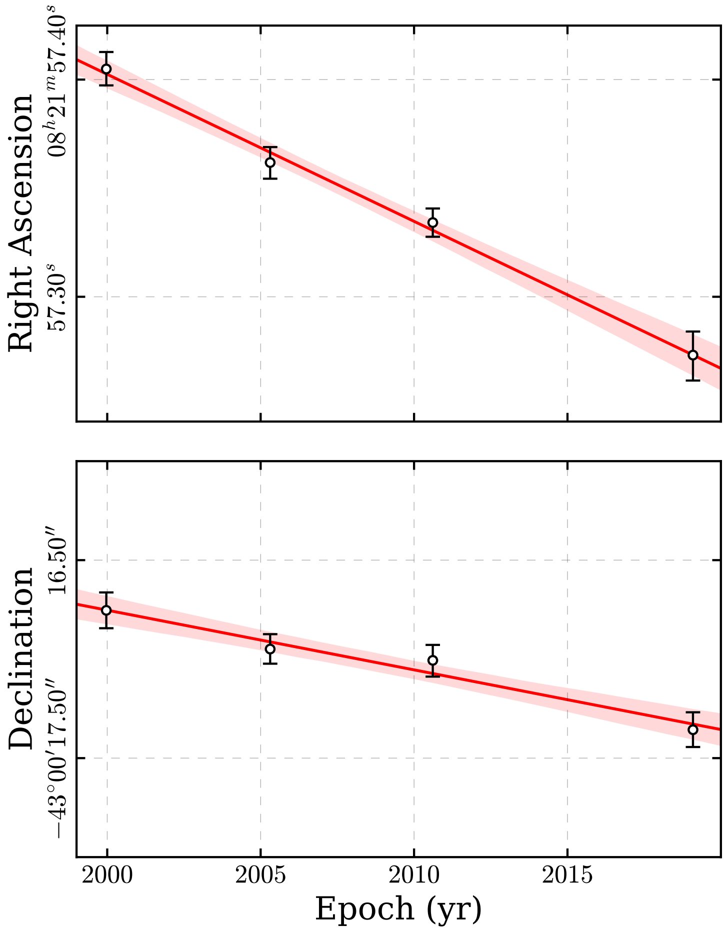

Figure 3.4: Fits to the proper motion of RX J0822−4300 projected onto the right ascension (*top*) and declination (*bottom*) axes. We indicate the median (best-fit) trajectory with a thick red line, and the 68% central interval of possible trajectories as red shaded regions.

higher proper motion and a slightly “shallower” position angle (when projected onto the sky). Naturally, our uncertainty on both values is smaller than theirs, since we have made use of a time baseline almost twice as long. Interestingly however, the relative increase in precision of the position angle is larger than that for the magnitude of proper motion. By looking at Figure 3.3, we can see that this is at least partly due to our position estimate for the observation from 2019, whose error contours are more extended along the direction of motion than perpendicular to it.

Gotthelf et al. (2013a) used an alternative method to constrain the proper motion of RX J0822−4300: They determined the locations of the NS and calibrator stars by measuring their centroids of the observed images. They then corrected the resulting value by the offset between centroid and source positions, as measured from simulated PSF images. They used only star A as a calibrator source, since it is the brightest of the three stars. If we apply this method to our data set, we obtain a proper motion of $(82 \pm 7)\,\mathrm{mas\,yr^{-1}}$ at a position angle of $(249 \pm 4)°$, entirely consistent with our result from PSF fitting.

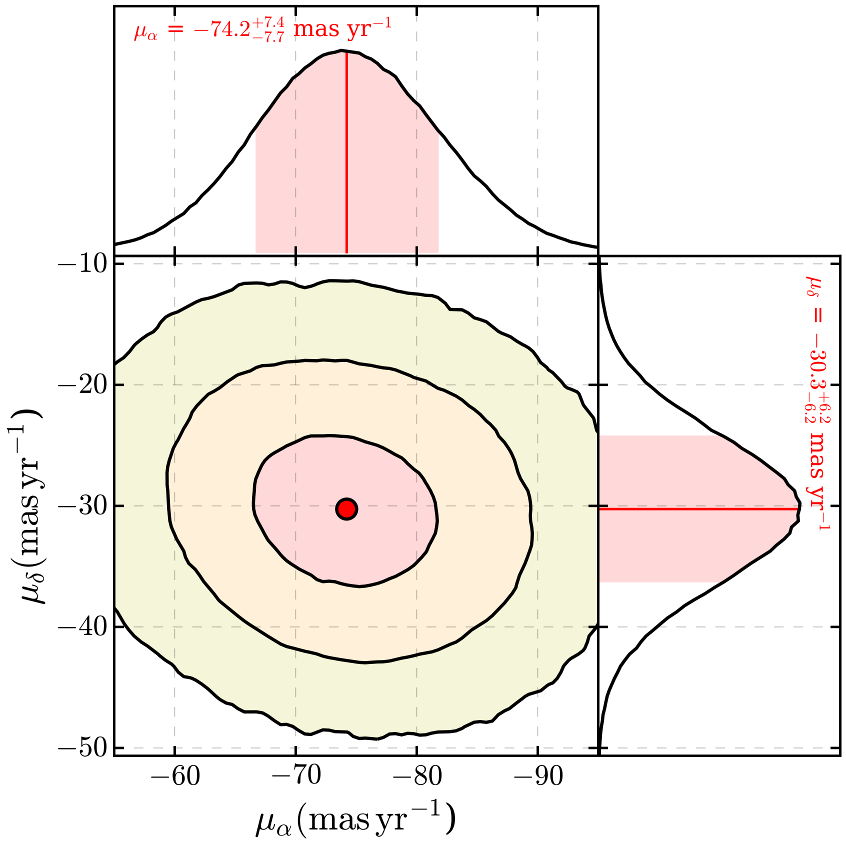

Figure 3.5: Two-dimensional distribution of the proper motion vector (μ_α, μ_δ). We show the best fit (red circle) and the contours corresponding to the cumulative probability within 1, 2, and 3σ, respectively. In the *top* & *right* panels, we show the corresponding marginalized probability distributions for Right Ascension & Declination components of proper motion. We indicate the median values & 68% central intervals for the marginalized quantities in red.

While the statistical errors here are comparable with those from our method, the Gotthelf et al. (2013a) centroid method uses only a single location on the detector to calibrate the astrometric reference frame, neglecting possible systematic distortions over the detector, which our scaling & rotation method includes. It is possible to extend this "corrected centroid" method to stars B and C, but this is non-trivial as it requires an iterative procedure, and it leads to increased statistical errors. We conclude that while both methods are consistent, our PSF fitting technique is the more robust one.

3.4 Discussion

3.4.1 Kinematics and kick mechanism

Our refined measurement of the proper motion of RX J0822−4300 agrees well with the results of Becker et al. (2012), while providing smaller error bars on its magnitude and position angle. Calculating the projected velocity of the neutron star tangential to the line of sight, v_{proj}, at an

Table 3.5: Final Results for the proper motion of RX J0822−4300

Method	μ_α	μ_δ	$\mu_{\rm tot}$	ϕ_0	α_0	δ_0
	(mas yr^{-1})	(mas yr^{-1})	(mas yr^{-1})	(°)	(h:m:s)	(d:m:s)
Translation	$-75.1^{+7.7}_{-8.0}$	$-31.0^{+6.4}_{-6.3}$	$81.6^{+7.5}_{-7.5}$	$247.5^{+4.7}_{-4.7}$	$08{:}21{:}57.272^{+0.009}_{-0.010}$	$-43{:}00{:}17.34^{+0.08}_{-0.08}$
Scaling & rotation	$-74.2^{+7.4}_{-7.7}$	$-30.3^{+6.2}_{-6.2}$	$80.4^{+7.7}_{-7.6}$	$247.8^{+4.3}_{-4.4}$	$08{:}21{:}57.274^{+0.009}_{-0.010}$	$-43{:}00{:}17.33^{+0.08}_{-0.08}$

Notes. The proper motion values in this table correspond to the medians and 68 % central intervals indicated in Figures 3.5 and 3.6. We provide (α_0, δ_0) as reference point for the absolute astrometric position of RX J0822−4300 at the epoch of our latest observation (2019.09, MJD 58516.5).

assumed distance d,[11] we obtain

$$v_{\rm proj} = 763^{+73}_{-72} \times \left(\frac{d}{2\,\rm kpc}\right) \rm km\,s^{-1}. \tag{3.9}$$

This in principle constitutes a lower limit on the kick which the neutron star experienced during the supernova explosion, and therefore an important constraint on supernova modelling. Generally, the conclusions on the kinematics of the system outlined by Becker et al. (2012) hold when considering our updated value. In dependence of neutron star mass $M_{\rm NS}$ and d, we obtain the following expressions for the tangential components (or lower limits) of momentum p and kinetic energy $E_{\rm kin}$ carried by the neutron star:

$$p = (2.12 \pm 0.20) \times \left(\frac{d}{2\,\rm kpc}\right)\left(\frac{M_{\rm NS}}{1.4\,M_\odot}\right) \times 10^{41}\,\rm g\,cm\,s^{-1} \tag{3.10}$$

$$E_{\rm kin} = 8.1^{+1.6}_{-1.5} \times \left(\frac{d}{2\,\rm kpc}\right)^2 \left(\frac{M_{\rm NS}}{1.4\,M_\odot}\right) \times 10^{48}\,\rm erg. \tag{3.11}$$

Assuming a neutron star of mass $1.4\,M_\odot$ at a distance of 2 kpc, we obtain an estimate for the momentum of the CCO of $p = (2.12 \pm 0.20) \times 10^{41}\,\rm g\,cm\,s^{-1}$. This is consistent with the approximate momentum attributed to the ejecta, seen to be expanding toward the northeast as fast, optically emitting filaments (Winkler & Kirshner 1985; Winkler & Petre 2007). For the kinetic energy of the neutron star, we obtain $E_{\rm kin} = 8.1^{+1.6}_{-1.5} \times 10^{48}$ ergs, corresponding to a fraction $f \sim 0.8\,\%$ of the energy released in a canonical core-collapse supernova explosion of 10^{51} ergs.

While older measurements suggest a distance of around 2.2 kpc to Puppis A (e.g. Reynoso et al. 2003), several recent investigations favor a considerably lower distance of around 1.3 kpc (Woermann et al. 2000; Aschenbach 2015; Reynoso et al. 2017). Assuming this lower distance would lead to a significantly smaller projected velocity of $\sim 500\,\rm km\,s^{-1}$, in even better agreement with the upper end of the neutron star velocity distribution (see e.g. Hobbs et al. 2005). Furthermore, the inferred momentum and kinetic energy would be reduced accordingly to around $p \sim 1.4 \times 10^{41}\,\rm g\,cm\,s^{-1}$ and $E_{\rm kin} \sim 3.4 \times 10^{48}$ ergs, respectively. Distance measurements to

---

[11] For the sake of comparability with earlier publications on this topic, we adopt a distance $d = 2$ kpc as reference scale.

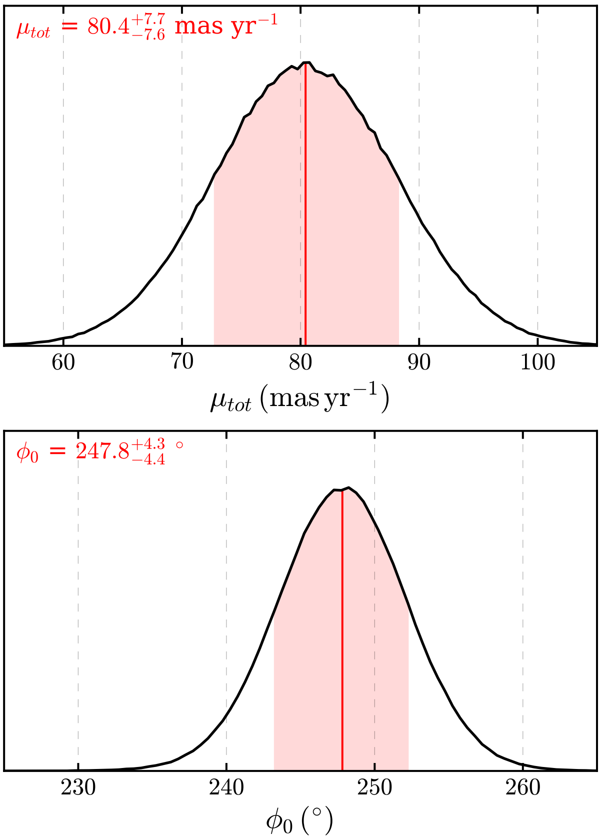

Figure 3.6: *Top:* Marginalized distribution of the total proper motion μ_{tot} with median and 68 % central interval indicated in red. *Bottom:* Same for the position angle ϕ_0.

Galactic supernova remnants are inherently difficult, since most are based on measuring H I or OH absorption features in their (continuum) radio spectrum, and using the presence (or absence) of such features, together with Galactic rotation models, to place lower and upper limits on the distance. Alternative methods based on optical and/or X-ray absorption are typically at least as uncertain.

In principle, natal kicks on neutron stars can occur e.g. via asymmetric neutrino emission during the explosion or via asymmetric ejection of matter due to hydrodynamic instabilities. The latter scenario is supported by the observed relationship between total ejecta mass and neutron star kick velocity (Bray & Eldridge 2016). Wongwathanarat et al. (2013) coined the term “gravitational tug-boat mechanism” for the underlying hydrodynamic mechanism: Massive, slowly moving ejecta on the side opposite the most violent explosion exert a gravitational pull on the newly born neutron star. This results in possible kick velocities on the order of $\sim 1000\,\mathrm{km\,s^{-1}}$ for strongly asymmetric explosions (Janka 2017b). Therefore, our proper motion estimate for RX J0822−4300, and the associated projected velocity are consistent with theoretical considerations for any reasonable assumption on the distance.

The hydrodynamic nature of the kick mechanism is supported by an investigation of the spin properties of RX J0822−4300: While the CCO does exhibit pulsed emission at a period of 0.112 s, its origin is likely to be purely thermal, resulting from periodic modulation of blackbody emission from two antipodal hotspots on the neutron star surface (Gotthelf & Halpern 2009; Gotthelf et al. 2010). The specific properties of these hotspots (temperature and effective area) lead to a phase-reversal of the pulse profile at an energy of around 1.2 keV, rendering the broad-band detection of pulsed emission difficult. Through the analysis of phase-coherent timing observations, Gotthelf et al. (2013a) were able to measure a total period derivative of $\dot{P} = (9.28 \pm 0.36) \times 10^{-18}$ for the pulses of RX J0822−4300. After consideration of the kinematic contribution of the neutron star motion via the Shklovskii effect (Shklovskii 1970), they derived a magnetic field of around 2.9×10^{10} G and a “spin-down age” corresponding to $\sim 2.5 \times 10^{8}$ yr.

The latter quantity is, of course, an unrealistic age estimate, which shows that the implicit assumption of the neutron star being born rotating much faster than today is wrong for this object. In conjunction with the very weak magnetic field they inferred, this contradicts electromagnetic powering of the kick mechanism. Such would require the newly born neutron star to rotate very fast or exhibit a very large magnetic field (Lai 2001). The low magnetic field and small period derivative are shared with other members of the CCO class, thus justifying their designation as “anti-magnetars” (Gotthelf et al. 2013a). A possible explanation for the weak observed dipole field could be that it has been buried by rapid fallback accretion of supernova ejecta after the explosion, and only slowly diffuses back to the surface on a time scale of around 10^4 yr (Bogdanov 2014; Luo et al. 2015).

3.4.2 Age of Puppis A

By extrapolating the motion of the neutron star back in time, our revised proper motion measurement of RX J0822−4300 also provides an updated estimate for the age of Puppis A. Winkler et al. (1988) analyzed the motion of faint, oxygen-rich filaments of the SNR in the optical. They found expansion at very high velocities (up to 1500 km s^{-1}) from a common center located at $\alpha(J2000) = 08^{\mathrm{h}}22^{\mathrm{m}}27.5^{\mathrm{s}}$, $\delta(J2000) = -42°57'29''$. The semi-major axis of the 68 % confidence ellipse on this position is oriented almost exactly along the line toward the CCO (position angle $\phi = 242°$ east of north), and measures $56''$; the semi-minor axis is $34''$ in the transverse direction.[12] Under the assumption of undecelerated trajectories for these dense knots, this center can be considered an estimate for the supernova explosion site. Assuming the errors on the expansion center to be approximately Gaussian, and comparing the coordinates of the expansion center with the position of the CCO in 2019, ($\alpha \approx 08^{\mathrm{h}}21^{\mathrm{m}}57.3^{\mathrm{s}}$, $\delta \approx -43°00'17''$, Table 3.5), we find that the neutron star is located at an angular distance of $372'' \pm 37''$ from the expansion center determined by Winkler et al. (1988). The inferred direction of motion is $243° \pm 4°$, which overlaps, within the errors, with the position angle we measured for the proper motion of RX J0822−4300 in X-rays. We illustrate its past trajectory and the location of the optical expansion center in Figure 3.7.

By weighting our sample of trajectories (Figure 3.5), according to their likelihood of overlap with the observed expansion center and determining the amount of time needed for the CCO to

---

[12] The 68% error ellipse comes from an updated analysis of the original data, and is (naturally) smaller than the 90%-confidence ellipse shown in Winkler et al. (1988).

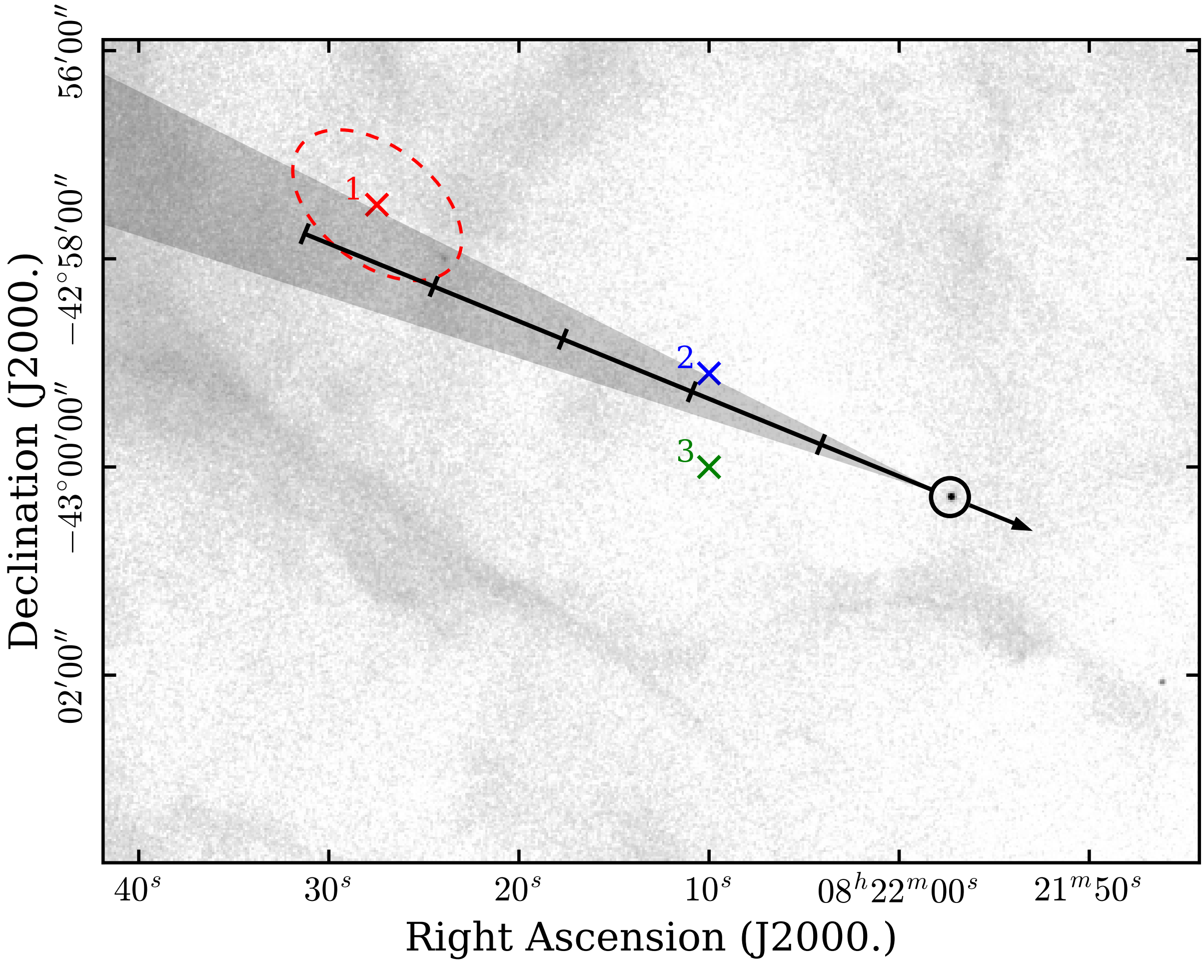

Figure 3.7: X-ray image of the central region of Puppis A with the past trajectory of RX J0822−4300 and directional uncertainties indicated. The optical expansion center of Winkler et al. (1988) and its 68 % confidence ellipse is indicated in red and marked as 1. We also show the location of the alternative remnant center provided by Aschenbach (2015) and the remnant center obtained from radio data (see Green 2019) which are marked as 2 and 3, respectively. For RX J0822−4300, the distance travelled every 1000 years is indicated with ticks.

cover the observed angular distance given the respective proper motion, we obtained an estimate for the kinematic age τ of Puppis A:

$$\tau = 4.6^{+0.7}_{-0.6} \times 10^{3}\,\mathrm{yr}. \tag{3.12}$$

This value is somewhat greater than the SNR age inferred from motion of the optical filaments alone, which Winkler et al. (1988) found to be $(3.7 \pm 0.3) \times 10^{3}$ yr, though the two values agree within the errors. The errors in the total displacement and position angle of the NS from its origin, and in the age of the SNR, are dominated by uncertainties in the expansion center for the system of ejecta filaments.

The neutron star itself is unlikely to have experienced any past deceleration, while the optically visible ejecta might have, due to their far lower density. Therefore, including a uniform deceleration model for the ejecta could possibly increase the minor tension between the two measurements, since the age inferred from optical filaments alone would then be reduced. As Winkler et al. (1988) already noted, the apparent center of the radio shell is offset from the optical expansion center by $\sim 4'$ toward the southwest. Therefore, it may be worthwhile to consider that the actual explosion site might be located closer to RX J0822−4300 than inferred, which would lead to a lower measured age from neutron star proper motion.

Aschenbach (2015) proposed to include an ejecta deceleration model that is not radially symmetric, but allows for different degrees of deceleration along two perpendicular axes. Repeating his approach with our updated proper motion value, the inferred age would be radically reduced by a factor ~ 2.4 to around 1950 yr.[13] The implied location of the remnant center would then be at $\alpha = 08^{\mathrm{h}}22^{\mathrm{m}}10.0^{\mathrm{s}}$, $\delta = -42°59'06''$, lying within one arcminute of the center of the radio shell of the SNR as given in the Green catalogue (Green 2019). While the exact methodology may be a matter of debate here, this example highlights how strongly the kinematic age estimate can be systematically affected by input assumptions, such as an assumed (or neglected) deceleration model.

3.4.3 Proper motion measurements of other CCOs

Proper motion studies of neutron stars are generally a powerful tool for inferring their origin and age as well as the kinematics of the supernova explosion. For radio pulsars, such measurements exist in large numbers, allowing for statistical studies of their distribution (e.g. Hobbs et al. 2005). However, for neutron stars without radio emission, particularly CCOs, there are few such measurements, due to the paucity of objects and the challenging nature of such measurements at other wavelengths.

Apart from the measurement here and in previous works for RX J0822−4300, X-ray proper motion results have been reported for three other CCOs, all with much lower transverse velocities than that of RX J0822−4300. For 1E 1207.4−5209, located in the SNR PKS 1209−51/52, Halpern & Gotthelf (2015) measured a relatively small proper motion of $(15 \pm 7)\,\mathrm{mas\,yr^{-1}}$, $v_{\mathrm{proj}} < 180\,\mathrm{km\,s^{-1}}$ for a distance of 2 kpc. For CXO J232327.8+584842 in Cas A, DeLaney & Satterfield (2013) measured a marginally significant projected velocity of $(390 \pm 400)\,\mathrm{km\,s^{-1}}$ for a distance of 3.4 kpc, which corresponds to a proper motion of $(24 \pm 25)\,\mathrm{mas\,yr^{-1}}$. Lastly, for the proper motion of CXO J085201.4-461753 in the Vela Jr. SNR (G266.2−1.2), only a 3σ upper limit of $< 300\,\mathrm{mas\,yr^{-1}}$, corresponding to $< 1400\,\mathrm{km\,s^{-1}}$ for a distance upper limit of 1 kpc, could be determined (Mignani et al. 2019). The latter two cases suffered from a lack of nearby calibrator sources, explaining their relatively large statistical errors.

All this illustrates that in order to perform proper motion measurements of CCOs to similar precision as in this work, the temporal baseline covered by the data must be quite long, the object should be located relatively nearby, and there must be astrometric calibrator sources in the field

---

[13] Aschenbach (2015) originally states an age of (1990 ± 150) yr, based on the proper motion of Becker et al. (2012), which enters his calculations explicitly.

of view.

3.5 Summary

We have incorporated a new *Chandra* observation of the central region of Puppis A to perform the most precise proper motion measurement of RX J0822−4300 to date. In particular, we have generalized the treatment of positional errors and used all available information from optical calibrator stars to obtain reliable position estimates and errors at all epochs. Our results are consistent within errors with those of Becker et al. (2012). We obtain a projected velocity of $763^{+73}_{-72}\,\mathrm{km\,s^{-1}}$, for a distance of 2 kpc to Puppis A. While this value lies on the upper end of the observed neutron star velocity distribution, it does not pose a challenge for theoretical supernova models, since such speeds are achievable with hydrodynamical kick mechanisms. If the actual distance to Puppis A is smaller, as recent measurements suggest, then the velocity will become proportionally smaller as well.

The direction of neutron star motion is consistent with the measurement of the supernova explosion site from optical filament expansion by Winkler et al. (1988). Our new measurement of the proper motion implies an age of 4600^{+700}_{-600} yr for the remnant, which is somewhat older than that derived from proper motions of the optical filaments alone. An important pillar for our age determination of Puppis A is the location of the optical center of expansion. The best currently available estimate is now over 30 years old and was based on digitization of photographic plates from three epochs over a total baseline of only 8 years. An updated measurement of the proper motions for the ejecta filaments based on CCD images, ideally from several epochs over an extended baseline, is long overdue. Images for such a measurement are in-hand, and the results will be reported separately (Winkler et al., in prep.). If one then finds a significant disagreement between the age based on the motion of optical filaments and that from extrapolation of the neutron star trajectory, this could point toward non-ballistic motion of the supernova ejecta clumps due to their interaction with the surrounding ISM.

Chapter 4

A kinematic study of central compact objects and their host supernova remnants

This chapter is largely based on a work published as Mayer & Becker (2021) in Astronomy & Astrophysics, Volume 651, A40, with the exception of Fig. 4.16, which was not included in the published paper.

4.1 Introduction

It is generally accepted that collapsing massive stars (i.e., core-collapse supernovae) leave behind a compact remnant, a neutron star (NS) or black hole. A natural consequence of asymmetries in core-collapse supernovae is a strong kick acting on the compact remnant (e.g., Wongwathanarat et al. 2013), whose kinematics are thus directly connected to explosion properties. Proper motion studies of NSs are therefore a powerful tool that allows a lower limit to be set on the kinetic energy and momentum transferred to the NS during the explosion of the progenitor. Beyond that, depending on its age, the proper motion of an NS may reveal its origin or even the exact supernova explosion site, which can be used to robustly infer the age of the NS and/or associated supernova remnant (SNR).

For radio pulsars, which make up the vast majority of known NSs, proper motion can be measured precisely for a comparatively large number of sources, using precise positions from pulsar timing or very-long-baseline interferometry. This allows for population studies of NS kinematics, as for example by Hobbs et al. (2005) and Verbunt et al. (2017). Such works establish the picture of NSs being very high-speed objects, with a mean three-dimensional velocity around $400\,\mathrm{km\,s^{-1}}$, and reliably measured projected velocities at least as high as $\sim 800\,\mathrm{km\,s^{-1}}$.

In contrast to radio pulsars, for NSs exhibiting at best weak radio and optical emission – such as magnetars, X-ray-dim isolated NSs, or central compact objects (CCOs) in SNRs – such measurements are much more challenging. While all three of these NS classes are characterized by primarily thermal X-ray emission, CCOs are particularly noteworthy for being exclusively young ($\lesssim 10^4$ yr) and nonvariable X-ray sources, located close to the center of SNRs. Unlike radio pulsars, they show no signs of interaction with their surroundings, such as extended nebu-

Table 4.1: CCOs with basic properties of their host SNRs.

SNR	CCO	Distance (kpc)	Age (yr)	References
G15.9+0.2	CXOU J181852.0−150213	7 – 16	2900 – 5700	1,2,3
Kes 79	CXOU J185238.6+004020	3.5 – 7.1	4400 – 6700	4,5,6,7
Cas A	CXOU J232327.9+584842	3.4	$\sim$ 350	8,9
Puppis A	RX J0822−4300	1.3 – 2.2	2000 – 5300	10,11,12,13,14
G266.1−1.2 (Vela Jr.)	CXOU J085201.4−461753	0.5 – 1.0	2400 – 5100	15
PKS 1209−51/52 (G296.5+10.0)	1E 1207.4−5209	1.3 – 3.9	$\sim$ 7000	16,17
G330.2+1.0	CXOU J160103.1−513353	4.9 – 10.0	$\lesssim$ 1000	18,19,20
RX J1713.7−3946 (G347.3−0.5)	1WGA J1713.4−3949	1.0 – 1.3	1500 – 2300	21,22,23,24
G350.1−0.3	XMMU J172054.5−372652	4.5	$\sim$ 600	25,26,27
G353.6−0.7	XMMU J173203.3−344518	$\sim$ 3.2	$\sim$ 27 000	28,29

Notes. The two SNRs G349.7+0.2 (Lazendic et al. 2005) and G296.8−0.3 (Sánchez-Ayaso et al. 2012) have been claimed to potentially host CCOs. Since *Chandra* data suitable for our purposes do not exist for either SNR, these sources are not considered further in our work.

References. (1) Tian et al. (2019), (2) Sasaki et al. (2018), (3) Maggi & Acero (2017), (4) Ranasinghe & Leahy (2018), (5) Kuriki et al. (2018), (6) Kilpatrick et al. (2016), (7) Zhou et al. (2016), (8) Fesen et al. (2006), (9) Alarie et al. (2014), (10) Reynoso et al. (2017), (11) Reynoso et al. (2003), (12) Aschenbach (2015), (13) Winkler et al. (1988), (14) Chapter 3 (Mayer et al. 2020), (15) Allen et al. (2015), (16) Giacani et al. (2000), (17) Roger et al. (1988), (18) McClure-Griffiths et al. (2001), (19) Williams et al. (2018), (20) Borkowski et al. (2018), (21) Fukui et al. (2003), (22) Cassam-Chenaï et al. (2004), (23) Acero et al. (2017), (24) Tsuji & Uchiyama (2016), (25) Lovchinsky et al. (2011), (26) Bitran et al. (1997), (27) Borkowski et al. (2020), (28) Maxted et al. (2018), (29) Tian et al. (2008).

lar or jet-like emission. Furthermore, their spectra can be described entirely using blackbody or NS atmosphere models with luminosities $\gtrsim 10^{33}\,\mathrm{erg\,s^{-1}}$, without any unambiguous evidence for nonthermal magnetospheric emission (see Becker 2009; Gotthelf et al. 2013a; De Luca 2017). Despite intensive searches (e.g., Mignani et al. 2008, 2019), no point-like or diffuse counterparts to any CCO at radio, infrared, or optical wavelengths have been found with present-day instrumentation. This places tight upper limits on the presence of potential binary companions and indicates no need for additional components to explain the observed spectral energy distribution.

We give an overview[1] of known CCOs in Table 4.1. Out of the ten known CCOs, X-ray pulsations have only been detected for those in Kes 79, Puppis A, and PKS 1209−51/52. These pulsations at 100−500 ms are likely attributable to the rotational modulation of the emission from hotspots on the NS surface (Gotthelf et al. 2010, 2005; Zavlin et al. 2000). Analysis of their spin-down points toward CCOs having a very weak magnetic dipole field. This, in combination with their steady emitting behavior, led to their designation as “anti-magnetars” (Gotthelf et al. 2013a; Halpern & Gotthelf 2010a).

An important issue is that, observationally, few orphaned CCOs, meaning older pulsars without an apparent nearby SNR but in a similar location of $(P, \dot{P})$–space, have been found (Luo

---

[1] For a more expansive review of CCOs and their characteristics, we refer to De Luca (2017) and the overview table on CCOs at `http://www.iasf-milano.inaf.it/~deluca/cco/main.htm`.

et al. 2015). It has therefore been suggested that the phenomenology of CCOs is caused by magnetic field burial due to the fallback accretion of material shortly after the supernova explosion. The magnetic field is then believed to resurface and evolve into a macroscopic dipolar field on timescales of $\sim 10^4$ yr, placing the object in a different region of parameter space (e.g., Bogdanov 2014; Luo et al. 2015; Gourgouliatos et al. 2020).

Since they are exclusively detected in X-rays, the proper motion of CCOs can currently only be measured directly using data from the *Chandra* X-ray Observatory, which presently is the only X-ray telescope providing sufficient spatial resolution for the task. Prior to this work, this has been attempted for five CCOs, with very diverse results: Most prominently, such measurements have been performed multiple times for RX J0822−4300, located in the SNR Puppis A (Hui & Becker 2006a; Winkler & Petre 2007; Becker et al. 2012; Gotthelf et al. 2013a; Mayer et al. 2020). Owing to the increasing temporal baseline, their precision has improved strongly over the years, the most recent value (see Chapter 3) being $(80.4 \pm 7.7)\,\mathrm{mas\,yr^{-1}}$, at 68% confidence. This corresponds to a projected velocity of $(763 \pm 73)\,\mathrm{km\,s^{-1}}$ for a distance of 2 kpc, which potentially places this CCO at the fast end of the NS velocity distribution.[2] In contrast, for the CCO in PKS 1209−51/52, Halpern & Gotthelf (2015) measured a much smaller proper motion of $(15 \pm 7)\,\mathrm{mas\,yr^{-1}}$, which corresponds to a projected velocity below $180\,\mathrm{km\,s^{-1}}$ for a distance of 2 kpc. Only weak constraints could be placed on the proper motions of the CCOs in Cas A (DeLaney & Satterfield 2013) and G266.2−1.2 (Vela Jr., Mignani et al. 2019), owing to a paucity of X-ray bright field sources for astrometric frame registration. Finally, very recently, Borkowski et al. (2020) have shown that the CCO in G350.1−0.3 seems to exhibit only modest proper motion, contrary to expectations (see Sect. 4.4.6).

Alternatively to a direct measurement, it can be feasible to infer the proper motion of an NS indirectly, if its origin (i.e., the explosion site) and the age of the SNR are known sufficiently precisely (e.g., Lovchinsky et al. 2011; Fesen et al. 2006). However, if the estimate for the explosion site is solely based on the apparent present-day morphology of the SNR, this method is much more prone to systematic biases than the direct one. The main reason is that the apparent geometric center of an SNR does not necessarily coincide with its true explosion site. This was first shown by Dohm-Palmer & Jones (1996), who demonstrated numerically that SNRs expanding into interstellar medium with a density gradient can show significant offsets between their morphological center and their true explosion site, despite maintaining a relatively circular shape.

A previous study by Holland-Ashford et al. (2017) explores the relationship between the proper motions of 18 young NSs (four of which are CCOs), and the morphology of their host SNRs. Several of their proper motion measurements are obtained directly from X-ray imaging data, with others (including those for all four CCOs) being inferred indirectly. They do not find any correlation between the magnitude of SNR asymmetry and the projected velocity of the NSs. However, they find that an anticorrelation exists between the direction of proper motion and the direction of brightest ejecta emission, a proxy to highest ejecta mass. A similar study based on six

---

[2] The main source of uncertainty in the projected velocity is the distance to Puppis A. While, in the past, values around 2 kpc were assumed, it has been most recently measured to be 1.3 kpc (Reynoso et al. 2017), implying a smaller velocity.

systems by Katsuda et al. (2018) confirms this observation. In addition, the latter work does find a positive correlation between the degree of SNR asymmetry and the NS kick velocity. These findings support a hydrodynamic kick mechanism, where the NS reaches its extreme velocity due to asymmetric ejection of matter during the explosion, rather than via a neutrino-induced channel.

The most immediate handle on the age of an SNR is the direct measurement of its expansion. This approach yields a robust upper limit on the age since any physically justifiable assumption about the expansion history of the SNR would result in an age estimate lower than that for free expansion.[3] Tracing the expansion of an SNR is in principle possible at all wavelengths that allow to resolve the relevant emission features at sufficiently high resolution, such as the radio, optical, and X-ray regimes. Typically, the optical regime yields the most precise age constraints since astrometric uncertainties are very small. Moreover, the optical emission usually originates from high density ejecta clumps, which are subject to little deceleration by the circumstellar medium. A popular example is Cas A, whose explosion date was quite precisely determined by Thorstensen et al. (2001) and Fesen et al. (2006) to around the year 1670.

However, many young SNRs are not visible at optical wavelengths, often due to Galactic absorption. In this case, X-ray expansion measurements are a powerful tool to constrain age and internal kinematics, despite the lower spatial resolution and higher deceleration of the observed features. Examples for the viability of this method include the confirmation of the nature of G1.9+0.3 as the youngest Galactic SNR (Borkowski et al. 2014), the analysis of the propagation of the northwestern rim of the "Vela Jr" SNR (G266.1−1.2, Allen et al. 2015), or multiple recent efforts to trace the shock wave propagation of the TeV SNR RX J1713.7−3946 (Acero et al. 2017; Tsuji & Uchiyama 2016; Tanaka et al. 2020). Measurements of precisely dated very young SNRs (such as Cas A, Tycho's, or Kepler's SNR) show that expansion as traced in X-rays typically appears somewhat decelerated compared to the expectation for free expansion (Patnaude & Fesen 2009; Hughes 2000; Vink 2008). This highlights that SNR expansion measurements generally provide only an upper limit on their true age.

Central compact objects together with their parent SNRs present an ideal target for combining kinematic information from both the NS and the supernova shock wave. Since such systems are exclusively young, one can expect to be able to measure large expansion velocities, corresponding to a significant fraction of their undecelerated value. In addition, a precisely measured proper motion of the CCO provides accurate constraints on the supernova explosion site, the exact origin of the SNR shock wave. Combining these constraints promises unbiased results on the SNR's kinematics and age as both the starting point and the present-day location of the shock wave are known.

The goal of this work is to establish a complete and internally consistent sample of proper motion measurements for CCOs and of expansion measurements for their host SNRs. We aim to provide direct constraints on the motion of all currently known CCOs (with appropriate data available) for which this task has not been previously performed. The ultimate target of this effort is to search for indications of violent supernova kicks, manifesting themselves in large velocities,

---

[3] A notable exception is the Crab nebula, whose expansion has been accelerated in the past, likely due to energy input from the central pulsar (Trimble 1968; Nugent 1998).

and to constrain the location of the true center of targeted SNRs, with respect to their present-day morphology. For the three SNRs for which an expansion measurement has not yet been carried out at the time of writing, we perform an independent expansion study using our combined data set.

Our paper is organized as follows: We outline our data selection and reduction in Sect. 4.2 and describe our analysis strategy in Sect. 4.3. We then give a detailed overview over the results for each individual CCO/SNR in Sect. 4.4. Finally, we discuss physical consequences of the compiled sample of proper motion and expansion measurements in Sect. 4.5, and summarize our results in Sect. 4.6. Unless stated otherwise, all errors given in this paper are computed at 68%, and all upper limits at 90% confidence.

4.2 Data selection and reduction

Our initial list of potential targets for analysis consisted of the SNRs listed in Table 4.1. From this list, we excluded Puppis A, PKS 1209−51/52 (due to already precisely measured proper motion of the CCO) and Vela Jr. (due to the established lack of astrometric calibrators, Mignani et al. 2019). Even though the proper motion of the CCO in Cas A has already been constrained directly (DeLaney & Satterfield 2013), we decided to include it in our target list, in order to apply our own methodology to the data.

We searched the *Chandra* Data Archive[4] for existing imaging observations covering the remaining potential targets. We took into account data sets from both *Chandra* imaging detectors, the High Resolution Camera (HRC Murray et al. 2000) and the Advanced CCD Imaging Spectrometer (ACIS, Garmire et al. 2003). Whenever possible, we preferred all our observations to be taken with the same detector. The archival data were required to span a minimum temporal baseline of five years in order to qualify for a proper motion measurement. Suitable sets of observations that fulfill these criteria were found for six targets, the SNRs G15.9+0.2, Kes 79 (G33.6+0.1), Cas A, G330.2+1.0, RX J1713.7−3946 (G347.3−0.5) and G350.1−0.3. For G353.6−0.7, we found only a single suitable observation in imaging mode (taken in 2008), not permitting further analysis for our purpose. Out of the six target SNRs, the expansion of three (Cas A, G330.2+1.0, RX J1713.7−3946) has been measured directly in past studies (Fesen et al. 2006; Borkowski et al. 2018; Acero et al. 2017; Tsuji & Uchiyama 2016; Tanaka et al. 2020).[5] This left us with the SNRs G15.9+0.2, Kes 79 and G350.1−0.3 as targets for an expansion measurement.

A journal of all observations used in our analysis is given in the appendix in Table B.1. For some of our targets, such as G330.2+1.0 and G350.1−0.3, there are multiple observations with very deep coverage, promising high-precision results. In contrast, for RX J1713.7−3946, we found only two shallow observations that contain the CCO, taken with different detectors. This made performing a meaningful measurement more challenging and prone to systematic effects. In all cases treated in our sample, the target is only covered at two epochs that are spaced far

---

[4] `https://cda.harvard.edu/chaser/`

[5] The expansion study of G350.1−0.3 by Borkowski et al. (2020) was published during the preparation of this work.

enough apart in time to perform a proper motion measurement, despite most having multiple closely spaced observations at one of the epochs.

We reprocessed all archival data using the *Chandra* Interactive Analysis of Observations (`CIAO`, Fruscione et al. 2006) task `chandra_repro` with standard settings, to create level 2 event lists calibrated according to current standards. For ACIS data, we enabled the option to use the Energy-Dependent Subpixel Event Repositioning (`EDSER`) algorithm (Li et al. 2004), to be able to exploit on-axis data at optimal spatial resolution. We used `CIAO` version 4.12 and the calibration database (CALDB) version 4.9.0 throughout the work described in this paper. After the reprocessing step, we screened all data for soft proton flares, excluding the few affected time intervals with background levels 3σ above the respective quiescent average, yielding cleaned and calibrated event lists on which we based our subsequent analysis.

4.3 Methods

Our main analysis strategy consisted of several steps: First, we searched for serendipitous field sources for astrometric calibration (Sect. 4.3.1), which we then used to align the coordinate frames of the observations and simultaneously fit for the CCO's proper motion (Sect. 4.3.2). For the three target SNRs of our expansion study, we exploited the astrometrically aligned data set to quantify the radial motion of key features of the SNR (Sect. 4.3.3).

4.3.1 Astrometric calibration sources

While the underlying principle of a proper motion analysis is rather straightforward, practically performing such a measurement in X-rays poses some challenges: Owing to uncertainties in aspect reconstruction, absolute source positions in *Chandra* images are only accurate to around $0.8''$ at 90% confidence.[6] In order to maximize the precision of the CCO's position and proper motion, it is thus necessary to align the coordinate system of our observations to an absolute reference, the International Celestial Reference System (ICRS). For this purpose, it is optimal to use serendipitous sources in the field of view with precisely known astrometric positions. Since most of our systems had not been studied in the context of a proper motion analysis previously, we searched for the presence of such calibrator sources systematically:

From the cleaned event lists, we extracted images over the entire detector area, which we binned at 1×1 and 2×2 detector pixels for ACIS and HRC, respectively. For ACIS, we included only events in the standard broad band, $0.5 - 7.0\,\mathrm{keV}$. We then employed the `CIAO` task `wavdetect` to perform wavelet-based source detection and rough astrometric localization at a detection threshold of 10^{-5}. We chose this rather "generous" threshold since we required the presence of a source in all observations in order for it to qualify as a calibrator. This eliminated the need to strictly reject potentially spurious sources in the individual detection runs.

For each of the observations, we matched the output source detection lists to the *Gaia* DR2 catalog[7] (Gaia Collaboration et al. 2016, 2018), which offers by far the best accuracy of all astro-

---

[6] `https://cxc.harvard.edu/cal/ASPECT/celmon/`

[7] `https://www.cosmos.esa.int/web/gaia/dr2`

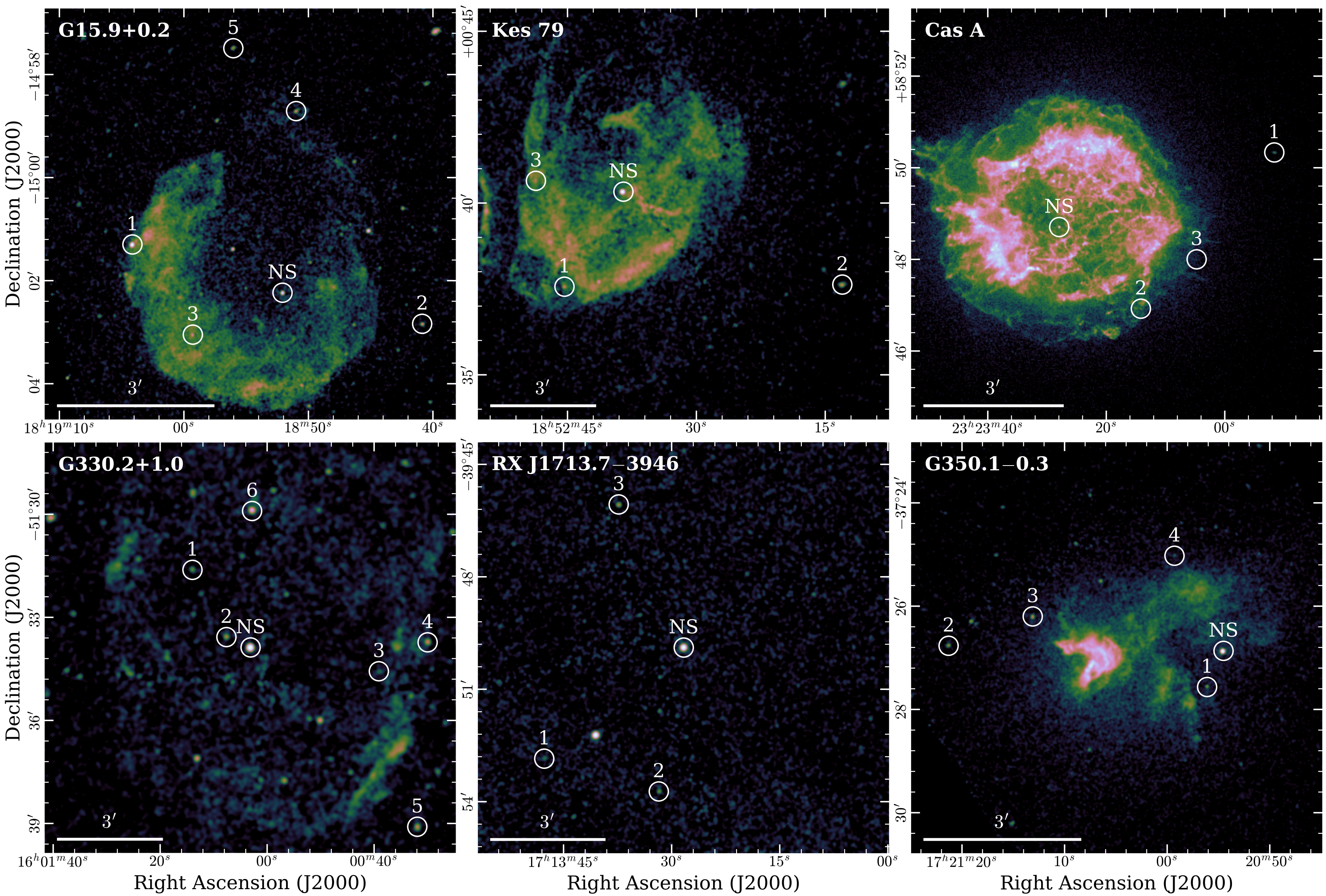

Figure 4.1: Overview over all target SNRs, with positions of the NS and the calibrator sources (labeled as in Table B.2) indicated on exposure-corrected images of the respective SNR. We show the deepest available observation for all targets except for RX J1713.7−3946, where we used the ACIS observation (ID 5559) instead of the HRC observation, due to its lower intrinsic noise level.

metric catalogs available at the time of writing. Those *Gaia* sources with an X-ray counterpart within at most 1.5″ in each observation made up our candidate list. We then visually inspected these candidates, excluding those sources that we deemed unreliable, for example because of large positional errors in X-rays or doubts in their correct optical identification. If many potential reference sources were found across the detector, we selected a subset of reliably identified and bright sources, spread evenly across the detector.

In further analysis steps, we occasionally decided to exclude objects from our list of frame registration sources. Reasons for this include the presence of a nearby overlapping source, the disagreement of positional offsets determined from different calibrator sources, or simply the failure to provide useful constraints compared to brighter sources. We display the calibrator source positions as well as the location of the respective target CCOs within their SNRs in Fig. 4.1. In addition, the list of astrometric reference sources used for our analysis is given in the appendix in Table B.2, where we also indicate which of the sources we decided to exclude in subsequent steps.

4.3.2 Proper motion analysis of CCOs

Our method for measuring the proper motion of CCOs followed the approach used in Chapter 3 and Becker et al. (2012). The main difference to these previous works is the performance of a simultaneous fit for the object's proper motion and the astrometric calibration of individual observations, which provides a natural way to deal with observations of varying depth (Sect. 4.3.2).

PSF modelling and fitting

The first step was the precise measurement of the positions of all sources, that is, of the CCO and calibrator objects, at each epoch. We closely followed the procedure outlined and discussed in depth in Sect. 3.3.1 to obtain models of the *Chandra* point spread function (PSF) via ray-tracing simulations, using the `ChaRT` (*Chandra* Ray Tracer) online tool[8] and the `MARX` software package[9] (Davis et al. 2012, version 5.4.0). As in Chapter 3, we fitted the respective PSF models to source image cutouts, using the spectral and image fitting program `Sherpa` (Freeman et al. 2001).[10] For each source in each observation, we obtained a profile of the logarithmic likelihood $\mathcal{L}_{ij}(x, y)$ of the source position on a finely spaced grid (typical spacing $\lesssim 20\,\mathrm{mas}$) in the region around the best fit (see Fig. 3.2). In our notation, the variables x and y describe relative positions as measured by *Chandra* in a tangent plane coordinate system around the approximate location of the CCO, while we use the indices i and j to label the individual observations and objects (including $j = 0$ for the CCO).

---

[8] `http://cxc.harvard.edu/chart/index.html`

[9] `http://space.mit.edu/CXC/MARX/`

[10] `http://cxc.harvard.edu/sherpa/`

Coordinate transformation and proper motion fit

In the next step, we corrected the astrometry of each observation for minor misalignment with the ICRS by applying a linear transformation to the *Chandra* coordinate system. This transformation allowed for a positional shift as well as a small stretch and rotation of the coordinate system. Prior to the analysis, two groups of "interesting" parameters were unknown:[11]

First, the astrometric solution of the CCO with the set of free parameters $\{\mu_\alpha, \mu_\delta, \alpha_0, \delta_0\}$,[12] describing its proper motion and its position at a reference epoch t_0, in right ascension (α) and declination (δ), respectively. Second, a set of transformation parameters $\{\Delta x_i, \Delta y_i, r_i, \theta_i\}$ per observation i, describing translation in the tangent plane, as well as minor scaling and rotation corrections to the coordinate frame.

We made the realistic assumption that the errors on *Gaia* positions of calibrator stars can be neglected when compared to the errors in measured X-ray source positions. Thus, the true[13] calibrator source positions were effectively known prior to the observation. Therefore, for each of our targets, there was a set $\mathbf{\Lambda} = \{\mu_\alpha, \mu_\delta, \alpha_0, \delta_0, \Delta x_1, \Delta y_1, ..., r_N, \theta_N\}$ of $4+4\times N$ parameters (with N the number of observations included), which were a priori unknown.

In order to constrain their values, we calculated the logarithmic likelihood for a given set of parameters, $\mathcal{L}_\mathrm{tot}(\mathbf{\Lambda})$, in the following manner: For a given astrometric solution $\{\mu_\alpha, \mu_\delta, \alpha_0, \delta_0\}$, we computed the true position of the CCO (x'_{i0}, y'_{i0}), at the epoch of observation i according to:

$$\begin{pmatrix} x'_{i0} \\ y'_{i0} \end{pmatrix} = \begin{pmatrix} -\mu_\alpha \\ \mu_\delta \end{pmatrix} \cdot (t_i - t_0) + \begin{pmatrix} \alpha_0 \\ \delta_0 \end{pmatrix}, \tag{4.1}$$

where t_i is the time of observation i. The fixed parameter t_0 describes the reference epoch, for which we always chose the time of the most recent observation in our respective data set. The true positions (x'_{ij}, y'_{ij}) of the calibrator sources were computed analogously, using their known *Gaia* astrometric solutions.

These true positions were then converted to measured positions (x_{ij}, y_{ij}), to account for a coordinate system shift modeled by the parameters $\{\Delta x_i, \Delta y_i, r_i, \theta_i\}$:

$$\begin{pmatrix} x_{ij} \\ y_{ij} \end{pmatrix} = r_i \begin{pmatrix} \cos\theta_i & -\sin\theta_i \\ \sin\theta_i & \cos\theta_i \end{pmatrix} \begin{pmatrix} x'_{ij} \\ y'_{ij} \end{pmatrix} + \begin{pmatrix} \Delta x_i \\ \Delta y_i \end{pmatrix}. \tag{4.2}$$

The likelihood of a given measured position was evaluated by interpolating the logarithmic likelihood grid $\mathcal{L}_{ij}(x, y)$, which we computed as described in the previous section. By summing over the contributions of all N observations and S sources, the total likelihood for a set of parameters $\mathbf{\Lambda}$ could then be straightforwardly calculated:

$$\mathcal{L}_\mathrm{tot}(\mathbf{\Lambda}) = \sum_{i=1}^{N} \sum_{j=0}^{S} \mathcal{L}_{ij}\left(x = x_{ij}(\mathbf{\Lambda}),\ y = y_{ij}(\mathbf{\Lambda})\right). \tag{4.3}$$

---

[11] Of course, other parameters such as source count rates and background levels were also unknown. However, for our purpose, the only globally interesting parameters are related to source positions.

[12] We follow the convention that $\mu_\alpha = \dot{\alpha}\cos(\delta)$, so that the proper motion is directly proportional to the object's physical velocity. Positive μ_α corresponds to motion from west to east.

[13] In the following, we refer to a position calibrated to the ICRS as "true" position, while a "measured" position describes the position determined in the coordinate system of a particular *Chandra* observation.

In order to extract the most likely proper motion solution, it is necessary to derive the posterior probability distribution for $\mathbf{\Lambda}$, which is implied by our likelihood function in its $(4 + 4 \times N)$–dimensional parameter space. To achieve this in practice, we used the `UltraNest`[14] software (Buchner 2021), which employs the nested sampling Monte Carlo algorithm `MLFriends` (Buchner 2016, 2019), to robustly tackle this multi-dimensional problem. We used uninformative (flat, truncated) priors on all variables since we wanted our study to be as independent as possible from external assumptions.

This method is equivalent to performing the PSF fits to all sources at all epochs simultaneously, under the constraints of NS motion at constant velocity and known positions of all calibrators. The advantage compared to a truly simultaneous implementation is that our method allows for very efficient evaluation of the likelihood function via interpolation on a precomputed grid. With our approach, sources with large measured positional uncertainties only add little weight to the fit, and thus do not "wash out" the final result. Furthermore, covariances between parameters as well as non-Gaussian errors are properly taken into account.

However, the main caveat of this approach is that it neglects the possible presence of any systematic offsets beyond the linear coordinate transformation allowed by our fit. Such offsets could be caused by subtle differences between different detectors and roll angles or by the possible misidentification of a frame registration source with the wrong astrometric counterpart. To identify such potential systematic effects, we visualized our model's predictions in the following way: For each point in the posterior sample of our fit, we computed the expected location of each source in the *Chandra* coordinate system (x_{ij}, y_{ij}). The distribution of these locations was then compared to the measured uncertainty contours, or equivalently the contours of $\mathcal{L}_{ij}(x, y)$. This allowed us to check whether the results given by our simultaneous fit were sensible for all objects, and to recognize potentially misidentified astrometric calibrators. An example of such a comparison, illustrating the strongly varying scales of our astrometric uncertainties, is shown in Fig. 4.2.

Correction for effects of solar motion and Galactic rotation

Ultimately, we attempt to extract physically meaningful quantities, such as NS velocity, with reference to the "rest frame" of the SNR. Therefore, it is necessary to take into account the expected motion of the NS from Galactic rotation alone (see e.g., Hobbs et al. 2005; Halpern & Gotthelf 2015). If this effect were not considered, our estimate of the physical CCO velocity would be contaminated by the motion of the sun and the rotation of the Galactic disk.

To determine the local standard of rest (LSR) of a system, we assumed the linear Galactic rotation curve and solar velocity given in (Mróz et al. 2019). For each system, the expected velocity for corotation with the disk was expressed as two components of proper motion in equatorial coordinates, $(\mu_\alpha^{\mathrm{LSR}}, \mu_\delta^{\mathrm{LSR}})$. From its distance d, proper motion, and LSR, it was then possible to determine the peculiar (projected) velocity of an object, v_{proj}^* as

$$v_{\mathrm{proj}}^* = \mu_{\mathrm{tot}}^* \times d = \sqrt{\left(\mu_\alpha - \mu_\alpha^{\mathrm{LSR}}\right)^2 + \left(\mu_\delta - \mu_\delta^{\mathrm{LSR}}\right)^2} \times d. \tag{4.4}$$

---

[14] `https://johannesbuchner.github.io/UltraNest/`

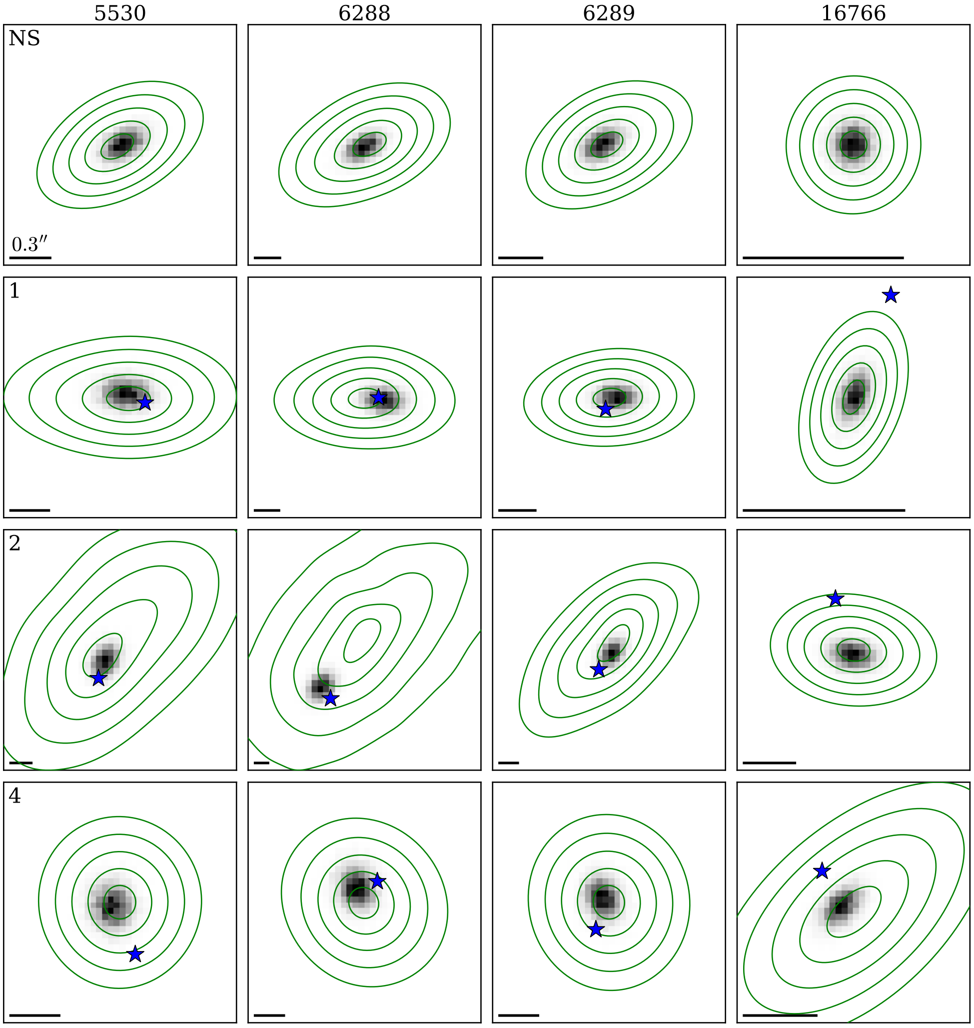

Figure 4.2: Illustration of PSF-fit likelihood for the source position and the prediction by our simultaneous proper motion fit for the CCO of G15.9+0.2. Each column corresponds to one individual epoch (with the observation ID displayed in the title), while each row represents one particular object. The one to five sigma contours of the PSF-fit likelihood $\mathcal{L}_{ij}(x, y)$ are shown in green, and the predicted positions obtained from our simultaneous fit (see posterior distribution in Fig. 4.4) are indicated using a grayscale two-dimensional histogram. In the lower left corner of each panel, we provide a reference scale of length $0.3''$. We display the true source position for our calibrator stars (known from *Gaia*) with a blue star. The uncertainty contours for observation 16766 are by far the smallest since the corresponding exposure was much deeper than at the other epochs (at $\sim 90\,\mathrm{ks}$).

One complication here is that, for some of our targets, the SNR distance d is not constrained precisely. For these cases, we assumed a flat probability distribution over the interval between its lower and upper limit (see Table 4.1 for available constraints). The resulting distribution of $(\mu_\alpha^{\mathrm{LSR}}, \mu_\delta^{\mathrm{LSR}})$ was then appropriately convolved with our distribution of the proper motion of the CCO. In practice, we found that the uncertainty on the LSR is significantly smaller than the uncertainty on the proper motion of all our targets.

A further technical issue is that, due to our choice of flat priors on (μ_α, μ_δ) in Sect. 4.3.2, the resulting probability distribution for μ^*_{tot} is biased toward large values. This is because, in the transformation to μ^*_{tot}, one essentially integrates over concentric circles of increasing radius, introducing an effective prior $\propto \mu^*_{\mathrm{tot}}$, and always leading to a peak of the distribution at nonzero μ^*_{tot}. Therefore, in order to not overestimate the projected velocity of our CCOs, we reweighted the posterior distributions by a factor $\propto 1/\mu^*_{\mathrm{tot}}$. The effect of this correction decreases with increasing significance of nonzero proper motion.

4.3.3 Expansion measurement of SNRs

When studying the dynamics of a young core-collapse SNR, a complementary tool to the analysis of the NS's proper motion is the measurement of the SNR's expansion. It provides the most immediate constraint on the shock velocity in its shell, and, by backward extrapolation, can be used to provide a very reliable constraint on its maximum age. Therefore, we took advantage of our results from the previous section, and measured the expansion of three CCO-hosting SNRs (G15.9+0.2, Kes 79, G350.1−0.3) in the following way:

First, we used the optimal transformation parameters $\{\Delta x_i, \Delta y_i, r_i, \theta_i\}$ for each observation i from Sect. 4.3.2, to perform the astrometric calibration of our data set. Since we fitted for the motion of the CCO and the frame calibration simultaneously, this had the advantage that, for observations taken close to each other in time, the position of the CCO (which is often the brightest source) was forced to be identical. This practically provided an additional reliable source for coordinate frame calibration. We aligned the data from all observations to a common coordinate system, using the `CIAO` task `wcs_update` with a `transformfile` customized to contain the optimal transformation parameters derived in Sect. 4.3.2. All data from observations taken at the same epoch were then merged and reprojected to a common tangent plane using `reproject_obs`. The systematic error in the coordinate frame alignment can be conservatively estimated from the combined statistical uncertainties of $\{\Delta x_i, \Delta y_i\}$, yielding typical values between $0.1''$ and $0.3''$.

In order to define the features of interest for our measurement, we extracted exposure-corrected images of each SNR in the standard ACIS broad band (0.5 − 7.0 keV). We then used `SAOImage ds9` (Joye & Mandel 2003) to interactively define rectangular regions containing emission features that we found suitable to trace the expansion of the SNR, for example sharp filaments or individual clumps. Since we were mostly interested in measuring radial motion, the orientation of these boxes was adapted to what we deemed the probable direction of motion given the shape of the feature and its location within the SNR.[15] In order to avoid any possible confirmation bias toward the detection of expansion, we refrained from excluding regions in retrospect, even if their motion turned out to be almost unconstrained by the available data.

At this point, it would be possible to determine the motion of an individual feature and its errors, for instance by fitting a model for the flux profile to the data of both epochs (e.g., Xi et al.

---

[15] We note that even for potential misalignment with the true direction of motion as large as 20°, the measured expansion speed would only deviate by $1 - \cos(20°) = 6\%$ from the true value.

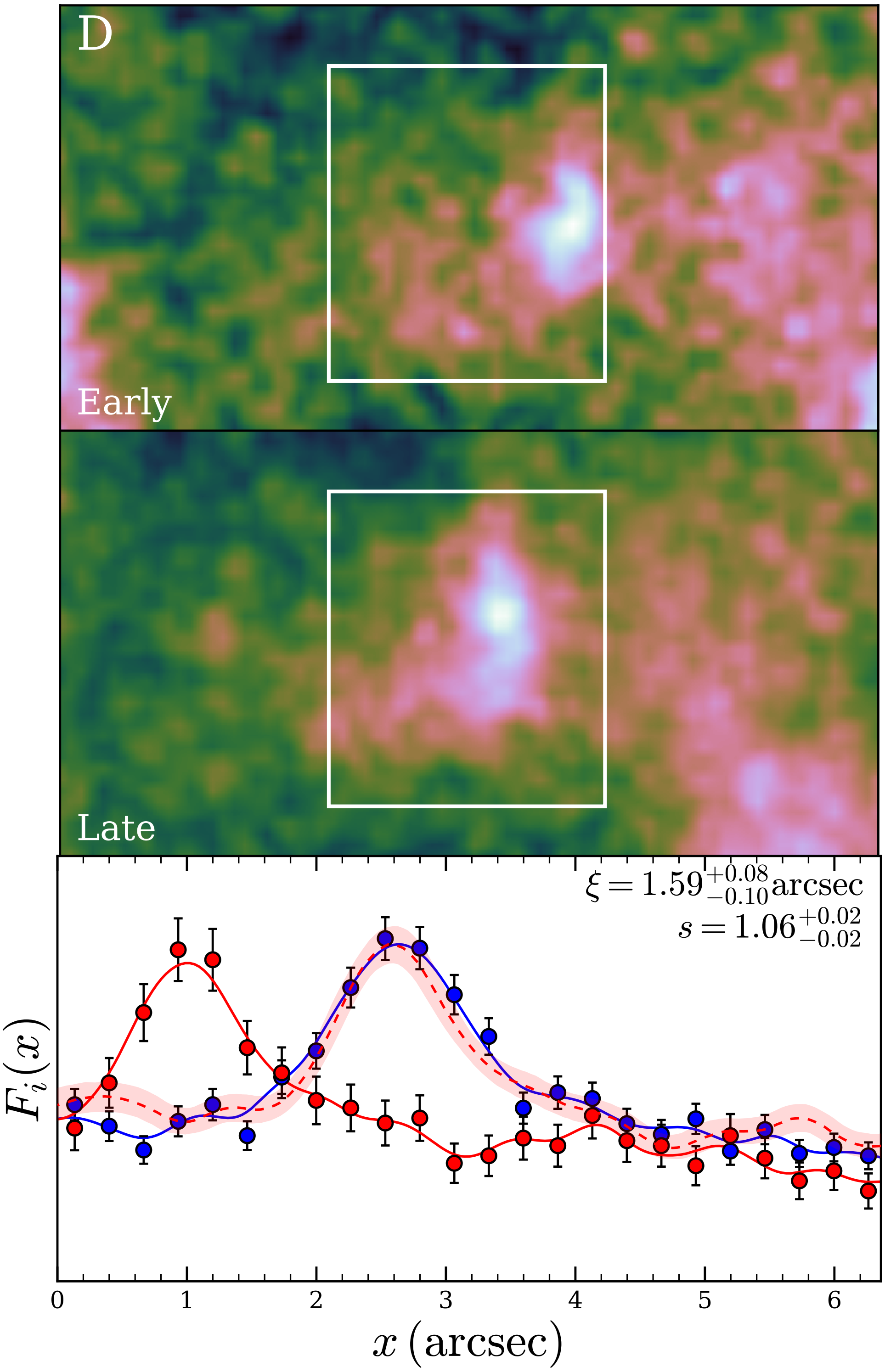

Figure 4.3: Example expansion measurement in region D of G350.1−0.3 (see Sect. 4.4.6). The *top* and *middle* panels depict the exposure corrected images at the early and late epoch, and the white rectangle marks the measurement region. The *bottom* panel displays the one-dimensional flux profiles $F_i(x)$ at the early (red) and late (blue) epoch. The markers display the binned distributions with errors, and the solid lines reflect the flux profiles smoothed by a Gaussian kernel. The dashed red line corresponds to the profile of the early epoch, shifted and rescaled by the indicated parameters (see upper right corner), with the shaded area displaying the associated uncertainty from bootstrapping. We define the x coordinate such that it increases in radial direction, meaning from west to east in this case.

2019). However, since some clumps and filaments targeted in this work show a rather complex profile, it seems infeasible to empirically model their shape, because the required number of free parameters would be high, or one would need to hand-tune the model for each feature. Alternatively, one could directly compare the observed emission profiles via a custom likelihood function (often some variant of χ^2) quantifying their deviation, in one (e.g., Tanaka et al. 2020; Tsuji & Uchiyama 2016), or two dimensions (e.g., Borkowski et al. 2020). However, after some initial testing, we found that such a likelihood function behaves quite erratically in many cases, meaning that small sub-pixel variations in the shift of the profiles lead to large "jumps" in the likelihood. This makes a direct determination of errors prone to systematics and irreproducible for varying bin sizes.

Thus, in order to avoid biased results or underestimated errors, we used a bootstrap resampling technique (Efron 1982) to estimate uncertainties for the motion of all our features: We extracted the set of X-ray event coordinates $\mathbf{x}_i$ (with $i = 1, 2$ labeling the early/late observational epoch) along the suspected direction of expansion, as well as the corresponding exposure profile, within the rectangular region of each feature. For both epochs, we created $N = 1000$ randomized realizations of the observed data set $\{\mathbf{x}^*_{1,i}, ..., \mathbf{x}^*_{N,i}\}$, via sampling with replacement from the list of observed events in the region. Thereby, the statistical uncertainty of the emission profile was approximated by the intrinsic scatter of our resampled data sets.

From each resampled data set $\mathbf{x}^*_{n,i}$, we extracted one-dimensional flux profiles $F_i(x)$ describing the emission along the (expected) direction of motion. For each bin x, we estimated a simple Gaussian flux error as $\sigma_i(x) = F_i(x)/\sqrt{C_i(x)}$, where $C_i(x)$ describes the number of events in the bin. In order to estimate the optimal shift between the epochs, we defined the function f, which quantifies the deviation between the emission profiles at early and late epochs, in dependence of a positional shift ξ and an amplitude scale factor s:

$$f(\xi, s) = \sum_x \frac{\left(sF_1(x-\xi) - F_2(x)\right)^2}{s^2\sigma_1^2(x-\xi) + \sigma_2^2(x)}, \tag{4.5}$$

where s was introduced to account for possible flux changes of the feature.

By minimizing f for each of the N realizations, we obtained a sample approximately distributed according to the likelihood of ξ. From this distribution, we extracted the angular speed μ_{exp} of the emission feature given by $\mu_{\mathrm{exp}} = \xi/\Delta t$, with Δt being the difference between the average event times of the early and late epochs. This is related to the projected expansion velocity via $v_{\mathrm{exp}} = \mu_{\mathrm{exp}} d$, where d corresponds to the (assumed) distance to the SNR.

The last step of estimating the global minimum of f is however complicated by the noisy nature of our function on small spatial scales. The reason for this is that the binning of events required to obtain an image is only an approximation to the underlying continuous flux distribution of a feature, which introduces a "granularity" in f. We resolved this issue by applying a Gaussian kernel to smooth the flux histograms $F_i(x)$ before computing f. The width of the kernel was chosen so as to not over-smooth the prominent features in each region, but at the same time eliminate most of the purely statistical bin-to-bin fluctuations. Other approaches, like smoothing only one of the profiles or applying Poisson statistics to directly compare the two unsmoothed profiles, were found to typically yield similar or larger intrinsic errors. The basic principle of our approach is visualized for an example region in G350.1−0.3 in Fig. 4.3.

The main advantage of our method is that we only extracted the optimal value of ξ for each realization. We therefore did not need to perform any "stepping" through parameter space to obtain the errors from a given likelihood threshold as we would consider this likely to yield underestimated statistical errors. Furthermore, our method allowed us to implicitly account for statistical fluctuations in both measurement epochs, which would be neglected when treating the deeper observation as a definitive "model" without intrinsic errors.

As a simple practical test of our approach, we used two late-time data sets of G350.1−0.3 (ObsIDs 21118 and 21119) and applied our method, as if trying to measure expansion. Naturally, the true shift of features between these two observations is essentially nonexistent due to the small time difference of around one day. Therefore, one expects the results of our experiment to cluster around zero, tracing not the motion of features but the intrinsic noise of our method. We find that the overall deviation from zero of our measurements can be satisfactorily accounted for with statistical and systematic errors. More quantitatively, the sum of normalized squared deviations from zero, $\chi^2 = \sum_{k=1}^{K} \xi_k^2 / \Delta\xi_k^2$, is found to be $\chi^2 = 19.1$ for $K = 18$ regions (i.e., "degrees of freedom"), when accounting only for statistical uncertainties. Adding in quadrature the estimated systematic error of $0.1''$, we obtain $\chi^2 = 14.3$. The expected 68% central interval of a χ^2 distribution with 18 degrees of freedom is $[12.1, 23.9]$. Therefore, our test demonstrates that we obtain reasonable estimates for our total uncertainty, and that our overall error estimates are likely rather conservative.

4.4 Results

4.4.1 G15.9+0.2

G15.9+0.2 is a small-diameter Galactic SNR, first detected in the radio by Clark et al. (1973). In X-rays, its morphology resembles that of an incomplete, but very symmetric, circular shell. It shows a northwestern "blowout" region with only weak apparent emission, likely due to reduced density of the circumstellar medium (Sasaki et al. 2018). Its distance is only constrained to a relatively uncertain range of values (7 – 16 kpc, Tian et al. 2019), and accordingly, the age shows correlated uncertainties of a factor of two (2900 – 5700 years, Sasaki et al. 2018).

The bright CCO CXOU J181852.0−150213 is quite clearly offset by around $35''$ from the apparent geometrical center of the SNR toward the west or southwest. As first noted by Reynolds et al. (2006), this seems to imply a quite large transverse velocity, or a proper motion of around 10 mas yr^{-1} for an assumed age of 3500 years.

Unfortunately, the available data at the early epoch are split into three nonconsecutive observations of 5.0, 9.2, and 15.1 ks length, with the detector aimpoint being located around $3'$ north of the CCO, which reduces the usability of this data set for our purpose. In contrast, the late observation is very deep (with an exposure around 90 ks) and aimed directly at the CCO, resulting in very small statistical errors on its late-time position.

The resulting posterior distribution from our astrometric fit can be seen in Fig. 4.4. The 68%

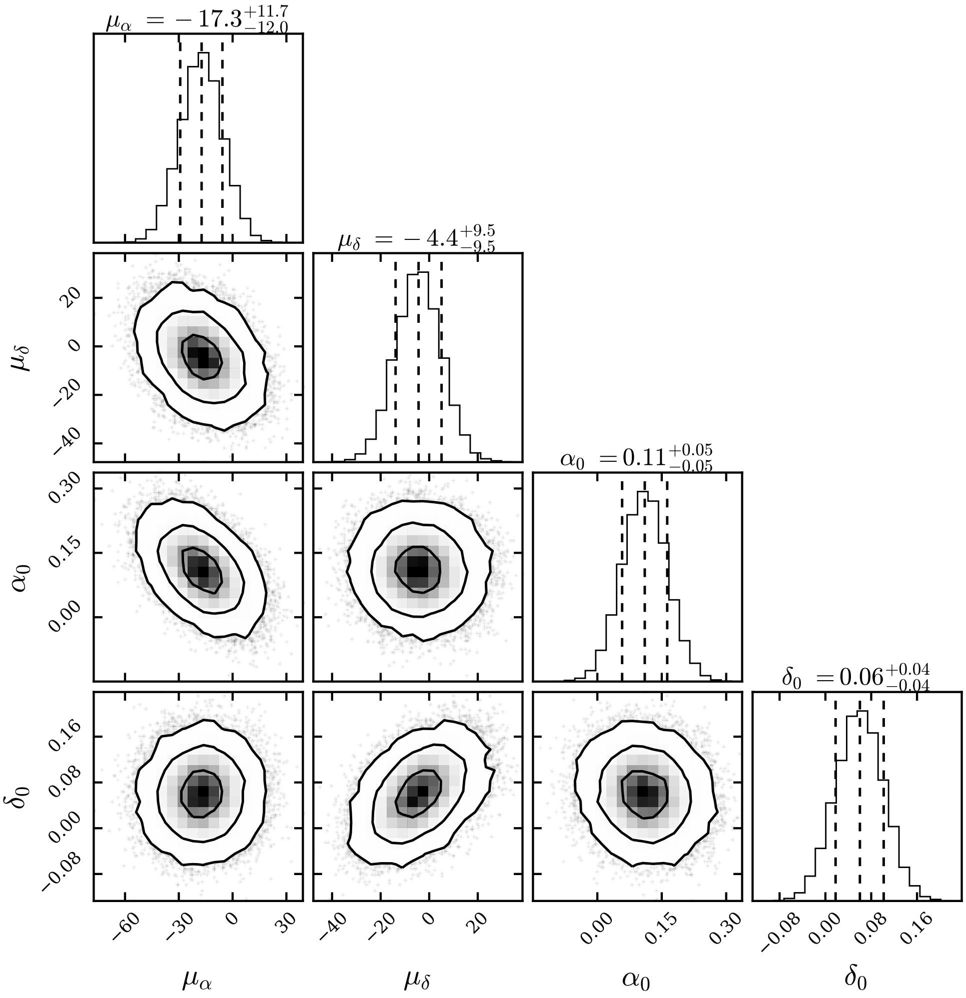

Figure 4.4: Corner plot displaying the joint and marginal posterior distributions for the parameters of the astrometric solution for the CCO in G15.9+0.2. The astrometric calibration parameters $\{\Delta x_i, \Delta y_i, r_i, \theta_i\}$ have been marginalized over, and are not shown here in order to keep the figure uncluttered (see Table B.3 for constraints on all parameters). In the two-dimensional correlation plots, we indicate the 1σ, 2σ, and 3σ contours, meaning the smallest regions containing 39.3%, 86.5%, and 98.9% of the total probability mass, with solid lines. In the marginalized one-dimensional histograms, we indicate the median and 68% central interval of the posterior probability distribution, with dashed lines. The units of proper motion and the astrometric zero-point are mas yr^{-1} and arcsec, respectively. This plot and analogous figures have been created using the `corner.py` package (Foreman-Mackey 2016).

central credible intervals for the proper motion are given by $(-17 \pm 12, -4 \pm 10)$ mas yr^{-1}, in right ascension and declination, respectively. This seems to agree well with the expected proper motion direction given the CCO's present-day location in the SNR.

While this cannot be counted as an unambiguous detection of significant proper motion for the CCO, a proper motion of the order of 15 mas yr^{-1} toward west seems realistic given the SNR geometry. It would imply a rather large projected velocity of the NS around 700 km s^{-1} when

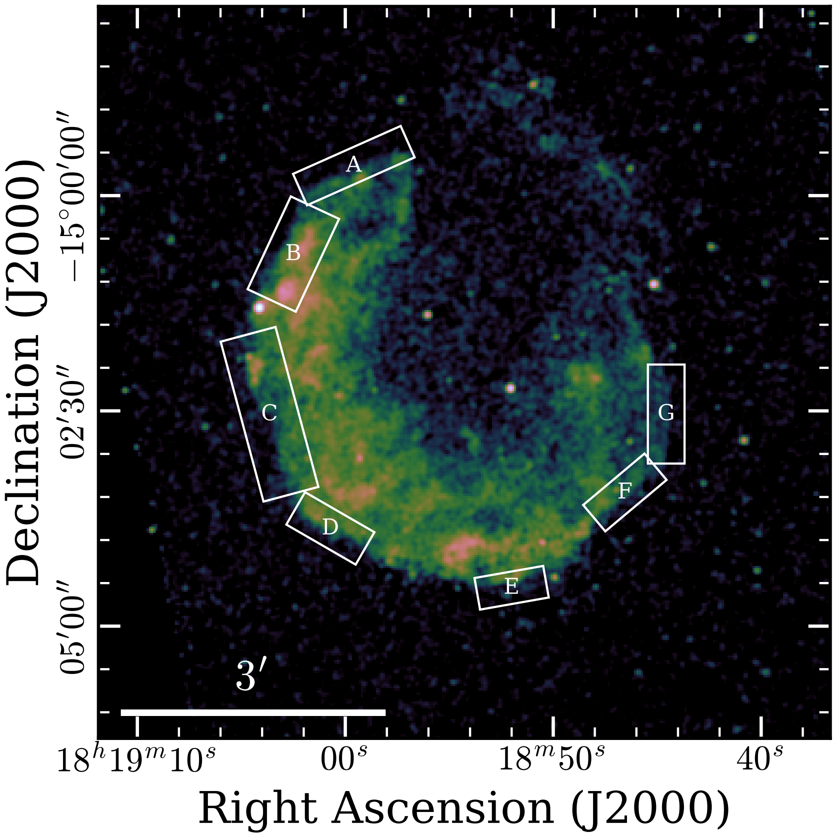

Figure 4.5: SNR G15.9+0.2 with regions used for the expansion measurement indicated. We show a smoothed, exposure-corrected image of the SNR with logarithmic scaling of the color map. We overlay the boxes from which we extracted the one-dimensional emission profiles for our expansion measurement, and label them alphabetically for easier identification and to avoid confusion with numeric labels for the astrometric calibrator stars.

scaling to a distance of 10 kpc. The formal 90% upper limit of 25 mas yr^{-1} (corresponding to 1200 km s^{-1} for that distance) on the total proper motion with respect to the LSR of G15.9+0.2 is physically unconstraining.

The almost perfectly circular shape of G15.9+0.2 allowed us to define quite intuitive regions along its outer rim for an expansion measurement. They are illustrated in Fig. 4.5. As can be seen, all regions trace the motion of the edge of the SNR shell, and due to the observed morphology, we would expect to observe quite similar expansion speeds along all directions. Minor problems faced in their definition were the bright star "1" superimposed on the eastern shell and a detector chip gap crossing the southernmost part of the remnant, both of which we avoided with our choice of regions.

In order to define a rough reference point for the expansion of the SNR, we used `SAOImage ds9` (Joye & Mandel 2003) to approximate the shell of the SNR with a circle. Its center at $(\alpha, \delta) = (18^{\rm h}18^{\rm m}54\overset{\rm s}{.}2, -15°01'55'')$ corresponds to the probable location of the explosion, with

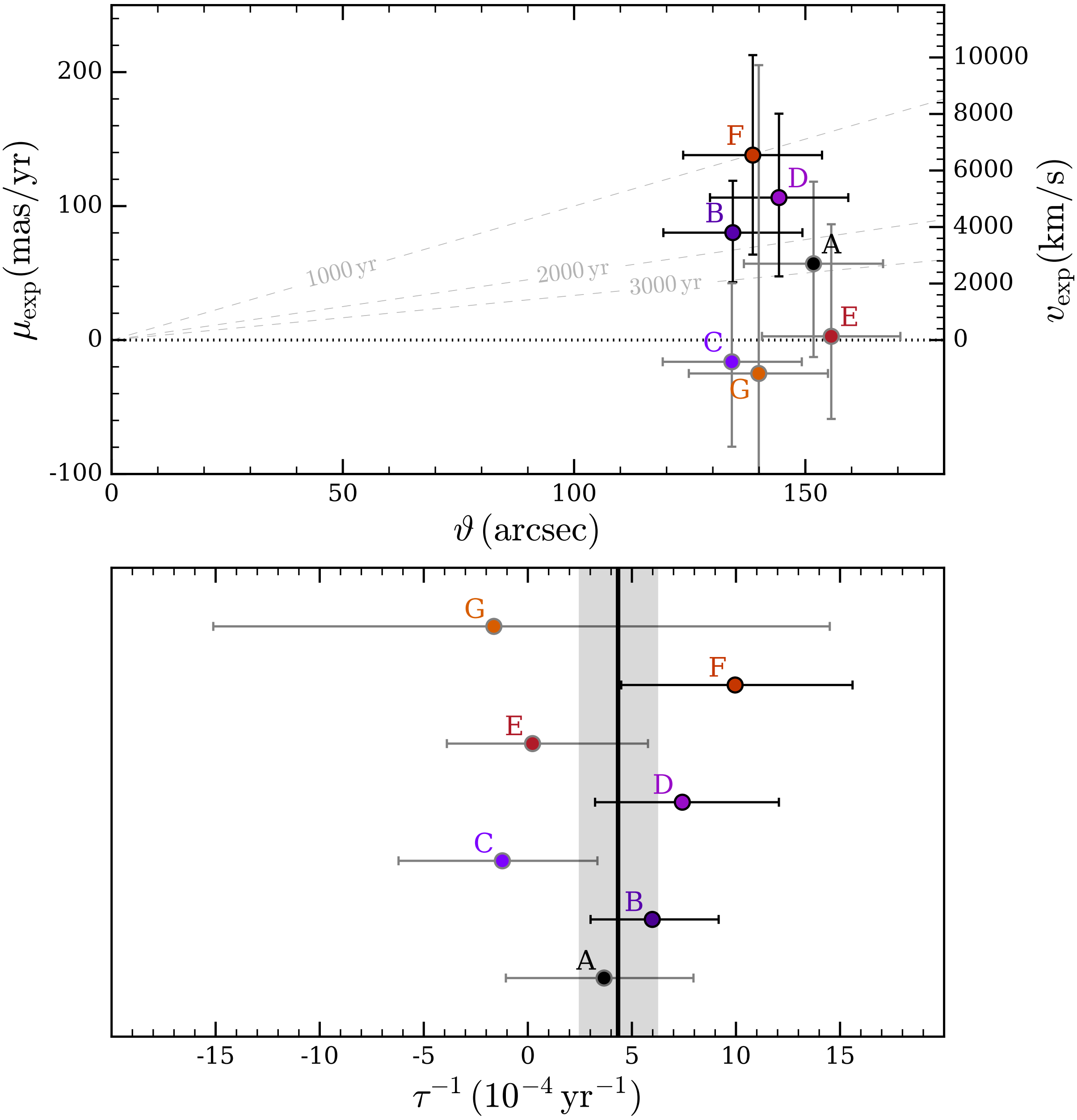

Figure 4.6: Constraints on the expansion of G15.9+0.2. *Top*: For each feature (labels as in Fig. 4.5), we plot the measured angular expansion speed $\mu_{\rm exp}$, and the corresponding projected velocity $v_{\rm exp}$ for a distance of 10 kpc, against its angular distance to the SNR center ϑ. To assess their respective significance, we have used black error bars for those measurements that enclose > 95% of the total probability mass on either side of 0, and gray for the others. In addition, we indicate the expected free expansion speed for ages of 1000, 2000, and 3000 years with dashed lines. *Bottom*: Expansion rate τ^{-1} as measured in each individual region. The thick black line with the gray-shaded area represents the combination of the individual measurements (or weighted average), assuming uniform expansion. All error bars are at 68% confidence. The data underlying this figure are given in Table B.4.

an assumed 1σ–error of $15''$, corresponding to around 10% of the SNR's radius. This is an intuitive way to estimate the origin of the SNR's expansion since the CCO is clearly offset with respect to the apparent center, and its proper motion is not constrained very precisely at this point. This reference point allowed us to obtain a rough estimate of the angular distance ϑ traveled by the shock wave at the location of each region.

The results of our expansion analysis are displayed in Fig. 4.6 (for a full illustration of the data at both epochs, see Fig. B.1). Due to the comparatively low exposure time available in the early epoch, the statistical error bars on the proper motion of the SNR shell are quite large. We estimate that the systematic error introduced by astrometric misalignment of the observations is at most $0.15''$ (see Table B.3), corresponding to a proper motion error around $15\,\mathrm{mas\,yr^{-1}}$. Therefore, the overall effect of this systematic error is rather small, also since there does not seem to be any bias toward detecting motion along a certain direction in our results.

We obtained a quantitative estimate of significance and rate of expansion in the following way: For each region, we combined the measured expansion speed $\mu_{\rm exp}$ with its distance from the SNR center ϑ to obtain an estimate of the expansion rate $\tau^{-1} = \mu_{\rm exp}/\vartheta$. In order to combine the constraints from individual boxes, we made the simplest possible assumption, which is that the SNR is expanding uniformly in all directions. The large size of the measured error bars presently does not warrant more complex (albeit more realistic) models, such as an azimuthal variation of the expansion velocity. Our assumption allowed us to directly multiply the inferred likelihoods from all regions to estimate an error-weighted average expansion rate of G15.9+0.2. In this process, we marginalized over systematic uncertainties introduced by astrometric misalignment of observations and the unknown location of the SNR center. This means we recalculated $\mu_{\rm exp}$ and ϑ many times for random samples drawn from possible center locations and systematic shifts, and summed up the combined distributions of τ^{-1} afterward. Thereby, we removed the need to artificially convolve distributions.

As can be seen in the lower panel of Fig. 4.6, our combined best estimate for the current average rate of expansion is $\tau^{-1} = (4.3 \pm 1.9) \times 10^{-4}\,\mathrm{yr^{-1}}$. This finding is moderately significant at around 2.5σ, as the probability for the true value to be less than or equal to zero is found to be 0.6%. Given the almost perfectly circular shape of the SNR, and the measured error bar sizes, presently there appears to be no obvious deviation from uniform expansion. Thus, while it is infeasible to constrain the kinematics of individual portions of the shell at this point, the statistical distribution of the results from our seven regions supports nonzero expansion. During the refinement of our analysis strategy, we attempted several techniques to measure the motion of the rim, and also attempted a simpler form of astrometric alignment of the two epochs (applying only a constant two-dimensional shift of the coordinate system). For all these cases, we found that overall expansion still holds.

It may therefore be tempting to state that, assuming perfectly free expansion, our average expansion rate would correspond to an age $\tau \sim 2500\,\mathrm{yr}$. Of course however, given the available data and the size of statistical errors, this value constitutes only a zeroth-order estimate for the SNR's age and is therefore to be taken with caution until the expansion of G15.9+0.2 has been independently measured.

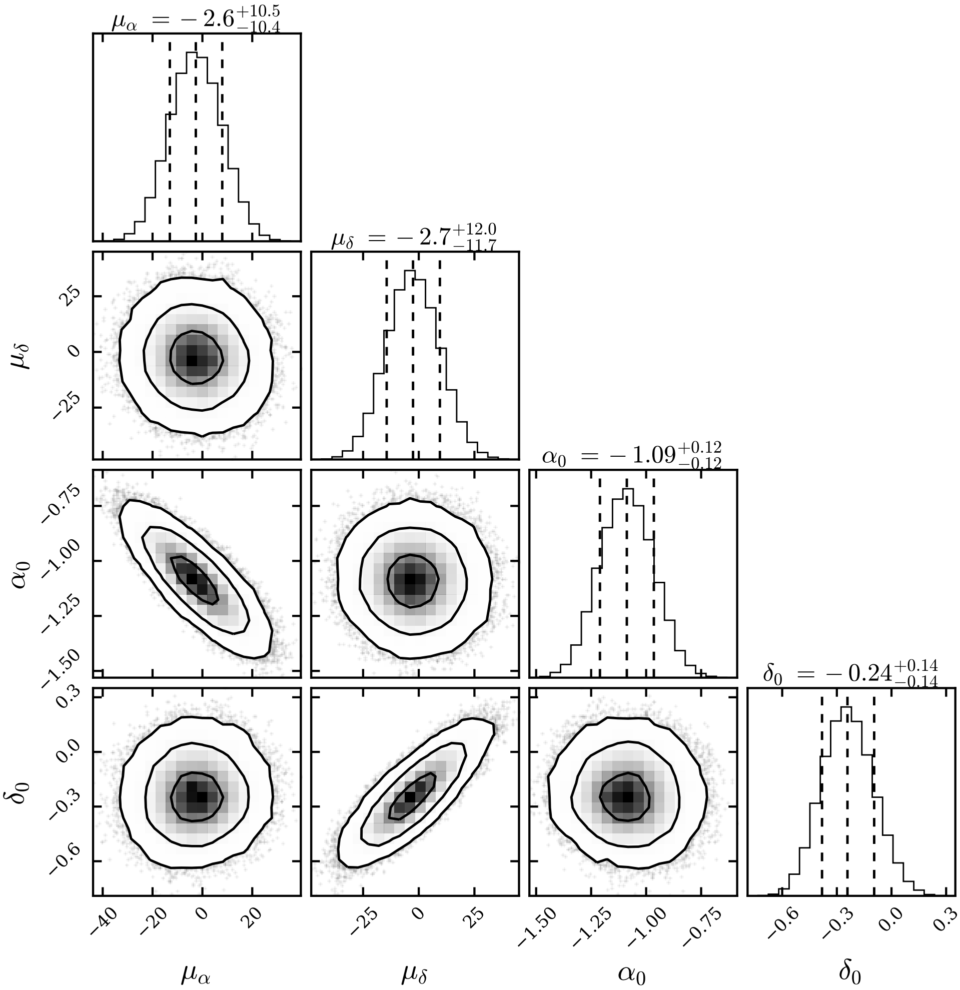

Figure 4.7: Corner plot (as in Fig. 4.4) showing the posterior distribution of the astrometric solution for the CCO in Kes 79. See Table B.3 for constraints on all parameters.

4.4.2 Kes 79

Kes 79 (G33.6+0.1) is a bright mixed-morphology SNR, whose X-ray appearance is dominated by multiple filaments and shells, as well as the bright central X-ray source CXOU J185238.6+004020 (Sun et al. 2004). In the radio and mid-infrared regimes, its morphology appears similarly complex and filamentary (Giacani et al. 2009; Zhou et al. 2016). The distance of Kes 79 is not very well constrained. One of the most recent estimates, inferred from H I absorption, yields a distance of 3.5 kpc (Ranasinghe & Leahy 2018), whereas CO observations (Kuriki et al. 2018) suggest a distance of 5.5 kpc. The age of Kes 79 is estimated via detailed X-ray spectroscopy to lie between 4.4 and 6.7 kyr (Zhou et al. 2016).

Our measurement of the CCO's proper motion (Fig. 4.7) is perfectly consistent with zero, the 68% central credible intervals being $(-3^{+11}_{-10}, -3^{+12}_{-11})\,\mathrm{mas\,yr^{-1}}$. This can be converted to a 90% upper limit on the CCO's peculiar proper motion of around 19 mas yr^{-1}. Equivalently, its

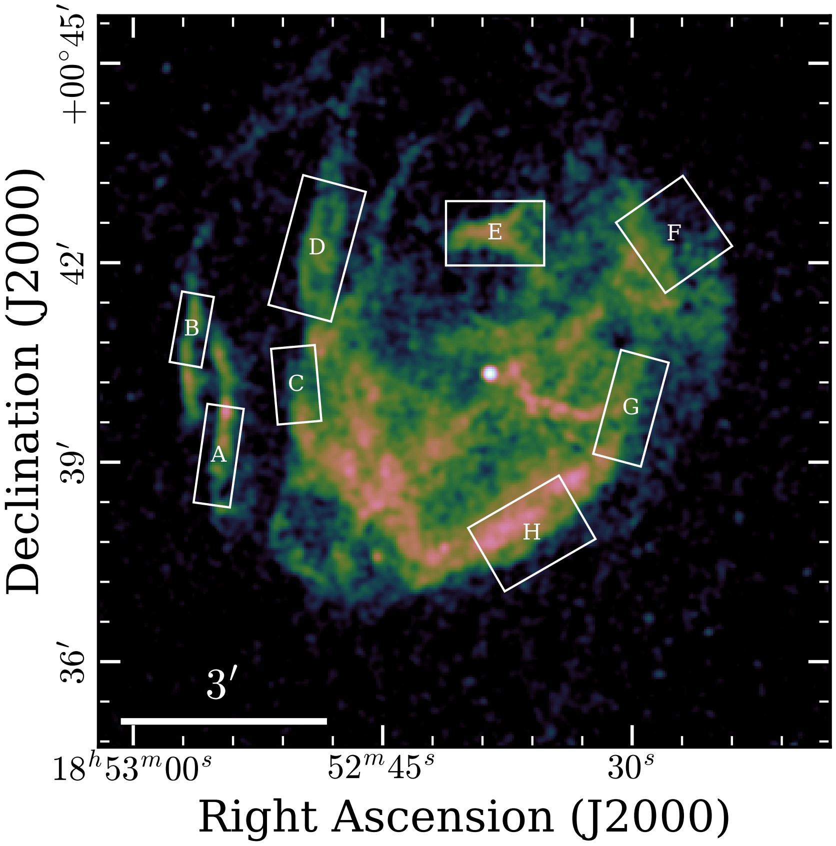

Figure 4.8: SNR Kes 79 with regions used for the expansion measurement indicated (as in Fig. 4.5).

tangential velocity is constrained at $< 450\,\mathrm{km\,s^{-1}}$, when scaled to a distance of 5 kpc.

While the limit on the CCO's transverse velocity is not very constraining by itself, our measurement has a noteworthy implication on the NS's timing properties, particularly its period derivative: The magnitude of the Shklovskii effect, an entirely kinematic contribution to the measured period derivative (Shklovskii 1970), can now be constrained to $< 4 \times 10^{-19}\,\mathrm{s\,s^{-1}}$ at 90% confidence (for a distance of 5 kpc). This corresponds to $< 5\%$ of the measured period derivative (Halpern & Gotthelf 2010a), which justifies to neglect this contribution to first order.

As can be seen in Fig. 4.8, Kes 79 exhibits several sharp filaments and shell fragments, which are in principle ideally suited for tracing the propagation of the supernova shock wave through the interstellar medium. However, our data set has several caveats: First, the exposure times of all observations are comparatively low (at 29.5, 9.8, and 10.0 ks), such that statistical fluctuations in the measured flux profiles are quite high. Second, for all three observations, the telescope pointing directions and roll angles were different. Therefore, since we attempted to avoid all the chip gaps of the ACIS-I detector, we had to exclude several emission features from our region definitions, which would otherwise have increased the measurable signal quite significantly (e.g., close to regions A, B, C, H). In order to quantify the distance between our emission features and the SNR center, we made use of our results in Sect. 4.5.2, establishing our estimated explosion

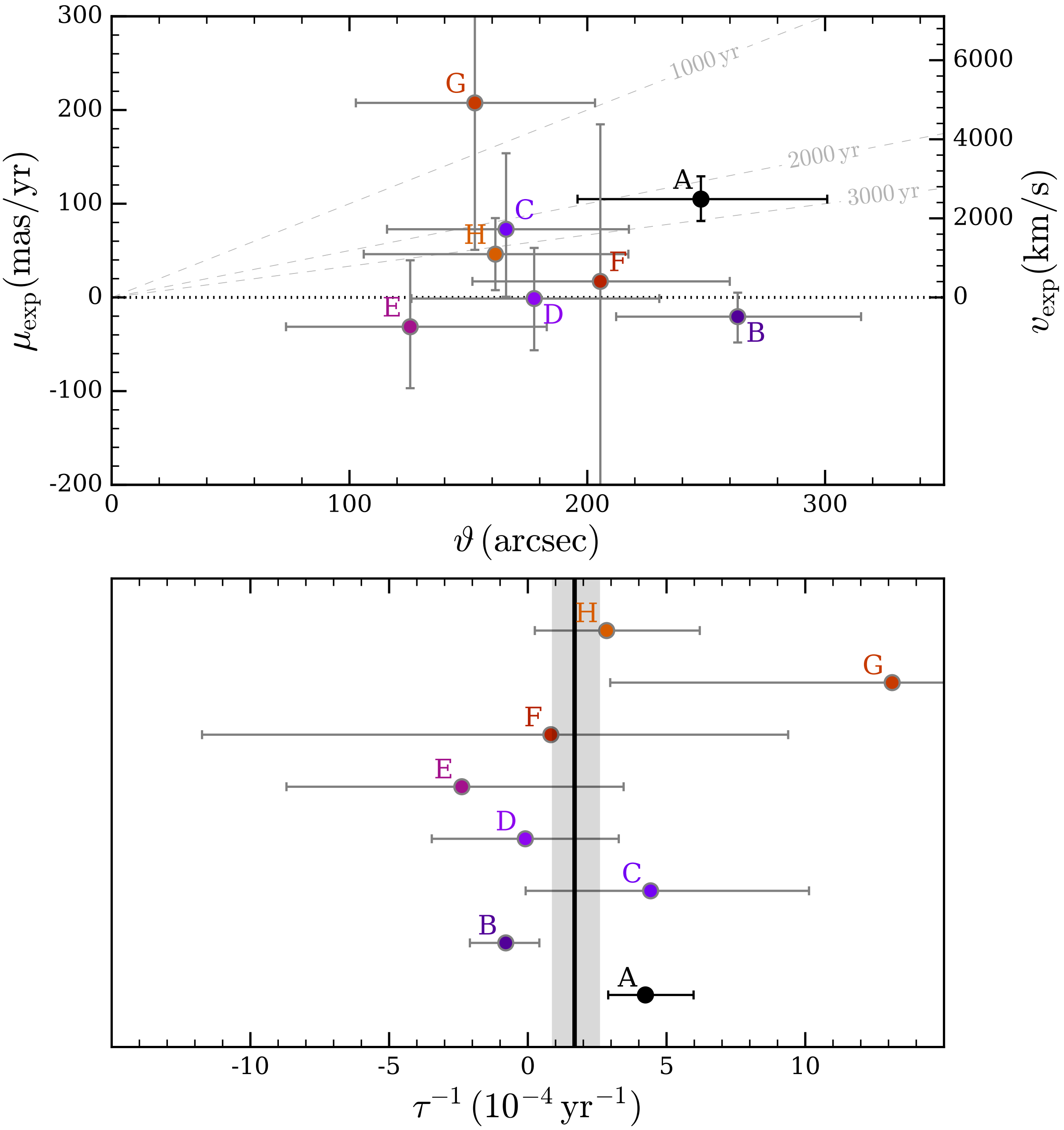

Figure 4.9: Constraints on the expansion of Kes 79 (as in Fig. 4.6). The assumed distance to Kes 79 for the conversion to v_{exp} is 5.0 kpc. The data underlying this figure are given in Table B.4.

site as (relatively uncertain) reference point.

The measured proper motion μ_{exp} of the shock wave in the individual regions is displayed in the upper panel of Fig. 4.9. Again, we observe that the overall picture is visually dominated by large statistical uncertainties, with most points scattered around zero, and several regions appearing almost unconstrained. However, the important exception is filament A as it, on its own, shows evidence for nonzero proper motion at $\sim 4\sigma$ statistical significance. In contrast, no regions show stronger deviations from zero than $\sim 1\sigma$ in the negative direction, which would be expected if this result was simply due to underestimated errors. We conservatively estimate the systematic astrometric error from coordinate system alignment to around $0.25''$ (see Table B.3), corresponding to an error on the angular motion around $17\,\mathrm{mas\,yr^{-1}}$. While the proximity of region A to a chip gap seems concerning for our overall interpretation, even an inspection by eye of the shock profiles in region A (see Fig. B.2) shows an obvious shift in the exposure-corrected flux profile, strengthening our confidence in the observed result.

Analogously to Sect. 4.4.1, we combined the measurements of individual regions to constrain the uniform expansion rate of Kes 79 at $\tau^{-1} = 1.7^{+0.9}_{-0.8}\times10^{-4}\,\mathrm{yr^{-1}}$. The probability for the true value to be less than or equal to zero is estimated to 1.6%. Thus, the nominal statistical significance of nonzero expansion is still low (at around 2σ). However, it should be noted that it is possible that certain features, traced for instance by the filament in region A, propagate more freely than others that could be more strongly decelerated. Therefore, the assumption of uniform expansion is likely unrealistic given the complex X-ray and radio morphology of Kes 79. Indirect signs of nonuniform expansion have actually been found in spatially resolved X-ray spectroscopy of Kes 79 by Zhou et al. (2016). If the expansion is indeed nonuniform, a combination of likelihoods is technically not valid, since one does not truly measure the same underlying quantity in different regions.

4.4.3 Cas A

Cas A (G111.7-2.1) is the youngest known Galactic core-collapse SNR at an age of around 350 years (e.g., Fesen et al. 2006; Alarie et al. 2014). Its X-ray morphology can be clearly separated into an inner, thermally emitting ejecta-dominated shell, and an outer forward shock region, which exhibits mainly synchrotron emission and expands at around $5000\,\mathrm{km\,s^{-1}}$ (DeLaney et al. 2004; Patnaude & Fesen 2007, 2009). The distance to Cas A has been precisely constrained to $(3.33 \pm 0.10)\,\mathrm{kpc}$ via an analysis of the expansion of filaments in the optical (Alarie et al. 2014).

The CCO CXOU J232327.9+584842 was discovered in the *Chandra* first-light image of Cas A (Tananbaum 1999). There exists a past proper motion analysis for the CCO performed by DeLaney & Satterfield (2013), which yielded a final measurement of the transverse velocity of $(390 \pm 400)\,\mathrm{km\,s^{-1}}$. This is equivalent to a total proper motion of $(24 \pm 25)\,\mathrm{mas\,yr^{-1}}$ toward the southwest, for their assumed distance of 3.4 kpc. Nevertheless, since they used different statistical methods than we did, and did not employ any PSF modeling, we decided to reanalyze the data to produce a comparable measurement to the other objects in this paper.

Our initial search for detectable calibrator sources yielded only one source common to all five observations (labeled as “1” here), which is identical to the one found in DeLaney & Satterfield (2013). However, instead of using quasi-stationary flocculi of Cas A for image registration, we decided to stack the late-time observations to increase our chance to detect faint sources. To do this, we aligned the observations using point-like sources found by `wavdetect` that were highly significant in all observations ($> 10\sigma$). These correspond mostly to bright clumps of emission of the SNR, which can be regarded as effectively stationary on the relevant timescales (< 10 days). We applied the `CIAO` task `wcs_match` to find the optimal transformation between two respective

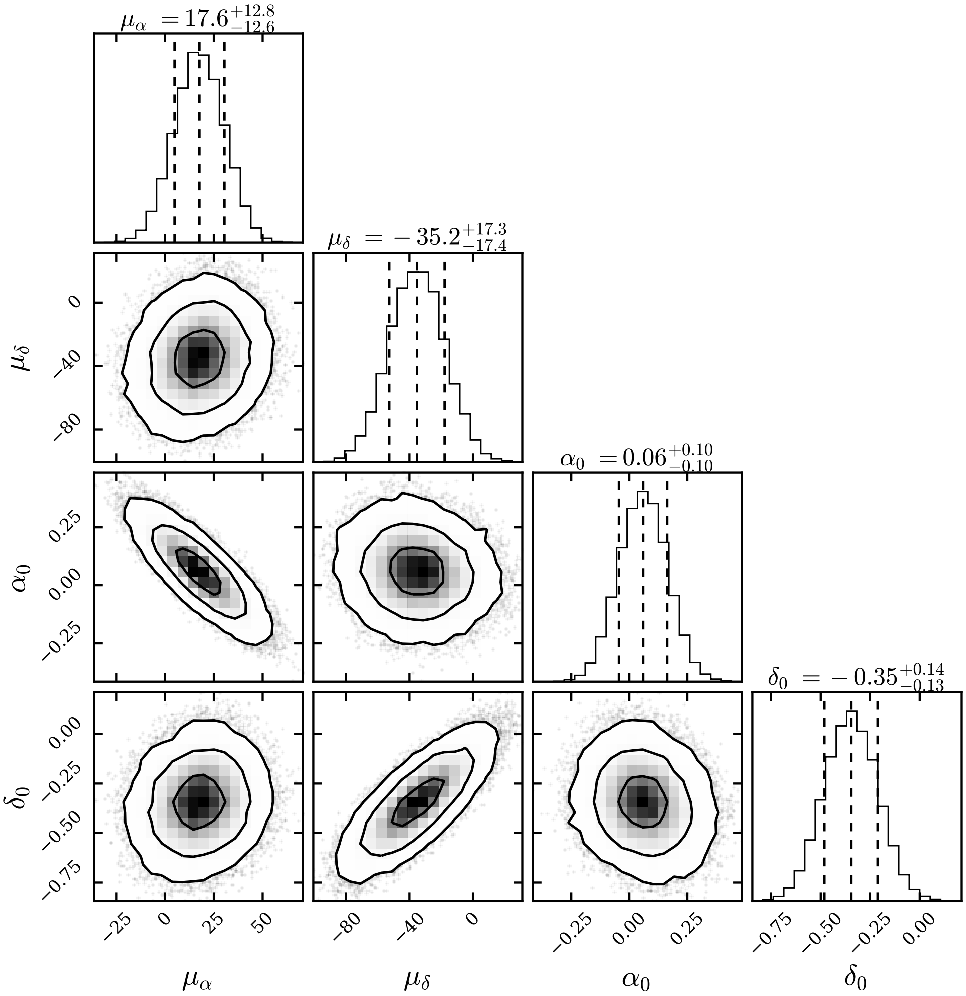

Figure 4.10: Corner plot (as in Fig. 4.4) showing the posterior distribution of the astrometric solution for the CCO in Cas A. See Table B.3 for constraints on all parameters.

epochs, and then reprojected and merged all late-time observations using the `wcs_update` and `reproject_obs` tasks.

Using this combined late-time data set, we detected two more point sources common to early and late observations, and with close positional match to *Gaia* stars (see Fig. 4.1 and Table B.2). Due to their location in the outer regions of Cas A (see Figure 4.1), we made some further considerations to ensure their correct identification: We verified that their spectral nature is softer than that of the surrounding emission, using an archival 1 Ms ACIS observation (ObsIDs 4634–4639, Hwang et al. 2004). Furthermore, we emphasize that if these sources were actually associated with ejecta clumps of the SNR rather than being foreground sources, they would be expected to show very large proper motion due to their location at the edge of the remnant shell. Such behavior would be clearly recognizable with respect to the secure source 1. Since we did not observe this, we concluded that all three astrometric calibrators are probably correctly identified.

The results of our proper motion measurement are displayed in Fig. 4.10. We find evidence for nonzero proper motion directed toward the southeast, with a best-fit value of $(18^{+12}_{-13}, -35^{+17}_{-18})\,\mathrm{mas\,yr^{-1}}$. An analogous fit to the data from the late epochs taken individually yielded a similar result, showing that the impact of our merging technique is rather small.

Converting our two-dimensional probability distribution for (μ_α, μ_δ) to a distribution for the absolute value of proper motion, we obtained a 68% central credible interval $\mu^*_{\mathrm{tot}} = 35^{+16}_{-15}\,\mathrm{mas\,yr^{-1}}$. This corresponds to a transverse physical velocity of $(570 \pm 260)\,\mathrm{km\,s^{-1}}$ at the distance to Cas A of 3.4 kpc. Here, including the effect of Galactic rotation does not considerably alter the result. Fesen et al. (2006) performed an analysis of the expansion of high-velocity optically emitting ejecta knots, yielding a precise estimate for the explosion date of Cas A (around the year 1670). Connecting the explosion site inferred in Thorstensen et al. (2001) with the present-day location of the CCO, they constrained its velocity to around $350\,\mathrm{km\,s^{-1}}$ at a position angle $169° \pm 8°$. Our measurement is marginally consistent with both that indirect estimate and the analysis of DeLaney & Satterfield (2013).

4.4.4 G330.2+1.0

The SNR G330.2+1.0 is located at a distance of at least 4.9 kpc (McClure-Griffiths et al. 2001), and can be seen as a faint but complete shell in X-rays. Its emission is almost entirely nonthermal in nature, except for a region in the east showing thermal emission (Williams et al. 2018). The analysis of shock-velocity and filament expansion points toward a rather young age of the remnant, likely below 1000 years (Williams et al. 2018; Borkowski et al. 2018). As part of their expansion analysis, Borkowski et al. (2018) noted that no evidence for “discernible motion” of the CCO CXOU J160103.1−513353 is found, which we attempted to further quantify here.

We can see the posterior distribution for the astrometric solution of the CCO in Fig. 4.11. We find a very small proper motion toward the south of $(-2.7^{+5.3}_{-5.4}, -6.4^{+5.5}_{-5.4})\,\mathrm{mas\,yr^{-1}}$. There are no obvious systematic discrepancies between the posterior predictions from our fit and the PSF fit contours, and we find no need to artificially add a systematic error component to the likelihood contours. Thus, due to the very long exposure times of the observations at early and late epochs, and the large number of clean astrometric calibrators, we find the small statistical error bars of our result plausible.

The expected proper motion of an object corotating with the Galactic disk at the location of G330.2+1.0 at a distance between 4.9 and 10.0 kpc is $(-4.9 \pm 0.8, -4.5 \pm 0.6)\,\mathrm{mas\,yr^{-1}}$ (Mróz et al. 2019). Thus, the measured proper motion of the CCO is perfectly consistent with zero when effects of Galactic rotation are taken into account. We quote the corresponding 90% upper limit on the CCO’s peculiar proper motion, which lies at $9.9\,\mathrm{mas\,yr^{-1}}$. This corresponds to a transverse kick velocity below $230\,\mathrm{km\,s^{-1}}$, assuming a distance of 5 kpc.

This case demonstrates that, even given the “poor” spatial resolution of X-ray data when compared to the optical, effects of Galactic rotation cannot generally be neglected for proper motion measurements. Furthermore, our very tight constraints on its motion imply that the maximum angular distance traveled by the CCO during the “lifetime” of G330.2+1.0 ($\lesssim$ 1000 years) is only around $10''$. This is close to negligible compared to the SNR’s present-day radius around $5'$, making CXOU J160103.1−513353 quite literally a “central” compact object.

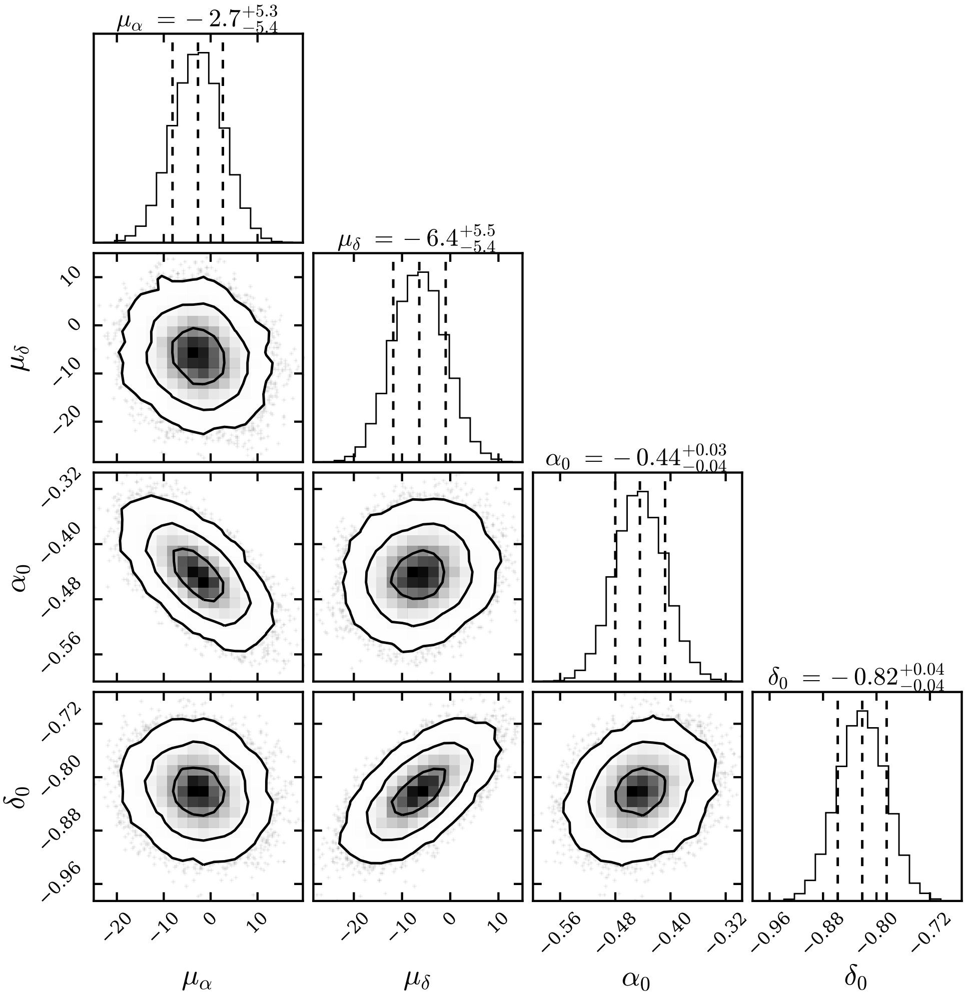

Figure 4.11: Corner plot (as in Fig. 4.4) showing the posterior distribution of the astrometric solution for the CCO in G330.2+1.0. See Table B.3 for constraints on all parameters.

4.4.5 RX J1713.7−3946

RX J1713.7−3946 (G347.3−0.5) is one of the brightest known emitters of very-high-energy gamma rays (e.g., H. E. S. S. Collaboration et al. 2018a). It appears quite luminous in X-rays and comparatively dim in the radio regime, with its X-ray spectrum being absolutely dominated by nonthermal synchrotron emission (Okuno et al. 2018). Morphologically, the SNR can be described as elliptically shaped, with the bright western shell appearing to consist of multiple ring-like structures, which in turn consist of thin filaments on smaller scales (Cassam-Chenaï et al. 2004). The distance to the SNR is estimated to be around 1.0 − 1.3 kpc, based on CO and H I observations of clouds interacting with the shock wave (Fukui et al. 2003; Cassam-Chenaï et al. 2004). The expansion of the outermost SNR filaments has been directly measured in three quadrants (Acero et al. 2017; Tsuji & Uchiyama 2016; Tanaka et al. 2020), yielding projected shock velocities up to 3900 km s^{-1} and implying an age for RX J1713.7−3946 between 1500 and

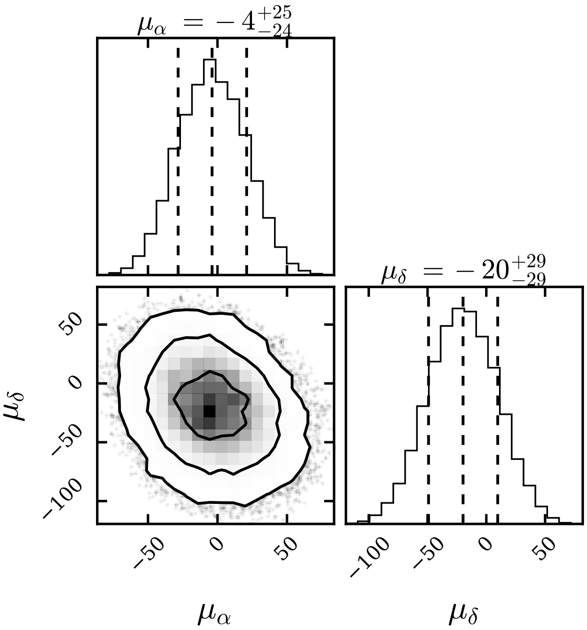

Figure 4.12: Corner plot (as in Fig. 4.4) showing the posterior distribution of the astrometric solution for the CCO in G347.3-0.5. For this target, a relative astrometric frame registration method was applied as described in the text. We therefore measured no absolute positions, but only relative source displacements, which correspond to the components of proper motion. See Table B.3 for constraints on all parameters.

2300 years.

The position of the CCO 1WGA J1713.4−3949 is slightly offset from the apparent center of the SNR (Pfeffermann & Aschenbach 1996) by around 4.5′ toward the southwest. Since the system is located quite nearby and the SNR age is likely rather low, it therefore seems reasonable to expect significant proper motion. For instance, assuming the geometric center to correspond to the explosion site, we would expect motion of around 130 mas yr^{-1} for an age of 2000 years.

There are three archival *Chandra* observations of the CCO,[16] one from 2005 using ACIS-I, one from 2013 using HRC-I, and one from 2015 (ID 15967) using ACIS-I. The latter observation was carried out using only a subarray of the detector, and with an offset aimpoint. Therefore, it is not suitable for our analysis, leaving us with only two moderately deep observations.

Due to the intrinsically high noise level in the HRC observation, it proved very difficult to find adequate reference sources that could be convincingly cross-matched to a *Gaia* counterpart. Thus, in order to avoid having to rely on potentially erroneous optical associations, we decided to modify our approach, measuring relative source offsets between our two observations directly instead of measuring absolute positions. To achieve this, for each source, we convolved the PSF-fit likelihood contours of the late epoch with the “mirrored” contours of the early epoch (meaning we set $x \to -x$, $y \to -y$). This effectively subtracts the two positions from each other, resulting in a probability distribution for the astrometric offset between the two observations for a given

---

[16] Due to the large extent of the SNR, the CCO is outside the field of view of the numerous observations of the SNR shell.

object. To account for the unknown possible proper motion of our calibrators, we convolved their offset distributions with a Gaussian of width $\sigma = 10\,\mathrm{mas\,yr^{-1}} \times \Delta t$, where $\Delta t = 7.9$ yr corresponds to the time difference between the two epochs. We then performed our astrometric fit with only $\{\mu_\alpha, \mu_\delta\}$ and a single set of frame registration parameters $\{\Delta x, \Delta y, r, \theta\}$ as free parameters. The advantage of this method is that it does not require precisely knowing the true source positions, and "only" assumes their motions to not be much larger than $10\,\mathrm{mas\,yr^{-1}}$.

The resulting posterior distribution can be seen in Fig. 4.12. We measure a proper motion of $(-4^{+25}_{-24}, -20 \pm 29)\,\mathrm{mas\,yr^{-1}}$, which is consistent with zero within its quite large statistical uncertainties. We verified this result by checking that for both of our calibrators taken as the sole astrometric reference (applying only a simple translation of the coordinate system), we also obtain proper motion consistent with zero. This demonstrates that our result is not overly biased by our method or choice of calibration sources. We estimate the 90% credible upper limit on the peculiar proper motion to be around $48\,\mathrm{mas\,yr^{-1}}$, corresponding to a limit on the two-dimensional space velocity of around $230\,\mathrm{km\,s^{-1}}$ for a distance of 1 kpc. A future observation would certainly allow these large error bars on the CCO's proper motion to be greatly reduced. Given the issues we faced, it would probably be advantageous to use the ACIS detector for such a task as it is generally better suited for the detection of faint sources than the HRC.

4.4.6 G350.1−0.3

G350.1−0.3 exhibits a very unusual morphology at multiple wavelengths: In the radio, it shows a distorted and elongated shape (Gaensler et al. 2008), and in X-rays, a very bright irregularly shaped clump in the east dominates the overall morphology with only weak emission otherwise. The most likely explanation for the bright clumpy X-ray emission is the interaction of hot, metal-rich ejecta with a molecular cloud, based on which a distance of 4.5 kpc seems likely (Bitran et al. 1997; Gaensler et al. 2008). Lovchinsky et al. (2011) performed spectral analysis of a deep ACIS-S observation of the SNR and from that estimated an age of 600 – 1200 years for the SNR.

The bright X-ray source XMMU J172054.5−372652 is located 3′ west of the dominant emission region, quite offset from the apparent center of the remnant. Assuming the origin of the CCO to be located at the apparent center of emission of the SNR, Lovchinsky et al. (2011) predicted a projected velocity of $1400 - 2600\,\mathrm{km\,s^{-1}}$ for the NS. This would require an extremely strong kick to have acted on the NS during the supernova explosion, and the implied proper motion of $65 - 130\,\mathrm{mas\,yr^{-1}}$ should be easily detectable for us.

During the preparation of this work, Borkowski et al. (2020) published a study on the expansion and age of G350.1−0.3.[17] They provided a detailed analysis of the motion of many individual emission clumps as well as a brief measurement of the CCO's proper motion. Their main results include the measurement of rapid expansion of the SNR, constraining its age to be at most around 600 yr. Moreover, they detected comparatively slow motion of the CCO toward the north, at significant uncertainty. Using our independent methods, we aimed to confirm their measurement of the SNR's expansion and obtain quantitative constraints on the proper motion

---

[17] Just prior to the submission of this work, a similar paper by Tsuchioka et al. (2021) became available as preprint; however, it did not substantially further influence our work.

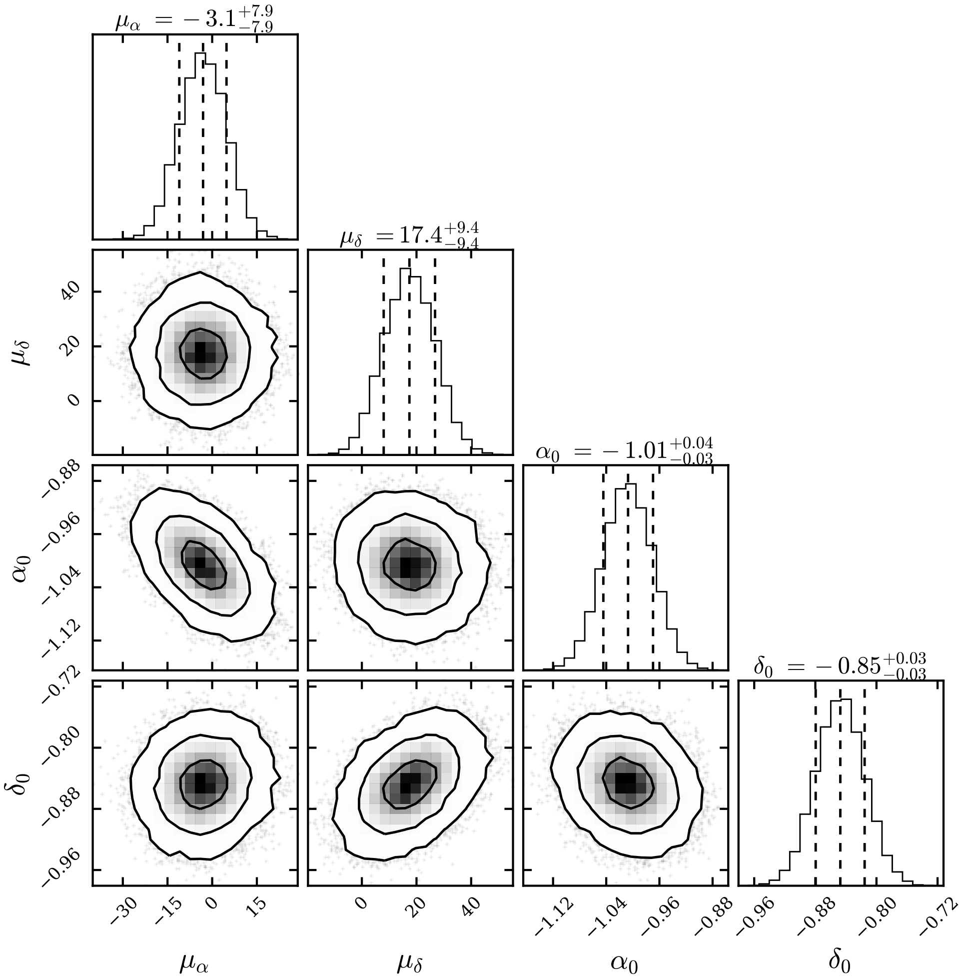

Figure 4.13: Corner plot (as in Fig. 4.4) showing the posterior distribution of the astrometric solution of the CCO in G350.1−0.3. See Table B.3 for constraints on all parameters.

of the CCO.

The total exposure of the data set at both early and late epochs is exquisite, at around 100 and 200 ks, respectively. The data are therefore ideal for obtaining precise constraints on the motion of both the CCO and the SNR ejecta in the nine-year time span between the two epochs.

From our proper-motion fit, where we treated all five late-time observations independently, we obtained the posterior distribution shown in Fig. 4.13. We find that the CCO appears to be moving northward (with large uncertainty), at $(-3 \pm 8, 17^{+10}_{-9})$ mas yr^{-1}. From this, we obtain a 68% central credible interval for the peculiar proper motion of $\mu^*_{\mathrm{tot}} = 15^{+10}_{-9}$ mas yr^{-1}, corresponding to a transverse velocity component of 320^{+210}_{-190} km s^{-1} at a distance of 4.5 kpc. Borkowski et al. (2020), using positions from Gaussian fits to the CCO and field sources, found a proper motion of (−5, 14) mas yr^{-1}, which is consistent with our finding of slow motion approximately due north. Both measured values are certainly much lower in magnitude (and quite likely different in direction) than what was predicted from the SNR geometry in Lovchinsky et al. (2011).

The implications of this will be discussed in Sect. 4.5.2.

As a first test for the expansion of G350.1−0.3, we performed a simple image subtraction of the early-time from the late-time image, to check for obvious changes between the two epochs. The lower panel of Fig. 4.14 displays the differential between the merged, exposure-corrected and smoothed images. There is very obvious evidence for substantial eastward motion of the bright ejecta clump, which appears more significant toward its outer edge. In addition, the image nicely confirms the measured proper motion of the CCO, with its position showing a small but visible offset between the two epochs. This image is a very useful qualitative confirmation of the SNR's rapid expansion, independent of the exact method used for quantitative analysis.

As can be seen in the upper panel of Fig. 4.14, the complex morphology and bright emission of the eastern clump allowed us to define numerous small-scale features of emission. Their propagation was measured in order to infer the internal kinematics and global expansion behavior of the ejecta. In contrast, for the much fainter emission in the north and south of the SNR, we defined regions of diffuse emission on much larger scales, which we hoped would allow us to trace the interaction of the shock wave with the interstellar medium.

For each feature, we used the indirectly inferred location of the explosion site from Sect. 4.5.2 to estimate the angular distance ϑ that has been traversed since the supernova. The measured expansion speeds $\mu_{\rm exp}$ for all 18 regions can be seen in the upper panel of Fig. 4.15 (for a full illustration of the data at both epochs, see Fig. B.3). We estimate systematic uncertainties due to astrometric frame registration to be smaller than $0.1''$, or equivalently $11\,{\rm mas\,yr^{-1}}$. The proper motion of most features is much better constrained than for those in Sects. 4.4.1 and 4.4.2. Therefore, we combined our probability distributions for ϑ and $\mu_{\rm exp}$ directly to obtain the free expansion age of the SNR, defined as $\tau = \vartheta/\mu_{\rm exp}$. The resulting constraints on τ are displayed in the lower panel of Fig. 4.15.

As we can see, there is spectacular evidence for significant expansion in almost all regions investigated. The maximal observed expansion speed is around $250\,{\rm mas\,yr^{-1}}$, corresponding to a projected shock wave velocity close to $6000\,{\rm km\,s^{-1}}$, for a distance of 4.5 kpc. In combination with its angular distance from the SNR center, we find the lowest expansion age for region E, at $\tau = (580 \pm 50)\,{\rm yr}$, including systematic errors. These findings are in great agreement with those from Borkowski et al. (2020), who measure the fastest expansion at a very similar location (labeled "B3" by them, finding $\tau = 590\,{\rm yr}$) despite a different region shape. Among the "runners-up" in terms of likely expansion rate are the regions A, B, F, M, P, all of which show values consistent with $\tau \sim 700\,{\rm yr}$. However, none of these regions independently confirms that $\tau < 700\,{\rm yr}$. In principle, the highest undecelerated expansion age τ can be considered a hard upper limit on the true age.[18] However, it seems important to ask why region E would indicate expansion at a higher rate than regions B or C. Its location does not appear to be "special" in the sense that it is not located close to the edge of the bright interacting ejecta clump. Naively, one would expect the least decelerated expansion there, if the bent shape of the clump was caused by the direct interaction of the shock wave with an obstacle. We thus chose to place a more

---

[18] Mathematically, the expansion at this evolutionary stage can ideally be described by the relation between radius and age $R \propto t^m$, with m, the deceleration parameter, expected to range between 0.4 and 1 for the Sedov-Taylor stage (Sedov 1959; Taylor 1950) and free expansion, respectively. The true age t is therefore related to the expansion age $\tau = R/\dot{R}$ via $t = m\tau \leq \tau$.

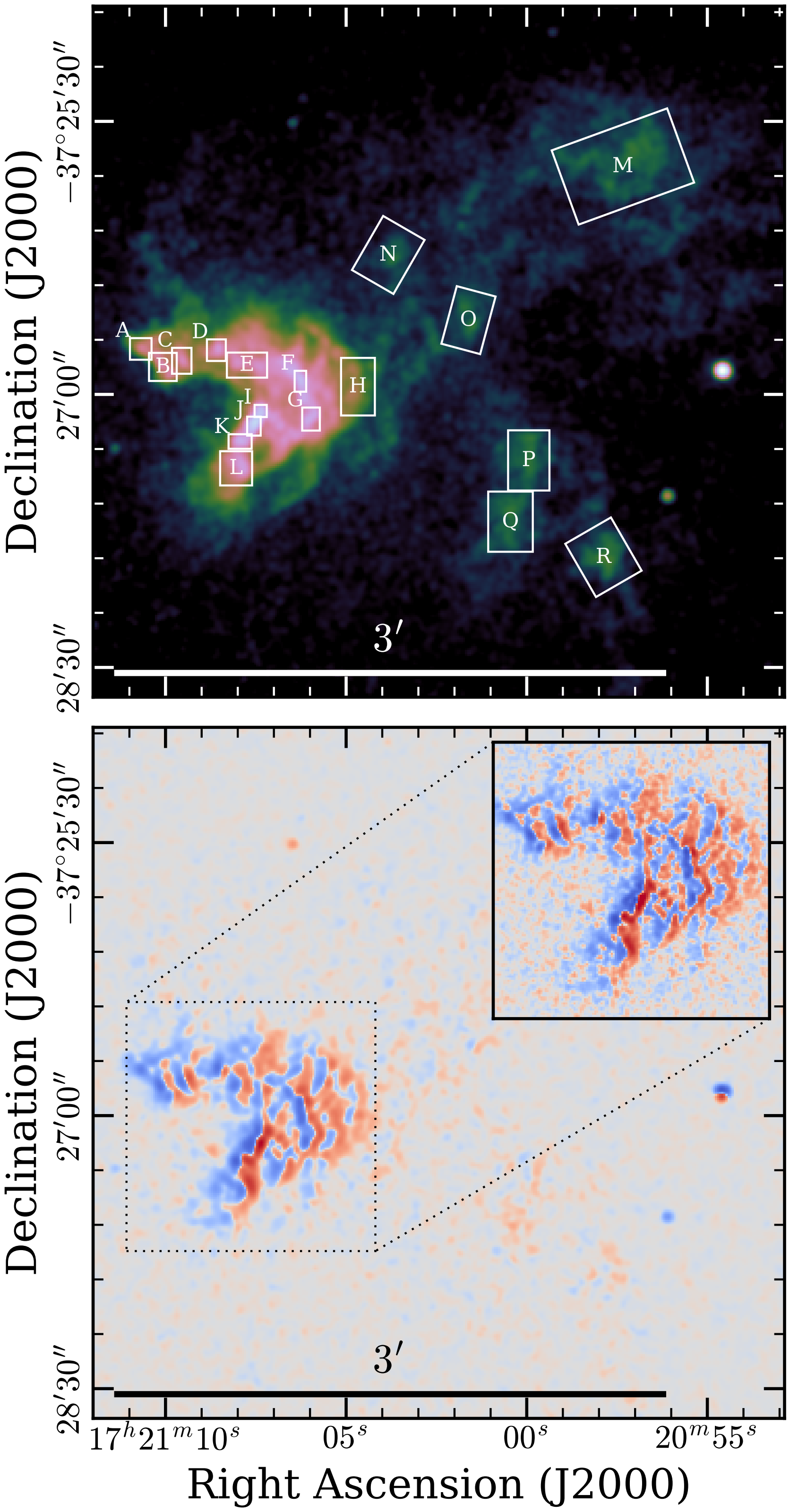

Figure 4.14: SNR G350.1−0.3 with regions used for the expansion measurement indicated in the *top* panel. The *bottom* panel shows a difference image between the early and late epochs. We use a symmetric logarithmic color scale to highlight features on small scales, with blue corresponding to the late-epoch emission being brighter, and red being the opposite. For the main image, we smoothed the data with a Gaussian kernel of 1″, while in the inset we show the region of the bright clump smoothed with only 0.5″

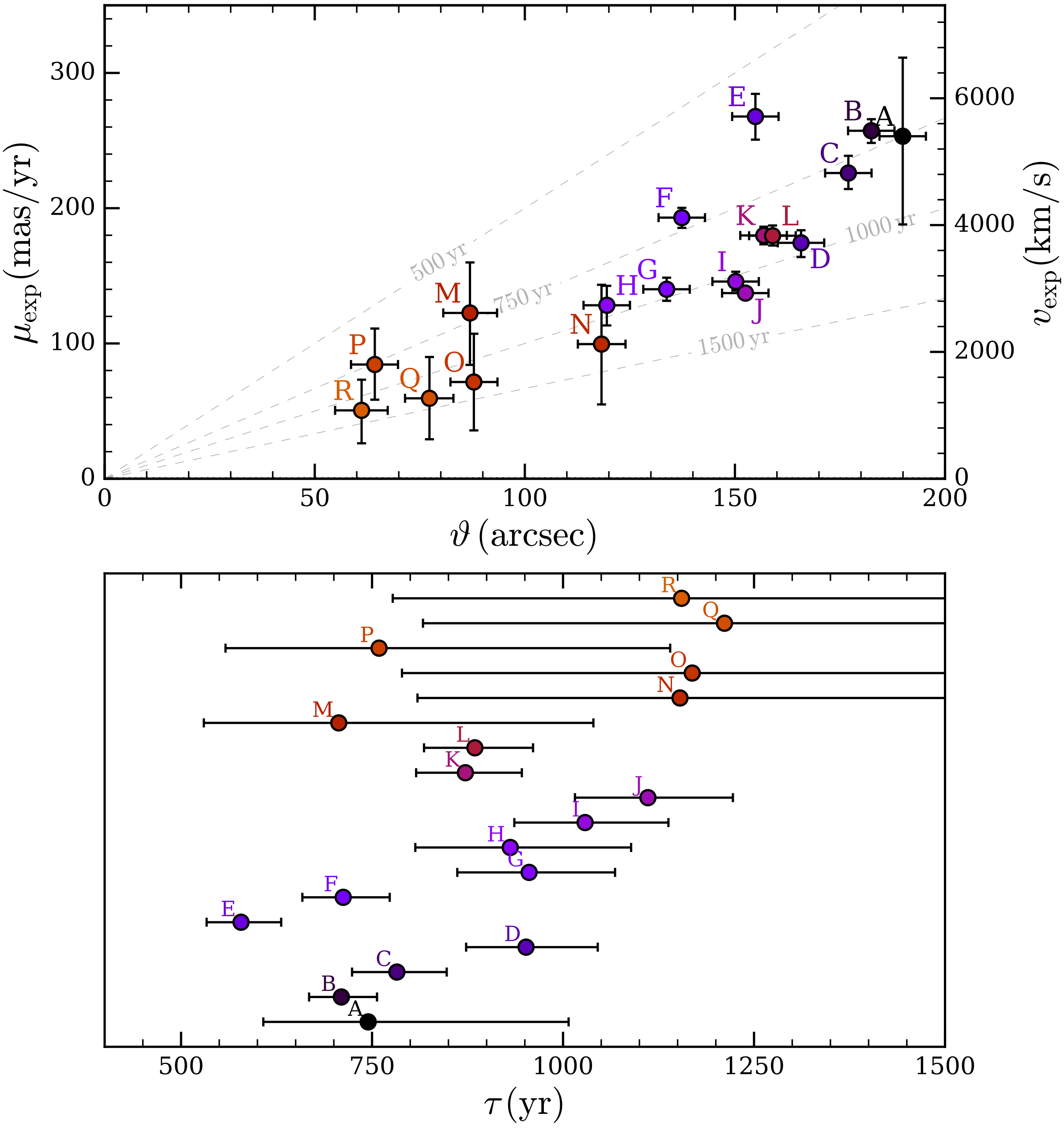

Figure 4.15: Expansion and age estimate for G350.1−0.3. *Top* panel as in Fig. 4.6, with an assumed distance of 4.5 kpc. *Bottom*: Constraints on the expansion age τ from each individual region, with error bars at 68% confidence. The data underlying this figure are given in Table B.4.

conservative upper limit of 700 yr on the true age of G350.1−0.3, which nonetheless confirms it as one of the three youngest known Galactic core-collapse SNRs (see Borkowski et al. 2020).

The internal kinematics of the bright eastern clump are found to vary quite significantly with location: In particular, its southern elongated feature shows a significant velocity gradient, with the regions I and J being decelerated more strongly than the southern regions K and L. Similarly, the easternmost regions B and C display quite rapid motion when compared with the rest of the clump, especially the nearby region D. Furthermore, upon closer inspection of flux profiles at early and late epochs, it becomes evident that some features in the clump, for example regions J and K, have evolved in shape and decreased in brightness (see Fig. B.3) over the time span of nine years. The general trend seems to be that the X-ray emission in these regions becomes less "clumpy" and more diffuse as the SNR evolves. All these findings trace the interaction of the ejecta with an X-ray dark obstacle (Gaensler et al. 2008), which appears to cause the unique outward bent shape of the clump. Clearly, the interaction is the strongest close to the center of the clump, leading to the lowest measured expansion rates there (regions I and J), and higher velocities for its eastern and southern parts. In this scenario, if parts of the shock wave encounter a reduced ambient density after having passed by the obstacle, morphological changes of associated emission features could be a natural consequence.

Finally, we clearly detect the motion of the larger, more diffuse emission features in the north and south of the SNR (labeled M to R). The expansion rates we find here are a lot less certain, but on average appear comparable to or slightly smaller, than those in the bright emission clump. Here, there are some subtle differences between our findings and those of Borkowski et al. (2020), for instance, for the faint regions M and O (labeled "NNE" and "K" by them). In these regions, they infer rapid, almost undecelerated expansion, corresponding to expansion ages $< 700\,\mathrm{yr}$, with quite small statistical errors. While our measurement for region M is formally consistent with theirs, we find much larger statistical errors in both regions M and O, making our constraints on the local degree of deceleration of the shock wave rather weak. These differences in uncertainty could be caused by different shapes or orientations of the measurement regions. However, we consider the most likely origin to be the difference in analysis methods, with our one-dimensional resampling technique yielding more conservative errors than a direct comparison of two-dimensional flux images.

Overall, we do not find significant evidence for spatially varying degrees of deceleration within the faint diffuse emission regions. The fact that every single region of the SNR shows (more or less) significant signatures of expansion away from a common center clearly proves that the unusual morphology of the SNR is not caused by the superposition of two unrelated objects, as was conjectured by Gaensler et al. (2008). Instead, G350.1−0.3 is indeed a single and highly peculiar SNR.

4.5 Discussion

4.5.1 Proper motion and NS kinematics

This work constitutes the first step toward the ambitious goal of building a sample of consistently measured transverse velocities for all CCOs. At the present time, only four members of the class (the CCOs in Puppis A, Cas A, G350.1−0.3 and PKS 1209−51/52) have a measured nonzero proper motion. However, we hope that future observations will aid in reducing error bars and obtaining more precise constraints for those CCOs for which only upper limits on the proper

Table 4.2: Overview of direct proper motion measurements and exact positions for all CCOs.

SNR	CCO	α_0 (J2000.) (h:m:s)	δ_0 (J2000.) (d:m:s)	t_0 (MJD)	μ_α (mas yr^{-1})	μ_δ (mas yr^{-1})	$\mu_{\rm tot}$ (mas yr^{-1})	d' (kpc)	$v_{\rm proj}$ (km s^{-1})	Reference
G15.9+0.2	CXOU J181852.0−150213	$18{:}18{:}52.072^{+0.004}_{-0.004}$	$-15{:}02{:}14.05^{+0.04}_{-0.04}$	57 233	-17 ± 12	-4 ± 10	< 25	10	< 1200	This work
Kes 79	CXOU J185238.6+004020	$18{:}52{:}38.561^{+0.008}_{-0.008}$	$+00{:}40{:}19.60^{+0.15}_{-0.14}$	57 441	-3^{+11}_{-10}	-3^{+12}_{-11}	< 19	5.0	< 450	This work
Cas A	CXOU J232327.9+584842	$23{:}23{:}27.932^{+0.013}_{-0.013}$	$+58{:}48{:}42.05^{+0.13}_{-0.13}$	55 179	18^{+12}_{-13}	-35^{+17}_{-18}	35^{+16}_{-15}	3.4	570 ± 260	This work
Puppis A	RX J0822−4300	$08{:}21{:}57.274^{+0.009}_{-0.010}$	$-43{:}00{:}17.33^{+0.08}_{-0.08}$	58 517	$-74.2^{+7.4}_{-7.7}$	-30.3 ± 6.2	80.4 ± 7.7	2.0	763 ± 73[b]	1
G266.1−1.2 (Vela Jr.)	CXOU J085201.4−461753	08:52:01.37[a]	−46:17:53.5[a]	51 843	...[c]	...[c]	< 300	1.0	< 1400	2,3
PKS 1209−51/52	1E 1207.4−5209	$12{:}10{:}00.913^{+0.003}_{-0.003}$	$-52{:}26{:}28.30\ ^{+0.04}_{-0.04}$	54 823	...[c]	...[c]	15 ± 7	2.0	< 180	4
G330.2+1.0	CXOU J160103.1−513353	$16{:}01{:}03.148^{+0.004}_{-0.004}$	$-51{:}33{:}53.82^{+0.04}_{-0.04}$	57 878	$-2.7^{+5.3}_{-5.4}$	$-6.4^{+5.5}_{-5.4}$	< 9.9	5.0	< 230	This work
RX J1713.7−3946	1WGA J1713.4−3949	17:13:28.30[a]	−39:49:53.1[a]	56 360	-4^{+25}_{-24}	-20 ± 29	< 48	1.0	< 230	This work
G350.1−0.3	XMMU J172054.5−372652	$17{:}20{:}54.585^{+0.003}_{-0.003}$	$-37{:}26{:}52.85^{+0.03}_{-0.03}$	58 308	-3 ± 8	17^{+10}_{-9}	15^{+10}_{-9}	4.5	320^{+210}_{-190}	This work
G353.6−0.7	XMMU J173203.3−344518	17:32:03.41[a]	−34:45:16.6[a]	54 584	...	...	...[d]	3.2	...[d]	5,6

Notes. To provide a complete four-parameter astrometric solution, we display the best-fit positions of the CCO (α_0, δ_0) at a given epoch t_0, corresponding to the latest available observation of the respective target. The values for the projected physical velocity $v_{\rm proj}$ are scaled to an assumed distance d', without the inclusion of any additional errors to account for uncertainties in d'. The measurements of total proper motion $\mu_{\rm tot}$ and projected velocity $v_{\rm proj}$ from this work have been corrected for the effect of Galactic rotation. All our measurements and errors correspond to the median and 68% central interval of the underlying probability distribution. All upper limits derived in this work are at 90% confidence.

[a] The positions without listed uncertainties have not been corrected for *Chandra*'s absolute astrometric inaccuracy, and therefore have estimated 1σ–errors on the order of 0.4″, corresponding to an 0.8″ radius of the two-dimensional 90% confidence region.

[b] The most recent distance measurement of around 1.3 kpc (Reynoso et al. 2017) to Puppis A would imply a transverse velocity of $v_{\rm proj} = (496 \pm 47)\,{\rm km\,s^{-1}}$ for the CCO.

[c] No explicit values for μ_α, μ_δ were given.

[d] Due to the lack of suitable data, no proper-motion measurement currently exists for the CCO of G353.6−0.7.

References. (1) Chapter 3 (Mayer et al. 2020), (2) Mignani et al. (2007), (3) Mignani et al. (2019), (4) Halpern & Gotthelf (2015), (5) Halpern & Gotthelf (2010b), (6) Maxted et al. (2018).

motion could be established here.

We display an overview of the astrometric solutions of all known CCOs, derived in this work and previous studies, in Table 4.2, and compare their projected velocities to the distribution of radio pulsar velocities in Fig. 4.16. Our work almost doubles the number of CCOs with quantitative proper-motion measurements from five to nine. For several systems in this work, the results of our proper motion measurements are markedly different from reasonable expectations. For instance, for both G350.1−0.3 and RX J1713.7−3946, the present-day location of the CCO within the SNR suggested measurable nonzero proper motion. For RX J1713.7−3946, we were unable to obtain any significant signature of proper motion despite the small distance to the system. For G350.1−0.3, we did measure a mildly significant nonzero value, which is however considerably smaller than what the SNR morphology would suggest. This is similar to the case of PKS 1209−51/52, where Halpern & Gotthelf (2015) measured very small proper motion, despite a striking offset of the CCO from the apparent SNR center. These examples illustrate that estimates of the NS kick purely based on SNR geometry have to be interpreted with care, and in most cases cannot replace a direct measurement.

As demonstrated by Dohm-Palmer & Jones (1996), an inhomogeneous circumstellar medium can easily result in an offset between the SNR's explosion site and its apparent center, as the shock wave experiences different degrees of deceleration in different directions, leading to a distortion of the remnant's morphology. This effect was investigated in detail for Tycho's SNR by Williams et al. (2013), who showed that the observed density and shock velocity variations along its outer rim imply a significant offset between the apparent and true SNR center, by up to 20% of its radius. Therefore, even if a central NS appears clearly offset from its host's morphological center, such an offset need not be due to its proper motion, but may also be caused – solely or to some fraction – by the SNR's distorted shape.

The two most important factors limiting the precision of the measurements in this work are the availability of reliable astrometric calibration sources and their photon statistics. For instance, the uncertainties on CCO proper motion in G15.9+0.2 and Kes 79 are primarily due to the (comparatively) short exposures at the former and latter of the two epochs, respectively, which lead to a small number of photons available for precise astrometric localization. In contrast, for RX J1713.7−3946, we were hindered by the lack of observed X-ray sources with reliable astrometric counterparts in the HRC observation. We argue that the main reason for this is the smaller effective area and higher intrinsic background rate of the *Chandra* HRC when compared to the ACIS instrument. In principle, the design of the HRC as a microchannel plate instrument (Murray et al. 2000) is ideal for astrometric measurements. However, such measurements can only be performed in an absolute manner in the presence of coordinate frame calibration sources, for which the ACIS usually possesses better detection prospects, unless their X-ray emission is very soft.

By combining the measured total proper motion μ_{tot} with an estimate for the distance d to the SNR, one can constrain the projected velocity of the CCO in the plane of the sky $v_{\text{proj}} = \mu_{\text{tot}} d$. This can be viewed as a lower limit to the physical velocity of the NS and thus serves as a proxy to the violent kick experienced by the proto-NS at its birth. Therefore, by comparing the fastest measured NS velocities to theoretical considerations and numerical simulations of

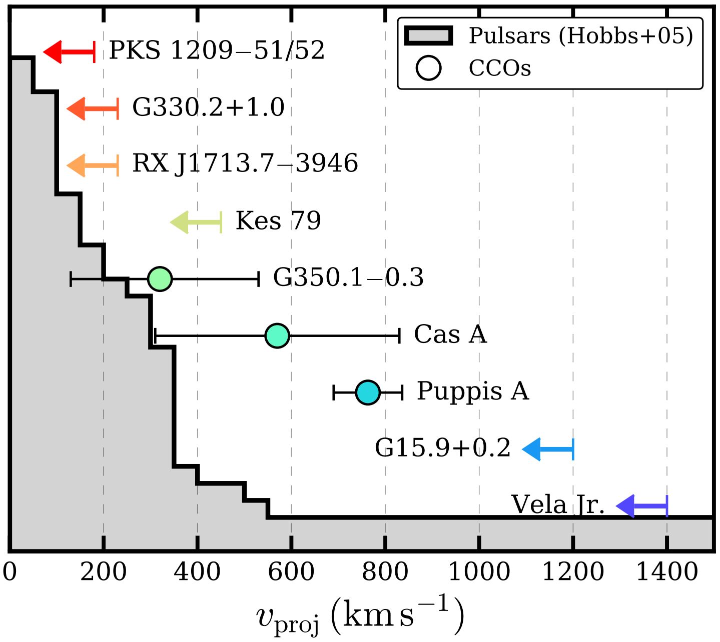

Figure 4.16: Comparison of CCO and radio pulsar kinematics. The gray histogram displays the inverse cumulative distribution of the projected velocities $v_{\rm proj}$ of young radio pulsars taken from Hobbs et al. (2005). This is compared with the available constraints on CCOs from this and other works (see Table 4.2), with the colored arrows indicating upper limits, and the error bars indicating 1σ uncertainties.

core-collapse supernovae, one can attempt to constrain the kick mechanism and the degree of explosion asymmetry.

Currently, the CCO with the largest securely measured velocity is RX J0822−4300 in Puppis A, with a value of $v_{\rm proj} = (763 \pm 73)\,{\rm km\,s^{-1}}$, scaled to a distance of 2 kpc. As is displayed in Table 4.2 and Fig. 4.16, none of the other known CCOs (except possibly those in G15.9+0.2 and Vela Jr. for which sufficient precision has not yet been achieved in a direct measurement) are likely to show a projected velocity in excess of $\sim 800\,{\rm km\,s^{-1}}$. A likely mechanism by which large NS kick velocities are achieved is the "gravitational tug-boat," in which an asymmetric ejecta distribution accelerates the proto-NS by exerting a gravitational pull in the direction of slow and massive ejecta clumps (Wongwathanarat et al. 2013). As it has been shown that kick velocities above $1000\,{\rm km\,s^{-1}}$ can be achieved in realistic explosion scenarios (Janka 2017b), none of the measured CCO velocities are in serious conflict with theoretical expectations.

At the present time, the observed distribution of CCO velocities shows no obvious departure from that for radio pulsars (see Fig. 4.16). For instance, assuming a Maxwellian velocity distribution[19] with one-dimensional $\sigma = 265\,{\rm km\,s^{-1}}$ as given by Hobbs et al. (2005), the probability of measuring $v_{\rm proj} \leq 250\,{\rm km\,s^{-1}}$ is around 35%. Therefore, observing three such cases in our sample is unsurprising. However, the current sample of measured CCO velocities is neither large

---

[19] The projection of a three-dimensional Maxwellian into the observed two dimensions yields a Rayleigh distribution $p(v_{\rm proj}) \propto v_{\rm proj} \times \exp\left(-v_{\rm proj}^2/2\sigma^2\right)$.

nor precise enough for definite conclusions on the velocity distribution of CCOs to be drawn.

Most likely, the task of performing a statistically meaningful comparison between kick velocities of radio pulsars and CCOs will require a lot of time and observational effort to complete (including the detection of new CCOs). However, it may ultimately help in shedding light on the question of what is the fundamental difference driving the phenomenological diversity of young NSs. At the present time, it is unclear how the difference in magnetic field strengths between CCOs, rotation-powered pulsars, and magnetars is related to the conditions before, during, or after the supernova explosion.

4.5.2 SNR expansion and explosion sites

Our proper motion measurements provide a constraint on the CCO's position over time, back to the explosion date of the supernova. This provides additional input to the physical interpretation of the present-day expansion and morphology of the SNR as the location of its true center can be estimated. With this in mind, we inferred explosion sites of our six SNRs by extrapolating our posterior distribution of the CCO's proper motion backward from its present-day location, to the assumed supernova explosion time. We then obtained the smallest two-dimensional regions containing 39.3% and 86.5% of the total probability mass, corresponding to 1σ and 2σ constraints on the explosion location, which can be regarded as the true center of the SNR. For this purpose, we assumed the following input ages, along the lines of available constraints (Table 4.1): 4000 yr (G15.9+0.2), 5000 yr (Kes 79), 340 yr (Cas A), 1000 yr (G330.2+1.0), 2000 yr (RX J1713.7−3946), and 700 yr (G350.1−0.3).

We compare the explosion sites to the present-day morphology of our six SNRs in Fig. 4.17. The extent of RX J1713.7−3946 is much larger than the *Chandra* field of view, which is why we used an archival *ROSAT* PSPC observation (Pfeffermann & Aschenbach 1996) to illustrate the characteristic structure of this SNR.

G15.9+0.2 and Kes 79: Possible direct evidence for expansion

It is immediately obvious that, for some SNRs, our proper motion measurements are physically much less constraining than for others. For instance, the extent of the uncertainty contours of the explosion sites of G15.9+0.2 and Kes 79 is almost comparable to the extent of the two SNRs themselves. The reason for this is the comparatively shallow exposure of part of the used data sets, in combination with the small intrinsic angular size and large age of the SNRs.

Nevertheless, we measured possible direct signatures of expansion for both remnants, which at this point appear slightly more significant for G15.9+0.2. If the true age of G15.9+0.2 were indeed lower than the 4000 yr that we assumed for estimating the explosion site, its uncertainty contours would "shrink" closer toward the CCO. The resulting constraints would likely still be consistent with what we estimate as the geometric center of the SNR.

For both objects, we have demonstrated the feasibility of an exploratory proper motion and expansion study, whose constraints could be significantly improved with future *Chandra* follow-up observations. For instance, a dedicated observation of Kes 79 around the year 2025 with a depth of $\sim$ 30 ks would extend the measurement baseline to $\sim$ 25 yr in combination with the

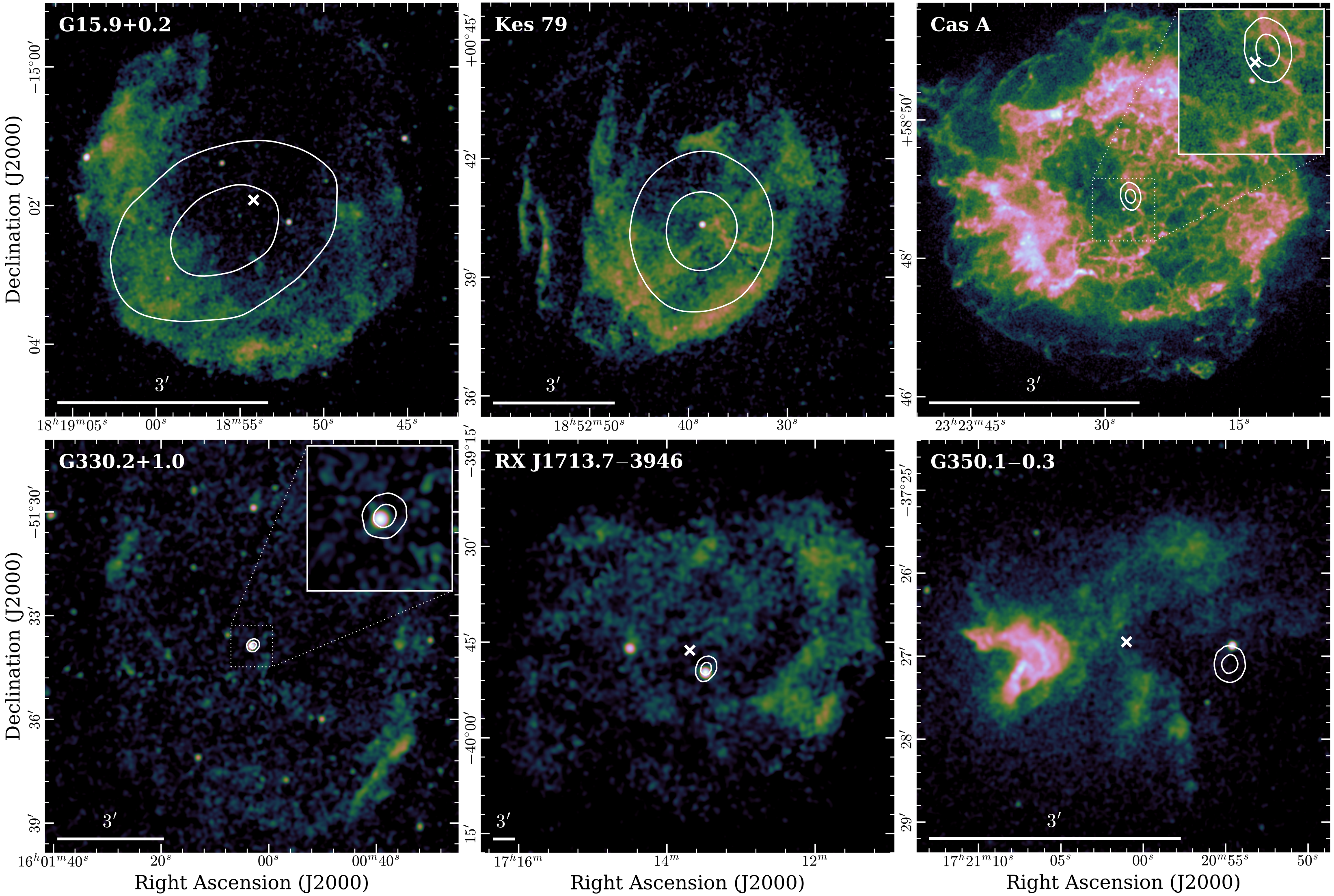

Figure 4.17: Constraints on the explosion sites of the six SNRs targeted in this paper. We show exposure-corrected images of the SNRs (with logarithmic intensity scaling), overlaid with 1σ and 2σ contours for the most likely origin of the CCO. The apparent geometrical centers of G15.9+0.2 (estimated in this work), RX J1713.7−3946 (Pfeffermann & Aschenbach 1996) and G350.1−0.3 (Lovchinsky et al. 2011) are indicated with white crosses. For Cas A, we plot the precisely constrained expansion center from Thorstensen et al. (2001) in an inset to make it more easily distinguishable. All images were created from the *Chandra* data used in this work, except for RX J1713.7−3946, where we used an archival *ROSAT* observation.

2001 observation. This would be expected to reduce the errors on proper motion and expansion by a factor of ~ 2. For G15.9+0.2, given that the very deep late-time observation was carried out in 2015, a followup observation appears to be feasible only after 2025. For example, a ~ 60 ks observation would effect an error reduction by a factor of ~ 1.9. In combination, reduced error bars on the motion of both the CCO and the SNR shell would provide insights into the kinematics and temporal evolution of filaments at the shock front as well as the SNR age. Moreover, a more accurate measurement of the proper motion of the CCO in G15.9+0.2 would further constrain its kick velocity. This would allow us to verify if its offset location within the SNR is indeed caused by a rather violent kick or is simply due to an asymmetric expansion of the SNR.

G330.2+1.0: Rapid shockwave expansion away from a stationary CCO

In contrast to G15.9+0.2 and Kes 79, we have provided stringent upper limits on the proper motion of the CCO of G330.2+1.0. Thus, its present-day location can be regarded as an almost perfect approximation to the SNR expansion center. The most immediate application of this is a comparison with the present-day expansion of the SNR. Borkowski et al. (2018) measured rapid motion away from the CCO, at up to $\sim 9000\,\mathrm{km\,s^{-1}}$ (for a distance of 5 kpc) for most parts of the SNR shell. In contrast, they detected a far smaller rate of expansion for parts of the southwestern rim, as well as significant temporal decline in its brightness. This, together with the relatively symmetric present-day morphology of the SNR, points toward a quite recent collision of the blast wave with a dense cloud in the southwestern region, causing significant deceleration after almost free expansion for the majority of the SNR's lifetime (Borkowski et al. 2018).

G350.1−0.3: A very young and highly peculiar SNR

Contrary to all other SNRs that host a CCO, the explosion site of G350.1−0.3 deduced in this work was found to be strongly offset from the remnant's emission center, but matches the position of the CCO closely (see Fig. 4.17). Consequently, the striking asymmetry of the SNR is further enhanced by our inferred explosion site: Only the rapidly propagating eastern "half" of the remnant appears to be visible at all, while the supposed half west of its true center, if present, remains almost entirely undetected. In any case, conservation of momentum requires the presence of a large amount of mass (either in the form of a compact object or ejecta) moving toward the west.

It is interesting to observe that, when ignoring the presence of the bright eastern clump, the remaining part of the SNR appears to form an almost circular incomplete shell, centered approximately on our inferred explosion site (indicated in Fig. 4.18). In this context, the bright eastern clump is required to be connected to fast ejecta as it is located far outside this potential shell, and shows the highest physical expansion velocities. As significant expansion was detected in all investigated regions, including the more diffuse northern and southern parts of the shell, it seems conceivable that the initial explosion imprinted a quadrupolar asymmetry on the ejecta distribution.

We consider a possible explanation for the missing western SNR shell to be a large density gradient in the surrounding interstellar medium (Gaensler et al. 2008). The alternative, a dipolar

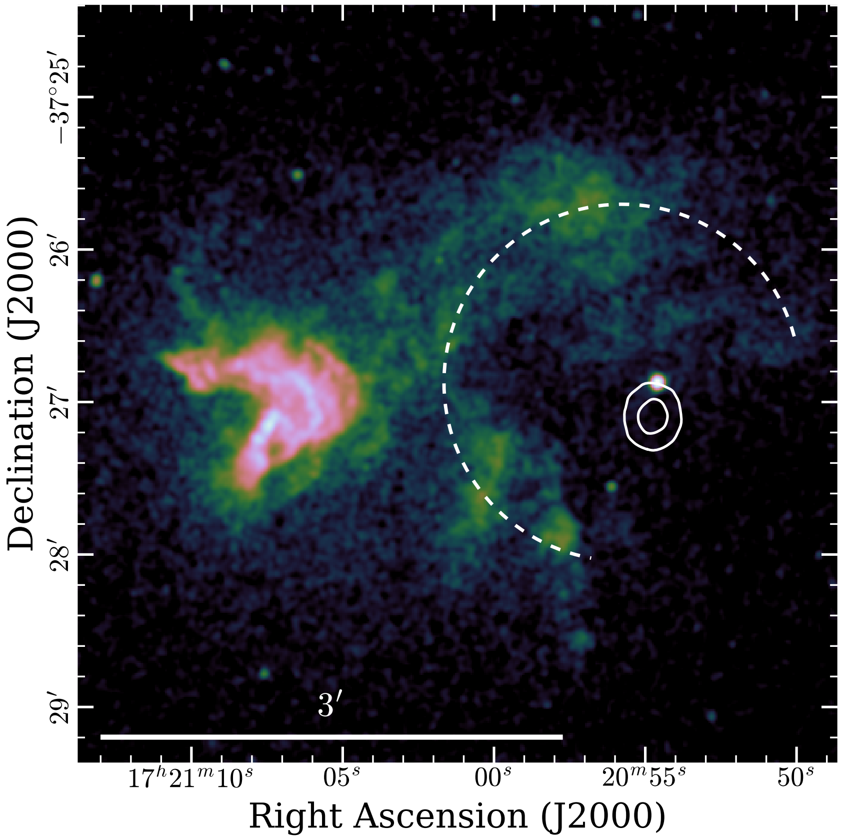

Figure 4.18: Potential diffuse shell of G350.1−0.3. We show the exposure-corrected image of G350.1−0.3 and its explosion site as in Fig. 4.17, overlaid with the incomplete circular shell tracing the SNR's diffuse emission (dashed line).

asymmetry in the amount of ejected material, would necessarily have imprinted a very strong westward kick on the CCO. Given our measurement of its modest northward proper motion, this seems rather unlikely. The detection of rapid eastward expansion of the shockwave at up to 5000 − 6000 km s^{-1} here and in Borkowski et al. (2020) only strengthens this conclusion, since it increases the momentum attributed to the bright eastern clump and thus the implied recoil. Furthermore, the expansion measurement leads to a precisely constrained explosion site, due to the now certain very low age of the SNR. Therefore, it can be stated with high confidence that the circumstellar material around G350.1−0.3 is highly inhomogeneous: It likely exhibits a density gradient from east to west and a significant localized density enhancement in the east. This eastern clump causes, as we have shown, a local velocity gradient in the expanding ejecta, which manifests itself in the fascinating outward-bent shape of the interacting shock wave.

Given our observations, we can infer that the true extent of the remnant is necessarily greater than apparent in X-rays, with a radius of at least 3.5′ (the approximate distance between the bright eastern ejecta clumps and the current location of the CCO), larger than the 2.5′ estimated in Lovchinsky et al. (2011). Since the remnant is larger, but also expanding much faster, than predicted, their age estimate of 600 – 1200 years is still consistent with the 600 – 700 years found by Borkowski et al. (2020) and deduced in our analysis.

The overall multiwavelength morphology of G350.1−0.3 is quite rich, and can aid in understanding its peculiar appearance in X-rays. As shown by Lovchinsky et al. (2011), the bright eastern clump has an obvious counterpart in the mid-infrared (24 μm), likely due to dust shocked by the interaction of the supernova ejecta with a molecular cloud. In its fainter regions, the 24 μm image of the SNR shows features corresponding to the southern part of the diffuse X-ray shell, but little apparent emission in the north. In contrast, as displayed by Gaensler et al. (2008), the SNR as viewed in the radio domain (at 4.8 GHz) exhibits a horizontal "bar," coincident with the northern part of the shell seen in X-rays. In turn, there appears to be no radio emission originating from the southern region. Keeping these points in mind, it is interesting to observe that the X-ray emission in these two regions also shows spectral differences, with the north emitting harder and the south softer radiation (see Fig. 1 in Borkowski et al. 2020). We interpret these findings as a further signature of inhomogeneous circumstellar medium, where denser circumstellar material in the south causes stronger interaction with the supernova blast wave, and thus leads to infrared emission from shocked or heated dust. Less dense material in the north interacts weakly with the shock wave, allowing it to propagate more freely, consistent with the observed radio and harder X-ray emission. Borkowski et al. (2020) come to a related conclusion, demonstrating that the northern part of the SNR shows little evidence for the presence of ejecta, and its emission is thus likely attributable to the propagation of the supernova blast wave through a comparatively thin medium.

Given the youth of G350.1−0.3, we checked the catalog of "guest stars" by Stephenson & Green (2009) for any potential historical counterpart. There is no obvious match to our SNR, except possibly one reported guest star in AD 1437, which would imply an age $\sim$ 580 yr. The specified position of this historic event is $(\alpha, \delta) = (16^{\mathrm{h}}55^{\mathrm{m}}, -38^{\circ})$, which places it about five degrees from the position of G350.1−0.3 (Stephenson & Green 2009). This spatial discrepancy and the possible nova explanation preferred by the authors argue against an association of this guest star with G350.1−0.3. In fact, the observed hydrogen column density $N_H \sim 4 \times 10^{22}\,\mathrm{cm}^{-2}$ (Lovchinsky et al. 2011) implies a visual extinction by around $A_V \sim 22$ mag, according to the relation of Predehl & Schmitt (1995). Combining this with an assumed peak absolute magnitude $M_V \sim -18$ for a core-collapse supernova at a distance of 4.5 kpc results in an observed apparent magnitude $m_V \sim 18$. It therefore seems very unlikely that the supernova associated with G350.1−0.3 would have been observable with the naked eye at all.

RX J1713.7−3946: Evidence for nonuniform expansion history

For RX J1713.7−3946, we have determined that the supernova explosion site is likely located within $\sim 2'$ of the present-day location of the CCO, which is somewhat at odds with the apparent geometrical center (Pfeffermann & Aschenbach 1996). The expansion of the SNR has been independently measured along three sectors of its shell, in the southeast, southwest, and northwest, in three individual studies (Acero et al. 2017; Tsuji & Uchiyama 2016; Tanaka et al. 2020). Interestingly, these works all showed that the maximal expansion speed of the shockwave is remarkably uniform, on the order of 4000 km s^{-1} (or 800 mas yr^{-1}), in all directions.[20]

With our determination of the expansion center of the SNR, we can provide updated constraints on the age of RX J1713.7−3946, by combining the location of its true center with the proper motion of the fastest "blobs" in the three regions, in analogy to Sect. 4.4.6: Comparing our inferred explosion site with the estimated position of "blob A" in the southwest (Tanaka et al. 2020), we find the angular distance covered by the shock wave up to today to be around $\vartheta = 1290'' \pm 50''$. Together with its measured proper motion of $\mu_{\mathrm{exp}} = (810 \pm 30)$ mas yr^{-1}, this yields an undecelerated expansion age of $\tau = (1590 \pm 80)$ yr. Since it is likely that the shock wave has been somewhat decelerated during its expansion history, we quote only the corresponding 90% upper limit on the expansion age of the SNR at $\tau < 1700$ yr. An analogous investigation using the reported values and errors for the northwest (Tsuji & Uchiyama 2016) and the southeast (Acero et al. 2017) rims yields higher formal limits of $\tau < 2520$ yr and $\tau < 3240$ yr, respectively, as illustrated in Fig. 4.19. We should note here that assuming a different age as input to the computation of the SNR's explosion site would slightly alter the size of the uncertainties on its expansion age. However, it would have little effect on the overall result since only significant nonzero motion of the CCO would bias our computation in any direction.

Therefore, if we assume all input expansion velocities and errors to be reliable, we can infer that the shock wave must have been decelerated nonuniformly, leading to the by far largest present-day expansion rate inferred for the southwest filament. Generally, it can be considered unlikely that any physical mechanism could have substantially accelerated the blast wave in the past, while it is very probable for the shock wave to have experienced some degree of deceleration due to past interaction with the surrounding medium. Therefore, we choose to quote the smallest out of the three measurements of τ, corresponding to a true age of < 1700 yr. This is a quite constraining result, as other recent age estimates are in the range 1500 – 2300 yr (Acero et al. 2017; Tsuji & Uchiyama 2016), depending on the exact model assumed for the density profiles of ejecta and the interstellar medium. In particular, our value is still consistent with the tentative association of RX J1713.7−3946 with the historical guest star, a possible supernova, observed by Chinese astronomers in the year 393 (Wang et al. 1997), if we assume parts of the southwest shell to be expanding almost freely.

However, it is somewhat puzzling that the shock wave seems to show the least decelerated expansion along the southwestern direction, in particular for blob A. The observed X-ray emission from blob A is much softer than its surroundings with a power law spectral index $\Gamma = 2.74 \pm 0.07$ (Tanaka et al. 2020). Using the simplest assumptions, this implies a shock velocity of only ~ 2800 km s^{-1} (Okuno et al. 2018), around 1000 km s^{-1} smaller than the measured value. Additionally, X-ray and molecular gas observations imply that the shock wave is expanding in a cavity blown by the progenitor in the southeast, whereas it has likely relatively recently struck the dense cavity wall in the west (Cassam-Chenaï et al. 2004; Fukui et al. 2012). Thus, one would naively expect to measure the least decelerated expansion of the shock wave in the southeast of RX J1713.7−3946. We therefore emphasize that our age estimate is largely based on the pub-

---

[20] All three studies measured the motion of several clumps or filaments. However, here, we focus on the highest respective velocities since these are expected to be closest to the undecelerated speed of the shock wave in that particular region.

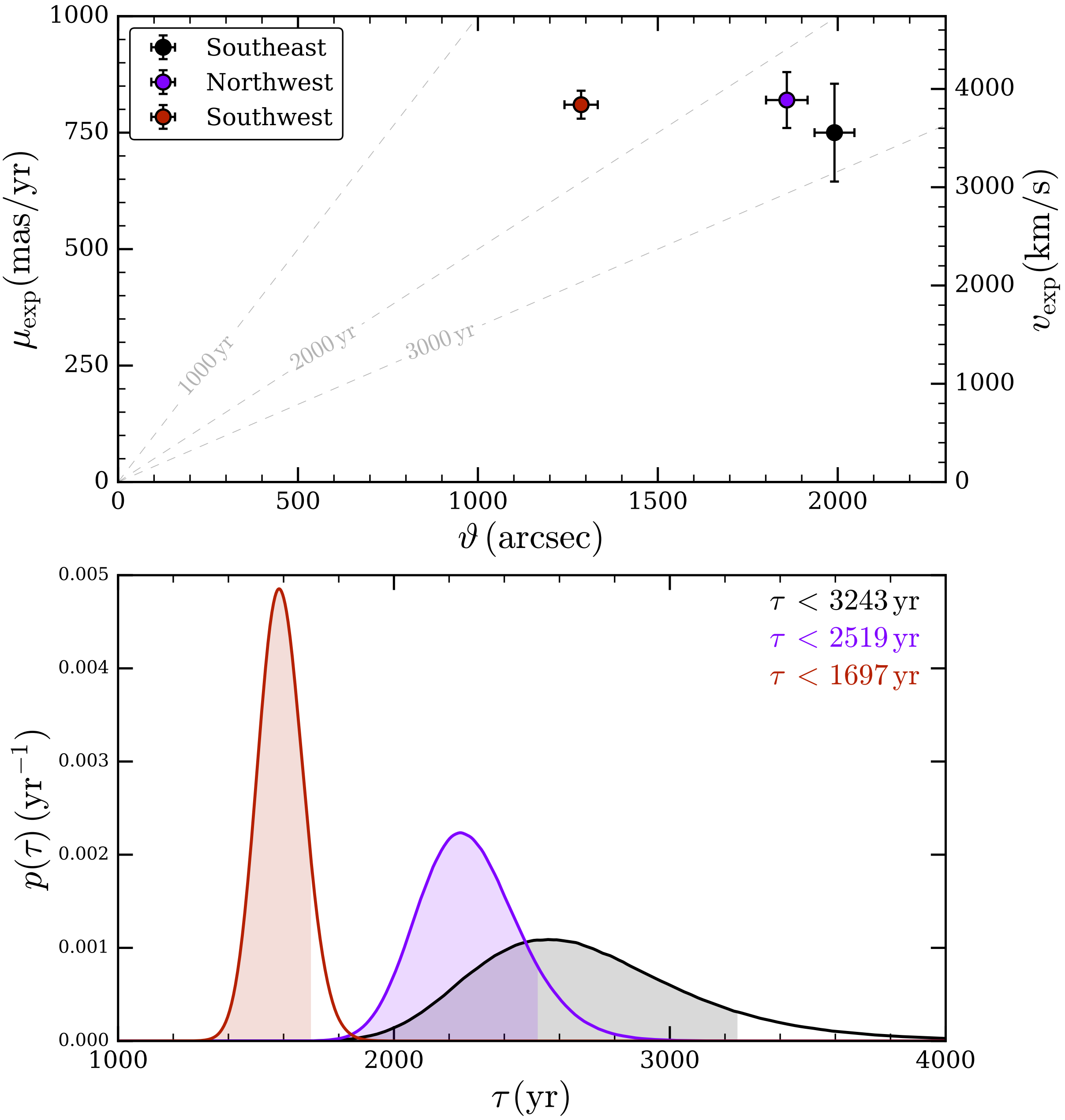

Figure 4.19: Expansion and age estimate for RX J1713.7−3946. The *top* panel shows the measured maximal proper motion $\mu_{\rm exp}$ of filaments in the expanding shell versus their angular distance ϑ from the explosion site. We indicate values from the literature for the southeast (Acero et al. 2017), northwest (Tsuji & Uchiyama 2016), and southwest (Tanaka et al. 2020) regions, respectively. For the proper motion, we display the error bars as given in the respective papers, scaled to 68% confidence and including systematic errors for Acero et al. (2017). The *bottom* panel shows the derived likelihood and corresponding 90% confidence upper limits for the undecelerated expansion age τ, inferred for the respective filaments.

lished proper motion of only a single blob in the southwest of the SNR by Tanaka et al. (2020), and is therefore to be taken with caution. In order to confirm these constraints, future followup observations and/or independent reanalyses are needed to verify both the proper motion of the CCO and that of blob A.

In this context, we consider again the double ring-like morphology of RX J1713.7−3946 in X-rays, which is most striking for the western shell (see Fig. 4.17). As pointed out by Cassam-Chenaï et al. (2004), both the inner and outer apparent ring exhibit a deformed elliptical structure. This structure appears nearly continuous around the entire SNR, and for the inner part, is matched well by the SNR's radio morphology. It is interesting to observe that the southern and eastern portions of this inner ring appear to be located quite close to our derived explosion site, as could be expected from a reverse shock. However, due to the overall weakness of thermal X-ray emission (Katsuda et al. 2015) and the radio detection of the inner ring, such an interpretation seems quite unlikely for this feature. Alternatively, one could also imagine that the complicated morphology stems from the superposition of two unrelated SNRs. This however can be considered unlikely due to the observed dominance of nonthermal X-ray emission across the entire remnant (e.g., Okuno et al. 2018) and the similar observed expansion velocities in multiple regions. The most likely scenario is that the SNR's peculiar morphology is caused by the projection of different parts of the shock wave, expanding into an anisotropic wind-blown cavity from the progenitor star. Locally varying collision times with the cavity wall are also a reasonable explanation for the observed differences in the relative expansion rate of the SNR.

Cas A: Adding independent constraints to optical expansion measurements

Finally, for Cas A, the situation is quite unique: While X-ray measurements of the propagation of the supernova shock wave do exist (e.g., Vink et al. 1998; Patnaude & Fesen 2009), their general target was to trace the exact location and propagation of the forward shock along the SNR shell. These studies were able to demonstrate that the forward shock of Cas A travels at a speed around (4200−5200) km s^{-1}, implying significant deceleration of the shockwave compared to free expansion. Direct expansion and age measurements for this infant SNR can be performed with much higher precision by tracing the motion of clumpy filaments in optical line emission. Prominent examples are the works by Fesen et al. (2006) and Thorstensen et al. (2001), who determined the explosion date of Cas A to around the year 1670.

Our constraint on the explosion site via NS proper motion is presently far less precise than the constraints from optical filament expansion. However, the accuracy of the latter result depends on the presence of systematic effects, for example from nonsymmetric deceleration of ejecta knots. If we imagine being able to use a potential future observation to extend our temporal baseline from around 10 to more than 20 years, we can envisage greatly reduced error bars on our X-ray measurement of the CCO's proper motion. For instance, we estimate that a further HRC observation of similar depth as the 1999 data set ($\sim$ 50 ks) would reduce the uncertainty on the proper motion by a factor of $\sim$ 2.5. The trajectory of the NS, which is almost perpendicular to the motion of the fastest optical knots (Fesen et al. 2006), could then serve as a complementary and completely independent ingredient to measuring the age and location of the expansion center of Cas A. The main advantage is that, due to its enormous density, the NS can be regarded as a "bullet," moving through its surroundings at effectively constant velocity. This makes its proper motion a useful tool to search for systematics in the motion of the fastest optical ejecta knots, possibly improving the accuracy of the age estimate for Cas A.

As pointed out by Fesen et al. (2006), it is interesting to observe that the NS in Cas A appears to be moving in a direction unrelated to that of the prominent "jets" of high-velocity ejecta. Instead, the CCO moves into the direction roughly opposite the brightest ejecta emission (Holland-Ashford et al. 2017). This is likely a manifestation of the NS kick mechanism, in which the proto-NS experiences the "gravitational tug" of slow and massive ejecta during the first seconds of the explosion (Wongwathanarat et al. 2013).

4.6 Summary

In this work, we have analyzed several sets of archival *Chandra* observations with the aim of deducing proper motion measurements consistently for all known CCOs with suitable data. Important elements of our analysis were the systematic search for serendipitous sources for astrometric frame calibration, the fitting of models of the *Chandra* PSF to the data to obtain unbiased source positions, and the alignment of measured positions with a calibrated reference frame. The final results were obtained by a simultaneous fit to the data from all observational epochs, to provide accurate estimates of the proper motion of the target. In this way, we attempted to exclude biases by PSF morphology, aspect reconstruction uncertainties, or the effects of Galactic rotation.

In total, we have presented six new measurements of NS proper motion, four of which had not been directly targeted prior to this work. Thus, we have approximately doubled the existing sample of CCOs with quantitatively constrained kinematics. We find moderately significant nonzero proper motion only for two objects in our sample, the NSs in Cas A and G350.1−0.3, with no evidence for any hypervelocity CCOs. In contrast, we set comparatively tight upper limits on the motion of several objects in our sample. For instance, the transverse physical velocities of the CCOs in G330.2+1.0 and RX J1713.7−3946 are constrained at $< 230\,\mathrm{km\,s^{-1}}$ at distances of 5 kpc and 1 kpc, respectively.

Complementarily, we have used our astrometrically coaligned data sets to directly measure the expansion of three SNRs, by comparing the one-dimensional emission profiles of characteristic features at different epochs. For the SNRs G15.9+0.2 and Kes 79, we applied our methods to comparatively shallow data sets to systematically search for signatures of expansion. For both objects, we find tentative evidence for the expansion of fragments of the SNR shell away from its center, at $2 - 2.5\sigma$ formal statistical significance. However, at the present time, the suboptimal exposure times and pointing configurations of the archival data sets prohibit a more detailed analysis of internal kinematics or an exact age estimate.

For the much younger SNR G350.1−0.3, we qualitatively confirm, using our independent methods, recently published results by Borkowski et al. (2020), most importantly the SNR's rapid expansion at close to $6000\,\mathrm{km\,s^{-1}}$. Conservative interpretation of our measurement implies an upper limit on the SNR's age of 700 years, which places G350.1−0.3 among the three youngest Galactic core-collapse SNRs. Additionally, we directly confirm that kinematics within the SNR vary on small scales within its bright eastern clump, likely due to the strong interaction of ejecta with a molecular cloud. Furthermore, expansion is visible also for much fainter emission features, proving that the peculiar observed morphology of G350.1−0.3 is in fact not due to chance superposition of two SNRs.

We have used our CCO proper motion measurements to constrain the exact explosion locations of the six SNRs in our sample. For instance, for the young SNR G330.2+1-0, we show that its supernova occurred within only 10″ of the present-day location of the CCO. A very interesting finding is the confirmation of a striking asymmetry in the SNR G350.1−0.3, whose explosion site is located far west of its apparent geometric center. This finding has severe implications on the properties of the SNR, requiring strong density inhomogeneities in the circumstellar environment of one of the youngest and most bizarre Galactic SNRs.

Finally, we have combined several published expansion measurements of RX J1713.7−3946 with our estimate of the supernova explosion site. We find that the current expansion rate significantly differs between individual regions. In particular, we show that part of the southwestern shock wave has likely experienced much weaker past deceleration than other regions, since otherwise its present-day velocity could not be reconciled with its origin. Using the most stringent resulting constraint, we determine an upper limit of 1700 years on the age of RX J1713.7−3946.

Some of our findings, as any multi-epoch astrometric analysis, would certainly profit from future *Chandra* follow-up observations, ideally similar to the 19-year campaign to measure the proper motion of the CCO in Puppis A (see Chapter 3). For instance, a future *Chandra* observation to be taken a few years from today would allow us to constrain the age and NS kick velocity of G15.9+0.2 and Kes 79, via an analysis of the kinematics of the CCO and the SNR shell. Additionally, a more precise trajectory of the NS could be used to indirectly constrain deceleration of optical ejecta filaments in Cas A, identifying potential systematic errors in its age estimate. Similarly, combining X-ray measurements of expansion for RX J1713.7−3946 with a more precise measurement of the proper motion of its CCO may help in supporting or rejecting its association with the historical SN 393. We hope that some of these exciting questions can be addressed during the lifetime of *Chandra*, as it is the only instrument allowing for the required high precision in X-ray astrometry – now, as in the foreseeable future.

Chapter 5

A global view of shocked plasma in the supernova remnant Puppis A provided by SRG/eROSITA

This chapter is largely based on a work published as Mayer et al. (2022) in Astronomy & Astrophysics, Volume 661, A31. However, Fig. 5.11 was not included in the published paper.

5.1 Introduction

Puppis A (G260.4−3.4) is a nearby Galactic core-collapse supernova remnant (SNR), which is particularly noteworthy for being one of the most prominent extended X-ray sources in the sky. It is most luminous at X-ray and infrared energies, where it appears as a deformed shell of around $56'$ in diameter, with a rich substructure that is formed by multiple filaments, clumps, and arcs (Arendt et al. 2010; Dubner et al. 2013). At those wavelengths, it exhibits a strong brightness gradient from northeast to southwest (Petre et al. 1982), likely caused by a density gradient in the surrounding interstellar medium (ISM). The distance to Puppis A has most recently been estimated to 1.3 ± 0.3 kpc via an H I absorption study (Reynoso et al. 2017), which places it behind the very extended nearby Vela SNR. Puppis A is detected across almost the entire electromagnetic spectrum, reaching from radio up until GeV energies (Xin et al. 2017). However, it has so far eluded detection at TeV energies, which is somewhat at odds with expectations (H. E. S. S. Collaboration et al. 2015).

Puppis A hosts the central compact object (CCO) RX J0822−4300. CCOs are a peculiar class of young neutron stars that have exclusively been observed in X-rays, and that are notable for the fact that their emission appears to be of a purely thermal nature (De Luca 2008), and in some cases for their very small magnetic fields (Gotthelf et al. 2013a). Studies of this particular CCO's large proper motion, as well as optical expansion studies of oxygen-rich ejecta knots, have provided kinematic age estimates for Puppis A in the range of 3700 – 4600 yr (Mayer et al. 2020; Becker et al. 2012; Winkler et al. 1988). This makes Puppis A much older than X-ray bright SNRs such as Cas A, Kepler, or Tycho, but significantly younger than the neighboring

Vela SNR.

Numerous previous works have identified and discussed prominent morphological features visible in Puppis A. These include the very luminous bright eastern knot (BEK), where the supernova shock wave interacts with a concentrated ISM density enhancement, leading to an indentation in the X-ray shell (Hwang et al. 2005). Moreover, Hwang et al. (2008) and Katsuda et al. (2008) independently discovered the presence of a localized enhancement of metal abundances (O, Ne, Mg, Si, and Fe), consistent with the presence of a compact ejecta knot and a more extended ejecta-rich region somewhat north of the SNR center, whereas they found little ejecta enrichment in the remaining SNR fraction under investigation. Similarly, Katsuda et al. (2010) found an apparent enrichment in ejecta in an underionized filament running parallel to the northeast rim of Puppis A. Detailed insights into the radiation processes acting within the BEK became available with *XMM-Newton* reflection grating spectroscopy. Via the analysis of line ratios, tensions with a purely thermal plasma emission model were revealed, which can possibly be relieved when including charge exchange processes (Katsuda et al. 2012). Using the same instrument, Katsuda et al. (2013) investigated the dynamics of the ejecta knot mentioned above, finding a radial velocity around $1500\,\mathrm{km\,s^{-1}}$, and providing a rare constraint on the oxygen temperature at $\lesssim 30\,\mathrm{keV}$.

The most sensitive and complete X-ray-view of the entirety of Puppis A was compiled by Dubner et al. (2013), who combined numerous pointed observations of *XMM-Newton* and *Chandra* to obtain a remarkable level of detail in a broad-band mosaic image of Puppis A. Luna et al. (2016) used this data set to introduce an interesting new method for creating spectral extraction regions. They briefly discussed their findings on temperature structure, foreground absorption, and elemental abundances, however only using a relatively coarse spatial resolution in the displayed maps. At this time, no comprehensive, spatially resolved spectral analysis of the entire Puppis A SNR has been carried out using data from only a single instrument.

eROSITA (Predehl et al. 2021) is the soft X-ray instrument aboard the German-Russian *Spectrum-Roentgen-Gamma* mission (Sunyaev et al. 2021). It consists of seven identical X-ray imaging telescope modules (TMs) with a field of view with a diameter around one degree, which are sensitive to X-ray emission in the $0.2-10.0\,\mathrm{keV}$ band. Its main task is the performance of eight consecutive all-sky surveys, which cumulatively will be around 25 times deeper in the $0.2-2.3\,\mathrm{keV}$ band than the *ROSAT* all-sky survey, and achieve an average spatial resolution around $26''$ (Merloni et al. 2012; Predehl et al. 2021).

In this work, we use an early eROSITA calibration observation to conduct a detailed spectro-imaging analysis of the X-ray emission of Puppis A. Our data set constitutes by far the most sensitive single observation to date that captures the emission from the entire SNR. Furthermore, it offers relatively uniform exposure over its extent, eliminating the need to create mosaics from many individual observations. Our paper is organized as follows: Sect. 5.2 presents basic characteristics of our data set and initial steps taken to ensure its correct treatment. We describe our methods and results in imaging and spectroscopic analysis in Sect. 5.3, with the core results of spatially resolved spectroscopy being presented in Sect. 5.3.3. Finally, in Sects. 5.4 and 5.5, we summarize our results and discuss their physical implications.

5.2 Observations and data preparation

The primary observation of Puppis A used in this work was carried out on 29 and 30 November 2019 as part of the calibration and performance verification campaign of eROSITA. Its main purpose was to calibrate the response and vignetting of the telescope. The observation was performed in field-scan mode, covering a region of around 2 × 2 degrees, including the entire Puppis A SNR and a western region of Vela. The total duration of the observation was 60 ks. Due to telemetry constraints, an electronic "chopper" was set that discards every second frame taken by the cameras, yielding an effective observation duration of 30 ks. Furthermore, only the detectors with on-chip filters (TMs 1, 2, 3, 4, and 6) were used. As the observation was performed in scanning mode, the effective spatial resolution of the data is similar to the survey average, at around 26″ (half-energy width). Due to slightly varying scanning patterns, the observation was formally divided into two parts of approximately equal length (ObsIDs 700199 and 700200), separated by a gap of about 2.5 ks.

For our entire analysis, we used the processing version `c001` of the data set, identical to the data released as part of the eROSITA early Data Release (EDR).[1] The data were analyzed using the publicly released version of the eROSITA science analysis software, `eSASSusers_201009` (Brunner et al. 2021).

As a first step, we used the task `evtool` to merge the data from the individual TMs and the two subobservations, allowing all valid patterns (`pattern=15`), which left a total of around 39 million valid events in the energy range 0.2 – 10.0 keV. The next step constitutes an important special treatment of the data, which was made necessary due to an error in the treatment of chopper values > 1 in the `c001` processing version of the data:[2] on one hand, the chopper settings were handled by introducing an individual good time interval (GTI) per valid frame (with a length around 50 ms). Therefore, in total, there are around 600 000 GTIs for each TM, which makes the runtime required for the computation of exposure-related quantities (exposure maps, ARFs) extremely long. In addition, a dead time correction factor (stored in the event file extensions `DEADCOR`) was introduced to account for the exposure loss, which effectively divides the total exposure by the chopper value for a second, unnecessary time. To tackle both issues, we manually modified the `GTI` extensions in the merged event file by joining all those GTIs constituting only of a single frame that were also separated only by the duration of a single frame. This step strongly speeds up downstream analysis, and corrects for the artificial exposure underestimation, as the factor 2 is now incorporated in the `DEADCOR` extensions only. We note that this issue is only present in the present processing version of the EDR data (`c001`), and will eventually be corrected in a future public update of the data, making the outlined treatment obsolete.

In addition to our main data set, we attempted to incorporate a second, more recent observation campaign of Puppis A (see Krivonos et al. 2021). This was carried out on 24 and 25 May 2021 as a grid of pointings toward the center and northeast of the SNR, with the purpose of cross-calibration with the Mikhail Pavlinsky ART-XC instrument (Pavlinsky et al. 2021).

---

[1] See https://erosita.mpe.mpg.de/edr/index.php

[2] See also https://erosita.mpe.mpg.de/edr/FAQ/

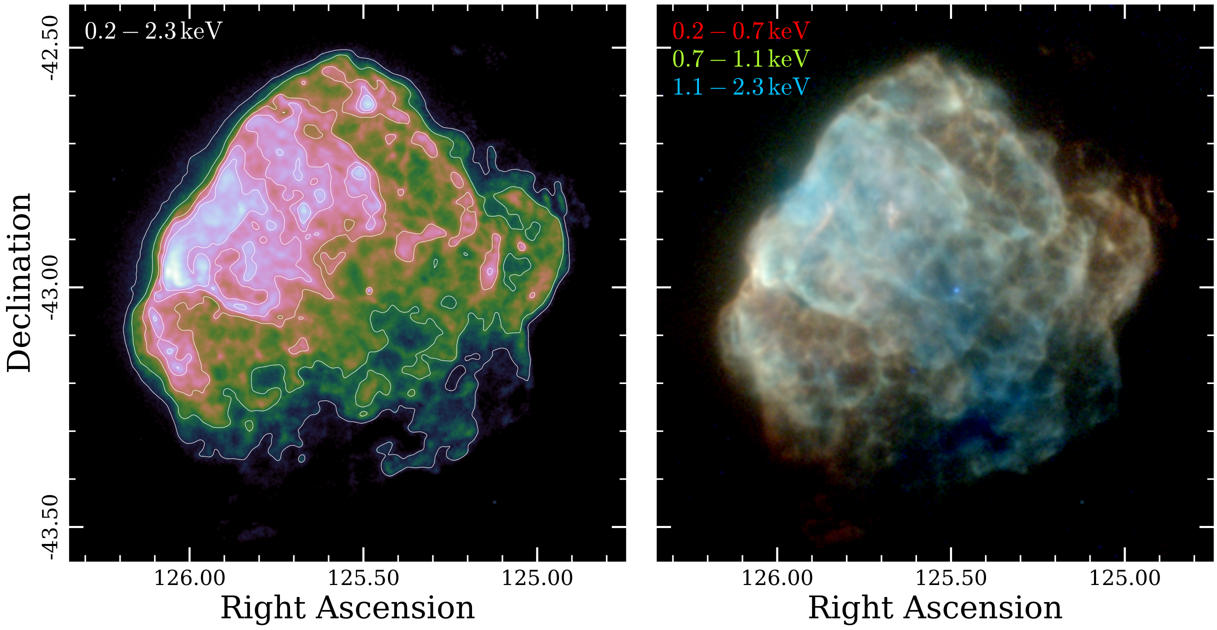

Figure 5.1: Single-band (*left*) and false-color (*right*) exposure-corrected images of Puppis A in the 0.2 – 2.3 keV range as seen by eROSITA. Both images were smoothed using a Gaussian kernel of width 6″. The color scale in this, as in all images shown in this work, is logarithmic. The contours in the *left* panel trace the 0.2 – 2.3 keV emission at levels of $1\times10^{-4}, 3\times10^{-4}, 1\times10^{-3}, 2\times10^{-3}, 3\times10^{-3}$ ct s^{-1} arcsec^{-2}. For comparison, the local background level in the broad band, measured in a region around 30′ northeast of the rim of Puppis A using the same observation, is around 1.2×10^{-5} ct s^{-1} arcsec^{-2}.

Usable eROSITA data with a chopper-corrected total exposure around 10 ks were obtained by the pointings with the eROSITA ObsIDs 730071–730092.[3] Unfortunately, less conservative instrument settings during these pointings led to exceeded event quotas on board. Therefore, a significant fraction of recorded frames were lost, preventing the determination of accurate normalizations from extracted spectra. We therefore only use this data set for brief imaging analysis (see Sect. 5.3.1), as it nonetheless provides an improved spatial resolution in the northeast SNR quadrant due to the different pointing strategy than in the primary observation.

5.3 Analysis and results

5.3.1 Broad-band morphology

As a first visualization of the eROSITA view of the morphology of Puppis A, we created images and exposure maps in the broad energy band 0.2 – 2.3 keV, as well as in soft, medium, and hard bands adapted to the SNR's spectrum at 0.2 – 0.7, 0.7 – 1.1, and 1.1 – 2.3 keV, which closely match the bands of Dubner et al. (2013). We chose the 0.2 – 2.3 keV range for our images, as

---

[3] These observations were assigned the experiment numbers 12110052003–12110052044 in the *SRG* mission program, which is the terminology used to identify the corresponding ART-XC data set in Krivonos et al. (2021).

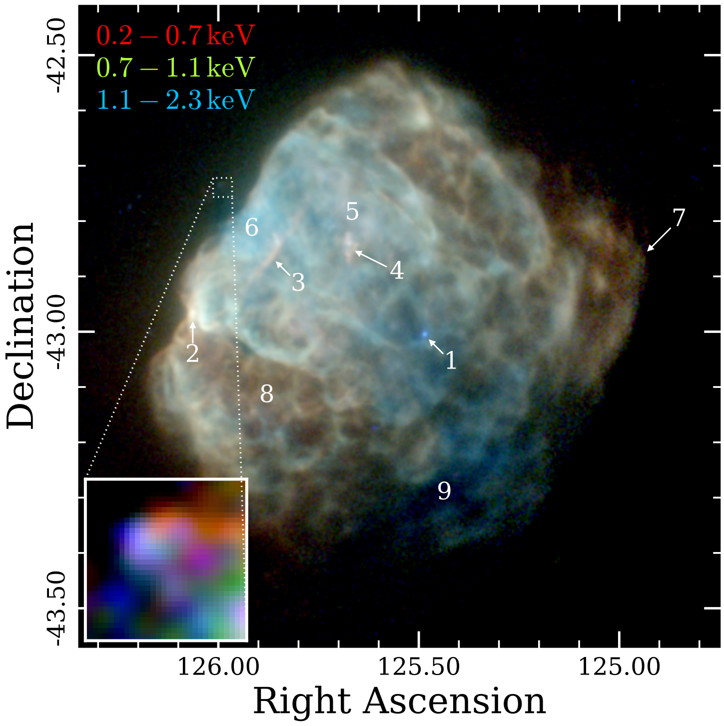

Figure 5.2: Guide to the main features of Puppis A. We show an exposure-corrected false-color image of Puppis A in the same energy bands as in Fig. 5.1, created from the data set taken in May 2021, with an inset highlighting the location and shape of the bullet-like feature. The numbers label the following characteristic features of Puppis A discussed in the text: (1) CCO, (2) BEK (see Hwang et al. 2005), (3) northeast filament (Katsuda et al. 2010), (4) ejecta knot (Katsuda et al. 2008), (5) ejecta-rich region (Hwang et al. 2008), (6) northeast rim, (7) western arc, (8) faint southeast, (9) southern hole (Dubner et al. 2013)

.

it contains both the most sensitive region of the eROSITA response, and the vast majority of the X-ray emission of Puppis A. All images and exposure maps here and in the following were constructed using the `evtool` and `expmap` tasks, using an angular binning of $4''$. As the local background level, which below 2.3 keV mainly originates from the nearby Vela SNR, is at least around an order of magnitude below the brightness level of Puppis A, except for its faintest and most absorbed regions, we did not attempt to subtract any background component to produce our broad-band images. We found that the noise in the images can already be sufficiently suppressed using a $\sigma = 6''$ smoothing kernel due to the excellent available statistics, with absolute count numbers ranging between around 2×10^3 ct arcmin^{-2} and 3×10^5 ct arcmin^{-2} across the SNR.

The resulting exposure-corrected broad-band and false-color images of Puppis A can be seen in Fig. 5.1. The global and small-scale morphology of Puppis A, first compiled in Dubner et al. (2013), is very well reproduced in our eROSITA observation. Numerous features, such as the characteristic strip of hard emission crossing the SNR from northeast to southwest, its hot CCO, an almost circular arc-like feature in the west, and numerous clumps and filaments across the

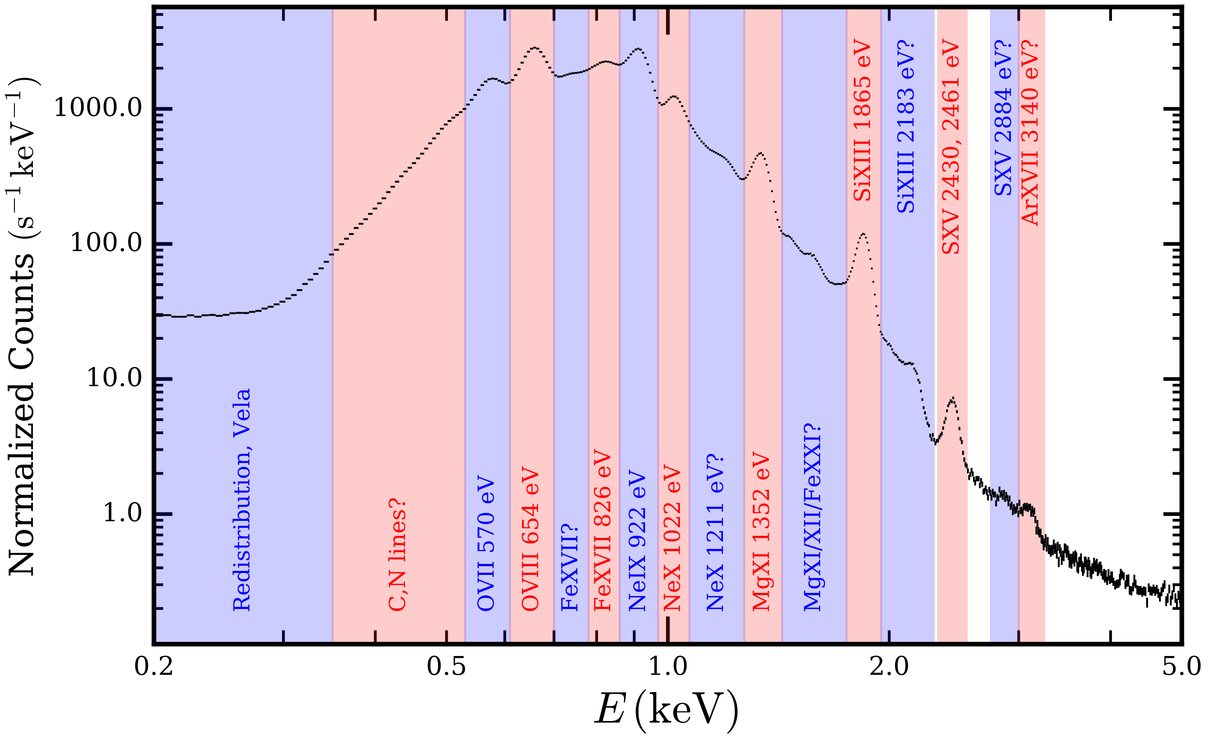

Figure 5.3: Integrated spectrum of the entire Puppis A SNR in the range 0.2 – 5.0 keV. The energy bands defined for narrow-band imaging are indicated in blue and red, together with the main contributions to the emission in the band. Line components marked with a question mark are likely present but subdominant with respect to the continuum.

SNR, are clearly visible. As far as the performance of eROSITA is concerned, it is particularly noteworthy that the image shown here was obtained using only a single observation with a total effective duration of 30 ks, distributed over a 2×2 degree field of view, leading to an effective vignetted exposure of Puppis A around 5 ks in the relevant band. In contrast, the image of Dubner et al. (2013) consists of a mosaic of many *Chandra* and *XMM-Newton* observations, with a total of several hundreds of kiloseconds exposure time.

Figure 5.2 displays an analogous false-color image to Fig. 5.1 that was created from the calibration observations carried out in May 2021. In this figure, we have labeled prominent features of Puppis A that are discussed here and in the following sections, in order to ease their identification by the reader. While the displayed data set largely provides an identical impression to Fig. 5.1, it exhibits a somewhat better spatial resolution in the northeast of Puppis A, as the pointings were mainly aimed there. This reveals a previously unknown feature located outside the northeast rim of the remnant. Located at around $(\alpha, \delta) = (08^{\mathrm{h}}23^{\mathrm{m}}59^{\mathrm{s}}, -42^{\circ}44')$, just outside the field of view of previous *Chandra* and *XMM-Newton* observations, it shows a cone-like morphology, and thereby resembles the well-known but much larger Vela “shrapnels”, which are interpreted as fragments of ejecta outside the SNR shell (Aschenbach et al. 1995; Miyata et al. 2001). Unfortunately, the emission of the feature is comparatively faint, preventing any further spectral analysis. Assuming a shocked plasma model typical for Puppis A (see Sect. 5.3.3), the observed count rate of $0.05\,\mathrm{ct\,s^{-1}}$ suggests an incident flux of $\sim 4 \times 10^{-14}\,\mathrm{erg\,s^{-1}\,cm^{-2}}$ in the $0.2 - 2.3\,\mathrm{keV}$ band, on top of a dominant background.

5.3.2 Narrow-band imaging and ratio images

The improved spectral resolution and reduced low-energy redistribution of the eROSITA CCDs with respect to those of *XMM-Newton* EPIC-pn (Meidinger et al. 2020) allow us to obtain cleaner narrow-band images of Puppis A that isolate the emission of individual lines or line complexes. In order to define the ideal bands to isolate such lines, we extracted an integrated spectrum of the entire remnant using `srctool`, and investigated the presence of strong lines in it (see Fig. 5.3). While the physical meaningfulness of a detailed fit to this integrated spectrum would be limited due to the superposition of plasmas at different conditions and absorbed by different column densities, it is a useful tool to identify the presence also of weaker lines at high energies. Based on this integrated spectrum, we defined 16 narrow energy bands (indicated in Fig. 5.3), covering strong and weak line complexes and pseudo-continuum regions across the energy range $0.2 - 3.25\,\mathrm{keV}$.

An array of exposure-corrected images in these 16 bands is shown in Fig. 5.4. For each image, we used a logarithmic intensity scale whose zero point was set to the median brightness of all pixels, thus preserving comparability of the bands despite varying dynamic ranges. We chose to refrain from attempting to correct for the presence of background in this part of our analysis, for the following reasons: in the softest bands, the dominant background component, the Vela SNR, has a nonuniform and unknown morphology, making any attempted correction dependent on the assumption of a highly uncertain spatial template. In the hard bands ($> 2.3\,\mathrm{keV}$), the dominant component is the instrumental background, which generally exhibits little flaring (Freyberg et al. 2020), and is approximately uniform on the spatial scales of the instrumental field of view ($\sim 1°$), which is why we consider its presence to have little impact on our imaging analysis.

One of the most prominent characteristics visible is the strong absorption of the southwest quadrant of Puppis A, recognizable in the lack of observed emission at low energies. Furthermore, while at low energies, the BEK clearly dominates the SNR's emission, at the highest energies, its morphology is dominated by a region at the northeast rim, and by the CCO, which emits as a hot blackbody. More subtle differences between individual energy bands become visible upon close inspection, in particular if one overlays the individual narrow-band images.[4]

In order to make the presence of such differences between narrow-band images quantifiable and visible on paper, we created maps displaying the ratio of selected energy bands in the following way: first, in order to obtain sufficient signal in all regions, we decided to rebin rather than smooth the data in each image, to preserve the independence of neighboring regions and not create any artifacts close to edges. To achieve this, we used the adaptive Voronoi binning algorithm by Cappellari & Copin (2003), requiring a minimum signal-to-noise ratio in the $0.2 - 2.3\,\mathrm{keV}$

---

[4] A movie looping through the emission of Puppis A in the individual energy bands shown in Fig. 5.4 is available at `https://www.aanda.org/articles/aa/olm/2022/05/aa42517-21/aa42517-21.html` as online supplementary material to the published version of this chapter.

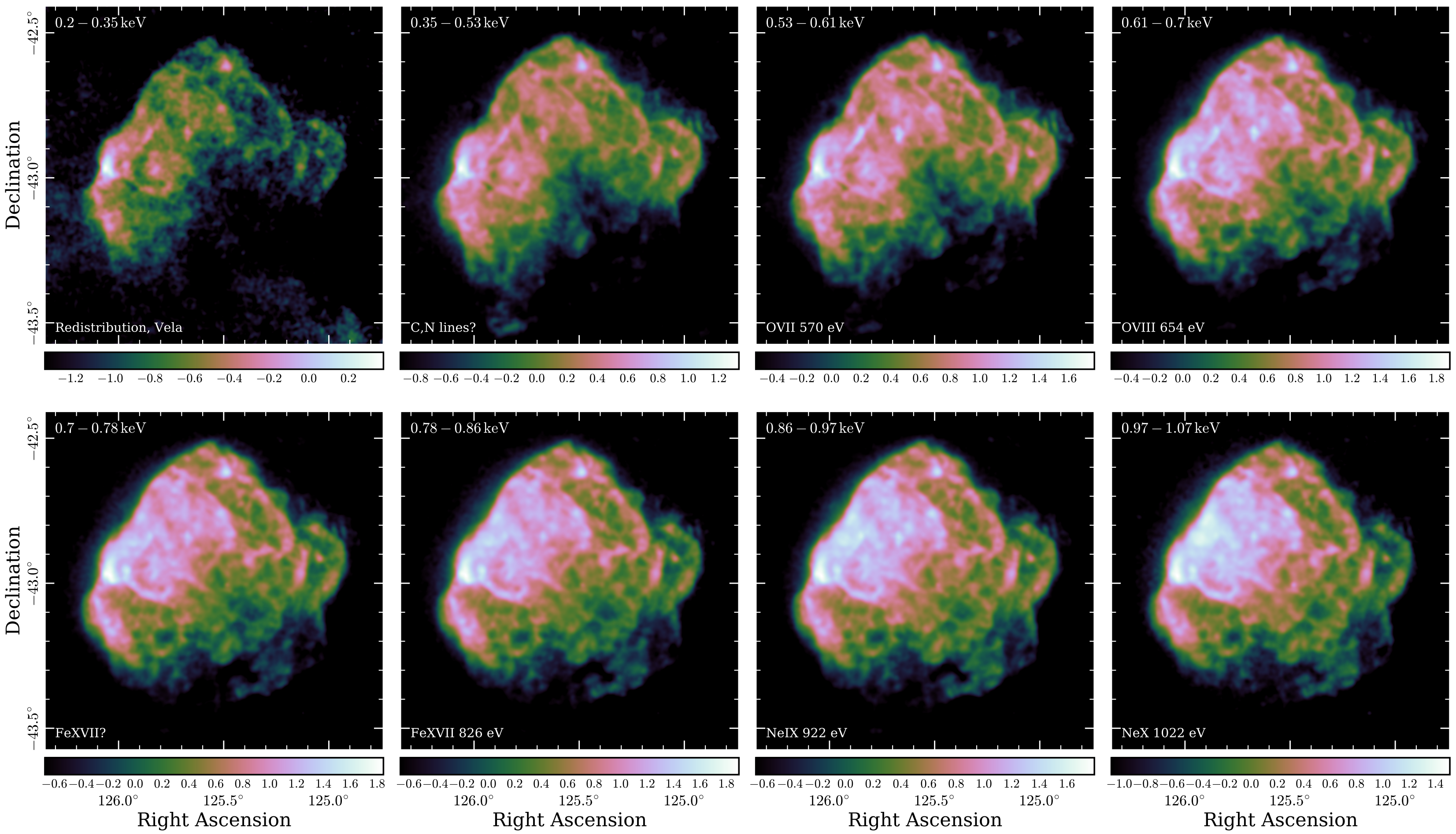

Figure 5.4: Exposure-corrected narrowband images of Puppis A. For all bands below 2.3 keV, we used a uniform smoothing kernel of 20″, while for those above 2.3 keV, we used 60″. These kernels were chosen in order to ensure maximum comparability between bands, while taking into account the much poorer statistics at high energies. In each image, we used a logarithmic color scale with the maximum at the peak count rate, and the minimum at the median count rate of all displayed pixels. The color bar underneath each panel indicates the displayed range of the logarithmic count rate in units of ct s^{-1} keV^{-1} $arcmin^{-2}$, to illustrate the dynamic range of each image. The upper left corner of each panel indicates the energy band covered by the image, while in the lower left corner, we indicate the physical content of the respective energy range. Components marked with a question mark are expected to be subdominant with respect to the (apparent) continuum.

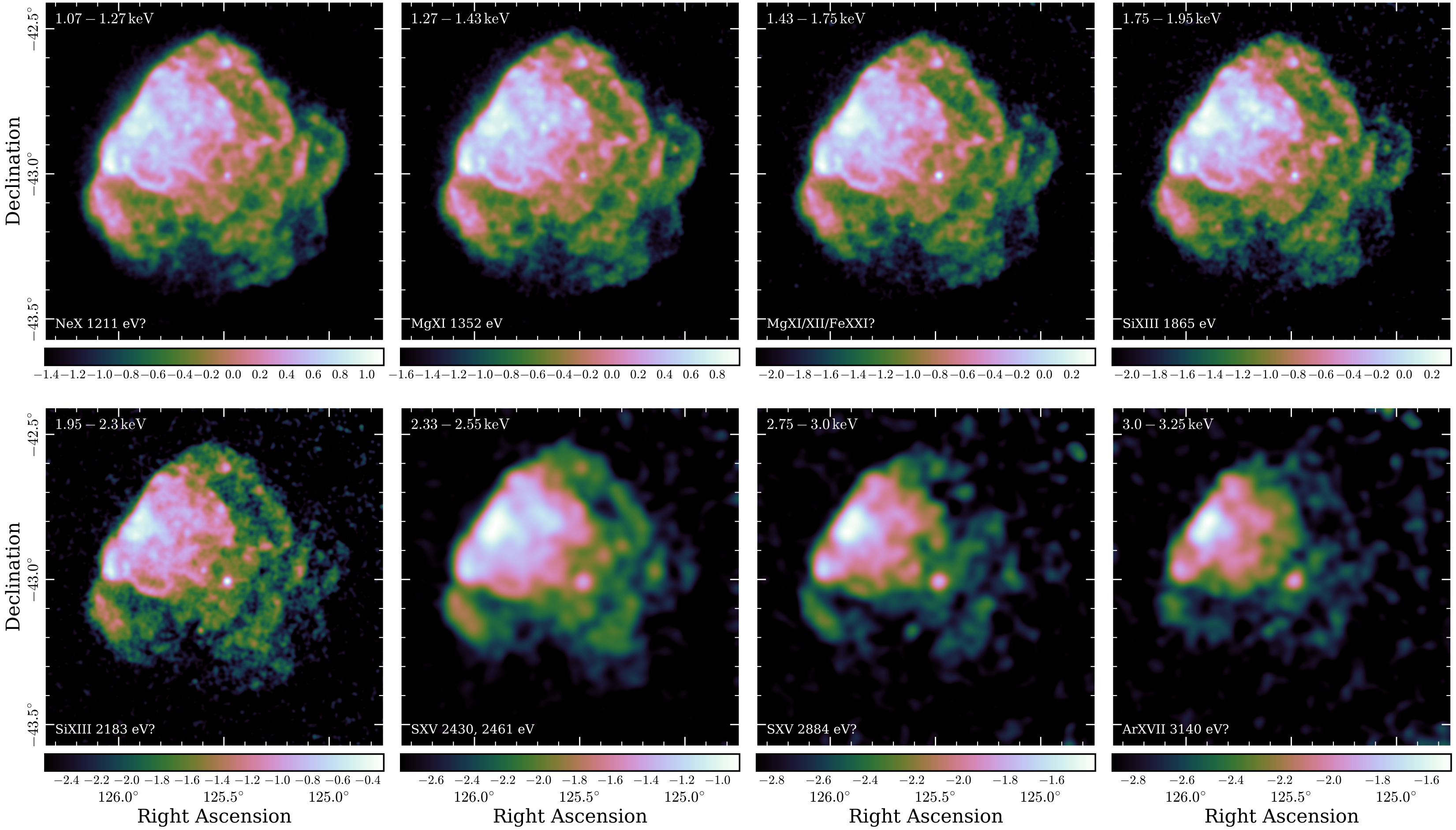

Figure 5.4: Continued.

band of $S/N = 200$. Prior to the binning, the CCO was masked in the input image, as we were mostly interested in the diffuse emission in its surroundings.

In order to obtain diagnostic maps of plasma conditions and elemental abundances, we chose to compare selected adjacent energy bands, such that the relative difference introduced by spatially variable absorption columns is reduced as much as possible, and does not fully mask the effect of locally varying physical conditions. To put these comparisons on a quantitative scale, we created maps of the band ratio H, which we defined as

$$H = \frac{R_2/A_2}{R_1/A_1}, \tag{5.1}$$

where R_1 (R_2) refers to the vignetting-corrected count rate in the softer (harder) of the two adjacent bands, and A_1 (A_2) describes the on-axis effective area of the telescope averaged over the respective energy range. This effective area correction allows us to directly compare observed line strengths, removing the effect of the telescope's energy-dependent response.

The resulting maps of the ratio H between selected energy bands are shown in Fig. 5.5. Most panels in this figure reflect the strength of emission lines of metals typical for ejecta, as they display the ratio of a line-dominated to a (pseudo-)continuum-dominated band. While these band ratios are of course also influenced by other factors, such as plasma temperature or ionization age, strong line emission may point toward a large abundance of the respective element. For instance, a prominent peak of emission line strength from the species O VII, Ne IX, Mg XI, Si XIII, and S XV is visible in a region located somewhat north of the SNR center, corresponding to the features labeled 4 and 5 in Fig. 5.2. This is consistent with the previously established presence of ejecta there (see Katsuda et al. 2008, 2013; Hwang et al. 2008). In contrast, the region of the BEK, for instance, does not show any apparent enhancement in these emission lines, as is expected from emission dominated by the collision of the blast wave with a density enhancement of the ISM (Hwang et al. 2005).

From a physical standpoint, the top right panel of Fig. 5.5 has a somewhat different interpretation: it displays the line ratio of two ionization states of oxygen, that is, the ratio of O VIII to O VII. Consequently, a relative enhancement of this ratio indicates that the material exists in a higher ionization state compared to the average. Conversely, a relative deficiency corresponds to a lower ionization state, introduced either by colder or by underionized, meaning recently shocked, plasma. Comparing our results to the line ratio map published by Hwang et al. (2008), we recover the low degree of ionization of plasma in the northeast filament, as well as in a relatively faintly emitting region in the southeast (labeled as 8 in Fig. 5.2). Similarly, we find a relative deficiency of O VIII emission along the entire northwest rim of Puppis A, which may be connected to a systematically smaller plasma temperature, particularly for the western arc, in accordance with its very soft broad-band emission (see Fig. 5.1). The northeast rim is the region most strongly dominated by O VIII emission. In combination with its increasingly dominant character toward high energies in imaging (see Fig. 5.4), this indicates that this region likely exhibits an elevated temperature and/or conditions close to collisional ionization equilibrium.

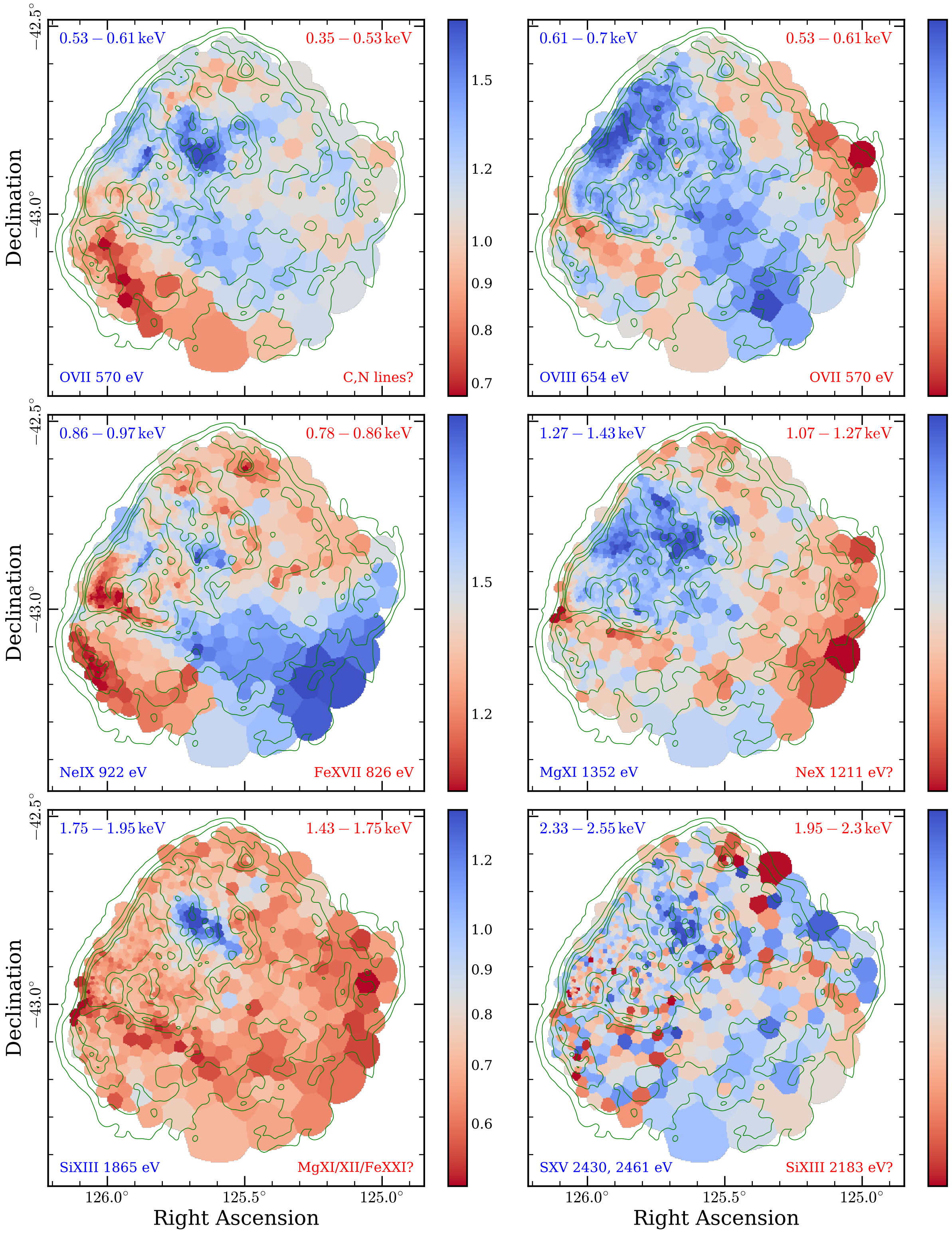

Figure 5.5: Maps of the ratio H calculated from selected adjacent narrow energy bands. In each panel, we indicate a larger relative strength of the harder (softer) band in blue (red), with the respective energy ranges indicated in the upper left (right) corner. The median 1σ uncertainties of H, which illustrate the typical statistical noise level in each panel, are (from *left* to *right*) 0.029 and 0.032 in the *top* row, 0.023 and 0.015 in the *middle* row, and 0.040 and 0.13 in the *bottom* row. The green contours trace the broad-band surface brightness of Puppis A, as displayed in Fig. 5.1.

5.3.3 Spatially resolved spectroscopy

In order to obtain a quantitative and in-depth picture of the physical conditions of the X-ray emitting plasma in Puppis A, it is necessary to go beyond the computation of band ratios, by forward-modeling the spectra extracted from different regions of the SNR. In order to achieve that, similarly to Sect. 5.3.2, we used the adaptive Voronoi binning scheme of Cappellari & Copin (2003) to define extraction regions from the broad-band $(0.2 - 2.3\,\mathrm{keV})$ count image, masking the location of the CCO. The resulting bins were saved as bit masks into FITS files, and individually fed into the `eSASS` task `srctool` to extract the corresponding spectra and ancillary response files (ARFs).[5] In order to test different trade-offs between photon statistics and spatial resolution, we performed three separate runs, with target signal-to-noise ratios of $S/N = 200$, 300, and 500, resulting in 772, 345, and 114 bins containing around 40 000, 90 000, and 250 000 counts, respectively.

We used `PyXspec`,[6] the Python implementation of `Xspec` (version 12.11.0, Arnaud 1996), to fit the spectra from our individual regions. To describe the emission of Puppis A, we used a model of a plane-parallel shocked plasma (Borkowski et al. 2001) with nonequilibrium ionization (NEI), and foreground absorption following the Tübingen-Boulder model with the corresponding abundances (Wilms et al. 2000). This model is expressed as `TBabs*vpshock` in `Xspec`. Similarly to previous works, we thawed the abundances of the most prominent line-emitting elements in the spectral range of Puppis A (O, Ne, Mg, Si, S, and Fe), while all remaining metal abundances were fixed to solar values. The lower limit of the ionization timescale as well as the redshift were fixed to zero. Attempts to leave the redshift free to constrain line-of-sight velocities are not viable with the given data, as the absolute energy calibration in the `c001` processing is not yet at the necessary level to allow for the reliable detection and quantification of the expected blue- or redshifts from velocities on the order of $\sim 1500\,\mathrm{km\,s^{-1}}$ (Katsuda et al. 2013). While our model is not overly complex, we consider it a useful approximation to the observed spectra, which can be employed to constrain the average chemical and physical plasma properties throughout the SNR.

The background was modeled with three additional physical components: the first component, the instrumental background, is expected to be more or less homogeneous in spectral shape, irrespective of sky location. This can be justified with the rare occurrence of soft proton flares during solar minimum at the L2 environment of eROSITA and the weak nature of fluorescence lines on the detector (Freyberg et al. 2020). Therefore, the only parameter left free in our fits was a multiplicative constant setting the global background normalization in the respective region, whereas its relative shape was taken from models fitted to filter-wheel-closed data.[7] The model we used consisted of a combination of two power laws and several Gaussian emission lines, reflecting the particle-induced background continuum and instrumental fluorescence lines, respectively. As these components do not correspond to actual X-ray photons, the instrumental background model was not multiplied by the ARF. The second component, the nonthermal X-

---

[5] Since `srctool` currently writes only the default redistribution matrix file (RMF), irrespective of, for example, the detector coordinates, we only extracted a single RMF, which we used to fit all spectra.

[6] `https://heasarc.gsfc.nasa.gov/xanadu/xspec/python/html/index.html#notes`

[7] Models are available at `https://erosita.mpe.mpg.de/edr/eROSITAObservations/EDRFWC`

ray background introduced by unresolved AGN, was modeled using a single absorbed power law with a photon index of 1.46 and fixed normalization per unit area following De Luca & Molendi (2004).

Finally, the thermal X-ray "background" in the relevant sky area requires careful treatment. Its dominant component at low energies is in fact a foreground, originating from the very extended Vela SNR, whose emission cannot be assumed to be spatially uniform. Vela is characterized by quite soft emission, generally at a lower surface brightness than Puppis A. However, we found that in particular for regions in which the observed emission of Puppis A is faint at low energies (e.g., in the south), its inclusion has a significant improving effect on the spectral fitting. We modeled the contribution of this component in the following way: we extracted a spectrum from a nearby bright Vela filament within the field of view of our observation, and fitted it using a `TBabs*(vapec+vpshock)` model (e.g., Silich et al. 2020), in addition to the aforementioned instrumental and nonthermal components. Our primary goal in this step was finding a good fit to the data, rather than obtaining a straightforward physical interpretation for the background model. We therefore left the abundances of all relevant elements free to vary independently to achieve maximum model flexibility. During the fit of the spectra of Puppis A, the shape of this model was fixed, and only the overall normalization of the thermal background left free. We note that Vela is located at a distance of approximately 290 pc (Dodson et al. 2003), around one quarter of the distance to Puppis A. This means that the soft portion of the thermal foreground and background component is subject to much less absorption than the emission of Puppis A, and any correlation between source and background absorption column densities will be rather weak. This justifies fixing the column density in our background template to a uniform value for all regions, rather than attempting to correct for its unknown possible variation across Puppis A.

Even though virtually all physical emission from Puppis A is encountered between around 0.4 and 4.0 keV, in order to be able to robustly constrain the normalization of both the soft thermal X-ray background and the high-energy tail of the instrumental background, we used a very wide energy range of 0.20 – 8.50 keV for spectral modeling. In order to avoid rebinning the spectra prior to their analysis, we used Poissonian (i.e. , Cash) statistics for all our fits (Cash 1979). For the source spectra, elemental abundances were first kept frozen and then thawed after an initial run. Finally, the `error` command was run to reduce the odds of converging toward secondary minima, and to obtain a rough estimate of the statistical uncertainty of our parameters. By repeating the outlined procedure for all adaptively binned spectra and recombining the results with the celestial location of the regions, we created maps of the physical parameters constrained by our model.

The `Xspec` expression for the emission measure, EM, acts as a normalization of the model and encodes information about the density of the emitting plasma:[8]

$$\mathrm{EM} = \frac{10^{-14}}{4\pi d^2} \int n_e n_\mathrm{H} \,\mathrm{d}V, \tag{5.2}$$

where d describes the distance to Puppis A, n_e and n_H describe the post-shock number densities of electrons and hydrogen atoms, respectively, and the integral runs over the emitting physical

---

[8] See `https://heasarc.gsfc.nasa.gov/xanadu/xspec/manual/`

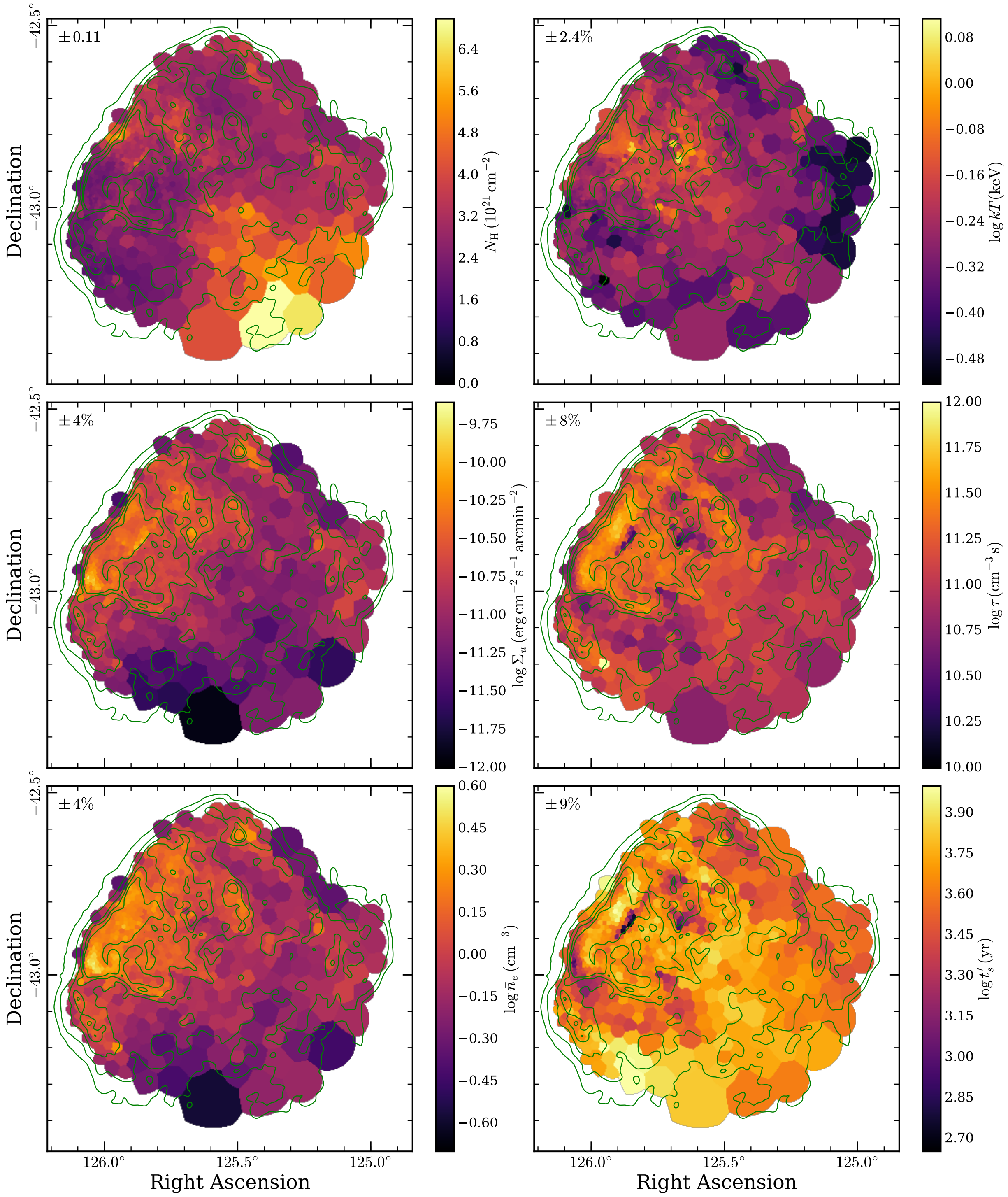

Figure 5.6: Parameter maps obtained from spectral fits to adaptively binned regions with $S/N = 200$. The color bar on the right of each panel indicates the displayed range of the respective parameter. The quantities displayed in the individual panels are the absorption column density $N_{\rm H}$, the plasma temperature kT, the unabsorbed surface brightness Σ_u in the $0.2 - 5.0$ keV band, the ionization age τ, the electron density proxy $\bar{n}_e$, and the pseudo-shock-age t'_s. All bins that extend up until the edge of our input image were masked, as these are dominated by background. In the upper left corner of each panel, we indicate the typical statistical uncertainty of the displayed quantity, which corresponds to the median over all bins of the observed 1σ errors. For all logarithmically displayed quantities, the characteristic fractional error is reported in per cent. For those displayed on a linear scale, the error is given in the same units as indicated on the color bar. The green contours in each panel trace the broad-band count rate of Puppis A, shown in Fig. 5.1.

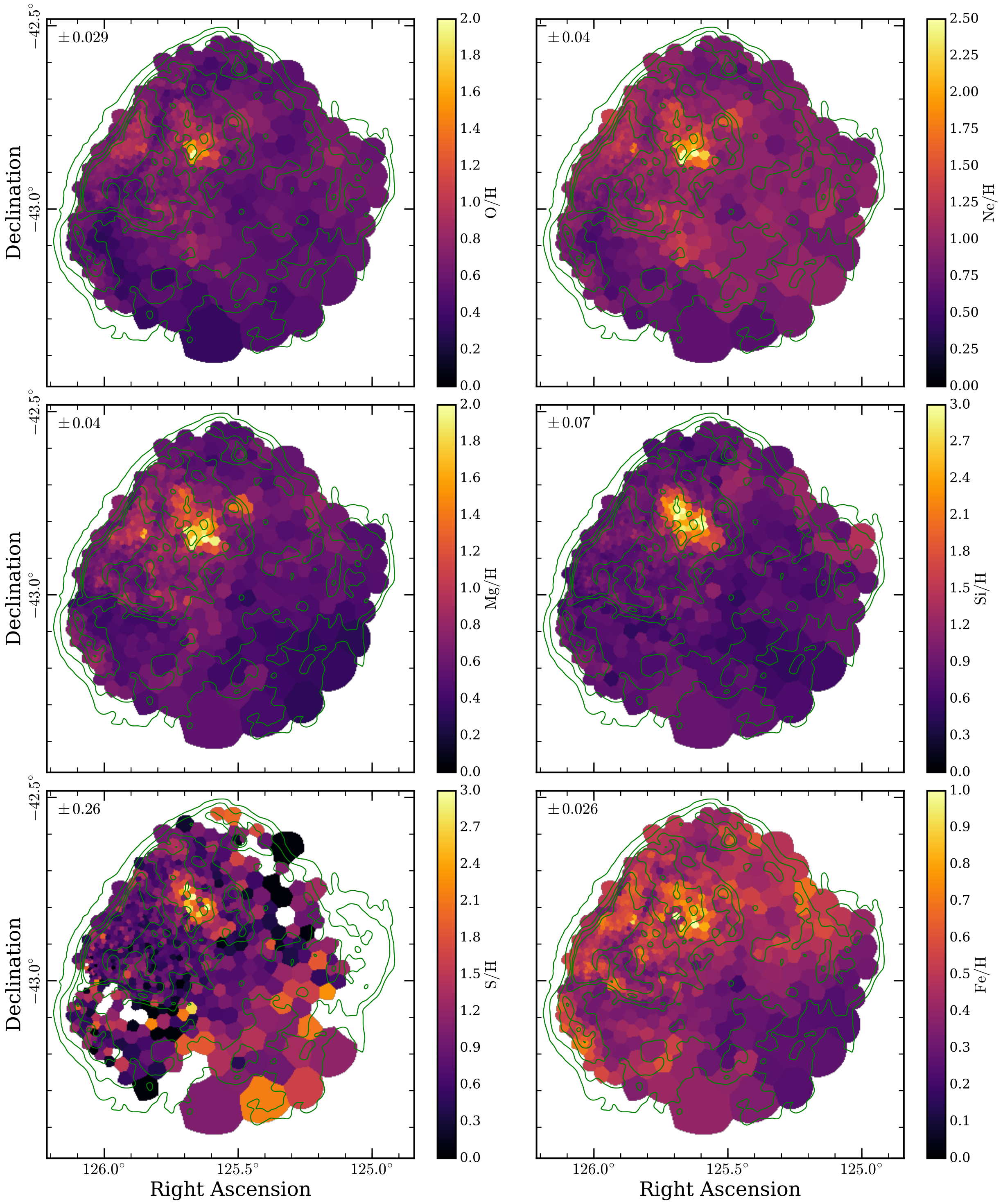

Figure 5.6: Continued. Here, we show the abundances of oxygen, neon, magnesium, silicon, sulfur, and iron normalized to solar values. An additional masking was applied to the map of sulfur abundances, as described in the text.

volume dV. From this, using the fitted emission measure normalized by the angular size Ω of the extraction region (in steradian), one can derive the quantity:

$$\bar{n}_e = 10^7 \sqrt{\frac{4\pi c_e}{D_{\mathrm{LoS}} f} \times \frac{\mathrm{EM}}{\Omega}}, \tag{5.3}$$

where $c_e \approx 1.2$ is equal to the ratio of electrons to hydrogen atoms for a typical ionized plasma with approximately solar abundances. Furthermore, D_{LoS} is an estimate of the depth of the emitting plasma along the line of sight, which we set to 20 pc here. This assumes a depth similar to the angular extent of Puppis A at a distance of 1.3 kpc (Reynoso et al. 2017). Finally, the filling factor f accounts for an inhomogeneous density distribution within the considered emitting region. For simplicity, at this point, we omit f, so that the resulting quantity is equivalent to $\bar{n}_e = \sqrt{\langle n_e^2 \rangle}$, where the average runs over the full volume of depth D_{LoS}. The main advantage of our assumptions is that $\bar{n}_e$ can be calculated without invoking uncertain assumptions dependent on the three-dimensional density structure of Puppis A. Thus, while it constitutes an average over a large, likely inhomogeneous volume, $\bar{n}_e$ serves as a useful proxy to the density of the post-shock plasma. The true average density over the full considered volume of an extraction region will always be smaller than $\bar{n}_e$, unless the material is distributed perfectly homogeneously within the entire volume. However, the peak density, which also presents the largest relative contribution to the overall emission, will always be larger. In order to obtain quantitative mass estimates (see Sect. 5.4.3), it is necessary to make more realistic assumptions on the density structure of Puppis A.

The model ionization age is defined as $\tau = n_e t_{\mathrm{s}}$, where t_{s} is the time since the emitting material was first struck by the shock wave (Borkowski et al. 2001). It describes the upper limit to observed ionization timescales in the plasma, which in turn quantify the degree of departure from collisional ionization equilibrium (CIE). In order to account for the dependence of τ on the post-shock density and attempt to reconstruct the propagation history of the blast wave, we define the shock pseudo-age as $t'_{\mathrm{s}} = \tau / \bar{n}_e$. This quantity should not be seen as an exact quantitative estimate of the collision time of the supernova shock wave with circumstellar material, as that would assume a truly uniform density distribution over the emitting volume as well as a constant density over time in the post-shock region. However, the measured distribution of t'_{s} over the extent of Puppis A serves as an indicator of the relative recency of the interaction between shock and ISM (or ejecta) in different parts of Puppis A.

In the resulting parameter maps, we generally found that the trade-off between statistical noise and spatial resolution appeared optimal for the lowest binning threshold $S/N = 200$. In the following, we therefore discuss the parameter maps binned to $S/N = 200$, which are displayed in Fig. 5.6. However, for weakly constrained parameters (e.g., the sulfur abundance), a coarser binning tends to lead to a clearer picture due to the improved suppression of noise. We therefore show similar plots with $S/N = 300$ and 500 in Figs. C.1 and C.2 in the appendix.

Absorption and plasma conditions

We clearly find a varying degree of foreground absorption across the remnant, as previously suspected by numerous authors (e.g., Aschenbach 1993; Hui & Becker 2006b; Dubner et al. 2013).

While the distribution of measured hydrogen column densities seems to exhibit a relatively sharp lower cutoff around $N_\mathrm{H} \approx 2 \times 10^{21}\,\mathrm{cm}^{-2}$ (see also Fig. C.3), the southwest quadrant of Puppis A appears to be strongly absorbed with our measurements reaching up to around $7 \times 10^{21}\,\mathrm{cm}^{-2}$, consistent with the relatively hard emission there (see Figs. 5.1 and 5.4) and with the detection of cold foreground dust in this region (Arendt et al. 2010; Dubner et al. 2013). The region in which the strongest far-infrared emission at $160\,\mu\mathrm{m}$ is found is consistent with what appears like a "hole" in the soft X-ray emission toward the southern edge of the shell (see Fig. 5.2). However, due to insufficient photon statistics in this area, in our N_H map, this region is mixed with neighboring, less absorbed regions, making it challenging to infer what the true maximum column density toward Puppis A is. Therefore, we dedicate some further attention to this region in Sect. 5.3.4.

Throughout the SNR, there are a few subtle features of enhanced absorption, which appear significant considering that statistical errors are estimated to be only on the order of $1 \times 10^{20}\,\mathrm{cm}^{-2}$: at the very northeast rim of the SNR, there appears to be a small-scale enhancement of absorption with measured column densities up to $5 \times 10^{21}\,\mathrm{cm}^{-2}$, coincident with an apparent indentation of the rim. An explanation for this could be additional absorption introduced by a possibly cospatial density enhancement of the ISM toward the Galactic plane, visible also at infrared wavelengths (Reynoso et al. 2017; Dubner et al. 2013; Arendt et al. 2010), with which the supernova shock wave is colliding. Furthermore, we note that the northeast filament also appears to show enhanced absorption (see Sect. 5.3.4).

Similarly to the broad-band count rate, our map of absorption-corrected surface brightness Σ_u exhibits a large gradient, ranging over about two orders of magnitude across the SNR. The highest fluxes are found at the northeast rim and the BEK, with values up to $\Sigma_u \sim 10^{-10}\,\mathrm{erg\,s^{-1}\,cm^{-2}\,arcmin^{-2}}$. By integrating the flux of the source model over all unmasked regions in Fig. 5.6, we estimate the total unabsorbed flux of Puppis A to be $F_u = 2.64 \times 10^{-8}\,\mathrm{erg\,s^{-1}\,cm^{-2}}$ in the $0.2 - 5.0\,\mathrm{keV}$ band, which corresponds to an intrinsic luminosity $L_X = 5.3 \times 10^{36}\,\mathrm{erg\,s^{-1}}$ at a distance of 1.3 kpc (Reynoso et al. 2017). The dominant uncertainty in this measurement is not of statistical nature, as the statistical error of the flux, derived by adding the uncertainties of all bins in quadrature, is only at a level of 0.2%. Instead, it is caused by the combined systematic effects of effective area calibration uncertainties (see also Sect. 5.3.5), the particular model choice, and the somewhat arbitrary definition of the SNR extent. We estimate the combined systematic uncertainty of our measurement to be on the order of 15%, if and only if one assumes the used spectral model to be the correct one. If one wanted to include the possibility that, for instance, a two-component model may be closer to reality in some regions, larger uncertainties would likely apply.

Converting our measurement to the $0.3 - 8.0\,\mathrm{keV}$ energy range, the corresponding flux of $F_u = 2.43 \times 10^{-8}\,\mathrm{erg\,s^{-1}\,cm^{-2}}$ (implying $L_X = 4.9 \times 10^{36}\,\mathrm{erg\,s^{-1}}$) is consistent with the broad uncertainty range derived by Dubner et al. (2013). However, it appears discrepant with the measurement of $F_u = (1.5 \pm 0.2) \times 10^{-8}\,\mathrm{erg\,s^{-1}\,cm^{-2}}$ for the same energy range by Silich et al. (2020). This is likely primarily caused by the difference between a spatially resolved and a spatially integrated treatment of the emission: we find a variation of the absorbing column density by a factor of a few over the SNR, whereas Silich et al. (2020) found weaker average absorption with a column density of $N_\mathrm{H} \sim 2 \times 10^{21}\,\mathrm{cm}^{-2}$, which implies a larger fraction of intrinsic SNR flux reaching the observer. Given the smoothly varying structure of our N_H map, we believe that our flux measurement is more reliable. The resulting luminosity, and thereby the energetics of Puppis A, are subject to the systematic error of the assumed distance to Puppis A (Reynoso et al. 2017), in addition to the factors affecting the flux measurement.

The line-of-sight density average of the post-shock plasma, $\bar{n}_e$, is rather tightly correlated with Σ_u, as it is computed based on the normalization of the spectrum. Unsurprisingly, the highest densities are found along the northeast rim and at the BEK, where it has been established that the shock wave is interacting with a small-scale density enhancement, possibly a molecular cloud (Hwang et al. 2005). Densities in the south and west of the SNR are found to be up to an order of magnitude lower, consistent with a thinner environment in the direction away from the Galactic plane.

The distribution of the plasma temperature kT over the SNR exhibits a median (and 68% central interval) of $kT = 0.55^{+0.14}_{-0.09}$ keV (see Fig. C.3). A few regions appear noteworthy in our map of kT. For instance, we find localized very high plasma temperatures close to the northeast filament and the ejecta knot (see Katsuda et al. 2008, 2010) at around 1.0 keV. This should however be treated as a somewhat uncertain finding, as regions rich in ejecta would realistically require modeling with multiple emission components (see Sect. 5.3.3), which would affect the inferred plasma temperature. In contrast, the western arc of Puppis A is found to exhibit temperatures as low as 0.35 keV. It may be possible that the soft emission here could be related to the existence of a local ISM cavity that would explain the almost circular structure of this feature. An extended region along the northeast rim stands out quite clearly, with coherently elevated temperatures spanning the range 0.7 – 0.8 keV, which is a highly significant enhancement considering the typical statistical noise level of only 2.4%. Together with comparatively large ionization ages on the order $\tau \sim 3 \times 10^{11}$ cm^{-3} s measured here, the high plasma temperature provides a convincing explanation for the brightness of this region above 2 keV (Fig. 5.4).

Finally, a fascinating picture is offered by the map of the shock pseudo-age t'_s where numerous regions of freshly shocked plasma appear quite prominent. First, the northeast filament shows by far the lowest values of t'_s, making this the region which appears to have experienced the most recent shock interaction in Puppis A. Similarly, the ejecta knot and part of the extended ejecta-rich region in the north of the SNR also appear to have been shocked quite recently. It should be noted that, since these features most likely do not extend along the whole line of sight through Puppis A, the inferred value of $\bar{n}_e$ is likely an underestimate of the true density. Consequently, the true shock age of these features is likely even lower than indicated in our map (see Sect. 5.3.4). On larger scales, we recover the underionized nature of relatively faintly emitting material in the southeast of Puppis A (feature 8 in Fig. 5.2) observed by Hwang et al. (2008).

Since most regions hosting a young shock are not located at the apparent edge of the remnant, a possible conclusion could be that their emission originates primarily behind or in front of the apparent surroundings. The apparent location of the features on the inside of the shell would then be due to projection effects along the line of sight only. An alternative, which may be more likely for regions associated with ejecta, could be that the emitting material has recently interacted with the reverse shock, leading to its reheating and strong departure from CIE. The western half of Puppis A does not appear to exhibit any similar recently shocked regions. On one hand, this may simply be an artifact of the fainter emission there, leading to larger bins for spectral extraction, which may mask the presence of small-scale features far from CIE. On the other hand, one could also imagine that our inability to observe clear signatures of a reverse shock there (see also Katsuda et al. 2010) may be due to a smaller amount of heated ejecta. Since the ISM is much thinner in the west, the mass swept up by the forward shock there is likely lower, leading to a shallower penetration of the reverse shock into the ejecta.

At the BEK, we find a quite clear dependence of t'_s on the angular distance from the SNR center, with the outermost regions exhibiting the youngest shock. This illustrates very nicely the gradual penetration of the shock into the ISM, as regions further inside have naturally been struck by the shock at an earlier time. This is very much consistent with the results of Hwang et al. (2005), as they concluded that the "bar" and "cap" structures are the remnants of a mature shock-cloud interaction, which occurred $2000 - 4000$ yr ago. In contrast, the compact knot located at the easternmost edge of the BEK region is undergoing an intense interaction with dense ISM at the present time.

A final interesting note to make is that the median value of t'_s over all regions is around 4200 yr (see Fig. C.3), which is comparable to quite precise kinematic age estimates of Puppis A (Winkler et al. 1988; Mayer et al. 2020), which range between 3700 and 4600 yr. However, most likely, this apparent agreement is partly coincidental, as the assumptions going into the computation of t'_s are extremely crude. For instance, the neglect of temporal changes in the density of the shocked plasma or of a possible nonuniform distribution of the emitting material likely do not hold under realistic conditions.

Elemental abundances

Our approach of decomposing the emission of Puppis A into many individual regions allows us to construct flux-weighted distribution functions of chemical abundances (see also Fig. C.4). We find that the median metal abundances across the SNR, normalized by the abundance table of Wilms et al. (2000), are given by $\mathrm{O/H} = 0.62^{+0.15}_{-0.10}$, $\mathrm{Ne/H} = 0.94^{+0.20}_{-0.13}$, $\mathrm{Mg/H} = 0.60^{+0.22}_{-0.13}$, $\mathrm{Si/H} = 0.83^{+0.20}_{-0.13}$, $\mathrm{S/H} = 0.88^{+0.59}_{-0.29}$, and $\mathrm{Fe/H} = 0.45^{+0.12}_{-0.11}$, with the quoted errors marking the 68% central intervals. The low median iron abundance and its relatively homogeneous distribution over the SNR do not indicate any significant enrichment of the emitting plasma with iron ejecta. Interestingly, the highest abundances relative to solar values across the remnant are found for neon, whereas the median oxygen abundance is considerably smaller (see Sect. 5.4.2).

Our abundance maps very clearly confirm the high metal content of the ejecta enhancements discussed in Katsuda et al. (2008) and Hwang et al. (2008) and labeled 4 and 5 in Fig. 5.2, as we find coherently elevated abundances of oxygen, neon, magnesium, silicon, and sulfur there. Iron abundances appear to be only weakly (if at all) enhanced in this area compared to surrounding regions, as even the maximum measured abundances are only about solar. Interestingly, while the peak of the light-element (O, Ne, and Mg) distribution is concentrated on the clumpy ejecta knot in the south of the enriched region, the heavier elements (Si and S) show enhancements spread over a larger elongated region. This is illustrated more clearly by the maps in Fig. 5.7, which display the ratios Ne/O, Si/O, and Fe/O deduced from the abundance maps in Fig. 5.6. A clear peak in the silicon-to-oxygen ratio is visible for the extended ejecta-rich region, whereas the compact ejecta knot to its south shows a relative enhancement in oxygen abundance.

The metal distribution across the remainder of Puppis A shows much more modest variations,

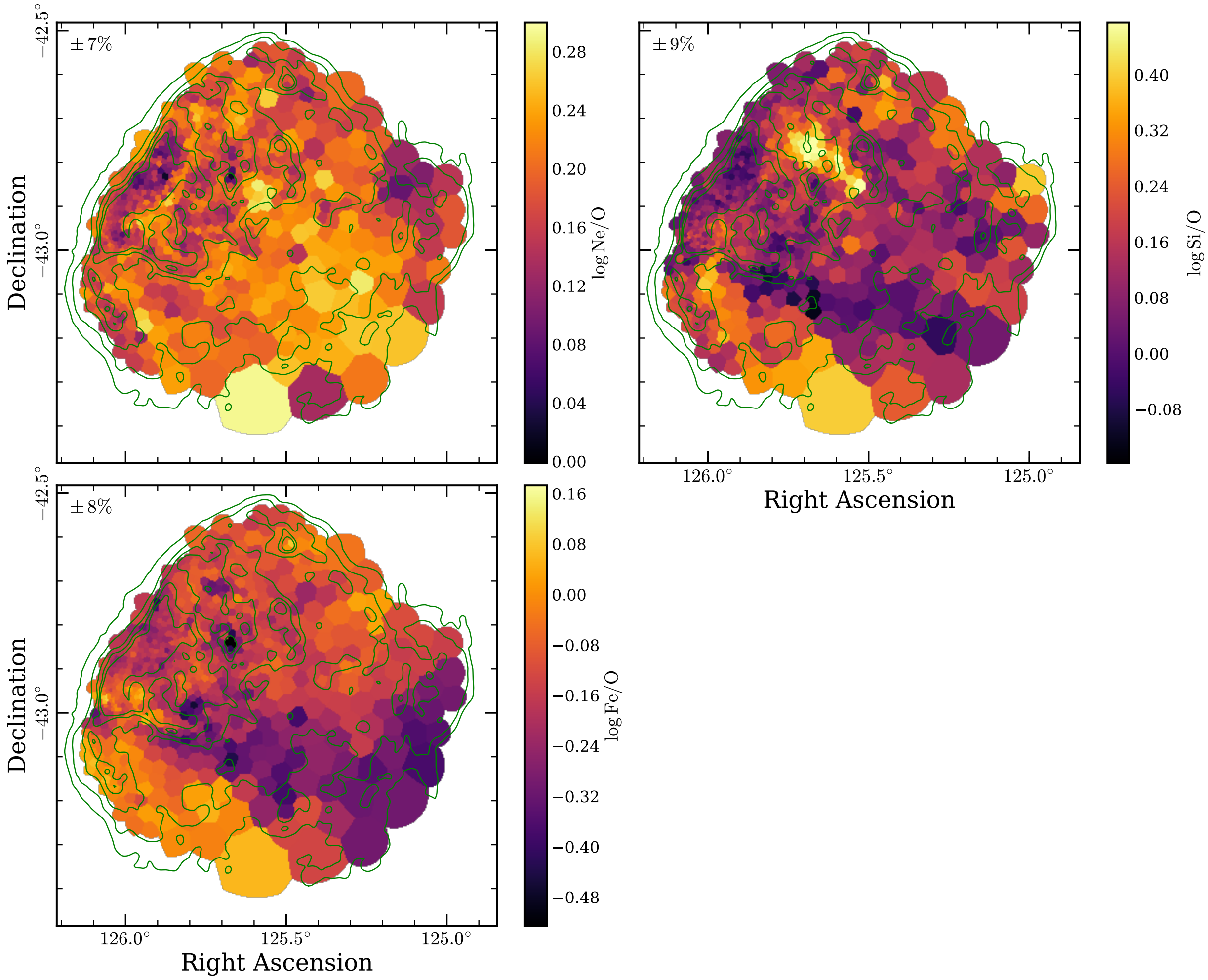

Figure 5.7: Ratio of selected elemental abundances with respect to the solar value, obtained from spectral fits to adaptively binned regions of $S/N = 200$ (see Fig. 5.6). The contours, region masking, and indication of the fractional uncertainty are as in Fig. 5.6.

which only appear visible for the lighter elements in Fig. 5.6. For instance, there seems to be a weak enhancement in neon and magnesium at a location about 10′ northwest of the prominent ejecta knot, coincident with a clumpy feature in the broad-band image of Puppis A. A further example is the hot northeast rim, which seems to show a relative oxygen enhancement, particularly visible in the Ne/O map. Generally, the maps displayed in Fig. 5.7 appear to show some interesting large-scale structure, as, for instance, a broad strip along the southeast rim of Puppis A appears to show enhanced Si/O and Fe/O ratios, whereas the region to the north and west of it seems to be more enriched in oxygen in a relative sense.

The distribution of sulfur abundances suffers from a large fraction of spurious measurements, with a significant number of unrealistically high ($\mathrm{S/H} \gtrsim 3$) or low values. We found that the majority of spurious elevated abundances can be suppressed by masking all those bins with a statistical 1σ-error larger than 0.8, which produces the map shown in Fig. 5.6. While this map

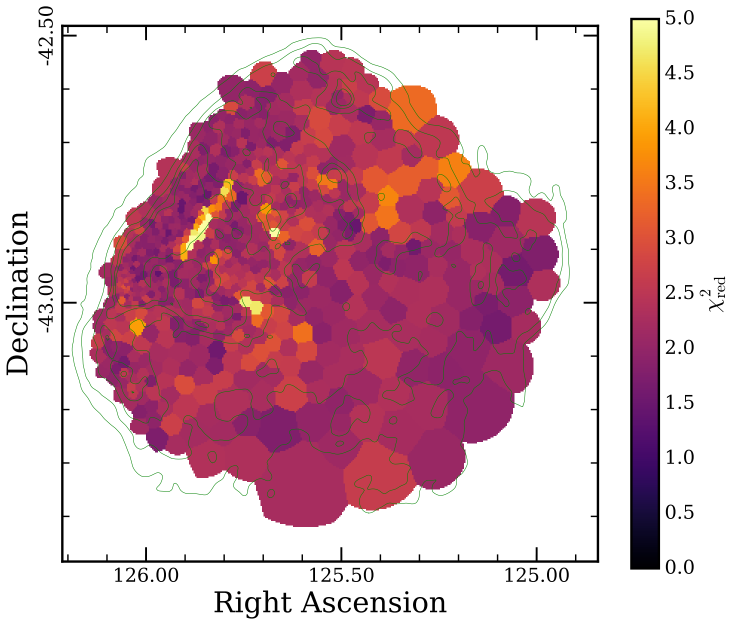

Figure 5.8: Map of the reduced χ^2 statistic computed for the best-fit (parameters as displayed in Fig. 5.6) in each bin. The number of degrees of freedom per bin varies between around 120 and 160 over the extent of the map, as each spectrum is rebinned individually to the target signal-to-noise ratio.

displays a convincing agreement between enhancements of sulfur and silicon in the extended ejecta-rich region, the entire western arc of Puppis A had to be masked, as it yielded unreasonably high values for S/H. A likely explanation for such behavior in the west of the SNR is the presence of a subdominant second emission component with higher plasma temperature. This hypothesized component would produce much stronger S xv line emission than expected from the best-fit single-temperature model with ISM abundances, thus driving the inferred sulfur abundance to unrealistically high, albeit formally statistically significant, values (see also region I in Sect. 5.3.4). Apart from the occurrence of such systematic outliers, large statistical fluctuations, including the presence of bins with S/H $\sim$ 0, are apparent in the map. These are likely caused by the poor statistics of our spectra in the band most sensitive to emission from sulfur, which is above 2.3 keV, where the eROSITA response exhibits a sharp drop. Indeed, the measured statistical errors are several times larger than for all our other abundance measurements, at a median 1σ-error of 0.26.

Model choice

At this point, a valid question to ask may be whether the employed physical model is really a sufficient representation of the conditions in Puppis A. In order to investigate this matter, after rebinning the spectrum and best-fit model to a signal-to-noise ratio of five in each bin, we manually computed the "reduced" χ^2 statistic for each spectrum, as a rough measure of goodness of fit. The resulting map is shown in Fig. 5.8. It shows that, while the fits in a few regions are clearly suboptimal, the large majority of regions exhibit $\chi^2_{\rm red} \sim 2$. Considering the large number of total counts per spectrum and the early stage of energy and response calibration, we believe that this value indicates an acceptable fit.

A possible origin of the poor fit quality of our model in a few regions may be the assumption of only one emission component with a single set of parameters, which neglects the possibility of physically different conditions projected along the same line of sight. By evaluating the improvement of the fit likelihood when including a further `vpshock` component, we verified that a second plasma component is indeed needed in those regions with a bad fit, in particular around the northeast filament. To tackle the observed issue there, we applied a more sophisticated treatment of the local background introduced by the emission of surrounding shocked ISM in Sect. 5.3.4. In contrast to the northeast filament, those regions with $\chi^2_{\text{red}} \sim 2$ in Fig. 5.8 generally show only minor improvements, indicating that the remaining imperfections of the fit there may indeed be mostly due to calibration uncertainties, not modeling issues. Generally, it should be noted that, while a two-component model naturally always leads to an equally good or improved fit, with the available spectral resolution, it is difficult to precisely constrain the individual parameters of both plasma components without making additional restricting assumptions, due to the large amount of parameter degeneracies introduced.

As a further test of the validity of our particular model choice, we repeated our fitting procedure using the frequently employed single-ionization-timescale NEI plasma model `vnei`. This approach qualitatively preserved many characteristic structures in our parameter maps, for instance the recently shocked regions and the abundance peaks in the ejecta-rich regions. However, compared to the `vpshock` model, it led to deteriorated fit statistics in the vast majority of bins, the resulting maps appeared much noisier overall, and the fraction of outliers for weakly constrained parameters was larger. Furthermore, from a physical standpoint, the model of a plane-parallel shock plasma is likely more appropriate for realistic SNRs dominated by an interaction with the ISM, as it applies a continuous distribution of ionization timescales within the emitting plasma, rather than assuming all material to have been struck by the shockwave at a single point in time (Borkowski et al. 2001). For the given data set, we therefore believe that an absorbed single-component `vpshock` model constitutes the optimal compromise between interpretability and physical accuracy of our spectral model.

5.3.4 Detailed modeling of selected regions

Following up on some open questions from the previous section, we now investigate in more detail the spectra of some isolated features of Puppis A, which were selected based on our images and parameter maps. The extraction regions used for our features are indicated in Fig. 5.9. Our targets include the northeast filament (regions A and B), the compact ejecta knot (C and D), the extended ejecta-rich region (E), the hot northeast rim (F), and the cold western arc (I). In addition, we included the southern hole in soft emission (G) to investigate the foreground absorption there, as well as an extremely faint filamentary feature at the southwest edge of Puppis A (H), which exhibits the softest visible emission associated to Puppis A.

As in the spatially resolved spectroscopic analysis described in Sect. 5.3.3, the source emission was described by an absorbed plane-parallel shocked plasma, expressed as `TBabs*vpshock`. To be comparable with previous studies (e.g., Katsuda et al. 2010, 2008), we tested two different

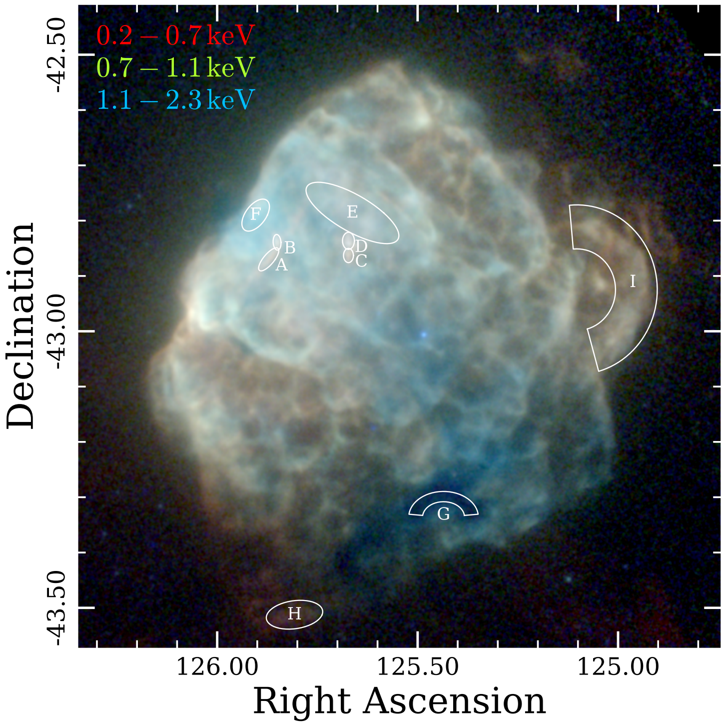

Figure 5.9: Regions for the extraction of the spectra in Fig. 5.10 overlaid on the false-color image of Puppis A (same data as in Fig. 5.1). To highlight the faint feature H, the zero point of the color scale was set lower than in Fig. 5.1.

approaches for treating elemental abundances: (i) we allowed the abundances of O, Ne, Mg, Si, S, and Fe to freely vary between 0 and 50, reflecting ISM possibly enriched by ejecta. (ii) We fixed the oxygen abundance at a value of 2000 (Winkler & Kirshner 1985), to allow for the possibility of pure metal ejecta, where the continuum bremsstrahlung emission is dominated by heavy elements.

For each source region, we defined a nearby region from which we extracted a local background spectrum. As regions A–E are intended to single out prominent features from the surrounding ISM-dominated emission of the SNR, their background regions were chosen to approximate the local emission from Puppis A. For all other features, the regions were chosen such as to trace the "true" local background outside the SNR shell. As a background model, we used again the combination of thermal, nonthermal and instrumental components outlined in Sect. 5.3.3. The spectra of the source and background regions were fitted simultaneously, with the relative normalization of the background initially tied between the two regions. After this initial fit, the X-ray background normalization was allowed to vary for the source region by up to a factor of two, to accommodate possible spatial variations in the flux of the background component. Such spatial variations may become important in particular if the background component traces the emission of Puppis A itself.

The resulting fits to source and background spectra are displayed in Fig. 5.10. While our models are generally able to qualitatively reproduce the shape of the observed data very well, a few

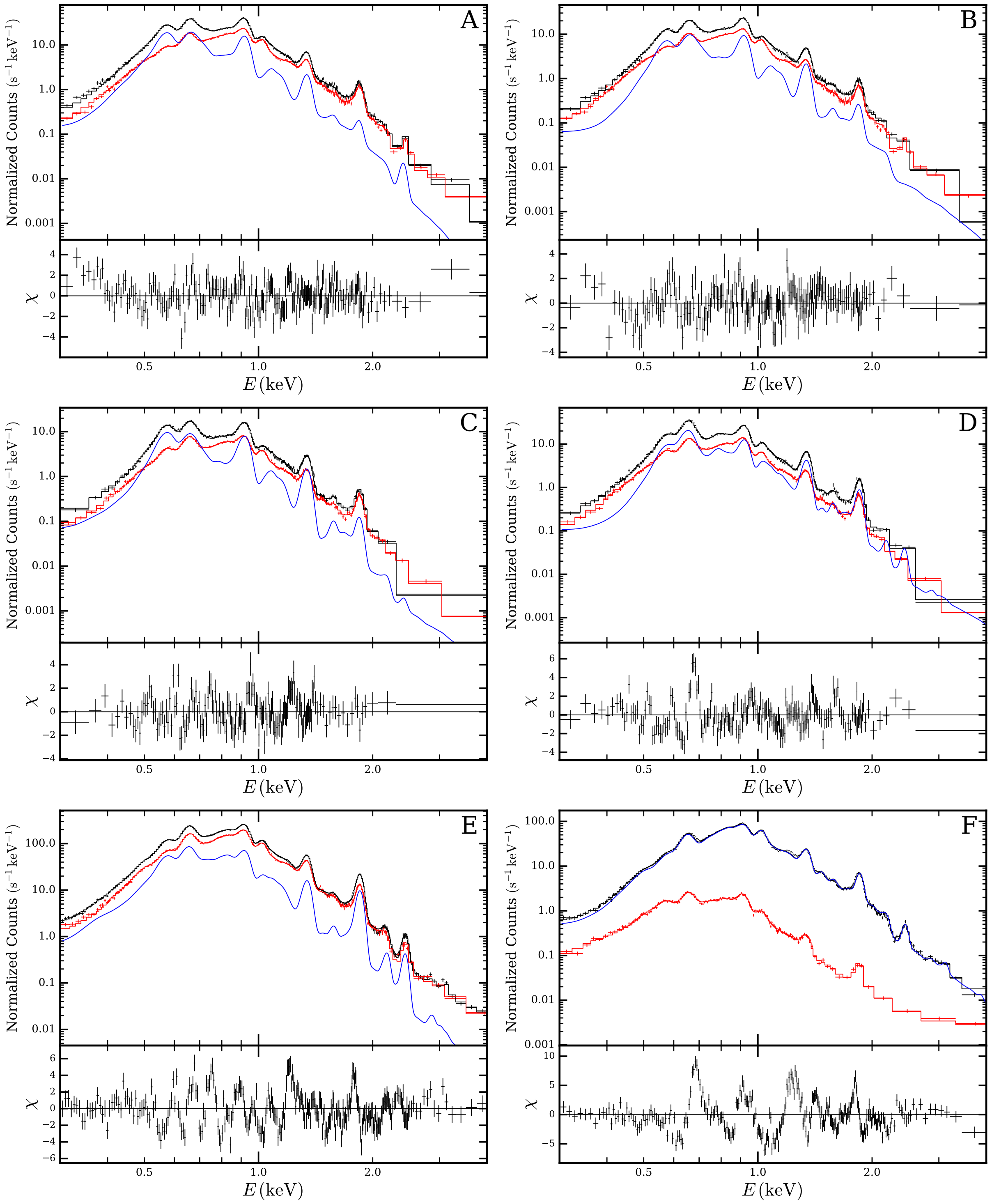

Figure 5.10: Fits to source and background spectra extracted from the regions indicated in Fig. 5.9 and labeled accordingly. In each panel, the background spectrum and binned model are displayed in red, while the total spectrum and model for the source region are shown in black. The blue line indicates the "background-subtracted" best-fit source model. The background spectra and models have been rescaled to represent their absolute contribution to the source region spectrum. The lower part of each panel indicates the residuals of the spectrum in the source region with respect to its best-fit model for source plus background. The fits displayed here correspond to case (i) outlined in the text, meaning metal abundances were left free to vary within a range typical for (enriched) ISM. The spectra and models were rebinned, for plotting purposes only, to a minimum signal-to-noise ratio of 5.

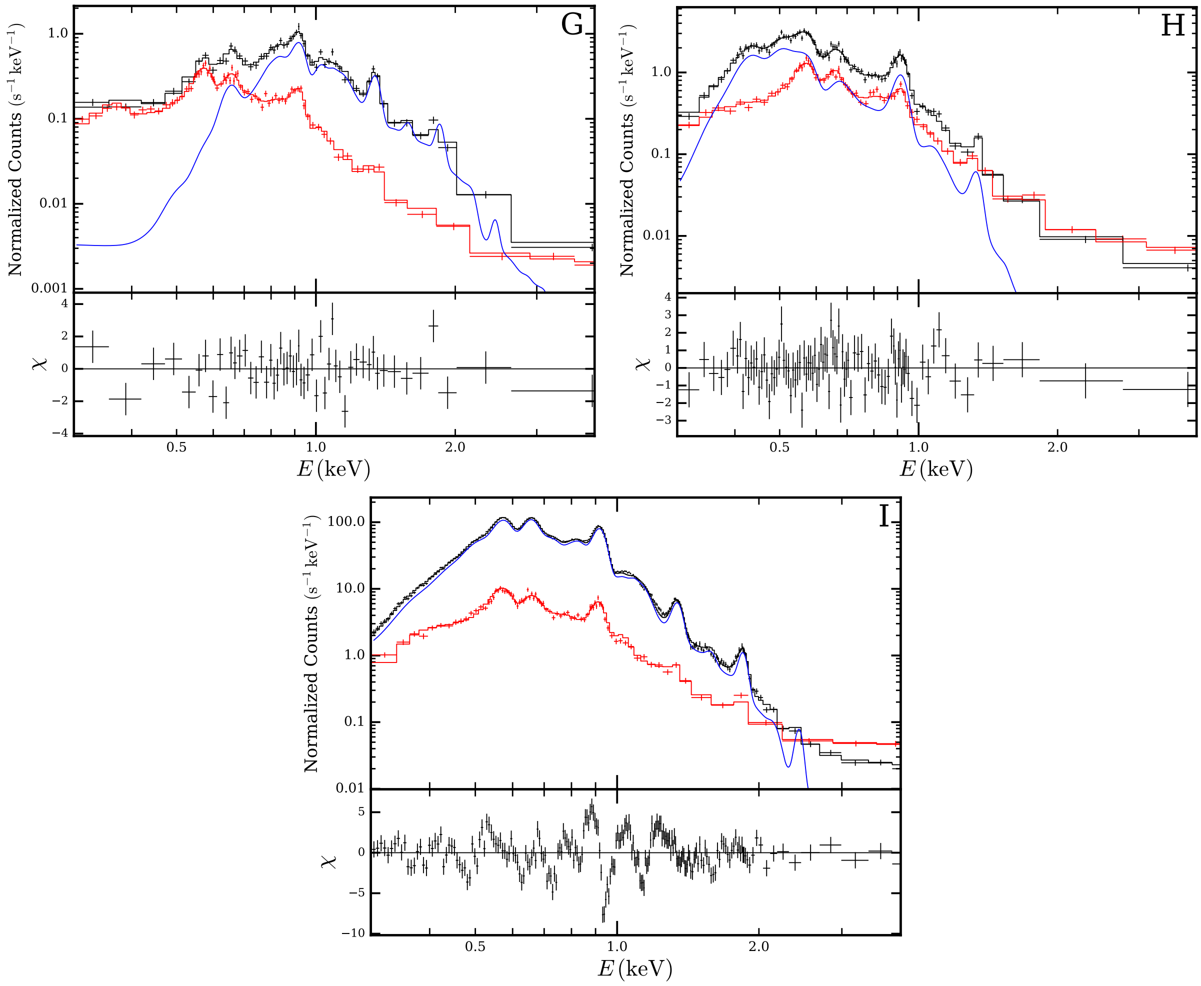

Figure 5.10: Continued

shortcomings become apparent: first, several of our spectra (e.g., regions E, F, and I) show strong systematic deviations from their best-fit model, clearly visible because of the excellent photon statistics. This indicates that statistical errors produced with standard methods are likely underestimated with respect to realistic uncertainties of model parameters, whose dominant source is of systematic nature. Possible reasons for the observed fit residuals include imperfect energy or response calibration, line shifts or line broadening due to nonzero radial velocities of the plasma, the presence of multiple plasma components along the same line of sight, or shifts in the centroid of line complexes due to physical processes not described by our model. For instance, Katsuda et al. (2012) found that, in the targeted regions in the east and north of Puppis A, forbidden-to-resonance line ratios in the Heα triplets of N, O, and Ne are higher than expected from purely thermal models, and require charge-exchange processes in order to be satisfactorily explained. A further subtle but fundamental issue of our approach is the assumption of the spectrum in the local background region being representative of the actual background contribution to the source region, which is generally reasonable, but cannot be guaranteed. This is especially important for those regions where source and background levels are comparable, such as A−E and the low- and high-energy portions of G and H, which makes them vulnerable to slight background variations not considered by the model. For regions A−E, variations on small scales are particularly likely, as their background consists of the surrounding emission from Puppis A, which is certainly more spatially inhomogeneous than the emission outside the SNR shell.

Nonetheless, while being aware of the above issues regarding modeling uncertainties, we believe that a discussion of the implications of our fits (see Table 5.1 for the best-fit parameters) is warranted. For a few regions, approaches (i) and (ii) yielded comparable fit qualities, for all others we show only the results of approach (i). Similarly to the previous section, we constructed density and shock age estimates for the emitting plasma from the emission measure and ionization timescale, with two modifications: first, for those features which visually appear as clumps (i.e., regions A−E), we assumed a line-of-sight depth of the emitting plasma similar to their extent in the image domain. This means we assumed their depth to be equal to the geometric mean of the major and minor axis of the ellipse used as extraction region. Second, for the case of pure-metal abundances (ii), we explicitly calculated the average atomic mass per hydrogen atom and the ratio of electrons to hydrogen atoms from the measured abundances, as the usual assumptions, valid for ISM conditions, break down here. To achieve this, for each region, we calculated the ion fractions for each element from the best-fit parameters, by averaging over the flat distribution of ionization timescales from zero to its maximum, τ, using the AtomDB code (Foster et al. 2012).

The spectra of regions A and B, extracted at the northeast filament, clearly confirm the low ionization age of the plasma that we found in Sect. 5.3.3. Comparing our results for case (i) with the maps in Fig. 5.6, our isolated treatment of this region and the more realistic assumption of a compact three-dimensional structure yield larger density estimates on the order of $10\,\mathrm{cm}^{-3}$, which imply smaller shock ages $\sim 100\,\mathrm{yr}$. Such recent interaction with a shock seems to agree well with the – to our knowledge unpublished – suspected flux decline over time in this filament (see Katsuda 2010), which would be a natural expectation for a comparatively young feature evolving on a short timescale.

Moreover, it is interesting to note that both regions A and B tend toward a quite large absorption column around $N_{\mathrm{H}} \approx 5.5 \times 10^{21}\,\mathrm{cm}^{-2}$, much larger than in adjacent regions, where $N_{\mathrm{H}} \approx 3 \times 10^{21}\,\mathrm{cm}^{-2}$ (weakly visible also in Fig. 5.6). This is also found if one keeps the relative background normalization fixed, and is therefore not an artifact of background over-subtraction at low energies. Furthermore, Katsuda et al. (2010) noted a similar behavior in their analysis before fixing N_{H} to a smaller, more “reasonable” value, which is why we consider it a possibility that the enhanced absorption may indeed be physical (see Sect. 5.4.1). Our higher absorption has a considerable effect on the measured abundances: we generally recover supersolar abundances of O, Ne, Mg, and Si in both regions, with the northern end of the filament (region B) exhibiting somewhat higher values. However, the ratios Ne/O and Mg/O are considerably below those found by Katsuda et al. (2010), who obtained values approximately twice solar. This is likely due to the higher absorption suppressing the soft oxygen line emission in the model spectrum, requiring an increased abundance to match the observed line flux.

Regions C and D represent the southern and northern part of the compact ejecta knot. In both cases, a fit with pure-ejecta abundances (ii) provides only a slightly worse fit compared to ISM

Table 5.1: Best-fit parameters from modeling of the spectra shown in Fig. 5.10.

Region	N_H	kT	τ	EM[b]	$\bar{n}_e$	t'_s	O/H	Ne/H	Mg/H	Si/H	S/H	Fe/H	C[d]
	10^{21} cm^{-2}	keV	10^{11} cm^{-3} s	10^{12} cm^{-5}	cm^{-3}	10^3yr							
A	$5.42^{+0.12}_{-0.05}$	$0.430^{+0.010}_{-0.021}$	$0.264^{+0.027}_{-0.012}$	$2.09^{+0.31}_{-0.17}$	7.7 ± 0.4	0.109 ± 0.010	$1.89^{+0.09}_{-0.08}$	$1.69^{+0.10}_{-0.04}$	$1.61^{+0.11}_{-0.13}$	$1.7^{+0.4}_{-0.4}$	...[c]	$0.32^{+0.04}_{-0.04}$	1683.5
A[a]	$6.18^{+0.10}_{-0.08}$	$0.342^{+0.004}_{-0.023}$	$0.36^{+0.06}_{-0.02}$	$0.0038^{+0.0008}_{-0.0002}$	0.90 ± 0.06	1.25 ± 0.16	2000[a]	1520^{+20}_{-50}	1620^{+90}_{-110}	1800^{+700}_{-700}	...[c]	140^{+40}_{-40}	1699.0
B	$5.64^{+0.20}_{-0.29}$	$0.69^{+0.12}_{-0.07}$	$0.177^{+0.027}_{-0.028}$	$0.38^{+0.10}_{-0.11}$	6.7 ± 0.9	0.084 ± 0.018	$3.5^{+0.6}_{-0.3}$	$3.3^{+0.7}_{-0.4}$	$3.8^{+0.8}_{-0.4}$	$3.3^{+0.8}_{-0.6}$	< 1.1	$0.13^{+0.12}_{-0.09}$	1607.5
B[a]	$5.3^{+0.4}_{-0.3}$	$0.59^{+0.14}_{-0.12}$	$0.21^{+0.10}_{-0.05}$	$0.00057^{+0.00028}_{-0.00014}$	0.76 ± 0.14	0.9 ± 0.4	2000[a]	2050^{+80}_{-100}	2900^{+200}_{-180}	2900^{+400}_{-500}	< 1100	< 11	1620.4
C	$3.39^{+0.30}_{-0.21}$	$0.72^{+0.09}_{-0.11}$	$0.19^{+0.05}_{-0.03}$	$0.050^{+0.029}_{-0.017}$	2.1 ± 0.5	0.28 ± 0.09	9^{+5}_{-2}	12^{+7}_{-4}	15^{+6}_{-4}	9^{+5}_{-3}	< 16	< 0.12	1345.6
C[a]	$3.57^{+0.22}_{-0.13}$	$0.59^{+0.05}_{-0.05}$	$0.24^{+0.05}_{-0.04}$	$0.00026^{+0.00005}_{-0.00005}$	0.46 ± 0.04	1.6 ± 0.3	2000[a]	2790^{+140}_{-130}	3650^{+220}_{-150}	2600^{+500}_{-500}	4300^{+1600}_{-1500}	< 13	1360.7
D	$4.57^{+0.10}_{-0.10}$	$1.14^{+0.11}_{-0.09}$	$0.35^{+0.05}_{-0.03}$	$0.080^{+0.031}_{-0.023}$	2.1 ± 0.4	0.52 ± 0.11	16^{+6}_{-4}	13^{+5}_{-3}	14^{+6}_{-4}	12^{+4}_{-3}	$8.0^{+2.1}_{-2.0}$	< 0.037	1561.6
D[a]	$4.46^{+0.11}_{-0.09}$	$1.27^{+0.13}_{-0.12}$	$0.323^{+0.017}_{-0.029}$	$0.00059^{+0.00004}_{-0.00003}$	0.509 ± 0.016	2.01 ± 0.16	2000[a]	1640^{+40}_{-50}	1710^{+70}_{-80}	1410^{+60}_{-60}	1020^{+240}_{-230}	< 3.0	1593.4
E	$3.45^{+0.05}_{-0.07}$	$0.727^{+0.003}_{-0.008}$	$0.443^{+0.023}_{-0.020}$	$1.39^{+0.03}_{-0.12}$	0.949 ± 0.025	1.48 ± 0.08	$3.19^{+0.17}_{-0.11}$	$4.22^{+0.23}_{-0.27}$	$4.8^{+0.3}_{-0.3}$	$17.5^{+1.4}_{-1.1}$	$20.2^{+2.4}_{-2.3}$	$2.37^{+0.18}_{-0.15}$	2687.2
F	$4.103^{+0.012}_{-0.021}$	$0.7403^{+0.0007}_{-0.0015}$	$3.14^{+0.06}_{-0.02}$	$9.81^{+0.01}_{-0.09}$	2.982 ± 0.008	3.34 ± 0.04	$0.907^{+0.016}_{-0.010}$	$1.143^{+0.011}_{-0.008}$	$0.812^{+0.009}_{-0.008}$	$0.885^{+0.014}_{-0.013}$	$0.78^{+0.05}_{-0.05}$	$0.5551^{+0.0041}_{-0.0016}$	3460.0
G	$11.0^{+1.1}_{-1.0}$	$0.68^{+0.08}_{-0.08}$	$0.61^{+0.43}_{-0.13}$	$0.33^{+0.23}_{-0.07}$	0.46 ± 0.11	4.2 ± 2.2	$0.9^{+0.8}_{-0.4}$	$0.9^{+0.4}_{-0.2}$	$0.55^{+0.12}_{-0.10}$	$0.52^{+0.13}_{-0.11}$	$0.7^{+0.8}_{-0.6}$	$0.48^{+0.11}_{-0.11}$	1811.2
H	$4.92^{+0.13}_{-0.15}$	$0.142^{+0.002}_{-0.018}$	$0.37^{+0.14}_{-0.14}$	20^{+4}_{-5}	3.0 ± 0.3	0.40 ± 0.16	$0.072^{+0.008}_{-0.006}$	$0.39^{+0.12}_{-0.07}$	$3.7^{+2.5}_{-1.5}$	< 15	< 13	< 2.2	1773.4
I	$3.581^{+0.027}_{-0.025}$	$0.3511^{+0.0004}_{-0.0007}$	$0.960^{+0.018}_{-0.015}$	$21.5^{+0.4}_{-0.5}$	1.228 ± 0.014	2.48 ± 0.05	$0.650^{+0.011}_{-0.015}$	$0.915^{+0.016}_{-0.021}$	$0.483^{+0.013}_{-0.011}$	$1.10^{+0.05}_{-0.05}$	$8.2^{+1.7}_{-0.7}$	$0.356^{+0.005}_{-0.009}$	2552.6

Notes. All errors and upper limits of fitted parameters were estimated using the built-in `error` command, and are given at a 1σ level. Uncertainties of derived quantities were estimated using Gaussian error propagation. The column C displays the combined Cash statistic of the best fit to source and background spectra.

[a] In these cases, the approach of fixing the oxygen abundance to a value of 2000 to represent pure ejecta emission (case ii), was found to provide a fit of comparable or slightly poorer quality to case (i).

[b] This corresponds to the definition of EM in `Xspec` (see Eq. 5.2), omitting the arbitrary factor 10^{-14}.

[c] Here, our fit was unable to provide any constraints within the allowed abundance range.

[d] The associated number of degrees of freedom is 1550 and 1551 for cases (i) and (ii), respectively.

abundances (i). While it is hard to make exact statements about temperature and ionization age due to the difficult access to associated continuum emission, the northern part appears to exhibit a hotter plasma, which is somewhat closer to CIE. Furthermore, we find that in the northern part of the clump, oxygen seems to be the most strongly enhanced element, while in the south, neon, magnesium, and possibly silicon are more concentrated. Interestingly, we find no need to include emission from iron in any of the assumed scenarios in either region. The spectrum of region E, corresponding to the more extended ejecta-rich region, significantly contrasts with those of regions C and D, as it clearly exhibits very strong silicon line emission, consistent with the extreme measured abundance thereof. At the same time, the abundances of O, Ne, and Mg, while also found to be enhanced, are around a factor of $3-5$ lower. This provides a clear confirmation of the spatial separation of silicon from lighter elements in the ejecta of Puppis A.

Spectrum F corresponds to the northeast rim, which stands out clearly as the hardest extended source of emission within Puppis A. Our fits confirm the high plasma temperature around 0.75 keV and large ionization age here, which in combination lead to a pronounced tail toward high energies in the spectrum (see also Krivonos et al. 2021). In this context, it is interesting to note that this region of hard emission appears to coincide approximately with the peak of emission of Puppis A in GeV gamma rays (Xin et al. 2017). However, our observation does not appear to suggest any indication of nonthermal emission, which would be expected if there was a contribution to the X-ray emission by synchrotron radiation from accelerated particles. In addition to providing a quantitative temperature measurement, we recover weakly enhanced elemental abundances in our region (compared to the median over the SNR) as well as a ratio of $\mathrm{Ne/O} \approx 1.25$, which is somewhat lower than in other ISM-dominated parts of the remnant (see Fig. 5.7).

As expected, the spectrum of Region G, the southern hole in soft emission, is strongly absorbed, with source emission only being detected above around 0.6 keV. While most physical parameters are not remarkable, the obtained column density of $N_{\mathrm{H}} \approx 11 \times 10^{21}\,\mathrm{cm}^{-2}$ is far higher than in any other region of Puppis A, consistent with the peak in foreground dust emission (Arendt et al. 2010; Dubner et al. 2013). In addition, one should note that the measured temperature of around 0.7 keV is quite large compared to the immediate surroundings, as apparent in Fig. 5.6, which may point toward a problematic fit. For instance, a possible superposition of different absorption column densities in the same spectrum would tend to mimic an increased plasma temperature. The reason for this is that the low-energy portion of the spectrum, which would be dominated by the least absorbed component, would force the fit toward a small value of N_{H}, due to the exponential effect of absorption on the observed spectrum. The additional hard emission introduced by more heavily absorbed components would then lead to an artificial increase in the fitted plasma temperature for a single-component model (for an example of this effect, see Locatelli et al. 2022). In addition, the scenario of different superimposed absorption columns is also consistent with the expectation for a compact absorbing cloud (Arendt et al. 2010), which would likely not have uniform optical thickness across region G. In conclusion, the true maximum column density toward the southern hole may be significantly larger than $11 \times 10^{21}\,\mathrm{cm}^{-2}$.

Region H exhibits a quite curious spectrum, whose best-fit parameters appear implausible, as they tend toward a strongly absorbed and comparatively cold plasma with strong departure from

CIE. Nevertheless, the observed spectral shape is distinctly different from any other spectrum in Fig. 5.10, as the source emission is the brightest around 0.4 − 0.6 keV but exhibits an extremely sharp cutoff toward lower energies. This appears to make the high column density and low temperature at least somewhat plausible. However, also the fitted elemental abundances appear quite peculiar: while the large magnesium abundance could likely be resolved by including a second, hotter plasma component in emission, the extremely low measured oxygen abundance is remarkable, especially since it is robustly recovered by our fit, independent of the exact modeling approach for source or background.

Finally, region I was defined in order to test for the presence of enhanced sulfur abundances in the western arc, as these were found to often diverge in previous fits with low signal-to-noise. Our best-fit single-component model recovers the previously found low plasma temperature, confirming that the region around the western arc, on average, hosts significantly colder plasma than the vast majority of Puppis A. It is interesting to note that the western arc appears distinct from the rest of the SNR, not only from a spectral but also from a morphological point of view, given its almost circular structure, which appears somewhat separate from the rest of the shell (see Fig. 5.1). A possible explanation for the formation of such “ear”-like structures in SNRs could be the expansion of the shock wave into a nonisotropic ISM, which may for instance be formed by an equatorially concentrated wind from the progenitor (Chiotellis et al. 2021).

Apart from the low plasma temperature, our spectral fit of region I indeed yields a strongly enhanced sulfur abundance at around eight times the solar value. This result should be treated with extreme caution, however. For instance, if we allow for a second plasma component in emission (with abundances tied to the first), we obtain an alternative fit with an improved statistic by around $\Delta C \approx -200$. This second thermal component is hotter than the primary one at a temperature of 0.5 keV, and completely removes the need for any sulfur line emission in the model. The conclusion is therefore that the putative sulfur enhancement, while formally statistically significant in our basic model, may in reality be an artifact of a hard tail of the spectrum, which is incompatible with the lower temperature of a single emission component. This case illustrates that, in theory, recreating realistic physical conditions of shocked plasma in SNRs would often require a complex multicomponent treatment of the emission, or even a nontrivial continuous distribution of temperatures and ionization timescales. However, when in practice fitting present-day CCD-resolution spectra, it is often challenging to convincingly disentangle even two emission components without imposing significant restrictions on the allowed parameter space.

5.3.5 The spectrum of the CCO

For completeness, we dedicate some further attention to the CCO of Puppis A, RX J0822−4300, visible as a hard point source in imaging. The timing of the CCO has been investigated in detail in the past (e.g., Gotthelf et al. 2013a), and the temporal resolution of 50 ms delivered by eROSITA is insufficient to provide any new insights in this respect. However, we can use its spectrum to verify if the results of our measurements are generally sensible, as variations of the spectrum are not expected on timescales of years to even decades. We thus extracted its spectrum from a circular aperture of a radius of $30''$ centered on the CCO, while we determined the local background from a concentric annulus with inner and outer radii of $50''$ and $90''$. For the

Table 5.2: Best-fit parameters for single (BB) and double (2BB) blackbody fits to the spectrum of the CCO.

	This work		Hui & Becker (2006b)	
	BB	2BB	BB	2BB
N_H (10^{21} cm^{-2})	$3.14^{+0.14}_{-0.14}$	$4.65^{+0.83}_{-0.53}$	$2.67^{+0.09}_{-0.09}$	$4.54^{+0.49}_{-0.43}$
kT_1 (keV)	$0.347^{+0.005}_{-0.005}$	$0.404^{+0.039}_{-0.026}$	$0.372^{+0.003}_{-0.003}$	$0.434^{+0.024}_{-0.017}$
R_1 (km)[a]	$0.89^{+0.03}_{-0.03}$	$0.56^{+0.16}_{-0.17}$	$0.73^{+0.02}_{-0.01}$	$0.44^{+0.07}_{-0.09}$
kT_2 (keV)	...	$0.215^{+0.040}_{-0.040}$	...	$0.225^{+0.026}_{-0.022}$
R_2 (km)[a]	...	$1.95^{+0.99}_{-0.53}$	...	$1.94^{+0.66}_{-0.44}$
F_a (10^{-12} erg s^{-1} cm^{-2})[b]	$4.54^{+0.04}_{-0.07}$	$4.70^{+0.07}_{-0.07}$	4.42	4.88
F_u (10^{-12} erg s^{-1} cm^{-2})[c]	$6.66^{+0.12}_{-0.12}$	$8.78^{+1.47}_{-0.81}$	6.05	8.94

Notes. Errors were estimated using the built-in `Xspec` command.

[a] Size of the circular emitting region, converted assuming a distance of 1.3 kpc.

[b] Observed (i.e., absorbed) flux of the source in the 0.5 – 10 keV range.

[c] Absorption-corrected flux of the source in the 0.5 – 10 keV range.

background modeling, we used the same approach as in the previous section. Following Hui & Becker (2006b), we used absorbed single (BB) and double (2BB) blackbody models to describe the emission of the CCO, from which we obtained the fit parameters displayed in Table 5.2.

For the BB model, our measurement appears statistically discordant with the study of Hui & Becker (2006b), who found a slightly hotter and less absorbed blackbody with somewhat smaller emitting area than our analysis suggests. However, it is important to keep in mind the systematic effect of the worse spatial resolution of eROSITA compared to *Chandra* and *XMM-Newton*, as the stronger blending of source and background likely outweighs the statistical errors derived in `Xspec`. Furthermore, since the BB model is likely not the optimal description of the spectrum (Hui & Becker 2006b), the smaller hard response of eROSITA leads to a weaker weighting of the high-energy tail of the spectrum, which naturally entails a lower measured effective temperature.

In this light, it is quite reassuring to notice that all measured parameters for the likely more accurate 2BB model agree within their statistical uncertainties, as we recover two blackbody components of temperatures around 0.2 and 0.4 keV with emission areas significantly smaller than the neutron star surface. Furthermore, all four fits described in Table 5.2 yield observed broad-band fluxes of the CCO that show a convincing agreement to within ten percent. A similar agreement can be found for the intrinsic fluxes when comparing identical models fitted here and in Hui & Becker (2006b). The apparent disagreement between unabsorbed fluxes of the BB and 2BB models can be attributed to the vastly different measured column densities. Apart from confirming the results of Hui & Becker (2006b), we believe that this brief analysis demonstrates that the absolute calibration of the eROSITA response in our observation is reliable up to a level of approximately ten percent.

5.4 Discussion

5.4.1 X-ray absorption toward Puppis A

While often regarded as somewhat of a nuisance parameter when analyzing spectra, the X-ray absorption toward Puppis A warrants some further discussion for several reasons: first, we find that the absorption column density shows strong variations of at least a factor five over the SNR's extent, from around $2 \times 10^{21}\,\mathrm{cm}^{-2}$ in the east and northwest to around $11 \times 10^{21}\,\mathrm{cm}^{-2}$ in the very south of Puppis A (Sect. 5.3.4). Therefore, a spatially integrated treatment of the emission from this SNR is not adequate, as it would not only combine emission from regions of different temperatures but also of different absorption columns. Strictly speaking, the resulting integrated spectrum is therefore not describable with a single-component model, and the derived parameters, such as temperature and intrinsic flux, can thus be strongly biased (see Sect. 5.3.3).

Second, with our analysis, we have shed some further light on the question of what causes the peculiar strip of hard emission crossing Puppis A from northeast to southwest (see Fig. 5.1). Numerous previous studies (Aschenbach 1993; Hui & Becker 2006b; Dubner et al. 2013) have, with good reason, argued that this strip is exclusively caused by an absorbing filament, which is visible in H I emission. However, our analysis suggests that the observed hard strip is not only due to foreground absorption, but caused by a combination of strong absorption in the southwest and elevated plasma temperatures in the center and northeast of the SNR. Apart from our spectral modeling, this is further supported by the fact that the northeast rim of Puppis A becomes the increasingly dominant source of emission above 2 keV (see final panels of Fig. 5.4 and Krivonos et al. 2021), where one would expect the spectral hardness to be mostly dependent on temperature rather than absorption.

Finally, both our work and the study of Katsuda et al. (2010) find locally enhanced absorption toward the northeast filament at $N_\mathrm{H} \sim 5.5 \times 10^{21}\,\mathrm{cm}^{-2}$. Katsuda et al. (2010) chose to discard this finding, since enhanced absorption appears counterintuitive for a feature that exhibits softer emission than its surroundings. However, since an elevated hydrogen column density is independently detected with two different instruments, we believe that it is at least a possibility that filaments such as this one may exhibit localized enhanced X-ray absorption. Additional support for this idea comes from Fig. 1 in Arendt et al. (2010), an overlay of mid-infrared (MIR) and X-ray emission of Puppis A, which shows superb agreement between the two regimes for a large fraction of the SNR, including the northeast filament. Thus, as the MIR is believed to trace the emission of shocked or heated dust, we suggest that the material that contributes additional small-scale absorption may actually be located within Puppis A, and could likely be (possibly destroyed) dust within the northeast filament.

5.4.2 The distribution of ejecta

The only previous spatially resolved abundance measurements covering the entirety of Puppis A were published by Luna et al. (2016). However, the map of oxygen abundance displayed in their work does not show any clear peak close to the ejecta knot visible in our corresponding plot in Fig. 5.6, likely due to the much larger size of their spatial bins. Furthermore, the average abundances obtained in their study are significantly lower than in ours. As both studies use the same reference abundance table, the reason for this is unclear, but may be related to different model versions or spectral analysis packages used.

Much better agreement exists between our results and the study of the eastern half of Puppis A by Hwang et al. (2008), concerning both the peak location and the average abundance values. First, we confirm their observation of overall subsolar abundances, finding median abundances ranging between around 0.4 for iron, and around 0.8 for silicon. Furthermore, we do not detect any significant large-scale oxygen enrichment to supersolar values, contrary to the natural expectation for an SNR that appears oxygen-rich in the optical (Winkler & Kirshner 1985). The generally low iron abundance and the lack of well localized iron enhancements throughout Puppis A could indicate a lack of iron ejecta enriching the ISM. Alternatively, the majority of iron ejecta may be in physical conditions outside the X-ray-emitting regime, as, for instance, they may not have been overrun by the reverse shock yet.

A somewhat special case is neon, which shows the highest median abundance of all metals in ISM-dominated regions. In the light of the bright dust emission in Puppis A, a promising explanation for this, introduced by Hwang et al. (2008), is the depletion of the other elements onto dust grains. Such dust depletion would reduce their measured X-ray abundances while preserving those of neon at around solar. The fact that the oxygen-to-neon ratio seems to be enhanced in the hot plasma at the northeast rim might be relevant in this context, as one could imagine that this may be a signature of a lower fraction of dust depletion, possibly due to its prior destruction. Of course, alternative explanations, such as a large-scale enrichment of the region with oxygen-rich ejecta material or intrinsic abundance gradients in the local ISM, are also conceivable.

A further observation by Hwang et al. (2008), uncertain at the time due to the limited spatial resolution and statistics of the observation, was that of apparently different spatial distributions of silicon and oxygen within the ejecta enhancement discovered by them. Thanks to the improvement in resolution and statistics provided by our data set, we are not only able to confirm this hypothesis, but can also see that the lighter elements (O, Ne, and Mg) are considerably more concentrated than the heavier elements (Si and S), which show an elongated distribution oriented along the northeast-southwest direction. This is the first clear confirmation of nonuniform mixing of hydrostatically and explosively synthesized ejecta elements on large scales in Puppis A. This is especially interesting since the heavier elements, synthesized toward the interior of the star, appear to be preferentially located further out in the SNR.

A less drastic case of nonuniform element distribution is detected within the compact ejecta knot that was previously investigated by Katsuda et al. (2008, 2013). Our results of spectral fits to the northern and southern portion of the clump (Sect. 5.3.4) are in broad qualitative agreement with those previous results, given the different approaches and models used. We find that the two parts show different chemical compositions, with the measured abundance ratios of neon and magnesium to oxygen being higher in the south than in the north. This observation is somewhat counterintuitive, as the southern part is considered to be associated with the oxygen-rich optically emitting "Ω filament" (Katsuda et al. 2008; Winkler & Kirshner 1985). This may indicate that a larger fraction of oxygen in the southern portion of the clump has cooled to temperatures below the X-ray emitting regime. A further characteristic separating the two portions of the ejecta knot is the fact that the southern part shows much stronger MIR emission than the northern part (Arendt et al. 2010). This indicates a higher concentration of heated dust in the south, which may be cospatial with the ejecta observed in X-rays or the optical. Finally, we note that our measurements and those of Katsuda et al. (2013) show little evidence for significant iron line emission in either part of the knot, indicating that its major constituents are in fact lighter elements, and any explosively synthesized iron, if present, is likely subdominant.

Our elemental abundance maps show only a single region with strong enhancements of O, Ne, Mg, Si, and S, with little indication of other X-ray emitting ejecta clumps throughout the remainder of the SNR. Therefore, a natural question to ask is why only such a small amount of ejecta is visible in Puppis A. In the context of this question, it is interesting to note that all detected compact ejecta clumps appear to be strongly underionized, implying relatively recent shock interaction. This is a natural expectation if ejecta material shocked earlier in time has already become unidentifiable as such. Apart from the advanced age of Puppis A, which implies that any X-ray emission from ejecta is superimposed with a dominant ISM-driven component, possible explanations for the apparent lack of ejecta include their cooling or the destruction of compact ejecta clumps. While the cooling of ejecta out of the X-ray-emitting regime is expected to operate slowly, the destruction of ejecta clumps after their interaction with the reverse shock may occur quite rapidly. We can roughly estimate the "clump-crushing" timescale for Puppis A, in analogy to the characteristic timescale for the interaction of shock waves with interstellar clouds (Klein et al. 1994): assuming an initial density contrast between an ejecta clump and ambient unshocked medium $\chi \lesssim 10$, a characteristic clump radius $a_0 \sim 0.2\,\mathrm{pc}$, similar to the apparent size of the observed ejecta knots, and a reverse shock velocity on the order of $v_s \sim 1000\,\mathrm{km\,s^{-1}}$ (Katsuda et al. 2013), the clump-crushing timescale $t_{\rm cc} = \chi^{1/2}\, a_0 / v_s$ is determined to be $t_{\rm cc} \lesssim 600\,\mathrm{yr}$. Since a clump is typically destroyed on the order of a few $t_{\rm cc}$ (Klein et al. 1994), ejecta knots overrun by the reverse shock early on in the evolution of Puppis A are expected to have significantly fragmented. The implied reduction of the density contrast between a clump and ambient medium likely hampers the identification of such older ejecta-rich features in X-rays.

If we assume our abundance maps to be approximately representative of the true ejecta distribution, they allow for an interesting comparison with the kinematics of the explosion: the CCO RX J0822−4300 has a quite precisely measured proper motion (Chapter 3), which, assuming a distance of 1.3 kpc, implies a transverse velocity of around $500\,\mathrm{km\,s^{-1}}$ toward southwest (position angle $\phi_0 \approx 248^\circ$ east of north). In a hydrodynamic kick scenario (e.g., Wongwathanarat et al. 2013), one expects heavy-element ejecta to be expelled preferentially in the opposite direction of the recoil experienced by the neutron star, which our abundance maps seem to qualitatively support. In particular, the silicon map in Fig. 5.6 indicates that close to all X-ray emitting silicon-rich ejecta are located in the northeast quadrant.

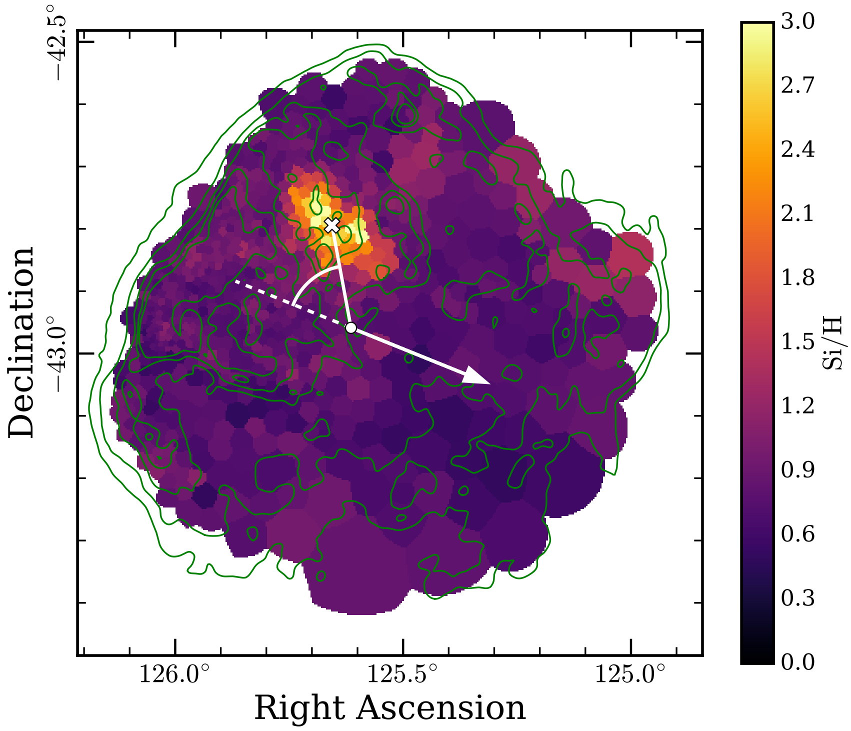

Figure 5.11: IME ejecta and NS kinematics in Puppis A. We show the distribution of IME ejecta, traced by the relative silicon abundance (as in Fig. 5.6), and indicate its computed center of mass (see text) with an "X". The arrow indicates the direction of NS motion (Chapter 3), away from the SNR's expansion center (marked by a dot; Winkler et al. 1988), and the dashed line marks the expected preferred ejecta recoil direction, which deviates significantly from the observed location of silicon ejecta.

A more quantitative comparison was performed by Katsuda et al. (2018), who performed a linear decomposition of the X-ray emission of Puppis A into physical components, aiming to isolate regions rich in intermediate-mass-element (IME) ejecta such as silicon. They found a general agreement between the direction of neutron-star motion and the distribution of these elements. However, upon closer inspection, it appears as if their method picked up part of the region of hot plasma at the northeast rim as IME-enriched, which is not confirmed by our analysis. Instead, this may be an artifact of enhanced silicon line emission introduced by the comparably high plasma temperature there, rather than enhanced abundances.

We performed a computation of the center of mass of the silicon abundance map in Fig. 5.6 (considering only clearly silicon-rich bins with Si/H > 1.2 and weighting each region according to the measured abundance), from which we obtained the location $(\alpha, \delta) = (08^{\mathrm{h}}22^{\mathrm{m}}38^{\mathrm{s}}, -42^{\circ}47'40'')$. This estimate of the centroid of IME ejecta lies at a position angle of 11° east of north from the commonly adopted center of expansion (Winkler et al. 1988). The deviation from the ideally expected recoil direction is around 57°, as is illustrated in Fig. 5.11, which is a much stronger discrepancy than apparent in Katsuda et al. (2018). We note however that our computation assumes a perfectly well known SNR center, which in reality is highly dependent on input assumptions (see Sect. 3.4). Furthermore, the observed distribution of silicon-rich ejecta may well be biased by the location of the reverse shock, as for a mature SNR such as Puppis A, only recently heated ejecta are expected to be visible. Nonetheless, an observation of IME-rich ejecta in a direction apparently unrelated to the expectation from a neutron star recoil scenario is not unheard of. For instance, the SNR N49 in the Large Magellanic Cloud was found to exhibit a deviation around 70° between the computed centroid of IME ejecta and the expectation from the apparent recoil direction of its magnetar (Katsuda et al. 2018).

Optical observations exhibit a qualitatively similar picture to X-rays, concerning the prevalence of ejecta, as oxygen-rich knots are found only in the northeast quadrant of Puppis A. Furthermore, they seem to possess an overall momentum directed in a direction roughly opposite that of the CCO (Winkler et al. 1988; Winkler & Petre 2007). An important remark in this context is that, ideally, one would investigate the distribution of heavy ejecta elements, such as iron or nickel, as those are expected to show the greatest anisotropies introduced by strong kicks (Wongwathanarat et al. 2013). However, as this and previous works have shown, these elements are notoriously difficult to trace for Puppis A.

A final interesting, though at this point uncertain, piece of evidence is the shrapnel-like feature displayed in Fig. 5.2, whose position with respect to the neutron star is almost opposite its proper motion direction. Its location outside the blast wave as well as the shape of the associated shock front visible in Fig. 5.2 seem to suggest that this feature is caused by a dense clump propagating into the ISM, and experiencing reduced deceleration due to its comparatively high density. A possible interpretation in analogy to the Vela shrapnels (e.g., Miyata et al. 2001) would be that this clump is composed of dense ejecta material, which, given its direction of motion, would fit well into a hydrodynamic recoil scenario. However, comparable features observed in the SNR RCW 103, which is similarly old as Puppis A, were found to show unremarkable abundances, contradicting their interpretation as ejecta clumps (Frank et al. 2015; Braun et al. 2019).

5.4.3 Estimating the mass of ejecta clumps and swept-up ISM

In Sect. 5.3.3, we have obtained the emission measure distribution across the whole SNR. This allows us to perform a rough estimate of the swept-up mass contributing to thermal X-ray emission in the forward shock, by integrating the product of average density and region volume over all analyzed regions associated to Puppis A. In order to improve the quantitative estimate of the electron density in the individual regions, it is necessary to make a more realistic assumption for the line-of-sight distribution of emitting plasma than the assumed uniform distribution over 20 pc that entered the map in Fig. 5.6.

We made the simplifying assumption that the shell of Puppis A is spherically symmetric, with a radius corresponding to the approximate observed diameter of 56′ at a distance of 1.3 kpc, implying a shockwave radius of $r \approx 10.6\,\mathrm{pc}$. Further, we assumed that the density along the radial direction follows a profile typical for an SNR in the Sedov-Taylor phase (Cox & Anderson 1982). Using this approach, we found numerically that the quantity that effectively enters the mass and density computations (see Eq. 5.3), the product of filling factor and line-of-sight depth $D_{\mathrm{LoS}}f$, is expected to range between around 5 and 9 pc over the majority of the SNR. In conjunction with the assumption of a mean atomic mass per hydrogen atom of $1.4\,m_{\mathrm{p}}$, typical for cosmic abundances, we obtained realistic estimates of the density in each region, and from that

Table 5.3: Estimated masses of features containing ejecta from spectral fits.

Region	M_{tot} $10^{-3}M_\odot$	M_{O} $10^{-3}M_\odot$	M_{Ne} $10^{-3}M_\odot$	M_{Mg} $10^{-3}M_\odot$	M_{Si} $10^{-3}M_\odot$	M_{Fe} $10^{-3}M_\odot$
A	66 ± 4	0.69 ± 0.05	0.118 ± 0.008	0.064 ± 0.006	0.075 ± 0.020	0.025 ± 0.004
A[a]	16.2 ± 1.0	11.2 ± 0.7	1.62 ± 0.11	0.99 ± 0.09	1.3 ± 0.5	0.17 ± 0.05
B	13.8 ± 1.9	0.26 ± 0.05	0.048 ± 0.010	0.031 ± 0.007	0.031 ± 0.008	< 0.0037
B[a]	3.2 ± 0.6	2.0 ± 0.4	0.39 ± 0.07	0.32 ± 0.06	0.36 ± 0.09	< 0.0011
C	6.0 ± 1.4	0.27 ± 0.12	0.07 ± 0.03	0.050 ± 0.021	0.036 ± 0.019	< 0.0005
C[a]	2.61 ± 0.25	1.52 ± 0.15	0.40 ± 0.04	0.31 ± 0.03	0.24 ± 0.06	< 0.0010
D	10.1 ± 1.7	0.82 ± 0.29	0.13 ± 0.05	0.075 ± 0.028	0.072 ± 0.026	< 0.00031
D[a]	4.38 ± 0.14	3.07 ± 0.10	0.479 ± 0.020	0.288 ± 0.015	0.269 ± 0.014	< 0.0005
E	362 ± 10	6.2 ± 0.3	1.57 ± 0.10	1.03 ± 0.08	4.3 ± 0.3	0.97 ± 0.07

Notes. The total and element-specific masses shown here were derived from the best-fit parameters shown in Table 5.1.

[a] Here, the best-fit parameters with the oxygen abundance fixed to a value of 2000 were used.

an estimate for the total emitting plasma mass of

$$M_{\mathrm{ISM}} = (78 - 87) \left(\frac{d}{1.3\,\mathrm{kpc}}\right)^{5/2} M_\odot. \tag{5.4}$$

The given uncertainty range was obtained by comparing the results of assuming different effective SNR extents and of using different Voronoi bin sizes. Formally derived statistical error bars would be much smaller than this heuristic systematic uncertainty range due to the large number of contributing regions.

On an elementary level, our result confirms that the overall mass budget of Puppis A is indeed dominated by swept-up ISM rather than by ejecta, which is a key assumption of the Sedov-Taylor model. Of course, this is unsurprising, as the blast wave is likely to have been decelerated substantially by heavy interaction with ISM at multiple locations. Using the approximate present-day radius of the shock wave $r \approx 10.6\,\mathrm{pc}$, and assuming the contribution of ejecta mass to M_{ISM} to be small, our estimate indicates a pre-explosion ISM density of around $1.1\times10^{-24}\,\mathrm{g\,cm^{-3}}$ when averaged over the present-day volume of Puppis A. Assuming an SNR age of $t \approx 4000\,\mathrm{yr}$, the expected explosion energy needed to produce a Sedov-Taylor shock wave (Sedov 1959) equivalent to the observed SNR size is thus

$$E = (1.22 - 1.36) \left(\frac{r}{10.6\,\mathrm{pc}}\right)^{9/2} \left(\frac{t}{4000\,\mathrm{yr}}\right)^{-2} \times 10^{51}\,\mathrm{erg}, \tag{5.5}$$

which is quite close to the canonical value of 10^{51} erg.[9] The fact that this approach yields a realistic result is quite reassuring, concerning in particular the distance to Puppis A, as the previously accepted value of 2.2 kpc (Reynoso et al. 2003) would yield a factor ~ 10 larger energy. However, it is important to keep in mind that the assumptions made here are extremely crude, implying significant systematic uncertainties on the explosion energy. For instance, an explosion into an ISM of uniform density seems extremely unlikely, considering the strong brightness gradient between the northeast and southwest of Puppis A. Moreover, the shock wave of Puppis A is in reality clearly not perfectly spherical given its appearance on the sky.

By combining our density estimate for each bin with the measured elemental abundances, it is straightforward to analogously estimate the masses of individual elements contributing to the observed emission in Puppis A. For those elements to which our fit is sufficiently sensitive, we obtain the following estimates: $M_{\mathrm{O}} \approx 0.29\,M_{\odot}$, $M_{\mathrm{Ne}} \approx 0.085\,M_{\odot}$, $M_{\mathrm{Mg}} \approx 0.032\,M_{\odot}$, $M_{\mathrm{Si}} \approx 0.052\,M_{\odot}$, $M_{\mathrm{Fe}} \approx 0.043\,M_{\odot}$. While it is certain that a limited contribution to the emission of these elements comes from ejecta material, the major contribution to the observed masses most likely originates from the ISM. Therefore, these estimates probably represent the composition of the local ISM around Puppis A, whereas the composition of the actual ejecta should be inferred directly from regions where these can be sufficiently isolated from their surroundings.

Therefore, to attempt to obtain mass estimates of individual ejecta clumps, we used our fit results given in Table 5.1 for the ejecta-enhanced regions A−E and proceeded analogously to our mass estimate for the whole remnant, with the modifications concerning assumed extent and electron-to-hydrogen ratio outlined in Sect. 5.3.4. The resulting mass estimates, in total and for individual elements, are given in Table 5.3.

It can be immediately seen that approaches (i) and (ii) yield differences by up to an order of magnitude for both the total and the element-specific masses. Therefore, making quantitative statements about the mass of individual ejecta knots is subject to large uncertainty, as both approaches are physically viable, and would likely require the spectral resolution of microcalorimeter detectors to be distinguishable (Greco et al. 2020). This is aggravated by additional large sources of systematic uncertainty such as the assumed three-dimensional extent of the respective feature, as well as the distance to Puppis A. This can be seen for regions C and D, where even after correcting for the different assumed distances,[10] our mass estimates and those for analogous regions by Katsuda et al. (2013) are discordant by a factor of a few, underlining the great importance of the assumed region volume for such computations. For instance, the oxygen mass M_{O} in the southern portion of the ejecta knot (region C) obtained in their study corresponds to $1.0 \times 10^{-4}\,M_{\odot}$ for normal, and $5.0 \times 10^{-4}\,M_{\odot}$ for pure-metal abundances, whereas we find values of $2.7 \times 10^{-4}\,M_{\odot}$ and $15 \times 10^{-4}\,M_{\odot}$, respectively.

While not particularly constraining in an absolute sense, our analysis implies that most X-ray emitting ejecta mass in Puppis A is located in region E, which is the largest more or less contiguous region of strongly enhanced abundances in the SNR. It is somewhat unexpected that such a region would show a significant silicon enhancement, reaching an overall mass ratio

---

[9] The dependence on $r^{9/2}$ arises from the combination of the mean density being proportional to $r^{-1/2}$ and the blast-wave energy being proportional to r^5.

[10] The estimated mass depends on $d^{5/2}$, due to the contributions of emitting volume ($\propto d^3$) and density ($\propto d^{-1/2}$).

$M_{\rm Si}/M_{\rm O} \sim 0.7$. Given the large size of this silicon-enriched region, and the compact nature of the more oxygen-rich ejecta knot (see Figs. 5.5 and 5.6), it seems reasonable to conclude that the average composition of all X-ray emitting ejecta clumps is dominated by the elemental composition measured in region E. The implied mass ratio $M_{\rm Si}/M_{\rm O} \sim 0.7$ would be extremely high if it were to be seen as representative of the average composition of the nucleosynthetic products of the supernova, as numerical modeling tends to predict $M_{\rm Si}/M_{\rm O} \lesssim 0.2$ (e.g., Sukhbold et al. 2016; Tominaga et al. 2007; Rauscher et al. 2002) for the integrated yield of core-collapse supernova ejecta. Since it is certain that Puppis A is the remnant of a core-collapse supernova, this apparent contradiction illustrates that, even thousands of years after the explosion, individual ejecta elements, which originate from different layers of the progenitor star, have not fully mixed and exist in separate clumps. The apparent lack of lighter elements with respect to Si might be caused by an, on average, earlier reheating of the outer ejecta layers, which are rich in O, Ne, and Mg, by the reverse shock. This may mask the presence of a large fraction of light-element ejecta among macroscopic variations of elemental abundances across the SNR. Apart from the uncertain possibility of ejecta cooling out of the X-ray-emitting regime, the rapid destruction of compact ejecta clumps by the reverse shock (see Sect. 5.4.2) may play a key role in this process, as it is expected to lead to stronger mixing with the ambient medium for ejecta material shocked earlier in time. The heavy impact of these effects on the apparent composition of the observed ejecta is the reason why any attempt to infer the progenitor mass of Puppis A based on the integrated composition of its X-ray-emitting ejecta budget is likely flawed.

5.5 Summary

At this time, the data set presented in this paper constitutes the deepest and highest-spatial-resolution X-ray observation of the entire Puppis A SNR that was taken with a single instrument. By dissecting the emission into narrow energy bands and performing spatially resolved spectral analysis, we have inferred the physical conditions and composition of the plasma across the entire SNR at hitherto unmatched sensitivity.

Our analysis has confirmed previous suggestions that parts of Puppis A, in particular in the southwest, are subject to strong foreground absorption (Dubner et al. 2013). The overall variation of the absorption column over Puppis A is found to be at least of a factor five. Part of the absorption on small spatial scales may be contributed by dust within Puppis A, which is visible in the MIR (Arendt et al. 2010). Furthermore, we have shown that large-scale variations in plasma temperature span a range of around a factor two, ranging between around 0.35 keV in the western arc and 0.75 keV at the northeast rim. Thanks to being comparatively close to CIE, the latter region exhibits the hardest X-ray emission in Puppis A, becoming dominant above 2 keV in imaging. The combination of hot plasma in the northeast and enhanced absorption in the southwest is identified as the likely origin of the characteristic strip of hard emission crossing the SNR.

From the plasma ionization age and emission measure distributions, we have reconstructed the time of shock interaction of the emitting material, providing an interesting new look at Puppis A: several features, such as the northeast filament (Katsuda et al. 2010), the ejecta knot (Katsuda et al. 2008; Hwang et al. 2008) and the eastern edge of the BEK (Hwang et al. 2005) stand out prominently, as the material in all these regions appears to have recently interacted with a forward or reverse shock. No clear analogous signatures of recent shock interaction are observed in the western half of Puppis A, which may be related to the thinner ISM there.

We have constructed elemental abundance maps of Puppis A, which reveal that elements typical for core-collapse SN ejecta (O, Ne, Mg, Si, and S) only show a few concentrated enhancements in X-rays, which are spatially consistent with the location of ejecta enhancements identified by Katsuda et al. (2008, 2010) and Hwang et al. (2008). We have confirmed the spatially disjoint nature of light-element and IME ejecta, as the peak of oxygen, neon, and magnesium is clearly separated from the more spatially extended silicon and sulfur emission. None of the regions investigated are found to exhibit a convincing signature of enrichment with iron ejecta. The X-ray emission of the remainder of Puppis A generally implies solar or subsolar abundances for all elements, with only mild large-scale variations. The highest average abundances are found for neon, which may be related to the possible depletion of other elements onto dust grains (Hwang et al. 2008), which would most strongly affect magnesium, silicon, and iron.

Our investigation of the distribution of silicon-rich ejecta with respect to the recoil direction of the neutron star has yielded a deviation of around 57° from the expectation, significantly higher than previously measured (Katsuda et al. 2018). However, an important shortcoming of this type of measurement is the unknown location of the reverse shock that may severely bias the observed distribution of ejecta material in Puppis A, which would also explain the apparent lack of ejecta clumps over the majority of the SNR.

Our spatially resolved treatment of the emission has allowed us to calculate the mass of the swept-up ISM contributing to the observed X-ray emission of Puppis A, which we determine to around $78-87\,M_\odot$. We use this to crudely estimate the explosion energy needed to create a Sedov-Taylor blast wave equivalent to the approximate present-day radius of Puppis A, finding a value reasonably close to the canonical explosion energy of 10^{51} erg. Furthermore, we have performed estimates of individual element masses in ejecta enhancements, finding that the largest ejecta-rich region exhibits an extremely high silicon-to-oxygen ratio when compared to the expected integrated yield of any core-collapse supernova. This may be a further consequence of the biased view on the inherent ejecta composition in this mature SNR, as much of the light-element ejecta may have mixed with ISM or cooled below X-ray emitting temperatures since their passage through the reverse shock.

The completion of the four-year eROSITA all-sky survey was originally planned for the end of 2023, but survey operations have been halted since February 2022, with around 4.5 out of 8 surveys complete.[11] Regardless of the future continuation of science operations, eROSITA has already mapped the entire X-ray sky at unprecedented sensitivity and spatial resolution. While the acquired exposure and statistics for SNRs in the all-sky survey are of course not comparable to this study, we hope to have demonstrated the excellent capabilities of eROSITA regarding the detection and characterization of diffuse emission. This is in particular relevant for the search for new Galactic SNRs (e.g., Churazov et al. 2021; Becker et al. 2021), which may help reduce the discrepancy between the expected and observed number thereof. Furthermore, the survey

---

[11] `https://www.mpe.mpg.de/7856215/news20220303`

allows carrying out systematic studies of the spectral and morphological properties of the entire X-ray-detected SNR population using a homogeneous data set (W. Becker et al., in prep.).

Chapter 6

A detailed look at thermal and nonthermal X-ray emission from the Vela supernova remnant with SRG/eROSITA

This chapter is based on a paper draft which will be submitted to Astronomy & Astrophysics as Mayer et al. (2023).

6.1 Introduction

Few objects dominate the X-ray sky like G263.9−3.3, the Vela supernova remnant (SNR). This composite core-collapse SNR was originally discovered as three separate radio structures named Vela X, Y, and Z (Rishbeth 1958). In X-rays, it appears as a large bright shell of around 8° diameter with a central pulsar (PSR B0833−45, the "Vela pulsar") and its associated pulsar wind nebula (PWN), commonly referred to as Vela X. The distance to the system is quite precisely known to 287^{+19}_{-17} pc, owing to measurements of optical absorption lines toward Vela and of the pulsar parallax in the radio and optical (Dodson et al. 2003; Cha et al. 1999; Caraveo et al. 2001). In contrast, the age of the SNR is not known precisely, and is commonly assumed to be equal to the characteristic spin-down age of the pulsar, around 11 kyr (Manchester et al. 2005). The true age may however deviate significantly from this value, and might even be as large as $\sim$ 30 kyr, as the pulsar appears to exhibit a braking index much lower than the commonly assumed value (Lyne et al. 1996; Espinoza et al. 2017). In any case, Vela can likely be considered an evolved SNR, significantly older than, for instance, the overlapping X-ray-bright SNR Puppis A (Winkler et al. 1988; Mayer et al. 2020).

Thanks to its proximity and evolved state, Vela allows studying the X-ray emission of an SNR at a level of depth and detail that is not attainable for most other SNRs at a larger distance. In the soft band, Vela appears as a relatively cool thermally emitting shell with significant substructure (Lu & Aschenbach 2000). A revolutionary finding was the discovery of the Vela "shrapnels" with *ROSAT* (Aschenbach et al. 1995), which are likely to be the signatures of dense ejecta clumps, produced in an inhomogeneous explosion, overtaking the main blast wave and penetrating the unshocked interstellar medium (ISM). This interpretation is probable, not only because of their characteristic bow shocks and their apparent trajectories consistent with an origin close to the SNR center, but also because of enhanced abundances of typical ejecta elements contributing to their X-ray emission. In particular, the shrapnels labeled B and D by Aschenbach et al. (1995) seem to be strongly enriched with oxygen, neon, and magnesium (Katsuda & Tsunemi 2005; Yamaguchi & Katsuda 2009), whereas shrapnel A and the more recently studied feature G appear to form a bilateral jet-like structure rich in silicon (Tsunemi et al. 1999; Miyata et al. 2001; Katsuda & Tsunemi 2006; García et al. 2017).

At harder X-ray energies ($\gtrsim 1.3\,\mathrm{keV}$), a completely different morphology emerges: Apart from the overlapping circular shell of the SNR RX J0852.0−4622 (Aschenbach 1998), which is most likely unrelated to the Vela SNR, strong nonthermal emission from the PWN is detected. The emission appears concentrated on a feature dubbed the “cocoon” extending around one degree southward from the pulsar, which was originally interpreted as a pulsar jet (Markwardt & Ögelman 1995). However, high-resolution X-ray observations disproved this interpretation. Data from the *Chandra* X-ray observatory revealed a complex structure in the immediate surroundings of the pulsar, including an equatorial torus and the actual pulsar jet, which emanates from it toward the northwest, along its proper motion direction (Helfand et al. 2001; Pavlov et al. 2003). Recently, observations by the *IXPE* mission have shown that the X-ray emission in this region is highly polarized, arguing in favor of a highly ordered magnetic field structure in the region of the torus (Xie et al. 2022). The question regarding the true nature of the cocoon has not been resolved beyond doubt, but several authors (e.g., Blondin et al. 2001; Slane et al. 2018) have proposed an interesting model in which an asymmetric reverse shock has crushed the PWN and shifted its apparent center off the pulsar toward the south, in agreement with its observed position and morphology in X-rays. Evidence for the presence of nonthermal X-ray emission in regions beyond the cocoon has been presented by several studies using pointed observations (Katsuda et al. 2011; Slane et al. 2018), and data from coded-mask instruments at higher X-ray energies (Willmore et al. 1992; Mattana et al. 2011). At the present time, it is however unclear how large the true extent of the Vela PWN in the X-ray regime is.

Emission associated to Vela has been identified and studied across the entire electromagnetic spectrum, from the radio domain (e.g. Duncan et al. 1996; Frail et al. 1997; Bock et al. 1998; Alvarez et al. 2001) up to very high-energy (VHE) gamma-rays (Aharonian et al. 2006a; Abdo et al. 2010; Abramowski et al. 2012; Grondin et al. 2013; Tibaldo et al. 2018; H. E. S. S. Collaboration et al. 2019). The radio band clearly reveals the composite nature of the Vela SNR, with prominent nonthermal emission originating from narrow filaments forming the SNR shell and from Vela X. In the latter region, the population of electrons accelerated in the pulsar wind creates a chaotic extended network of filaments with a flat spectrum (Bock et al. 1998; Alvarez et al. 2001), as typical for PWNe. Similarly, at gamma-ray energies $< 100\,\mathrm{GeV}$, extended diffuse emission is observed, approximately consistent with the extent of the radio halo (Grondin et al. 2013; Tibaldo et al. 2018). In contrast, at TeV energies, primarily the cocoon and its immediate surroundings are visible, whereas a large part of the radio-bright Vela X region and the SNR shell are not detected (Abramowski et al. 2012; Tibaldo et al. 2018). These findings may be interpreted as the signature of the existence of two separate electron populations in Vela X, where the lower-energy population is responsible for the extended halo emission in the GeV and radio bands, via inverse Compton and synchrotron emission, respectively. A "younger", more energetic electron population would accordingly produce the observed TeV and X-ray emission in the cocoon (de Jager et al. 2008).

In this work, we present and analyze the X-ray data set of the Vela region gathered by the eROSITA telescope on board the *SRG* mission (Predehl et al. 2021; Sunyaev et al. 2021) during its first four all-sky surveys. Our observations provide higher sensitivity and much better spectral resolution than available in the *ROSAT* all-sky survey (Aschenbach 1993). Furthermore, its effectively infinite field of view contrasts the comparatively small regions within and around Vela covered by pointings or even mosaics with instruments such as *Suzaku* or *XMM-Newton* (e.g., Katsuda & Tsunemi 2005, 2006; Miceli et al. 2008; Yamaguchi & Katsuda 2009; García et al. 2017; Slane et al. 2018). The ability to resolve spectral emission lines across the entirety of Vela is a crucial tool for separating and characterizing the contributions of thermal emission from hot plasma and nonthermal synchrotron emission in imaging and spectroscopy throughout the SNR.

Our paper is organized as follows: after a brief description of data assembly and cleaning procedures (Sect. 6.2), we perform imaging and spectroscopic analysis of the X-ray emission of the Vela SNR shell, the Vela shrapnels, and the central PWN in Sect. 6.3. The implications of our findings on the distribution and composition of intervening material, the presence of ejecta inside and outside the shell, and the size and multiwavelength properties of Vela X are discussed in Sect. 6.4, and our results summarized in Sect. 6.5.

6.2 Observations and data preparation

The region of Vela is observed every six months during the eROSITA all-sky survey (eRASS)[1]. eROSITA scans the sky along great circles of constant ecliptic longitude, at a rate of four hours per revolution, accumulating around 40 s of exposure per scan, while slowly advancing the scanning axis by around one degree per day (Predehl et al. 2021). Here, we concentrate on the combined data set of the Vela region taken during the first four surveys (commonly referred to as eRASS:4), taken between May 2020 and November 2021. The total unvignetted exposure acquired during these four surveys ranges between around 1000 and 1400 s over the extent of Vela.

We started our work by merging the data in the `c020` processing version from all eROSITA sky tiles in a 15° × 15° region centered on the Vela pulsar[2]. Compared to the earlier versions `c946`/`c001`, this current eROSITA processing entails strongly suppressed electronic noise at low energies, increased precision of boresight corrections, and an improved handling of different event pattern types (A. Merloni et al., in prep.). For the merging of the individual sky tiles, we used the `evtool` task of the latest internal release of the eROSITA science analysis software (Brunner et al. 2021), `eSASSusers_211214`, to combine data from all seven telescope modules

---

[1] At the time of writing, science operations of eROSITA are interrupted, in response to the Russian invasion of Ukraine.

[2] The whole "German" eRASS data set will be released incrementally, with the processing `c020` being the most current version of the eRASS:4 data set. Currently, the release of the first all-sky survey is scheduled for May 2023, with the second release, likely including data up to eRASS4, projected for the second quarter of 2024.

(TMs), while using the recommended `flag` and `pattern` filter keywords.[3]

Prior to beginning scientific analysis, we performed a thorough check of the acquired data set for time-variable artifacts visible in imaging, focussing especially on the low- and high-energy ends of the spectral range. While eROSITA is typically not too strongly affected by temporal background variations due to enhanced solar activity (Freyberg et al. 2020), we found a few stripes exhibiting an enhanced high-energy count rate oriented along the telescope's scanning direction, typical for such flares. We used the `flaregti` tool, applying a fixed count rate threshold of $1.2\,\mathrm{ct\,s^{-1}\,deg^{-2}}$ in the $4.0 - 8.5\,\mathrm{keV}$ range, to filter out those time intervals most strongly affected by enhanced background, while only losing around 1% of all events.

In the energy range $0.2 - 0.3\,\mathrm{keV}$, we encountered two further stripe-like artifacts in the south and southeast of Vela, which we found originated in TM4 and during eRASS3 and eRASS4 alone. TM4 was struck by a micrometeorite during the third survey (Freyberg et al. 2022), rendering several thousands of pixels bright, hence unusable. Therefore, the likely reason for the occurrence of these low-energy stripes in the data is the variability of a few affected unmasked pixels, which may have temporarily exceeded the on-board threshold, producing spurious low-energy events. We were able to completely filter out the spurious feature in eRASS3 by removing the TM4 good time intervals (GTIs) corresponding to a single scan at around 2021-05-21 18:20:00 (UTC) from the event file. In contrast, the stripe in eRASS4 was found to occur during multiple scans, but to originate only from a single bright row of pixels in TM4 (with the pixel coordinate `RAWX=150`), and was filtered out accordingly. The final cleaned event file on which we based our analysis contains around 19 million entries. In the following, all our imaging analysis is based on the combination of events from all seven TMs, while, for spectroscopy, we excluded TMs 5 and 7, leaving a total of around 12 million events, as their contamination by optical light (Predehl et al. 2021) makes them less suitable for this purpose.

6.3 Analysis and results

6.3.1 Energy-dependent morphology

While imaging of Vela in the *ROSAT* era was usually limited to a soft and a hard band, the energy resolution of the eROSITA CCDs (Predehl et al. 2021; Meidinger et al. 2020) allows us to study the morphology of the entire SNR across a larger number of independent energy bands for the first time. In order to obtain a three-band false-color image of our target, we used the `evtool` and `expmap` tasks to create exposure-corrected images of the Vela region, binned to a pixel size of $30''$. We used typical energy bands covering the most sensitive range of the eROSITA response, $0.2 - 0.7$, $0.7 - 1.1$, and $1.1 - 2.3\,\mathrm{keV}$, as well as a broad band $0.2 - 2.3\,\mathrm{keV}$.

Figure 6.1 displays the resulting single-band and false-color images of Vela, using a logarithmic brightness scale in order to represent the full dynamic range covered by our data set. In order to emphasize spectral variations in the bright portions of the SNR, this is complemented by Fig. 6.2, which displays a false-color image of the same data set after adaptive smoothing of each

---

[3] `https://erosita.mpe.mpg.de/edr/DataAnalysis/esasscookbook.html`

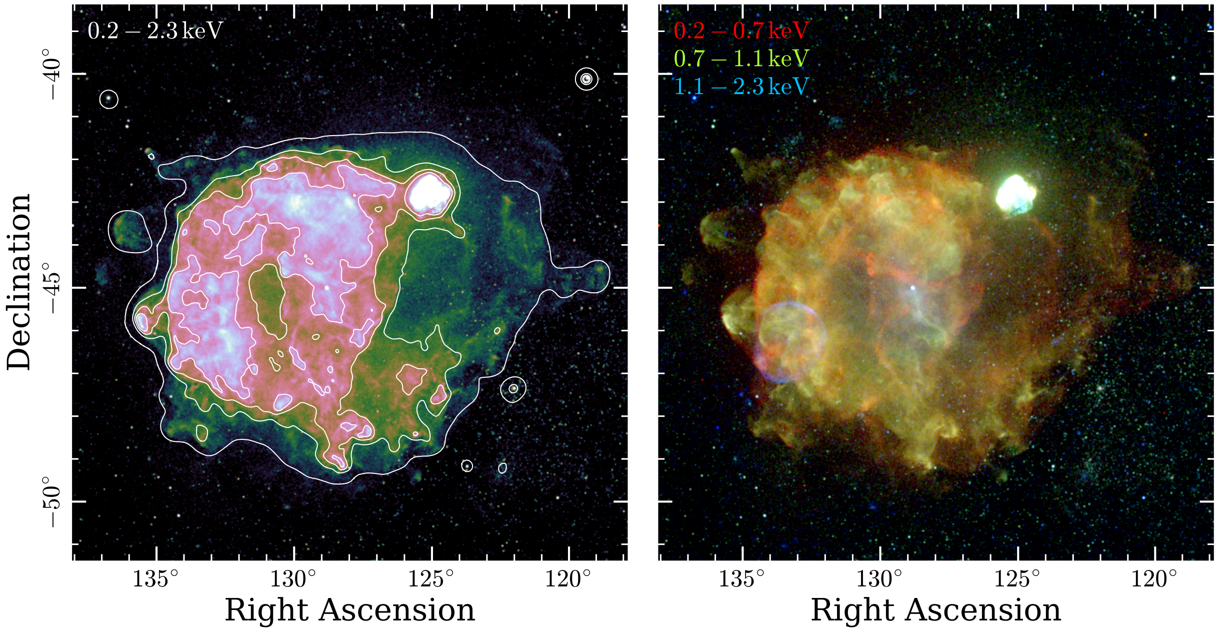

Figure 6.1: Exposure-corrected images of the Vela SNR displayed in the broad band (*left*) and as an RGB false-color image (*right*) in the energy range 0.2 – 2.3 keV. Gaussian smoothing with a kernel size of $\sigma = 45''$ was applied to both images, and a logarithmic brightness scale was used. The contours in the *left* panel trace the heavily smoothed 0.2 – 2.3 keV emission at levels of 1.4×10^{-2}, 4.0×10^{-2}, 8.0×10^{-2}, 1.6×10^{-1} ct s^{-1} arcmin^{-2}.

band to $S/N = 30$[4], and using a linear brightness scale. In addition, we display an image in a logarithmic brightness scale, but with an artificially enhanced color contrast through a quadratic stretch applied to the RGB array, which preserves the visibility of faint features. The excellent statistics and spectral resolution of our data set permit also the construction of a set of narrow-band images, isolating the contribution of prominent emission lines to the SNR's morphology. In Fig. 6.3, we show exposure-corrected images of the Vela region in 16 non-overlapping bands of increasing energy.

The X-ray emission of Vela exhibits a quite complex morphology, which varies strongly with energy, with its filled shell being visible across an extent around 10° × 8°. A strong horizontal brightness gradient is visible in the thermal emission, with the west generally exhibiting a much lower surface brightness level, and only some faint soft filaments tracing what appears to be the western SNR shell. This may be related to a density gradient in the surrounding ISM, which likely exhibits higher densities toward north and east (e.g. Moriguchi et al. 2001; Sushch et al. 2011; Slane et al. 2018). Furthermore, Fig. 6.2 reveals the presence of multiple morphological components: the soft energy band exhibits a diffuse shell of emission toward north and east, as well as several thick filamentary structures, extending in a tangential direction with respect to the center. In contrast, structures at intermediate energies seem to be preferentially oriented radially, with several "fingers" of emission appearing to intersect almost perpendicularly with the soft

---

[4] `https://xmm-tools.cosmos.esa.int/external/sas/current/doc/asmooth/index.html`

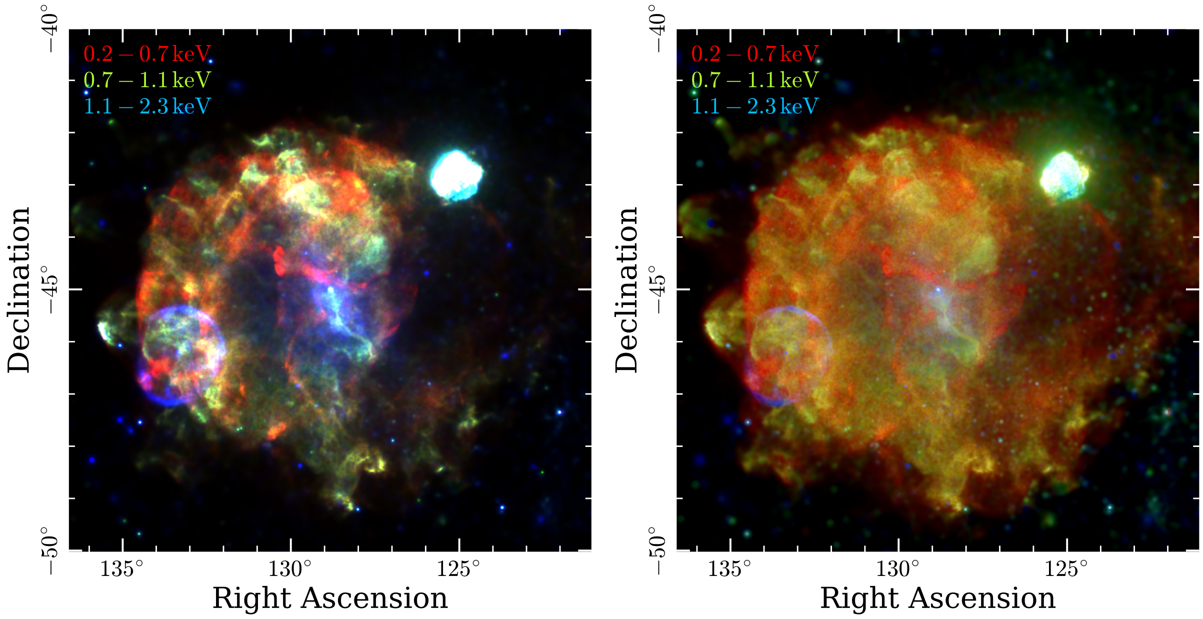

Figure 6.2: Color-enhanced images of Vela. The *left* panel shows the RGB image from Fig. 6.1 in linear brightness scale, with the saturation of each band at the 99.5th percentile of the observed brightness distribution; the *right* panel keeps the image in a logarithmic brightness scale, but with a quadratic stretch applied to the RGB colors.

shell in the northeast. As can be seen in Fig. 6.3, the transition between the two components seems to occur at around 0.6 keV, between the two bands dominated by line emission from different ionization states of oxygen, O vii and O viii, respectively. Therefore, it seems likely that the difference in morphology is at least partly caused by different plasma temperatures in the emitting components.

Apart from thermal emission from the SNR shell, several shrapnels in the east, most prominently those labelled A, B, and D (Aschenbach et al. 1995) are clearly visible through their characteristic bow shocks, created as the ejecta clumps penetrate into the ISM. In addition to the originally established shrapnels, our image reveals several similar structures, preferentially just outside the southern part of the shell, which may also be interpreted as signatures of dense clumps of outward-protruding material (see García et al. 2017). It is conceivable that these features correspond to ejecta shrapnels at an earlier stage, which do not exhibit an equally visible bow shock. A more detailed imaging and spectroscopic study of known and suspected shrapnels is performed in Sect. 6.3.3.

The Vela pulsar is clearly visible as a bright point source across the whole energy range, with the nonthermal emission of its plerion dominating the hard energy band above (> 1.1 keV). The cocoon south of the pulsar constitutes the brightest portion of the extended nonthermal emission, which is spatially coincident with thermal emission seen in the medium energy band (Slane et al. 2018). In addition, Fig. 6.2 clearly reveals the presence of nonthermal emission beyond the cocoon, in particular in the northern direction. While indications for the presence of more

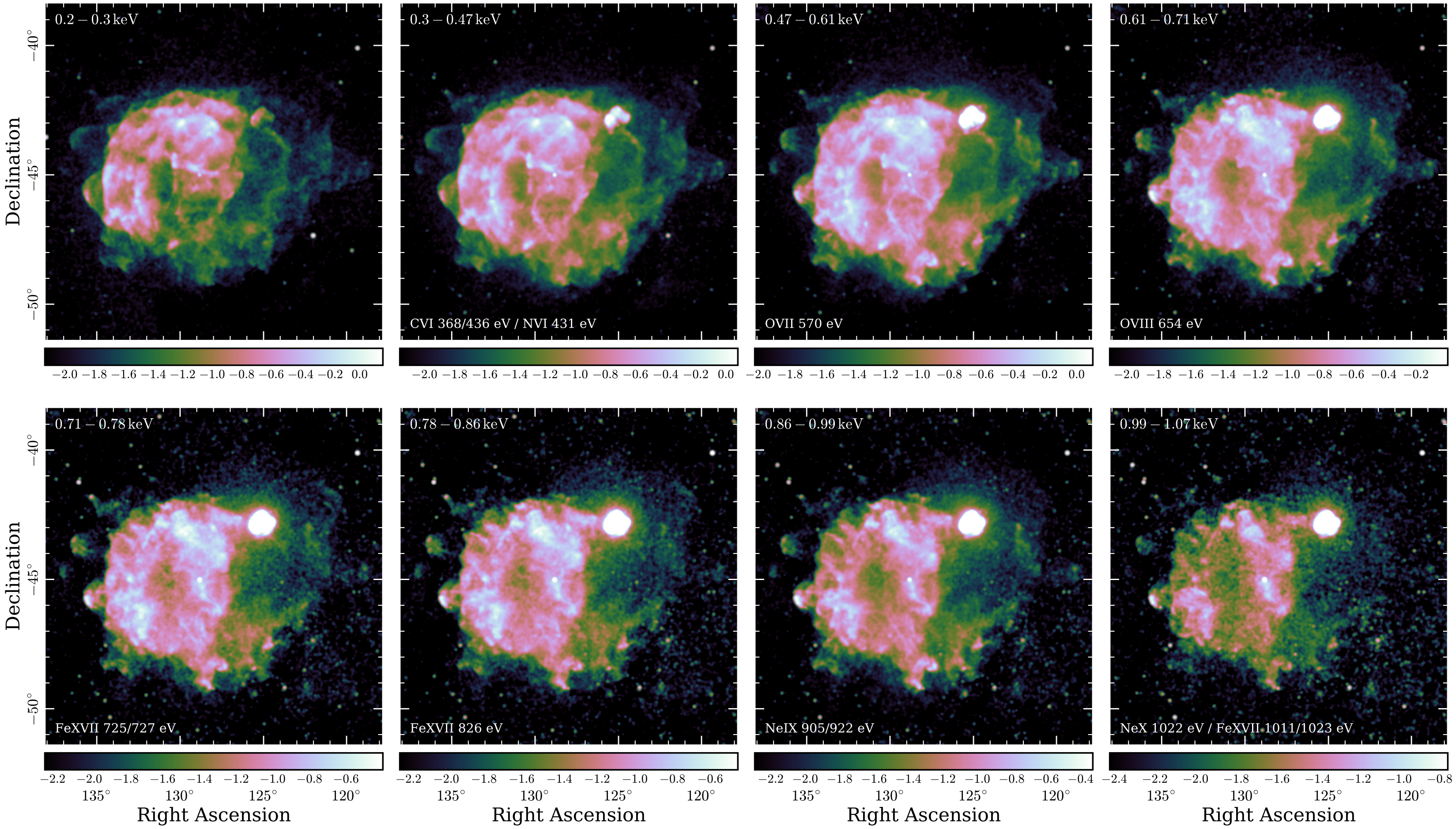

Figure 6.3: Exposure-corrected images of Vela in 16 narrow bands of ascending energy. The image in each band was smoothed with a 2.5′ Gaussian kernel. The upper right corner of each panel denotes the displayed energy band, whereas, in the lower left corner, we indicate strong spectral lines expected to contribute to the emission in the respective band. The color bar underneath each panel indicates the logarithmic range of the displayed count rate, specified in units of ct s^{-1} keV^{-1} $arcmin^{-2}$.

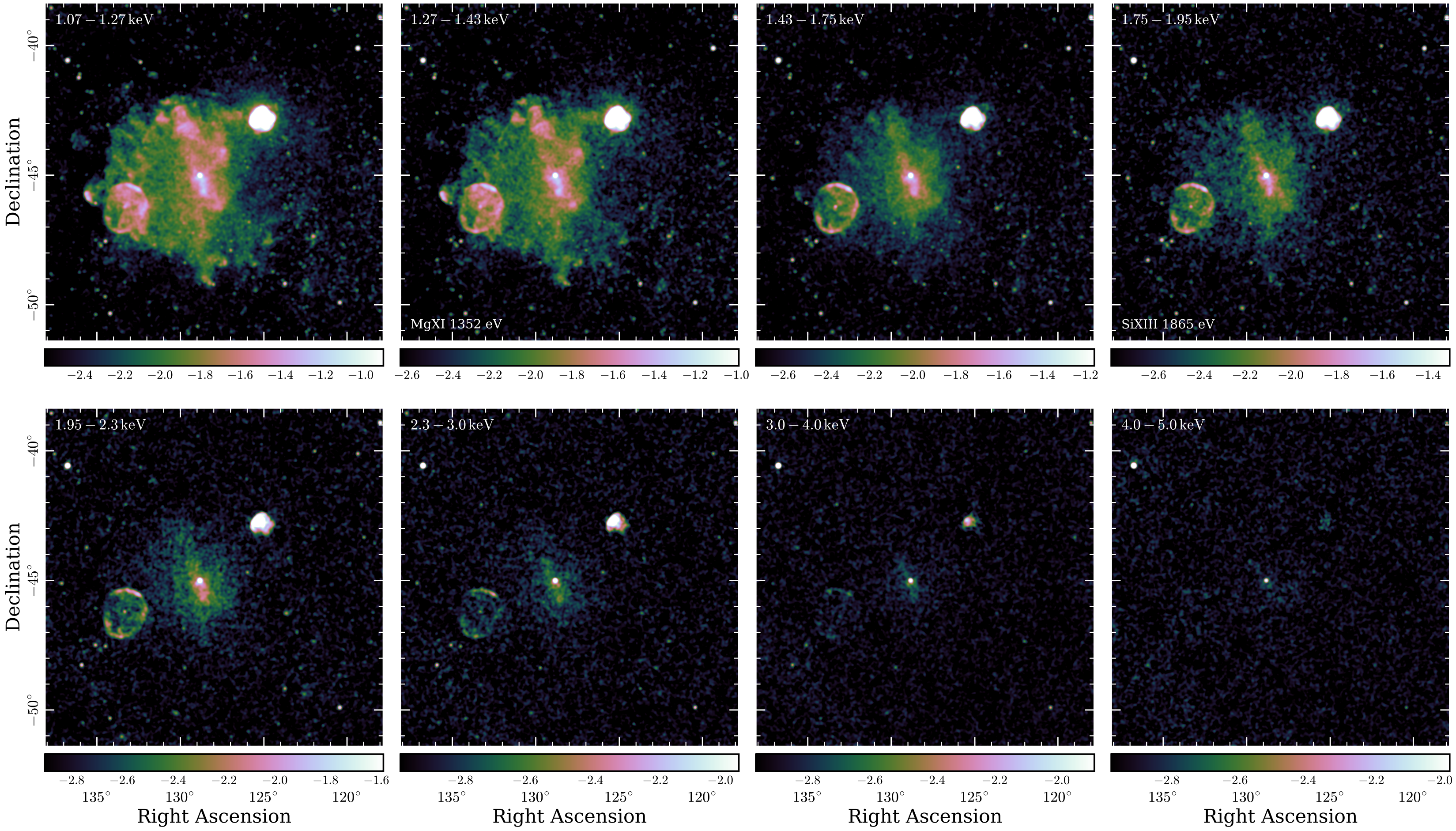

Figure 6.3: Continued.

extended hard X-ray emission had been found previously in pointed observations (e.g. Katsuda et al. 2011; Slane et al. 2018) and weak hints were visible also in the *ROSAT* hard band (Fig. 1 in Aschenbach 1998), our imaging data demonstrates the contiguous nature of the extended hard X-ray emission centered on the pulsar. In Fig. 6.3, we can see that, above 1.4 keV, the contribution from the presumably thermal morphological components becomes negligible. Thus, the emission detected in energy bands without strong expected emission lines, for instance 1.43 − 1.75 keV and 1.95 − 2.30 keV, likely traces only the emission from Vela X. These bands reveal a vast extent of the plerion, with an apparent diameter around five degrees in the north-south direction. The fact that the apparent size of Vela X seems to decrease toward higher energies may be interpreted as a signature of synchrotron cooling of the emitting electrons (Tang & Chevalier 2012). However, a more quantitative analysis is needed to confirm this hypothesis, in particular since the relative particle background contribution rises strongly with energy (see Sect. 6.4.3).

Multiple physically unrelated objects stand out against the large, soft shell of Vela. Apart from the high-mass X-ray binary Vela X-1 in the northeast, a few star clusters in the southwest, and numerous, mostly stellar, point sources, this includes the extremely bright SNR Puppis A in the northwest, and the hard, almost circular shell of SNR RX J0852.0−4622 (“Vela Jr.”, Aschenbach 1998), in the southeast. Both Puppis A (Chapter 5) and Vela Jr. (Camilloni et al. 2023) have recently been studied using eROSITA data, and will therefore not be discussed in detail here. However, the large field of view of our data set allows for two brief observations regarding the periphery of Puppis A: First, there exists a diffuse halo of emission centered on the SNR, visible most clearly in the “green” energy band. Given the considerable amount of intervening material toward Puppis A (Sect. 5.4.1), this could be interpreted as a dust-scattering halo. Second, a previously unknown faint arc is visible just outside the northwest rim of Puppis A. At the present time, it is unclear whether this feature is physically associated to Puppis A, to Vela, or to neither of the two.

6.3.2 Spatially resolved spectroscopy

Binning and modelling

In this section, we aim to disentangle and characterize the thermal and nonthermal contributions to the observed X-ray emission in different regions of Vela by performing spatially resolved spectroscopy. We followed the general approach of subdividing the emission into spatial bins using Voronoi tessellation (Cappellari & Copin 2003) with the modification proposed by Diehl & Statler (2006), similarly to Sect. 5.3.3. Subsequently, we fitted the spectrum of each region using `Xspec` (version 12.11.0, Arnaud 1996), in order to extract physically meaningful parameters.

In order to prevent contamination by the emission from bright fore- and background sources, we masked out all highly significant point-like sources (i.e., those sources with `DET_LIKE_0` > 50 and `EXT_LIKE` = 0) in the eRASS1 catalog (A. Merloni et al., in prep.) in the input broadband (0.2 − 2.3 keV) image, prior to performing the binning. In addition, the region of Puppis A and a 3′ radius around the Vela pulsar were excluded. In order to avoid obtaining unnecessarily many bins dominated by background counts alone, we subtracted an estimated background count map from the input signal image. This map was created by multiplying a flat background count rate, measured in an “empty” region far from the shell of Vela, with the broadband exposure map. We decided to use a target signal-to-noise threshold of $S/N = 100$ for the tessellation, which provides decent spatial resolution and around 500 resulting bins across the SNR, while retaining sufficient statistics to perform meaningful spectral fits in each bin.

Similarly to Sect. 5.3.3, we extracted all spectra from TMs $1-4$ and 6 using `srctool`, and subsequently fitted them with a physical source model combined with several background templates. The latter consisted of a model of the instrumental background, determined from filter-wheel-closed data in the `c020` processing (M. Yeung et al., submitted), a fixed absorbed extragalactic X-ray background (De Luca & Molendi 2004), and a thermal background component. The thermal component was constrained by fitting the spectrum of an empty region northeast of the SNR shell with a model consisting of the above components and a model expressed as `acx+apec+TBabs*(apec+apec)` (Smith et al. 2014, 2001; Wilms et al. 2000). The individual components reflect charge exchange emission originating within the heliosphere,[5] the unabsorbed contribution of thermal plasma in the local hot bubble, as well as absorbed thermal emission from the Galactic halo and a possible hot component from unresolved stars in the Galactic plane (see Wulf et al. 2019), respectively. The best-fit shape of the thermal background was fixed and used as a template in our modelling of the source spectra, where only its global normalization was allowed to vary by up to a factor 2. Generally, it should be noted that, due to the bright soft thermal emission of Vela, this thermal background component has a relatively minor effect on our spectral modelling, as, in most regions, it is outshone by source emission at all relevant energies.

As observed in Sect. 6.3.1, both thermal and nonthermal components contribute to the emission of Vela. In order to reflect this fact, we modelled the source contribution to each spatial bin using a combination of a thermal plane-parallel shocked plasma with non-equilibrium ionization (NEI; Borkowski et al. 2001) and a power law model, with foreground absorption following the Tübingen-Boulder model (Wilms et al. 2000). In the following, we refer to this thermal-nonthermal model, which is expressed as `TBabs*(vpshock+powerlaw)` in `Xspec`, as the “TNT” model. While this model allows for the realistic possibility of underionized plasma close to shock fronts, it entails a severe degeneracy between plasma temperature and ionization age, especially in the presence of a possible nonthermal component contributing to continuum emission. We found that a decent alternative is given by a model consisting of two thermal plasmas in collisional ionization equilibrium (CIE; Smith et al. 2001) and one nonthermal component, expressed as `TBabs*(vapec+vapec+powerlaw)`, and labeled “2TNT” in the following. A similar two-component model in CIE has been used previously to describe the thermal emission of Vela (e.g. Miceli et al. 2008), and is likely a good approximation of the spectrum inside the SNR shell, as for instance Slane et al. (2018) did not detect any clear deviations from CIE around Vela X. For both models, the abundances of N, O, Ne, Mg, and Fe were thawed, as these are the elements with the highest impact on line emission in the observed spectra, whereas all other abundances were fixed to the reference values of Wilms et al. (2000). For the 2TNT model, the abundances of all elements were tied between the two thermal components, in order

---

[5] While solar wind charge exchange is not actually a thermal process, we include it in this “thermal” background, as the phenomenology of a line-dominated soft spectrum is quite similar to the truly thermal components.

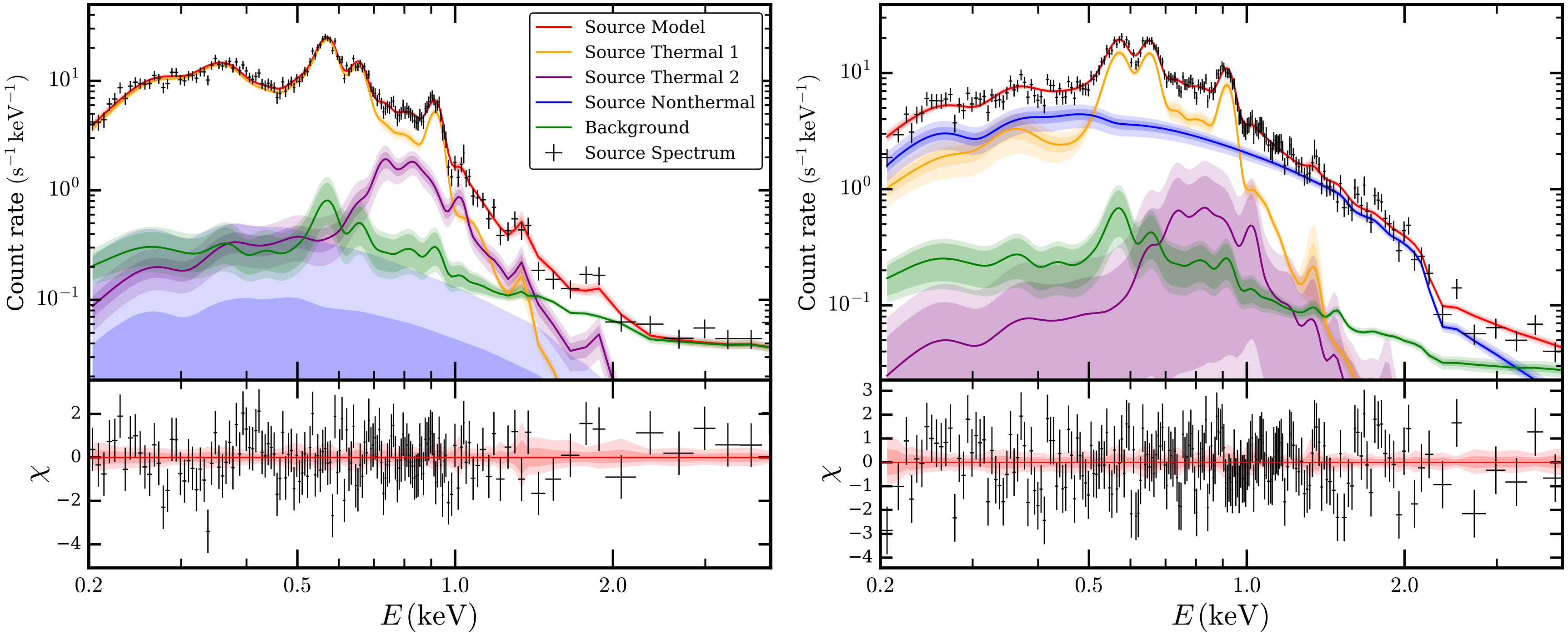

Figure 6.4: Fully modelled spectra of two sample regions. The region in the *left* panel (see Fig. 6.5) is dominated only by thermal emission, while the *right* panel exhibits a strong nonthermal contribution. In both panels, the model range predicted by the posterior distribution of the 2TNT spectral model parameters is displayed, with the contributions of background, nonthermal, and the two thermal components indicated in different colors. The background model shown here encompasses both instrumental and astrophysical components, as detailed in the text. The dark and light shaded areas correspond to the 68% and 95% central intervals of the posterior prediction of the respective model component. The lower portion of the panels indicate the residuals of the data, normalized by their error bars, with respect to the model range allowed by the posterior.

to reduce the number of degenerate model parameters. Initially, we attempted to also leave the silicon abundance free to vary, in order to quantify the presence of Si XIII Heα emission at around ~ 1.85 keV. However, we found that, at the relevant temperatures, this parameter would mostly affect L-shell ionization states of Si emitting at energies below 0.3 keV. This resulted in unrealistically high Si abundances in absorbed regions, which is why we decided to fix it to the solar value.

In order to make optimal usage of the available statistics, and in particular to explore parameter degeneracies, we decided to use a Markov chain Monte Carlo (MCMC) approach to constrain the physical parameters for each of our spectra: after an initial minimization of the fit statistic within `Xspec` in the $0.2 - 8.5$ keV range, we ran the affine-invariant ensemble sampler `emcee` (Foreman-Mackey et al. 2013; Goodman & Weare 2010), using a likelihood given by $\ln \mathcal{L} = -C/2$, where C is the Cash statistic (Cash 1979) evaluated for a given set of model parameters. The 50 walkers were initialized in a “ball” around the best fit, following a multivariate normal distribution, and run for 1000 burn-in and 2000 sampling steps.

We used a uniform prior on the absorption column density N_{H}, and logarithmically uniform priors on all other parameters. After extensive testing, we found that the power-law spectral index Γ requires very careful treatment. This is because, in regions without detectable nonthermal emission, it is essentially an ill-defined quantity, which in our tests would often hit the upper limit under a uniform prior, contributing to the spectrum only at very soft energies. We therefore fixed Γ to a value of 2.5 during our initial `Xspec` fit, and applied a Gaussian prior centered on this value with a width of 0.5 during our MCMC run. This approach has negligible impact on regions with bright nonthermal emission, and avoids a contamination of our model at soft energies in purely thermal regions.

Figure 6.4 illustrates the motivation for our complex approach by displaying spectra and fitted 2TNT models of two representative regions, one dominated by thermal emission, and one with a strong nonthermal contribution. In both cases, one can observe that model components which are not required to satisfactorily fit the spectrum are unconstrained within a large range, as intended. Furthermore, degeneracies between the thermal and nonthermal model components in certain spectral ranges are reflected in their increased uncertainties. After performing our MCMC sampling procedure, for each parameter, we used the median and the 68% central interval of the marginalized posterior as an estimate of its most probable value and approximate error. By repeating this for all spectral extraction regions with the 2TNT and TNT models, we created the physical parameter maps shown in Figs. 6.5 and D.4, respectively.

Distribution of physical parameters across Vela

For the vast majority of Voronoi bins, the 2TNT model was found to yield satisfactory fits from a statistical standpoint. This is illustrated in Fig. 6.6, which displays rough estimates of the “reduced χ^2” statistic of each region, based on observed and median model spectra rebinned to a 5σ significance in each spectral bin. While this quantity is technically inapplicable to our Bayesian methodology, it may still serve as an estimator of the deviation of the observed spectrum from a typical model. The median value of $\chi^2_{\mathrm{red}} \sim 1.2$ and the negligible number of outliers make us confident in the statistical quality of our parameter constraints. Generally, we did not

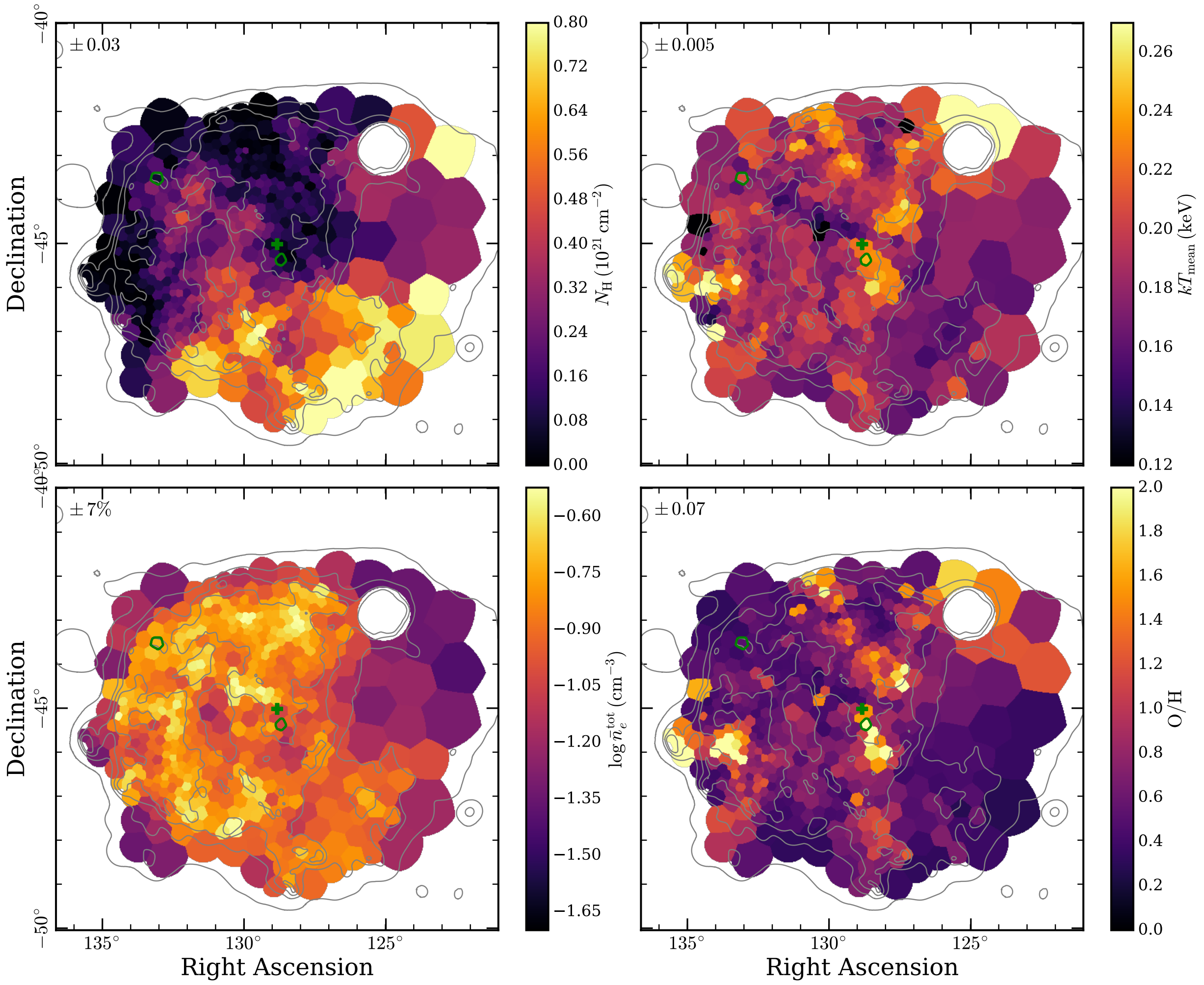

Figure 6.5: Parameter maps from spatially resolved spectroscopy of Vela, using the 2TNT model. We display the distribution of the following physical quantities: absorption column density N_H, mean temperature kT_mean, total electron density $\bar{n}_e^\mathrm{tot}$, and relative abundance of oxygen, normalized to the solar value, of the thermal components. To provide a rough estimate of the typical noise level, the upper left corner of each panel indicates the median uncertainty for the respective parameter across all bins. The gray contours reflect the broad-band count rate of Vela, and are identical to those displayed in Fig. 6.1. The green polygons mark the two regions whose spectra are displayed in Fig. 6.4, and the green "+" sign marks the position of the Vela pulsar.

find evidence for a significant global difference between the statistical quality of fits of the two models across the SNR. Nonetheless, in the following, we mainly discuss the parameter maps determined via the 2TNT model (Fig. 6.5), for the simple reason that these are somewhat less affected by parameter degeneracies, thus appearing less noisy. Wherever relevant, we point out differences between the global results of the two models.

The map of the equivalent hydrogen column density N_H shows that most of the Vela SNR experiences quite little absorption, with the vast majority of regions exhibiting $N_\mathrm{H} < 8 \times 10^{20}\,\mathrm{cm}^{-2}$. This is unsurprising given the small distance to Vela of only 290 pc. We observe a clear structure in the distribution of N_H toward Vela, with the southern part of the SNR experiencing much

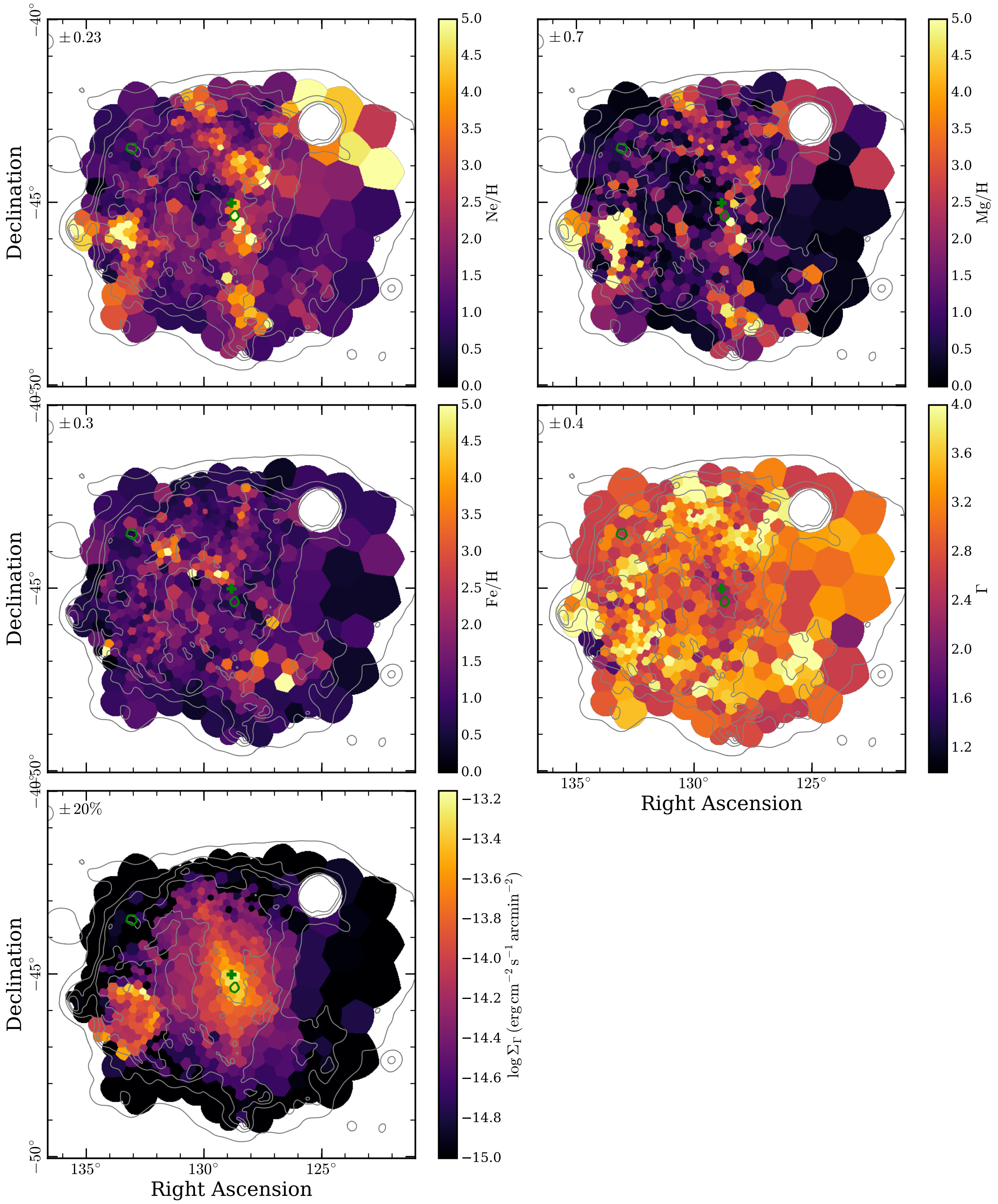

Figure 6.5: Continued. Here, we display the relative elemental abundances of neon, magnesium, and iron in the thermal components, as well as spectral index Γ and surface brightness Σ_Γ in the 1.0 – 5.0 keV range, of the nonthermal component.

higher absorption than the north. The north exhibits regions which appear entirely unabsorbed, in the very east and in the center, whereas the far west and the region around a right ascension of

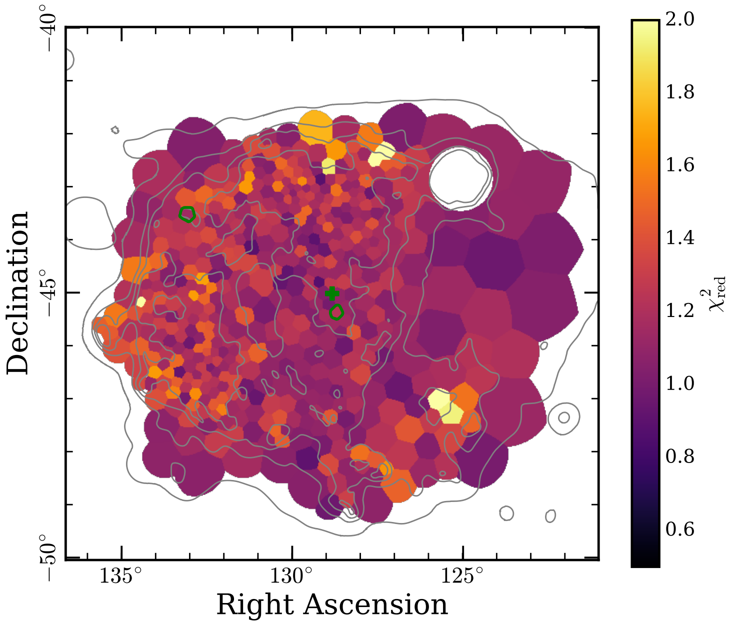

Figure 6.6: "Reduced χ^2" statistic computed for each Voronoi bin across the Vela SNR for the fits with the 2TNT model. Contours and markers are as in Fig. 6.5.

$\alpha \sim 133°$ display values in the range $2{-}5 \times 10^{20}\,\mathrm{cm}^{-2}$. On smaller scales, a few apparent filaments and clumps of enhanced absorption seem to be present, for instance around $(\alpha, \delta) \sim (133°, -44°)$. It is striking that the $N_{\rm H}$ map from the TNT model (Fig. D.4) exhibits the same qualitative features as in the 2TNT model, but appears systematically shifted to lower values, by a factor ~ 1.5. This is most likely caused by the larger soft intrinsic flux in the 2TNT model from the cooler thermal component, and demonstrates that the quantitative determination of the degree of X-ray absorption is strongly model-dependent.

We define the mean temperature of our two-component thermal model as the average of the individual component temperatures kT_i, weighted by their respective emission measures EM_i:

$$kT_{\rm mean} = \frac{\mathrm{EM}_1\, kT_1 + \mathrm{EM}_2\, kT_2}{\mathrm{EM}_1 + \mathrm{EM}_2}. \tag{6.1}$$

The mean plasma temperature spans a quite narrow range across Vela, with virtually all regions in the range $0.15\,\mathrm{keV} < kT_{\rm mean} < 0.25\,\mathrm{keV}$ and a median value around $0.19^{+0.03}_{-0.02}\,\mathrm{keV}$ (errors representing the 68% central interval of the distribution). This quantity is dominated by the temperature of the cold component, as the respective median temperatures are $kT_1 \sim 0.18^{+0.02}_{-0.02}\,\mathrm{keV}$ and $kT_2 \sim 0.60^{+0.50}_{-0.15}\,\mathrm{keV}$ for the cold and hot components, respectively. A few regions stand out in our mean temperature map: we find that a filament of very low-temperature plasma runs from the central pulsar in a northeastern direction, which naturally manifests itself in the extremely soft emission visible from this feature (Fig. 6.2). In contrast, several coherent structures of hotter-than-average plasma are visible. This includes the region of the cocoon, as already indicated by the temperature maps of Slane et al. (2018), as well as blobs of high-temperature material in the direction of shrapnel D, and toward the northern rim. Finally, enhanced temperatures are visible also in the northwestern periphery of the pulsar, apparently pointing in a direction roughly consistent with that of the pulsar jet (Helfand et al. 2001; Pavlov et al. 2003).

Our proxy for the total electron density is computed as $\bar{n}_e^{\mathrm{tot}} = \bar{n}_{e,1} + \bar{n}_{e,2}$, where the density estimates of the individual components $\bar{n}_{e,i}$ are calculated from the corresponding emission measures EM_i as in Sect. 5.3.3, assuming a distance of 290 pc and a shell diameter of 8°. The distribution of $\bar{n}_e^{\mathrm{tot}}$ is highly inhomogeneous across Vela, with many thick filaments and clumps standing out, similar to those visible in the soft band in Figs. 6.2 and 6.3. The measured density estimates reach up to $0.3\,\mathrm{cm}^{-3}$, with thinner intervening regions down to $0.07\,\mathrm{cm}^{-3}$. The south and especially the west of Vela seem to exhibit a lower average density in their emitting material, consistent with the suspected expansion of these regions into a thin ISM (Sushch et al. 2011). Generally, while useful for comparing relative densities, it should be emphasized that $\bar{n}_e^{\mathrm{tot}}$ is computed by assuming a perfectly homogeneous density distribution over a known volume, without accounting for the unknown volume filling factor. This means that the quantitative values given here should at most be seen as a lower limit to the true characteristic emitting density of the X-ray-luminous material.

The elemental abundance maps of oxygen, neon, and magnesium in Fig. 6.5 show several prominent peaks, mostly consistent in position between the individual elements, which we interpret as evidence for the presence of ejecta contributing to the X-ray emission. The locations of these putative ejecta enhancements – toward shrapnel D, around the cocoon (see Slane et al. 2018), and to the north and northwest of the pulsar – seem to agree quite well with the regions exhibiting elevated temperatures. Generally, the observed range of neon abundances is higher by around a factor of two than that of oxygen. This is roughly consistent with abundance patterns typically identified in ejecta in the Vela shrapnels (Miyata et al. 2001; Katsuda & Tsunemi 2005, 2006; Yamaguchi & Katsuda 2009), and therefore may be a general property of the X-ray emitting ejecta in Vela. In contrast, the map of iron abundance does not appear correlated with the distribution of the lighter elements. We observe an apparent iron peak at the location of a soft filament around two degrees northeast of the pulsar. We investigate the spectrum of this region in detail in Sect. 6.3.3, in order to evaluate whether this clump indeed contains a physical iron enhancement.

The last panel in Fig. 6.5 displays the non-thermal surface brightness Σ_Γ, that is, the flux per unit area of the power-law component, evaluated in the comparatively hard energy range 1.0 – 5.0 keV. This energy range was chosen in order to avoid being biased by unphysically large fluxes from extremely steep power laws, which may mimic a very soft thermal continuum in regions without a significant nonthermal contribution to the spectrum. Apart from the clear identification of the nonthermal shell associated to Vela Jr. in the southeast (Camilloni et al. 2023), the measured distribution of Σ_Γ indicates an extremely large region of significant nonthermal emission in Vela. Its surface brightness is highest at the location of the pulsar and the cocoon, consistent with previous observations (Markwardt & Ögelman 1995; Slane et al. 2018). However, the emission of what appears to be an extended PWN seems to reach up to distances around two to three degrees from the pulsar. This extended nonthermal plerion seems to show an asymmetric structure in emission, with the largest extent along an axis around 15° east of north, and a narrower profile in the perpendicular direction. These findings of an extremely large and likely asymmetric X-ray PWN are broadly consistent with what can be observed directly in imaging: in the energy range 1.4 – 2.3 keV, Fig. 6.3 displays a structure quite similar in size and morphology to the one found in spectral modelling. This makes the possibility of a systematic issue in either of the two methods appear unlikely.

The spectral index Γ of our power law component, on the other hand, is difficult to constrain and prone to systematic and statistical errors, as the data and our instrument only offer a relatively short spectral range as a baseline for its measurement. Below 1.0 keV, most spectra are strongly dominated by thermal emission from Vela, while above 2.3 keV, the eROSITA effective area decreases sharply, so that the instrumental background quickly becomes dominant. Nonetheless, we observe realistic, albeit significantly scattered, spectral indices of $\Gamma \sim 2.2$ in the vicinity of the pulsar, consistent with the range observed there by Slane et al. (2018). Furthermore, an apparent increase in Γ with distance from the central pulsar is visible. Even though this finding is clearly quite uncertain, an intriguing physical explanation for this phenomenon could be that radiative losses of the underlying electron population lead to a gradual steepening of the nonthermal spectrum toward larger distances from the source.

Our spectral fits with the TNT model (see Fig. D.4) reveal patterns which are mostly qualitatively consistent with those discussed above. Even though the values of certain parameters, such as absorption or plasma temperature, appear to quantitatively disagree with our measurements above, we believe the observed similarity to be encouraging, since two significantly differing physical models were applied to describe the thermal component. In particular, the physical interpretation of the “temperature” of a plasma with NEI is fundamentally different from that of a plasma in CIE, where electrons, ions, and protons have fully equilibrated with each other (Borkowski et al. 2001). The ionization age fitted in the TNT model, which is the product of post-shock density and shock age, $\tau = n_e\, t_s$ is poorly constrained across the extent of Vela. Generally, the observed median value around $2 \times 10^{12}\,\mathrm{s\,cm^{-3}}$ suggests weak overall departure from CIE, meaning there is no ubiquitous evidence for NEI across the SNR. In a few of the hotter regions, however, departures from CIE with $\tau < 10^{11}\,\mathrm{s\,cm^{-3}}$ seem to be present. However, given the strong model degeneracies involved, in particular that between kT and τ, we believe that these findings of possible localized departures from CIE should be taken with caution.

Our spatially resolved spectral analysis permits the computation of the total intrinsic flux of Vela, by integrating the unabsorbed background-subtracted flux of the 2TNT model over all bins within or overlapping the shell. We obtain $F_X = 2.84 \times 10^{-8}\,\mathrm{erg\,s^{-1}\,cm^{-2}}$ in the $0.2 - 5.0$ keV range, corresponding to an X-ray luminosity of $L_X = 2.9 \times 10^{35}\,\mathrm{erg\,s^{-1}}$ at a distance of 290 pc. The formal statistical uncertainty of this result is at a sub-percent level, but a relative systematic error of at least 15% due to effective area uncertainties and the assumed extent of Vela is to be expected (see also Sect. 5.3.3). A further systematic uncertainty is illustrated by the fact that the TNT model yields a total intrinsic flux of $F_X = 2.48 \times 10^{-8}\,\mathrm{erg\,s^{-1}\,cm^{-2}}$, which is around 13% lower than the value given by the 2TNT model. The origin of this discrepancy lies mainly in the systematically lower absorption column required by the TNT model, since this is the quantity that sets the fraction of intrinsic flux which is ultimately detected by the telescope.

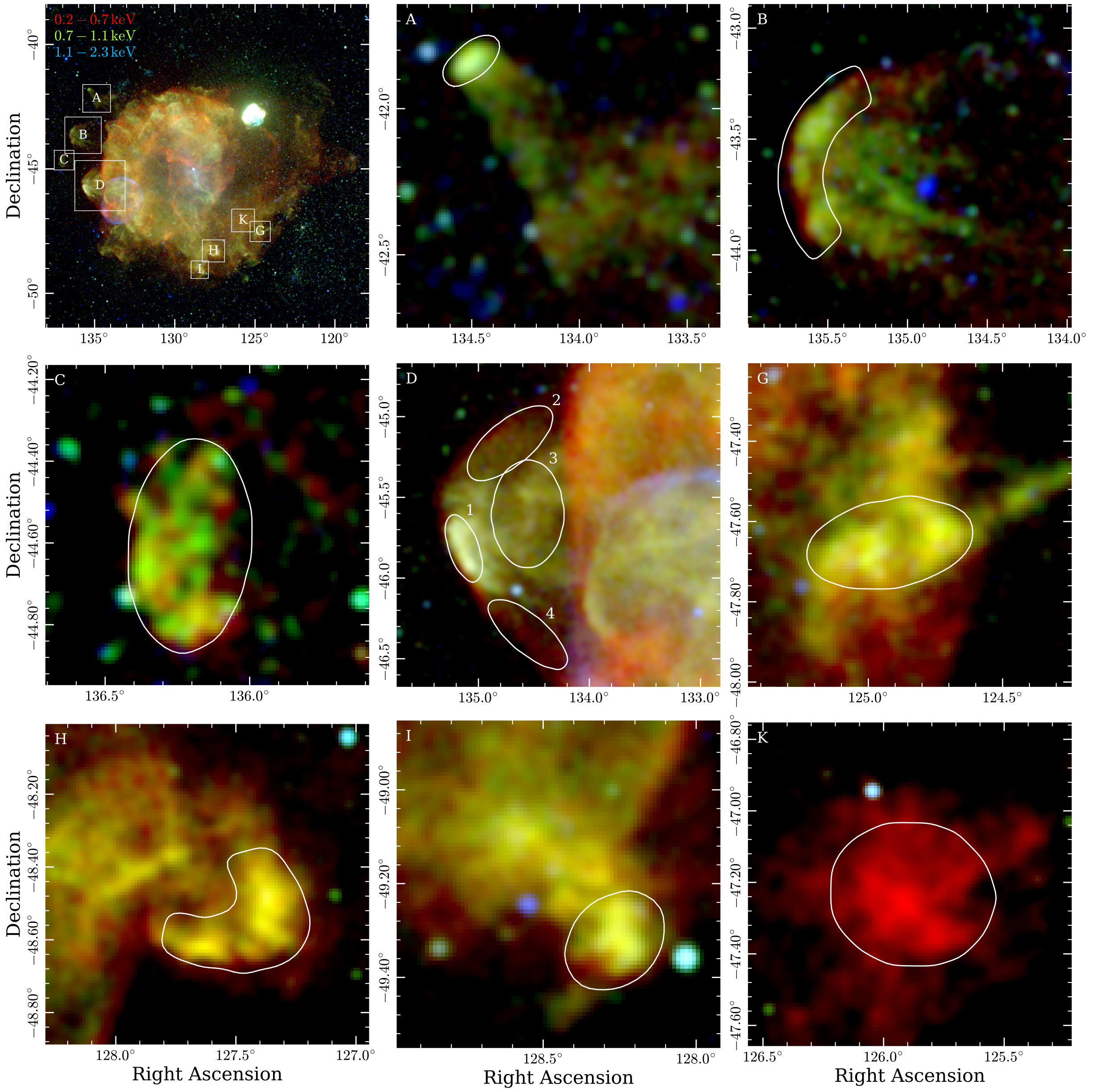

Figure 6.7: Morphological features of Vela. The *upper left* panel displays the false-color image of Vela shown in Fig. 6.1, with white boxes outlining the regions depicted by each of the other panels, which are identified with the corresponding letter. The brightness scale used in each sub-panel preserves the relative colors of the original image, via a truncation of the original brightness scale at equal quantiles for the soft, medium, and hard bands, with the goal of optimally displaying the morphology of the features. In each panel, we indicate the regions used for extraction of the spectra shown in Fig. 6.8 in white, with numbers distinguishing the individual spectra in case of multiple regions.

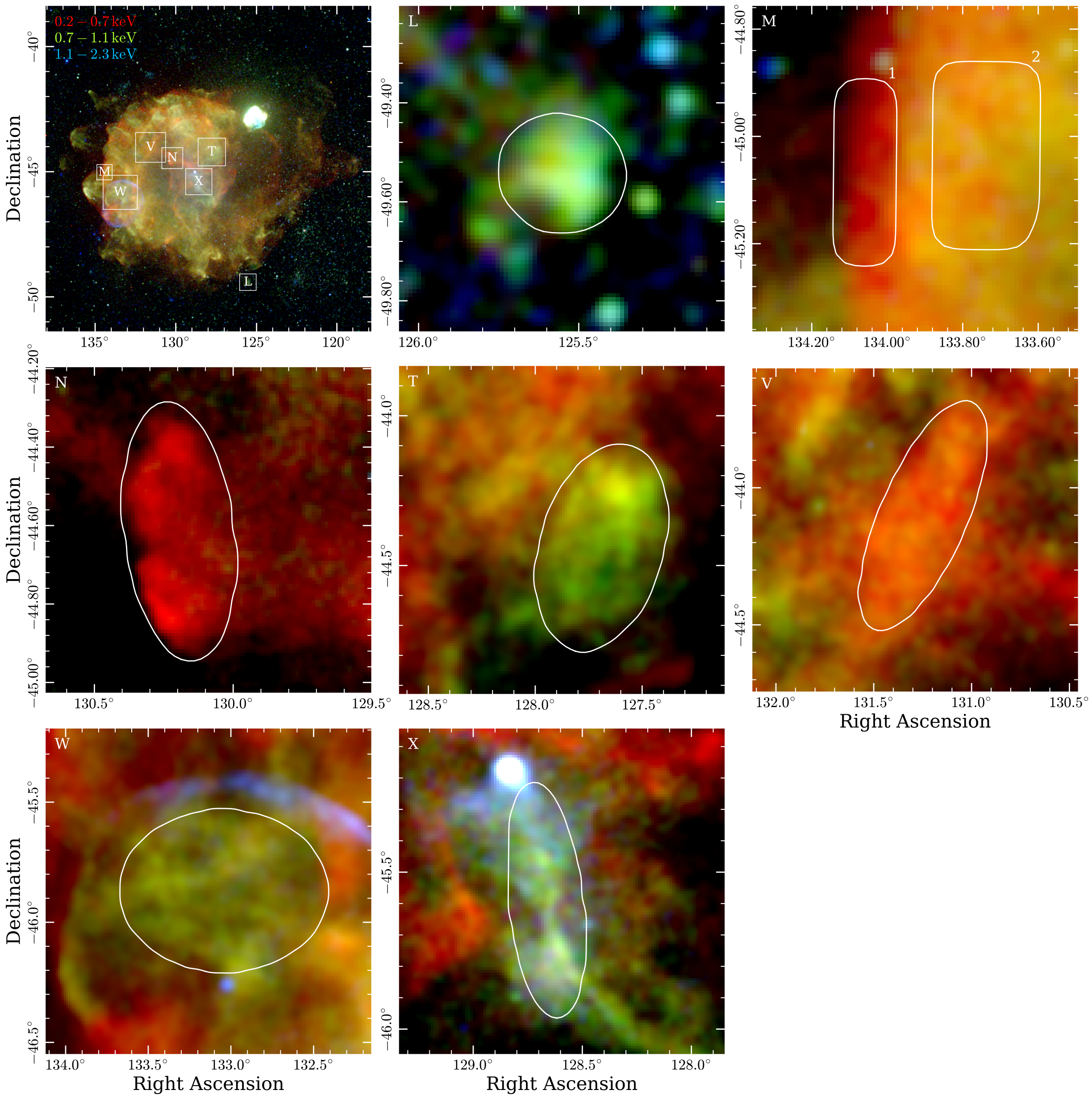

Figure 6.7: Continued.

6.3.3 A closer look at prominent features of Vela

The analysis presented in the previous section has allowed us to obtain an impression of the global properties of shocked thermal plasma, as well as the distribution of relativistic particles from the pulsar wind throughout Vela, in a way that is completely agnostic toward the underlying shapes of features. In this section, we complement this with the imaging and spectroscopic investigation of selected features defined by morphological, rather than purely statistical, criteria.

Figure 6.7 displays the location and energy-dependent morphology of prominent features selected for further study. These include the Vela shrapnels A to D (Aschenbach et al. 1995), as well as potentially similar features discussed in later studies (García et al. 2017; Sapienza et al. 2021), labelled G, H, I, and K. Furthermore, we follow up on several regions that stood out in the previous sections, due to high elemental abundances (T, V, W, X), peculiar temperatures (N, V), or morphological criteria (L, M).

In order to investigate the physical conditions within our features, we extracted spectra from the regions indicated in Fig. 6.7. These spectra were modelled in analogous fashion to the previous section. This concerns the choice of background and source models, as well as the usage of an MCMC sampler for obtaining parameter constraints. However, here, we allowed the silicon abundance parameter to vary, as the presence or absence of silicon is an important aspect to explore in the many ejecta-rich regions we investigate. In order to evaluate which of our models describes the individual spectra better, we computed approximate Bayesian model evidences from the probabilities of our posterior sample. We accomplished this by using the modified harmonic mean approximation detailed by Robert & Wraith (2009). We display the investigated spectra, along with their fitted TNT models, in Fig. 6.8. The corresponding constraints on physical parameters are detailed in Tables 6.1 and 6.2 for the TNT and 2TNT models, respectively.

Our data set allows us to resolve for the first time the energy dependence of the morphology of the Vela shrapnels labelled A to D by Aschenbach et al. (1995). Features B and D clearly show spatially varying hardness in their X-ray emission, with the hardest emission originating close to the apex of the broad bow-shock, and much softer emission (visible in red in Fig. 6.7) along the sides. While the spectra at the head of the shrapnels A, B, D have been studied in detail elsewhere (e.g., Katsuda & Tsunemi 2005, 2006; Yamaguchi & Katsuda 2009), Fig. 6.8 illustrates very clearly that feature A exhibits a fundamentally different spectrum from the other shrapnels. This applies in particular at $0.7 - 0.9\,\mathrm{keV}$, where line emission of Fe xvii seems to contribute. While the statistics of our data set for shrapnel A are limited, we find enhanced abundance ratios of iron relative to lighter elements (e.g. $\mathrm{Fe/O} = 1.4^{+0.6}_{-0.4}$), similarly to Katsuda & Tsunemi (2006). This may be a signature either of a strong contribution of shocked ISM of at least solar iron content to the emission or of enhanced mixing of explosively synthesized iron into this silicon-rich ejecta clump. In shrapnel B, we have detected significant silicon line emission, which may indicate a larger abundance thereof than previously established for this feature (Yamaguchi & Katsuda 2009).

During the inspection of broad-band images of Vela, we discovered a previously unnoticed compact clump southwest of the SNR shell, which we have labelled feature L. Due to its apparent faint tail in the northeast direction and the clump's highest brightness in the medium energy band, it seems reasonable to propose that this feature may be a potential analog to shrapnel A. Its observed spectrum is quite curious, however: it exhibits a signature of a comparatively high temperature, as well as very high absorption, with a fitted value around $2 \times 10^{21}\,\mathrm{cm}^{-2}$. The latter fact makes a reconciliation with the distance of Vela problematic, as one would in principle expect much less intervening material. Nonetheless, to our knowledge, there is no known potentially X-ray emitting object that would appear extended (e.g., galaxy cluster or star cluster) at the location of our feature. Therefore, an association with the Vela SNR cannot be ruled out, in particular since the feature is located close to the most absorbed part of the SNR. Follow-up observations of this clump may be desirable in order to infer both its composition and

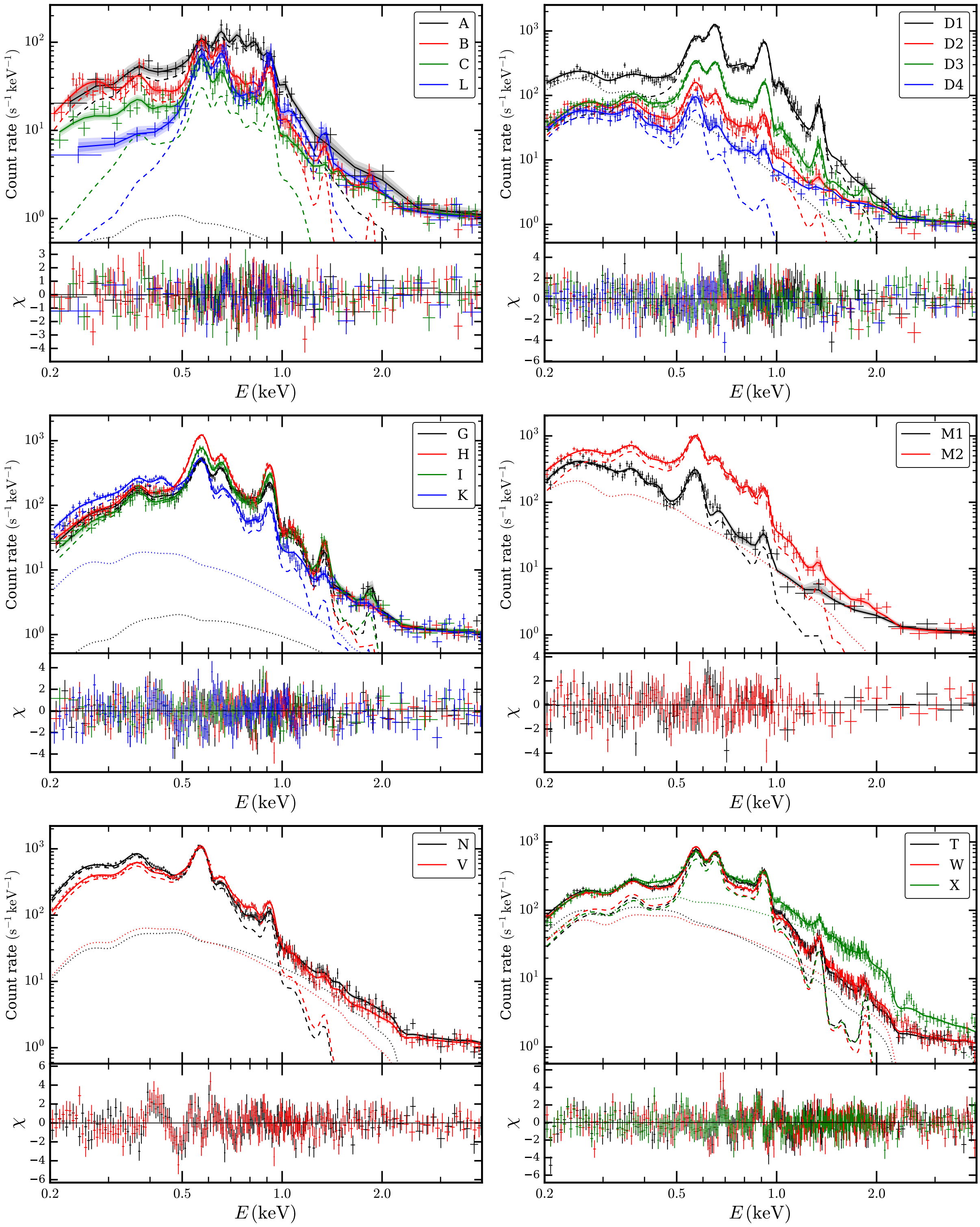

Figure 6.8: Spectra of prominent morphological features of Vela. The extraction regions of all spectra are outlined in Fig. 6.7 and identified according to their assigned labels in the figure legends. For all panels, we display the results of the TNT spectral model, which in a few cases gave considerably better fits than the 2TNT model. In each subplot, the displayed spectral model corresponds to the median of the prediction obtained from the posterior sample of our MCMC procedure. The dashed (dotted) line represents the median contribution from the thermal (nonthermal) source model component. For the sake of comparability, all spectra and models have been normalized dividing by their `BACKSCAL` keyword, resulting in equal levels of particle background.

Table 6.1: Parameter constraints from modelling of the spectra shown in Fig. 6.8 with the TNT model.

Feature	N_{H}	kT	log τ	log EM	N/H	O/H	Ne/H	Mg/H	Si/H	Fe/H	Γ	log F_{Γ}	ln $\mathcal{B}^{(a)}$
	10^{21} cm^{-2}	keV	cm^{-3} s	cm^{-5}								erg cm^{-2} s^{-1}	
A	**$0.19^{+0.15}_{-0.12}$**	**$0.43^{+0.11}_{-0.09}$**	**$11.59^{+0.20}_{-0.38}$**	**$11.06^{+0.16}_{-0.27}$**	**$0.4^{+0.6}_{-0.3}$**	**$0.56^{+0.25}_{-0.14}$**	**$1.0^{+0.5}_{-0.3}$**	**$0.5^{+0.6}_{-0.4}$**	**$3.5^{+3.7}_{-2.1}$**	**$0.80^{+0.47}_{-0.24}$**	**$2.6^{+0.6}_{-0.5}$**	**$-13.65^{+0.28}_{-1.02}$**	**0.4**
B	**$0.040^{+0.052}_{-0.029}$**	**$0.37^{+0.06}_{-0.06}$**	**$11.39^{+0.14}_{-0.22}$**	**$11.55^{+0.08}_{-0.10}$**	**$0.089^{+0.069}_{-0.029}$**	**$0.82^{+0.12}_{-0.08}$**	**$1.96^{+0.38}_{-0.24}$**	**$1.4^{+0.6}_{-0.4}$**	**$6.4^{+1.9}_{-1.3}$**	**$0.48^{+0.10}_{-0.07}$**	**$2.6^{+0.5}_{-0.5}$**	**$-14.17^{+0.26}_{-0.75}$**	**0.9**
C	**$0.6^{+0.4}_{-0.3}$**	**$0.30^{+0.25}_{-0.09}$**	**$11.45^{+0.26}_{-0.74}$**	**$11.17^{+0.22}_{-0.49}$**	**$0.18^{+0.36}_{-0.11}$**	**$0.69^{+0.30}_{-0.20}$**	**$1.8^{+0.9}_{-0.6}$**	**$0.19^{+0.46}_{-0.12}$**	**$1.4^{+6.3}_{-1.2}$**	**$1.0^{+0.6}_{-0.4}$**	**$2.5^{+0.5}_{-0.5}$**	**$-14.07^{+0.26}_{-0.77}$**	**1.5**
L	**$2.2^{+0.5}_{-0.7}$**	**$0.80^{+0.14}_{-0.17}$**	**$10.53^{+0.10}_{-0.13}$**	**$10.59^{+0.20}_{-0.39}$**	**$0.31^{+0.92}_{-0.22}$**	**$2.1^{+2.5}_{-1.0}$**	**$4.9^{+6.5}_{-2.4}$**	**$3.0^{+4.0}_{-1.6}$**	**$1.1^{+3.5}_{-1.0}$**	**$0.32^{+0.56}_{-0.20}$**	**$2.5^{+0.5}_{-0.5}$**	**$-13.82^{+0.28}_{-0.94}$**	**9.5**
D1	$0.08^{+0.04}_{-0.04}$	$0.285^{+0.003}_{-0.003}$	$12.92^{+0.08}_{-0.10}$	$11.72^{+0.07}_{-0.09}$	$0.11^{+0.13}_{-0.04}$	$8.5^{+2.0}_{-2.2}$	15^{+3}_{-4}	15^{+3}_{-4}	$1.2^{+2.6}_{-1.0}$	$1.11^{+0.26}_{-0.27}$	$4.72^{+0.28}_{-0.28}$	$-12.59^{+0.11}_{-0.15}$	−2.0
D2	$0.009^{+0.014}_{-0.007}$	$0.210^{+0.024}_{-0.007}$	$12.64^{+0.24}_{-0.61}$	$11.98^{+0.09}_{-0.11}$	$0.09^{+0.08}_{-0.03}$	$0.69^{+0.07}_{-0.06}$	$1.76^{+0.25}_{-0.26}$	$1.2^{+1.2}_{-0.9}$	$4.3^{+1.8}_{-1.1}$	$0.53^{+0.17}_{-0.18}$	$2.8^{+0.9}_{-0.6}$	$-13.61^{+0.28}_{-1.12}$	−2.5
D3	**$0.007^{+0.012}_{-0.006}$**	**$0.330^{+0.018}_{-0.023}$**	**$11.62^{+0.09}_{-0.11}$**	**$12.20^{+0.05}_{-0.05}$**	**$0.13^{+0.09}_{-0.06}$**	**$1.14^{+0.09}_{-0.07}$**	**$2.41^{+0.20}_{-0.17}$**	**$2.30^{+0.34}_{-0.29}$**	**$4.1^{+0.5}_{-0.5}$**	**$0.271^{+0.035}_{-0.029}$**	**$2.8^{+0.8}_{-0.6}$**	**$-13.15^{+0.29}_{-1.32}$**	**4.1**
D4	$0.13^{+0.15}_{-0.10}$	$0.23^{+0.07}_{-0.07}$	$10.37^{+0.17}_{-0.28}$	$11.33^{+0.13}_{-0.19}$	$0.35^{+0.17}_{-0.19}$	$0.46^{+0.08}_{-0.07}$	$0.36^{+0.37}_{-0.23}$	$0.4^{+1.9}_{-0.3}$	$5.1^{+4.7}_{-2.7}$	$0.8^{+4.0}_{-0.7}$	$2.6^{+0.6}_{-0.5}$	$-14.28^{+0.25}_{-0.64}$	−1.1
G	$0.35^{+0.10}_{-0.09}$	$0.37^{+0.06}_{-0.05}$	$11.12^{+0.12}_{-0.17}$	$11.91^{+0.10}_{-0.12}$	$0.45^{+0.15}_{-0.15}$	$0.68^{+0.07}_{-0.06}$	$1.64^{+0.16}_{-0.15}$	$1.20^{+0.24}_{-0.20}$	$3.6^{+1.1}_{-1.0}$	$0.43^{+0.06}_{-0.05}$	$2.7^{+0.6}_{-0.5}$	$-12.85^{+0.29}_{-1.45}$	−1.3
H	**$0.31^{+0.11}_{-0.09}$**	**$0.336^{+0.020}_{-0.026}$**	**$10.97^{+0.07}_{-0.08}$**	**$11.85^{+0.07}_{-0.08}$**	**$0.71^{+0.15}_{-0.14}$**	**$1.91^{+0.17}_{-0.16}$**	**$5.3^{+0.6}_{-0.5}$**	**$4.1^{+0.6}_{-0.6}$**	**$2.2^{+1.4}_{-1.2}$**	**$0.48^{+0.08}_{-0.07}$**	**$2.6^{+0.5}_{-0.5}$**	**$-13.47^{+0.29}_{-1.18}$**	**28.0**
I	**$0.54^{+0.13}_{-0.14}$**	**$0.37^{+0.06}_{-0.04}$**	**$10.96^{+0.12}_{-0.16}$**	**$11.56^{+0.11}_{-0.15}$**	**$0.15^{+0.16}_{-0.08}$**	**$1.14^{+0.17}_{-0.12}$**	**$2.8^{+0.4}_{-0.3}$**	**$2.9^{+0.6}_{-0.5}$**	**$4.2^{+2.1}_{-1.7}$**	**$0.29^{+0.07}_{-0.06}$**	**$2.5^{+0.5}_{-0.5}$**	**$-13.93^{+0.27}_{-0.88}$**	**16.0**
K	$0.28^{+0.11}_{-0.09}$	$0.47^{+0.04}_{-0.05}$	$10.07^{+0.05}_{-0.05}$	$11.83^{+0.06}_{-0.07}$	$1.57^{+0.14}_{-0.14}$	$0.72^{+0.07}_{-0.06}$	$1.37^{+0.19}_{-0.16}$	$0.8^{+0.4}_{-0.4}$	$2.8^{+2.3}_{-1.6}$	$1.5^{+0.5}_{-0.4}$	$3.6^{+0.5}_{-0.7}$	$-12.19^{+0.11}_{-0.15}$	−8.2
M1	$0.30^{+0.05}_{-0.06}$	$0.221^{+0.036}_{-0.029}$	$10.16^{+0.09}_{-0.11}$	$11.79^{+0.10}_{-0.13}$	$0.57^{+0.08}_{-0.07}$	$0.330^{+0.037}_{-0.028}$	$0.70^{+0.28}_{-0.21}$	$2.2^{+6.7}_{-2.0}$	$15.5^{+3.0}_{-3.7}$	8^{+6}_{-5}	$2.6^{+0.5}_{-0.5}$	$-13.93^{+0.27}_{-0.84}$	−12.5
M2	$0.033^{+0.051}_{-0.026}$	$0.220^{+0.016}_{-0.015}$	$11.76^{+0.13}_{-0.18}$	$12.48^{+0.06}_{-0.07}$	$0.45^{+0.11}_{-0.11}$	$0.498^{+0.031}_{-0.027}$	$0.85^{+0.08}_{-0.08}$	$0.8^{+0.4}_{-0.3}$	$2.4^{+0.6}_{-0.6}$	$0.69^{+0.20}_{-0.12}$	$4.32^{+0.29}_{-0.30}$	$-12.28^{+0.08}_{-0.10}$	−7.9
N	$0.27^{+0.06}_{-0.05}$	$0.164^{+0.007}_{-0.008}$	$11.88^{+0.10}_{-0.13}$	$13.15^{+0.07}_{-0.08}$	$0.41^{+0.05}_{-0.05}$	$0.412^{+0.029}_{-0.030}$	$0.72^{+0.06}_{-0.06}$	$0.6^{+0.6}_{-0.4}$	$2.7^{+0.7}_{-0.6}$	$1.5^{+0.8}_{-0.4}$	$3.06^{+0.25}_{-0.24}$	$-11.44^{+0.03}_{-0.04}$	−18.0
V	**$0.37^{+0.06}_{-0.04}$**	**$0.164^{+0.006}_{-0.005}$**	**$12.23^{+0.11}_{-0.15}$**	**$13.35^{+0.06}_{-0.08}$**	**$0.55^{+0.07}_{-0.07}$**	**$0.49^{+0.04}_{-0.03}$**	**$1.15^{+0.09}_{-0.09}$**	**$0.8^{+0.4}_{-0.4}$**	**$2.5^{+0.7}_{-0.5}$**	**$2.7^{+0.9}_{-0.7}$**	**$3.7^{+0.4}_{-0.4}$**	**$-11.48^{+0.03}_{-0.04}$**	**5.2**
T	**$0.14^{+0.03}_{-0.04}$**	**$0.402^{+0.026}_{-0.031}$**	**$11.24^{+0.07}_{-0.08}$**	**$12.29^{+0.06}_{-0.08}$**	**$0.22^{+0.14}_{-0.12}$**	**$1.40^{+0.21}_{-0.17}$**	**$3.1^{+0.5}_{-0.4}$**	**$2.25^{+0.40}_{-0.29}$**	**$4.1^{+0.8}_{-0.6}$**	**$0.75^{+0.11}_{-0.08}$**	**$3.41^{+0.13}_{-0.16}$**	**$-11.214^{+0.029}_{-0.031}$**	**6.0**
W	**$0.095^{+0.017}_{-0.016}$**	**$0.335^{+0.009}_{-0.015}$**	**$11.43^{+0.04}_{-0.05}$**	**$12.70^{+0.03}_{-0.04}$**	**$0.082^{+0.050}_{-0.023}$**	**$1.42^{+0.08}_{-0.07}$**	**$3.18^{+0.19}_{-0.17}$**	**$2.77^{+0.23}_{-0.22}$**	**$3.6^{+0.5}_{-0.4}$**	**$0.468^{+0.031}_{-0.028}$**	**$2.94^{+0.07}_{-0.08}$**	**$-10.733^{+0.016}_{-0.016}$**	**43.4**
X	**$0.130^{+0.027}_{-0.028}$**	**$0.40^{+0.05}_{-0.04}$**	**$11.29^{+0.11}_{-0.14}$**	**$12.05^{+0.07}_{-0.09}$**	**$0.34^{+0.22}_{-0.21}$**	**$1.31^{+0.20}_{-0.15}$**	**$2.8^{+0.5}_{-0.3}$**	**$2.3^{+0.5}_{-0.4}$**	**$5.8^{+1.7}_{-1.2}$**	**$0.56^{+0.08}_{-0.06}$**	**$2.30^{+0.08}_{-0.08}$**	**$-10.569^{+0.013}_{-0.014}$**	**6.9**

Notes. All parameters are defined as in Sect. 6.3.2. The emission measure EM quantifies the normalization of the thermal component, whereas F_{Γ} indicates the unabsorbed nonthermal flux integrated over the range 1.0 – 5.0 keV. The given values and uncertainties correspond to the median and 68% central interval of the posterior parameter distribution. The parameters corresponding to spectra shown in the same panel in Fig. 6.8 are delimited by horizontal lines.

[a] Approximate Bayes factor from the ratio of model evidence estimates $\mathcal{B} = \mathcal{Z}_{\mathrm{TNT}}/\mathcal{Z}_{\mathrm{2TNT}}$. Regions with a positive value of ln $\mathcal{B}$, indicating statistical preference for the TNT model, are highlighted in bold.

Table 6.2: Same as Table 6.1, but for the 2TNT model.

Feature	N_H 10^{21} cm^{-2}	kT_1 keV	log EM$_1$ cm^{-5}	kT_2 keV	log EM$_2$ cm^{-5}	N/H	O/H	Ne/H	Mg/H	Si/H	Fe/H	Γ	log F_Γ erg cm^{-2} s^{-1}
A	$0.30^{+0.18}_{-0.14}$	$0.269^{+0.025}_{-0.024}$	$11.24^{+0.12}_{-0.16}$	$0.54^{+0.26}_{-0.23}$	$10.34^{+0.22}_{-0.48}$	$0.35^{+0.99}_{-0.25}$	$0.78^{+0.27}_{-0.17}$	$1.3^{+0.6}_{-0.4}$	$0.7^{+0.9}_{-0.5}$	5^{+6}_{-3}	$0.90^{+0.42}_{-0.26}$	$2.6^{+0.5}_{-0.5}$	$-13.75^{+0.28}_{-0.94}$
B	$0.07^{+0.08}_{-0.05}$	$0.227^{+0.007}_{-0.006}$	$11.79^{+0.06}_{-0.06}$	$0.62^{+0.26}_{-0.23}$	$10.38^{+0.21}_{-0.42}$	$0.11^{+0.13}_{-0.05}$	$1.22^{+0.14}_{-0.11}$	$3.3^{+0.4}_{-0.4}$	$2.9^{+1.4}_{-1.2}$	$5.8^{+2.9}_{-1.9}$	$0.87^{+0.18}_{-0.14}$	$2.6^{+0.5}_{-0.5}$	$-14.10^{+0.26}_{-0.74}$
C	$0.9^{+0.4}_{-0.3}$	$0.194^{+0.012}_{-0.011}$	$11.69^{+0.14}_{-0.20}$	$0.52^{+0.45}_{-0.26}$	$10.03^{+0.19}_{-0.35}$	$0.14^{+0.26}_{-0.07}$	$0.61^{+0.25}_{-0.18}$	$1.9^{+0.9}_{-0.7}$	$0.25^{+0.60}_{-0.17}$	$2.2^{+8.4}_{-1.9}$	$1.5^{+1.0}_{-0.5}$	$2.5^{+0.6}_{-0.5}$	$-14.05^{+0.27}_{-0.80}$
L	$2.60^{+0.29}_{-0.62}$	$0.203^{+0.017}_{-0.015}$	$11.44^{+0.19}_{-0.36}$	$0.36^{+0.19}_{-0.07}$	$10.57^{+0.22}_{-0.45}$	$0.22^{+0.77}_{-0.14}$	$2.0^{+1.9}_{-0.9}$	$5.7^{+6.0}_{-2.7}$	$5.1^{+5.6}_{-2.6}$	$1.5^{+7.3}_{-1.4}$	$0.39^{+0.52}_{-0.23}$	$2.5^{+0.5}_{-0.5}$	$-13.37^{+0.29}_{-1.19}$
D1	**$0.04^{+0.04}_{-0.03}$**	**$0.2736^{+0.0026}_{-0.0024}$**	**$11.79^{+0.09}_{-0.11}$**	**$0.31^{+0.42}_{-0.06}$**	**$9.97^{+0.19}_{-0.33}$**	**$0.10^{+0.12}_{-0.04}$**	**$7.2^{+1.9}_{-1.5}$**	**$12.8^{+3.2}_{-2.7}$**	**$14.0^{+3.4}_{-2.9}$**	**$2.3^{+2.5}_{-1.9}$**	**$1.01^{+0.25}_{-0.20}$**	**$4.54^{+0.26}_{-0.22}$**	**$-12.56^{+0.11}_{-0.15}$**
D2	**$0.009^{+0.015}_{-0.007}$**	**$0.195^{+0.004}_{-0.005}$**	**$12.04^{+0.04}_{-0.04}$**	**$0.49^{+0.66}_{-0.19}$**	**$10.49^{+0.21}_{-0.43}$**	**$0.11^{+0.10}_{-0.04}$**	**$0.70^{+0.05}_{-0.04}$**	**$1.77^{+0.21}_{-0.21}$**	**$1.0^{+1.1}_{-0.8}$**	**$2.8^{+0.7}_{-0.7}$**	**$0.62^{+0.24}_{-0.17}$**	**$2.6^{+0.6}_{-0.5}$**	**$-14.08^{+0.26}_{-0.76}$**
D3	$0.013^{+0.020}_{-0.009}$	$0.32^{+0.05}_{-0.11}$	$11.57^{+0.17}_{-0.29}$	$0.223^{+0.057}_{-0.005}$	$12.31^{+0.18}_{-0.31}$	$0.44^{+0.18}_{-0.18}$	$1.68^{+0.08}_{-0.07}$	$3.65^{+0.25}_{-0.25}$	$4.3^{+0.6}_{-0.6}$	$2.7^{+0.5}_{-0.5}$	$0.54^{+0.05}_{-0.05}$	$2.5^{+0.5}_{-0.5}$	$-13.33^{+0.29}_{-1.25}$
D4	**$0.14^{+0.19}_{-0.07}$**	**$0.075^{+0.005}_{-0.005}$**	**$12.53^{+0.11}_{-0.15}$**	**$0.231^{+0.043}_{-0.022}$**	**$10.83^{+0.12}_{-0.16}$**	**$0.76^{+0.25}_{-0.24}$**	**$1.7^{+0.4}_{-0.3}$**	**$1.4^{+1.2}_{-1.0}$**	**$0.4^{+1.6}_{-0.3}$**	**$0.5^{+3.8}_{-0.4}$**	**$0.6^{+0.8}_{-0.4}$**	**$2.6^{+0.5}_{-0.5}$**	**$-14.41^{+0.24}_{-0.57}$**
G	**$0.84^{+0.08}_{-0.09}$**	**$0.163^{+0.016}_{-0.019}$**	**$12.51^{+0.06}_{-0.07}$**	**$0.257^{+0.020}_{-0.013}$**	**$12.25^{+0.15}_{-0.23}$**	**$0.15^{+0.11}_{-0.07}$**	**$0.63^{+0.05}_{-0.04}$**	**$1.54^{+0.15}_{-0.12}$**	**$1.46^{+0.35}_{-0.28}$**	**$6.9^{+2.4}_{-1.9}$**	**$0.47^{+0.08}_{-0.07}$**	**$2.5^{+0.5}_{-0.5}$**	**$-13.60^{+0.28}_{-1.09}$**
H	$1.14^{+0.09}_{-0.11}$	$0.1671^{+0.0017}_{-0.0019}$	$12.88^{+0.04}_{-0.04}$	$0.47^{+1.24}_{-0.20}$	$10.38^{+0.21}_{-0.44}$	$0.12^{+0.08}_{-0.05}$	$1.24^{+0.11}_{-0.09}$	$4.7^{+0.4}_{-0.4}$	$6.7^{+1.1}_{-1.0}$	11^{+5}_{-4}	$1.5^{+0.4}_{-0.3}$	$2.6^{+0.5}_{-0.5}$	$-13.74^{+0.28}_{-0.95}$
I	$1.09^{+0.11}_{-0.15}$	$0.180^{+0.004}_{-0.005}$	$12.33^{+0.07}_{-0.08}$	$0.26^{+0.45}_{-0.05}$	$10.49^{+0.25}_{-0.69}$	$0.077^{+0.054}_{-0.021}$	$1.06^{+0.11}_{-0.11}$	$3.6^{+0.5}_{-0.4}$	$7.2^{+1.5}_{-1.3}$	12^{+5}_{-6}	$0.84^{+0.23}_{-0.19}$	$2.4^{+0.5}_{-0.5}$	$-13.00^{+0.29}_{-1.22}$
K	**$0.49^{+0.06}_{-0.06}$**	**$0.083^{+0.007}_{-0.005}$**	**$13.15^{+0.09}_{-0.11}$**	**$0.205^{+0.008}_{-0.004}$**	**$11.80^{+0.09}_{-0.11}$**	**$2.25^{+0.27}_{-0.25}$**	**$2.4^{+0.6}_{-0.6}$**	**$7.3^{+2.0}_{-1.8}$**	**$3.5^{+2.6}_{-2.5}$**	**$0.21^{+0.63}_{-0.13}$**	**$2.9^{+0.8}_{-0.7}$**	**$4.32^{+0.25}_{-0.32}$**	**$-12.00^{+0.06}_{-0.07}$**
M1	**$0.460^{+0.025}_{-0.035}$**	**$0.0677^{+0.0028}_{-0.0024}$**	**$13.29^{+0.07}_{-0.09}$**	**$0.240^{+0.025}_{-0.025}$**	**$11.17^{+0.07}_{-0.09}$**	**$0.61^{+0.13}_{-0.12}$**	**$1.24^{+0.20}_{-0.19}$**	**$1.6^{+0.5}_{-0.4}$**	**$1.4^{+2.7}_{-1.2}$**	**$17.3^{+1.9}_{-3.3}$**	**$0.50^{+0.34}_{-0.23}$**	**$2.5^{+0.5}_{-0.5}$**	**$-14.22^{+0.25}_{-0.67}$**
M2	**$0.21^{+0.09}_{-0.10}$**	**$0.115^{+0.008}_{-0.008}$**	**$12.87^{+0.07}_{-0.09}$**	**$0.212^{+0.013}_{-0.008}$**	**$12.49^{+0.05}_{-0.06}$**	**$0.68^{+0.09}_{-0.09}$**	**$0.55^{+0.05}_{-0.04}$**	**$0.91^{+0.12}_{-0.11}$**	**$1.0^{+0.4}_{-0.3}$**	**$2.4^{+1.5}_{-1.2}$**	**$0.84^{+0.19}_{-0.19}$**	**$2.4^{+0.5}_{-0.5}$**	**$-12.45^{+0.23}_{-0.54}$**
N	**$0.242^{+0.026}_{-0.019}$**	**$0.0833^{+0.0019}_{-0.0018}$**	**$13.64^{+0.04}_{-0.04}$**	**$0.204^{+0.007}_{-0.003}$**	**$12.08^{+0.05}_{-0.05}$**	**$0.83^{+0.07}_{-0.07}$**	**$1.55^{+0.12}_{-0.12}$**	**$2.87^{+0.31}_{-0.29}$**	**$0.29^{+0.90}_{-0.21}$**	**$0.10^{+0.13}_{-0.04}$**	**$1.50^{+0.26}_{-0.24}$**	**$3.81^{+0.14}_{-0.15}$**	**$-11.509^{+0.027}_{-0.029}$**
V	$0.48^{+0.05}_{-0.04}$	$0.1502^{+0.0012}_{-0.0013}$	$13.57^{+0.04}_{-0.05}$	$0.40^{+0.36}_{-0.17}$	$10.05^{+0.20}_{-0.37}$	$0.42^{+0.05}_{-0.06}$	$0.410^{+0.037}_{-0.023}$	$1.07^{+0.12}_{-0.09}$	$1.0^{+0.5}_{-0.5}$	$2.1^{+0.7}_{-0.5}$	$5.2^{+0.8}_{-0.8}$	$3.6^{+0.5}_{-0.5}$	$-11.49^{+0.04}_{-0.04}$
T	$0.18^{+0.03}_{-0.03}$	$0.2163^{+0.0014}_{-0.0015}$	$12.66^{+0.05}_{-0.06}$	$0.53^{+0.03}_{-0.03}$	$11.59^{+0.07}_{-0.08}$	$0.56^{+0.24}_{-0.27}$	$1.94^{+0.31}_{-0.23}$	$5.1^{+0.8}_{-0.6}$	$3.9^{+0.7}_{-0.5}$	$4.4^{+1.1}_{-0.8}$	$1.23^{+0.20}_{-0.15}$	$3.46^{+0.16}_{-0.19}$	$-11.28^{+0.04}_{-0.04}$
W	$0.140^{+0.014}_{-0.014}$	$0.2128^{+0.0010}_{-0.0010}$	$12.969^{+0.023}_{-0.025}$	$0.48^{+0.07}_{-0.09}$	$11.41^{+0.09}_{-0.12}$	$0.10^{+0.08}_{-0.04}$	$2.05^{+0.12}_{-0.11}$	$5.3^{+0.3}_{-0.3}$	$5.9^{+0.6}_{-0.6}$	$2.4^{+0.5}_{-0.5}$	$1.08^{+0.08}_{-0.07}$	$2.99^{+0.06}_{-0.07}$	$-10.726^{+0.021}_{-0.022}$
X	$0.157^{+0.026}_{-0.025}$	$0.2205^{+0.0022}_{-0.0022}$	$12.35^{+0.06}_{-0.07}$	$0.64^{+0.07}_{-0.07}$	$11.17^{+0.12}_{-0.17}$	$0.6^{+0.4}_{-0.4}$	$2.03^{+0.34}_{-0.25}$	$4.9^{+0.9}_{-0.7}$	$4.7^{+1.3}_{-1.0}$	$5.2^{+1.6}_{-1.3}$	$1.08^{+0.21}_{-0.17}$	$2.34^{+0.07}_{-0.08}$	$-10.576^{+0.014}_{-0.015}$

Notes. The parameters kT_1 (kT_2) and EM$_1$ (EM$_2$) refer to the temperatures and emission measures of the cooler (hotter) thermal component, respectively.

its distance, similarly to García et al. (2017).

Spectra extracted from multiple regions across shrapnel D exhibit a vast range of electron temperatures and ionization ages, particularly visible in the varying ratio of O VIII to O VII line emission. The highest ratio is visible at the apex of the bow shock (D1), while it is lowest along the sides (D2 and D4), and exhibits intermediate values further downstream (D3). Our detection of extreme abundances of oxygen, neon, and magnesium at the apex, with Ne/O and Mg/O ratios around two, and no strong iron enhancement, is completely consistent with the results of Katsuda & Tsunemi (2005), cementing the interpretation of this hot feature as a light-element ejecta-rich clump. Interestingly, the plasma in this region shows no convincing signature for departure from CIE, which is somewhat unexpected for material which should have recently been shocked by interaction with the ISM. The spectra of the lateral regions D2 and D4 generally exhibit much lower light-element abundances, consistent with the dominant contribution coming from shock-heated ISM. Furthermore, the low observed temperature appears consistent with an interaction with a shock that is likely moving more slowly than at the apex of the structure.

The features G, H, I, and K were identified in García et al. (2017) and Sapienza et al. (2021) with G, H, and I proposed as potential analogues to the established shrapnels. Our imaging demonstrates that their energy-dependent morphologies show similarities with feature D: they exhibit clumpy emission mainly in the $0.7 - 1.1\,\mathrm{keV}$ band which appears to be protruding outward, surrounded by diffuse, softer emission, likely from shocked ISM. Spectral modelling indicates that all three clumps exhibit enhanced elemental abundances, as expected if the features correspond to ejecta clumps. It is interesting to observe that the spectra of two features, G and I, exhibit a clear signature of Si XIII emission at around 1.85 keV, indicating a significant amount of silicon mixed into the ejecta (see also García et al. 2017), which implies an origin at a deeper layer in the progenitor star than for instance feature H. Feature K exhibits a quite unique spectrum. It can be fitted either with a strong departure from CIE, at an ionization age of $\tau \sim 10^{10}\,\mathrm{s\,cm^{-3}}$, or with a combination of low-temperature plasmas. In addition, a pronounced emission line at 0.43 keV is present. Our modelling attributes this line to a supersolar nitrogen abundance, which we do not observe in a single other investigated region. Feature K appears to intersect with an extended soft filament, interpreted as residual stellar wind material by Sapienza et al. (2021). Therefore, one may speculate that the observed clump consists of nitrogen-rich material ejected by the progenitor, which was only recently overrun by the blast wave.

Region M presents a close look at thermal emission close to the forward shock, focussing on a relatively “clean” location, where the shock appears close to plane-parallel. Our imaging reveals a clear hardness gradient, with the soft band becoming increasingly dominant close to the shock front. This is confirmed by the spectra extracted from regions M1 and M2, with the former exhibiting its peak count rate at the extremely low energy of 0.25 keV. While the 2TNT model is preferred for both regions from a statistical point of view, physically, one would expect NEI plasma this close to the shock front. Intriguingly, our spectral fits with the TNT model attribute the observed difference in hardness mostly to different ionization ages in the two regions. While the almost perfect agreement in plasma temperature is probably partly coincidental, an inward increase of the ionization age is perfectly consistent with expectations, as material located further downstream should have interacted with the forward shock at an earlier time. An important point to make is that the extremely high measured silicon abundance in region M1 is most likely not physical, as we expect this region to be dominated by shocked ISM. Instead, it probably originates from the statistically highly significant downward curvature of the spectrum below 0.25 keV, which our model can only reproduce by increasing both the emission from the silicon L-shell and the absorption column density. In reality, this curvature could be caused for instance by an overestimated response of eROSITA at these very low energies, or by the true energy dependence of the absorption cross-section differing from the `TBabs` model. Thus, we argue that any potentially enhanced silicon abundance is only credible in combination with the detection of Si xiii emission at 1.85 keV.

Regions N and V were selected for further study due to their appearance as broad and cold filamentary structures, and, in case of region V, for the apparent iron enrichment encountered in Sect. 6.3.2. Feature N is found to exhibit an intriguing morphology in the soft band below 0.7 keV, as it appears as a clumpy structure, with a well-defined brightened edge at its eastern boundary. The spectra of the two regions appear quite similar, revealing soft thermal components with little departure from CIE. This is superimposed by significant nonthermal emission from the PWN. In both regions, our spectral fits argue in favor of supersolar abundances of iron. One may thus speculate that heavy-element ejecta may be present in these cold and thick filamentary structures. However, we found that, in our modelling, the iron abundance is heavily correlated with other model parameters, such as plasma temperature or ionization age (for the TNT model), and thus we cannot exclude that the detected overabundances might also be a signature of systematic issues, such as an imperfect model choice.

Finally, features T, W, and X were defined around regions found to be rich in typical ejecta elements in Sect. 6.3.2, those being the northwest periphery of the pulsar (T), the northern interior of the shell of Vela Jr. (W), and the Vela cocoon (X). All three regions are characterized by a relative dominance of the intermediate energy band in imaging, which is expected to trace neon or iron emission lines. First, we note that the power law spectral index Γ found in region X agrees very well with the typical value $\Gamma \approx 2.2 - 2.3$ observed for the inner portion of the Vela cocoon (LaMassa et al. 2008; Slane et al. 2018; H. E. S. S. Collaboration et al. 2019). This shows that our data set allows us to characterize bright nonthermal emission reasonably well. All three investigated regions exhibit similar thermal plasma properties, with moderate NEI at $\tau \sim 2 \times 10^{11}\,\mathrm{s\,cm^{-3}}$. Also, they appear to show comparable abundance patterns, with enhancements in the light ejecta elements oxygen, neon, and magnesium, at O/H ∼ 1.4, Ne/H ∼ 3, Mg/H ∼ 2.5 (for the TNT model). Intriguingly, all three regions exhibit significant Si xiii line emission, consistent with a strong contribution of silicon to the emission of these ejecta-rich clumps. In contrast, no indication of a supersolar iron enrichment is observed.

6.4 Discussion

6.4.1 X-ray absorption toward Vela in a multiwavelength context

The absorption column density toward Vela (Fig. 6.5) exhibits a rich structure with a strong north-south asymmetry and several clumps or filaments of enhanced absorption, tracing the in-

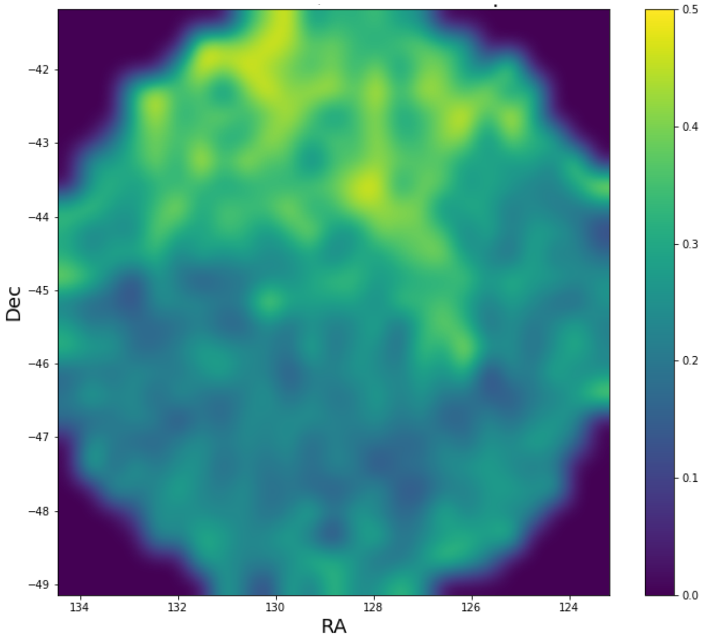

Figure 6.9: Spatially resolved integrated optical extinction in the direction of Vela, assumed to lie at a distance of 290 pc, using the catalog based on the `StarHorse` code (Anders et al. 2022). The color bar indicates the value of A_V in units of magnitude. Figure credit: P. Predehl.

homogeneous distribution of foreground material. Our absorption map strongly resembles that based on *ROSAT* data (Lu & Aschenbach 2000), even though we seem to recover a systematically larger absorption column. This may be due to differences in the model choice, such as different thermal plasma or absorption models. As noted already by Lu & Aschenbach (2000), the large-scale distribution of N_H appears to be anticorrelated with the observed distribution of neutral hydrogen and CO in the direction of Vela: while the latter two appear most concentrated toward the north and east (Dubner et al. 1998; Moriguchi et al. 2001), we observe the highest X-ray absorption in the south. However, even though tentative signs of interaction between the SNR and neutral material are found, the major drawback of the maps of Dubner et al. (1998) and Moriguchi et al. (2001) is that they may include material that is in reality located behind Vela. In contrast, the three-dimensional dust-extinction information extracted from the photometric and astrometric data analyzed with the `StarHorse` SED fitting code (Queiroz et al. 2018; Anders et al. 2022) allows us to predict the amount of intervening material in a distance-resolved manner. We achieved this based on the integrated optical extinction A_V in the catalog, which we evaluated in a slice around the precisely known distance of 290 pc (Dodson et al. 2003) to Vela. Using the fact that optical extinction and X-ray absorption are expected to correlate with an approximate relation of $N_H = 2.08 \times 10^{21} A_V \,\mathrm{cm}^{-2}$ (Zhu et al. 2017), a comparison between the two is expected to reveal similar spatial distributions of intervening material.

As displayed in Fig. 6.9, the prediction based on `StarHorse` is also opposite to what is seen in X-ray absorption. Similarly to the neutral gas tracers, it exhibits the largest column density of absorbing material in the north of Vela, contrasting the observed peak of X-ray absorption in its south. Even though optical and X-ray absorption trace components of the ISM that are not necessarily identical, dust grains and (mostly) metals, respectively, such a strong disagreement between the two is quite unexpected, as their tight correlation is well established on larger Galactic scales (Predehl & Schmitt 1995; Güver & Özel 2009; Zhu et al. 2017).

A possible avenue toward the resolution of this conundrum may lie in dust destruction: given the fact that the massive progenitor of the Vela SNR likely exploded in a star-forming region which may have been dust-rich, and that the immediate neighborhood of the sun appears to be almost dust-free (Lallement et al. 2019), it seems reasonable to assume that the majority of intervening dust was located close to the SNR. Assuming a shock velocity $\gtrsim 200\,\mathrm{km\,s^{-1}}$ (Slavin et al. 2015), it is thus imaginable that the destruction of dust grains within the reach of the SNR shock wave has significantly reduced the integrated dust budget along the entire line of sight to Vela (Zhu et al. 2019). In this scenario, the X-ray absorption would be unaffected, as heavy elements would still contribute absorption, but optical light would be less attenuated. An analogous scenario has been invoked to explain the apparent lack of optical extinction toward Cas A (Predehl & Schmitt 1995; Hartmann et al. 1997). However, it is unclear why the destruction of dust would have an asymmetric effect on dust along the line of sight, and preferentially destroy dust in the southern portion of the SNR, unless a larger fraction of dust were to be located out of reach of the shock wave in the north.

Furthermore, a serious discrepancy exists between the dust extinction within the surroundings of the sun predicted by `StarHorse` and the results of three-dimensional inversion techniques (Lallement et al. 2019, 2022; Vergely et al. 2022), with the latter predicting a smaller integrated extinction $A_V < 0.1$ up to 290 pc in the direction of Vela. This disagreement may be caused by the large statistical scatter for individual stars in `StarHorse`, which may drive the estimated local average extinction to unrealistically large values, in comparison with the hierarchical spatial inversion technique which reconstructs the differential extinction in each volume element. As an example, in the catalog of Anders et al. (2022), the average extinction toward stars within 100 pc of the sun in the direction of Vela is around 0.15, which seems significantly too large for objects within the local hot bubble, which should be more or less free of dust.

As noted by Lu & Aschenbach (2000), the X-ray absorption column density appears to correlate well with optical Hα line emission. In Fig. 6.10, we visualize this by comparing a smoothed version of our N_H map (Fig. 6.5) to the smoothed continuum-subtracted Hα map of the region, adapted from the public Southern H-Alpha Sky Survey Atlas (SHASSA; Gaustad et al. 2001). An almost step-like increase from north to south is clearly visible in both X-ray absorption and optical line intensity. The Hα emission in any evolved SNR is expected to be caused by low-velocity shocks interacting with a high-density medium, resulting in the observed filamentary structure. The presence of the highest average ISM density in the south appears to be contradicted by both our density map, computed from the emission measure of the spectra (Fig. 6.5), and the larger shell radius there (Slane et al. 2018), both of which imply the densest ISM in the northeast. One may however speculate that the ISM is, on average, more clumpy in the south, despite exhibiting a lower mean density. This would explain the larger shock radius there, as the expansion behavior would be determined by the least dense component (Sushch et al. 2011). Furthermore, this could be reconciled with the lower X-ray emission measure in the south, if the volume filling factor is much smaller than in the north, as would be expected for a clumpy medium. In this

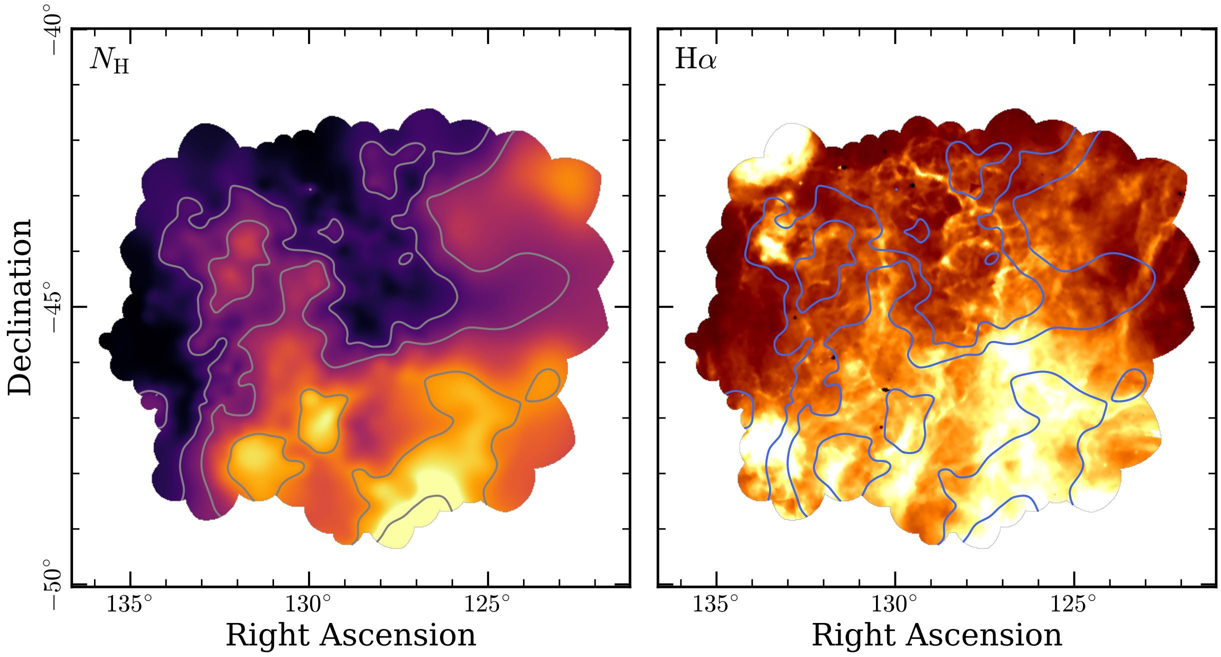

Figure 6.10: Comparison between X-ray absorption and Hα emission. The *left* panel displays a smoothed map of our measured $N_{\rm H}$ values toward Vela, with contours at the level of $N_{\rm H} = 1.7, 3.0, 6.0, 10.0 \times 10^{20}$ cm^{-2}. The same contours are overlaid on an Hα emission map of the region in the *right* panel. Both panels employ a linear color scale, and have been masked as in Fig. 6.5.

scenario, if the X-ray emission in the south really originates preferentially from dense filaments and clumps, it is imaginable that these contribute a large amount of additional absorption, on top of what would be expected from the "spatial average" given by optical extinction or neutral gas tracers.

6.4.2 Thermal emission from the Vela SNR

Temperature distribution and shocks

Our eRASS:4 data set has allowed us to identify the multi-component nature of the thermally emitting plasma in the Vela SNR in imaging. Cooler material seems to be concentrated in several thick shells and filaments, whereas the hotter component appears to dominate in thin radially oriented structures. This complex morphology can clearly not be described in its entirety with spherically symmetric models of the density structure of SNRs. Nonetheless, it is tempting to identify the colder thermal component as representative of a "typical" SNR shell, as it exhibits several smooth structures which appear to delineate the local boundary between shocked, X-ray-emitting and unshocked, X-ray-dark ISM, in particular in the northeast. The thinner radial filaments making up the hotter component could be associated to overdense clumps originating from deeper layers, which are now penetrating outward, due to the smaller deceleration they experience. This would be akin to the more pronounced shrapnels, which have already protruded out further into the unshocked ISM.

Our spatially resolved spectroscopy in Sect. 6.3.2 demonstrates that the median temperature of X-ray emitting plasma in Vela is very low, at $kT \sim 0.19\,\mathrm{keV}$. Assuming that this value is approximately representative of the equilibrium temperature that the plasma in the shell reaches a sufficiently long time after its forward shock interaction, this implies a late-time shock velocity of

$$v_s = \left(\frac{16}{3}\frac{kT}{\bar{m}}\right)^{1/2} \sim 400\,\mathrm{km\,s^{-1}}. \tag{6.2}$$

Here, we have assumed an average particle mass of $\bar{m} = 0.61\,m_p$, typical for a fully ionized plasma of ISM composition. If we further assume that the forward shock expansion of Vela has been approximately following the expectation for a Sedov-Taylor blast wave throughout the majority of its lifetime, we obtain a crude estimate for the SNR age of $t = (2r_s)/(5v_s) \sim 20\,\mathrm{kyr}$, given a current shell radius $r_s \approx 20\,\mathrm{pc}$. While this value is around a factor of two larger than the characteristic age of the Vela pulsar (Manchester et al. 2005), a pulsar age up to 30 kyr is considered plausible, given the uncertain spin-down history of the frequently glitching object (Espinoza et al. 2017). Therefore, an age around 20 kyr for the Vela SNR and its pulsar is certainly reasonable, for instance if the pulsar was born with a non-negligible fraction of its present-day spin period, or if it has exhibited a higher braking index in the past.

A close look at an almost plane-parallel portion of the forward shock (region M in Sect. 6.3.3) has revealed a drastic softening of the thermal X-ray emission toward the shock front, which could point toward a decrease in shock age. In this scenario, the plasma right behind the shock is presently still strongly underionized, suppressing the line emission from high ionization states, whereas plasma further downstream has almost reached CIE. While, our ionization age measurements are extremely uncertain, in principle, they can be related to the expected amount of time passed between shock interaction in the two regions. Assuming a shock velocity of $400\,\mathrm{km\,s^{-1}}$, and a shock compression factor of 4, one expects material to move downstream at around $100\,\mathrm{km\,s^{-1}}$ in the rest frame of the shock. Given the angular separation of around $15'$ between the two regions, this implies a difference in shock ages on the order of $\Delta t_s \sim 10\,\mathrm{kyr}$. This can be compared with the (quite uncertain) ionization age difference $\Delta\tau \sim 6 \times 10^{11}\,\mathrm{cm^{-3}\,s}$, to estimate the post-shock electron density $n_e \sim \Delta\tau/\Delta t_s \sim 2\,\mathrm{cm^{-3}}$, corresponding to a proton density around $n_\mathrm{H} \sim 0.4\,\mathrm{cm^{-3}}$ in the unshocked ISM. This value is a factor of a few higher than ISM densities typically inferred from X-ray emission in the east of Vela (Katsuda & Tsunemi 2005; Yamaguchi & Katsuda 2009), which one may justifiably attribute to the large uncertainties involved, for instance when estimating the past velocity of the blast wave. However, alternatively, a resolution might also be given by a clumpy ISM, in which a low-density component controls the expansion behavior, while a denser component acts as the main source of X-ray emission (Sushch et al. 2011; Slane et al. 2018), biasing the spectrally estimated parameters.

Shrapnel D is a prototypical target for studying the temperature and morphology of an overdense clump, which has overtaken the main blast wave and is penetrating the unshocked ISM. In Sect. 6.3.3, we have found a strong temperature gradient across the feature: the hottest material is encountered at the presumable apex of the structure, where the highest concentration of ejecta material is also observed, whereas much colder plasma is found in the outer portions of the bow shock. Miceli et al. (2013) have successfully reproduced the observed X-ray brightness distribution of shrapnel D, by modelling the evolution of a moderately overdense ejecta clump, initially located at $1/3$ of the ejecta radius, throughout the lifetime of Vela. While they did not publish a prediction on the observed spectrum in different regions of the shrapnel, Fig. 5 in their paper seems to indicate that the densest region, which contributes the brightest X-ray emission, should exhibit a lower temperature than the rest of the bow shock. This appears to be in tension with our observation of comparatively hard emission originating from a hot CIE plasma at the X-ray-brightest portion of the shrapnel. This could indicate that an additional source of heating, for instance through the reverse shock, may have affected the ejecta overdensity during its outward propagation. Alternatively, the initial conditions of Miceli et al. (2013), where, to maintain pressure equilibrium, the overdensity has a much lower initial temperature than ambient ejecta material, might be violated in practice. Another possibility may be that the densest portion of ejecta material is actually still too cold to be visible in X-rays, in which case the measured temperature might reflect that of shocked ISM in front of the clump, which indeed should be highest at the apex of the bow shock (Miceli et al. 2013).

Ejecta inside and outside the SNR shell

Spatial distribution Throughout this work, we have encountered signatures of ejecta of the Vela SNR both in spatially resolved spectroscopy, agnostic to feature morphologies (Sect. 6.3.2), and in the dedicated spectral analysis of interesting structures (Sect. 6.3.3). As many previous works have found, X-ray emitting ejecta are present both inside and outside the limits of the SNR shell. Clumpy features located outside the SNR shell in the plane of the sky are relatively easily identifiable as such, as there is no background emission from swept-up ISM. This is why the original six shrapnels were the first identified ejecta clumps in Vela (Aschenbach et al. 1995; Miyata et al. 2001; Katsuda & Tsunemi 2005, 2006; Yamaguchi & Katsuda 2009). It has been shown, here and in García et al. (2017), that several features emanating from the shell in the southward direction are rich in neon, magnesium, and silicon, and may thus be dense ejecta clumps, similarly to the shrapnels. Their less prominent appearance may be linked to a thinner ISM in the southwest direction (Sushch et al. 2011; Slane et al. 2018), leading to a later breakout from the forward shock. Miceli et al. (2008) found signatures of several clumps of neon- and magnesium-rich material close to the northern rim of Vela, which they interpreted as ejecta shrapnels located inside the SNR shell in projection. Our analysis has revealed several peaks in metal abundances inside the shell, which may constitute similar cases, for instance close to the eastern rim (region W in Sect. 6.3.3). This may indicate that in the evolved Vela SNR, a significant fraction of ejecta heated to X-ray-emitting temperatures is located in outward-protruding overdense clumps, many of which have overtaken the main SNR blast wave already.

In contrast, Slane et al. (2018) observed a concentration of X-ray emitting ejecta also at the very center of Vela. They provided an interesting model to explain the morphology of the ejecta-infused cocoon, in which the northeast portion of the reverse shock arrives at the pulsar's location first, asymmetrically crushing the PWN. This leads to a shift in the peak of the distribution of both relativistic electrons and ejecta toward the southwest, consistent with the current location of the cocoon. Our analysis clearly confirms this ejecta enhancement inside the cocoon. Furthermore, our maps in Fig. 6.5 show that the associated peak in oxygen and neon abundance is indeed confined to a narrow stripe extending southward from the pulsar.

In addition, we have discovered a further abundance enhancement about one degree northwest of the pulsar (region T in Sect. 6.3.3). While one may naturally ascribe this to a further isolated ejecta clump seen merely in projection, we believe that our X-ray images indicate a direct association between the pulsar and this feature. In particular, in Fig. 6.2, one can see a thin filamentary structure emanating from the vicinity of the pulsar and connecting to our ejecta-rich feature, visible in the 0.7 − 1.1 keV energy band. While significantly fainter, its thin, curved morphology appears similar to that of the outer portion of the cocoon. Even though we cannot exclude the possibility that this apparent connection with the pulsar is merely coincidental, it is intriguing to note that the apparent base of our supposed filament is located in the northwest of the pulsar, approximately in the direction in which the jet of the Vela pulsar is being launched (Helfand et al. 2001; Pavlov et al. 2003). It may therefore be possible that energy input from mildly relativistic particles in the polar outflow of the pulsar plays a role in powering thermal emission in this region. Alternatively, observing the morphological similarity with the cocoon, one may suspect a similar scenario as in Slane et al. (2018): the thin filamentary structure could have been created by anisotropic crushing of ejecta-rich material by a secondary shock, causing the observed elongated shape.

A final interesting observation regarding the distribution of ejecta in Vela is that regions rich in ejecta seem to exhibit systematically higher temperatures, irrespective of the exact model setup (see Figs. 6.5 and D.4). The observation of this trend with two separate models makes us confident in its physical origin, rather than an origin in a systematic modelling issue. While the majority of X-ray emitting ISM in Vela has likely been heated by a strongly decelerated forward shock, one may thus conclude that the interaction between ejecta clumps and the reverse shock may have heated the ejecta to systematically higher temperatures. If we, conversely, assume that hot thermal emission in Vela tends to be linked to ejecta material, we can speculate that most structures that appear dominant in imaging in the 0.7 − 1.1 keV energy band (Fig. 6.2) are rich in ejecta. This scenario is especially intriguing because of the many radially oriented features visible in this energy band, which can be interpreted as ejecta clumps protruding outward, either through the decelerated shell associated to the forward shock or into the unshocked ISM.

Composition Several patterns emerge, concerning elemental abundances in the ejecta of Vela: throughout the SNR, the distributions of oxygen, neon, and magnesium show peaks which are generally well correlated, as expected from a common origin of these elements in the progenitor star. However, heavier, explosively synthesized elements, such as iron and silicon, seem to not follow this correlation. This can be observed in particular for the Vela shrapnels: while the head of shrapnel D is found to exhibit a large concentration of oxygen, neon, and magnesium, little evidence for silicon or iron emission is present. This is contrasted by shrapnel A, which exhibits a large amount of silicon ejecta (Miyata et al. 2001; Katsuda & Tsunemi 2006), with little evidence for an enrichment in lighter elements. This feature is particularly intriguing, since the narrow opening angle of the associated Mach cone indicates a higher current velocity than for other shrapnels. This implies that shrapnel A has overtaken clumps formed in outer ejecta layers due

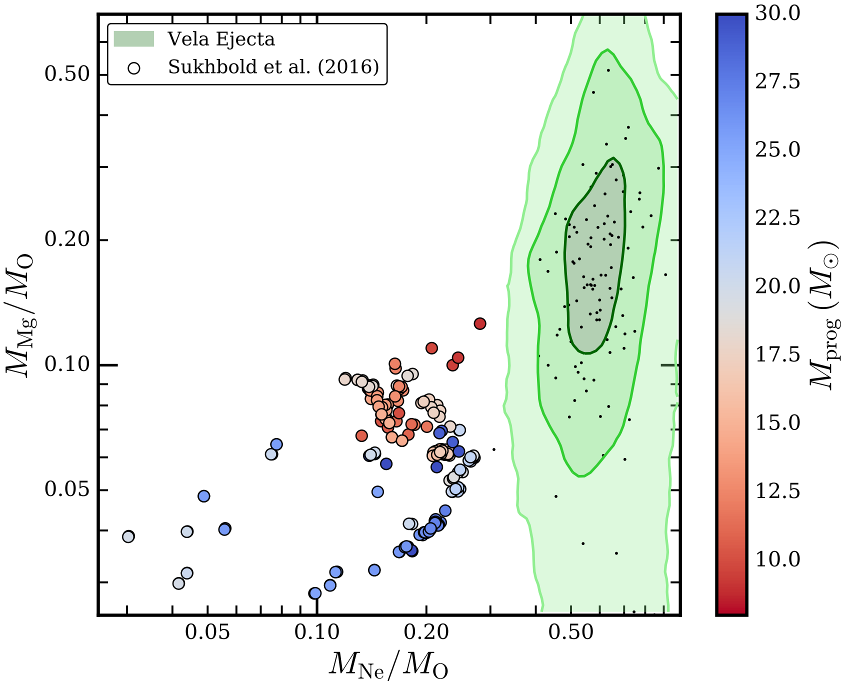

Figure 6.11: Comparison of observed light-element ejecta to theoretical predictions. In green, we show the one, two, and three sigma contours of the distribution of neon-to-oxygen and magnesium-to-oxygen mass ratios in the ejecta of Vela, based on the 2TNT model. The locations of the individual bins in this parameter space are indicated with black dots. This is compared to the predicted total element ratios for individual explosions in the simulations by Sukhbold et al. (2016), where the color coding of the circular markers indicates the simulated progenitor mass.

to either an extremely high density contrast or a large initial velocity, possibly as part of a silicon-rich jet from deeper ejecta layers (García et al. 2017). The observed dichotomy in composition is encountered also for the ejecta clumps studied in the south of Vela (see Sect. 6.3.3): the relative concentration of silicon with respect to neon and magnesium is much higher for features G and I than for feature H, implying an origin at different depths in the progenitor despite their similar angular distances from the center.

While silicon ejecta are clearly present in several clumps inside and outside the shell, evidence for the presence of X-ray-emitting iron ejecta is sparse. Shrapnel A does exhibit significant iron L-shell emission. However, given the small absolute abundances of all typical metals except silicon (Katsuda & Tsunemi 2006), one might ascribe this to a strong contribution of ISM with about solar iron abundance to the emission of the ejecta clump. Feature V is a further location where tentative enhanced emission from Fe xvii is observed to be originating in the soft filament. However, detailed follow-up analysis would be necessary to clarify whether this is actually caused by enhanced iron abundances, or may be explained by a particular superposition of plasma temperatures and/or ionization states. In principle, consulting the comprehensive simulations of core-collapse supernova nucleosynthesis by Sukhbold et al. (2016), a comparable concentration of iron and oxygen ejecta (relative to the solar composition) should be present in the integrated yield of the supernova, unless the progenitor was very massive. Given the fact that the reverse shock has likely traversed and reheated the entire ejecta material in the northeastern portion of Vela (Slane et al. 2018), one would certainly expect to observe iron-rich ejecta at X-ray emitting temperatures there.

An interesting observation regarding the composition of ejecta in Vela is that neon and magnesium seem to be consistently enriched with respect to oxygen, when compared to solar abundances. Typical abundance ratios in ejecta-rich regions appear to be around $\langle \mathrm{Ne/O} \rangle \sim 2.5$ and $\langle \mathrm{Mg/O} \rangle \sim 2.0$. The corresponding typical mass ratios $M_{\mathrm{Ne}}/M_{\mathrm{O}} \sim 0.6$ and $M_{\mathrm{Mg}}/M_{\mathrm{O}} \sim 0.15$ may thus be representative of the composition of the outer ejecta layers during the explosion. Similar compositions were observed by other authors for the ejecta located inside the shell in projection, and in several shrapnels outside the shell (Miceli et al. 2008; Katsuda & Tsunemi 2005, 2006; Yamaguchi & Katsuda 2009). Considering this ubiquitous trend, it is important to note that most studies of core-collapse supernova nucleosynthesis do not predict strongly supersolar concentrations of neon or magnesium with respect to oxygen for any progenitor mass (e.g., Woosley & Weaver 1995; Rauscher et al. 2002; Sukhbold et al. 2016), at least when integrated over the total ejecta yield. In Fig. 6.11, we indicate the observed distribution of O-Ne-Mg abundance ratios in the ejecta-rich regions of Vela, defined to include all those Voronoi bins in Fig. 6.5 with supersolar oxygen content, $\mathrm{O/H} > 1$. This is compared to explosion models of different progenitor masses by Sukhbold et al. (2016), none of which seem to reach the relative neon- and magnesium-concentration which we seem to observe throughout Vela. A very similar trend can be observed when using the results of the TNT model instead. We note that, for several $15\,M_{\odot}$-progenitor models, the simulations of Fryer et al. (2018), which assume a broad parametrization of the "supernova engine", seem to be able to produce similar abundance patterns as observed here. However, given the wide range of input values assumed for the explosion energy and timescale, and the resulting extremely wide spread of element abundances in their models, we believe that some skepticism is warranted concerning the applicability of their results to our case.

Qualitatively, the low relative oxygen concentration might be understood as a signature of a relatively light progenitor, as the implied high central density during helium burning would tend to disfavor the production of oxygen compared to carbon (Woosley et al. 2002). This could ultimately lead to a lack of oxygen ejecta with respect to the products of carbon burning, including neon and magnesium. Nonetheless, a major caveat of performing such comparisons is that, to our knowledge, all currently available nucleosynthesis predictions for a large sample of progenitors are based on one-dimensional supernova models, due to computational limitations. These are unable to fully represent three-dimensional effects during the explosion, and their consequences on nucleosynthesis in individual ejecta clumps. We therefore hope to learn in the future, if the predictions of potentially more realistic arrays of two- or three-dimensional models of supernova nucleosynthesis differ substantially from the studies discussed above. Naturally, it is also imaginable that the observed unusual patterns in X-ray abundances are caused by a systematic observational issue, such as the preferential cooling of oxygen ejecta out of the X-ray regime, or a spectral modelling issue, like an inadequate model or an insufficient number of model components.

6.4.3 The vast extent of nonthermal X-ray emission from Vela X

X-ray emission from arcsecond to degree scales

Morphology The X-ray synchrotron emission associated to the plerion of the Vela pulsar has been investigated extensively in previous studies. On small scales, a complex, spectrally hard structure similar to the one in the Crab nebula is visible (Helfand et al. 2001; Pavlov et al. 2003). A mildly relativistic jet-counterjet structure emanates from the pulsar toward northwest and southeast, approximately parallel to its spin axis and proper motion direction. In the pulsar's equatorial plane, a torus consisting of two arc-like structures, around 50″ in diameter, is visible (see Fig. 2.6). This likely corresponds to the location of the termination shock of the pulsar wind (Helfand et al. 2001), in which the local magnetic field appears to follow a highly ordered toroidal structure (Xie et al. 2022). This torus is embedded in larger-scale diffuse nonthermal emission, which is brightest toward the southwest. This diffuse component likely constitutes the base of the cocoon which is thought to contain relativistic electrons from the pulsar wind, crushed by a one-sided interaction with the reverse shock (Slane et al. 2018). In X-rays, the cocoon extends up until around 1.5° southwest of the pulsar.

In this work, we have for the first time surveyed the vast extent of nonthermal X-ray emission beyond the cocoon. While several previous studies have found evidence for a nonthermal X-ray component in other directions from the pulsar (Willmore et al. 1992; Mattana et al. 2011; Katsuda et al. 2011; Slane et al. 2018), this study has exposed the entirety of a diffuse synchrotron nebula extending two to three degrees from the Vela pulsar (Fig. 6.5). The size of our extended PWN is quantified in Fig. 6.12, which displays the evolution of the nonthermal surface brightness Σ_Γ with distance from the pulsar r_{PSR}. This reveals a smooth radial decrease of the diffuse nebula's brightness by 1.5 orders of magnitude across a large portion of the SNR shell. Interestingly, the nonthermal emission seems to show a quadrupolar asymmetry, with the largest extent seemingly running from north-northeast to south-southwest (along a position angle $\sim$ 15° east of north), which, if real, may indicate a preferred direction of particle transport in the nebula.

Size and energetics Using our constraints on the brightness of synchrotron emission in the entire Vela SNR (Fig. 6.5), we can compute the total nonthermal flux of the plerion of the Vela pulsar. Apart from the central 3′ radius around the pulsar which was masked already during spectral fitting, we excluded a 1.2° region around Vela Jr., and integrated the nonthermal flux within a 4° radius around the pulsar. Since our spectral modelling approach enforces a nonnegative value of the power law normalization in each bin, even if the true flux is negligible, it is possible that a simple integration over all bins overestimates the total flux. Therefore, a conservative flux estimate is provided by only including those bins whose flux posterior indicates a nonzero value by at least 5σ significance. This yields an estimate of $F_\Gamma = 4.6 \times 10^{-10}\,\mathrm{erg\,cm^{-2}\,s^{-1}}$ in the $1.0 - 5.0\,\mathrm{keV}$ band, and a corresponding synchrotron luminosity of $L_\Gamma = 4.7 \times 10^{33}\,\mathrm{erg\,s^{-1}}$. In order to be able to compare this with published energetics of other X-ray PWNe, we also compute the luminosity in the $0.5 - 8.0\,\mathrm{keV}$ band, finding $L_\Gamma = 1.02 \times 10^{34}\,\mathrm{erg\,s^{-1}}$. This does not include the emission from the core of the PWN, which would contribute on the level of a few percent only, assuming the luminosity given by Helfand et al. (2001). While this broad energy

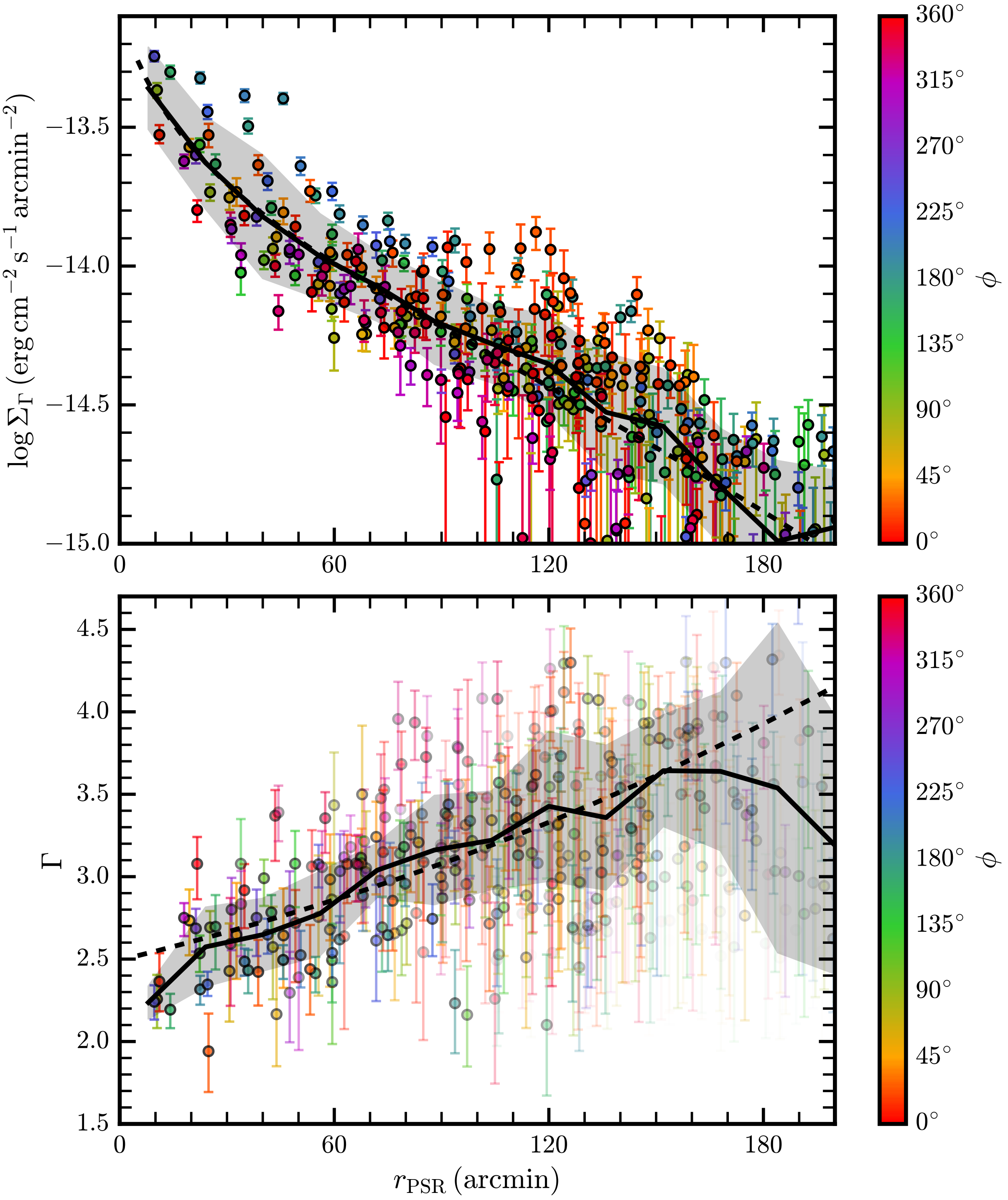

Figure 6.12: Radial evolution of nonthermal emission from Vela X. The *top* panel depicts the nonthermal surface brightness Σ_Γ of each Voronoi bin in the 1.0 – 5.0 keV range from the 2TNT model, plotted against its angular distance r_{PSR} from the pulsar. The *bottom* panel shows the measured spectral index Γ versus r_{PSR}, where the transparency of the individual markers indicates the relative contribution of the nonthermal component to the hard spectrum. In each panel, the marker color indicates the position of the bin, that is, its relative angle ϕ (east of north) with respect to the pulsar position. In both plots, the solid black line and shaded area indicate the weighted average and associated standard deviation of the measured quantities, determined within narrow radial bins. The dashed lines indicate the best fit of the brightness profile (*top*) and radial spectral softening (*bottom*), using the models described in the text. All bins located within 1.2° from the center of Vela Jr. have been excluded from this figure to remove any contamination by its nonthermal shell.

band may be considered “standard” for the quantification of X-ray fluxes, we caution the reader that the extrapolation of the nonthermal component to below 1.0 keV is somewhat problematic, since at lower energies, its emission is strongly overpowered by the thermal component. Thus, our spectral fits are not sensitive to the true contribution of the nonthermal component there.

Comparing our measured luminosity with the well-known spin-down power of the pulsar $\dot{E} = 6.9 \times 10^{36}\,\mathrm{erg\,s^{-1}}$ (Dodson et al. 2007), we obtain an approximate PWN efficiency, that is, the ratio of X-ray luminosity to the present-day pulsar spin-down power, of $\eta_{\mathrm{PWN}} \sim 1.5 \times 10^{-3}$. While this value is still far below the efficiency of young and X-ray-bright PWNe, such as the Crab or PSR B0540−69, it appears to be almost two orders of magnitude higher than other estimates for Vela X ($\eta_{\mathrm{PWN}} \sim 2 \times 10^{-5}$, Kargaltsev & Pavlov (2008)). We note however, that this is not really an “apples to apples” comparison, as other studies only took the arcminute-size PWN core into account. Our estimate considers a much more extended region and therefore integrates over a much longer history of particle injection from the pulsar wind, as older electrons likely contribute to the diffuse outer X-ray emission. In any case, our measurement challenges the picture of the Vela plerion being particularly underluminous in X-rays.

While there does not appear to be any abrupt outer border to the synchrotron emission from our extended PWN, we attempted to roughly quantify its size, using a model for the emission profile of a diffusive nonthermal halo, assuming a constant magnetic field. We modelled the observed radial surface brightness evolution using the brightness profile given by Abeysekara et al. (2017), for simplicity, evaluated at a single effective energy only (see Appendix D.1). The best fit is indicated in the upper panel of Fig. 6.12, and corresponds to a characteristic angular size $\theta_D = 164 \pm 6$ arcmin, which, at the distance of Vela, corresponds to a physical diffusion radius of around $r_D = 13.8 \pm 0.5$ pc.

While the relative size of the nebula in the plane of the sky and compared to its host SNR is astonishing, its absolute physical size is not inexplicably large by itself, considering that TeV PWNe regularly reach tens of parsec in size (Kargaltsev et al. 2013). Furthermore, Bamba et al. (2010) listed two X-ray PWNe comparable in size to our nebula for pulsars slightly older than the Vela pulsar. A similar case to Vela X may be given by PSR J1826−1334, corresponding to the TeV source HESS J1825−137, whose X-ray PWN has been measured to extend up to 17 pc from the pulsar (Uchiyama et al. 2009). It is intriguing to note that both the characteristic age of 21 kyr and the spin-down power of $2.8 \times 10^{36}\,\mathrm{erg\,s^{-1}}$ are comparable to the properties of the Vela pulsar. Thus, the energetic PSR J1826−1334 and the very extended PWN in HESS J1825−137 might be seen as a slightly more evolved analog of the extended PWN in Vela X. By analogy, one would thus expect a rather low magnetic field in Vela X, similar to the measurement $B \sim 4-5\,\mu\mathrm{G}$ in HESS J1825−137, inferred from the relative intensities and extents of X-ray and gamma-ray emission (Principe et al. 2020). Therefore, while some skepticism regarding the large physical PWN size from a relatively young pulsar may be warranted, the measured extent is by no means unphysical. In particular, the observation of Vela X presented here seems ideal for the detection of faint, diffuse nonthermal X-ray emission, given its dominant character down to ~ 1.0 keV, the physical proximity and negligible foreground absorption of Vela, and the homogeneous and sensitive coverage of the region in the eROSITA all-sky survey.

While its diffuse and extended nature make it tempting to identify our nonthermal nebula as a “pulsar halo”, it does not technically qualify as such in the evolutionary picture of PWNe presented by Giacinti et al. (2020). Instead, Vela X is classified to be in an intermediate stage (stage 2 in Giacinti et al. 2020) of its evolution, where a highly irregular relic PWN (i.e., the cocoon) has been created by the interaction between pulsar and SNR, but diffusive escape from the PWN core has become possible. Synchrotron emission from these escaped electrons may provide an explanation for the observed extended X-ray emission of Vela X. This stage differs from the "true" halo stage in that the pulsar has not yet left its parent SNR shell, meaning the escaped electrons are not diffusing through the unperturbed ISM, but through a more turbulent medium inside the SNR. Given the large physical size of the X-ray PWN revealed here, it seems quite plausible that Vela X is indeed closely related to the population of gamma-ray halos seen around middle-aged pulsars.

In order to robustly quantify the behavior of the physical quantities regulating the observed properties of the X-ray PWN, such as the magnetic field and diffusion constant, one would likely need to model the full X-ray/gamma-ray spectral energy distribution of the region in a spatially resolved manner, which is beyond the scope of this paper. However, with the given data set, we can attempt to infer the order of magnitude of the involved quantities in our extended nebula with the following considerations: The "characteristic" energy E_e of an electron emitting synchrotron emission at an energy E_X in a transverse magnetic field $B_\perp = B_{\mu\mathrm{G}}\,\mu\mathrm{G}$ can be written as (de Jager & Djannati-Ataï 2009)

$$E_e = 220 \times B_{\mu\mathrm{G}}^{-1/2} \left(\frac{E_X}{1\,\mathrm{keV}}\right)^{1/2} \mathrm{TeV}. \tag{6.3}$$

The corresponding approximate lifetime of the electron under losses from synchrotron emission and inverse Compton scattering in the Klein-Nishina regime is (Aharonian et al. 2006c)

$$\tau = 18 \times \frac{1}{1 + 0.144\,B_{\mu\mathrm{G}}^2} \left(\frac{E_e}{100\,\mathrm{TeV}}\right)^{-1} \mathrm{kyr}. \tag{6.4}$$

Combining this with the expectation for the diffusion constant D_B in the Bohm limit

$$D_B = 3.3 \times 10^{27} B_{\mu\mathrm{G}}^{-1} \left(\frac{E_e}{100\,\mathrm{TeV}}\right) \mathrm{cm^2\,s^{-1}}, \tag{6.5}$$

one can derive a characteristic energy-independent radius $r_B \sim (4 D_B \tau)^{1/2}$ covered by an electron transported through Bohm diffusion during its lifetime

$$r_B \sim 28 \times \frac{B_{\mu\mathrm{G}}^{-1/2}}{\left(1 + 0.144\,B_{\mu\mathrm{G}}^2\right)^{1/2}}\,\mathrm{pc}. \tag{6.6}$$

By equating this with the observed PWN size on the order of 14 pc, we can derive an approximate magnetic field strength in the Bohm limit of $B_\perp \sim 2.3\,\mu\mathrm{G}$. This estimate for the extended nebula is around half that measured in SED modelling of the cocoon (H. E. S. S. Collaboration et al. 2019), and slightly below the typical ISM magnetic field strength of $3\,\mu\mathrm{G}$ (Minter & Spangler 1996). The lifetime of an electron emitting at the X-ray energy where the nonthermal component is typically best-constrained in our data, $E_X \approx 1.6\,\mathrm{keV}$,[6] is around $\tau \sim 5.2\,\mathrm{kyr}$. The corresponding Bohm diffusion coefficient would be $D_B \sim 2.6 \times 10^{27}\,\mathrm{cm}^2\,\mathrm{s}^{-1}$.

If the above equations are taken at face value, this low magnetic field implies a very high characteristic energy of the electrons responsible for synchrotron emission at 1.6 keV of $E_e \sim 180\,\mathrm{TeV}$. This energy is more than high enough for escape from the spatial scales of the cocoon, with $B \sim 6\,\mu\mathrm{G}$ (H. E. S. S. Collaboration et al. 2019) and a perpendicular extent $\sim 1\,\mathrm{pc}$, to be possible if particle transport occurs via diffusion. The escape timescale would be $\sim 130\,\mathrm{yr}$ for Bohm diffusion (de Jager & Djannati-Ataï 2009; Tang & Chevalier 2012), which is much shorter than the expected synchrotron lifetime for this energy in the cocoon around $\tau \sim 1.6\,\mathrm{kyr}$. However, a fundamental problem with this high electron energy is that it is in apparent contradiction with the energy cutoff at $\sim 100\,\mathrm{TeV}$ inferred for the outer cocoon regions by H. E. S. S. Collaboration et al. (2019). If this energy cutoff is indicative of radiative energy losses, rather than the escape of high-energy particles (see Hinton et al. 2011), it seems doubtful whether more energetic electrons could have survived out to even larger distances. Furthermore, our low inferred magnetic field seems questionable given that, even with no energy cutoff, the ratio of the integrated X-ray to the VHE gamma-ray flux in a given region is expected to increase with the magnetic field approximately as $F_X/F_\gamma \propto B^2$ (Aharonian et al. 1997), and that, at this time, most of our extended nebula has not been detected at TeV energies (see below).

A possible mitigation of the above issues may lie in assuming a higher diffusion coefficient than implied by the Bohm limit, which would increase the inferred magnetic field, and correspondingly reduce the required energy of synchrotron-emitting electrons and their expected brightness in the TeV band. However, the electron lifetime would be reduced accordingly. A further fundamental aspect is that, in reality, the electron synchrotron emissivity is not describable by a delta function at a single peak energy, but by a rather wide distribution, which implies that X-ray synchrotron emission is also expected significantly beyond the characteristic energy corresponding to the cutoff. In conclusion, it is likely that either the electrons emitting in our extended X-ray PWN exhibit only a small fraction of the age of Vela itself, or that we are observing the significantly steepened part of the nonthermal spectrum located beyond the cutoff energy.

Tentative detection of radiative cooling Given the vast extent of the detected PWN, it seems natural to expect a significant degree of energy loss via synchrotron and inverse Compton emission affecting the highest-energy electron population, as it diffuses to large distances from the pulsar. The effect of synchrotron cooling has been directly observed for the electron population in the cocoon, where the energy loss manifests itself in a steepening of the nonthermal X-ray spectrum from a photon index of $\Gamma = 2.2$ to $\Gamma = 2.6$ within a distance of $100'$ from the pulsar (Slane et al. 2018). A similar effect seems to be observed in our data set as well (see Fig. 6.12), even though our ability to constrain the spectral slope in all but the brightest nonthermal regions is severely hampered by statistical noise. This is due to the relatively short spectral baseline available for constraining Γ, which is effectively limited by the bright thermal emission from Vela below 1.0 keV and the sharp drop in instrumental response above 2.3 keV (Predehl et al.

---

[6] For typical spectra with nonthermal contributions (e.g., regions W and T in Fig. 6.8), one can observe that the relative strength of the nonthermal component is maximal at around this energy.

2021), respectively. Thus, in order to reduce the potentially spurious impact of soft energies on the measurement of the average nonthermal slope with radius, we introduced a weighting scheme designed to reflect the relative contribution of the nonthermal component to the total observed spectrum above 1.0 keV (see Appendix D.1). This weighting factor is reflected in the transparency of the data points in the lower panel of Fig. 6.12, and was used to reweight the individual bins to compute the radial averages shown in the figure.

Despite the large overall noise level in the photon index, a significant outward steepening from $\Gamma \sim 2.2$ in the inner $15'$ to a maximum of $\Gamma \sim 3.6$ around $160'$ from the pulsar is apparent in the radial average of the spectral slope. The apparent decrease in Γ even further out can likely be explained with our prior becoming dominant, as Γ is almost unconstrained there. We attempted to test whether the observed increase of Γ with r_{PSR} can be reconciled with the expectation from radiative energy loss in a PWN in which particle transport is regulated by diffusion. To do this, we performed a fit of the pure diffusion model presented by Tang & Chevalier (2012) based on Gratton (1972) to the observed radial dependence of the photon index. However, given the likely importance of inverse Compton scattering due to the low suspected magnetic fields, we introduced a modification to take into account both synchrotron and inverse Compton losses (see Appendix D.1). We assumed a distance of 290 pc, a PWN age equal to the approximate age of Vela, $t = 20$ kyr, and that our constraints on the X-ray photon index correspond to a measurement at an effective energy of 1.6 keV. The model-predicted power law slope is given by

$$\Gamma(r) = 1 - \left.\frac{\mathrm{d}\log P(\nu, r, t)}{\mathrm{d}\log \nu}\right|_{h\nu\,=\,1.6\,\mathrm{keV}} \tag{6.7}$$

where $P(\nu, r, t)$ corresponds to the synchrotron power radiated at a frequency ν at a projected radius r from the pulsar, integrated along the line of sight following the modified Tang & Chevalier (2012) model. In the steady-state regime, where the lifetime of X-ray emitting electrons is shorter than the pulsar age, the predicted slope at a given radius only depends on the energy slope of the injected particles p ($\mathrm{d}N/\mathrm{d}E_e \propto E_e^{-p}$), and on a combination of diffusion coefficient D and transverse magnetic field $B_\perp$, which are assumed to be spatially uniform on the relevant scales. The degeneracy between D and $B_\perp$ cannot be lifted based on X-ray data alone without further assumptions, but would require the measurement of the level of the corresponding inverse Compton emission at TeV energies. The physical parameters constrained by the model are p and a characteristic "cooling radius" $r_C := (4D\tau)^{1/2}$, describing the degree of radial steepening, where the electron lifetime τ is computed as in Eqs. 6.3 and 6.4. We extracted the parameter constraints by modelling the range $r_{\mathrm{PSR}} < 200'$ via MCMC sampling with `emcee` (Foreman-Mackey et al. 2013), using a uniform prior on p and a logarithmic prior on r_C.

Our best fit is indicated as a dashed line in the lower panel of Fig. 6.12, and yields an electron power law index of $p = 4.00 \pm 0.11$, and a characteristic radius of $r_C = 14.7^{+1.3}_{-1.1}$ pc. This electron index predicts an X-ray photon index of $\Gamma = (p + 1)/2 \approx 2.5$ at the center of the PWN, clearly somewhat above the observed value. This may indicate that the electron population powering the extended PWN has already undergone significant cooling losses when leaving the PWN core, in possible conflict with the input assumption of an injected electron spectrum without cutoff. For a typical ISM magnetic field of $B_\perp = 3\,\mu$G, our measurement implies a diffusion constant of

$D = 3.6^{+0.6}_{-0.5} \times 10^{27}\,\mathrm{cm}^2\,\mathrm{s}^{-1}$. However, as shown by Tang & Chevalier (2012), if in reality the diffusion coefficient increases with energy as $D \propto E_e^{\alpha}$, the radial spectral index profile would be flattened. In the idealized case of Bohm diffusion ($\alpha = 1$), the profile of Γ would even become constant, as in the steady-state regime, the cooling radius would be energy-independent. Therefore, a more realistic constraint on the diffusion constant D at X-ray-emitting electron energies, assuming an ISM-level magnetic field, is given by

$$D = 3.6^{+0.6}_{-0.5} \times 10^{27}\,(1-\alpha)^2\ \mathrm{cm}^2\,\mathrm{s}^{-1}. \tag{6.8}$$

Given the large statistical and systematic uncertainties of our measurement, and the large number of simplifying assumptions entering the fitted model, this value should be seen only as an order-of-magnitude estimate of the average regime of diffusion in our extended PWN. However, our measurement of the radiative cooling radius agrees greatly with the characteristic PWN size of 14 pc, measured via the radial brightness profile, above. For comparison, the latter value yields a diffusion constant of $D = (3.14 \pm 0.26) \times 10^{27}\,\mathrm{cm}^2\,\mathrm{s}^{-1}$, assuming $B_\perp = 3\,\mu\mathrm{G}$. Intriguingly, both estimates are on a similar level as the diffusion constant estimated for 100 TeV-electrons in the pulsar halos of Geminga and PSR B0656+14 (Abeysekara et al. 2017).

While the determination of the exact level of radial steepening in the nonthermal spectrum is clearly challenging due to limited statistics, we believe that the observed effect of radiative cooling in our data set is most likely physical. We verified this hypothesis by performing a second set of spectral fits only on the hard portion of the observed X-ray spectra, to exclude possible biases introduced in spectral modelling. This allowed us to qualitatively reproduce both the radial brightness profile of the PWN and the radial increase of the nonthermal photon index (see Appendix D.2).

The connection to radio, GeV, and TeV emission

The Vela X PWN exhibits a complex multiwavelength morphology. In order to visualize the contrast between different energy bands, we compiled observations of the PWN at radio and TeV energies, and compared them with the observed nonthermal X-ray emission in Fig. 6.13. To display the large-scale low-frequency radio emission, we extracted an image in the 170 – 231 MHz band from the public data of the Galactic and Extra-Galactic All-sky MWA survey (GLEAM; Hurley-Walker et al. 2017, 2019). TeV observations of the region are available as part of the HESS Galactic plane survey (H. E. S. S. Collaboration et al. 2018b), from which we have used the > 1 TeV flux map with a 0.1° correlation radius. In order to reflect the nonthermal X-ray emission of the plerion, we used an image extracted from our data set in the 1.95 − 2.30 keV band, above any significant line emission from Vela, but below the drop in the eROSITA effective area.

While at radio energies, an extended filamentary structure extending over 3° × 2° is visible (Bock et al. 1998), until now, in X-rays, only the elongated cocoon, extending around 1.5° south of the pulsar (Slane et al. 2018) was known to be powered by the pulsar wind. At gamma-ray energies below around 100 GeV, a diffuse structure similar to the radio nebula is visible, together with a (possibly unrelated) point-like source west of the pulsar (Grondin et al. 2013; Tibaldo et al. 2018). In contrast, VHE gamma-ray emission appears to trace the shape of the cocoon, albeit

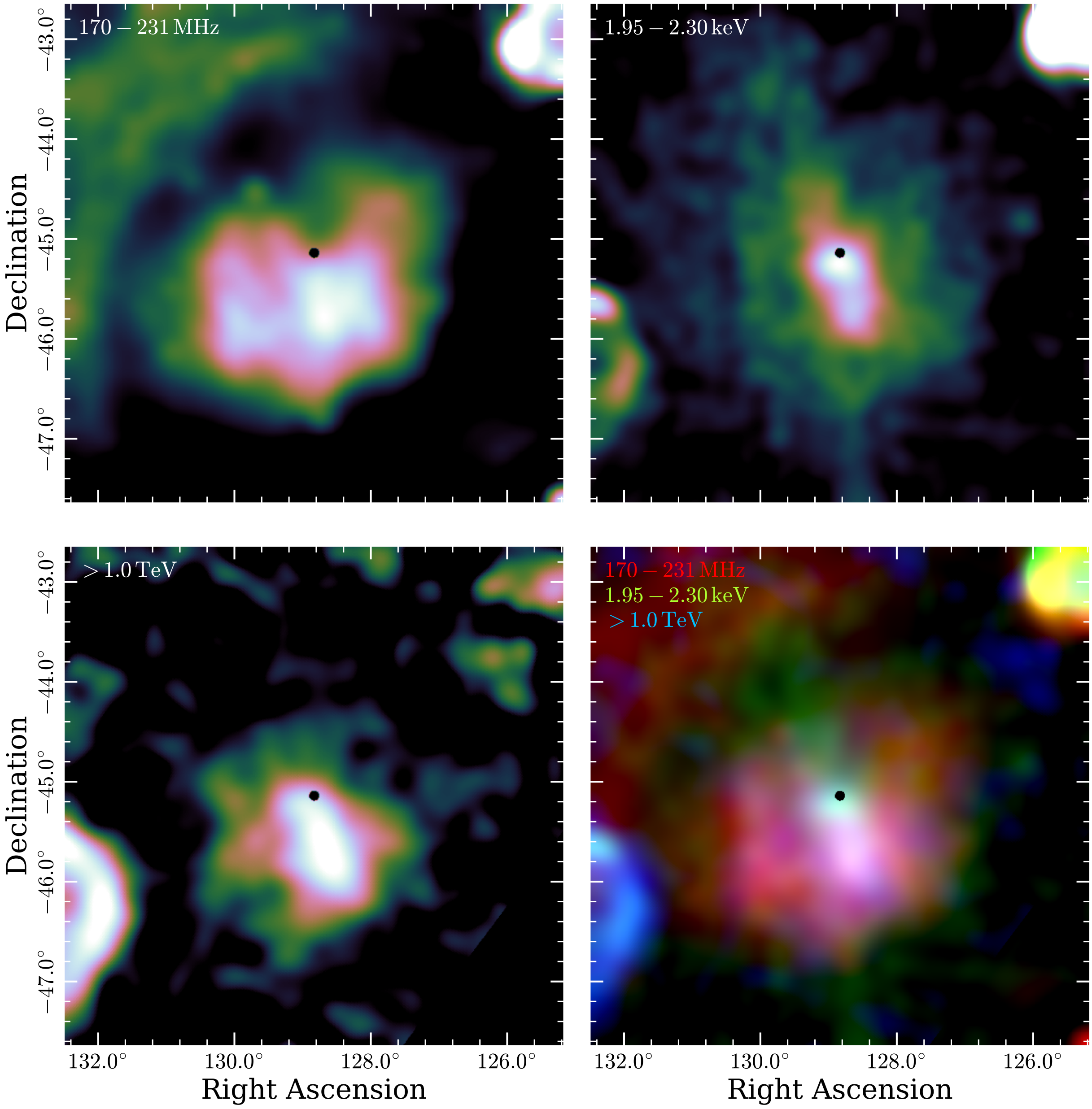

Figure 6.13: Multiwavelength morphology of Vela X. The individual panels show the morphology of nonthermal emission in a 5° × 5° region around the Vela pulsar in a low-frequency radio band (*top left*), in the nonthermal X-ray regime (*top right*), and at TeV energies (*bottom left*). The *bottom right* panel displays a false-color superposition of the three bands. In the radio and X-ray images, a $3'$ radius around the pulsar was masked, before they were smoothed with a Gaussian kernel of $\sigma = 6'$ to match the resolution of the TeV band. In all three bands, we used a square-root brightness scale, spanning a factor of 30 in dynamic range.

with a larger lateral extent than seen in X-rays (Aharonian et al. 2006a; Abramowski et al. 2012; H. E. S. S. Collaboration et al. 2019).

A two-zone leptonic model has been invoked in order to explain these multiwavelength observations (de Jager et al. 2008). In this model, a lower-energy electron population with a cutoff on the order of 100 GeV (Grondin et al. 2013) produces the radio synchrotron component, whereas inverse Compton scattering is responsible for the GeV component. Analogously, the TeV and X-ray emission components originate from a more energetic component with a cutoff around 100 TeV (H. E. S. S. Collaboration et al. 2019). So far, the somewhat wider extent of TeV emission has been explained by the shorter expected lifetime of the electron population visible through X-ray synchrotron emission, as the TeV emission traces longer-lived particles down to lower energies.

This view is however challenged by our detection of a diffuse nonthermal X-ray nebula, which extends far beyond the dimensions of the cocoon and the established TeV emission region. Since the newly detected emission is likely solely due to synchrotron radiation, its explanation requires the presence also of an associated diffuse gamma-ray PWN, which has not been observed at TeV energies, so far (Aharonian et al. 2006a; Abramowski et al. 2012). Since the diffuse X-ray component exhibits a softer and fainter character than the cocoon, the associated electron population is likely older, and exhibits a lower cutoff energy from radiative losses (H. E. S. S. Collaboration et al. 2019).

It is interesting to observe that the extent of our X-ray nebula appears to exceed even that of the radio emission associated to Vela X, which traces a less energetic particle population, which is generally assumed to be even older. Furthermore, the diffuse X-ray component is observed to exhibit an apparent elongation in the north-south direction. This contrasts the radio emission, which is widest in the east-west direction, and is clearly centered south of the pulsar, likely due to an asymmetric interaction with the reverse shock (Bock et al. 1998; de Jager & Djannati-Ataï 2009; Slane et al. 2018). If this is truly caused by different spatial distributions of the underlying particle populations, the highest-energy electrons seem to have mitigated the strong influence of the reverse shock. This could be attributed to a comparatively recent injection by the pulsar, after the central PWN portion had already been crushed by the reverse shock. Alternatively, this may the signature of an increase in diffusivity with electron energy preventing the long-term confinement of X-ray emitting electrons in the cocoon.

An interesting comparison was made between Vela X and the Geminga pulsar by Fang et al. (2019). In their work, they showed that the vast TeV halo of Geminga can be explained by confinement in a turbulent slow-diffusion environment created by the shock wave of its parent SNR. They argued that a similar process may be at play in Vela X, where electrons escaped from the PWN core are diffusing through the turbulent environment inside the SNR shell, producing a relatively smooth extended synchrotron nebula. The topic of particle escape was addressed also by Hinton et al. (2011), who argued that the extremely soft GeV spectrum of the radio nebula can be explained by the escape of particles from Vela X. They interpreted the presumed lack of spectral variability of the cocoon in the TeV band as evidence for it being advection-dominated, preventing higher-energy electrons from easily escaping. Evidence for spectral variability along the cocoon has since been found in the X-ray band here and elsewhere (Slane et al. 2018; H. E. S. S. Collaboration et al. 2019), which may be interpreted as evidence for energy losses through synchrotron radiation or particle escape.

In summary, there remain two fundamental questions regarding our scenario of an extended diffusive X-ray nebula: first, it is unclear whether sufficiently energetic electrons can escape from the PWN core or the cocoon without losing the majority of their energy. Second, even though the assumption of an ISM-level magnetic field outside the cocoon leads to sufficiently long electron lifetimes, and sufficiently large diffusion distances, to reach the observed extent, it also requires the presence of similarly extended TeV emission from relatively energetic particles (up to $\sim 100\,\mathrm{TeV}$), in order to explain the detection of nonthermal X-ray emission above $1\,\mathrm{keV}$, in contrast with existing data.

We hope that our discovery of an extended nonthermal X-ray nebula can be reconciled with future observations of Vela X at TeV energies, which might reach a higher sensitivity toward extended emission. Only the combination of TeV and X-ray data across the entire PWN (similarly to H. E. S. S. Collaboration et al. 2019) can provide a full picture of the high-energy particle content, particle propagation, and magnetic field structure inside the Vela X PWN, a prototypical PWN in an evolved SNR. If observations were able to exclude the presence of a gamma-ray counterpart to our X-ray nebula at the required level, one would have to search for alternative scenarios which mimic the spatially smooth and spectrally featureless characteristics observed here in X-ray imaging and spectroscopy (see Figs. 6.3 and 6.5).

6.5 Summary

The observations during the first four eROSITA all-sky surveys constitute by far the deepest X-ray data set of the whole Vela SNR acquired to date, and will likely stay so for the foreseeable future, providing enormous potential for scientific exploitation by the community after its public release. In this work, we have used this data set to explore the distribution and properties of shock-heated plasma and relativistic electrons throughout the entire remnant at unprecedented spatial and spectral resolution. Our analysis included the dissection of emission of Vela into broad and narrow energy bands for imaging, the spatially resolved spectroscopy of over 500 independent regions across the SNR, and the dedicated investigation of several prominent morphological structures, such as the Vela shrapnels.

We found that the energy-dependent morphology of Vela exhibits at least three separate components: the soft band is dominated by a diffuse shell and thick filaments, which are likely related to heated ISM behind the forward shock. At intermediate energies (i.e., starting at the O VIII lines at $0.65\,\mathrm{keV}$), thin radial structures become visible, which may be tracing the outward propagation of dense ejecta fragments. In the harder bands, above around $1.4\,\mathrm{keV}$, the emission is dominated by an extended nonthermal nebula, centered on the Vela pulsar.

Owing to the eight-degree angular extent of Vela, the foreground absorption toward the SNR was observed to be inhomogeneous and highly structured. Our study reinforces previous findings of a puzzling anticorrelation between X-ray absorption, which is strongest in the south, and optical extinction as well as neutral hydrogen column density, both of which are highest in the north of Vela. A possible, yet highly speculative, solution to this contradiction may lie in dust destruction in the SNR blast wave. This process may have disintegrated the local dust grains, responsible for optical extinction, while preserving the X-ray absorption. Alternatively, a clumpy ISM in the south, possibly traced also by Hα emission, may introduce additional absorption on top of a homogeneous background there.

The majority of shocked ISM in Vela was found to be relatively cold, at a median temperature of 0.19 keV, and to show no significant deviations from CIE. If this temperature corresponds to full equilibration of the blast wave's kinetic energy, the forward shock is presently expanding into the ISM at a velocity around $400\,\mathrm{km\,s^{-1}}$. However, close looks at the outermost region of the shell and at the bow shock of shrapnel D have revealed large hardness gradients, possibly due to recent shock-heating of the ISM. Dedicated observations of such regions could permit to trace in detail the transition between underionized and equilibrated plasma, and reconstruct the ionization history of material behind a rather slow shock.

We have encountered ample evidence for the presence of ejecta produced during the explosion. This includes dense ejecta fragments in the shrapnels, as well as several newly detected clumps protruding into the ISM in the south of Vela. Furthermore, significantly enhanced elemental abundances inside the shell indicate the presence of further ejecta-rich features, which are possibly located outside the shell but seen in projection. Interestingly, two regions in the vicinity of the central pulsar show similar signatures, which may point toward a recent crushing of ejecta and relativistic pulsar wind particles by secondary shocks.

The X-ray-detected ejecta signatures appear to be almost universally enriched in oxygen, neon, and magnesium, which are expected to originate from the outer ejecta layers of the progenitor star. Interestingly, in virtually all ejecta clumps, neon and magnesium were found to be strongly enhanced with respect to oxygen at about twice the solar ratio, which cannot be easily reconciled with expectations for supernova nucleosynthesis. Silicon ejecta are encountered in several clumps (e.g., shrapnel A) inside and outside the shell, but appear to be almost absent in a few cases (e.g., shrapnel D), indicating that the X-ray-bright ejecta trace a varying mix of hydrostatically and explosively synthesized elements released during the supernova. In contrast to the lighter elements, no secure signature of iron ejecta was found anywhere in the SNR.

Thanks to the improved sensitivity and spectral resolution of our data set with respect to *ROSAT*, we were able to isolate the nonthermal contribution to the X-ray emission, revealing the vast size of the plerion of the Vela pulsar. The extended synchrotron nebula, which extends up to three degrees or 14 pc from the pulsar, exceeds the PWN core by almost two orders of magnitude, both in total luminosity and size. Thus, the conversion efficiency of spin-down power into PWN X-ray luminosity is much larger than estimated for the core alone, at around 1.5×10^{-3}.

The suspected physical origin for this extended nonthermal emission lies in synchrotron emission of relativistic electrons from the pulsar wind. These particles have escaped confinement in the PWN core or the cocoon, and are likely transported via diffusion through the turbulent medium inside the SNR shell. In order to be able to reach such a large physical size within the electron radiative lifetime, a rather small magnetic field is required, around $3\,\mu\mathrm{G}$ if diffusion occurs at a similar rate as observed in gamma-ray pulsar halos. Observing nonthermal X-ray emission above 1 keV thus requires the escape of electrons up to 100 TeV into the diffuse nebula, unless the magnetic field is significantly stronger. We have tentatively observed and quantified the effect of radiative energy loss on the electron population, traced by the steepening of the nonthermal X-ray spectrum toward larger distances from the pulsar, which appears to be at a level consistent with the estimated physical parameters.

Generally, it appears puzzling that our X-ray nebula extends further away from the pulsar than the PWN seen at radio and GeV energies, which are generally expected to trace a less energetic, older electron population. Furthermore, up until now, observed emission in the VHE gamma-ray band is dominated by a comparatively small region around the cocoon, with no detected counterpart to our extended X-ray nebula, in particular in the north of the pulsar. This is potentially problematic since electrons at multi-TeV energies are required for the production of the detected X-ray synchrotron radiation, and should be visible in the TeV band via inverse Compton emission. Therefore, we hope that future observations of the Vela region in the VHE gamma-ray band will detect the suspected population of energetic electrons in the diffuse nebula, in order to independently confirm and complete the picture of one of the largest X-ray PWNe observed to date.

Chapter 7

Discussion

7.1 Exploring and exploiting the NS-SNR connection

In this thesis, I have presented detailed investigations of the kinematics and spectral properties of core-collapse SNRs and their central NSs. A recurring theme throughout this work is that of the connection between NS and their parent SNRs. Traditionally, NSs, specifically pulsars, and SNRs have been studied separately, due to inherently different detection channels, even though they are known to be produced by the same process. However, especially for young systems, the connection between the two can be both exploited to gain physical information, and explored, in order to learn about the physics of freshly born NSs as well as evolved PWNe.

In Chapter 3, we have measured the proper motion of the CCO RX J0822−4300 in Puppis A, which implies a physical kick velocity of around $(500 \pm 50)\,\mathrm{km\,s^{-1}}$ (assuming the most likely distance of 1.3 kpc, Reynoso et al. 2017), and tightly constrains the past trajectory of central NS. Using the fact that the SNR and NS must have been born at the same place and time, we combined our measurement with the expansion center of the SNR measured in the optical (Winkler et al. 1988), finding an approximate age of (4600±700) yr. This agrees within around 1σ with the value of (3700 ± 300) yr based on optical expansion alone. Thus, this exercise serves as an independent verification of the assumption that the optically emitting ejecta clumps can be treated as "bullets", meaning they are dense enough to move through the ISM without significant deceleration. Apart from extremely young SNRs or those with historical counterparts, this makes Puppis A one of the SNRs with the most reliable age estimate. As shown in Chapter 4, while current errors on the proper motion of the CCO in Cas A are still relatively large, a similar comparison would become possible with a future X-ray observation with high spatial resolution on the order of $0.5''$.

Inverting this approach, we have used the rather insignificant motion of the CCOs in RX J1713.7−3946 (G347.3−0.5) and G350.1−0.3 to constrain possible SN explosion sites in Chapter 4. By assuming these to be equal to the center of the SNR in combination with X-ray expansion measurements, we were able to estimate a stringent upper limit on the age of RX J1713.7−3946 of 1700 yr, and expose its likely asymmetric expansion behavior. Further, we have confirmed the results of Borkowski et al. (2020) with our independent methods, showing not only that G350.1−0.3 is rapidly expanding and is at most 600 − 700 yr old, but also verifying that its explosion site is in fact far off the apparent morphological center. Thus, by combining the motion of the CCO and the expansion of the SNR, we have demonstrated that this peculiar remnant in fact seems to be missing its "western half". Considering the explosion kinematics, we found that the lack of radio, mid-infrared, or X-ray emission west of the CCO (Gaensler & Slane 2006; Lovchinsky et al. 2011), likely requires the SNR's expansion into an extreme ISM gradient. It would be interesting to see if hydrodynamical simulations of the expansion of a blast wave into an inhomogeneous ISM are in fact capable of reproducing the extraordinary multi-wavelength morphology of G350.1−0.3.

The mechanism giving rise to the NS kick velocity in Puppis A is directly probed by the comparison performed in Chapter 5, where we combined our spectroscopic abundance measurements with the NS trajectory determined in Chapter 3. Using the fact that the SNR center is relatively accurately determined (Winkler et al. 1988), we were able to measure the ejection direction of intermediate-mass element ejecta, traced by the relative silicon abundance, quite precisely. This yielded an unexpectedly large deviation from the expected direction of ejection, which would be opposite the NS recoil direction, contradicting a previous study by Katsuda et al. (2018), in which no direct spectral fitting was performed. On one hand, this deviation may be explicable by observational biases in the X-ray regime. For instance, the observed ejecta centroid could be shifted if silicon ejecta clumps in part of the SNR are invisible either due to their rapid dissolution by the reverse shock, or because heating to X-ray-emitting temperatures has not yet occurred. On the other hand, our finding may also imply a significant physical misalignment between the NS recoil direction and the preferential ejection direction of the inner ejecta layers, which may serve as a constraint on the kick mechanism. In any case, applying our approach of combining directly measured NS kinematics with the SNR's elemental abundances constrained through complete spectral fits (rather than e.g., emission line strengths alone) to other systems would certainly be worthwhile, despite the large observational and analysis-related effort. In this way, the predictions of NS recoil in the gravitational tug-boat scenario (Scheck et al. 2006; Wongwathanarat et al. 2013) or alternative, more exotic kick mechanisms (e.g., Fuller et al. 2003; Fryer & Kusenko 2006) could be tested accurately.

A different flavor of the NS-SNR connection was probed by our observations in Chapter 6, namely the interaction between the relativistic particles originating from the wind of the Vela pulsar and the reverse shock of its host SNR. The processes shaping the X-ray bright elongated cocoon south of the pulsar can likely be understood in the following scenario (Blondin et al. 2001; Slane et al. 2018): Higher ISM densities in the northeast of the SNR cause a stronger deceleration of the forward shock there, and a faster return of the reverse shock to the SNR center. The asymmetric interaction between the PWN and the reverse shock leads to the compression of material into the elongated cocoon, in which a relic population of relativistic electrons is mixed with ejecta, consistent with the region's spectroscopic properties in X-rays.

Intriguingly, our observation has revealed the existence of fainter, but much more extended X-ray synchrotron emission beyond the cocoon and the PWN core, with an extent up to three degrees (or 14 pc) from the pulsar. A possible interpretation for this structure is that of an object transitioning from a compact PWN phase into an extended pulsar halo, similar to what is seen around middle-aged pulsars ($\sim 10^5 - 10^6$ yr) in the TeV band (Abeysekara et al. 2017; Giacinti et al. 2020). This is motivated by the fact that both Vela X and the population of pulsar halos are visible through the emission of escaping high-energy electrons, which are diffusing through the ambient medium at compatible, relatively small speeds ($D \sim 10^{27}\,\mathrm{cm^2\,s^{-1}}$). For Vela X, we observe X-ray synchrotron emission from particles diffusing through the material swept up by the SNR, whereas in pulsar halos, usually, inverse Compton radiation from electrons in the unperturbed ISM is detected. While this is certainly an exciting scenario, the interpretation of our extended X-ray nebula in the context of electrons escaped from the inner PWN is not unproblematic from a theoretical point of view. For instance, it has been suggested (Aharonian et al. 1997; Hinton et al. 2011) that the inner portions of young PWNe are advection-dominated and exhibit high magnetic fields, preventing the loss-free escape of high-energy particles. Furthermore, the existence of X-ray-bright synchrotron emission at large distances from the pulsar may require relatively high particle energies or magnetic fields in comparison with those measured in the outer cocoon (H. E. S. S. Collaboration et al. 2019). In any case, the presented findings on Vela X, possibly in combination with TeV observations, will likely constitute an important future data point for modelling the characteristics and evolution of PWNe, at the transition between young PWNe and older pulsar halos.

7.2 Challenges and future opportunities

With this thesis, I hope to have illustrated the potential of the direct X-ray measurements of NS and SNR kinematics, the composition and physical state of shocked gas in SNRs, and the properties of relativistic particles in evolved PWNe, with present-day instrumentation, especially the relatively recent *SRG*/eROSITA telescope. However, our data and analysis are not devoid of systematic errors and modelling biases affecting their interpretation. Here, I describe their nature and effects, along with possible future remedies for the underlying issues.

7.2.1 Astrometric measurements in X-rays

Virtually all our results in Chapters 3 and 4 concern the kinematics of CCOs and their parent SNRs, as measured through their motion in the plane of the sky between X-ray observations spaced by several years. The fundamental challenge we had to overcome was that of the pointing uncertainty of the *Chandra* telescope on the order of $0.8''$, which prevents the accurate localization of sources in an absolute reference frame. We tackled this issue by individually calibrating the reference frame of each observation using serendipitous X-ray-detected sources in the field of view with precise astrometric information available in the *Gaia* DR2 catalog. This however entails two subtle, interconnected issues: first, we assumed that the coordinate system can in fact be aligned to an absolute reference frame using a simple four-parameter linear transformation. The maximum permissible relative error introduced by nonlinear distortions is around $\sim 1/1000$, since individual sources were spaced on arcminute scales, and the precision ultimately reached was usually on the level of $0.1''$. Second, the number of astrometric calibration sources per observation was relatively small, on the order of $2-5$, which is insufficient to reveal possible deviations from the assumed linear mapping to the reference system. This lack of calibration sources, which introduces statistical and systematic errors, is caused by the relatively low sensi-

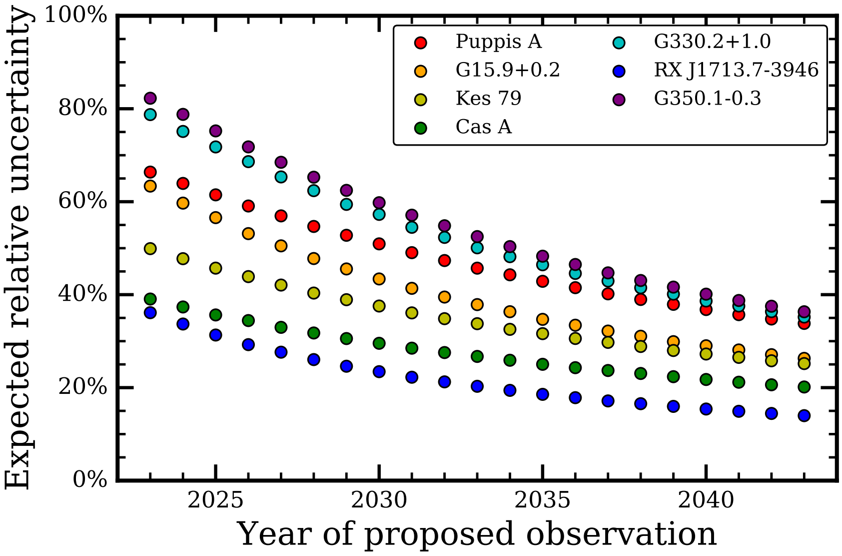

Figure 7.1: Prediction for proper motion measurements with future observations. For each of the seven CCOs discussed in Chapters 3 and 4, the expected reduction in uncertainty of the proper motion is indicated, assuming a future *Chandra* observation with an exposure of 50 ks at the given time. This figure was created by simulating a large number of possible measurements at the times of the actual and hypothetical observations, and assuming that their relative astrometric errors scale with the inverse square root of the exposure time.

tivity to off-axis point sources with the two imaging detectors aboard the *Chandra* observatory: the HRC exhibits relatively high intrinsic noise related to its microchannel plate design (Murray et al. 2000), whereas the ACIS suffers from a loss of response at low energies due to contamination of the detector, which is increasing over time (Marshall et al. 2004).

The impact of all these issues on measurements of the proper motion of NSs or the expansion of SNRs can be alleviated with one conceptually simple measure: using longer temporal baselines reduces both statistical and systematic errors on the proper motion as $\sim t^{-1}$, as the signature of a positional offset introduced by the constant NS velocity becomes more prominent over time, compared to the error sources. In Fig. 7.1, we illustrate the predicted relative reduction of the proper motion errors, for the seven CCOs investigated in Chapters 3 and 4, assuming the execution of a future *Chandra* follow-up observation. This demonstrates that the statistical errors could be reduced within the 2020s by at least a factor of two for four CCOs. This would be especially intriguing for the cases of Cas A and RX J1713.7−3946, where it would allow for much more precise comparisons with the SNRs' expansion behavior.

While *Chandra* is presently the only X-ray instrument feasible for astrometric measurements with the required accuracy, in the future, *Chandra* legacy data may be combined with observations from new planned missions. For instance, the proposed probe-class mission *Advanced X-ray Imaging Satellite* (*AXIS*, Mushotzky 2018) would be expected to provide a similar spatial resolution to *Chandra* at 0.4″, combined with a significantly higher effective area, which would yield reduced absolute positional errors compared to *Chandra*. In contrast, the Wide-

Field Imager (WFI) on the planned ESA L-Class mission *Advanced Telescope for High-Energy Astrophysics* (*ATHENA*, Nandra et al. 2013) is expected to have a spatial resolution of 5″, which is significantly worse than the on-axis resolution of 0.5″ of *Chandra*. However, the high effective area, wide field of view, and uniform PSF size across the detector will allow for a large number of reasonably well-localized sources across the field of view. In combination, this may allow reducing absolute astrometric uncertainties sufficiently to provide a meaningful extension of the available baseline for proper motion measurements, at least for diffuse emission (e.g., SNR shells), even in the absence of a telescope with *Chandra*-level resolution.[1]

7.2.2 Spectroscopy of thermally emitting shocked plasma

The thermal X-ray emission of collisionally ionized shocked gas in the SNRs Puppis A and Vela was our main analysis target in Chapters 5 and 6, with a heavy emphasis on the spatially resolved interpretation of the observed spectra. Generally, our approach would be to assume a spectral model with one or multiple thermal emission components from collisionally ionized plasma, modified by an assumed absorption model. This model was folded through the instrument's response and statistically compared to the observed spectra to infer the set of physical parameters, which optimally reproduces the data.

One important source of systematic uncertainties in this process can be ascribed to the relatively early state of the eROSITA mission, and the consequent imperfect calibration of the instrument's response. To some extent, this is a "luxury problem", as it concerns in particular spectra with large numbers of counts (such as in Chapter 5), where small uncertainties in the telescope's energy resolution or absolute energy scale can lead to large residuals in the resulting model fits. Fortunately, the calibration of the instrument's response, along with aspects such as its point spread function or vignetting, is continually being improved using ground-based and in-orbit calibration data (Dennerl et al. 2020).

In the case of line-dominated soft spectra, as in Puppis A and Vela, there are several unavoidable shortcomings also to the modelling approach itself, as parameter degeneracies tend to be inevitable: first, unless qualitative arguments based on physical reasoning or imaging are consulted, it is unclear how many model components are really necessary to reflect the suspected physically separate origins of the emission. For instance, in young SNRs, the observed emission could originate from both forward-shocked ISM and reverse-shocked ejecta. With the spectral resolution of present-day CCD detectors, it is hard to discriminate between these two scenarios. A closely related second point concerns the determination of physical densities and masses of the emitting material. Since the total X-ray emission measure characterizes the volume integral of the density squared, an assumption needs to be made about the distribution of plasma along the line of sight to estimate a volume filling factor (see Sect. 5.4.3). This is typically very hard to base on anything other than simple geometric models, such as the density structure behind a Sedov-Taylor blast wave (e.g., Cox & Anderson 1982), and naturally introduces large systematic

---

[1] In 2022, ESA announced that the predicted cost of the current *ATHENA* concept would exceed the allocated budget, such that the mission will likely have to be redesigned in order to meet the cost requirements. Thus, it is possible that the finalized mission will not quantitatively meet the specifics discussed here.

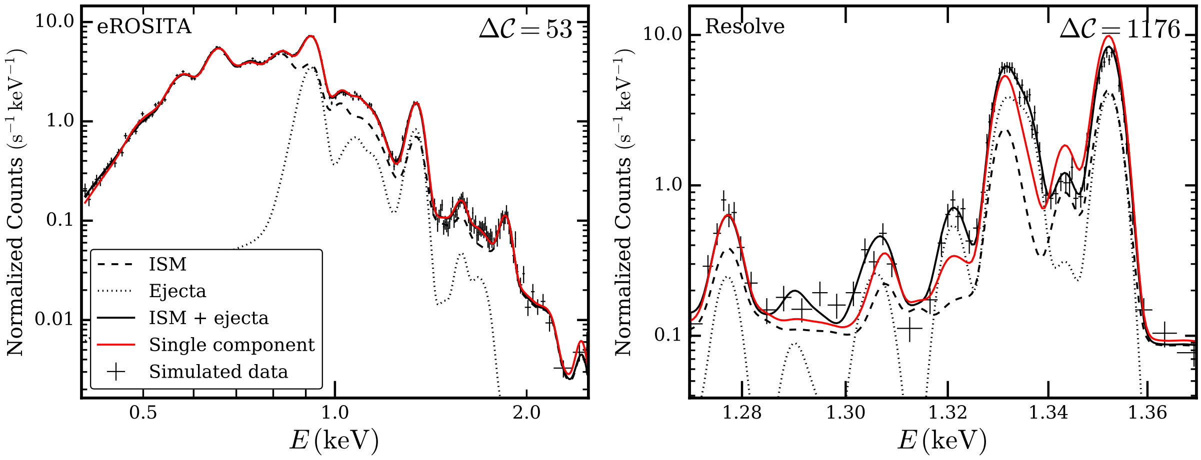

Figure 7.2: Modelling of a typical SNR spectrum with *SRG*/eROSITA (*left*) and *XRISM*/Resolve (*right*). I simulated a 50 ks observation[2]of a plausible spectrum (black line and points) of a compact region inside an SNR, in which the emission from shocked ISM (`vpshock`, $kT = 0.5\,\mathrm{keV}$, $\tau = 10^{11}\,\mathrm{cm}^{-3}\,\mathrm{s}$) with solar abundances is superimposed by the faint emission from a recently shocked clump (`vpshock`, $kT = 2.0\,\mathrm{keV}$, $\tau = 10^{10}\,\mathrm{cm}^{-3}\,\mathrm{s}$) of pure neon and magnesium ejecta. A single `vpshock` component (red) was fitted to the simulated data, to estimate the statistical evidence for the presence of two separate components, traced by the deterioration in fit statistic C shown in the upper right corner. For Resolve, I display only the region surrounding the Mg XI Heα triplet.

uncertainties in any mass or density estimate.

Furthermore, measuring fractional elemental abundances with respect to hydrogen is complicated by the fact that the ratio of line emission to the true bremsstrahlung continuum is often hard to infer in X-rays, as the contributions of weak unresolved lines may form a pseudo-continuum between the peaks of strong emission lines, in particular at $\lesssim 1\,\mathrm{keV}$. For ejecta-rich material, this is aggravated by the contribution of heavy elements to the bremsstrahlung continuum becoming significant, requiring the detection of radiative recombination continua to lift the model degeneracy between material enriched with ejecta and pure ejecta clumps (Greco et al. 2020).

Finally, absorption models such as `TBabs` (Wilms et al. 2000) are frequently treated as a "black box", with only a single free parameter, describing the column density of absorbing material. In reality however, the energy-dependent degree of absorption is sensitive also to the ionization state and elemental composition of the absorbing material, which may vary across different sight lines. Since CCD detectors do not have sufficient spectral resolution to resolve the strength of many absorption edges (Morrison & McCammon 1983) introduced by individual elements, it is possible that assuming a perfectly known composition of the intervening ISM introduces a hidden bias into the spectral analysis.

Several of these issues can likely be resolved or mitigated with the increased spectral resolution which will be introduced by microcalorimeter detectors in X-ray astronomy, such as the X-ray Integral Field Unit (X-IFU, Barret et al. 2018) planned for the *ATHENA* mission. Its projected typical spectral resolution of 2.5 eV across its entire spectral range would constitute a giant leap in spectral information content compared to CCD detectors such as those of eROSITA, which yield resolutions around 70 eV and 140 eV at energies of 1 keV and 6 keV, respectively (Predehl et al. 2021). Many years prior to the somewhat uncertain launch of *ATHENA*, the Resolve instrument on board the *X-ray Imaging and Spectroscopy Mission* (*XRISM*, XRISM Science Team 2020) will provide an impression of the capabilities of X-ray microcalorimeter detectors, at a predicted resolution of ~ 5 eV. Despite its very limited spatial resolution and field of view, it will allow investigating compact interesting regions inside SNRs at thus far unprecedented detail. Furthermore, the ambitious proposed probe-class mission *Line Emission Mapper* (*LEM*, Kraft et al. 2022) is aimed at resolving soft emission lines within $0.2 - 2.0$ keV at a comparable spectral resolution to X-IFU, but over a large field of view of $30'$ diameter and with decent spatial resolution $\sim 10''$. Despite its primary focus being extragalactic astrophysics, its target capabilities in spatially resolved mapping of thermal emission, if technically realizable, would make it very attractive for the analysis of moderately extended SNRs, such as Puppis A.

The ability of microcalorimeters to resolve and characterize individual emission lines will be extremely helpful in separating contributions of components of different temperatures or ionization states. Furthermore, the true bremsstrahlung continuum as well as radiative recombination features in SNR spectra could be distinguished from the emission lines, allowing a quantitative characterization of extremely ejecta-rich material (Greco et al. 2020). In Fig. 7.2, we compare the capabilities of present-day CCD detectors with those of microcalorimeters in this regard, using simulations of a plausible spectrum of shocked ISM mixed with a faint ejecta component. This clearly illustrates how the ability to resolve individual lines rather than blurred line complexes allows for disentangling different superimposed components with different ionization states with great significance, both visually and statistically. Similarly to emission lines, absorption edges would be resolvable for the relevant metals at mildly absorbed energies, yielding constraints on the composition of intervening ISM in a particular direction (similarly to Gatuzz & Churazov 2018). Finally, it is likely that the distribution of material along the line of sight in SNRs will always be dependent on assumptions. However, high resolution spectra would significantly improve our ability to detect line red-/blueshifts, since individual lines with precisely known intrinsic energies would become resolvable, rather than a single unresolved line complex with a centroid energy that is dependent on microphysics. Such line shifts would indicate motion of material along the line of sight, and thus also allow separating components of different velocities at the same location on the sky. This information could then be used indirectly to estimate where within the expanding SNR shell how much emitting material is located.

The fundamental downside of these future missions with microcalorimeter detectors is their extremely limited field of view, which means investigations of extended SNRs, such as Puppis A, will likely be limited to bright compact regions. The notable exception is the proposed *LEM* mission, which will however be limited to the soft X-ray band below 2.0 keV.

Aside from improvements in X-ray instrumentation, several methods have been developed by the scientific community which may prove useful in understanding both morphological and spectroscopic properties of the emission of SNRs, by combining spatial and spectral analysis tech-

---

[2] For eROSITA, I used a representative response including TMs 1–4 and 6, as for the observation of Puppis A in Chapter 5. For Resolve, I used the response files available at `https://xrism.isas.jaxa.jp/research/proposer/obsplan/response/index.html`.

niques. Examples include the smoothed particle inference technique (e.g., Siegel et al. 2020), which directly fits the data cube given by an X-ray event file with spatial-spectral models, or the generalized morphological component analysis (GMCA, Picquenot et al. 2019, 2021), which uses a blind source separation technique to decompose observed X-ray data sets into their morphological components and their associated spectra. In principle, such methods are ideally suited for analyzing X-ray data which encompass a large number of resolution elements in both the spectral and spatial domain, such as the eROSITA data of extended SNRs presented in this thesis. For instance, GMCA could be used to separate the ISM contributions to the X-ray emission of our SNRs from those from ejecta or a PWN, without having to assume explicit spectral or morphological models.

7.2.3 Characterizing the nonthermal emission from Vela X

One of the most intriguing findings in this thesis is the discovery and characterization of the extended X-ray synchrotron emission of Vela X in Chapter 6. The sensitivity of eROSITA above 1 keV, and especially its ability to quantify the contribution from thermal emission at higher energies, has allowed us to isolate the nonthermal contribution to the spectrum across the SNR, providing strong constraints on its integrated flux above 1 keV. One fundamental challenge in our observation, however, is that the photon index Γ of the nonthermal emission can only be constrained with large systematic and statistical uncertainty. This is caused by the short effective spectral baseline for its determination, due to the “contamination” by soft thermal emission from Vela at low energies, and the drop in eROSITA’s response above 2.3 keV. Even though we were able to obtain realistic spectral slopes in the PWN center and also found tentative evidence for a radial steepening of the spectrum, the quantitative reliability of our photon index measurements in the outer X-ray PWN is limited by their large statistical scatter.

An issue in the physical interpretation of the detected X-ray synchrotron emission is the fact that presently published emission profiles of Vela X at TeV energies do not exhibit a similarly large extent as we find in X-rays. At first sight, this appears problematic, as X-ray synchrotron emission necessarily originates from electrons with TeV energies (de Jager & Djannati-Ataï 2009), and these energetic electrons are expected to be visible at TeV energies via the emission of inverse Compton radiation in the presence of ambient radiation fields (Aharonian et al. 1997). It may however be possible that the presently published gamma-ray observations with H.E.S.S. (Abramowski et al. 2012; H. E. S. S. Collaboration et al. 2019) are not sensitive enough to detect the suspected faint diffuse counterpart to our X-ray PWN, since the angular scales involved are uncomfortably large for the instrument. Alternatively, one might invoke a possibly enhanced magnetic field to explain the relative brightness of the X-ray emission, since the integrated synchrotron and inverse Compton fluxes scale as $F_X/F_\gamma \propto B^2$ (Aharonian et al. 1997). This would however significantly reduce the lifetime of the electrons under radiative losses, requiring their very efficient outward diffusion to explain the observed extent of the X-ray PWN.

There are two possible remedies which could resolve the relatively unclear physical interpretation of the X-ray PWN: first, observing the extended nonthermal emission with an instrument with larger effective area at hard energies than eROSITA could provide the required sensitivity to robustly constrain the spectral index of synchrotron emission across the PWN. This would

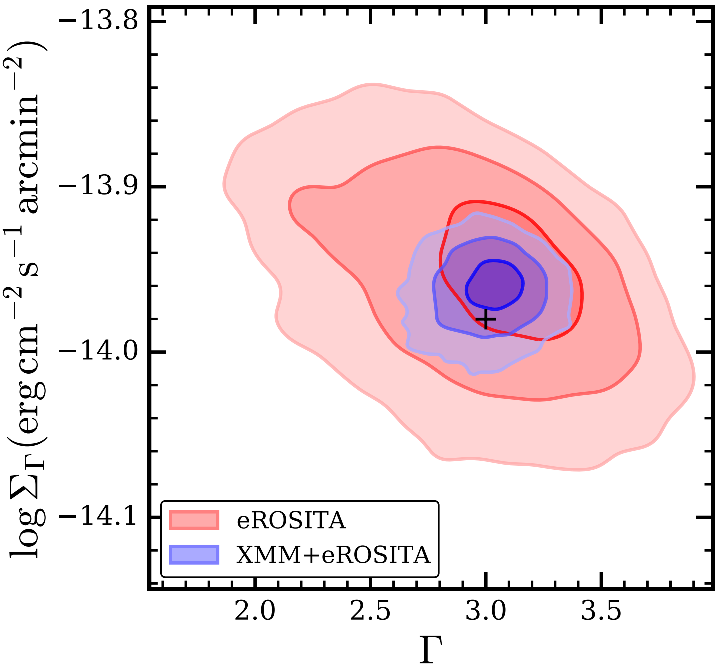

Figure 7.3: Constraining nonthermal X-ray emission from Vela X with *XMM-Newton*. I show a simulation of the constraints resulting from a short 2 ks exposure with EPIC-pn and MOS of a typical X-ray spectrum in the outer regions of the PWN with thermal contamination from the Vela SNR, with the input parameters marked by a black cross-hair. The joint $1\sigma, 2\sigma, 3\sigma$ constraints[3] on photon index Γ and nonthermal surface brightness Σ_Γ combining *XMM-Newton* and eRASS:4 data are compared to those from eRASS:4 alone, showing an error shrinkage by factors of 2.8 and 2.6, respectively.

allow characterizing the radial and azimuthal brightness profile of the extended PWN at a higher accuracy than possible here, and quantifying the level of synchrotron cooling experienced by the electrons diffusing away from their source. The best currently available instrument for this endeavor would likely be *XMM-Newton*, thanks to its large field of view and combined effective area, especially above 2 keV (Strüder et al. 2001; Turner et al. 2001). Keeping in mind that the eROSITA results presented in Chapter 6 are based on an average on-source time of only $\sim$ 1200 s, an array of shallow observations probing the PWN regions outside the cocoon could yield a significant improvement on our constraints, especially in combination with the existing observation mosaic presented by Slane et al. (2018). At a rough estimate, approximately 50 individual pointings would be needed to complete the *XMM-Newton* view of a two-degree radius around the pulsar. Thus, a mosaic observation with 100 ks usable science exposure, corresponding to an average of 2 ks per pointing, would be sufficient to obtain a $\sim$ 5 times deeper view of the emission of Vela X at 2.3 – 5.0 keV than available in eRASS:4, improving the constraints on both nonthermal flux and spectral index by a factor $\sim$ 2.5 (see Fig. 7.3). This does however not take into account the possible presence of background flares in *XMM-Newton* (e.g., Kuntz & Snowden 2008), which in practice might make a somewhat longer observation necessary. The cutoff energy of the synchrotron emission could be further probed by combining the existing data with observations in a harder X-ray band, for instance with the *NuStar* telescope (Harrison et al. 2013), or its proposed successor mission *HEX-P* (Madsen et al. 2019). However, this effort would only be feasible to carry out for a few pencil-beam observations, owing to the limited fields of view and sensitivities of the involved instruments. Similarly, deep pencil-beam observations of the outer regions of Vela X with a polarization-sensitive X-ray telescope, such as *IXPE* (Weisskopf et al. 2016), might be able to constrain the orientation and degree of turbulence of the magnetic field in which the observed X-ray synchrotron emission originates. This would be particularly interesting in comparison with the highly ordered toroidal magnetic field observed in the PWN core (Xie et al. 2022).

Even in the absence of improved X-ray constraints on the synchrotron emission, a detection and spatially resolved characterization of the corresponding emission at TeV energies would be extremely valuable, for several reasons. First, the combination of absolute flux levels from synchrotron and inverse Compton radiation would directly constrain the magnetic field strength (Aharonian et al. 1997), lifting the degeneracy between magnetic field and diffusion constant, which arises in the analysis of the X-ray flux and spectral index profiles alone (See Sect. 6.4.3). Second, the gamma-ray emission would provide constraints on the spectrum of the underlying electron distribution over a much wider spectral range, constraining not only the possible cutoff energy, but also indirectly the range of possible X-ray photon indices. It remains to be seen if these ambitious goals can be fulfilled with the joint analysis of X-ray data and deep gamma-ray observations by the H.E.S.S. telescope (Aharonian et al. 2006b), or if they will only become possible with future TeV observatories, such as the Cherenkov Telescope Array (CTA, Cherenkov Telescope Array Consortium et al. 2019). The CTA will provide better spatial resolution, higher sensitivity, and a larger field of view than present-day very-high-energy gamma-ray observatories. The latter two developments are likely to allow for a more efficient mapping of the degree-scale gamma-ray emission that we expect based on the detection of our very extended X-ray PWN.

---

[3] Note that, for a two-dimensional joint probability distribution, the "1σ contour" is expected to enclose the true parameter value only with 39.3% probability. Statistically speaking, it is thus unremarkable that one of the two displayed contours does not include the true value.

Appendix A

Contributions to scientific publications as a co-author

Hoinga - A supernova remnant discovered in the SRG/eROSITA all-sky survey eRASS1

Becker, W., Hurley-Walker, N., Weinberger, Ch., Nicastro, L., *Mayer, M. G. F.*, Merloni, A., Sanders, J. 2021, A&A, 648, A30
`https://ui.adsabs.harvard.edu/abs/2021A%26A...648A..30B/abstract`

This work reports on the discovery of the Hoinga SNR (G249.5+24.5), the largest SNR ever discovered in X-rays. Hoinga was detected as a diffuse, soft shell with a diameter around 4° in eRASS1, indicating a rather nearby, evolved SNR far off the Galactic plane. The analysis of archival radio observations revealed a nonthermal shell at the location of Hoinga, confirming its SNR nature beyond doubt. Assuming a Vela-like size for Hoinga implies a distance $\sim 500\,\mathrm{pc}$.

My contribution to this work consisted in the analysis of Hoinga's X-ray spectrum, finding that it is well represented by a low-temperature CIE plasma with $kT = 0.10 \pm 0.02\,\mathrm{keV}$. Further, the measured absorption column is significantly smaller than the integrated Galactic column density in the direction of the SNR, supporting the hypothesis that Hoinga is a rather local SNR.

The TRAPUM L-band survey for pulsars in Fermi-LAT gamma-ray sources

Clark, C. J., Breton, R. P., Barr, E. D., Burgay, M., Thongmeearkom, T., Nieder, L., Buchner, S., Stappers, B., Kramer, M., Becker, W., *Mayer, M.*, et al. 2023a, MNRAS, 519, 5590
`https://ui.adsabs.harvard.edu/abs/2023MNRAS.519.5590C/abstract`

This paper reports on the results of a radio survey searching for pulsars, carried out by the TRAPUM collaboration using the MeerKAT telescope. The survey was targeted at the error ellipses of unidentified gamma-ray sources detected by the *Fermi*-LAT instrument, which have a high likelihood of being pulsars. Nine new millisecond pulsars were found and characterized in this search, most of which are located in binary systems. Two of the detected systems were found to be so-called redbacks, binaries in which the pulsar wind continually ablates its companion main-sequence star, causing a large amount of diffuse intrabinary material.

Our (i.e., W. Becker and myself) contribution to this work was the discovery of the X-ray emission from one of the redbacks, PSR J1803−6707, in a search for X-ray counterparts to *Fermi*-LAT sources in eRASS1. The fact that this source is relatively X-ray bright compared to the gamma-regime may be attributable to excess emission from an intrabinary shock.

SRG/eROSITA and XMM-Newton observations of Vela Jr

Camilloni, F., Becker, W., Predehl, P., Dennerl, K., Freyberg, M., *Mayer, M. G. F.*, Sasaki, M. 2023, submitted to A&A

This work describes the first X-ray spectro-imaging analysis of the entirety of the nonthermal shell-type SNR "Vela Jr" (G266.2-1.2), using data from eRASS:4 and archival *XMM-Newton* observations. The spectral analysis of its emission is complicated by the bright, soft thermal emission from the overlapping Vela SNR. Through joint modelling of background and source contributions, we found that the emission from Vela Jr is likely mostly synchrotron radiation, indicating a tenuous ISM. Further, we derived a likely distance to Vela Jr above $\sim 750\,\mathrm{pc}$, based on arguments related to optical and X-ray absorption, and the shock velocity needed for particle acceleration.

Since the shell of Vela Jr overlaps with the area investigated in Chapter 6, I contributed a spatially resolved spectral analysis of Vela Jr employing a similar Voronoi binning approach as presented here. This analysis revealed intriguingly flat nonthermal emission in the southwest part of the SNR, possibly due to enhanced absorption by a localized molecular cloud. Further, I contributed to the implementation of advanced spectral fitting methods used thoughout the paper.

Appendix B

Observational details and fit results on the kinematics of CCOs and SNRs

Table B.1: Journal of *Chandra* observations used for our analysis

SNR	Detector	ObsID	Date	Exposure (s)	R.A.	Dec.	Roll
G15.9+0.2	ACIS-S	5530	2005 May 23	9062	274.7150	−14.9841	105.8
	ACIS-S	6288	2005 May 25	4896	274.7149	−14.9841	105.8
	ACIS-S	6289	2005 May 28	14 934	274.7150	−14.9841	105.8
	ACIS-S	16766	2015 Jul 30/31	92 021	274.7197	−15.0420	259.1
Kes 79	ACIS-I	1982	2001 Jul 31/Aug 01	29 571	283.1585	+0.6642	234.3
	ACIS-I	17453	2015 Jul 20	9647	283.1545	+0.6019	215.0
	ACIS-I	17659	2016 Feb 23	9926	283.1594	+0.6173	77.2
Cas A	HRC-I	1505	1999 Dec 19	48 720	350.8566	+58.8101	287.1
	HRC-I	12057	2009 Dec 13	10 465	350.8570	+58.8105	287.0
	HRC-I	12059	2009 Dec 15	12 294	350.8568	+58.8106	287.0
	HRC-I	12058	2009 Dec 16	8865	350.8571	+58.8105	287.0
	HRC-I	11240	2009 Dec 20	12 400	350.8568	+58.8106	287.0
G330.2+1.0	ACIS-I	6687	2006 May 21/22	49 977	240.2458	−51.5714	3.3
	ACIS-I	19163	2017 May 02/03	74 143	240.2304	−51.5508	30.2
	ACIS-I	20068	2017 May 05/06	74 140	240.2315	−51.5497	30.2
RX J1713.7−3946	ACIS-I	5559	2005 Apr 19	9645	258.3739	−39.8275	72.5
	HRC-I	13284	2013 Mar 08/09	37 018	258.3724	−39.8271	85.8
G350.1−0.3	ACIS-S	10102	2009 May 21/22	82 976	260.2653	−37.4388	57.9
	ACIS-S	20312	2018 Jul 02	40 579	260.2711	−37.4497	296.2
	ACIS-S	20313	2018 Jul 04	19 840	260.2702	−37.4491	296.2
	ACIS-S	21120	2018 Jul 05	37 619	260.2707	−37.4494	296.2
	ACIS-S	21119	2018 Jul 07/08	48 289	260.2709	−37.4496	296.2
	ACIS-S	21118	2018 Jul 08/09	42 907	260.2703	−37.4492	296.2

Notes. The column “Exposure” lists the effective unvignetted exposure time of each observation, referring to the sum of all good time intervals, corrected for the dead time fraction of the specific detector. The columns “R.A.” and “Dec.” specify the right ascension and declination of the telescope pointing, given in decimal degrees, respectively. The column “Roll” describes the telescope roll angle west of north, given in degrees.

Table B.2: Overview of astrometric calibrator objects for all targets.

SNR	Designation		Position (Epoch 2015.5)		Proper Motion		Used[a]
	Number	*Gaia* DR2 Source ID	R.A. (ICRS) (h:m:s)	Dec. (ICRS) (d:m:s)	μ_α ($\mathrm{mas\ yr^{-1}}$)	μ_δ ($\mathrm{mas\ yr^{-1}}$)	
G15.9+0.2	1	4146177809117217024	18:19:04.1362(0)	−15:01:17.914(0)	−2.99 ± 0.05	−11.13 ± 0.05	Y
	2	4146176679563359744	18:18:40.8608(0)	−15:02:50.272(0)	−4.74 ± 0.12	−11.63 ± 0.10	Y
	3	4146177396800326016	18:18:59.2871(0)	−15:03:02.877(0)	0.58 ± 0.36	−0.19 ± 0.34	N
	4	4146178977348360192	18:18:50.9880(0)	−14:58:42.607(0)	0.01 ± 0.09	−5.59 ± 0.08	Y
	5	4146179114787324800	18:18:56.0305(0)	−14:57:29.414(0)	2.16 ± 0.16	0.31 ± 0.15	N
Kes 79	1	4266507644409347712	18:52:45.3536(0)	+00:37:33.883(0)	2.71 ± 0.34	−5.48 ± 0.37	Y
	2	4266506952913023488	18:52:13.0122(0)	+00:37:37.579(0)	−2.48 ± 0.58	−4.97 ± 0.50	Y
	3	4266508464741698816	18:52:48.6778(0)	+00:40:38.852(0)	−1.11 ± 0.45	−2.45 ± 0.41	Y
Cas A	1	2010478284367990016	23:22:51.6664(0)	+58:50:19.792(0)	15.64 ± 0.09	0.30 ± 0.08	Y
	2	2010477356655102592	23:23:14.1850(0)	+58:46:55.429(0)	13.78 ± 0.04	−0.16 ± 0.04	Y
	3	2010477253575869184	23:23:04.7862(0)	+58:48:00.022(0)	−1.22 ± 0.03	−1.53 ± 0.03	N
G330.2+1.0	1	5981660915203664384	16:01:13.9674(0)	−51:31:37.490(0)	−5.01 ± 0.23	−5.03 ± 0.15	Y
	2	5981660743404965120	16:01:07.6243(0)	−51:33:34.908(0)	10.35 ± 0.18	9.56 ± 0.13	Y
	3	5981637791098864128	16:00:39.0792(0)	−51:34:34.539(0)	−9.87 ± 0.07	−10.89 ± 0.05	N
	4	5981640814756329088	16:00:29.9561(0)	−51:33:43.894(0)	−6.15 ± 0.23	−7.64 ± 0.17	Y
	5	5981636932105333632	16:00:31.8387(0)	−51:39:05.986(0)	0.49 ± 0.08	−1.31 ± 0.06	Y
	6	5981661774197144448	16:01:02.8106(0)	−51:29:54.717(0)	−18.74 ± 0.30	−19.66 ± 0.23	Y
RX J1713.7−3946	1	5972217652195355392	17:13:47.7129(0)	−39:52:51.150(0)	−2.82 ± 0.07	−8.38 ± 0.05	N
	2	5972124679069981440	17:13:31.7884(0)	−39:53:43.687(0)	0.37 ± 0.09	−1.99 ± 0.06	Y[c]
	3	5972266138099405696	17:13:37.3502(15)	−39:46:04.196(20)	...[b]	...[b]	Y[c]
G350.1−0.3	1	5972890935584476288	17:20:56.1029(0)	−37:27:34.016(0)	−3.07 ± 0.18	−4.57 ± 0.14	Y
	2	5972880112266871936	17:21:21.3165(0)	−37:26:46.025(0)	−2.48 ± 0.17	−1.02 ± 0.12	Y
	3	5972880558943480448	17:21:13.1090(0)	−37:26:11.996(0)	1.06 ± 0.10	1.50 ± 0.07	N
	4	5972892516132452608	17:20:59.2872(0)	−37:25:01.514(0)	2.41 ± 0.37	2.25 ± 0.25	N

Notes. We display the astrometric solutions for all our initially selected reference sources as listed in the *Gaia* DR2 catalog (Gaia Collaboration et al. 2018). We state the rounded 1σ uncertainties of Right Ascension and Declination at the reference epoch in parentheses to illustrate their negligible character for almost all objects. The proper motion components along the Right Ascension and Declination axes are labeled as μ_α and μ_δ, respectively.

[a] The column "Used" indicates whether an individual source was included in the final proper motion analysis or excluded for a specific reason (see subsections on the individual objects in Sect. 4.4).

[b] No proper motion information in *Gaia* DR2.

[c] For these two sources, the absolute *Gaia* positions were not used in our analysis since we considered their identification unreliable. Instead, the individual coordinate frames were directly registered with each other based on relative positions alone (see Sect. 4.4.5 for details).

Table B.3: Full results of proper motion measurements and astrometric calibration of the individual observations for the six CCOs targeted in this work.

SNR	CCO	μ_α (mas yr^{-1})	μ_δ (mas yr^{-1})	α_0 (arcsec)	δ_0 (arcsec)
G15.9+0.2	CXOU J181852.0−150213	$-17.29^{+11.65}_{-12.00}$	$-4.38^{+9.51}_{-9.54}$	$0.110^{+0.052}_{-0.053}$	$0.060^{+0.042}_{-0.043}$
Kes 79	CXOU J185238.6+004020	$-2.59^{+10.49}_{-10.37}$	$-2.72^{+12.03}_{-11.65}$	$-1.089^{+0.123}_{-0.120}$	$-0.244^{+0.147}_{-0.137}$
Cas A	CXOU J232327.9+584842	$17.58^{+12.78}_{-12.62}$	$-35.23^{+17.33}_{-17.37}$	$0.060^{+0.103}_{-0.104}$	$-0.346^{+0.134}_{-0.134}$
G330.2+1.0	CXOU J160103.1−513353	$-2.70^{+5.30}_{-5.44}$	$-6.39^{+5.47}_{-5.43}$	$-0.444^{+0.037}_{-0.036}$	$-0.821^{+0.037}_{-0.037}$
RX J1713.7−3946	1WGA J1713.4−3949	$-3.90^{+24.43}_{-23.92}$	$-19.63^{+28.67}_{-28.93}$	...[a]	...[a]
G350.1−0.3	XMMU J172054.5−372652	$-3.06^{+7.89}_{-7.98}$	$17.42^{+9.41}_{-9.42}$	$-1.007^{+0.038}_{-0.037}$	$-0.847^{+0.032}_{-0.032}$
SNR	Observation ID	Δx_i (arcsec)	Δy_i (arcsec)	$r_i - 1$ (10^{-4})	θ_i (10^{-4} rad)
G15.9+0.2	5530	$-0.010^{+0.105}_{-0.102}$	$0.153^{+0.086}_{-0.087}$	$5.7^{+5.1}_{-5.0}$	$6.6^{+5.2}_{-4.9}$
	6288	$-0.066^{+0.143}_{-0.142}$	$0.129^{+0.112}_{-0.117}$	$-9.7^{+7.4}_{-7.2}$	$6.1^{+7.3}_{-7.4}$
	6289	$0.171^{+0.096}_{-0.097}$	$0.176^{+0.081}_{-0.081}$	$2.3^{+4.7}_{-4.8}$	$5.4^{+5.0}_{-5.1}$
	16766	$0.020^{+0.047}_{-0.047}$	$-0.260^{+0.033}_{-0.033}$	$5.8^{+2.5}_{-2.5}$	$-2.5^{+1.7}_{-1.8}$
Kes 79	17453	$0.128^{+0.115}_{-0.117}$	$-0.323^{+0.131}_{-0.137}$	$1.2^{+6.4}_{-7.1}$	$-4.5^{+6.1}_{-5.7}$
	17659	$0.548^{+0.121}_{-0.124}$	$-0.156^{+0.136}_{-0.151}$	$-2.5^{+6.5}_{-7.2}$	$-6.0^{+8.2}_{-11.0}$
	1982	$-0.164^{+0.085}_{-0.091}$	$0.026^{+0.093}_{-0.097}$	$2.5^{+4.1}_{-5.0}$	$-8.2^{+3.5}_{-3.5}$
Cas A	1505	$-0.243^{+0.071}_{-0.072}$	$0.056^{+0.108}_{-0.110}$	$0.6^{+4.1}_{-4.2}$	$-10.7^{+5.0}_{-4.9}$
	Late[b]	$-0.526^{+0.104}_{-0.102}$	$0.267^{+0.134}_{-0.134}$	$10.9^{+4.7}_{-4.8}$	$-15.9^{+5.9}_{-5.9}$
G330.2+1.0	19163	$-0.164^{+0.035}_{-0.036}$	$0.606^{+0.036}_{-0.036}$	$2.4^{+2.2}_{-2.2}$	$-1.5^{+2.1}_{-2.1}$
	20068	$-0.104^{+0.036}_{-0.037}$	$0.216^{+0.036}_{-0.036}$	$2.0^{+1.8}_{-1.8}$	$-4.1^{+2.0}_{-2.0}$
	6687	$0.027^{+0.044}_{-0.043}$	$0.221^{+0.043}_{-0.043}$	$1.4^{+1.9}_{-1.9}$	$-2.0^{+1.6}_{-1.6}$
RX J1713.7−3946	5559 − 13284[a]	$-0.292^{+0.189}_{-0.192}$	$-0.255^{+0.225}_{-0.228}$	$0.8^{+8.0}_{-8.1}$	$-4.9^{+8.9}_{-9.2}$
G350.1−0.3	10102	$-0.072^{+0.061}_{-0.062}$	$0.568^{+0.077}_{-0.079}$	$0.9^{+3.7}_{-3.7}$	$4.4^{+3.3}_{-3.3}$
	20312	$0.423^{+0.040}_{-0.040}$	$0.094^{+0.035}_{-0.034}$	$-1.4^{+4.7}_{-4.7}$	$-15.3^{+5.3}_{-5.4}$
	20313	$0.438^{+0.042}_{-0.042}$	$0.087^{+0.036}_{-0.036}$	$2.0^{+6.2}_{-6.5}$	$-21.5^{+9.8}_{-10.1}$
	21118	$0.343^{+0.036}_{-0.036}$	$0.098^{+0.031}_{-0.032}$	$4.0^{+3.0}_{-3.1}$	$-4.4^{+4.6}_{-4.7}$
	21119	$0.531^{+0.039}_{-0.039}$	$0.269^{+0.033}_{-0.034}$	$9.1^{+3.6}_{-3.7}$	$1.3^{+4.5}_{-4.4}$
	21120	$0.449^{+0.040}_{-0.040}$	$0.158^{+0.034}_{-0.034}$	$7.9^{+3.7}_{-3.7}$	$-0.7^{+4.6}_{-4.7}$

Notes. The upper part of the table displays the best-fit astrometric solution for each CCO – proper motion and position at a reference time – as resulting from our fit. In the lower part, we show for all systems the optimal determined astrometric calibration parameters – describing translation, stretch and rotation of the coordinate system – for each individual observation.

[a] For RX J1713.7−3946, only relative astrometric analysis was performed, via direct subtraction of positions from the two epochs. Therefore, our fit provides no absolute source positions.

[b] For Cas A, the closely spaced individual observations (IDs 11240, 12057, 12058, 12059) were merged to create a single late-time data set.

The tangent points that we used for conversion of celestial coordinates to a (right-handed) local Cartesian coordinate system and as center of scaling and rotation, were ($18^h18^m52\overset{s}{.}080$, $-15^\circ02'14\overset{''}{.}11$) for G15.9+0.2, ($18^h52^m38\overset{s}{.}4888$, $+00^\circ40'19\overset{''}{.}848$) for Kes 79, ($23^h23^m27\overset{s}{.}940$, $58^\circ48'42\overset{''}{.}40$) for Cas A, ($16^h01^m03\overset{s}{.}100$, $-51^\circ33'53\overset{''}{.}00$) for G330.2+1.0, ($17^h13^m28\overset{s}{.}320$, $-39^\circ49'53\overset{''}{.}34$) for RX J1713.7−3946, and ($17^h20^m54\overset{s}{.}500$, $-37^\circ26'52\overset{''}{.}00$) for G350.1−0.3.

Table B.4: Results of expansion measurements in individual regions for G15.9+0.2, Kes 79, and G350.1−0.3

SNR	Region	ϑ (arcsec)	μ_{exp} (mas yr^{-1})	τ^{-1} (10^{-4} yr^{-1})	τ (yr)
G15.9+0.2	A	152^{+15}_{-15}	57^{+61}_{-70}	$3.66^{+4.38}_{-4.83}$	...
	B	134^{+15}_{-15}	80^{+39}_{-37}	$5.99^{+3.30}_{-3.15}$	...
	C	134^{+15}_{-15}	-16^{+59}_{-63}	$-1.23^{+4.68}_{-5.13}$	...
	D	144^{+15}_{-15}	106^{+63}_{-59}	$7.44^{+4.71}_{-4.29}$	...
	E	156^{+15}_{-15}	3^{+84}_{-62}	$0.24^{+5.60}_{-4.21}$	...
	F	139^{+15}_{-15}	138^{+75}_{-74}	$9.97^{+5.68}_{-5.55}$	...
	G	140^{+15}_{-15}	-25^{+230}_{-183}	$-1.58^{+16.11}_{-13.55}$	...
Kes 79	A	248^{+53}_{-52}	105^{+24}_{-23}	$4.24^{+1.74}_{-1.34}$	...
	B	263^{+52}_{-51}	-21^{+26}_{-28}	$-0.80^{+1.20}_{-1.30}$	...
	C	166^{+52}_{-50}	73^{+81}_{-72}	$4.41^{+5.73}_{-4.50}$	...
	D	178^{+53}_{-52}	-1^{+54}_{-55}	$-0.08^{+3.38}_{-3.38}$	...
	E	126^{+57}_{-52}	-31^{+71}_{-66}	$-2.36^{+5.80}_{-6.36}$	...
	F	205^{+54}_{-54}	17^{+168}_{-255}	$0.80^{+8.61}_{-12.55}$	...
	G	153^{+51}_{-50}	208^{+143}_{-157}	$13.05^{+10.06}_{-10.13}$	...
	H	161^{+56}_{-55}	46^{+38}_{-38}	$2.85^{+3.36}_{-2.60}$	...
G350.1−0.3	A	190^{+6}_{-6}	253^{+58}_{-65}	$13.39^{+3.07}_{-3.59}$	745^{+263}_{-138}
	B	182^{+6}_{-6}	257^{+9}_{-9}	$14.09^{+0.89}_{-0.87}$	710^{+47}_{-42}
	C	177^{+6}_{-6}	226^{+13}_{-12}	$12.78^{+1.03}_{-0.99}$	782^{+66}_{-58}
	D	166^{+6}_{-6}	174^{+9}_{-11}	$10.51^{+0.94}_{-0.94}$	952^{+94}_{-78}
	E	155^{+6}_{-6}	268^{+17}_{-17}	$17.28^{+1.46}_{-1.44}$	579^{+52}_{-45}
	F	137^{+6}_{-6}	193^{+7}_{-8}	$14.04^{+1.14}_{-1.11}$	712^{+61}_{-54}
	G	134^{+5}_{-6}	140^{+9}_{-9}	$10.47^{+1.14}_{-1.11}$	955^{+113}_{-94}
	H	120^{+6}_{-6}	128^{+14}_{-15}	$10.75^{+1.64}_{-1.59}$	930^{+161}_{-123}
	I	150^{+5}_{-6}	146^{+7}_{-7}	$9.72^{+0.96}_{-0.93}$	1029^{+109}_{-92}
	J	153^{+5}_{-6}	137^{+4}_{-4}	$9.01^{+0.85}_{-0.83}$	1110^{+112}_{-95}
	K	157^{+5}_{-6}	180^{+6}_{-7}	$11.47^{+0.92}_{-0.89}$	872^{+74}_{-65}
	L	159^{+5}_{-6}	180^{+8}_{-7}	$11.30^{+0.93}_{-0.90}$	885^{+77}_{-67}
	M	87^{+6}_{-6}	123^{+37}_{-38}	$14.13^{+4.77}_{-4.64}$	706^{+336}_{-177}
	N	118^{+6}_{-6}	100^{+44}_{-45}	$8.40^{+3.82}_{-3.92}$	1154^{+772}_{-345}
	O	88^{+6}_{-6}	71^{+36}_{-36}	$8.11^{+4.29}_{-4.31}$	1172^{+860}_{-381}
	P	64^{+6}_{-6}	84^{+27}_{-26}	$13.13^{+4.76}_{-4.46}$	760^{+382}_{-201}
	Q	77^{+6}_{-6}	59^{+31}_{-30}	$7.73^{+4.24}_{-4.37}$	1211^{+943}_{-395}
	R	61^{+6}_{-6}	51^{+23}_{-24}	$8.26^{+4.35}_{-4.32}$	1157^{+854}_{-378}

Notes. The table shows the quantities underlying Figs. 4.6, 4.9 and 4.15. To ease comparison between the systems, we provide the resulting constraints on the expansion rate τ^{-1} for all three SNRs. In addition, we provide its inverse, the free expansion age τ, only for G350.1−0.3 since the expansion rate has to be significantly different from zero to obtain a sensible value for individual regions.

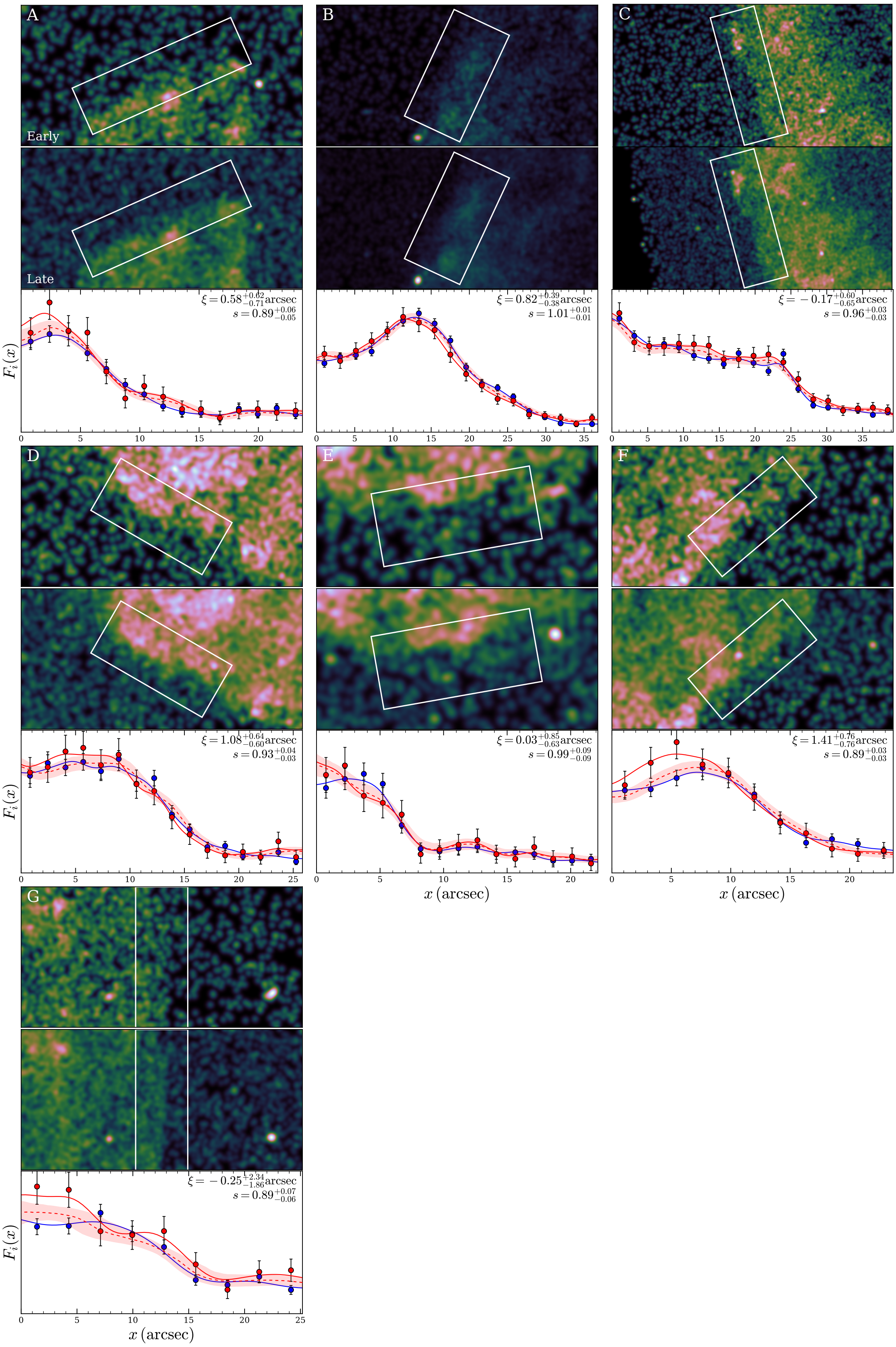

Figure B.1: Direct comparison of flux profiles in different regions of G15.9+0.2. The layout of each subpanel is identical to Fig. 4.3, with the letter in the upper left corner corresponding to the respective region.

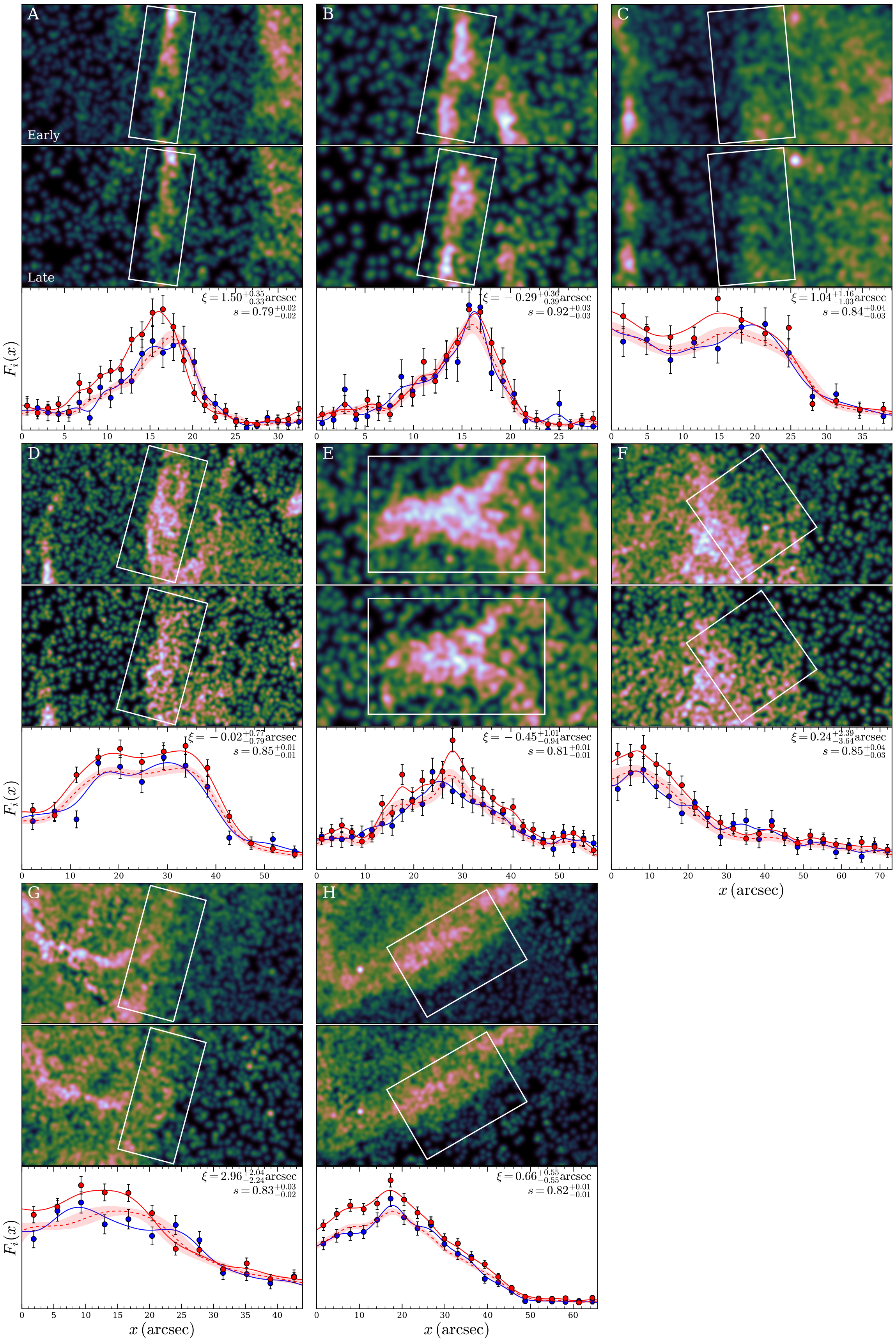

Figure B.2: Direct comparison of flux profiles in different regions of Kes 79 (as in Fig. B.1).

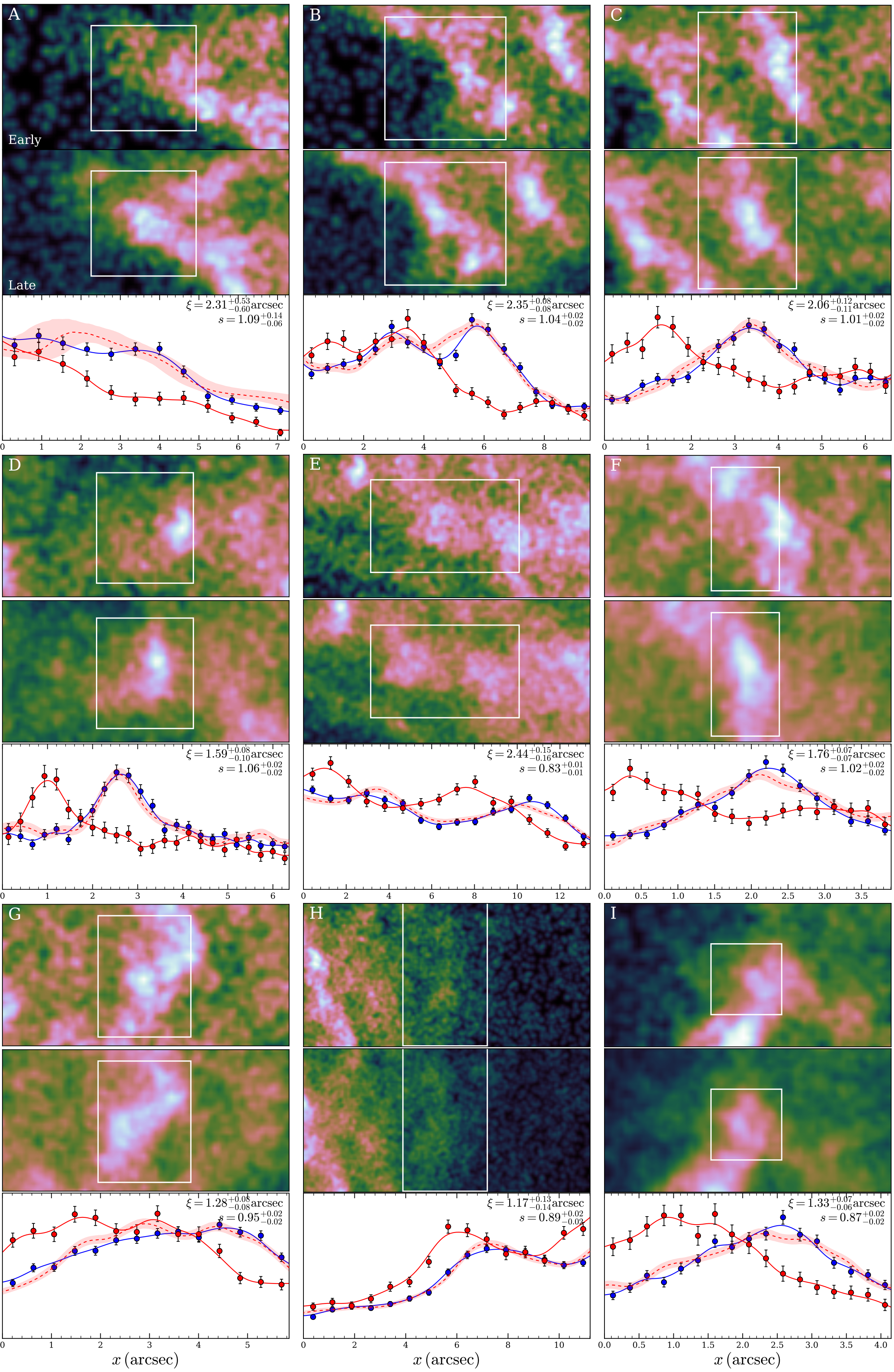

Figure B.3: Direct comparison of flux profiles of G350.1−0.3 (as in Fig. B.1).

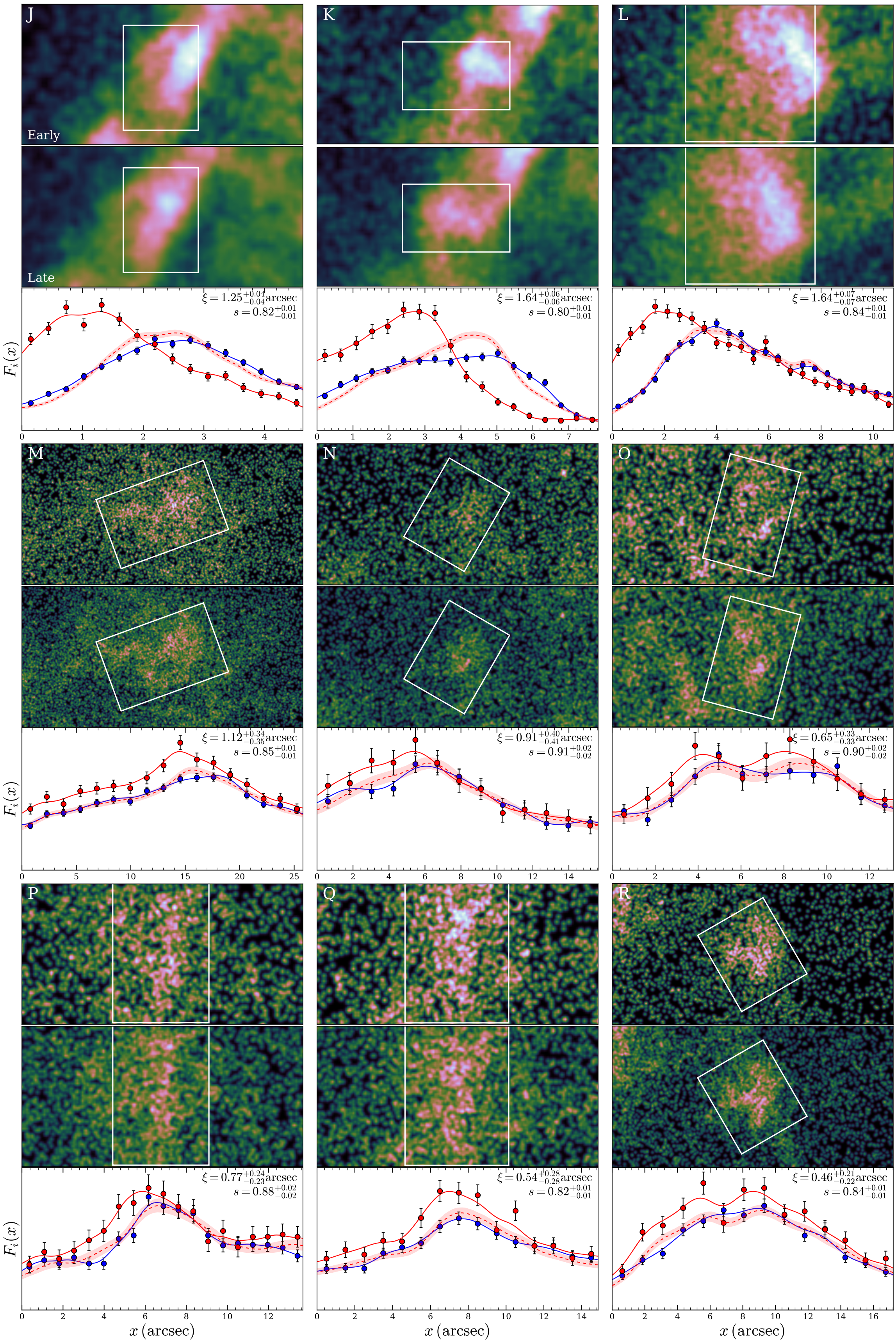

Figure B.3: Continued

Appendix C

Parameter distributions from spectral fitting of Puppis A

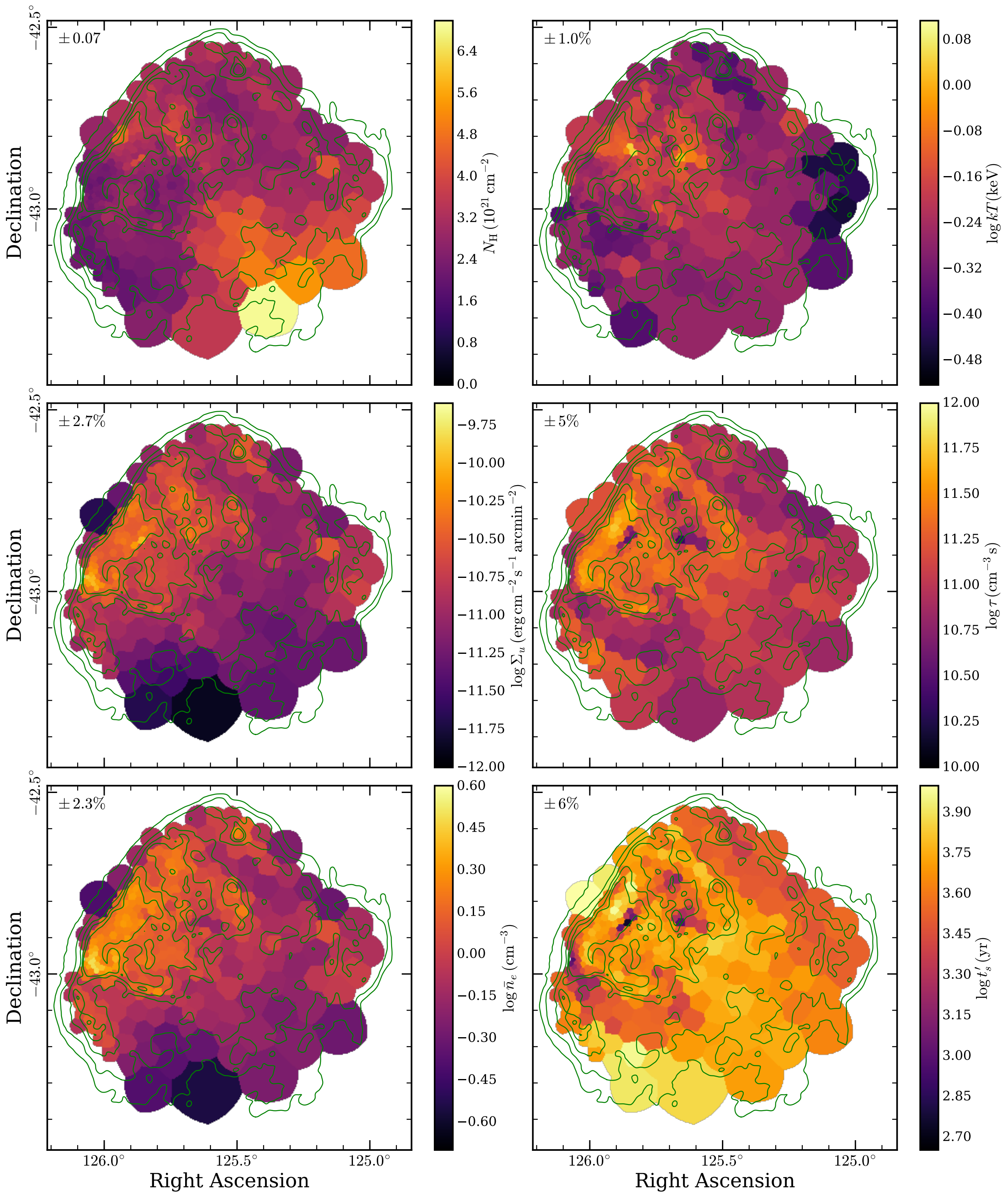

Figure C.1: Same as Fig. 5.6, but with coarser binning due to a larger threshold of $S/N = 300$.

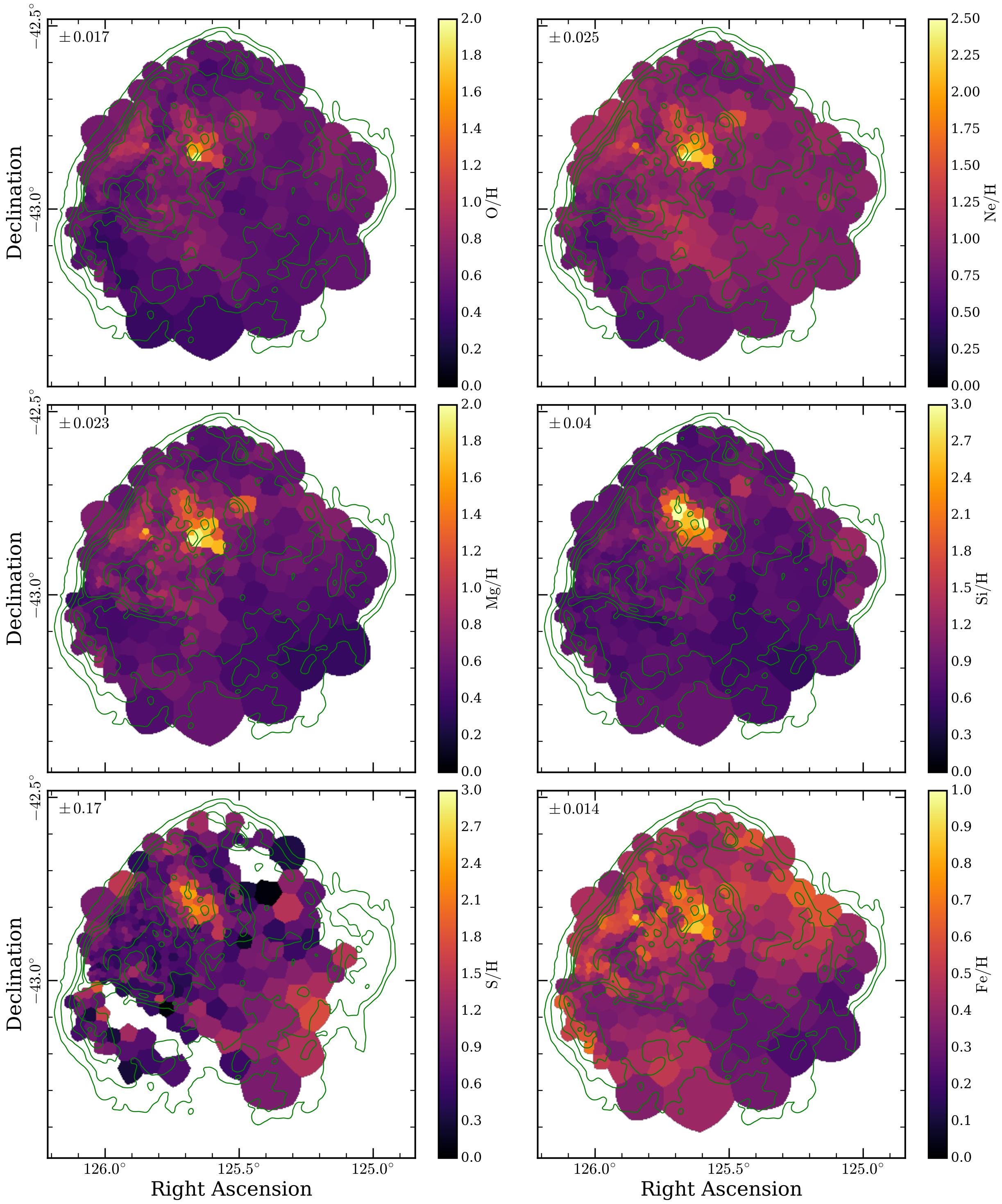

Figure C.1: Continued. In the map of S/H, all bins with an absolute error larger than 0.4 were masked.

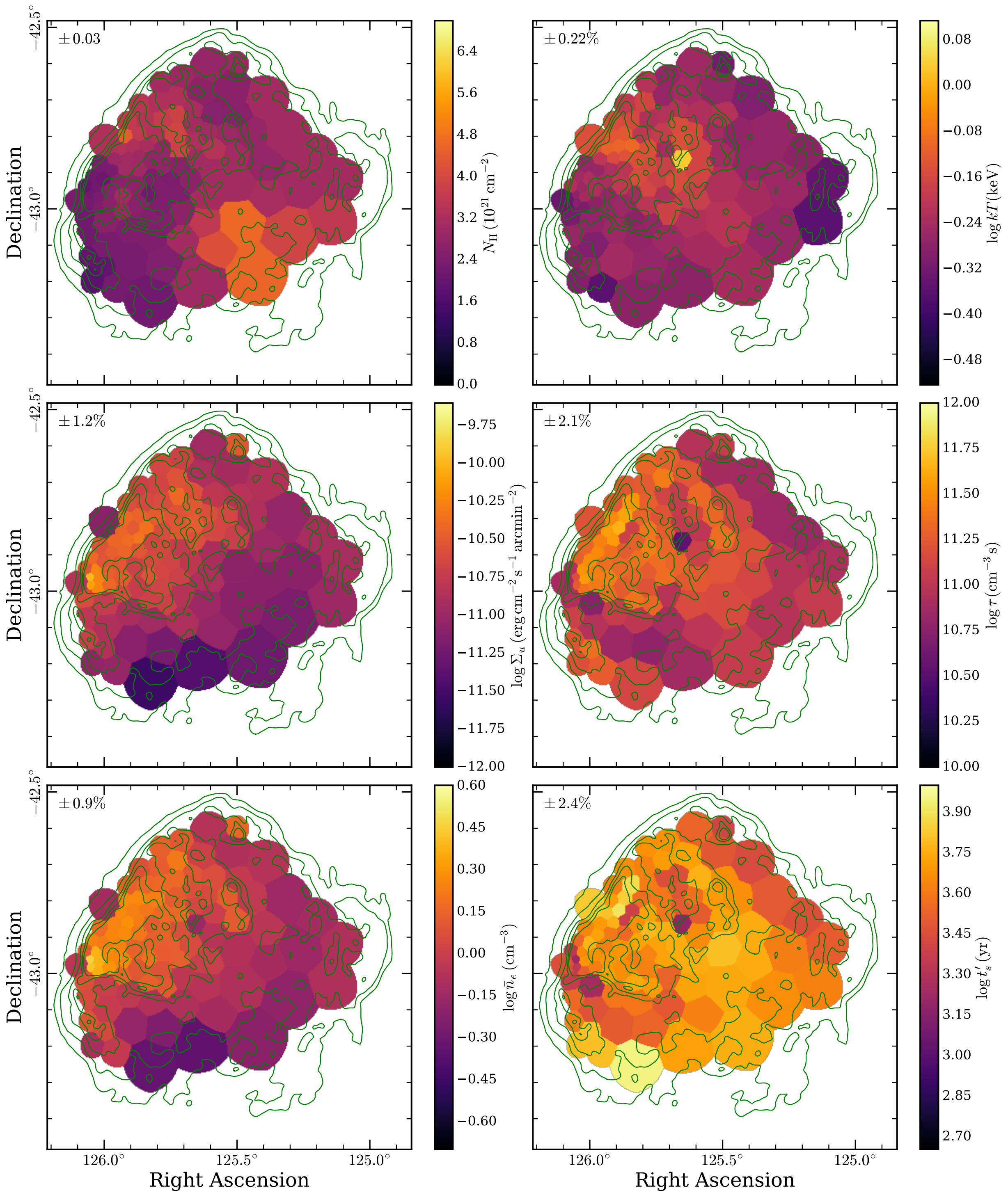

Figure C.2: Same as Fig. 5.6, but with coarser binning due to a larger threshold of $S/N = 500$.

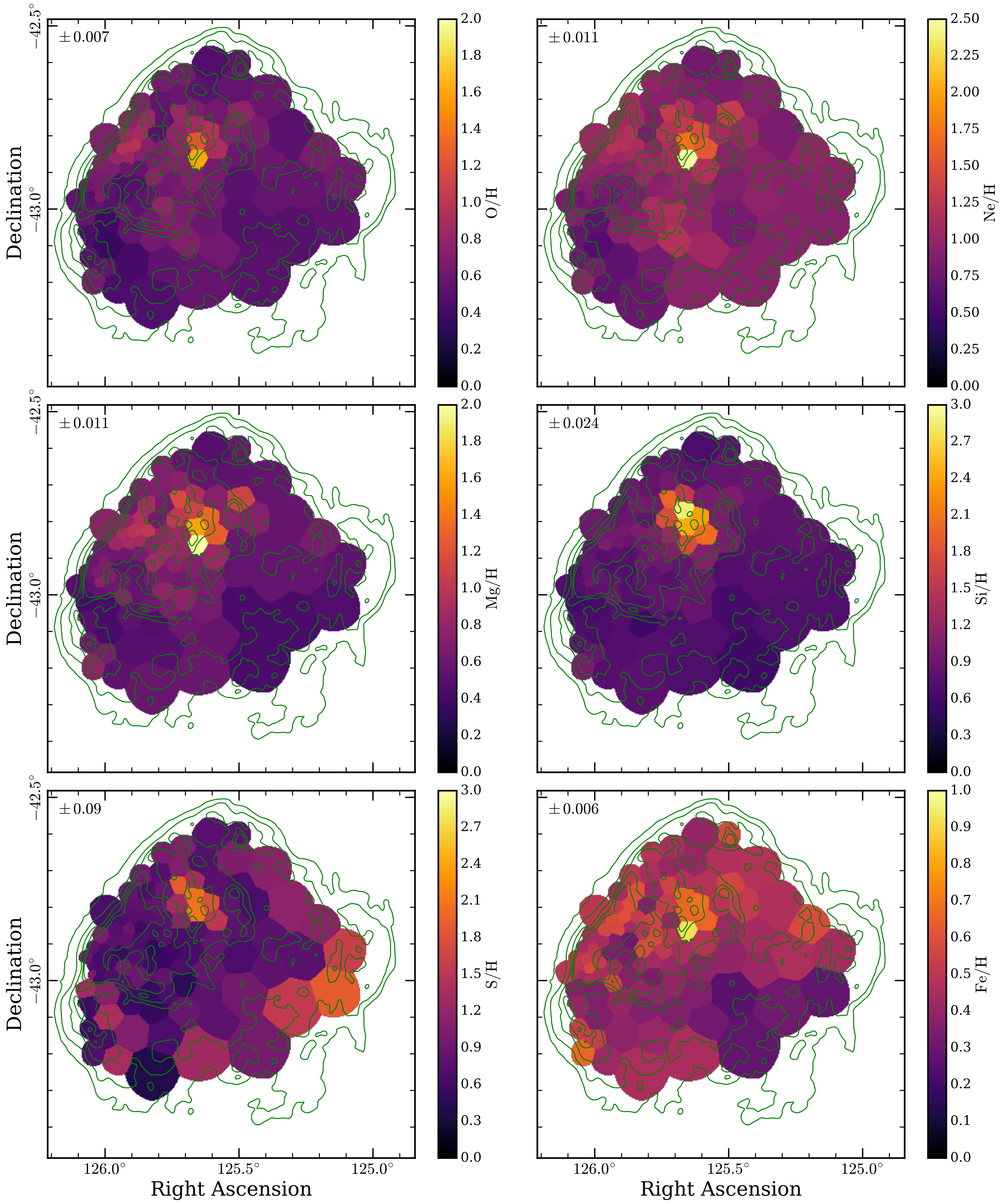

Figure C.2: Continued.

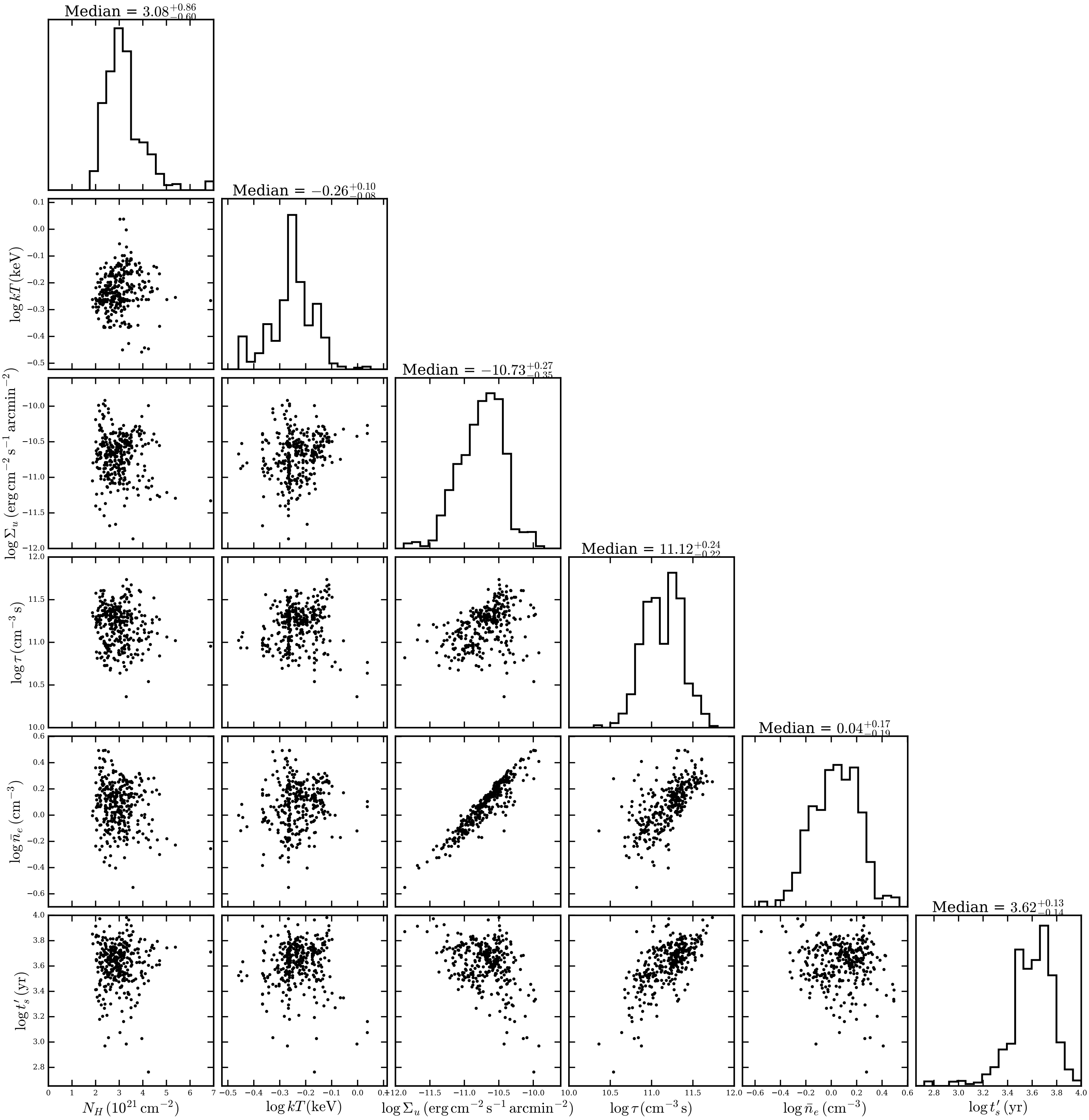

Figure C.3: Correlation plot of the parameters describing foreground absorption and plasma conditions in the individual regions in Fig. C.1. In order to suppress scatter in the resulting distributions, we used the $S/N = 300$ binning here, to reduce the statistical fluctuations in the individual points. The distributions on the diagonal represent flux-weighted histograms of the respective parameter across the remnant, with the median and 68% central interval indicated above.

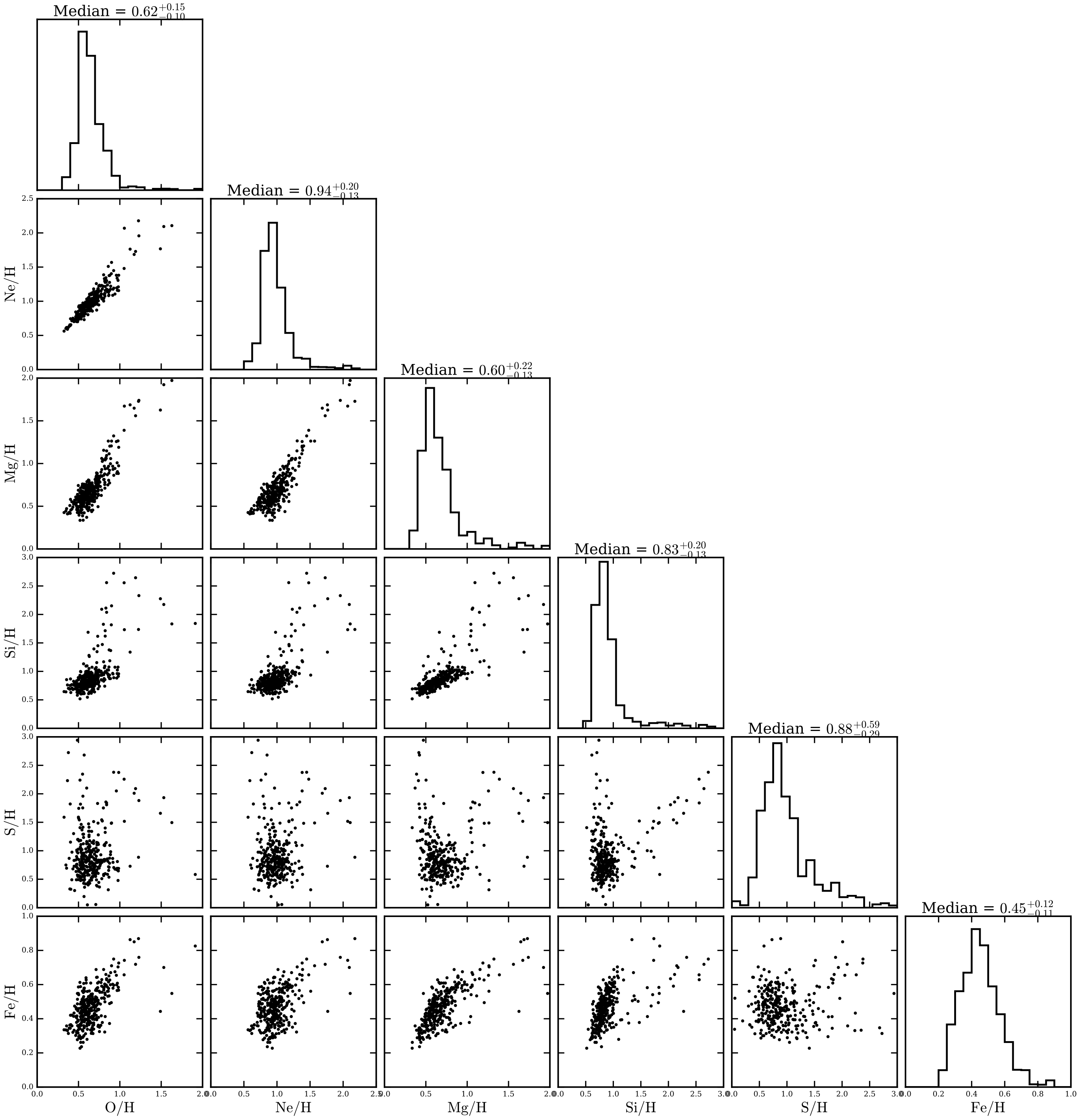

Figure C.4: Same as Fig. C.3, but for the parameters describing elemental abundances.

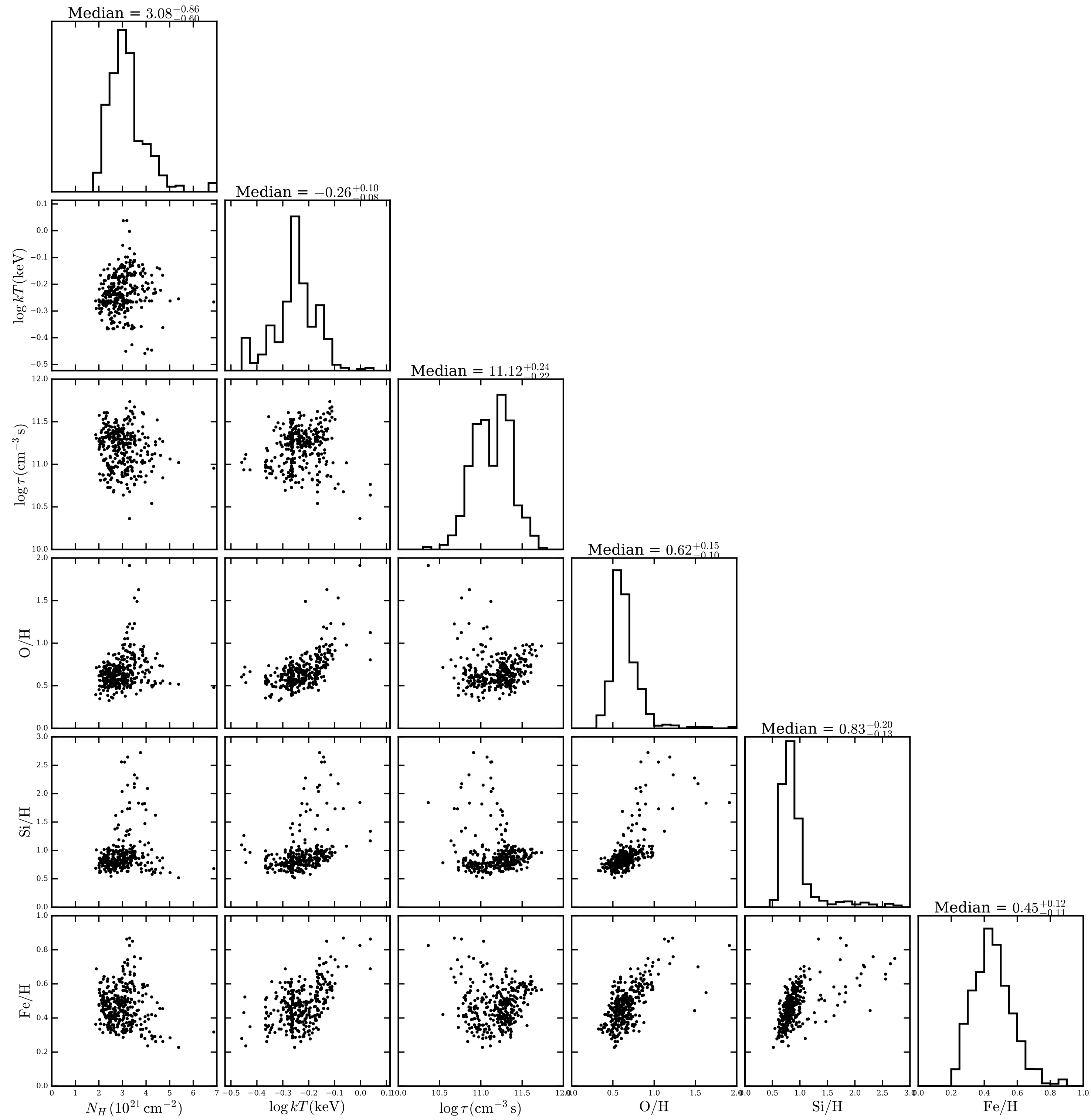

Figure C.5: Same as Fig. C.3, but illustrating the correlation between N_H, kT, and τ and the abundances of the characteristic elements O, Si, and Fe.

Appendix D

Details on modelling the X-ray emission of the Vela SNR

D.1 Application of physical models to the emission of Vela X

Here, we expand on the physically motivated toy models used to characterize the radial profiles of the nonthermal brightness and photon index of Vela X in Sect. 6.4.3. In analogy to Abeysekara et al. (2017), the intensity of nonthermal emission in a pulsar halo at a single electron energy E_e, assuming a constant magnetic field and particle transport via isotropic diffusion, is approximately proportional to

$$F(\theta, E_e) \propto \frac{\exp\left(-\theta^2/\theta_D^2(E_e)\right)}{\theta_D(E_e)\,(\theta + 0.06\,\theta_D(E_e))}, \tag{D.1}$$

where θ describes the angular distance to the pulsar, and θ_D is the "diffusion angle", the characteristic angular size of the emission on the sky at the given energy. In the steady-state regime, it is related to the diffusion constant D and electron lifetime τ following

$$r_D = \theta_D\, d = (4D\tau)^{1/2}\,, \tag{D.2}$$

where d is the distance to the Vela SNR. With the main goal of constraining the size of the PWN at an "effective" X-ray-emitting energy, we thus fitted the observed nonthermal brightness profile F (Fig. 6.12) with a model of the following form

$$F(\theta; A, \theta_D, C) = \frac{A}{\theta_D}\,\frac{\exp\left(-\theta^2/\theta_D^2\right)}{\theta + 0.06\,\theta_D} + C, \tag{D.3}$$

where A is proportional to the integrated PWN flux and C accounts for a possible spatially uniform background. During these fits we included an intrinsic relative scatter s around the radial average profile as a free parameter, so that the model likelihood is given by

$$\log\,\mathcal{L} = -\frac{1}{2}\sum_i \left(\log(2\pi\rho_i^2) + \left(\frac{F_i - F(\theta_i; A, \theta_D, C)}{\rho_i}\right)^2\right), \tag{D.4}$$

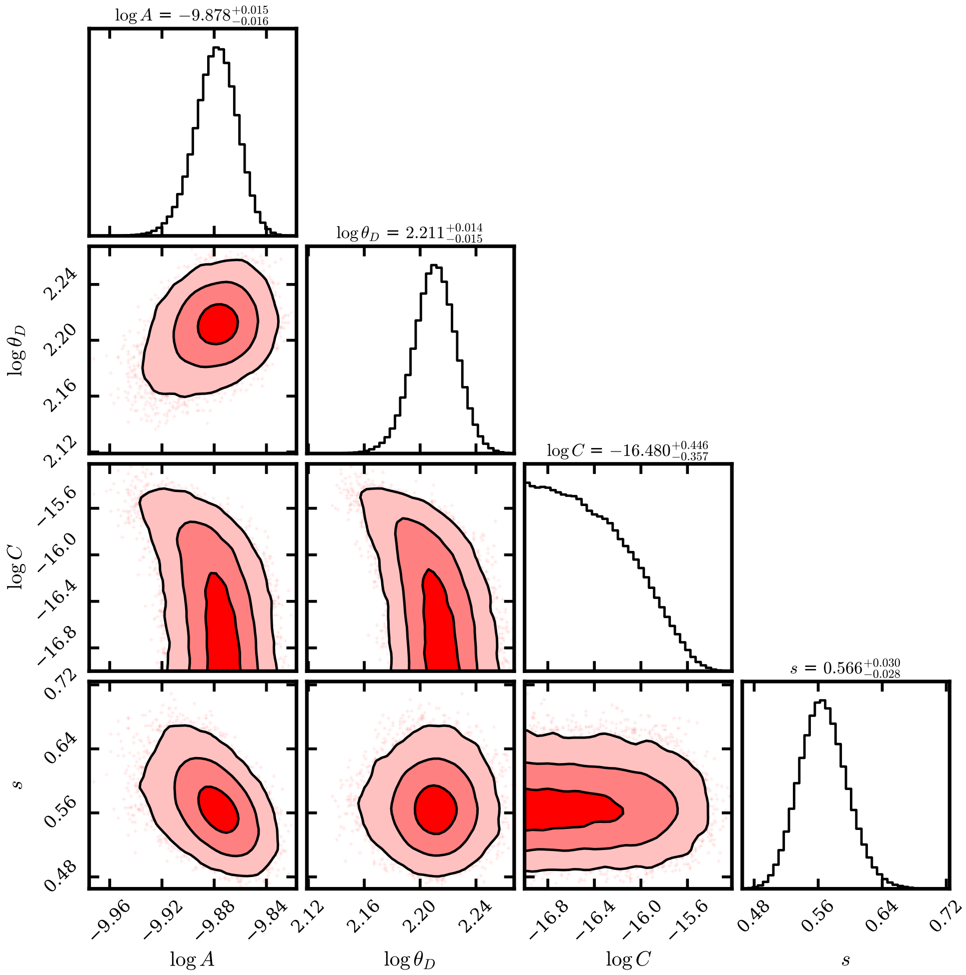

Figure D.1: Corner plot (Foreman-Mackey 2016) displaying the posterior distribution of the parameters of the brightness profile fit shown in Fig. 6.12. The diagonal plots display marginalized posterior distributions of the individual parameters. The contours in the off-diagonal plots correspond to 1σ, 2σ, 3σ constraints on the joint probability distribution of two parameters. The units of the parameters A, C, and θ_D are erg s^{-1} cm^{-2}, erg s^{-1} cm^{-2} arcmin^{-2}, and arcmin, respectively.

where the total error ρ_i of each bin is obtained from its purely statistical error σ_i as

$$\rho_i^2 = \sigma_i^2 + s^2\, F(\theta_i; A, \theta_D, C)^2. \tag{D.5}$$

The constraints on our model parameters were extracted via MCMC sampling with `emcee` (Foreman-Mackey et al. 2013) using logarithmically uniform priors on A, θ_D, and C and uniform priors on s. A total of 100 walkers were run for 5000 burn-in and sampling steps, respectively. This resulted in the posterior distribution displayed in Fig. D.1.

When fitting the radial profile of the photon index Γ, we found it crucial to only include those bins with a significant hard nonthermal contribution, in order to mitigate biases by the prior on Γ, or by potentially spurious power-law components fitting the soft band only. Thus, we

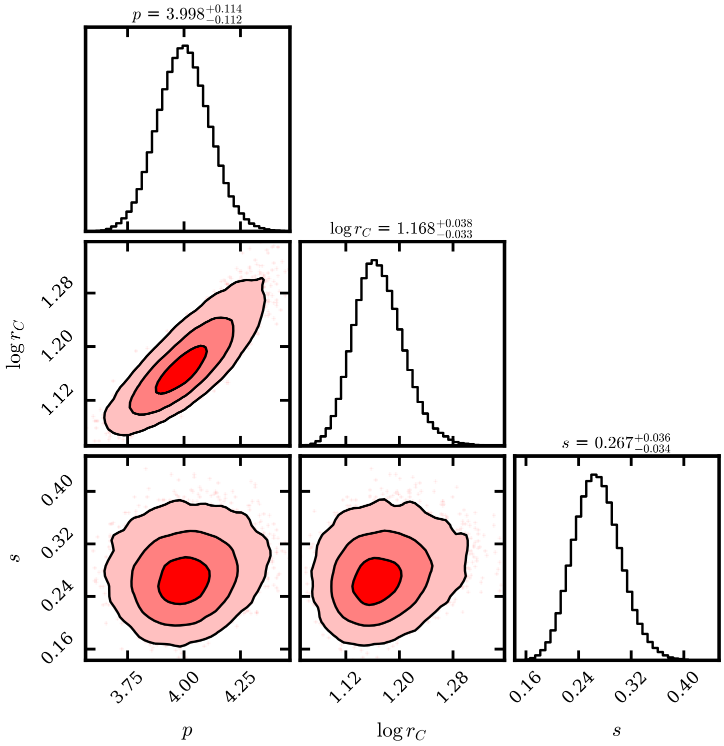

Figure D.2: Same as Fig. D.1, but for the fit of the radial photon index evolution shown in Fig. 6.12. The cooling radius r_C is given in pc, whereas p and s are unitless.

defined the following quantity g, with the target of quantifying the relative contribution of the hard nonthermal component to the spectrum:

$$g = \int_{1.0\,\mathrm{keV}}^{5.0\,\mathrm{keV}} \mathrm{d}E_X\, f(E_X) \frac{f_{\mathrm{NT}}(E_X)}{f(E_X) - f_{\mathrm{NT}}(E_X)} \bigg/ \int_{1.0\,\mathrm{keV}}^{5.0\,\mathrm{keV}} \mathrm{d}E_X\, f(E_X)\,, \tag{D.6}$$

where $f(E_X)$ and $f_{\mathrm{NT}}(E_X)$ describe the total (including backgrounds) and nonthermal forward-folded spectra fitted to the observed X-ray spectrum, respectively. Thus, g is equivalent to a flux-weighted average of the ratio of the nonthermal to all other contributions to the spectrum above 1 keV. For each spectrum, we defined a corresponding statistical weight w via the transformation

$$w = \frac{g}{1+g}, \tag{D.7}$$

which ranges from 0 for no significant hard contribution to 1 for a very dominant one.

We obtained a rough model of the effect of radiative energy loss on the nonthermal photon index in a diffusive PWN with the following approach: We modified the expression for the synchrotron power $P(\nu, r, t)$ at a given frequency ν, radius r, and time t, described in Eqs. 3 to 5 in Tang & Chevalier (2012), to include the effects of inverse Compton emission. In the prescription for energy loss $\mathrm{d}E/\mathrm{d}t = -Q\,E^2$, we achieved this by setting

$$Q = \left(2.37 \times 10^{-15}\, B_{\mu\mathrm{G}}^2 + 1.65 \times 10^{-14}\right) \mathrm{erg}^{-1}\,\mathrm{s}^{-1}, \tag{D.8}$$

where the first term accounts for synchrotron losses, and the second term for inverse Compton scattering on the cosmic microwave background in the Klein-Nishina regime (Aharonian et al. 2006c). From this, we computed the expected power-law index Γ at a given energy as:

$$\Gamma(\theta, \nu, t) = 1 - \frac{\mathrm{d}}{\mathrm{d}\log\nu}\log\left(\int_0^\infty \mathrm{d}z\, P(\nu,\, \sqrt{\theta^2 d^2 + z^2}, t)\right), \tag{D.9}$$

where we have integrated the emission profile along the line of sight, and used the distance to Vela d to convert from physical to angular scales. The degree of radial steepening in this model depends mostly on the quantity $r_C^2 := 4D\tau \propto D/Q$, meaning a characteristic cooling radius can be defined in analogy to Eq. D.2. In order to compare the predicted radial profile to our observations, we fixed the PWN age to $t = 20\,\mathrm{kyr}$, and chose $E_X = h\nu = 1.6\,\mathrm{keV}$ as a uniform effective measurement energy, as we found that this is the typical "pivot" energy, at which the relative uncertainty on the fitted power law component is minimal. The predicted model photon indices $\Gamma(\theta_i)$ were compared to our measurements Γ_i with errors σ_i in each bin, via the likelihood

$$\log\,\mathcal{L}_i = -\frac{1}{2}\left(\log(2\pi\rho_i^2) + \left(\frac{\Gamma_i - \Gamma(\theta_i; p, r_C)}{\rho_i}\right)^2\right), \tag{D.10}$$

$$\rho_i^2 = \sigma_i^2 + s^2. \tag{D.11}$$

This introduces the systematic error scale s, added in quadrature to the statistical errors, as an additional free parameter. Using the weights w_i defined as above, the total model likelihood was computed as

$$\log\,\mathcal{L} = \sum_i w_i \log\,\mathcal{L}_i. \tag{D.12}$$

In combination with uniform priors on p and s and a logarithmically uniform prior on r_C, we constrained the physical model parameters via the same MCMC approach as above. The resulting posterior distribution of the parameters is illustrated in Fig. D.2.

D.2 Characterization of the nonthermal emission of Vela X through spectral fits in the hard band

Here, we reproduce the results discussed in Sect. 6.4.3 regarding the properties of nonthermal X-ray emission of the extended Vela X PWN, using a more "traditional" method: rather than simultaneously modelling the thermal and nonthermal contributions to the broad-band spectra, we restricted our analysis to a relatively simple spectral fit to the hard band, which we defined to begin above the thermal emission lines from the Mg XI triplet, so that it extends over the range 1.43 – 8.50 keV. In order to obtain similar levels of statistics in each region, we extracted spectra from concentric annuli, centered on the pulsar, radially spaced by 30′, and each divided into four sectors of equal size. The same masks as described in Sect. 6.3.2 were applied to the regions, with the additional exclusion of a 1.2° radius around the center of Vela Jr. Despite the weak nature of thermal continuum emission in the employed energy band, we found it necessary to include a

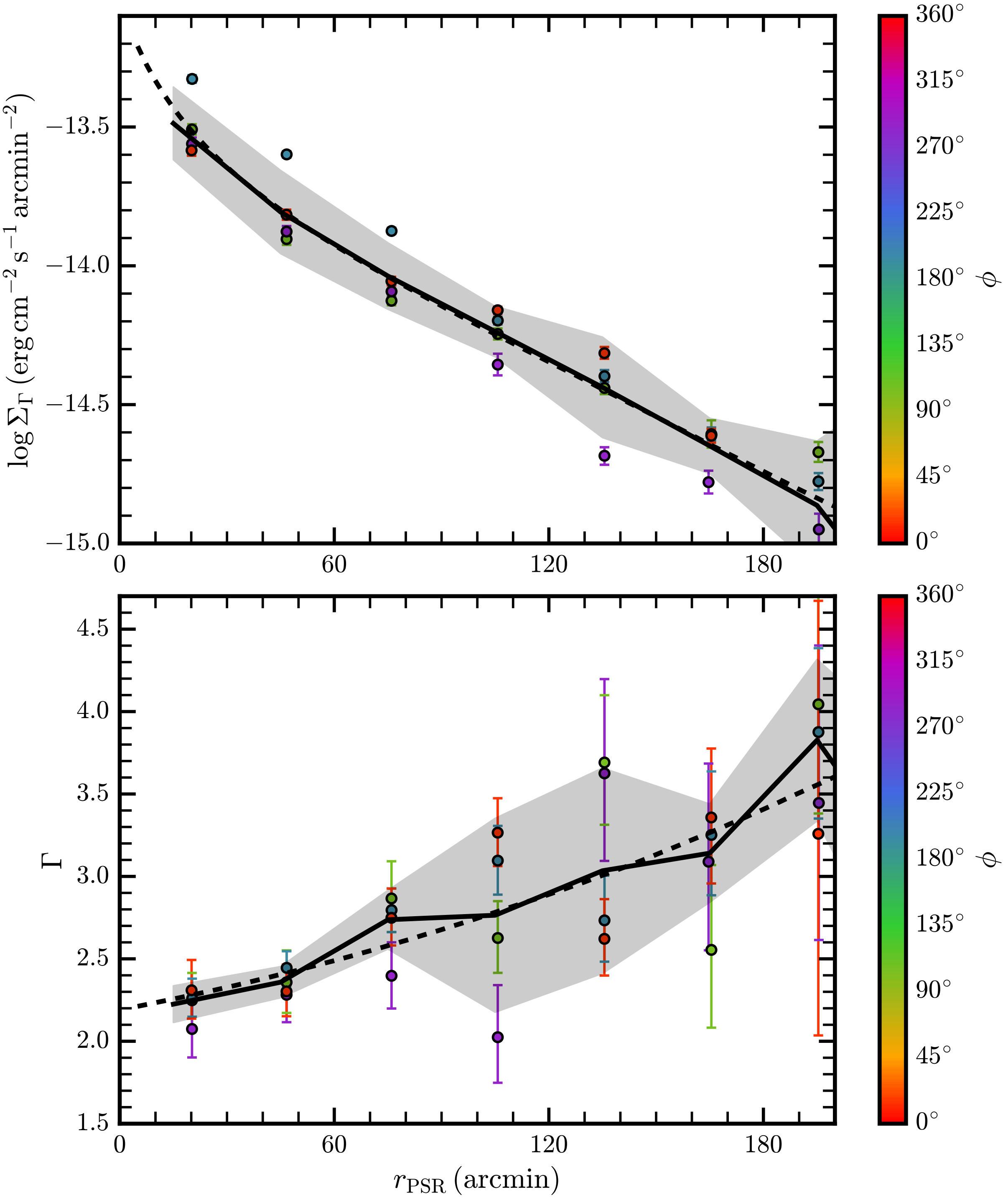

Figure D.3: Same as Fig. 6.12, but displaying the results of spectral fits in the 1.43 – 8.50 keV band, using the approach described here.

Gaussian emission line in our model, to account for Si xiii line emission around 1.85 keV, such that our complete source model was expressed as `powerlaw+gaussian`. Since the soft band was excluded here, a uniform prior on the power-law photon index was found sufficient. The rest of our methodology, including background treatment and parameter estimation, was identical to Sect. 6.3.2.

Figure D.3 illustrates the results of this approach, including radial averages and model fits as in Sect. 6.4.3. The radial brightness profile reproduces the results shown in Fig. 6.12 quite well, regarding both level and slope of the outward-declining flux profile. The characteristic size of the nebula matches our results from the fits of the full energy band, as is indicated by the best-fit diffusion angle of $\theta_D = 167^{+17}_{-25}$ arcmin.

The photon index Γ fitted by our model exhibits a significant radial increase, at a similar average slope as in our fits of the full spectra (Fig. 6.12), which is characterized by the resulting characteristic cooling radius of $r_C = 15.3^{+2.4}_{-1.6}$ pc. This confirms our observation of radiative losses in the extended nebula with a completely independent approach applied to the same data set. It is noteworthy however that, apart from the innermost bin, the fitted power-law slopes are on average lower than in our fits of the full spectral range, as is reflected also by the lower electron spectral index $p = 3.38 \pm 0.14$ in our diffusion model. This is somewhat unexpected, since a possible contaminating high-energy tail of thermal emission from the Vela SNR should lead to an increased inferred spectral slope, as its bremsstrahlung continuum will most likely decrease with energy faster than true nonthermal emission. Thus, while the large extent of the nonthermal emission and the presence of synchrotron and inverse Compton losses affecting the emitting electron population appear quite certain, a quantitative characterization of its energy loss likely requires a significantly deeper coverage in the hard band than available here.

D.3 Spectral parameter maps for the TNT model

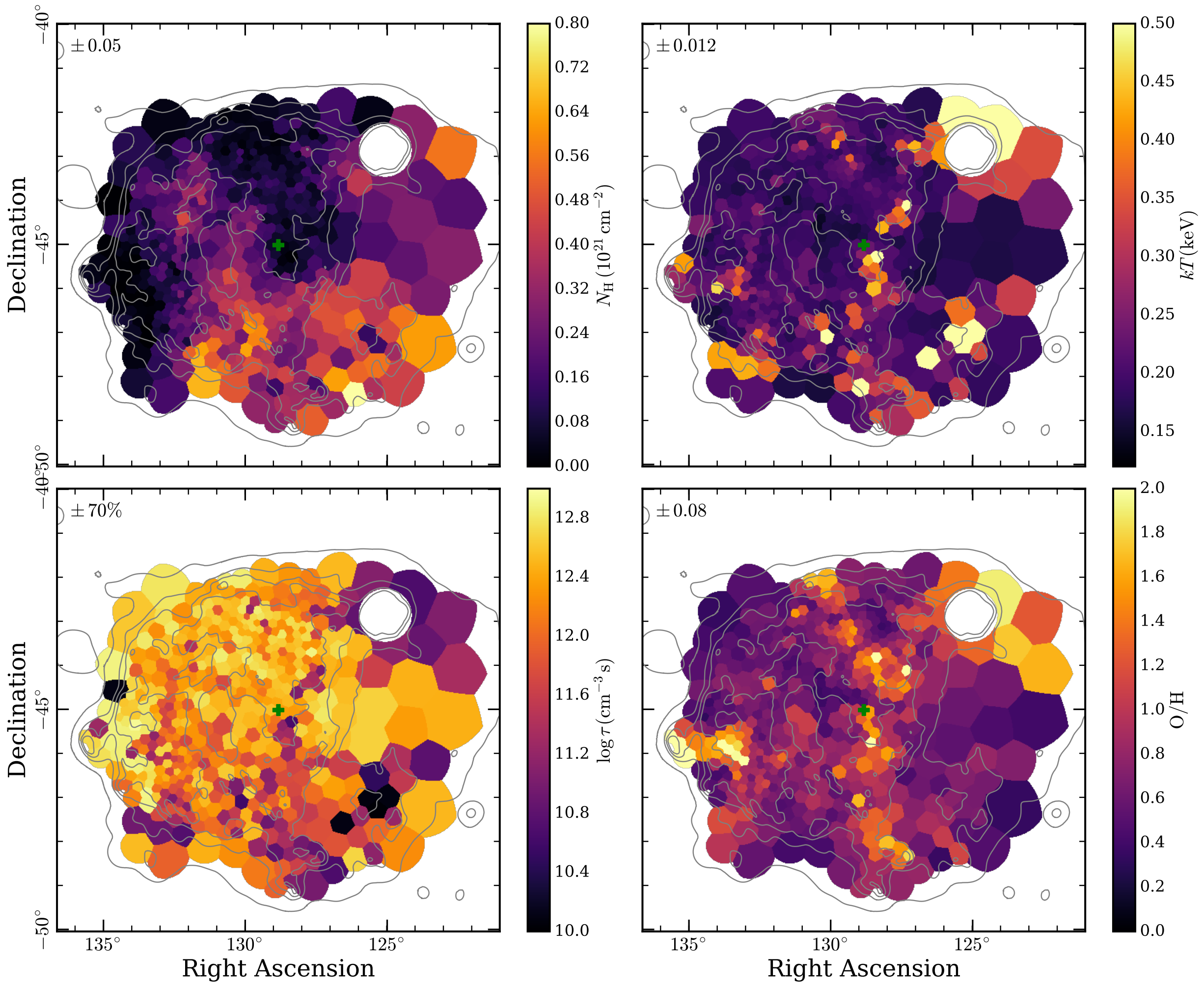

Figure D.4: Same as Fig. 6.5, but for the TNT model, with most panels displaying analogous quantities. However, the *upper right* panel displays the ionization age τ, corresponding to the degree of departure of the thermal plasma from CIE.

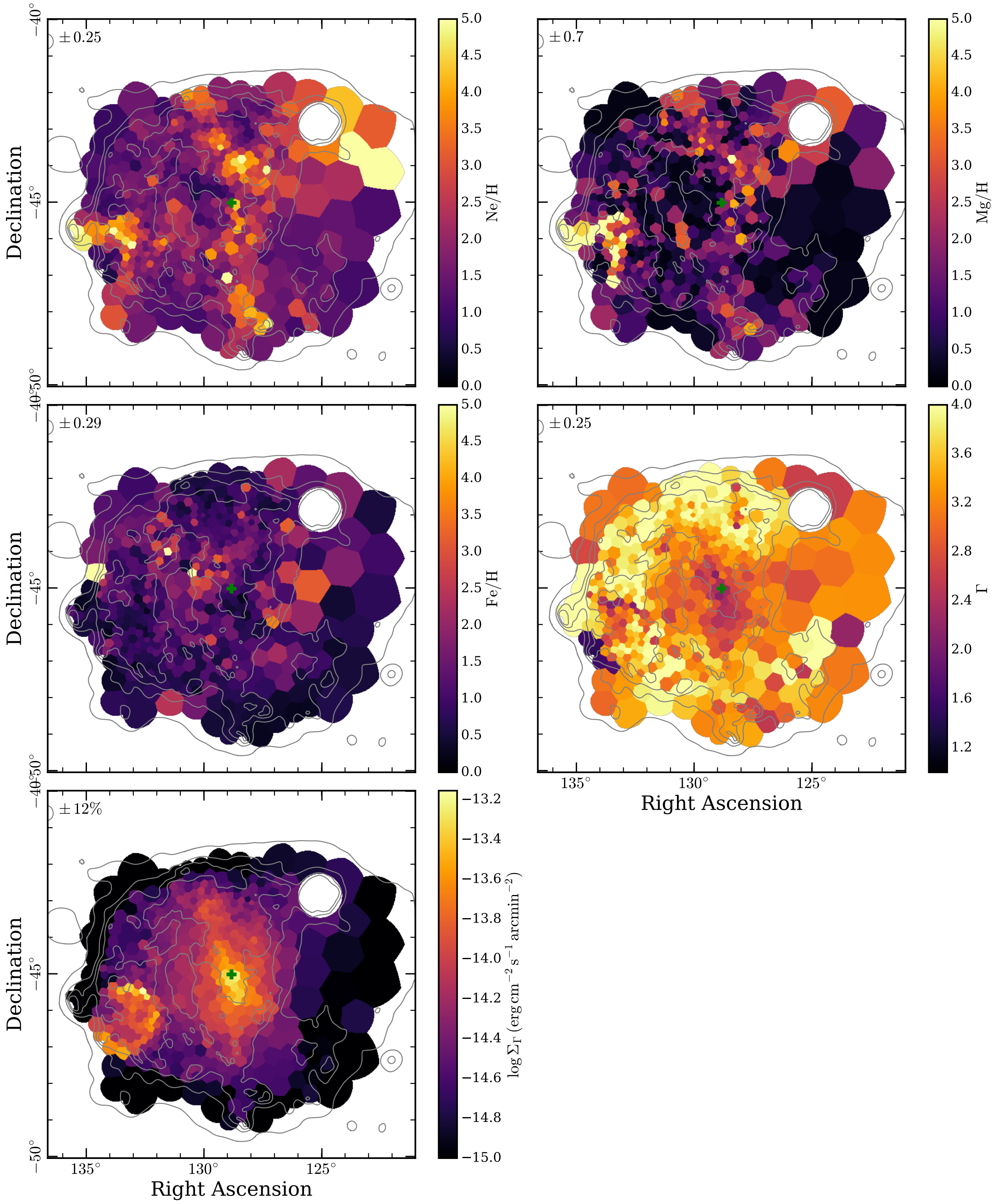

Figure D.4: Continued.

Bibliography

Abbott, B. P., Abbott, R., Abbott, T. D., et al. 2017, Phys. Rev. Lett., 119, 161101

Abdo, A. A., Ackermann, M., Ajello, M., et al. 2010, ApJ, 713, 146

Abdo, A. A., Ajello, M., Allafort, A., et al. 2013, ApJS, 208, 17

Abeysekara, A. U., Albert, A., Alfaro, R., et al. 2017, Science, 358, 911

Abramowski, A., Acero, F., Aharonian, F., et al. 2012, A&A, 548, A38

Accardo, L., Aguilar, M., Aisa, D., et al. 2014, Phys. Rev. Lett., 113, 121101

Acero, F., Katsuda, S., Ballet, J., & Petre, R. 2017, A&A, 597, A106

Aharonian, F., Akhperjanian, A. G., Bazer-Bachi, A. R., et al. 2006a, A&A, 448, L43

Aharonian, F., Akhperjanian, A. G., Bazer-Bachi, A. R., et al. 2006b, A&A, 457, 899

Aharonian, F., Akhperjanian, A. G., Bazer-Bachi, A. R., et al. 2006c, A&A, 460, 365

Aharonian, F. A., Atoyan, A. M., & Kifune, T. 1997, MNRAS, 291, 162

Ahnen, M. L., Ansoldi, S., Antonelli, L. A., et al. 2017, MNRAS, 472, 2956

Alarie, A., Bilodeau, A., & Drissen, L. 2014, MNRAS, 441, 2996

Alford, J. A. J. & Halpern, J. P. 2023, arXiv e-prints, arXiv:2302.05893

Allen, G. E., Chow, K., DeLaney, T., et al. 2015, ApJ, 798, 82

Alvarez, H., Aparici, J., May, J., & Reich, P. 2001, A&A, 372, 636

Anders, F., Khalatyan, A., Queiroz, A. B. A., et al. 2022, A&A, 658, A91

Anderson, M. C., Keohane, J. W., & Rudnick, L. 1995, ApJ, 441, 300

Antoni, T., Apel, W. D., Badea, A. F., et al. 2005, Astroparticle Physics, 24, 1

Arendt, R. G., Dwek, E., Blair, W. P., et al. 2010, ApJ, 725, 585

Arnaud, K. A. 1996, in Astronomical Society of the Pacific Conference Series, Vol. 101, Astronomical Data Analysis Software and Systems V, ed. G. H. Jacoby & J. Barnes, 17

Aschenbach, B. 1993, Advances in Space Research, 13, 45

Aschenbach, B. 1998, Nature, 396, 141

Aschenbach, B. 2015, in XI Multifrequency Behaviour of High Energy Cosmic Sources Workshop (MULTIF15), 21

Aschenbach, B., Egger, R., & Trümper, J. 1995, Nature, 373, 587

Atoyan, A. M. & Aharonian, F. A. 1996, MNRAS, 278, 525

Baade, W. & Zwicky, F. 1934a, Proceedings of the National Academy of Science, 20, 259

Baade, W. & Zwicky, F. 1934b, Proceedings of the National Academy of Science, 20, 254

Baade, W. & Zwicky, F. 1934c, Physical Review, 46, 76

Ballet, J. 2006, Advances in Space Research, 37, 1902

Bamba, A., Anada, T., Dotani, T., et al. 2010, ApJ, 719, L116

Barret, D., Lam Trong, T., den Herder, J.-W., et al. 2018, in Society of Photo-Optical Instrumentation Engineers (SPIE) Conference Series, Vol. 10699, Space Telescopes and Instrumentation 2018: Ultraviolet to Gamma Ray, ed. J.-W. A. den Herder, S. Nikzad, & K. Nakazawa, 106991G

Becker, W. 2009, in Astrophysics and Space Science Library, ed. W. Becker, Vol. 357, 91

Becker, W., Hurley-Walker, N., Weinberger, C., et al. 2021, A&A, 648, A30

Becker, W., Prinz, T., Winkler, P. F., & Petre, R. 2012, ApJ, 755, 141

Becker, W. & Trümper, J. 1997, A&A, 326, 682

Becker, W., Weisskopf, M. C., Tennant, A. F., et al. 2004, ApJ, 615, 908

Bednarek, W. & Bartosik, M. 2003, A&A, 405, 689

Berezhko, E. G., Ksenofontov, L. T., & Völk, H. J. 2003, A&A, 412, L11

Bitran, M., Alvarez, H., Bronfman, L., May, J., & Thaddeus, P. 1997, A&AS, 125, 99

Blondin, J. M., Chevalier, R. A., & Frierson, D. M. 2001, ApJ, 563, 806

Bock, D. C. J., Turtle, A. J., & Green, A. J. 1998, AJ, 116, 1886

Bogdanov, S. 2014, ApJ, 790, 94

Bogovalov, S. V., Chechetkin, V. M., Koldoba, A. V., & Ustyugova, G. V. 2005, MNRAS, 358, 705

Bollig, R., Yadav, N., Kresse, D., et al. 2021, ApJ, 915, 28

Borkowski, K. J., Lyerly, W. J., & Reynolds, S. P. 2001, ApJ, 548, 820

Borkowski, K. J., Miltich, W., & Reynolds, S. P. 2020, ApJ, 905, L19

Borkowski, K. J., Reynolds, S. P., Green, D. A., et al. 2014, ApJ, 790, L18

Borkowski, K. J., Reynolds, S. P., Williams, B. J., & Petre, R. 2018, ApJ, 868, L21

Braun, C., Safi-Harb, S., & Fryer, C. L. 2019, MNRAS, 489, 4444

Bray, J. C. & Eldridge, J. J. 2016, MNRAS, 461, 3747

Breuhaus, M., Reville, B., & Hinton, J. A. 2022, A&A, 660, A8

Brinkman, A. C., Gunsing, C. J. T., Kaastra, J. S., et al. 2000, ApJ, 530, L111

Brunner, H., Liu, T., Lamer, G., et al. 2021, arXiv e-prints, arXiv:2106.14517

Buchner, J. 2016, Statistics and Computing, 26, 383

Buchner, J. 2019, PASP, 131, 108005

Buchner, J. 2021, Journal of Open Source Software, 6, 3001

Burgay, M., D'Amico, N., Possenti, A., et al. 2003, Nature, 426, 531

Camilloni, F., Becker, W., Predehl, P., et al. 2023, submitted to A&A

Canizares, C. R., Davis, J. E., Dewey, D., et al. 2005, PASP, 117, 1144

Cao, Z., Aharonian, F. A., An, Q., et al. 2021, Nature, 594, 33

Cappellari, M. & Copin, Y. 2003, MNRAS, 342, 345

Caraveo, P. A. 1993, ApJ, 415, L111

Caraveo, P. A., De Luca, A., Mignani, R. P., & Bignami, G. F. 2001, ApJ, 561, 930

Cash, W. 1979, ApJ, 228, 939

Cassam-Chenaï, G., Decourchelle, A., Ballet, J., et al. 2004, A&A, 427, 199

Cha, A. N., Sembach, K. R., & Danks, A. C. 1999, ApJ, 515, L25

Chakrabarty, D., Pivovaroff, M. J., Hernquist, L. E., Heyl, J. S., & Narayan, R. 2001, ApJ, 548, 800

Cheng, K. S. 2009, in Astrophysics and Space Science Library, Vol. 357, Astrophysics and Space Science Library, ed. W. Becker, 481

Cheng, K. S., Ho, C., & Ruderman, M. 1986, ApJ, 300, 522

Cherenkov Telescope Array Consortium, Acharya, B. S., Agudo, I., et al. 2019, Science with the Cherenkov Telescope Array (World Scientific Publishing Co. Pte. Ltd.)

Chiotellis, A., Boumis, P., & Spetsieri, Z. T. 2021, MNRAS, 502, 176

Churazov, E. M., Khabibullin, I. I., Bykov, A. M., et al. 2021, MNRAS, 507, 971

Clark, C. J., Breton, R. P., Barr, E. D., et al. 2023a, MNRAS, 519, 5590

Clark, C. J., Kerr, M., Barr, E. D., et al. 2023b, Nature Astronomy

Clark, D. H., Caswell, J. L., & Green, A. J. 1973, Nature, 246, 28

Cox, D. P. & Anderson, P. R. 1982, ApJ, 253, 268

Davis, J. E., Bautz, M. W., Dewey, D., et al. 2012, in Society of Photo-Optical Instrumentation Engineers (SPIE) Conference Series, Vol. 8443, Space Telescopes and Instrumentation 2012: Ultraviolet to Gamma Ray, ed. T. Takahashi, S. S. Murray, & J.-W. A. den Herder, 84431A

de Jager, O. C. & Djannati-Ataï, A. 2009, in Astrophysics and Space Science Library, Vol. 357, Astrophysics and Space Science Library, ed. W. Becker, 451

de Jager, O. C., Slane, P. O., & LaMassa, S. 2008, ApJ, 689, L125

De Looze, I., Barlow, M. J., Swinyard, B. M., et al. 2017, MNRAS, 465, 3309

De Luca, A. 2008, in American Institute of Physics Conference Series, Vol. 983, 40 Years of Pulsars: Millisecond Pulsars, Magnetars and More, ed. C. Bassa, Z. Wang, A. Cumming, & V. M. Kaspi, 311–319

De Luca, A. 2017, in Journal of Physics Conference Series, Vol. 932, Journal of Physics Conference Series, 012006

De Luca, A., Caraveo, P. A., Mereghetti, S., Negroni, M., & Bignami, G. F. 2005, ApJ, 623, 1051

De Luca, A. & Molendi, S. 2004, A&A, 419, 837

DeLaney, T., Rudnick, L., Fesen, R. A., et al. 2004, ApJ, 613, 343

DeLaney, T. & Satterfield, J. 2013, arXiv e-prints, arXiv:1307.3539

den Hartog, P. R., Kuiper, L., Hermsen, W., et al. 2008, A&A, 489, 245

Dennerl, K., Andritschke, R., Bräuninger, H., et al. 2020, in Society of Photo-Optical Instrumentation Engineers (SPIE) Conference Series, Vol. 11444, Society of Photo-Optical Instrumentation Engineers (SPIE) Conference Series, 114444Q

Diehl, S. & Statler, T. S. 2006, MNRAS, 368, 497

Dodson, R., Legge, D., Reynolds, J. E., & McCulloch, P. M. 2003, ApJ, 596, 1137

Dodson, R., Lewis, D., & McCulloch, P. 2007, Ap&SS, 308, 585

Dohm-Palmer, R. C. & Jones, T. W. 1996, ApJ, 471, 279

Doroshenko, V., Suleimanov, V., Pühlhofer, G., & Santangelo, A. 2022, Nature Astronomy, 6, 1444

Drew, J. E., Greimel, R., Irwin, M. J., et al. 2005, MNRAS, 362, 753

Dubner, G., Loiseau, N., Rodríguez-Pascual, P., et al. 2013, A&A, 555, A9

Dubner, G. M., Green, A. J., Goss, W. M., Bock, D. C. J., & Giacani, E. 1998, AJ, 116, 813

Dubner, G. M., Velázquez, P. F., Goss, W. M., & Holdaway, M. A. 2000, AJ, 120, 1933

Duncan, A. R., Stewart, R. T., Haynes, R. F., & Jones, K. L. 1996, MNRAS, 280, 252

Dwek, E., Galliano, F., & Jones, A. P. 2007, ApJ, 662, 927

Efron, B. 1982, The Jackknife, the Bootstrap and other resampling plans (Society for Industrial and Applied Mathematics)

Enoto, T., Kisaka, S., & Shibata, S. 2019, Reports on Progress in Physics, 82, 106901

Espinoza, C. M., Lyne, A. G., & Stappers, B. W. 2017, MNRAS, 466, 147

Fang, K., Bi, X.-J., & Yin, P.-F. 2019, MNRAS, 488, 4074

Ferrand, G. & Safi-Harb, S. 2012, Advances in Space Research, 49, 1313

Fesen, R. A., Hammell, M. C., Morse, J., et al. 2006, ApJ, 645, 283

Foreman-Mackey, D. 2016, The Journal of Open Source Software, 1, 24

Foreman-Mackey, D., Hogg, D. W., Lang, D., & Goodman, J. 2013, PASP, 125, 306

Foster, A. R., Ji, L., Smith, R. K., & Brickhouse, N. S. 2012, ApJ, 756, 128

Frail, D. A., Bietenholz, M. F., & Markwardt, C. B. 1997, ApJ, 475, 224

Frail, D. A., Goss, W. M., & Whiteoak, J. B. Z. 1994, ApJ, 437, 781

Frank, K. A., Burrows, D. N., & Park, S. 2015, ApJ, 810, 113

Freeman, P., Doe, S., & Siemiginowska, A. 2001, in Society of Photo-Optical Instrumentation Engineers (SPIE) Conference Series, Vol. 4477, Astronomical Data Analysis, ed. J.-L. Starck & F. D. Murtagh, 76–87

Freyberg, M., Perinati, E., Pacaud, F., et al. 2020, in Society of Photo-Optical Instrumentation Engineers (SPIE) Conference Series, Vol. 11444, Society of Photo-Optical Instrumentation Engineers (SPIE) Conference Series, 114441O

Freyberg, M. J., Müller, T., Perinati, E., et al. 2022, in Society of Photo-Optical Instrumentation Engineers (SPIE) Conference Series, Vol. 12181, Society of Photo-Optical Instrumentation Engineers (SPIE) Conference Series, ed. J.-W. A. den Herder, S. Nikzad, & K. Nakazawa, 1218155

Fruscione, A., McDowell, J. C., Allen, G. E., et al. 2006, in Society of Photo-Optical Instrumentation Engineers (SPIE) Conference Series, Vol. 6270, Society of Photo-Optical Instrumentation Engineers (SPIE) Conference Series, ed. D. R. Silva & R. E. Doxsey, 62701V

Fryer, C. L., Andrews, S., Even, W., Heger, A., & Safi-Harb, S. 2018, ApJ, 856, 63

Fryer, C. L. & Kusenko, A. 2006, ApJS, 163, 335

Fukui, Y., Moriguchi, Y., Tamura, K., et al. 2003, PASJ, 55, L61

Fukui, Y., Sano, H., Sato, J., et al. 2012, ApJ, 746, 82

Fuller, G. M., Kusenko, A., Mocioiu, I., & Pascoli, S. 2003, Phys. Rev. D, 68, 103002

Gaensler, B. M. & Slane, P. O. 2006, ARA&A, 44, 17

Gaensler, B. M., Tanna, A., Slane, P. O., et al. 2008, ApJ, 680, L37

Gaia Collaboration, Brown, A. G. A., Vallenari, A., et al. 2018, A&A, 616, A1

Gaia Collaboration, Prusti, T., de Bruijne, J. H. J., et al. 2016, A&A, 595, A1

García, F., Suárez, A. E., Miceli, M., et al. 2017, A&A, 604, L5

Garmire, G. P., Bautz, M. W., Ford, P. G., Nousek, J. A., & Ricker, George R., J. 2003, in Society of Photo-Optical Instrumentation Engineers (SPIE) Conference Series, Vol. 4851, X-Ray and Gamma-Ray Telescopes and Instruments for Astronomy., ed. J. E. Trümper & H. D. Tananbaum, 28–44

Gatuzz, E. & Churazov, E. 2018, MNRAS, 474, 696

Gaustad, J. E., McCullough, P. R., Rosing, W., & Van Buren, D. 2001, PASP, 113, 1326

Ghavamian, P. & Williams, B. J. 2016, ApJ, 831, 188

Giacani, E., Smith, M. J. S., Dubner, G., et al. 2009, A&A, 507, 841

Giacani, E. B., Dubner, G. M., Green, A. J., Goss, W. M., & Gaensler, B. M. 2000, AJ, 119, 281

Giacinti, G., Mitchell, A. M. W., López-Coto, R., et al. 2020, A&A, 636, A113

Gil, J., Lyubarsky, Y., & Melikidze, G. I. 2004, ApJ, 600, 872

Gold, T. 1968, Nature, 218, 731

Gomez, H. L., Krause, O., Barlow, M. J., et al. 2012, ApJ, 760, 96

Goodman, J. & Weare, J. 2010, Communications in Applied Mathematics and Computational Science, 5, 65

Gotthelf, E. V. & Halpern, J. P. 2007, ApJ, 664, L35

Gotthelf, E. V. & Halpern, J. P. 2009, ApJ, 695, L35

Gotthelf, E. V. & Halpern, J. P. 2020, ApJ, 900, 159

Gotthelf, E. V., Halpern, J. P., & Alford, J. 2013a, ApJ, 765, 58

Gotthelf, E. V., Halpern, J. P., Allen, B., & Knispel, B. 2013b, ApJ, 773, 141

Gotthelf, E. V., Halpern, J. P., & Seward, F. D. 2005, ApJ, 627, 390

Gotthelf, E. V., Perna, R., & Halpern, J. P. 2010, ApJ, 724, 1316

Gourgouliatos, K. N., Hollerbach, R., & Igoshev, A. P. 2020, MNRAS, 495, 1692

Gratton, L. 1972, Ap&SS, 16, 81

Greco, E., Vink, J., Miceli, M., et al. 2020, A&A, 638, A101

Green, D. A. 2011, Bulletin of the Astronomical Society of India, 39, 289

Green, D. A. 2019, Journal of Astrophysics and Astronomy, 40, 36

Green, D. A. & Stephenson, F. R. 2003, in Supernovae and Gamma-Ray Bursters, ed. K. Weiler, Vol. 598 (Springer Berlin Heidelberg New York), 7–19

Grondin, M. H., Romani, R. W., Lemoine-Goumard, M., et al. 2013, ApJ, 774, 110

Güver, T. & Özel, F. 2009, MNRAS, 400, 2050

H. E. S. S. Collaboration, Abdalla, H., Abramowski, A., et al. 2018a, A&A, 612, A6

H. E. S. S. Collaboration, Abdalla, H., Abramowski, A., et al. 2018b, A&A, 612, A1

H. E. S. S. Collaboration, Abdalla, H., Aharonian, F., et al. 2019, A&A, 627, A100

H. E. S. S. Collaboration, Abramowski, A., Aharonian, F., et al. 2015, A&A, 575, A81

Haberl, F. 2007, Ap&SS, 308, 181

Halpern, J. P. & Gotthelf, E. V. 2010a, ApJ, 709, 436

Halpern, J. P. & Gotthelf, E. V. 2010b, ApJ, 710, 941

Halpern, J. P. & Gotthelf, E. V. 2015, ApJ, 812, 61

Harding, A. K. 2013, Frontiers of Physics, 8, 679

Harding, A. K. & Muslimov, A. G. 2002, ApJ, 568, 862

Harrison, F. A., Craig, W. W., Christensen, F. E., et al. 2013, ApJ, 770, 103

Hartmann, D. H., Predehl, P., Greiner, J., et al. 1997, Nucl. Phys. A, 621, 83

Heger, A., Fryer, C. L., Woosley, S. E., Langer, N., & Hartmann, D. H. 2003, ApJ, 591, 288

Helder, E. A., Vink, J., Bykov, A. M., et al. 2012, Space Sci. Rev., 173, 369

Helfand, D. J., Collins, B. F., & Gotthelf, E. V. 2003, ApJ, 582, 783

Helfand, D. J., Gotthelf, E. V., & Halpern, J. P. 2001, ApJ, 556, 380

Herbst, W. & Assousa, G. E. 1977, ApJ, 217, 473

Hessels, J. W. T., Ransom, S. M., Stairs, I. H., et al. 2006, Science, 311, 1901

Hewish, A., Bell, S. J., Pilkington, J. D. H., Scott, P. F., & Collins, R. A. 1968, Nature, 217, 709

Hinton, J. A., Funk, S., Parsons, R. D., & Ohm, S. 2011, ApJ, 743, L7

Ho, W. C. G. 2011, MNRAS, 414, 2567

Hobbs, G., Lorimer, D. R., Lyne, A. G., & Kramer, M. 2005, MNRAS, 360, 974

Hoeflich, P. 2017, in Handbook of Supernovae, ed. A. W. Alsabti & P. Murdin (Springer Cham), 1151

Holland-Ashford, T., Lopez, L. A., Auchettl, K., Temim, T., & Ramirez-Ruiz, E. 2017, ApJ, 844, 84

Hopkins, P. F., Quataert, E., & Murray, N. 2012, MNRAS, 421, 3522

Hughes, J. P. 2000, ApJ, 545, L53

Hughes, J. P., Hayashi, I., Helfand, D., et al. 1995, ApJ, 444, L81

Hui, C. Y. & Becker, W. 2006a, A&A, 457, L33

Hui, C. Y. & Becker, W. 2006b, A&A, 454, 543

Hulse, R. A. & Taylor, J. H. 1975, ApJ, 195, L51

Hurley-Walker, N., Callingham, J. R., Hancock, P. J., et al. 2017, MNRAS, 464, 1146

Hurley-Walker, N., Hancock, P. J., Franzen, T. M. O., et al. 2019, PASA, 36, e047

Hwang, U., Flanagan, K. A., & Petre, R. 2005, ApJ, 635, 355

Hwang, U. & Laming, J. M. 2012, ApJ, 746, 130

Hwang, U., Laming, J. M., Badenes, C., et al. 2004, ApJ, 615, L117

Hwang, U., Petre, R., & Flanagan, K. A. 2008, ApJ, 676, 378

Iwamoto, K., Brachwitz, F., Nomoto, K., et al. 1999, ApJS, 125, 439

Janka, H.-T. 2012, Annual Review of Nuclear and Particle Science, 62, 407

Janka, H.-T. 2017a, in Handbook of Supernovae, ed. A. W. Alsabti & P. Murdin (Springer Cham), 1095

Janka, H.-T. 2017b, ApJ, 837, 84

Joye, W. A. & Mandel, E. 2003, in Astronomical Society of the Pacific Conference Series, Vol. 295, Astronomical Data Analysis Software and Systems XII, ed. H. E. Payne, R. I. Jedrzejewski, & R. N. Hook, 489

Kahn, S. M. 2005, High-Energy Spectroscopic Astrophysics Saas Fee Advanced Course 30. Lecture Notes 2000. Swiss Society for Astrophysics and Astronomy, 1st edn., Saas-Fee Advanced Course, 30 (Berlin, Heidelberg: Springer Berlin Heidelberg)

Kaplan, D. L. 2008, in American Institute of Physics Conference Series, Vol. 983, 40 Years of Pulsars: Millisecond Pulsars, Magnetars and More, ed. C. Bassa, Z. Wang, A. Cumming, & V. M. Kaspi, 331–339

Kargaltsev, O., Cerutti, B., Lyubarsky, Y., & Striani, E. 2015, Space Sci. Rev., 191, 391

Kargaltsev, O. & Pavlov, G. G. 2008, in American Institute of Physics Conference Series, Vol. 983, 40 Years of Pulsars: Millisecond Pulsars, Magnetars and More, ed. C. Bassa, Z. Wang, A. Cumming, & V. M. Kaspi, 171–185

Kargaltsev, O., Rangelov, B., & Pavlov, G. 2013, in The Universe Evolution: Astrophysical and Nuclear Aspects. Edited by I. Strakovsky and L. Blokhintsev. Nova Science Publishers (Nova Science Publishers), 359–406

Kaspi, V. M. 2010, Proceedings of the National Academy of Science, 107, 7147

Katsuda, S. 2010, X-Ray Time Variability of an Ejecta Filament in Puppis A, Chandra Proposal

Katsuda, S., Acero, F., Tominaga, N., et al. 2015, ApJ, 814, 29

Katsuda, S., Hwang, U., Petre, R., et al. 2010, ApJ, 714, 1725

Katsuda, S., Mori, K., Petre, R., et al. 2011, PASJ, 63, S827

Katsuda, S., Mori, K., Tsunemi, H., et al. 2008, ApJ, 678, 297

Katsuda, S., Morii, M., Janka, H.-T., et al. 2018, ApJ, 856, 18

Katsuda, S., Ohira, Y., Mori, K., et al. 2013, ApJ, 768, 182

Katsuda, S. & Tsunemi, H. 2005, PASJ, 57, 621

Katsuda, S. & Tsunemi, H. 2006, ApJ, 642, 917

Katsuda, S., Tsunemi, H., Mori, K., et al. 2012, ApJ, 756, 49

Khokhlov, A. M. 1991, A&A, 245, 114

Kilpatrick, C. D., Bieging, J. H., & Rieke, G. H. 2016, ApJ, 816, 1

Kirk, J. G., Lyubarsky, Y., & Petri, J. 2009, in Astrophysics and Space Science Library, Vol. 357, Astrophysics and Space Science Library, ed. W. Becker, 421

Klein, R. I., McKee, C. F., & Colella, P. 1994, ApJ, 420, 213

Komissarov, S. S. & Lyubarsky, Y. E. 2004, MNRAS, 349, 779

Koyama, K., Petre, R., Gotthelf, E. V., et al. 1995, Nature, 378, 255

Kraft, R., Markevitch, M., Kilbourne, C., et al. 2022, arXiv e-prints, arXiv:2211.09827

Kramer, M., Stairs, I. H., Manchester, R. N., et al. 2021, Physical Review X, 11, 041050

Krivonos, R., Arefiev, V., Lapshov, I., et al. 2021, arXiv e-prints, arXiv:2107.05586

Kuntz, K. D. & Snowden, S. L. 2008, A&A, 478, 575

Kuriki, M., Sano, H., Kuno, N., et al. 2018, ApJ, 864, 161

Lagage, P. O., Claret, A., Ballet, J., et al. 1996, A&A, 315, L273

Lai, D. 2001, in Physics of Neutron Star Interiors, ed. D. Blaschke, N. K. Glendenning, & A. Sedrakian, Vol. 578 (Springer Berlin Heidelberg), 424

Lallement, R. 2004, A&A, 422, 391

Lallement, R., Babusiaux, C., Vergely, J. L., et al. 2019, A&A, 625, A135

Lallement, R., Vergely, J. L., Babusiaux, C., & Cox, N. L. J. 2022, A&A, 661, A147

LaMassa, S. M., Slane, P. O., & de Jager, O. C. 2008, ApJ, 689, L121

Lattimer, J. M., Pethick, C. J., Prakash, M., & Haensel, P. 1991, Phys. Rev. Lett., 66, 2701

Lazendic, J. S., Slane, P. O., Hughes, J. P., Chen, Y., & Dame, T. M. 2005, ApJ, 618, 733

Levenson, N. A., Graham, J. R., Keller, L. D., & Richter, M. J. 1998, ApJS, 118, 541

Li, B., Zhang, Y., Liu, T., Liu, R.-Y., & Wang, X.-Y. 2022, MNRAS, 513, 2884

Li, J., Kastner, J. H., Prigozhin, G. Y., et al. 2004, ApJ, 610, 1204

Li, W., Chornock, R., Leaman, J., et al. 2011a, MNRAS, 412, 1473

Li, W., Leaman, J., Chornock, R., et al. 2011b, MNRAS, 412, 1441

Locatelli, N., Ponti, G., & Bianchi, S. 2022, A&A, 659, A118

Lopez, L. A., Grefenstette, B. W., Reynolds, S. P., et al. 2015, ApJ, 814, 132

Lovchinsky, I., Slane, P., Gaensler, B. M., et al. 2011, ApJ, 731, 70

Lu, F. J. & Aschenbach, B. 2000, A&A, 362, 1083

Luna, G. J. M., Smith, M. J. S., Dubner, G., Giacani, E., & Castelletti, G. 2016, A&A, 590, A70

Lundqvist, P. & Fransson, C. 1996, ApJ, 464, 924

Luo, J., Ng, C. Y., Ho, W. C. G., et al. 2015, ApJ, 808, 130

Lyne, A. G., Pritchard, R. S., Graham-Smith, F., & Camilo, F. 1996, Nature, 381, 497

MacFadyen, A. I. & Woosley, S. E. 1999, ApJ, 524, 262

Madsen, K., Hickox, R., Bachetti, M., et al. 2019, Bulletin of the AAS, 51, https://baas.aas.org/pub/2020n7i166

Maggi, P. & Acero, F. 2017, A&A, 597, A65

Maguire, K. 2017, in Handbook of Supernovae, ed. A. W. Alsabti & P. Murdin (Springer Cham), 293

Maitra, C., Haberl, F., Sasaki, M., et al. 2022, A&A, 661, A30

Manchester, R. N., Hobbs, G. B., Teoh, A., & Hobbs, M. 2005, AJ, 129, 1993

Marcaide, J. M., Martí-Vidal, I., Alberdi, A., et al. 2009, A&A, 505, 927

Marelli, M., De Luca, A., & Caraveo, P. A. 2011, ApJ, 733, 82

Markwardt, C. B. & Ögelman, H. 1995, Nature, 375, 40

Marshall, H. L., Tennant, A., Grant, C. E., et al. 2004, in Society of Photo-Optical Instrumentation Engineers (SPIE) Conference Series, Vol. 5165, X-Ray and Gamma-Ray Instrumentation for Astronomy XIII, ed. K. A. Flanagan & O. H. W. Siegmund, 497–508

Mattana, F., Götz, D., Terrier, R., et al. 2011, ApJ, 743, L18

Maxted, N., Burton, M., Braiding, C., et al. 2018, MNRAS, 474, 662

Mayer, M., Becker, W., Patnaude, D., Winkler, P. F., & Kraft, R. 2020, ApJ, 899, 138

Mayer, M. G. F. & Becker, W. 2021, A&A, 651, A40

Mayer, M. G. F., Becker, W., Predehl, P., & Sasaki, M. 2023, to be submitted to A&A

Mayer, M. G. F., Becker, W., Predehl, P., Sasaki, M., & Freyberg, M. 2022, A&A, 661, A31

McClure-Griffiths, N. M., Green, A. J., Dickey, J. M., et al. 2001, ApJ, 551, 394

McCray, R. & Fransson, C. 2016, ARA&A, 54, 19

Meidinger, N., Andritschke, R., Dennerl, K., et al. 2020, in Society of Photo-Optical Instrumentation Engineers (SPIE) Conference Series, Vol. 11444, Society of Photo-Optical Instrumentation Engineers (SPIE) Conference Series, 114440

Merloni, A., Predehl, P., Becker, W., et al. 2012, arXiv e-prints, arXiv:1209.3114

Miceli, M., Bocchino, F., & Reale, F. 2008, ApJ, 676, 1064

Miceli, M., Orlando, S., Reale, F., Bocchino, F., & Peres, G. 2013, MNRAS, 430, 2864

Mignani, R. P., de Luca, A., Zaggia, S., et al. 2007, A&A, 473, 883

Mignani, R. P., De Luca, A., Zharikov, S., et al. 2019, MNRAS, 486, 5716

Mignani, R. P., Zaggia, S., de Luca, A., et al. 2008, A&A, 484, 457

Minter, A. H. & Spangler, S. R. 1996, ApJ, 458, 194

Miyata, E., Tsunemi, H., Aschenbach, B., & Mori, K. 2001, ApJ, 559, L45

Moriguchi, Y., Yamaguchi, N., Onishi, T., Mizuno, A., & Fukui, Y. 2001, PASJ, 53, 1025

Morrison, R. & McCammon, D. 1983, ApJ, 270, 119

Mróz, P., Udalski, A., Skowron, D. M., et al. 2019, ApJ, 870, L10

Murray, S. S., Austin, G. K., Chappell, J. H., et al. 2000, in Society of Photo-Optical Instrumentation

Engineers (SPIE) Conference Series, Vol. 4012, X-Ray Optics, Instruments, and Missions III, ed. J. E. Trümper & B. Aschenbach, 68–80

Mushotzky, R. 2018, in Society of Photo-Optical Instrumentation Engineers (SPIE) Conference Series, Vol. 10699, Space Telescopes and Instrumentation 2018: Ultraviolet to Gamma Ray, ed. J.-W. A. den Herder, S. Nikzad, & K. Nakazawa, 1069929

Nandra, K., Barret, D., Barcons, X., et al. 2013, arXiv e-prints, arXiv:1306.2307

Nomoto, K., Kobayashi, C., & Tominaga, N. 2013, ARA&A, 51, 457

Nugent, R. L. 1998, PASP, 110, 831

Ochelkov, I. P. & Usov, V. V. 1980, Ap&SS, 69, 439

Okuno, T., Tanaka, T., Uchida, H., Matsumura, H., & Tsuru, T. G. 2018, PASJ, 70, 77

Oppenheimer, J. R. & Volkoff, G. M. 1939, Physical Review, 55, 374

Ostriker, J. P. & Gunn, J. E. 1969, ApJ, 157, 1395

Ozawa, M., Koyama, K., Yamaguchi, H., Masai, K., & Tamagawa, T. 2009, ApJ, 706, L71

Pacini, F. 1967, Nature, 216, 567

Page, D. 2009, in Astrophysics and Space Science Library, Vol. 357, Astrophysics and Space Science Library, ed. W. Becker, 247

Page, D., Lattimer, J. M., Prakash, M., & Steiner, A. W. 2004, ApJS, 155, 623

Patnaude, D. J. & Fesen, R. A. 2007, AJ, 133, 147

Patnaude, D. J. & Fesen, R. A. 2009, ApJ, 697, 535

Pavlinsky, M., Tkachenko, A., Levin, V., et al. 2021, A&A, 650, A42

Pavlov, G. G., Teter, M. A., Kargaltsev, O., & Sanwal, D. 2003, ApJ, 591, 1157

Perlmutter, S., Aldering, G., Goldhaber, G., et al. 1999, ApJ, 517, 565

Petre, R., Becker, C. M., & Winkler, P. F. 1996, ApJ, 465, L43

Petre, R., Kriss, G. A., Winkler, P. F., & Canizares, C. R. 1982, ApJ, 258, 22

Pétri, J. 2019, MNRAS, 485, 4573

Pfeffermann, E. & Aschenbach, B. 1996, in Roentgenstrahlung from the Universe, ed. H. U. Zimmermann, J. Trümper, & H. Yorke, 267–268

Picquenot, A., Acero, F., Bobin, J., et al. 2019, A&A, 627, A139

Picquenot, A., Acero, F., Holland-Ashford, T., Lopez, L. A., & Bobin, J. 2021, A&A, 646, A82

Pillepich, A., Porciani, C., & Reiprich, T. H. 2012, MNRAS, 422, 44

Predehl, P., Andritschke, R., Arefiev, V., et al. 2021, A&A, 647, A1

Predehl, P. & Schmitt, J. H. M. M. 1995, A&A, 293, 889

Principe, G., Mitchell, A. M. W., Caroff, S., et al. 2020, A&A, 640, A76

Queiroz, A. B. A., Anders, F., Santiago, B. X., et al. 2018, MNRAS, 476, 2556

Rakowski, C. E., Ghavamian, P., & Hughes, J. P. 2003, ApJ, 590, 846

Ranasinghe, S. & Leahy, D. A. 2018, AJ, 155, 204

Rauscher, T., Heger, A., Hoffman, R. D., & Woosley, S. E. 2002, ApJ, 576, 323

Reynolds, S. P. 2008, ARA&A, 46, 89

Reynolds, S. P. 2017, in Handbook of Supernovae, ed. A. W. Alsabti & P. Murdin (Springer Cham), 1981

Reynolds, S. P., Borkowski, K. J., Hwang, U., et al. 2006, ApJ, 652, L45

Reynoso, E. M., Cichowolski, S., & Walsh, A. J. 2017, MNRAS, 464, 3029

Reynoso, E. M., Green, A. J., Johnston, S., et al. 2003, MNRAS, 345, 671

Rho, J. & Petre, R. 1998, ApJ, 503, L167

Rho, J., Reach, W. T., Tappe, A., et al. 2009, ApJ, 700, 579

Riess, A. G., Filippenko, A. V., Challis, P., et al. 1998, AJ, 116, 1009

Rishbeth, H. 1958, Australian Journal of Physics, 11, 550

Robert, C. P. & Wraith, D. 2009, in American Institute of Physics Conference Series, Vol. 1193, Bayesian Inference and Maximum Entropy Methods in Science and Engineering: The 29th International Workshop on Bayesian Inference and Maximum Entropy Methods in Science and Engineering, ed. P. M. Goggans & C.-Y. Chan, 251–262

Roberts, M. S. E. 2013, in Neutron Stars and Pulsars: Challenges and Opportunities after 80 years, ed. J. van Leeuwen, Vol. 291, 127–132

Roger, R. S., Milne, D. K., Kesteven, M. J., Wellington, K. J., & Haynes, R. F. 1988, ApJ, 332, 940

Sánchez-Ayaso, E., Combi, J. A., Albacete Colombo, J. F., et al. 2012, Ap&SS, 337, 573

Sapienza, V., Miceli, M., Bamba, A., et al. 2022, ApJ, 935, 152

Sapienza, V., Miceli, M., Peres, G., et al. 2021, A&A, 649, A56

Sasaki, M., Mäkelä, M. M., Klochkov, D., Santangelo, A., & Suleimanov, V. 2018, MNRAS, 479, 3033

Scheck, L., Kifonidis, K., Janka, H. T., & Müller, E. 2006, A&A, 457, 963

Sedov, L. I. 1959, Similarity and Dimensional Methods in Mechanics (Academic Press)

Shabaltas, N. & Lai, D. 2012, ApJ, 748, 148

Shibata, S., Watanabe, E., Yatsu, Y., Enoto, T., & Bamba, A. 2016, ApJ, 833, 59

Shklovskii, I. S. 1970, Soviet Ast., 13, 562

Shklovsky, J. S. 1968, Supernovae (John Wiley & Sons Ltd)

Siegel, J., Dwarkadas, V. V., Frank, K., Burrows, D. N., & Panfichi, A. 2020, Astronomische Nachrichten, 341, 163

Silich, E. M., Kaaret, P., Zajczyk, A., et al. 2020, AJ, 160, 20

Slane, P., Helfand, D. J., van der Swaluw, E., & Murray, S. S. 2004, ApJ, 616, 403

Slane, P., Lovchinsky, I., Kolb, C., et al. 2018, ApJ, 865, 86

Slavin, J. D., Dwek, E., & Jones, A. P. 2015, ApJ, 803, 7

Smith, R. K., Brickhouse, N. S., Liedahl, D. A., & Raymond, J. C. 2001, ApJ, 556, L91

Smith, R. K., Foster, A. R., Edgar, R. J., & Brickhouse, N. S. 2014, ApJ, 787, 77

Stephenson, F. R. & Green, D. A. 2009, Journal for the History of Astronomy, 40, 31

Strüder, L., Briel, U., Dennerl, K., et al. 2001, A&A, 365, L18

Sukhbold, T., Ertl, T., Woosley, S. E., Brown, J. M., & Janka, H. T. 2016, ApJ, 821, 38

Suleimanov, V., Potekhin, A. Y., & Werner, K. 2009, A&A, 500, 891

Sun, M., Seward, F. D., Smith, R. K., & Slane, P. O. 2004, ApJ, 605, 742

Sunyaev, R., Arefiev, V., Babyshkin, V., et al. 2021, arXiv e-prints, arXiv:2104.13267

Sushch, I., Hnatyk, B., & Neronov, A. 2011, A&A, 525, A154

Tanaka, T., Uchida, H., Sano, H., & Tsuru, T. G. 2020, ApJ, 900, L5

Tananbaum, H. 1999, IAU Circ., 7246, 1

Tang, X. & Chevalier, R. A. 2012, ApJ, 752, 83

Tappe, A., Rho, J., & Reach, W. T. 2006, ApJ, 653, 267

Taylor, G. 1950, Proceedings of the Royal Society of London Series A, 201, 159

Taylor, J. H. & Weisberg, J. M. 1982, ApJ, 253, 908

Thorstensen, J. R., Fesen, R. A., & van den Bergh, S. 2001, AJ, 122, 297

Tian, W. W., Leahy, D. A., Haverkorn, M., & Jiang, B. 2008, ApJ, 679, L85

Tian, W. W., Zhu, H., Zhang, M. F., et al. 2019, PASP, 131, 114301

Tibaldo, L., Zanin, R., Faggioli, G., et al. 2018, A&A, 617, A78

Tominaga, N., Umeda, H., & Nomoto, K. 2007, ApJ, 660, 516

Trimble, V. 1968, AJ, 73, 535

Truelove, J. K. & McKee, C. F. 1999, ApJS, 120, 299

Trümper, J. 1982, Advances in Space Research, 2, 241

Tsuchioka, T., Uchiyama, Y., Higurashi, R., et al. 2021, ApJ, 912, 131

Tsuji, N. & Uchiyama, Y. 2016, PASJ, 68, 108

Tsuji, N., Uchiyama, Y., Khangulyan, D., & Aharonian, F. 2021, ApJ, 907, 117

Tsunemi, H., Miyata, E., & Aschenbach, B. 1999, PASJ, 51, 711

Turner, M. J. L., Abbey, A., Arnaud, M., et al. 2001, A&A, 365, L27

Uchida, H., Koyama, K., Yamaguchi, H., et al. 2012, PASJ, 64, 141

Uchiyama, H., Matsumoto, H., Tsuru, T. G., Koyama, K., & Bamba, A. 2009, PASJ, 61, S189

Verbunt, F., Igoshev, A., & Cator, E. 2017, A&A, 608, A57

Vergely, J. L., Lallement, R., & Cox, N. L. J. 2022, A&A, 664, A174

Vink, J. 2008, ApJ, 689, 231

Vink, J. 2020, Physics and Evolution of Supernova Remnants (Springer Nature Switzerland)

Vink, J. 2022, arXiv e-prints, arXiv:2212.10677

Vink, J., Bloemen, H., Kaastra, J. S., & Bleeker, J. A. M. 1998, A&A, 339, 201

Vink, J. & Laming, J. M. 2003, ApJ, 584, 758

Vink, J., Prokhorov, D., Ferrazzoli, R., et al. 2022, ApJ, 938, 40

Wanajo, S., Nomoto, K., Janka, H. T., Kitaura, F. S., & Müller, B. 2009, ApJ, 695, 208

Wang, Z. R., Qu, Q. Y., & Chen, Y. 1997, A&A, 318, L59

Weber, F., Negreiros, R., & Rosenfield, P. 2009, in Astrophysics and Space Science Library, Vol. 357, Astrophysics and Space Science Library, ed. W. Becker, 213

Weisskopf, M. C., Ramsey, B., O'Dell, S., et al. 2016, in Society of Photo-Optical Instrumentation Engineers (SPIE) Conference Series, Vol. 9905, Space Telescopes and Instrumentation 2016: Ultraviolet to Gamma Ray, ed. J.-W. A. den Herder, T. Takahashi, & M. Bautz, 990517

Williams, B. J., Borkowski, K. J., Ghavamian, P., et al. 2013, ApJ, 770, 129

Williams, B. J., Hewitt, J. W., Petre, R., & Temim, T. 2018, ApJ, 855, 118

Willmore, A. P., Eyles, C. J., Skinner, G. K., & Watt, M. P. 1992, MNRAS, 254, 139

Wilms, J., Allen, A., & McCray, R. 2000, ApJ, 542, 914

Winkler, P. F. & Kirshner, R. P. 1985, ApJ, 299, 981

Winkler, P. F. & Petre, R. 2007, ApJ, 670, 635

Winkler, P. F., Tuttle, J. H., Kirshner, R. P., & Irwin, M. J. 1988, in IAU Colloq. 101: Supernova Remnants and the Interstellar Medium, ed. R. S. Roger & T. L. Landecker, 65

Woermann, B., Gaylard, M. J., & Otrupcek, R. 2000, MNRAS, 317, 421

Wongwathanarat, A., Janka, H. T., & Müller, E. 2013, A&A, 552, A126

Wongwathanarat, A., Janka, H.-T., Müller, E., Pllumbi, E., & Wanajo, S. 2017, ApJ, 842, 13

Woods, P. M. & Thompson, C. 2006, in Compact stellar X-ray sources, Vol. 39 (Cambridge University Press), 547–586

Woosley, S. E., Heger, A., & Weaver, T. A. 2002, Reviews of Modern Physics, 74, 1015

Woosley, S. E. & Weaver, T. A. 1995, ApJS, 101, 181

Wulf, D., Eckart, M. E., Galeazzi, M., et al. 2019, ApJ, 884, 120

Xi, L., Gaetz, T. J., Plucinsky, P. P., Hughes, J. P., & Patnaude, D. J. 2019, ApJ, 874, 14

Xie, F., Di Marco, A., La Monaca, F., et al. 2022, Nature, 612, 658

Xin, Y.-L., Guo, X.-L., Liao, N.-H., et al. 2017, ApJ, 843, 90

XRISM Science Team. 2020, arXiv e-prints, arXiv:2003.04962

Yakovlev, D. G. & Pethick, C. J. 2004, ARA&A, 42, 169

Yamaguchi, H., Badenes, C., Petre, R., et al. 2014, ApJ, 785, L27

Yamaguchi, H. & Katsuda, S. 2009, ApJ, 696, 1548

Yamaguchi, H., Ozawa, M., Koyama, K., et al. 2009, ApJ, 705, L6

Zacharias, N., Finch, C., Girard, T., et al. 2010, AJ, 139, 2184

Zavlin, V. E., Pavlov, G. G., Sanwal, D., & Trümper, J. 2000, ApJ, 540, L25

Zhou, P., Chen, Y., Safi-Harb, S., et al. 2016, ApJ, 831, 192

Zhu, H., Slane, P., Raymond, J., & Tian, W. W. 2019, ApJ, 882, 135

Zhu, H., Tian, W., Li, A., & Zhang, M. 2017, MNRAS, 471, 3494

Acknowledgments

Many people have contributed, directly or indirectly, to my 3.5-year scientific journey described in this thesis, and I am deeply grateful to all of them:

First and foremost, I would like to thank my supervisor, Prof. Werner Becker, for his valuable scientific mentorship during the past years, and for the many personal advices he gave me in our numerous meetings. It has been (and still is) a joy to work together! I would like to express my gratitude to Manami Sasaki, Michael Freyberg, and Bruno Leibundgut for participating in the long-term planning of my PhD, as members of my thesis committee. I am further grateful to Manami Sasaki, Peter Predehl, Michael Freyberg, Dan Patnaude, Frank Winkler, and, of course, Werner Becker, for our fruitful scientific collaboration on several research projects, which led to the publications presented in this thesis.

I would like to thank Kirpal Nandra, as well as Andrea Merloni and Peter Predehl, for allowing me to be part of a stimulating scientific environment in the MPE high-energy group, and within the eROSITA consortium, respectively. The PhD environment at MPE would not be the same without the patient support of Birgit Boller and Annette Hilbert on the administrative side, and Harald Baumgartner on any IT-problem, many thanks to them! Further, I would like to thank the entire eROSITA-DE team, especially Miriam Ramos, Ian Stewart, Alain Gueguen, Konrad Dennerl, and Jeremy Sanders, for their assistance on any bug or artifact I encountered.

The last years would have been incredibly dull without my (present and former) PhD colleagues. Many thanks to Adam, Alena, Catarina, Damien, David, Emre, Francesco, Iuliia, Isabelle, Julien, Linda, Mike, Riccardo, Ricky, Robert, Sophia, Soumya, Yru, and Zsofi for many entertaining lunch breaks and Friday beers! A special shoutout to my office mate Adam, for being my first contact person on many technical problems, to Francesco, for numerous discussions on our favorite objects, and to Riccardo, for passing on his recent experience on how this whole PhD submission thing works! I would like to further thank Christian, Emmanuel, Johan, Johannes, Matthias, Toska, and Vittorio, for many fun discussions during lunch and coffee breaks, during which I often learned lots, especially about clusters and cosmology.

I would like to express my gratitude to my friends outside MPE for their companionship over the years, whether they have suffered with me through our TUM bachelor's degree, lived with me in the best house of Studentenstadt, or sweated with me on the squash court. Finally, I would like to thank my loving family – my parents Rita and Erwin, and my sister Anna – without whose support over the last 28 years I would never have made it this far. Ihr seid die Besten! Last, but certainly not least, I want to thank my wonderful girlfriend Edmée, for being there, for listening, for laughing with me. TQM!